EXTREME PRECIPITATION EVENTS: SPATIO-TEMPORAL CONNECTIONS, FORECASTING, GENERATION, IMPACT ANALYSIS, VULNERABILITY AND RISK ASSESSMENT

EDITED BY: Sanjeev Kumar Jha, Hannes Müller-Thomy and Jaepil Cho
PUBLISHED IN: Frontiers in Earth Science

frontiers Research Topics

ISSN 1664-8714
ISBN 978-2-83251-898-4
DOI 10.3389/978-2-83251-898-4

About Frontiers

Frontiers is more than just an open-access publisher of scholarly articles: it is a pioneering approach to the world of academia, radically improving the way scholarly research is managed. The grand vision of Frontiers is a world where all people have an equal opportunity to seek, share and generate knowledge. Frontiers provides immediate and permanent online open access to all its publications, but this alone is not enough to realize our grand goals.

Frontiers Journal Series

The Frontiers Journal Series is a multi-tier and interdisciplinary set of open-access, online journals, promising a paradigm shift from the current review, selection and dissemination processes in academic publishing. All Frontiers journals are driven by researchers for researchers; therefore, they constitute a service to the scholarly community. At the same time, the Frontiers Journal Series operates on a revolutionary invention, the tiered publishing system, initially addressing specific communities of scholars, and gradually climbing up to broader public understanding, thus serving the interests of the lay society, too.

Dedication to Quality

Each Frontiers article is a landmark of the highest quality, thanks to genuinely collaborative interactions between authors and review editors, who include some of the world's best academicians. Research must be certified by peers before entering a stream of knowledge that may eventually reach the public - and shape society; therefore, Frontiers only applies the most rigorous and unbiased reviews.
Frontiers revolutionizes research publishing by freely delivering the most outstanding research, evaluated with no bias from both the academic and social point of view. By applying the most advanced information technologies, Frontiers is catapulting scholarly publishing into a new generation.

What are Frontiers Research Topics?

Frontiers Research Topics are very popular trademarks of the Frontiers Journals Series: they are collections of at least ten articles, all centered on a particular subject. With their unique mix of varied contributions from Original Research to Review Articles, Frontiers Research Topics unify the most influential researchers, the latest key findings and historical advances in a hot research area! Find out more on how to host your own Frontiers Research Topic or contribute to one as an author by contacting the Frontiers Editorial Office: frontiersin.org/about/contact

EXTREME PRECIPITATION EVENTS: SPATIO-TEMPORAL CONNECTIONS, FORECASTING, GENERATION, IMPACT ANALYSIS, VULNERABILITY AND RISK ASSESSMENT

Topic Editors:
Sanjeev Kumar Jha, Indian Institute of Science Education and Research, Bhopal, India
Hannes Müller-Thomy, Technische Universitat Braunschweig, Germany
Jaepil Cho, Integrated Watershed Management Institute, South Korea

Citation: Jha, S. K., Müller-Thomy, H., Cho, J., eds. (2023). Extreme Precipitation Events: Spatio-Temporal Connections, Forecasting, Generation, Impact Analysis, Vulnerability and Risk Assessment. Lausanne: Frontiers Media SA.
doi: 10.3389/978-2-83251-898-4

Table of Contents

frontiers | Frontiers in Earth Science

TYPE Editorial
PUBLISHED 21 October 2022
DOI 10.3389/feart.2022.1050027

OPEN ACCESS

EDITED AND REVIEWED BY
Wouter Buytaert,
Imperial College London,
United Kingdom

*CORRESPONDENCE
Sanjeev Kumar Jha,
sanjeevj@iiserb.ac.in

†Previous work by this author has been published under the name Hannes Müller

SPECIALTY SECTION
This article was submitted to Hydrosphere, a section of the journal Frontiers in Earth Science

RECEIVED 21 September 2022
ACCEPTED 06 October 2022
PUBLISHED 21 October 2022

CITATION
Jha SK, Müller-Thomy H and Cho J (2022), Editorial: Extreme precipitation events: Spatio-temporal connections, forecasting, generation, impact analysis, vulnerability and risk assessment. *Front. Earth Sci.* 10:1050027. doi: 10.3389/feart.2022.1050027

Editorial: Extreme precipitation events: Spatio-temporal connections, forecasting, generation, impact analysis, vulnerability and risk assessment

Sanjeev Kumar Jha[1]*, Hannes Müller-Thomy [2†] and Jaepil Cho[3]

[1]Indian Institute of Science Education and Research, Bhopal, India, [2]Department of Hydrology and River Basin Management, Leichtweiß-Institute for Hydraulic Engineering and Water Resources, TU Braunschweig, Braunschweig, Germany, [3]Integrated Watershed Management Institute Seoul, Seoul, South Korea

KEYWORDS

precipitation extremes, atmospheric circulation, numerical weather prediction, southwest vortex, urban flooding

Editorial on the Research Topic
Extreme precipitation events: Spatio-temporal connections, forecasting, generation, impact analysis, vulnerability and risk assessment

Extreme precipitation events (EPEs) have shown a significant increase in magnitude and frequency in various parts of the world. In the past decades, extreme precipitation has caused wide-ranging impacts on various sectors of society, leading to increased risk and vulnerability while decreasing resilience and adaptive capacity. Unfortunately, the frequency of EPEs is increasing and is estimated to even intensify in the future (Ali and Mishra, 2018). During the past decades, studies have used various approaches to understand the mechanism behind the formation of EPEs, their spatio-temporal characteristics, their impacts on various sectors of society, and ways to prevent adverse impacts (Singhal and Jha, 2021). On this vital research topic of Extreme Precipitation Events, 12 articles were accepted and published. Out of these, nine articles can be categorized under two broader themes: 1) understanding of mechanisms behind the generation of EPEs, and 2) challenges in urban and semi-urban areas due to increasing influences of anthropogenic activities on EPEs. The remaining three articles focus on various other aspects of extreme precipitation events.

Some parts of the world have been more prone to increased incidence of EPEs than others. One such region is Central Asia, where atmospheric processes and weather systems of different scales have significantly influenced the nature of extreme precipitation events. In this regard, Chen et al. assessed the mechanism behind the

unusually long duration of the rainy period in China during the 2020 Meiyu precipitation front. They found a meridional migration of the 2020 abnormal Meiyu rain belt from June to July, leading to extreme rainfall. Further, to better comprehend the characteristics of heavy precipitation occurring due to the Autumn Continuous Rain (ACR) in China, Yang et al. analysed daily precipitation data to assess the spatiotemporal variations in ACR and constructed a conceptual model including the factors such as sea surface temperature, arctic vortex and sub-tropical high. In another study, Wu et al. studied the dual-core southwest vortex and how the circulation process is affected by the release of latent heat and the local topography. They concluded that the release of latent heat significantly influenced the formation of the Dual-Core Southwest Vortex (DCSWV). At the same time, the topography of the Tibetan Plateau affected the location and duration of DCSWV in China. Similarly, Cao et al. explained the reasons behind increased EPEs over Central China by studying the moisture supply and water vapor transport throughout Europe and Asia. The authors used decomposed water vapor flux divergence with the Barnes filter and synoptic methods in different precipitation events. Further, Dong et al. investigated the characteristics and formation of two banded strong radar echoes over the Sichuan Basin of China in view of two vortices coupling.

Urban hydrology is an important research subject, especially in the context of climate change and extreme precipitation. Due to expanding anthropogenic influences, the world is witnessing abrupt changes in the hydrological and meteorological characteristics in various urban and semi-urban regions of the world. In this context, Singhal et al. developed a framework for generating impact-based forecasts by analysing extreme precipitation forecasts of 2017–2020 and estimated the impacts on various sectors of population, economy, and agriculture in a semi-urban region of northern India. Alongside this, the authors suggested corresponding preventive actions to mitigate the severity of the impacts. In another study, Davis et al. addressed the growing issue of urban flooding in India by setting up a Weather Research and Forecasting (WRF) model for the city of Bangalore, India. The authors used the hydrologic model PCSWMM to provide high-resolution flood forecasts using 6-h rainfall forecasts before the event. Further, Tian et al. used weather radars to obtain high-resolution and high-accuracy quantitative precipitation estimates. The authors used a deep neural network to improve the accuracy of rainfall estimates by including meteorological and geographical factors as covariates. Liu et al. analysed the rainfall trend taking into account the change in the categories of rain gauges from rural to urban. The authors applied an approach of dynamic sampling to find that the total annual and maximum daily precipitation has increased in the past 30 years in the Yangtze River basin of China.

Along with the aforementioned contributions, this Research Topic includes other significant articles focussing on various aspects of extreme precipitation, risk assessment and mitigation. For instance, Li et al. performed 32 experiments to find out the effect of porous fiber material (PFM) on the surface runoff and peak flow under the conditions of extreme precipitation in the Huaibei basin of China. Results show that PFM increases the water holding capacity and, as a result, reduces the risk of droughts and floods in the region. Tiwari et al. reviewed how the land surface plays a role in tropical cyclone intensification. The article reports about the advancement in the improved prediction of the north Indian Ocean Tropical Cyclone due to advancement in the atmospheric model and air-sea coupled models, and satellite-era. Wang et al. reproduced supercell precipitation by assimilating lightning data into the WRF model. The authors show that the assimilation of lightning data enhances the range and intensity of precipitation forecasts and compensates for the unavailability of observation data during supercell growth.

Author contributions

SKJ wrote the first draft of the Editorial. HM-T and JC proofread it.

Conflict of interest

The authors declare that the research was conducted in the absence of any commercial or financial relationships that could be construed as a potential conflict of interest.

Publisher's note

References

Ali, H., and Mishra, V. (2018). Increase in subdaily precipitation extremes in India under 1.5 and 2.0°C warming worlds. *Geophys. Res. Lett.* 45, 6972–6982. doi:10.1029/2018GL078689

Singhal, A., and Jha, S. K. (2021). An application of multiple-point statistics downscaling approach over North-West Himalayas in avalanche-prone areas. *Int. J. Climatol.* 42, 1902–1921. doi:10.1002/joc.7342

frontiers in Earth Science

ORIGINAL RESEARCH
published: 31 January 2022
doi: 10.3389/feart.2021.799104

Subseasonal Variation of 2020 Meiyu Rainfall With Extremely Long Duration Over the Yangtze–Huaihe River Basin in China

Shengjie Chen[1,2,3], *Zhiming Kang*[1,3]*, *Mei Liu*[1,3]*, *Runqing Lv*[1], *Jing Ma*[4] and *Jinhai He*[4]

[1]Jiangsu Meteorological Observatory, Nanjing, China, [2]School of Atmospheric Sciences, Nanjing University, Nanjing, China, [3]Key Laboratory of Transportation Meteorology, China Meteorological Administration Transportation, Nanjing, China, [4]Key Laboratory of Meteorological Disaster, Ministry of Education (KLME)/Joint International Research Laboratory of Climate and Environment Change (ILCEC)/Collaborative Innovation Center on Forecast and Evaluation of Meteorological Disasters (CIC–FEMD), Nanjing University of Information Science and Technology, Nanjing, China

OPEN ACCESS

Edited by:
Sanjeev Kumar Jha,
Indian Institute of Science Education and Research, India

Reviewed by:
Jasti S Chowdary,
Indian Institute of Tropical Meteorology (IITM), India
Huopo Chen,
Institute of Atmospheric Physics (CAS), China

***Correspondence:**
Mei Liu
lmkerry@163.com
Zhiming Kang
kangzm@cma.gov.cn

Specialty section:
This article was submitted to Atmospheric Science, a section of the journal Frontiers in Earth Science

Received: 21 October 2021
Accepted: 20 December 2021
Published: 31 January 2022

Citation:
Chen S, Kang Z, Liu M, Lv R, Ma J and He J (2022) Subseasonal Variation of 2020 Meiyu Rainfall With Extremely Long Duration Over the Yangtze–Huaihe River Basin in China. Front. Earth Sci. 9:799104. doi: 10.3389/feart.2021.799104

An observed fact is proposed that the 2020 record-breaking Meiyu over the Yangtze–Huaihe River Basin (YHRB) is characteristic of significant subseasonal variation. The anomalously enhanced rainfall experiences a southward retreat from the northern YHRB in June to the southern YHRB in July. The meridional shift of abnormal rainbelt is closely related to the different anomalous Meiyu front circulations. The first stage features a warm Meiyu front with an extremely strong northward transport of warm-and-wet air, whereas a cold front forms with a convergence between the strong northeasterlies and southwesterlies in July. Another significant subseasonal variation of the 2020 Meiyu is that the Meiyu rainfall evolves in a periodic quasi-biweekly oscillation (QBWO). On the scale of the QBWO, the cold air activities over East Asia contribute significantly to Meiyu; each intense southward invasion of cold air corresponds well to the enhancement of Meiyu rainfall. However, the location of the western Pacific subtropical high, the subtropical East Asia summer monsoon (SEASM), and the intensity of the East Asia subtropical westerly jet exhibit opposite QBWO characteristics in June and July. For an increasing (decreasing) of Meiyu rainfall, the western Pacific subtropical high marches northward (retreats southward), the subtropical East Asia summer monsoon weakens (strengthens), and the East Asia subtropical westerly jet accelerates (decelerates) in June. The opposite holds true in July. Further analyses reveal that the filtered cyclone over Northeast China benefiting the southward intrusion of cold air is associated with the eastward propagation of a wave train over the mid-high latitudes in June, whereas it arises from both the westward propagation of a wave train over the mid-high latitudes and the northward propagation of cyclonic circulation from the tropics in July.

Keywords: 2020 long-persisting meiyu, subseasonal variation, quasi-biweekly oscillation, East Asia summer monsoon systems, wave trains over the mid-high latitudes

INTRODUCTION

Severe rainstorms and devastating floods severely hit southern Japan and the Yangtze–Huaihe River Basins (YHRB) in China in the early summer of 2020. The rainy period is the well-known Meiyu in China (also called Baiu in Japan and Changma in Korea), a typical episode in the progression of East Asia summer monsoon (EASM) (Tao and Chen, 1987; Yihui and Chan, 2005). Climatologically, Meiyu starts in mid-June and ends in mid-July. However, by the monitoring of China National Climate Center, 2020 Meiyu persists from June 1 to August 1 with an earlier onset and a later ending. The long duration and the accumulated Meiyu precipitation around the Yangtze River Basins both broke the record since 1961 (Gan, 2020; Ding et al., 2021). The anomalously enhanced Meiyu precipitation causes great losses of life and property.

In each summer, the date when Meiyu begins/ends and the Meiyu precipitation amount are the most important issue concerned by meteorological, hydrological, and other services in such regions affected by Meiyu as China, Japan, and Korea. The mechanism and prediction of Meiyu have always been the hot topic (Ninomiya, 1984; Chen and Yu, 1988; Kodama, 1992; Webster et al., 1998; Huaqiang and Yongfu, 1999; Yihui and Chan, 2005; Huang et al., 2011; Yim et al., 2015; Li et al., 2019; Ding et al., 2020).

The onset/ending time, evolution, rainfall amount, and extreme weather events during the Meiyu season are all intimately related to the circulation components of the EASM regime. Generally, the Meiyu rainbelt is anchored over the region of the zonally elongated quasi-stationary Meiyu front. The front is formed by the interaction between the warm-and-wet air masses from the tropics and the cold-and-dry air masses from the mid-high latitudes. To the south of the Meiyu front, southwesterly winds along the northwestern flank of the western Pacific subtropical high (WPSH) supply abundant warm-and-wet air to the Meiyu regions. The northerly winds in the western part of low troughs or in the eastern high ridges over the mid-high latitudes at the middle and lower troposphere reinforce cold-and-dry air masses intruding into the north of Meiyu front. The persistent confrontation of warm and cold air contributes to the quasi-stationary rain belt (Ninomiya, 1984; Ding, 1992; Ninomiya, 2000; Ding, 2007). Variations of location and intensity of any circulation component of the EASM system could exert influence directly on Meiyu rainfall. For example, the northward shift of the East Asia subtropical westerly jet (EASWJ) to the north of the South Asian High in the upper troposphere and the poleward jump of the ridge line of the WPSH in a zonal shape would modulate the onset and ending time of Meiyu season (Tao and Chen, 1987; Yimin and Guoxiong, 2004; Zhang and Guo, 2005; Zhang et al., 2006; Xuan et al., 2011; Liu et al., 2019). The EASWJ anchors the Meiyu rainband by steering transient eddies and creating convective instability and adiabatic updrafts (Sampe and Xie, 2010; Chowdary et al., 2019; Chowdary et al., 2021). Zhou and Yu (2005) found that southwestward extension of the WPSH and southward shift of the EASWJ over East Asia are favorable for enhanced rainfall over the middle and lower reaches of the Yangtze River, whereas the northwestward extension of WPSH and an eastward shift of the EASWJ contribute to anomalous water vapor transports to the Huaihe River valley. In addition to warm and moist air affected by circulation in the tropics and subtropics, cold air intrusion associated with the mid-high latitude systems plays an equally important role in Meiyu rainfall (Lau et al., 2000; Ding et al., 2020). He et al. (2007) proposed that the frequent activity of the Northeast Cold Vortex, a crucial circulation system over Northeast Asia, is advantageous to more Meiyu rainfall.

The forecast of Meiyu and the associated rainstorms remains challenging, as Meiyu precipitation is characterized by multi-time scale variabilities. Significant differences exist in the influencing factors and the physical mechanisms of Meiyu's interdecadal, interannual, and subseasonal variations (Ding et al., 2020). On the interannual timescales, external forcings such as El Niño–Southern Oscillation over the Pacific Ocean (Wang et al., 2009; Kosaka et al., 2011; Zhu et al., 2013), sea surface temperature (SST) anomalies over the Indian Ocean (IO) (Xie et al., 2009; Wang et al., 2013; Xie et al., 2016; Takaya et al., 2020), Kuroshio SST front over the East China Sea (Xu et al., 2018), and snow cover of the Tibetan Plateau (Ge et al., 2014; Liu et al., 2014) have been verified to exert important impacts on Meiyu rainfall through air–sea coupling or atmospheric teleconnections. The Madden–Julian Oscillation (Li et al., 2018), the intraseasonal oscillation of EASM (Chen et al., 2015; Li et al., 2015; Song et al., 2016), and the summer North Atlantic Oscillation (NAO) (Bollasina and Messori, 2018; Liu et al., 2020) are viewed as crucial factors that modulate the subseasonal variation of Meiyu rainfall.

Considering the significant extremity, 2020 Meiyu is termed as a super Meiyu. The characteristics and the mechanisms of 2020 super Meiyu have been extensively examined (Li et al., 2020; Liu and Ding, 2020; Takaya et al., 2020; Ding et al., 2021; Guo et al., 2021; Niu et al., 2021; Pan et al., 2021; Zhou et al., 2021). Quite a few studies attribute the excessive rainfall over YHRB to an enlarged WPSH caused by the persistent warming over the tropical IO (Takaya et al., 2020; Ding et al., 2021; Niu et al., 2021; Pan et al., 2021), as well as a La Niña-like SST anomaly forcing in the equatorial Pacific (Pan et al., 2021). However, few details in the subseasonal variability of the 2020 Meiyu have been reported. As a matter of fact, a number of studies based on historical data showed that Meiyu is characterized by low-frequency oscillations with periods of 30–60 and 10–20 days [quasi-biweekly oscillation (QBWO)] (Lau and Li, 1984; Liang and Ding, 2012; Ding et al., 2020). Therefore, this study focuses on the characteristics of the subseasonal variation in 2020 Meiyu rainfall.

The rest of this paper is organized as follows. The data and methods are introduced in *Data and Method*. The *Results and Analysis* describes the characteristics and cause of the meridional migration of the 2020 abnormal Meiyu rainbelt from June to July and reveals a QBWO feature of daily Meiyu rainfall intensity and the corresponding atmospheric circulation characteristics. The *Conclusions and Discussions* contain some concluding remarks and a discussion of the results.

DATA AND METHODS

Data

To identify the characteristics of Meiyu rainfall over YHRB in 2020, we used the daily rainfall data at 2,417 meteorological

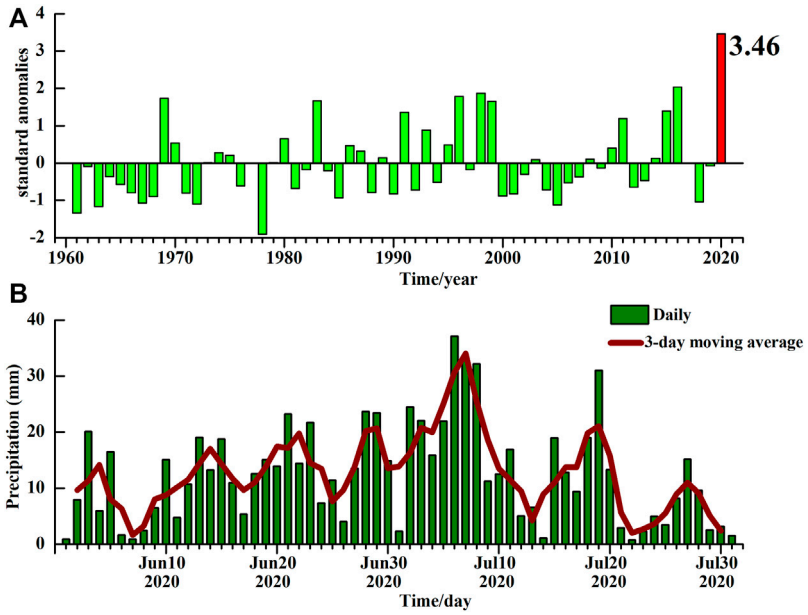

FIGURE 1 | (A) Interannual variations of standardized anomalies of total precipitation of June–July averaged at 277 observation stations over Meiyu monitoring area in China from 1961 to 2020. Value in 2020 is labeled. **(B)** Daily (bars) and 3-day moving mean (curve) precipitation averaged at 277 observation stations over Meiyu monitoring area in China from June 1, 2020, to July 31, 2020.

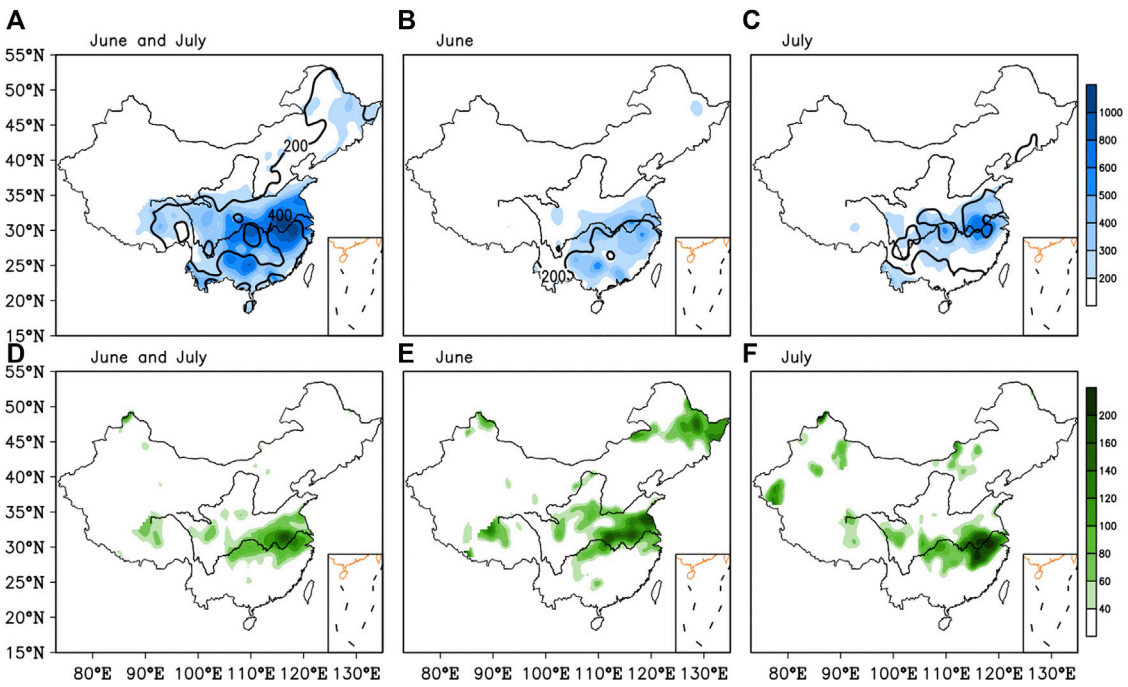

FIGURE 2 | Accumulated precipitation (shaded in **A–C**, unit: mm) and anomaly percentage of precipitation (shaded in **D–E**, unit: %) in June–July **(A,D)**, June **(B,E)**, and July **(C,F)** in 2020 over 2,417 stations of China. Contours in **A–C** are climatological mean precipitation of more than 200 mm with intervals of 200 mm. Climatology of precipitation is calculated from 1981 to 2010.

stations from 1961 to 2020 provided by the National Meteorological Information Center in China. The representative stations for monitoring Meiyu are 277 observation stations over YHRB according to China National standard GB/T 33671–2017. The daily circulation data at 02:00, 08:00, 14:00, and 20:00 Beijing local time in 2020 with a

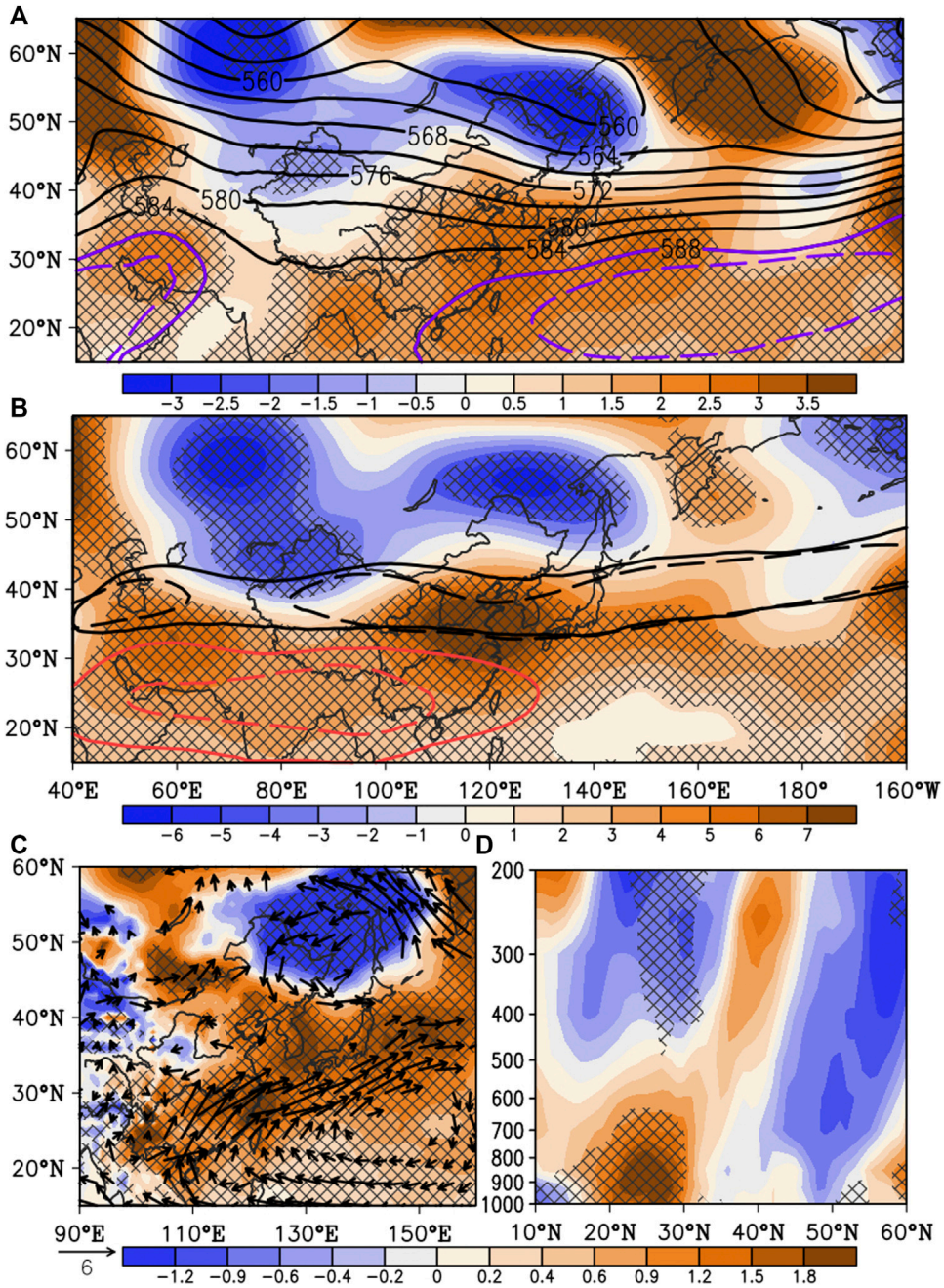

FIGURE 3 | (A) Composites of original values (contours, unit: dagpm) and anomalies (shaded, unit: dagpm) of 500-hPa geopotential heights averaged from June 1 to June 30, 2020. Purple solid and dashed lines are 2020 and climatological 588-dagpm contour of 500-hPa geopotential heights, respectively. **(B)** Composite anomalies of 200-hPa geopotential heights (shaded, unit: dagpm) averaged from June 1 to June 30, 2020. Black solid and dash lines are 2020 and climatological 30 m s^{-1} contour of 200-hPa zonal winds, respectively. Red solid and dash lines are 2020 and climatological 1,252-dagpm contour of 200-hPa geopotential heights, respectively. **(C)** Composite anomalies of 925-hPa air temperature (shaded, unit: °C) and winds (unit: m s^{-1}). Only anomaly winds value exceeding 0.05 significance level is shown by vectors. **(D)** Vertical section of composite anomalies of meridional winds (unit: m s^{-1}) averaged over East Asia along 105°E–135°E. Crossed area in each panel denotes anomalies exceeding 0.05 significance level.

horizontal resolution of 1° × 1° is derived from the fifth generation of European Centre for Medium-Range Weather Forecasts (ECMWF ERA-5) atmospheric reanalysis data (Hersbach et al., 2020).

METHODS

The start and end dates of Meiyu are defined in the China national standard (GB/T 33671–2017) and released by China

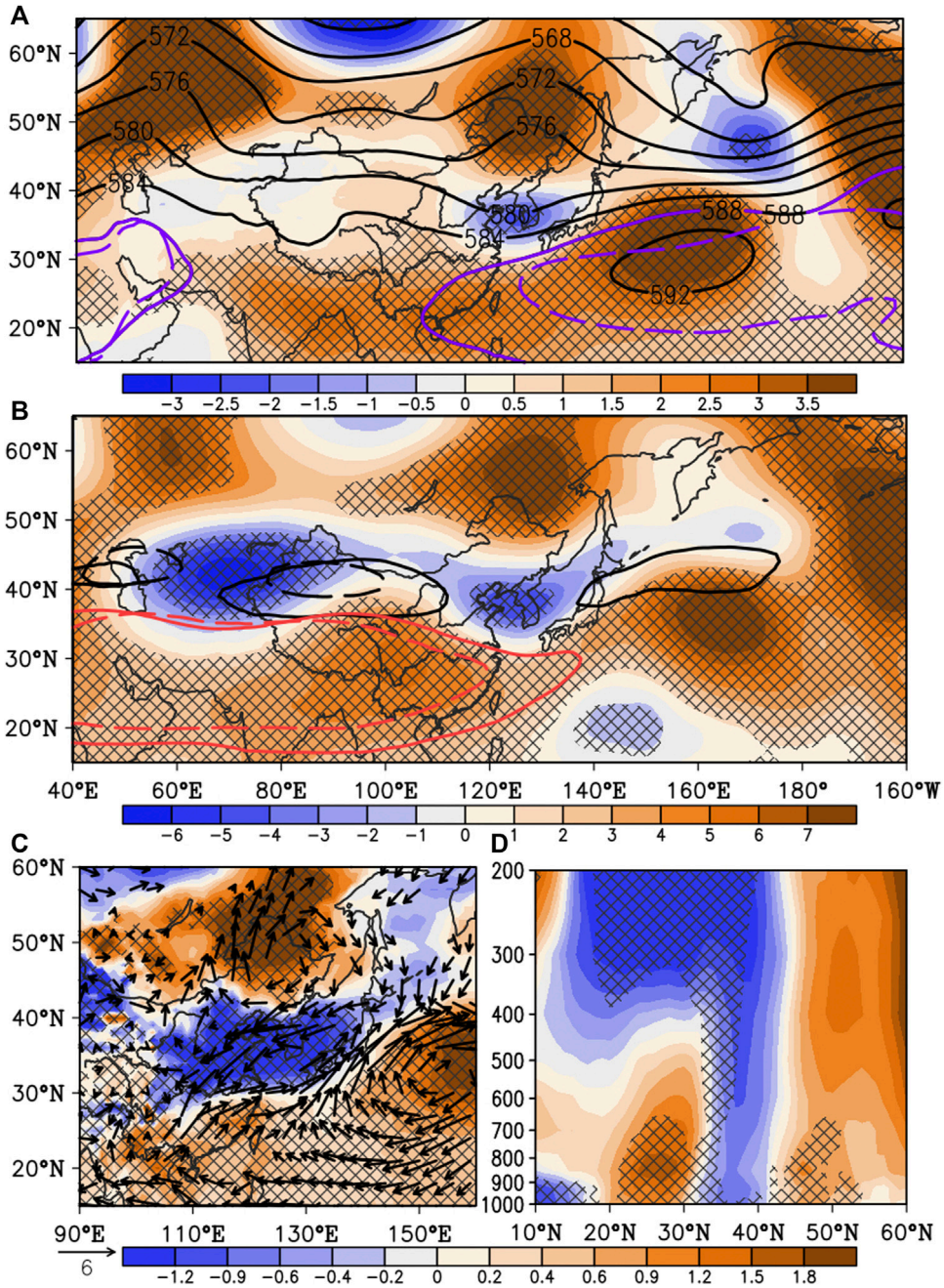

FIGURE 4 | As in **Figure 3** but for composite analysis from July 1 to July 31, 2020. **(A)** Composites of original values (contours, unit: dagpm) and anomalies (shaded, unit: dagpm) of 500-hPa geopotential heights averaged from June 1 to June 30, 2020. Purple solid and dashed lines are 2020 and climatological 588-dagpm contour of 500-hPa geopotential heights, respectively. **(B)** Composite anomalies of 200-hPa geopotential heights (shaded, unit: dagpm) averaged from June 1 to June 30, 2020. Black solid and dash lines are 2020 and climatological 30 m s^{-1} contour of 200-hPa zonal winds, respectively. Red solid and dash lines are 2020 and climatological 1,252-dagpm contour of 200-hPa geopotential heights, respectively. **(C)** Composite anomalies of 925-hPa air temperature (shaded, unit: °C) and winds (unit: m s^{-1}). Only anomaly winds value exceeding 0.05 significance level is shown by vectors. **(D)** Vertical section of composite anomalies of meridional winds (unit: m s^{-1}) averaged over East Asia along 105°E–135°E. Crossed area in each panel denotes anomalies exceeding 0.05 significance level.

National Climate Center. The 277 observation stations over YHRB in China are representative for monitoring Meiyu (**Supplementary Figure S1**). The daily Meiyu intensity is defined as the precipitation averaged over all the monitoring stations. The daily circulation is calculated by averaging the values four times in a day. The climatological mean state of each circulation variable is defined by the arithmetic mean of 1981–2010. Anomalies of variables are calculated as differences between the original data and the climatic means. The local wavelet power spectrum (Torrence

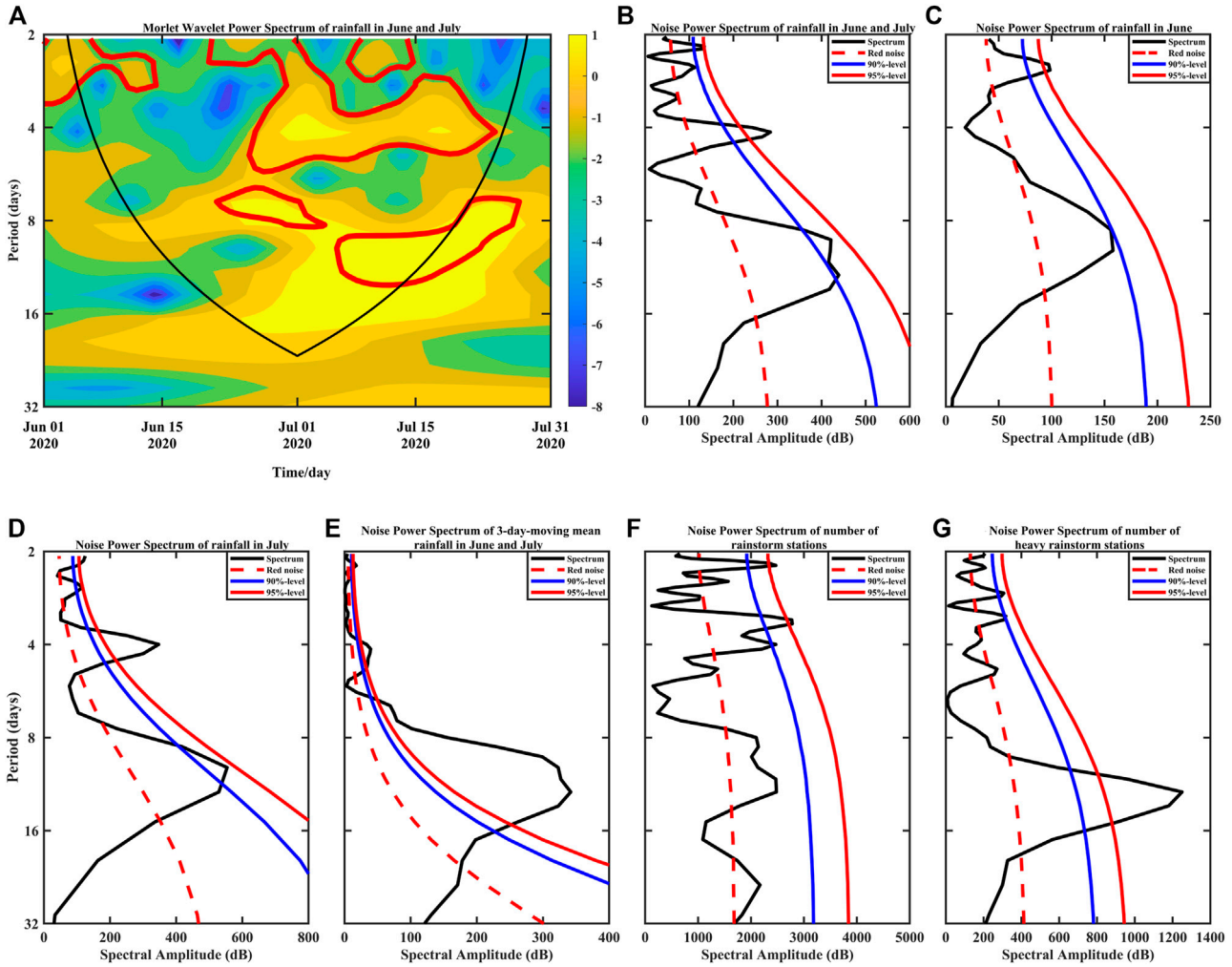

FIGURE 5 | (A) Local wavelet power spectrum of series of daily averaged precipitation from June 1, 2020, to July 31, 2020, in **Figure 1B** using Morlet wavelet analysis (thick red contour encloses regions of greater than 95% confidence for a red-noise process). **(B)** Noise power spectrum analysis of series of daily mean precipitation in **Figure 2B** (dashed red line is for red noise spectrum). Solid blue/red line is for 95/90% confidence level for spectrum. **(C)** as in **(B)** but for series of precipitation in June 2020. **(D)** as in **(B)** but for series of precipitation in July 2020. **(E)** as in **(B)** but for series of daily 3-day moving mean averaged precipitation in **Figure 2B**. **(F)** as in **(B)** but for series of daily number of rainstorm (daily rainfall ≥ 50 mm) stations. **(G)** as in **(B)** but for series of daily number of heavy rainstorm (daily rainfall ≥ 100 mm) stations.

and Compo, 1998) and the noise power spectrum analysis (Schulz and Mudelsee, 2002) are applied to show the significant timescale of the daily averaged Meiyu rainfall in 2020. The QBWO component of each variability is extracted by the Lanczos bandpass filter (Trenberth, 1984), retaining fluctuations with a period of 8–16 days.

RESULTS AND ANALYSIS

Subseasonal Variation of the Anomalous 2020 Meiyu Rainbelt

The 2020 Meiyu is labeled by a rarely long duration and record-breaking precipitation accumulation (**Figure 1**). Statistically, the total Meiyu amount reaches the extreme value with a standardized anomaly of 3.46, well breaking the record since 1961 (**Figure 1A**). The super 2020 Meiyu is mainly attributed to the frequent rainstorm processes with the severest intensity of approximately 38 mm at per Meiyu monitoring station. Removing the high-frequency weather signals within 3 days, there are seven peaks of heavy rainfall processes during the whole rainy season (**Figure 1B**). The Meiyu season persists in the whole of June and July of 2020 with extensively positive rainfall anomalies over the YHRB (**Figure 2**). The heaviest accumulated Meiyu precipitation is more than 800 mm, with the anomaly percentage exceeding 100% along the middle and lower reaches of the Yangtze River (**Figures 2A–D**). A robust subseasonal variation of the anomalous rainband is detected that the anomalous precipitation center shifts southward from June to July (**Figures 2B, C, E, F**). In the first stage, the northern edge of

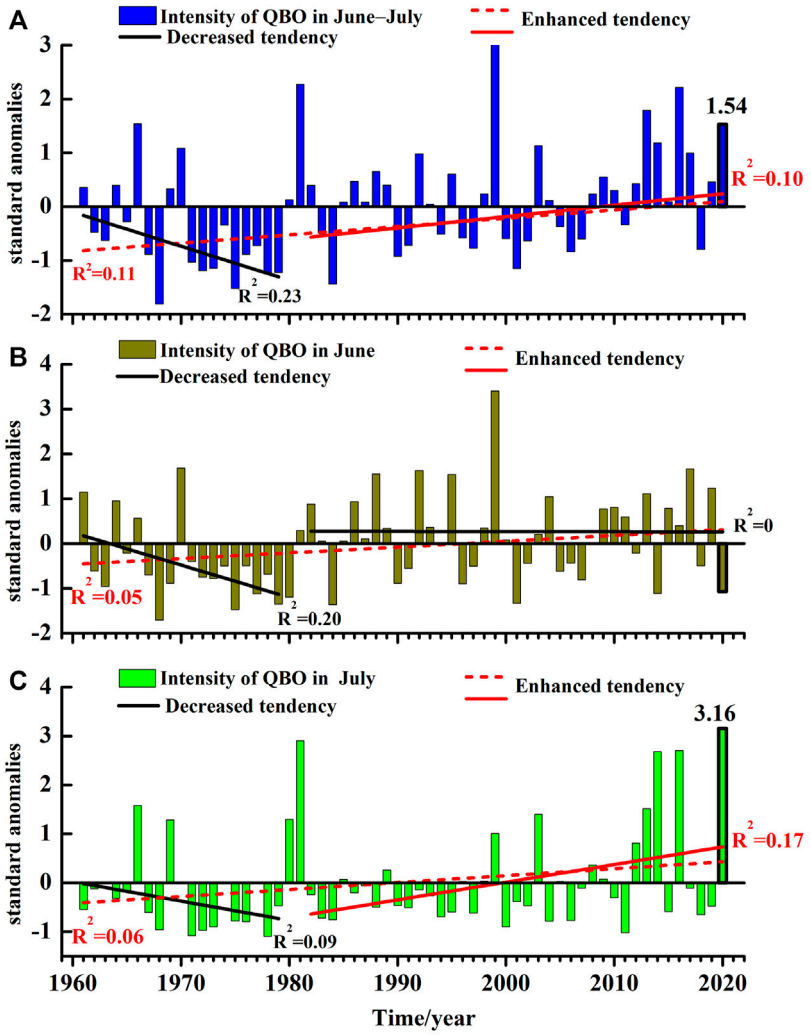

FIGURE 6 | (A) Interannual standardized anomalies of intensity of quasi-biweekly (8–16 days) oscillation (QBWOI) of precipitation of June and July (bars) from 1961 to 2020. Red dotted line is tendency of interannual series from 1961 to 2020. Solid lines are tendency of interannual series of 1961–1979 and 1982–2020. Red/black dotted line represents enhanced/decreased tendency. R^2 in left side of line is coefficient of determination of tendency of time span from 1961 to 2020. R^2 in right side is that of time span of 1961–1979 and 1982–2020. Value in 2020 is labeled. **(B)** as in **(A)** but for June. **(C)** as in **(A)** but for July.

precipitation over 200 mm extends to 35°N over East China, far exceeding the northern boundary of the climatological 200-mm contour. The two above-normal rainbands occur along the Huaihe and Yangtze River Basin, respectively (**Figure 2E**). In the later period, although the northern edge of rainbelt maintains over 35°N in agreement with the march of climatological rainbelt, the total rainfall amount over the Yangtze River Basin and the Jiang Nan Area is much heavier with anomalies exceeding the climate mean by 200% (**Figure 2F**).

As a typical stage of the EASM, Meiyu precipitation is a product of the interactions of circulation systems over the tropical, subtropical, and mid-high latitudes (Ninomiya, 1984; Tao and Chen, 1987; Ding, 1992; Yihui and Chan, 2005; Ding, 2007; Ding et al., 2018). The common Meiyu circulation pattern includes the WPSH in a zonal shape with warm and moist air transport in its northwestern flank, blocking-type circulation at the high latitudes and a low trough at the middle latitudes tending to carry cold and dry air. Owing to the necessity of good dynamic lifting conditions, the Meiyu rainbelt is generally located at the right entrance of the upper-level jet and the left exit of the lower-level jet. The typical circulation background summarized above applies for the 2020 Meiyu but cannot explain its extremity. Composite circulation anomalies in June and July show the possible cause of the extremely heavy and persistent Meiyu rainfall (**Figures 3**, **4**). During the whole Meiyu season, the anomalous anticyclone over the western North Pacific (WNPAC) induces the westward and northward expansion of WPSH (**Figures 3A**, **4B**). Correspondingly, the lower-level southwesterly winds in the northwestern flank of the WNPAC accelerate the transport of warm-and-wet air into the YHRB (**Figures 3C**, **4C**). As is known that the WNPAC could be maintained by the local air–sea interaction in the western

Pacific ocean or the "relay" role of the tropical Indian Ocean during El Niño decaying summers (Xie et al., 2009; Xie et al., 2016). By analyzing the evolutions of SST anomaly (SSTA) over the Indo and Pacific Ocean from 2020 January to July (**Supplementary Figure S2**), it is found that the basin-wide tropical IO warming persists from the winter to early summer of 2020 and a quick phase transition of an El Niño-like SSTA pattern over the equatorial central Pacific in the winter of 2020 to a La Niña-like SSTA pattern in the equatorial eastern Pacific in early summer. In agreement with Pan et al. (2021), both the warm SST anomaly forcing in the tropical Indian Ocean and the La Niña-like SST anomaly in the equatorial Pacific contribute to the formation and maintenance of the WNPAC. Additionally, the upper-level jet maintains at the climatological position with a much stronger intensity, favoring the persistence of 2020 Meiyu (**Figures 3B**, **4B**). The vertical circulation structure illustrates a stronger baroclinicity with southerly anomalies at the lower troposphere and northerly anomalies at the higher levels over the subtropics, boosting the classical monsoon circulation and promoting the above-normal ascending motion over the Meiyu region (**Figures 3D**, **4D**).

Despite the similarity of the atmospheric circulation anomalies in June and July, there exist distinct differences, which are responsible for the subseasonal variation of the anomalous 2020 Meiyu rainbelt location (**Figures 3**, **4**). In June, the quasi-barotropic positive geopotential height anomalies (GHAs) associated with anticyclonic anomalies (ACA) and negative GHAs related to cyclonic anomalies (CA) cover the South China Sea-western Pacific and the northern Asia continent, respectively, presenting a meridional dipole pattern. The positive GHAs of this dipole pattern, that is the WNPAC, contribute to the enhancement, northward expansion, and westward (eastward) extension of WPSH [South Asian High (SAH)], favoring the dynamic conditions for the abundant Meiyu rainfall over the YHRB and inducing the northward march of the anomalous rainbelt (**Figures 3A,B**). Although the quasi-barotropic negative GHAs of the dipole pattern over Northeast Asia and West Siberia favor the anomalous cold air accumulation in the high latitudes (**Figure 3A–C**), northerly anomalies to the north of the Meiyu rainbelt are relatively weak in June (**Figures 3C,D**), indicating the weak southward intrusion of cold air to the north of Meiyu front. The enhanced Meiyu is mainly attributed to the energetic northward warm-and-wet air transport from the lower latitudes (**Figures 3C,D**). The front edge of significantly abnormal lower-level southwesterly wind extends northward to 34°N. The dominance of the abnormally warm air suggests a warm Meiyu front feature.

Comparatively, in July, a meridional tripole seesaw pattern of anomalous circulation appears with positive GHAs (ACA) over the South China Sea-western Pacific, negative GHAs (CA) at the middle latitudes over Asia, and positive GHAs (ACA) at the high latitudes, resembling the Pacific–Japan pattern (Nitta, 1987) or the East Asia–Pacific pattern (Ronghui and Yifang, 1989; Huang and Sun, 1992) (**Figure 4**). Positive GHAs at the high latitudes centered over Northeast Asia and West Siberia indicate more active blocking highs over the mid-high latitudes. Positive GHAs at the lower latitudes cause an intensification and a westward (eastward) extension of the WPSH (SAH). With the obstruction of negative GHAs over the Sea of Japan–North China and the southward migration of the western WNPAC over the South China Sea, the 588-dagpm contour of WPSH features a weak northward expansion, and the ridge line of the western WPSH obviously retreats to the south of the climatological position in July (**Figures 4A,B**). This large-scale abnormal circulation is favorable for the southward shift of the rainband in July. In contrast to that, in June, the quasi-barotropic CA structure moves southward and maintains to the north of the Meiyu front. Accordingly, the anomalous northerly winds in the western flank of the CA bring cold-and-dry air into the YHRB and converge with the warm-and-moist air from the lower latitudes (**Figures 4C,D**). In this stage, the southward intrusion of cold air is remarkably enhanced, favoring the formation of a cold Meiyu front.

The 2020 Meiyu begins with a rapid northward march into the Huaihe River basin and experiences a meridional swing with the above-normal rainbelt from the northern YHRB in June to the southern YHRB in July. The two different structures of the Meiyu front regime are responsible for the subseasonal variation of the Meiyu rainband location. The enhanced Meiyu over the northern YHRB in June is primarily due to the extremely vigorous activity of northward warm air transporting moisture, whereas the abnormally abundant Meiyu over the southern YHRB in July is attributed to the significantly southward intrusion of cold air and the intimate meeting of anomalous cold and warm.

Quasi-Biweekly Oscillation of 2020 Meiyu

Characteristics of the Quasi-Biweekly Oscillation of 2020 Meiyu

Since the 2020 Meiyu has witnessed an obvious subseasonal variation (**Figure 1B**), we further investigated the subseasonal variability of mean Meiyu intensity using the period analysis methods. The Morlet wavelet analysis reveals that two significant periods dominate the 2020 Meiyu rainfall processes: 2–4 and 8–16 days (**Figure 5A**). The former is a high-frequency oscillation associated with synoptic transient eddies. The range of 8–16 days, about 2 weeks, is classified as an important low-frequency fluctuation time window on the subseasonal scale. In other words, the QBWO is significant in 2020 Meiyu intensity. The same results can be obtained in the noise power spectrum analysis of the daily Meiyu precipitation (**Figure 5B–D**). Both period windows of 2–4 and 8–16 days are obviously exceeding the red noise spectrum and the 90% confidence level, except that the range of 8–16 days in June is less than the 90% confidence level. After filtering out the high-frequency signal by the 3-day moving average of daily precipitation, the period of 8–16 days notably exceeds the 95% confidence level and acts as the primary period of Meiyu precipitation during 2020 June–July (**Figure 5E**). Considering that the 2020 Meiyu is attributed to frequent heavy rainfall processes, the period analyses were also conducted to the daily number of a rainstorm (daily rainfall ≥ 50 mm) and heavy rainstorm (daily rainfall ≥ 100 mm) stations (**Figure 5F–G**). The period of 2 and 4 days and approximately 2 weeks are all above the noise thresholds for the rainstorm

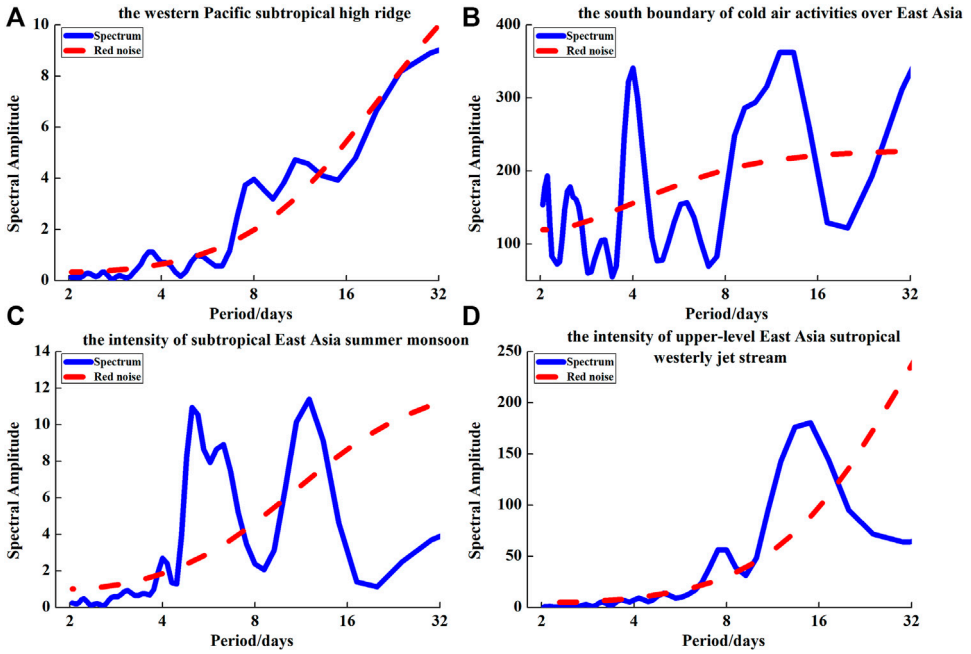

FIGURE 7 | Noise power spectrum analysis of series of daily index of western Pacific subtropical high (WPSH) ridge **(A)**, south boundary of cold air over East Asia **(B)**, intensity of subtropical East Asia summer monsoon (SEASM) **(C),** and intensity of upper-level East Asia subtropical westerly jet **(D)** in June and July 2020 (dashed red line is for red noise spectrum).

events. For rainstorms, 2 and 4 days associated with the high-frequency variation are much more evident, whereas, for the heavy rainstorm events, the QBWO is the most significant low-frequency component, by far exceeding the 95% confidence level. Therefore, rainfall variabilities with 8–16 days are a crucial period for the alarming 2020 Meiyu, especially for the severe rainstorm events, which require more attention when producing the medium and extended range forecast of rainfall.

The QBWO of Meiyu has been investigated by previous studies (Lau and Li, 1984; Liang and Ding, 2012; Ding et al., 2020). How much is the contribution of the QBWO component to the total rainfall amount? How strong is the QBWO of 2020 Meiyu? The intensities of the QBWO of Meiyu precipitation (QBWOI) are defined by calculating the variance of the daily series of 8–16-day Lanczos filter value of daily total precipitation over Meiyu monitoring regions for a specified period. For example, the QBWOI in June–July is referred to as the variance of the daily 8–16-day Lanczos filter precipitation averaged over 277 observation stations from June 1 to July 31, 2020. It is found that the QBWO component can explain 22% of the total variability of the 2020 Meiyu when calculating the variance contribution. The past 60 years have witnessed an obvious increasing tendency of the standardized QBWOI in both June and July since 1961, which passes the 95% confidence level (**Figure 6A**). A closer look finds a turning point in the early 1980s for the tendency of the QBWOI in both June and July using the Manner–Kendall test. From 1961 to 1979, the QBWOI in June–July, especially in June (**Figure 6B**), is characterized by a significantly decreasing tendency. In contrast, since 1981, the QBWOI is obviously intensified in June–July, especially in July (**Figure 6C**). The QBWOI in June–July of 2020 is abnormally high with a standardized anomaly of 1.54, ranked at the sixth place in history. Specially and interestingly, the QBWOI in July is markedly stronger than normal with a standardized anomaly of 3.16 and breaks the record, although the QBWOI in June is weaker than normal. It is noted that the significant subseasonal characteristic of QBWO is also presented in some other extreme Meiyu rainfall events such as 1998, 1999, and 2016 (**Figure 6A**).

Cause of the Quasi-Biweekly Oscillation of 2020 Meiyu

The QBWO mainly modulates the daily rainfall intensity of the super Meiyu in 2020. The QBWOI of Meiyu rainfall in July even broke the record. How does the QBWO of the Meiyu rainfall happen? As Meiyu rainfall is closely associated with the EASM atmospheric circulation systems, we conducted the spectrum analyses of specific atmospheric circulation systems, including the position of the WPSH ridge line at 120°E, the southern boundary of cold air over East Asia (the latitude of the 564 dagpm at 500-hPa geopotential heights averaged along 105°E–135°E), the intensity of subtropical East Asia summer monsoon (SEASM) (the average 925-hPa meridional winds over the region of 110°E–120°E, 25°N–35°N, defined as China National Meteorological trade standard QX/T 394–2017), and the intensity of EASWJ (the average 200-hPa zonal winds over the region of 120°E–160°E, 35°N–45°N). All of these EAMS variabilities exhibit a significant QBWO as Meiyu rainfall doe (**Figure 7**).

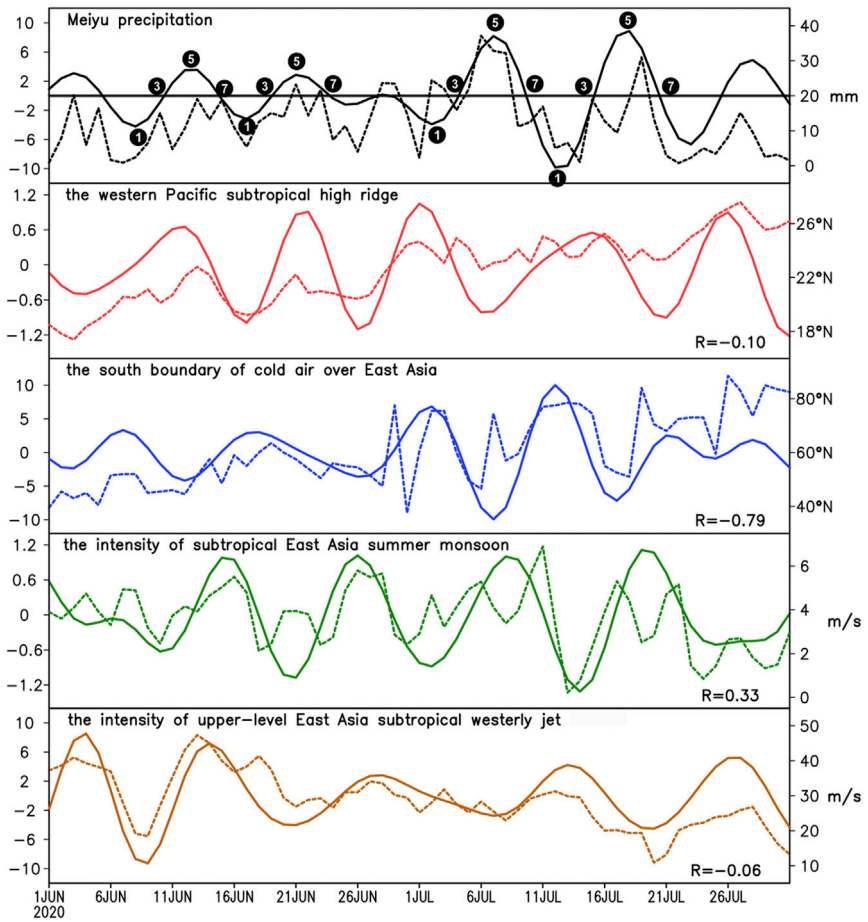

FIGURE 8 | 8-16-day Lanczos filter value (solid curves, left axes) and daily original value (dashed curves, right axes) of Meiyu precipitation, WPSH ridge, southern boundary of cold air over East Asia, intensity of SEASM, and intensity of upper-level East Asia subtropical westerly jet from June 1, 2020, to July 31, 2020 (numbers of "1," "3," "5," and "7" denote different phases of four processes of QWBO component during 2020 Meiyu season).

TABLE 1 | Behaviors of some ESAMS associated with first to seventh round of precipitation processes during 2020 Meiyu.

	First	Second	Third	Fourth	Fifth	Sixth	Seventh
WPSH ridge	Valley	Peak	Peak	Northward march	Valley	Southward retreat	Valley
South boundary of cold air over East Asia	Valley	Valley	Southward invasion	Valley	Valley	Valley	Southward invasion
Intensity of SEASM	Valley	Enhancement	Valley	Weakening	Peak	Peak	Enhancement
Intensity of upper-level East Asia subtropical westerly jet	Peak	Enhancement	Enhancement	Peak	Valley	Weakening	Weakening

The daily variation of the 8–16-day filtered Meiyu precipitation underlines seven precipitation processes with peaks occurring on June 3, 13, 21, and 28 and July 7, 18, and 28 and corresponding to the abundant Meiyu rainfall phases, respectively (**Figure 8**). They are named as the first to the seventh round of precipitation processes. The peak/valley of precipitation is referred to as the fifth/first phase of each round. By listing the behaviors of the EASM atmospheric circulation systems associated with the first to the seventh round of precipitation processes during the whole 2020 Meiyu (**Table 1**), it is found unexpectedly that only the southern boundary of the cold air activity over East Asia corresponds well to the Meiyu rainfall for all the seven processes. When the QBWO component of Meiyu reaches the peaks, the cold air over East Asia invades southward at best (in five processes) or is on the march of the southward invasion (in two processes). The correlation coefficient (CC) of the 8–16-day Lanczos filtered Meiyu precipitation and the latitudes of the southern boundary of cold air over East Asia from June 1 to July 31 is -0.79. The highly negative correlation indicates that the southward invasion of cold air over East Asia is

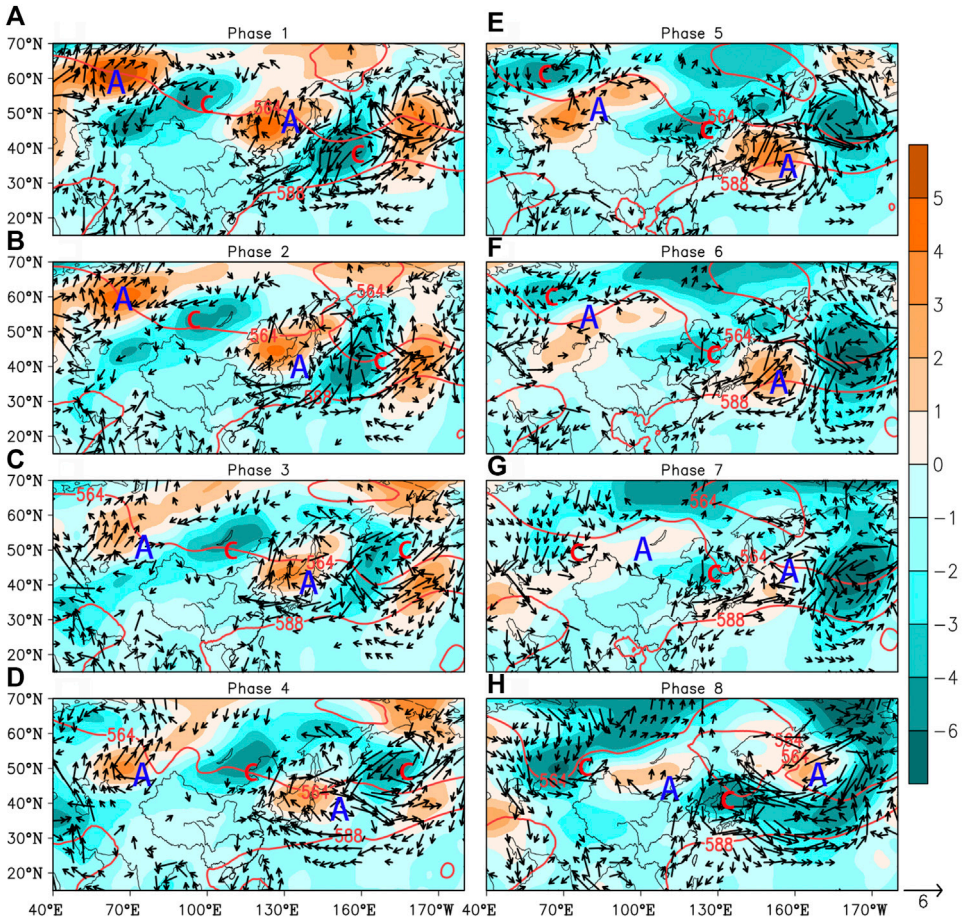

FIGURE 9 | Composite 8–16-day Lanczos filtered 500-hPa height (shaded, unit: dagpm) and 925-hPa winds (only filter value exceeding 1 m s^{-1} is shown by vectors). Marks of C/A denotes cyclonic/anticyclonic filtered circulation) corresponding to eight evolution phases of QWBO rainfall in second and third rainfall processes. Red lines denote 564- and 588-dagpm contours at unfiltered 500-hPa GHs. **A–H** correspond to the eight phases of the composite evolution of QWBO component of the the second to third rainfall processes.

well conducive to Meiyu rainfall. By contrast, the other EASM circulation systems have a weaker relationship with the Meiyu rainfall. Three peaks of QBWO rainfall witness the enhancement or peaks of the SEASM with CC = 0.55 between the filtered intensity of the SEASM and Meiyu rainfall in July while corresponding to the weakening or valleys of SEASM in the first, third, and fourth processes. Besides, the features of the meridional shift of the WPSH ridge and the intensity of the upper-level East Asia subtropical westerly jet during the peak phases of the QBWO rainfall in June are nearly opposite to those in July. The CCs of the QBWO component of the WPSH ridge (the intensity of the upper-level East Asia subtropical westerly jet) with the QBWO rainfall increase up to 0.45 (0.42) in June and decrease down to -0.40 (-0.31) in July. It suggests that the WPSH ridge at 120°E marches northward, and the upper-level East Asia subtropical westerly jet intensifies when the rainfall enhances in June, whereas the reverse applies in July.

To further clarify the QBWO of the atmospheric circulation favorable for the super Meiyu, the composite evolution of the EASM atmospheric circulation systems in the second to third and the fifth to sixth rounds is presented in **Figures 9–12**. The composite 8–16-day filtered circulations show almost opposite evolution patterns in the first to fourth phase to the fifth to eighth phase in June and July 2020, respectively (**Figure 9–12**). The filtered circulation pattern at phase 5 that corresponds to the peak phase of precipitation is contrary to that at phase 1.

In June, the increasing (decreasing) of rainfall on the 8–16-day time scale is accompanied by a northward march (southward retreat) of the WPSH and a southward intrusion (northward diminishing) of the cold air over Northeast Asia (**Figure 9**). At the peak phase (phase 5), a cyclonic circulation at 500 and 925 hPa occurs over Northeast China. The 588-dagpm contour at 500 hPa shifts northward to the Yangtze River valley, and the 564-dagpm contour arrives at the southernmost location. The meeting of the cold vortex and WPSH contributes to the intensification of Meiyu precipitation. The reverse is true for valley phase 1. The cyclone over Northeast China at phase 5 can be traced back to the cyclonic circulation west of Lake Baikal at phase 1, which is embedded in a wave train over the mid-high latitudes. At phase 1, the wave train is featured with high pressure/anticyclonic winds over the Ural

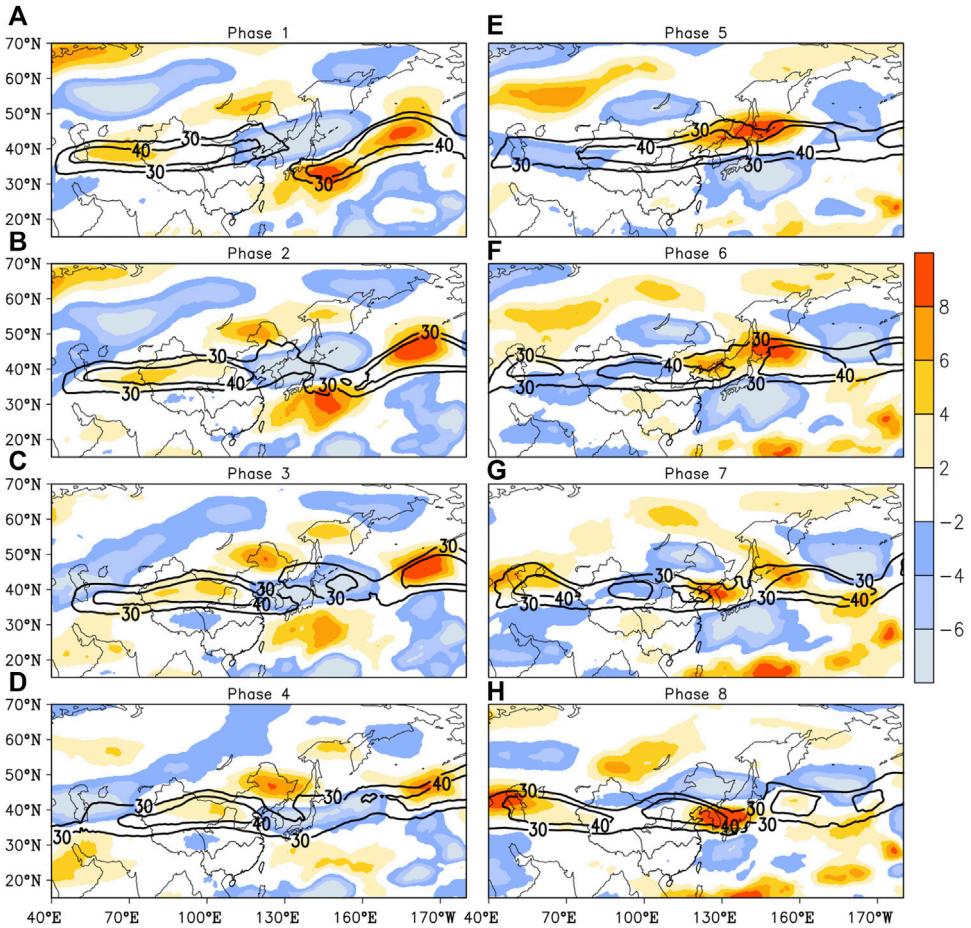

FIGURE 10 | Composite 8–16 days Lanczos filtered 200-hPa zonal winds (shaded, unit: m s^{-1}) corresponding to eight evolution phases of QWBO rainfall in second and third rainfall processes. Red lines denote 30 and 40 m s^{-1} contours at unfiltered 200-hPa zonal winds. **A–H** correspond to the eight phases of the composite evolution of QWBO component of the the second to third rainfall processes.

Mountains, low pressure/cyclonic winds west of Lake Baikal, high pressure/anticyclonic winds over Northeast China, and low pressure/cyclonic winds over the North Pacific east of Japan. With the enhancement of rainfall, the wave train moves southeastward. At phase 5, the wave train with the opposite sign to phase 1 takes place at the troposphere (**Figure 9**).

The eastward propagating wave train might be related to the EASWJ. Although the EASWJ cores persist over the latitudes of 30–40°N, benefiting the stationary rainbelt, its intensity exhibits a significant QBWO (**Figure 10**). The intensity of the EASWJ reaches the maximum with the positive filtered zonal wind over North China–Japan at phase 5, whereas the EASWJ belt broke with the negative filtered zonal wind over North China–Japan at phase 1. The enhancement of the EASWJ is favorable for the ascending motion, thereby enhancing Meiyu rainfall. On the other hand, it might contribute to the eastward propagating of the wave train as a waveguide.

As in June, broad filtered cyclonic winds at 925 hPa accompanied with a trough over Northeast Asia at 500 hPa favor a southward intrusion of cold air from the mid-high latitudes at the peak phase of Meiyu rainfall in July; the opposite holds true for the valley phase (**Figure 11**). At phase 5, over the broad low pressure in Northeast Asia, two cyclone centers are found north of Lake Baikal and over Northeast China. The cyclone center to the north of Lake Baikal originates from the northwestward propagation of the low pressure/cyclone over the Aleutian Islands at phase 1 carried by a wave train at the mid-high latitudes. The distribution of the wave train centers in July are distinct from those in June (**Figures 9**, **11**), and it comprises high pressure/anticyclonic winds north of the Ural Mountains, broad low pressure/cyclonic winds over Northeast China, and high pressure/anticyclonic winds over the Aleutian Islands. Another cyclone center over Northeast China might arise from the combination of the westward propagation of the wave train over mid-high latitudes and the northwestward propagation of the cyclonic circulation over the Philippine Sea at phase 1. As the cyclonic circulation over the Philippine Sea marches northward and slightly westward, an anticyclone from the tropics gradually takes its place, inducing the westward extension of the WPSH. Because of the northward migration of the cyclone along the East

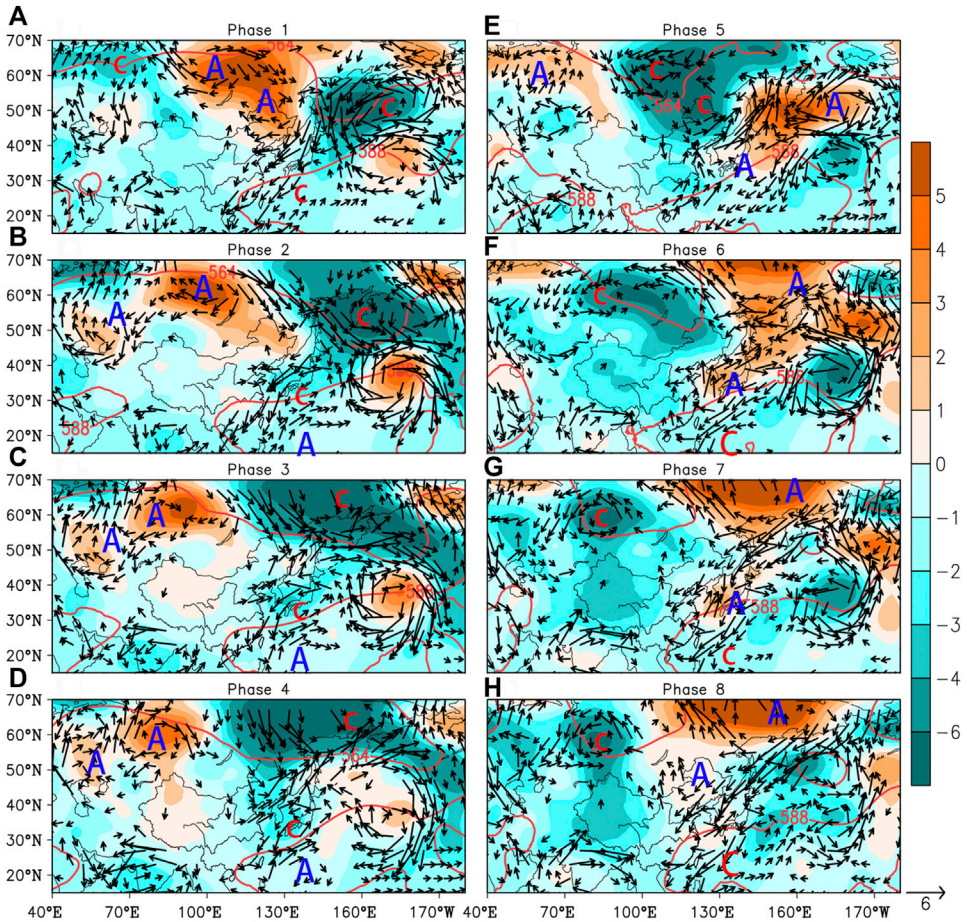

FIGURE 11 | As in **Figure 9** but for fifth and sixth rainfall processes. **A–H** correspond to the eight phases of the composite evolution of QWBO component of the the second to third rainfall processes.

Asia coast, the WPSH around 120°E retreats southward as Meiyu rainfall increases. Remarkably different from that in June, at phase 5, the southwest winds favorable for warm and wet air transport over southern China are more vigorous to meet with the northwest winds carrying cold and dry air from the north. The two flows contribute to an obvious lower pressure over southeast China, causing the WPSH to retreat to the southernmost (**Figure 11**). The westward propagation of the wave train over the mid-high latitudes of Eurasia is contrary to that in June, which may be related to that of the EASWJ weakened markedly from June to July. A contrary evolution of the intensity of the EASWJ associated with Meiyu rainfall stands out in July, as shown in **Figure 12**. At the peak phase of rainfall, the EASWJ weakens with the broad negative filtered zonal wind over East Asia, possibly related to the westward propagation of the wave activities on the scale of the QBWO.

To summarize, the evolutions of the EASM atmospheric circulation systems on the scale of 8–16 days in June and July both well capture the QBWO component of the 2020 Meiyu rainfall but exhibit two different ways. In addition to the opposite propagation of the wave train over the mid-high latitudes of Eurasia, the WPSH ridge, SEASM, and EASWJ exhibit opposite evolution behaviors in June and July.

CONCLUSIONS AND DISCUSSIONS

The super 2020 Meiyu onsets earlier and ends later than normal, with an extremely long duration of 62 days. Persistent rainfall accompanied with frequent heavy rainstorms brings a record-broking Meiyu event and causes devastating floods over the YHRB. The Meiyu rainfall is closely related to the anomalous EASM atmospheric circulation systems with westward and northward WPSH, evident expansion of the EASWJ and SAH, and the accelerated lower-level southwesterly flows.

When closely examining the characteristics of the Meiyu rainbelt migration, it is found that the centers of positive

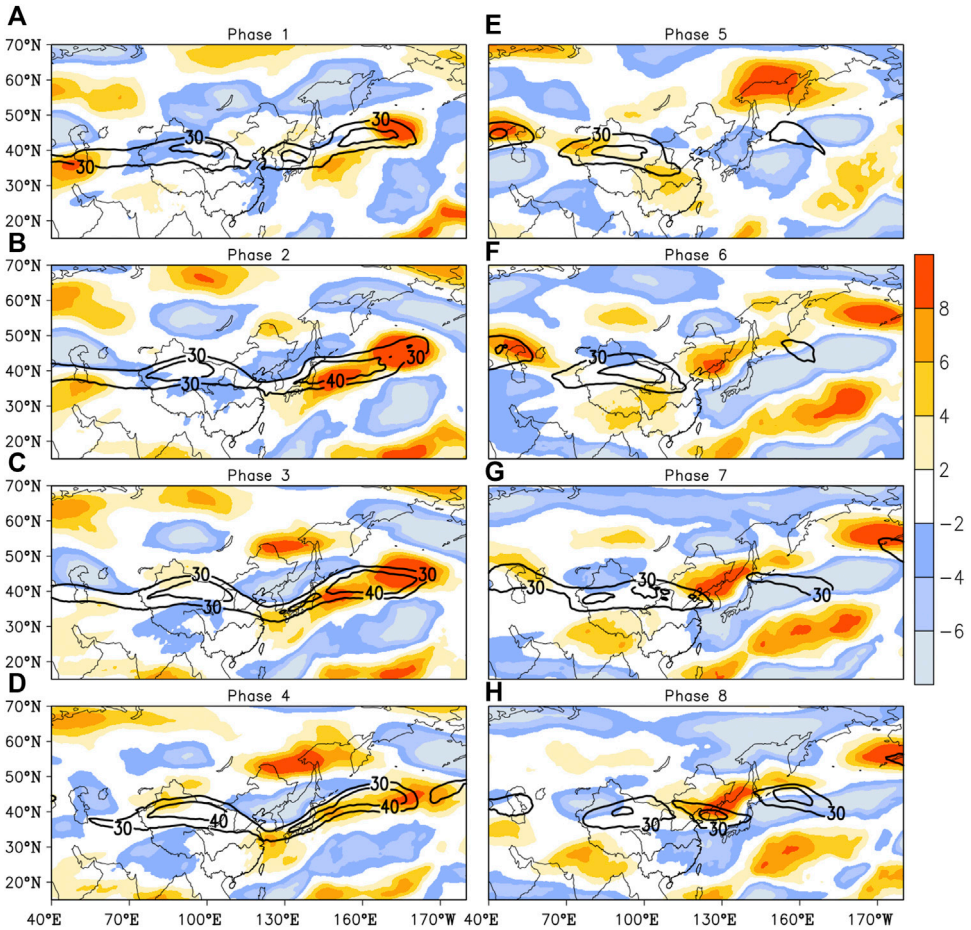

FIGURE 12 | As in **Figure 10** but for fifth and sixth rainfall processes. **A–H** correspond to the eight phases of the composite evolution of QWBO component of the the second to third rainfall processes.

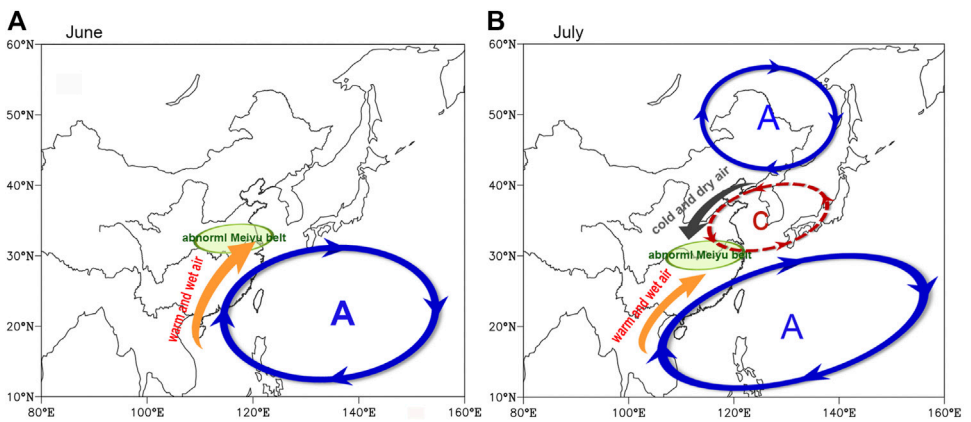

FIGURE 13 | Schematic diagram for explanation for abnormal Meiyu rainbelt in June **(A)** and July **(B)** 2020 (solid blue/dashed red cycle and blue/red letter A/C denote anticyclonic/cyclonic anomaly).

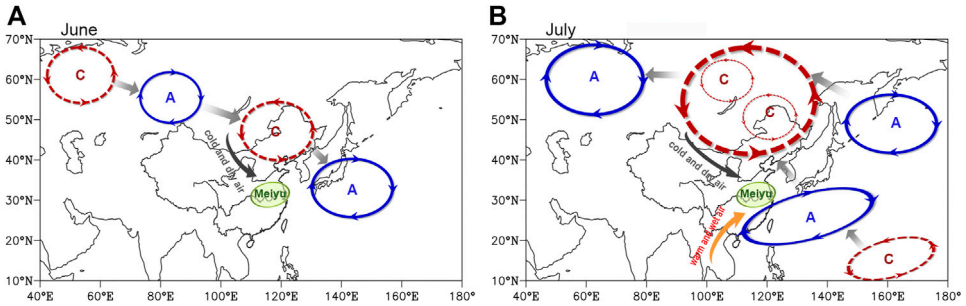

FIGURE 14 | Schematic diagram for circulations for Meiyu rainfall on scale of QBWO in June **(A)** and July **(B)** 2020 (Solid blue/dashed red cycles and blue/red letter A/C denote anticyclonic/cyclonic filtered circulation. Gray arrows denote propagation of wave train. Filtered circulation associated with valley phase of Meiyu is opposite to that at peak phase, as shown).

rainfall anomalies experience a southward retreat from June to July. The above-normal rainband was located over the northern YHRB in 2020 June and retreated southward to the southern YHRB in July. To better understand the rainbelt migration, the anomalous large-scale circulation patterns are illustrated in **Figure 13**. In June, extremely vigorous northward warm-and-wet air transported by the abnormal southwesterlies associated with the WPSH motivates a warm Meiyu front, anchoring the Meiyu rainbelt over the northern YHRB (**Figure 13A**). By comparison, in July, the significant northeast wind anomalies linked with the CA over the Sea of Japan–North China and the ACA over Northeast Asia induce cold air to invade into the lower latitudes and to converge with the abnormal southwesterlies in the northwestern flank of the ACA over the western Pacific. The intimate merging of cold and warm air is favorable for the Meiyu front formation and the rainbelt over the southern YHRB (**Figure 13B**).

During all the 2020 Meiyu season, no matter in June or July 2020, it is identified that an extremely strong WNPAC persists and induces abundant Meiyu rainfall over the YHRB. Consistent with Pan et al. (2021), the SSTA pattern over the Indo-Pacific ocean with a basin-wide IO warming persisting from the winter to early summer of 2020 and a quick phase transition of an El Niño-like SSTA pattern over the equatorial central Pacific in the winter to a La Niña-like SST pattern in the equatorial eastern Pacific in the early summer is a great contributor to the formation and maintenance of the WNPAC. However, the explanation for the subseasonal southward shift of the WNPAC over the South China Sea favorable for the meridional migration of the 2020 Meiyu rainbelt from June to July needs to be explored in our further studies.

Another significant subseasonal variation of the 2020 Meiyu precipitation is that the Meiyu rainfall evolves in periodic oscillations of approximately 2 weeks (8–16 days). Interestingly, the QBWO intensity of Meiyu rainfall, especially in 2020 July, has witnessed an obvious increasing tendency since the early 1980s. The QBWO intensity of Meiyu rainfall in 2020 July ranks first place since 1960.

Consistent with the Meiyu rainfall, the circulation systems also exhibit a QBWO feature. Pieces of evidence show that each southward intrusion of cold air over East Asia corresponds well to the increase of Meiyu precipitation on the scale of QBWO. However, other systems such as the WPSH, SEASM, and EASWJ behave in different and even contrary ways between June and July 2020. The results are unexpected and require more investigation of the details. When Meiyu rainfall enhances to the peaks, the WPSH marches northward (retreats southward), the SEASM weakens (strengthens), and the EASWJ accelerates (decelerates) in June (July) 2020. Moreover, the filtered cyclone over Northeast China available for the southward intrusion of cold air from the mid-high latitudes for Meiyu precipitation arises in different ways. In June, the cyclone is attributed to the eastward propagation of a wave train over the mid-high latitudes, whereas that in July is the result of the joint effect of the westward propagation of a wave train over the mid-high latitudes and the northward propagation of the cyclonic circulation from the tropics. Circulations at the peak phase of Meiyu rainfall on the scale of QBWO are summarized in **Figure 14**.

This study describes the characteristics and cause of the meridional migration of the 2020 Meiyu rainbelt from June to July and reveals a QBWO feature of daily Meiyu rainfall amount and the corresponding atmospheric circulation characteristics. The external forcings driving the subseasonal variation of the abnormal rainbelt and the QWBO variability require further investigations. Given that the QBWO intensity of Meiyu exhibits significant interannual and interdecadal variations, the influencing factors (e.g., the global SSTA), the associated physical processes, and the contribution to the prediction of Meiyu are still open questions.

DATA AVAILABILITY STATEMENT

The data analyzed in this study is subject to the following licenses/restrictions: The precipitation datasets presented in this article are not readily available because raw data supporting the conclusions of this article is high precision. High spatial and temporal resolution observations are confidential data and cannot be made public according to the data management regulation. Requests to access the datasets should be mailed to the author,

dg1728001@smail.nju.edu.cn. The ERA-5 datasets analyzed for this study can be found on the Copernicus Climate Change Service Climate Data Store (https://cds.climate.copernicus.eu/). Requests to access these datasets should be directed to dg1728001@smail.nju.edu.cn.

AUTHOR CONTRIBUTIONS

SC conceived the idea and performed the analysis. ML and KZ revised the interpretation of the results. The other authors contributed the writing.

FUNDING

This research was supported by the National Natural Science Foundation of China (41805051) and the Key Project of the Jiangsu Meteorological Bureau (KZ202101 and KZ202205).

SUPPLEMENTARY MATERIAL

The Supplementary Material for this article can be found online at: https://www.frontiersin.org/articles/10.3389/feart.2021.799104/full#supplementary-material

REFERENCES

Bollasina, M. A., and Messori, G. (2018). On the Link between the Subseasonal Evolution of the North Atlantic Oscillation and East Asian Climate. *Clim. Dyn.* 51, 3537–3557. doi:10.1007/s00382-018-4095-5

Chen, T. J. G., and Yu, C.-C. (1988). Study of Low-Level Jet and Extremely Heavy Rainfall over Northern Taiwan in the Mei-Yu Season. *Mon. Wea. Rev.* 116, 884–891. doi:10.1175/1520-0493(1988)116<0884:sollja>2.0.co;2

Chen, J., Wen, Z., Wu, R., Chen, Z., and Zhao, P. (2015). Influences of Northward Propagating 25-90-day and Quasi-Biweekly Oscillations on Eastern China Summer Rainfall. *Clim. Dyn.* 45, 105–124. doi:10.1007/s00382-014-2334-y

Chowdary, J. S., Hu, K., Srinivas, G., Kosaka, Y., Wang, L., and Rao, K. K. (2019). The Eurasian Jet Streams as Conduits for East Asian Monsoon Variability. *Curr. Clim. Change Rep.* 5, 233–244. doi:10.1007/s40641-019-00134-x

Chowdary, J. S., Vibhute, A. S., Darshana, P., Parekh, A., Gnanaseelan, C., and Attada, R. (2021). Meridional Displacement of the Asian Jet and its Impact on Indian Summer Monsoon Rainfall in Observations and CFSv2 Hindcast. *Clim. Dyn.* 57, 1432–0894. doi:10.1007/s00382-021-05935-1

Ding, Y., Si, D., Liu, Y., Wang, Z., Liu, Y., Zhao, L., et al. (2018). On the Characteristics, Driving Forces and Inter-decadal Variability of the East Asian Summer Monsoon. *Chin. J. Atmos. Sci.* 42, 533–558. doi:10.3878/j.issn.1006-9895.1712.17261

Ding, Y., Liang, P., Liu, Y., and Zhang, Y. (2020). Multiscale Variability of Meiyu and its Prediction: A New Review. *J. Geophys. Res. Atmos.* 125, e2019JD031496. doi:10.1029/2019JD031496

Ding, Y., Liu, Y., and Hu, Z.-Z. (2021). The Record-Breaking Mei-Yu in 2020 and Associated Atmospheric Circulation and Tropical SST Anomalies. *Adv. Atmos. Sci.* 38, 1980–1993. doi:10.1007/s00376-021-0361-2

Ding, Y. (1992). Summer Monsoon Rainfalls in China. *J. Meteorol. Soc. Jpn.* 70, 373–396. doi:10.2151/jmsj1965.70.1B_373

Ding, Y. (2007). The Variability of the Asian Summer Monsoon. *J. Meteorol. Soc. Jpn.* 85B, 21–54. doi:10.2151/jmsj.85B.21

Gan, N. (2020). China Has Just Contained the Coronavirus. Now It'sbattling Some of the Worst Floods in Decades. Available at: https://edition.cnn.com/2020/07/14/asia/china-flood-coronavirus-intl-hnk/index.html (Accessed on: July 14, 2020).

Ge, L., Ren-Guang, W., and Yuan-Zhi, Z. (2014). Persistence of Snow Cover Anomalies over the Tibetan Plateau and the Implications for Forecasting Summer Precipitation over the Meiyu-Baiu Region. *Atmos. Oceanic Sci. Lett.* 7, 115–119. doi:10.1080/16742834.2014.11447145

Guo, Y., Zhang, R., Wen, Z., Li, J., Zhang, C., and Zhou, Z. (2021). Understanding the Role of SST Anomaly in Extreme Rainfall of 2020 Meiyu Season from an Interdecadal Perspective. *Sci. China Earth Sci.* 64, 1619–1632. doi:10.1007/s11430-020-9762-0

He, J., Wu, Z., Jiang, Z., Miao, C., and Han, G. (2007). "Climate Effect" of the Northeast Cold Vortex and its Influences on Meiyu. *Chin. Sci. Bull.* 52, 671–679. doi:10.1007/s11434-007-0053-z

Hersbach, H., Bell, B., Berrisford, P., Hirahara, S., Horányi, A., Muñoz-Sabater, J., et al. (2020). The ERA5 Global Reanalysis. *Q. J. R. Meteorol. Soc.* 146, 1999–2049. doi:10.1002/qj.3803

Huang, R., and Sun, F. (1992). Impacts of the Tropical Western Pacific on the East Asian Summer Monsoon. *J. Meteorol. Soc. Jpn.* 70, 243–256. doi:10.2151/jmsj1965.70.1B_243

Huang, D., Zhu, J., and Kuang, X. (2011). Decadal Variation of Different Durations of Continuous Meiyu Precipitation and the Possible Cause. *Chin. Sci. Bull.* 56, 424–431. doi:10.1007/s11434-010-4241-x

Huaqiang, L., and Yongfu, Q. (1999). Numerical Simulations of Intense Meiyu Rainfall in 1991 over the Changjiang and Huaihe River Valleys by a Regional Climate Model with P- σ Incorporated Coordinate System. *Adv. Atmos. Sci.* 16, 395–404. doi:10.1007/s00376-999-0018-z

Kodama, Y. (1992). Large-Scale Common Features of Subtropical Precipitation Zones (The Baiu Frontal Zone, the SPCZ, and the SACZ) Part I: Characteristics of Subtropical Frontal Zones. *J. Meteorol. Soc. Jpn.* 70, 813–836. doi:10.2151/jmsj1965.70.4_813

Kosaka, Y., Xie, S.-P., and Nakamura, H. (2011). Dynamics of Interannual Variability in Summer Precipitation over East Asia*. *J. Clim.* 24, 5435–5453. doi:10.1175/2011JCLI4099.1

Lau, K.-M., and Li, M.-T. (1984). The Monsoon of East Asia and its Global Associations-A Survey. *Bull. Amer. Meteorol. Soc.* 65, 114–125. doi:10.1175/1520-0477(1984)065<0114:tmoeaa>2.0.co;2

Lau, K.-M., Kim, K.-M., and Yang, S. (2000). Dynamical and Boundary Forcing Characteristics of Regional Components of the Asian Summer Monsoon. *J. Clim.* 13, 2461–2482. doi:10.1175/1520-0442(2000)013<2461:dabfco>2.0.co;2

Li, J., Mao, J., and Wu, G. (2015). A Case Study of the Impact of Boreal Summer Intraseasonal Oscillations on Yangtze Rainfall. *Clim. Dyn.* 44, 2683–2702. doi:10.1007/s00382-014-2425-9

Li, X., Gollan, G., Greatbatch, R. J., and Lu, R. (2018). Intraseasonal Variation of the East Asian Summer Monsoon Associated with the Madden-Julian Oscillation. *Atmos. Sci. Lett.* 19, e794. doi:10.1002/asl.794

Li, H., He, S., Fan, K., and Wang, H. (2019). Relationship between the Onset Date of the Meiyu and the South Asian Anticyclone in April and the Related Mechanisms. *Clim. Dyn.* 52, 209–226. doi:10.1007/s00382-018-4131-5

Li, L., Zhu, C., Zhang, R., and Liu, B. (2020). Roles of the Tibetan Plateau Vortices in the Record Meiyu Rainfall in 2020. *Atmos. Sci. Lett.* 22, e1017. doi:10.1002/asl.1017

Liang, P., and Ding, Y. (2012). Climatologic Characteristics of the Intraseasonal Oscillation of East Asian Meiyu. *Acta Meteorol. Sin.* 70, 418–435. 0577-6619/2012/70(3)-0418-35

Liu, Y., and Ding, Y. (2020). Characteristics and Possible Causes for the Extreme Meiyu in 2020. *Meteorol. Mon.* 46, 1393–1404. doi:10.7519/j.issn.1000-0526.2020.11.001

Liu, G., Wu, R., Zhang, Y., and Nan, S. (2014). The Summer Snow Cover Anomaly over the Tibetan Plateau and its Association with Simultaneous Precipitation over the Mei-Yu-Baiu Region. *Adv. Atmos. Sci.* 31, 755–764. doi:10.1007/s00376-013-3183-z

Liu, B., Zhu, C., Su, J., Ma, S., and Xu, K. (2019). Record-Breaking Northward Shift of the Western North Pacific Subtropical High in July 2018. *J. Meteorol. Soc. Jpn.* 97, 913–925. doi:10.2151/jmsj.2019-047

Liu, B., Yan, Y., Zhu, C., Ma, S., and Li, J. (2020). Record-Breaking Meiyu Rainfall Around the Yangtze River in 2020 Regulated by the Subseasonal Phase

Transition of the North Atlantic Oscillation. *Geophys. Res. Lett.* 47, e2020GL090342. doi:10.1029/2020GL090342

Ninomiya, K. (1984). Characteristics of Baiu Front as a Predominant Subtropical Front in the Summer Northern Hemisphere. *J. Meteorol. Soc. Jpn.* 62, 880–894. doi:10.2151/jmsj1965.62.6_880

Ninomiya, K. (2000). Large- and Meso-α-Scale Characteristics of Meiyu/Baiu Front Associated with Intense Rainfalls in 1-10 July 1991. *J. Meteorol. Soc. Jpn.* 78, 141–157. doi:10.2151/jmsj1965.78.2_141

Nitta, T. (1987). Convective Activities in the Tropical Western Pacific and Their Impact on the Northern Hemisphere Summer Circulation. *J. Meteorol. Soc. Jpn.* 65, 373–390. doi:10.2151/jmsj1965.65.3_373

Niu, R., Zhai, P., and Tan, G. (2021). Anomalous Features of Extreme Meiyu in 2020 over the Yangtze-Huai River Basin and Attribution to Large-Scale Circulations. *J. Meteorol. Res.* 35, 799–814. doi:10.1007/s13351-021-1018-x

Pan, X., Li, T., Sun, Y., and Zhu, Z. (2021). Cause of Extreme Heavy and Persistent Rainfall over Yangtze River in Summer 2020. *Adv. Atmos. Sci.* 38, 1994–2009. doi:10.1007/s00376-021-0433-3

Ronghui, H., and Yifang, W. (1989). The Influence of ENSO on the Summer Climate Change in China and its Mechanism. *Adv. Atmos. Sci.* 6, 21–32. doi:10.1007/BF02656915

Sampe, T., and Xie, S.-P. (2010). Large-Scale Dynamics of the Meiyu-Baiu Rainband: Environmental Forcing by the Westerly Jet*. *J. Clim.* 23, 113–134. doi:10.1175/2009JCLI3128.1

Schulz, M., and Mudelsee, M. (2002). REDFIT: Estimating Red-Noise Spectra Directly from Unevenly Spaced Paleoclimatic Time Series. *Comput. Geosci.* 28, 421–426. doi:10.1016/S0098-3004(01)00044-9

Song, Z., Zhu, C., Su, J., and Liu, B. (2016). Coupling Modes of Climatological Intraseasonal Oscillation in the East Asian Summer Monsoon. *J. Clim.* 29, 6363–6382. doi:10.1175/JCLI-D-15-0794.1

Takaya, Y., Ishikawa, I., Kobayashi, C., Endo, H., and Ose, T. (2020). Enhanced Meiyu-Baiu Rainfall in Early Summer 2020: Aftermath of the 2019 Super IOD Event. *Geophys. Res. Lett.* 47, e2020GL090671. doi:10.1029/2020GL090671

Tao, S., and Chen, L. (1987). "A Review of Recent Research on the East Asian Summer Monsoon in China," in *Monsoon Meteorology*. Editors C.-P. Chang and T. N. Krishnamurti (Oxford UP, NY: Oxford University Press), 60–92.

Torrence, C., and Compo, G. P. (1998). A Practical Guide to Wavelet Analysis. *Bull. Amer. Meteorol. Soc.* 79, 61–78. doi:10.1175/1520-0477(1998)079<0061:apgtwa>2.0.co;2

Trenberth, K. E. (1984). Signal versus Noise in the Southern Oscillation. *Mon. Wea. Rev.* 112, 326–332. doi:10.1175/1520-0493(1984)112<0326:svnits>2.0.co;2

Wang, J., He, J., Liu, X., and Wu, B. (2009). Interannual Variability of the Meiyu Onset over Yangtze-Huaihe River Valley and Analyses of its Previous strong Influence Signal. *Chin. Sci. Bull.* 54, 687–695. doi:10.1007/s11434-008-0534-8

Wang, B., Xiang, B., and Lee, J.-Y. (2013). Subtropical High Predictability Establishes a Promising Way for Monsoon and Tropical Storm Predictions. *Proc. Natl. Acad. Sci.* 110, 2718–2722. doi:10.1073/pnas.1214626110

Webster, P. J., Magaña, V. O., Palmer, T. N., Shukla, J., Tomas, R. A., Yanai, M., et al. (1998). Monsoons: Processes, Predictability, and the Prospects for Prediction. *J. Geophys. Res.* 103, 14451–14510. doi:10.1029/97jc02719

Xie, S.-P., Hu, K., Hafner, J., Tokinaga, H., Du, Y., Huang, G., et al. (2009). Indian Ocean Capacitor Effect on Indo-Western Pacific Climate during the Summer Following El Niño. *J. Clim.* 22, 730–747. doi:10.1175/2008JCLI2544.1

Xie, S.-P., Kosaka, Y., Du, Y., Hu, K., Chowdary, J. S., and Huang, G. (2016). Indo-western Pacific Ocean Capacitor and Coherent Climate Anomalies in post-ENSO Summer: A Review. *Adv. Atmos. Sci.* 33, 411–432. doi:10.1007/s00376-015-5192-6

Xu, M., Xu, H., and Ren, H. (2018). Influence of Kuroshio SST Front in the East China Sea on the Climatological Evolution of Meiyu Rainband. *Clim. Dyn.* 50, 1243–1266. doi:10.1007/s00382-017-3681-2

Xuan, S., Zhang, Q., and Sun, S. (2011). Anomalous Midsummer Rainfall in Yangtze River-Huaihe River Valleys and its Association with the East Asia westerly Jet. *Adv. Atmos. Sci.* 28, 387–397. doi:10.1007/s00376-010-0111-3

Yihui, D., and Chan, J. C. L. (2005). The East Asian Summer Monsoon: an Overview. *Meteorol. Atmos. Phys.* 89, 117–142. doi:10.1007/s00703-005-0125-z

Yim, S.-Y., Wang, B., Xing, W., and Lu, M.-M. (2015). Prediction of Meiyu Rainfall in Taiwan by Multi-lead Physical-Empirical Models. *Clim. Dyn.* 44, 3033–3042. doi:10.1007/s00382-014-2340-0

Yimin, L., and Guoxiong, W. (2004). Progress in the Study on the Formation of the Summertime Subtropical Anticyclone. *Adv. Atmos. Sci.* 21, 322–342. doi:10.1007/BF02915562

Zhang, Y., and Guo, L. (2005). Relationship between the Simulated East Asian westerly Jet Biases and Seasonal Evolution of Rainbelt over Eastern China. *Chin. Sci. Bull.* 50, 1503–1508. doi:10.1360/982004-361

Zhang, Y., Kuang, X., Guo, W., and Zhou, T. (2006). Seasonal Evolution of the Upper-tropospheric westerly Jet Core over East Asia. *Geophys. Res. Lett.* 33, 2006GL026377. doi:10.1029/2006GL026377

Zhou, T.-J., and Yu, R. (2005). Atmospheric Water Vapor Transport Associated with Typical Anomalous Summer Rainfall Patterns in China. *J. Geophys. Res.* 110, D08104. doi:10.1029/2004JD005413

Zhou, Z.-Q., Xie, S.-P., and Zhang, R. (2021). Historic Yangtze Flooding of 2020 Tied to Extreme Indian Ocean Conditions. *Proc. Natl. Acad. Sci. USA* 118, e2022255118. doi:10.1073/pnas.2022255118

Zhu, J., Huang, D.-Q., Zhang, Y.-C., Huang, A.-N., Kuang, X.-Y., and Huang, Y. (2013). Decadal Changes of Meiyu Rainfall Around 1991 and its Relationship with Two Types of ENSO. *J. Geophys. Res. Atmos.* 118, 9766–9777. doi:10.1002/jgrd.50779

Conflict of Interest: The authors declare that the research was conducted in the absence of any commercial or financial relationships that could be construed as a potential conflict of interest.

Publisher's Note: All claims expressed in this article are solely those of the authors and do not necessarily represent those of their affiliated organizations or those of the publisher, the editors, and the reviewers. Any product that may be evaluated in this article, or claim that may be made by its manufacturer, is not guaranteed or endorsed by the publisher.

frontiers in Earth Science

ORIGINAL RESEARCH
published: 22 February 2022
doi: 10.3389/feart.2022.801075

Research on the Characteristics and Influence Factors of Autumn Continuous Rain in Qinghai Province

Hanwei Yang[1,2], *Hongyan Shen*[3], *Yue Ma*[4], *Yawei Yang*[1,2], *Xiaojuan Wang*[5]* *and Guolin Feng*[6]

[1]Shanghai Climate Centre, Shanghai, China, [2]Key Laboratory of Cities Mitigation and Adaptation to Climate Change in Shanghai, Shanghai, China, [3]Qinghai Climate Centre, Qinghai, China, [4]Shanghai Jiading District Meteorological Bureau, Shanghai, China, [5]Changshu Institute of Technology, Suzhou, China, [6]National Climate Center (China), Beijing, China

Using daily precipitation data of national meteorological stations in Qinghai Province and reanalysis data, the main patterns of autumn continuous rain (ACR) are extracted, and key SST areas and circulation factors are searched for to analyze the possible effects on the seasonal and sub-seasonal predictability of ACR in Qinghai Province. The factors with strong precursors mainly include sea surface temperature (SST), Arctic vortex, and subtropical high. The influence of oceanic factors on ACR is relatively independent, while there is an interaction between atmospheric circulation factors. The precursors in spring are from the equatorial east-central Pacific for the main pattern with consistent precipitation distribution, and the Indian Ocean for the pattern with "saddle type" distribution. SST anomalies from the Pacific and Indian Oceans force different circulation patterns that can enhance meridional circulation over Europe-Asia and lead to different precipitation pattern of ACR. The signals from the Arctic vortex and subtropical high in June to July are indicative for ACR. The southward, westward and strong Arctic vortex, together with the south-westward extension of subtropical high over the Atlantic and Pacific can promote more ACR in Qinghai Province. Under the SST forcing and configuration of high and low latitude circulation, the meridional circulation continues to be weak, and the latitudinal circulation to be enhanced over the Eurasia in the early period, and the circulation pattern changes from type-W to type-C, which lead to positive anomaly of ACR in Qinghai Province.

Keywords: autumn continuous rain, main patterns of rainfall, sea surface temperature anomaly, atmospheric circulation, predictable factors

OPEN ACCESS

Edited by:
Sanjeev Kumar Jha,
Indian Institute of Science Education and Research, Bhopal, India

Reviewed by:
Xichen Li,
Institute of Atmospheric Physics (CAS), China
Maoqiu Jian,
Sun Yat-sen University, China

***Correspondence:**
Xiaojuan Wang
mouse0903@126.com

Specialty section:
This article was submitted to Atmospheric Science, a section of the journal Frontiers in Earth Science

Received: *24 October 2021*
Accepted: *21 January 2022*
Published: *22 February 2022*

Citation:
Yang H, Shen H, Ma Y, Yang Y, Wang X and Feng G (2022) Research on the Characteristics and Influence Factors of Autumn Continuous Rain in Qinghai Province. Front. Earth Sci. 10:801075. doi: 10.3389/feart.2022.801075

INTRODUCTION

Autumn continuous rainfall (lasting for days or even more than 10 days, ACR) in Qinghai province has the characteristics of high frequency and long persistency, which is one of the dominant meteorological disasters in Qinghai Province (Shi, 2003). It comes along with the harvest of highland barley, spring wheat, rape and other plateau crop in Qinghai Province. ACR not only adversely affects autumn harvest works, but also easily cause food crops to go moldy (Yuan and Yan, 2017). In addition, the lasting lower temperatures along with ACR will lead to the delay of crop fertility or growth (Fu et al., 2004). Thus, it has important practical significance to guide agricultural production, effectively avoid disaster form ACR, and increase the meteorological disaster prevention and mitigation capacity by carrying out prediction research to strengthen the short-term climate prediction ability of ACR in Qinghai province.

TABLE 1 | ACR disaster lever and its classified factors.

No	Disaster level	Classified factors
1	Light	D ≥ 5, S ≤ 2.5, $p \geq 10$, and d < 2
2	Heavy	D ≥ 10, S ≤ 2.5, $p \geq 20$, and d < 3

Note: D - process Rainy Day (unit: day) P - process Precipitation (unit: mm). S - Sunshine Hours per day (unit: hour) D–Rainless Day (unit: day).

ACR is always the study focus of many researchers. Some good research results have obtained in internal structure of cloud, the definition, climate characteristics and physical mechanism of ACR. Toit (2010) found that large concentrations of raindrops having diameters of less than 0.5 mm were observed in a few thousand feet above the ground by Doppler radar observation. Through the study on the relationship of the sunshine duration and cloud cover, the new Qinghai ACR monitoring index was revised, and space-time distribution and intensity change characteristics were analyzed (Li, et al., 2018). Sun et al. (2016) analyzed the climate characteristics of ACR in China, and found that the cumulative frequency is larger in upper and middle reaches of Yangtze River, and with the increase of strength, the region of greater value move toward the southwest from the southeast of China. In Qinghai, its climate characteristics of spatial-temporal variation was analyzed by Ma (2008), showing that the occurrences frequency of ACR is slowly decreasing, and it is more in southeast than northwest. In synoptic scale forecasting, A continuing heavy rain process occurred in west of Sichuan Basin from 22 September 2008 to 27 September 2008 was analyzed and predicted in wave-packet propagation diagnosis method, and concluded that the evolution of wave packet is meaningful for prediction (Xiao, et al., 2010). In short-term climatic forecasting, it is found that subtropical high over western Pacific and SST in the equatorial central and eastern Pacific has important effects on ACR in northwest of China by the study on typical cases occurred in 2000 and 2001 (Lin and Zhang, 2003). Based on the theory of isentropic potential vorticity, diagnostic analysis is carried out on a continuous rainfall process occurring in northwest of China in late May 2005 by Cheng et al. (2007), thinking that the continuous rainfall process is caused by continuous plateau low vortex and cold air separated from the north, and the positive vorticity area of isentropic surface is closely related to the precipitation area, which can be used as an important predictor.

However, in the forecasting and prediction of ACR in Qinghai Province, most of the previous studies focused on the synoptic scale (Xu et al., 2010). In the short-term climate prediction of ACR, the objective forecasting methods and tools is lacked. On the other hand, it is also a lack of in-depth understanding of the formation mechanism of ACR and intuitive conceptual model is still not given. Therefore, in this work, we use the daily precipitation data observed from 50 national meteorological stations in Qinghai Province to extract the main rainfall modes of ACR in Qinghai Province to analyze its spatial-temporal variation characteristic. The key SST areas and circulation factors related to ACR are then searched for to analyze their influence and indicative significance on ACR, and furthermore construct the conceptual model of impact factors. This study will expand the understanding of the mechanism of ACR in highland areas and lay a solid foundation for the development of a combined dynamical-statistical prediction method.

Data and Method

The quality controlled daily precipitation data from 2000 stations sorted out by National Climate Center (NCC) of China for 1961-2017 were used, from which 50 stations with good continuity in Qinghai Province were selected for analysis. The monthly mean geopotential height form NCEP/NCAR reanalysis from 1,000 hPa to 10 hPa (2.5 ° × 2.5 °, Kalnay et al., 1996), and monthly SST reanalysis data (2 ° × 2 °) from NOAA were selected. The SST and atmospheric circulation indices were extracted from the dataset of 142 circulation indices. The dataset is treated by the Climate Diagnostics and Prediction Division of NCC and widely used in research and monitoring/prediction work, including global subtropical high indices (strength, area and position indices), Arctic vortex indices (strength, area and position indices) in difference continent, SST indices in global key oceanic regions, ocean-atmosphere oscillation indices, circulation pattern indices, and other forcing indices (sea ice, snow cover). Details of the indices used can be found in the **Supplementary Material**.

ACR refers to the disaster of long-lasting cloudy and rainy weather with high air humidity, which affects crop ripening, harvesting, drying and other farming activities. Following the local meteorological disaster standard of Qinghai Province, the ACR events can be classified to light level and heavy level (**Table 1**). In this work, the ACR is defined including both light and heavy event as the process rainy days (D) ≥ 5 days, sunshine hours per day (S) < 2.5 h, the process precipitation (P) ≥ 10 mm, as well as rainless days (d) < 2 days.

We use the empirical orthogonal function (EOF) (Shi, 2009) to extract the main rainfall modes of ACR in Qinghai Province. Regression, correlation, partial correlation and anomaly analyses (Wei, 2007) were used to analyze the impact on seasonal and sub-seasonal precipitation of ACR. The square root of the coefficient of determination was used in the regression analysis to be tested according to the significance test of the correlation coefficient.

THE MAIN RAINFALL PATTERNS OF ACR IN QINGHAI PROVINCE

Based on the definition of ACR events, we count the number of station with ACR occurrence in each month from 1961 to 2017 (**Table 2**). During the period of 1961–2017, there were 2,157 stations of ACR, all of which occurred in August-November. Among them, it was most frequent in August-September,

TABLE 2 | The number of occurred stations in each month of ACR in Qinghai Province.

Month	Frequency (station)	Percentage (%)
August	898	41.6
September	982	45.5
October	274	12.7
November	3	0.1
Total	2,157	100

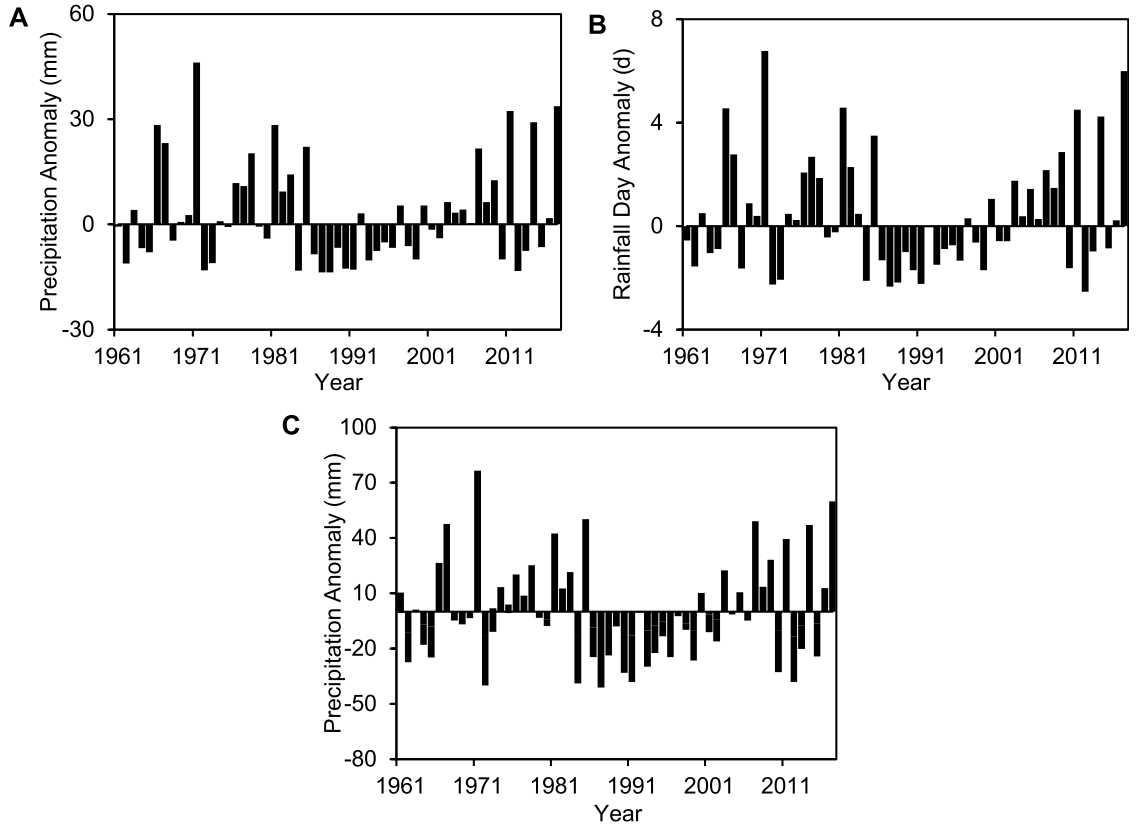

FIGURE 1 | Regional average precipitation anomaly **(A)**, unit: mm), rainday anomaly **(B)**, unit: day) and concerned domain **(C)**, unit: mm) average precipitation anomaly of ACR from August to September during 1961-2017.

reaching 898 (41.6%) and 982 (45.5%) stations respectively, and reaching nearly 90% accumulated. It was less frequent in October, with only 274 stations, accounting for 12.7%. It rarely occurred in November, with only 3 stations, accounting for 0.1%. Therefore, August-September is the time of high incidence of ACR in Qinghai Province, and the analysis below is mainly for this time period.

Using daily precipitation observations from 50 national meteorological stations in Qinghai Province, the anomaly of regional average continuous rainfall and rainday from August to September 1961-2017 are calculated (**Figure 1**). Similar variations are found in the time series of rainfall and rainday on both interannual and interdecadal scales. The correlation coefficient between the time series of rainfall and rainday in Qinghai Province reaches 0.97.

On the interdecadal scale, the amount of rainfall and the number of rainday in Qinghai Province have positive anomaly from the 1960s to the mid-1980s and from the beginning of the 21st century to the 2010s. While from the mid-1980s to the end of the 21st century, they have negative anomaly. On the interannual scale, the interannual variation of ACR is large, and there is obvious interannual difference.

The EOF analysis is conducted to extract the main rainfall patterns of ACR in Qinghai Province from 1961 to 2017. The explained variances of the first two modes reach 35.8 and 11.0% respectively, and the cumulative explained variance is 46.8%. It is tested that the first two modes of EOF analysis can pass the North test (North et al., 1982), meaning that the both modes are independent.

Mode EOF1 (**Figure 2A**) shows a spatial-consistent distribution pattern, which characterizes the main spatial pattern of ACR, and is similar to its climatic mean state. Also, the variation characteristics of its temporal coefficient (**Figure 2C**) is similar to those of the rainfall anomaly (**Figure 1A**), and the correlation coefficient between them can reach 0.95, i.e., the spatial distribution pattern of EOF1 can basically characterize its average condition.

Mode EOF2 (**Figure 2B**) is the second main mode after the climatic mean state, showing a "saddle-shaped" spatial distribution pattern. Two types of precipitation distribution are formed when coupled with the phase of time coefficients, namely southern rainfall type and East-West rainfall type.

Based on the distribution of EOF1 (**Figure 2A**), the anomalous center of ACR is located in the southeastern part of the Qinghai Province. The concerned domain is designated according to the spatial distribution (**Figure 3**) of the year-to-year variability by standard deviation (STD) > 30 mm. It can be found that its precipitation anomaly (**Figure 1C**) is similar with the region's, with the correlation coefficient reaching 0.94. Therefore, the rainfall of ACR can represent the temporal variations, which can be used to analyze the relationship between ACR and

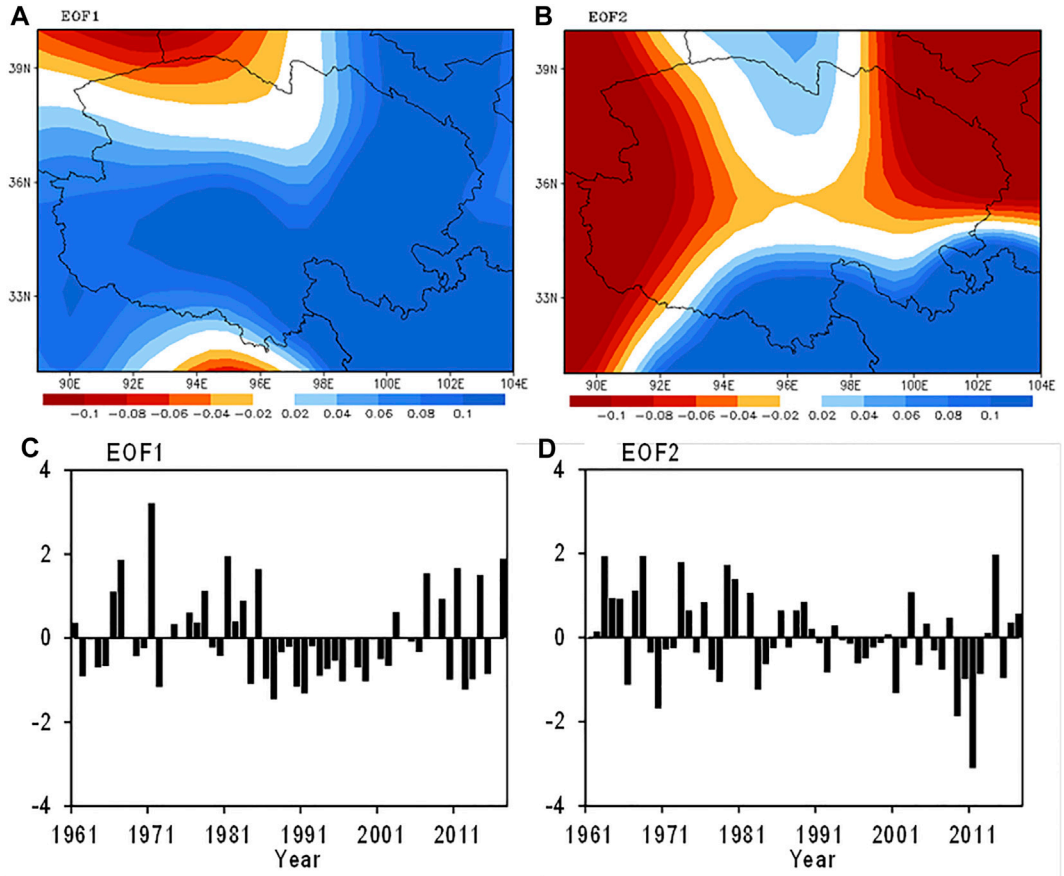

FIGURE 2 | Main modes and their time coefficients of ACR from 1961 to 2017. **(A)**: EOF1; **(B)**: EOF2; **(C)**: PC1; **(D)**: PC2.

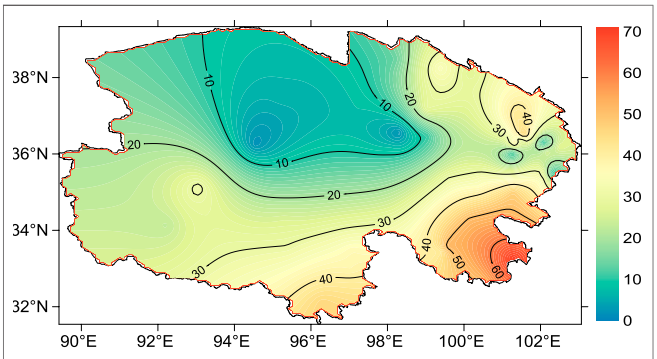

FIGURE 3 | Standard deviation of ACR in Qinghai Province during 1961-2017 (unit: mm).

ocean/atmospheric circulation, and exploring its seasonal and subseasonal predictability.

The Relationship Between ACR and SST

The oceanic forcing acts as one of the important driving factors affecting the occurrence and development of ACR in Qinghai Province. The temporal coefficients of the main rainfall patterns and the time series of ACR anomaly are correlated with SST and oceanic indexes from the ocean/circulation index dataset during the same and the previous period, respectively. To single out the effect of one factor on ACR, partial correlation analysis is also conducted and control variables are extracted by excluding factors of the same class. The key SST areas that influence the main rainfall distribution patterns are extracted, and their relationships are discussed to exploring their indicative effect.

The Relationship Between ACR and SST During the Same Period

A regression analysis was conducted using the temporal coefficients of the main modes of ACR on SST during the same period, respectively (**Figures 4C–F**). The key SST area for consistent precipitation distribution (EOF1) is located in the equatorial eastern central Pacific, and the relationship is significantly negatively correlated, i.e., the negative SST anomaly (La Niña event) in the equatorial eastern central Pacific is favorable to positive anomaly of ACR in Qinghai. The key SST region of "saddle-type" precipitation distribution (EOF2) is mainly located in the Indian Ocean, and presenting a significant negative correlation, i.e., the higher SST, especially in the western and southeastern Indian Ocean, is favorable to more ACR Qinghai during the same period.

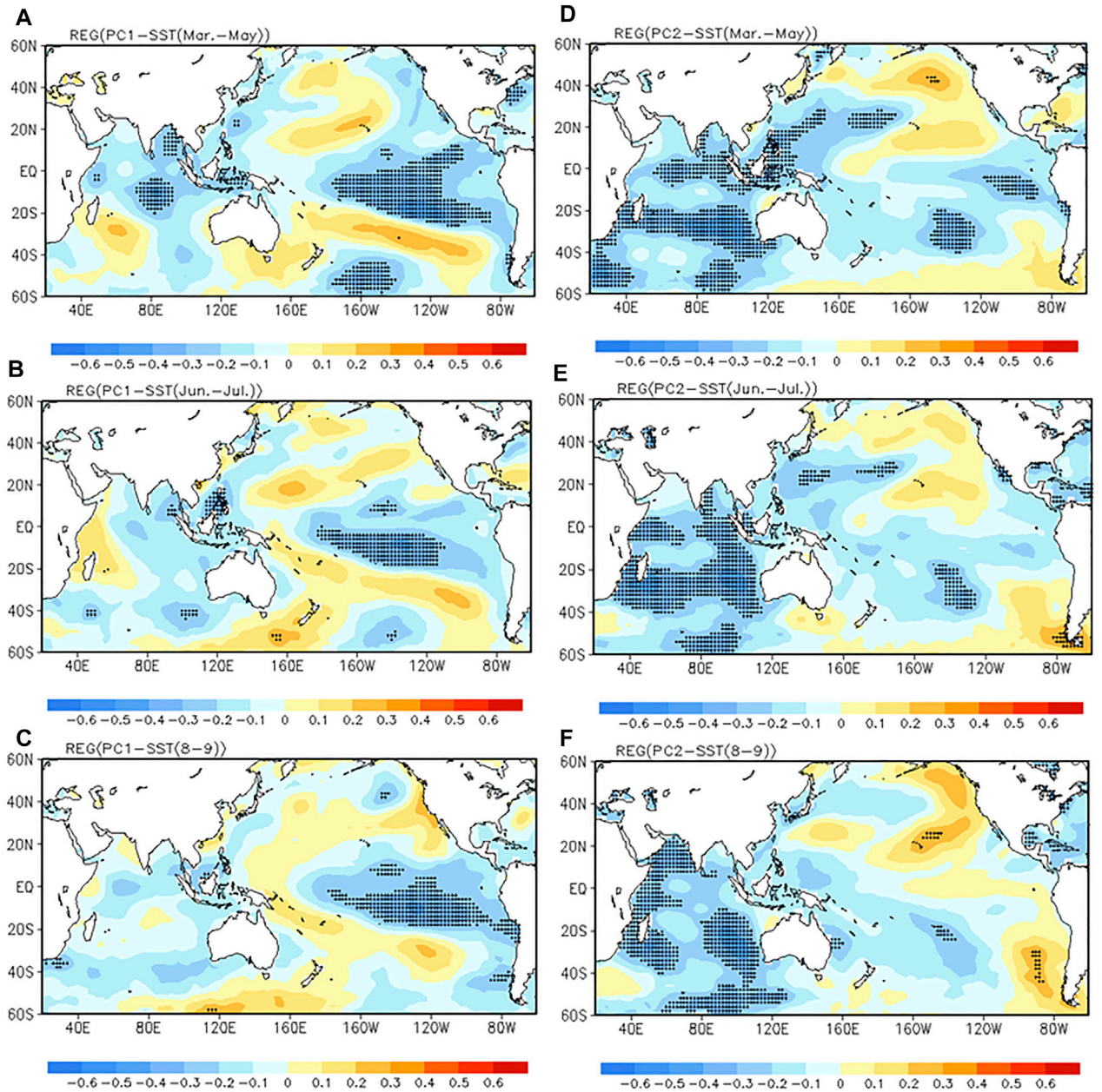

FIGURE 4 | Regressions on global SST in spring **(A,D)**, summer **(B,E)** and August-September **(C,F)** of PCs during 1961–2017. **(A–C)**: PC1; **(D–F)**: PC2; +: pass the significant level of 0.05).

The SST indices are selected from the index dataset, and correlated with the time series of ACR anomaly in August, September, and August-September from 1961 to 2017, respectively (**Table 3**). The SSTs of the same period in different areas have different indications for the sub-seasonal rainfall of ACR. The key area influencing the ACR in August is mainly from the tropical Indian Ocean, which shows a significant positive correlation between the TIOD with the rainfall of ACR. In September, the key areas shift to the Pacific Ocean, including NINO A and the Kuroshio region, both of which show a significant negative correlation. From the result of partial correlation, the correlation coefficients by excluding the influence for each other do not change, meaning that the effects from the equatorial eastern central Pacific and tropical Indian Ocean on ACR are independent.

The Relationship Between ACR and SST During the Previous Period

Figures 4A,B shows the regression of EOF1 temporal coefficients on earlier global SST. It can be found that the early ocean signal in spring mainly comes from the equatorial central-east Pacific and the tropical central Indian Ocean. In summer, the precursor of the equatorial central-east Pacific narrows to the central region, and the Indian

TABLE 3 | Correlation and partial correlation coefficients between ACR and the oceanic indexes in the same period from 1961 to 2017.

No	Oceanic index	Aut.-Sep	Aut	Sep.
1	SST anomaly in NINO A region	— —	— —	–0.28 (–0.28)
2	SST anomaly in Kuroshio region	— —	— —	–0.28 (–0.28)
3	TIOD index	— —	0.28 (0.28)	— —

Note: The partial correlation coefficient is indicated in parentheses. Only the correlation coefficients passing the 0.05 significance level are presented.

TABLE 4 | Correlation and partial correlation coefficients between ACR and ocean indexes during the previous period from 1961 to 2017.

ACR	Ocean index	Mar.-May	Jun.-jul	Mar.	Apr.	May	Jun.	Jul.
Aug.-Sep	TIOD index	0.28	—	—	—	0.28 (0.24)	— (0.25)	—
	SIOD index	—	—	—	0.31 (0.28)	—	—	—
Aug.	TIOD index	—	0.31 (0.35)	—	—	0.26 (0.25)	0.33 (0.35)	0.27 (0.31)
	SIOD index	—	—	—	0.26	—	—	—
Sep.	NINO SST index in region 1 + 2	—	—	–0.27 (–0.28)	—	—	—	—
	NINO SST index in region 3	—	—	–0.33 (–0.30)	—	—	—	—
	NWP warm pool index	—	—	–0.32 (–0.30)	—	—	—	—
	SOI	0.27	—	—	0.28	—	—	—

Note: The partial correlation coefficient is indicated in parentheses. Only the correlation coefficients that passed the 0.05 significance level test are represented in the table.

Ocean signal weakens. These relationships all show a significant negative correlation, i.e., the lower SST in the early period favors more precipitation in the main pattern of the consistent pattern of ACR. For EOF2 (**Figures 4D,E**), the precursory signal for the "saddle-type" precipitation distribution is mainly located in the Indian Ocean, and it can last from spring to summer. In addition, there is also some gradually weakening signal in the Kuroshio region from spring to summer.

The SST of tropical Indian Ocean in spring is indicative to the ACR in August-September. A positively correlated relationship is found between TIOD index and ACR. However, in sub-seasonal scale, the relationship from global SST is different. It is similar for ACR in August with a stronger signal in the tropical Indian Ocean, which can be advanced to the southern Indian Ocean in april and shift to the tropical Indian Ocean in May. While, the indicative signal of ACR in September appears in the equatorial east-central Pacific Ocean. Especially in March-April, the SST in NINO region shows a significant negative correlation with it. In addition, under the influence of SST, Southern Oscillation is also one of the indicative signals of the September ACR with significant positive correlation (**Table 4**). After excluding the influence from other oceans, the partial correlation coefficient can also pass the 0.05 significance level. Thus, the signals from tropical Indian Ocean and the equatorial east-central Pacific Ocean are with indicative significance and independence in the previous period.

Influence Mechanism of SST on ACR

The SST anomaly in the equatorial eastern central Pacific and the tropical Indian Ocean correspond to precipitation pattern of EOF1 and EOF2 respectively, and their precursor signals can be advanced to spring. In order to explore the impact of SSTs on the ACR, composite analysis is conducted by extracting typical years with STD >1.7 of PC1 (1967, 1971, 1981, and 2017) and PC2 (1963, 1968, 1973, 1979, and 2014).

Consistent with the correlation analysis, a strong La Niña event can be found from spring to September for EOF1 (**Figure 5A**). The SST anomaly in the equatorial eastern central Pacific will cause anomalous circulation over the middle and high latitudes of Eurasia, forming a strong positive anomaly over Europe and negative anomaly over Asia (**Figure 5C**). This circulation pattern will strengthen the meridional circulation over the Eurasian. At the same time, the negative anomaly of SST is strong enough to extend to Equatorial Western Pacific, and causing a weak and easterly western Pacific subtropical high (WPSH) by weakening the Hadley circulation. Thus, it forms a warm advection over the main rainfall region of the ACR in Qinghai Province (**Figure 6A**), and brings water vapor from Indian Ocean (**Figure 6C**) to leading the precipitation pattern of EOF1.

For the precipitation pattern of EOF2, the consistent negative anomaly of SST is also can be found in the tropical Indian Ocean (**Figure 5B**). The circulation anomaly caused is different with a La Niña event, forming a "+, -, +,-" pattern over the middle and high latitudes of Europe-Asia-Pacific (**Figure 5D**). This circulation pattern can also strengthen the meridional circulation over the Eurasian, especially the cyclonic circulation anomaly formed over north of Qinghai Province. Under this circulation pattern, water vapor from the Indian and Pacific Oceans mainly affects the eastern part of China and cannot be transported to Qinghai Province. The precipitation pattern of EOF2 is mainly due to the cyclonic circulation anomaly, which forms a cold advection over Qinghai Province and brings water vapor from the Arctic (**Figures 6B–D**).

Therefore, the enhanced meridional circulation is necessary to cause the ACR in Qinghai. However, SST anomalies from the

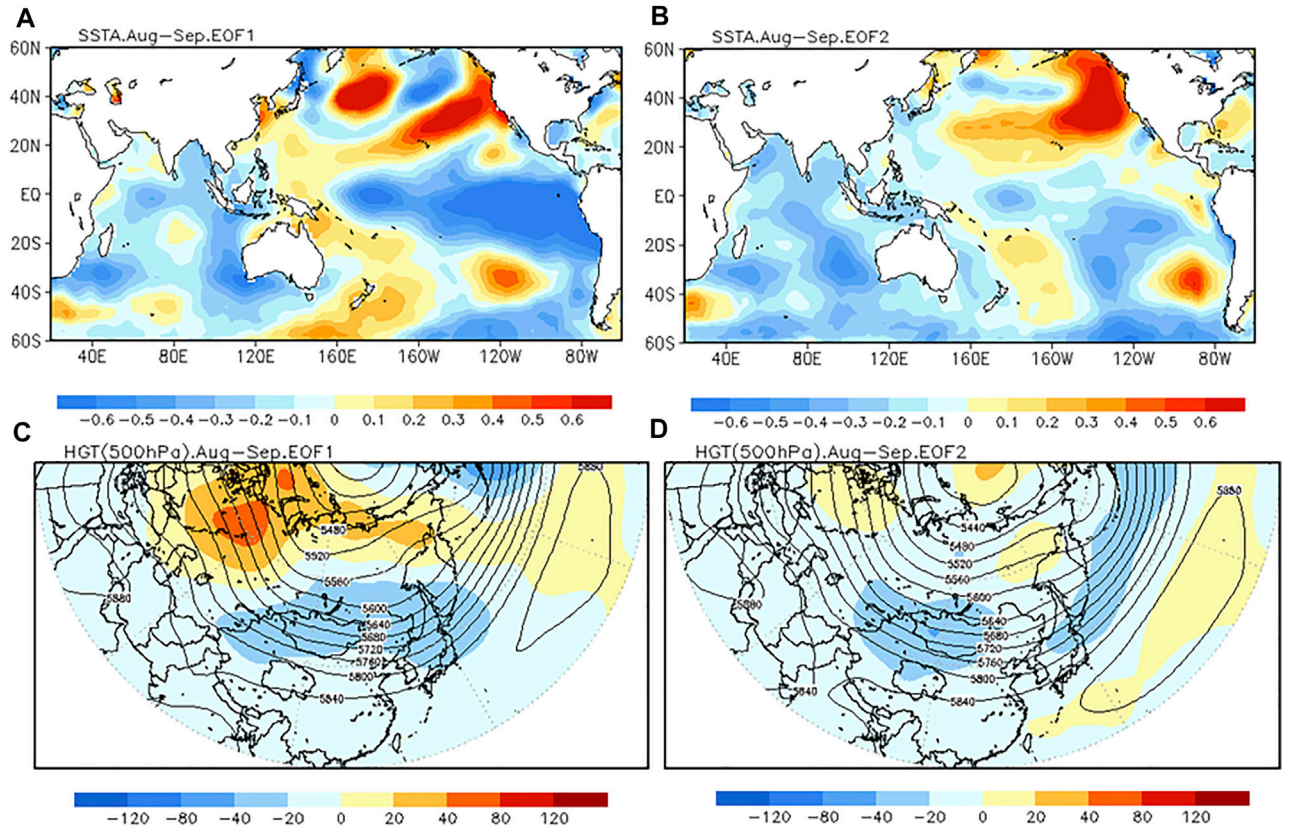

FIGURE 5 | Composite analysis of SST and geopotential height in 500 hPa for EOF1 **(A,C)** and EOF2 **(B,D)**. **(A,B)**: SST anomaly, unit: ˚C; **(C,D)**: geopotential height, contour line: geopotential height, shading: geopotential height anomaly, unit: gpm).

Pacific and Indian Oceans force different circulation patterns that lead to different precipitation pattern of ACR.

IMPACT OF ATMOSPHERIC CIRCULATION ON ACR IN QINGHAI PROVINCE

The atmospheric circulation configuration between high and low levels, north and south latitudes forced by SST anomaly are the direct factors leading to the ACR anomaly. Similar to the SST, the possible impact on seasonal and sub-seasonal ACR of atmospheric circulation is analyzed to explore their indicative effects.

The Relationship Between ACR and Atmospheric Circulation During the Same Period

A regression analysis was conducted using the temporal coefficients of the main modes of ACR with the 500hPa geopotential height field during the same period. The key area, which can affect the consistent pattern of ACR by causing the change of the trough and ridge over Qinghai Province, is located in the middle and high latitudes of the upper Eurasian continent showing a significant positive correlation (**Figure 7A**). The remote correlation wave train with significant correlation to the "saddle type" precipitation distribution pattern are located at middle and high latitudes, forming "-, +, -, +, -" from Central Asia to the west coast of North America, and this wave train plays an important role in the "saddle type" distribution of ACR (**Figure 7B**).

The atmospheric circulation that have important influence on ACR in the same period mainly come from subtropical high (No. 1–8) and high latitude circulation and remote correlation circulation pattern (No. 9–11) in the northern hemisphere (**Table 5**), and presenting different characteristics in seasonal and sub-seasonal scale. In August, the ACR is mainly positively correlated with the Pacific subtropical high pressure, especially over the eastern Pacific Ocean, while in September it is negatively correlated with the northern boundary of subtropical high over the North American-Atlantic.

The relationships between the high latitude circulation/remote correlation circulation pattern in the northern hemisphere and the ACR are mainly reflected in the seasonal scale, including the area of the polar vortex over the Atlantic-Europe (negative correlation), the Pacific Transition Pattern (PT) remote correlation circulation pattern (positive correlation), and C-type circulation over the Atlantic-Europe (positive correlation). Therefore, The circulation configuration with strong subtropical high over the Pacific, southward subtropical

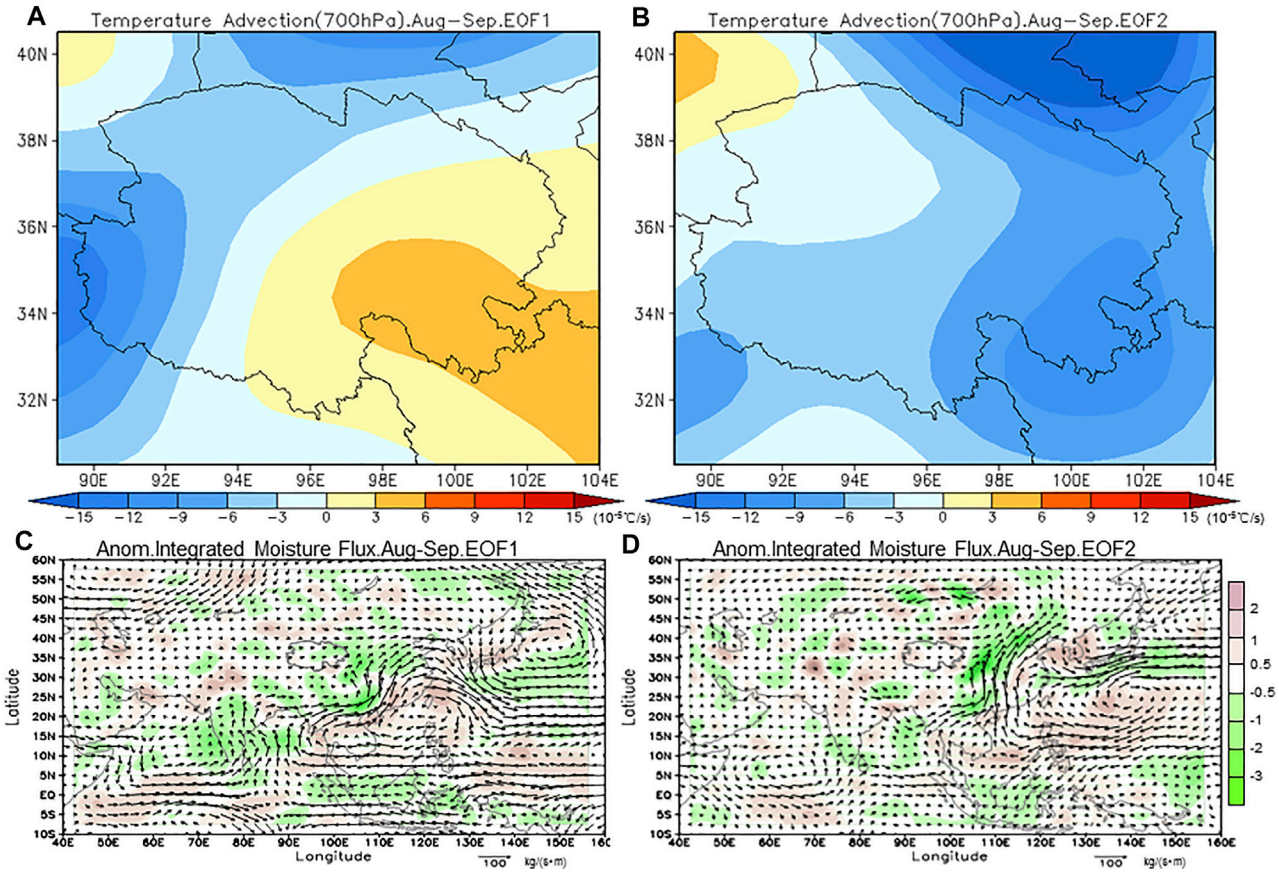

FIGURE 6 | Composite analysis of temperature advection in 700 hPa and integrated moisture flux anomaly (1000 hPa–300 hPa) for EOF1 **(A,C)** and EOF2 **(B,D)**. **(A,B)**: temperature advection, unit: 10^{-5} °C/s; **(C,D)**: integrated moisture flux anomaly, vector: moisture transport anomaly, unit: kg/s^{-1}•m^{-1}; shading: convergence and divergence anomaly field of moisture, unit: 10^{-5}kg/s^{-1}•m^{-2}).

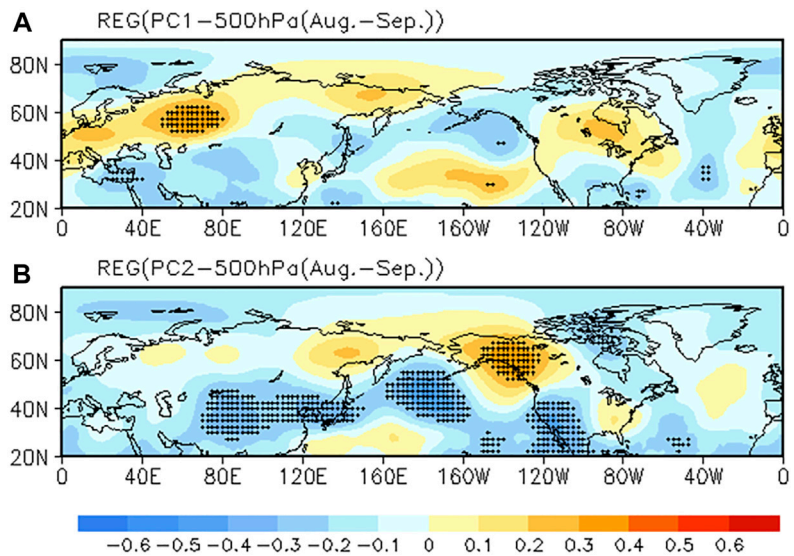

FIGURE 7 | Regressions on 500 hPa geopotential height field of temporal coefficients of ACR in August-September during the 1961–2017 period.**(A)**: PC1; **(B)**: PC2; +: pass the significant level of 0.05).

TABLE 5 | Correlation and partial correlation coefficients between ACR and atmospheric circulation indexes in the same period from 1961 to 2017.

No	Atmospheric circulation index	Aug-sep	Aug.	Sep.
1	Subtropical High Area index over the Eastern Pacific	−−	0.32 (0.40)	−−
2	Subtropical High Area index over the Pacific	−−	0.28 (0.36)	−−
3	Subtropical High Intensity index over the Eastern Pacific	−−	0.34 (0.41)	−−
4	Subtropical High Intensity index over the Pacific	−−	0.30 (0.37)	−−
5	Ridge Line of Subtropical High over the Eastern Pacific	0.34 (0.37)	−−	−−
6	Northern boundary of Subtropical High over the northern hemisphere	−−	0.31 (0.34)	−−
7	Northern boundary of Subtropical High over the Atlantic	-0.41 (-0.41)	−−	–0.43 (–0.41)
8	Northern boundary of Subtropical High over the North American-Atlantic	-0.41 (-0.41)	−−	–0.43 (–0.41)
9	Area index of the Arctic vortex over the Atlantic-Europe	-0.27	−−	–0.37 (–0.28)
10	Pacific Transition Pattern (PT)	0.28	−− (0.31)	−−
11	C-type circulation over the Atlantic-Europe	0.30 (0.26)	−−	−−

Note: The partial correlation coefficient is indicated in parentheses. Only the correlation coefficients that passed the 0.05 significance level test are represented in the table.

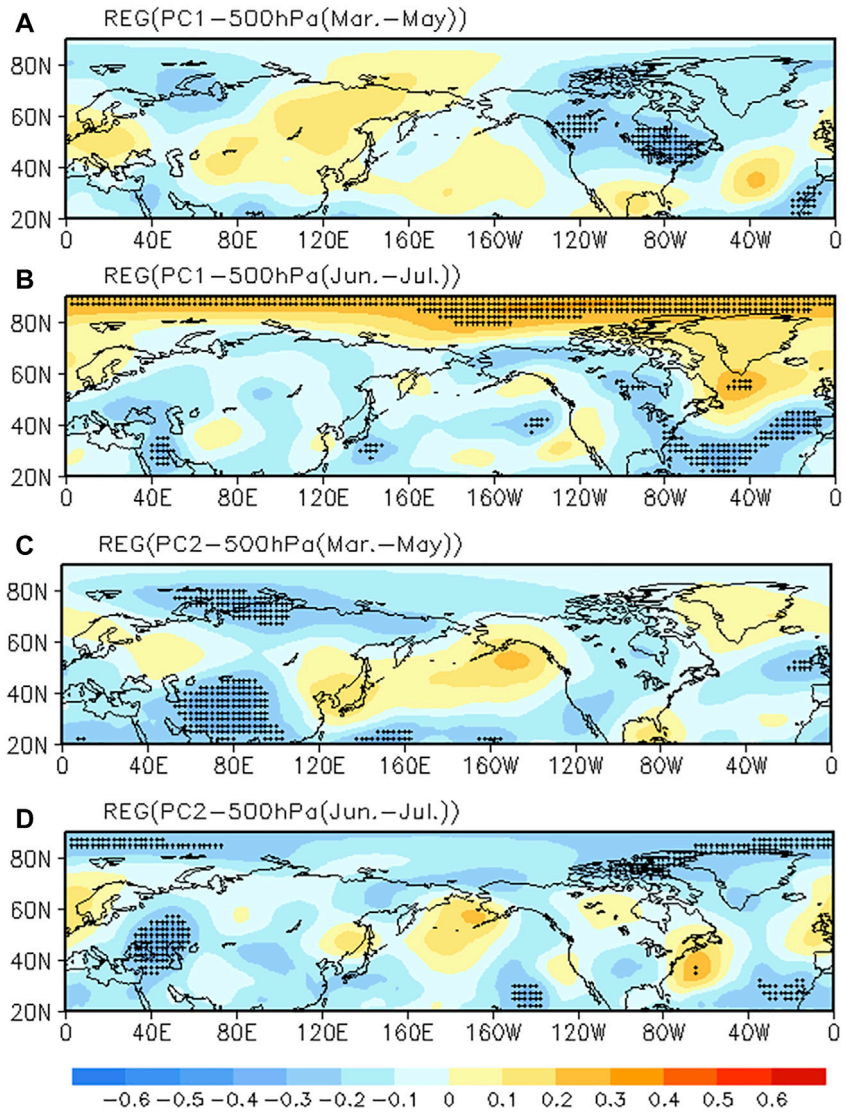

FIGURE 8 | Regressions on 500hPa geopotential height fields during the previous period of PC1 **(A,B)** and PC2 **(C,D)** from 1961 to 2017. **(A,C)**: March-May; **(B,D)**: June-July; +: pass the significant level of 0.05.

TABLE 6 | Correlation and partial correlation coefficients between ACR and atmospheric circulation indexes in previous period from 1961 to 2017.

No	Atmospheric circulation index	Mar.-May	Jun.-jul	Mar.	Apr.	May	Jun.	Jul.
1	Ridge line of subtropical high over the Atlantic	—	—	—	—	—	−0.28 (−0.33)	—
2	Northern boundary of Subtropical High over the Pacific	—	—	—	—	−0.27 (−0.29)	—	—
3	Ridge point of subtropical high over the western Pacific	—	—	—	—	−0.29 (−0.31)	—	—
4	Area index of the Arctic vortex over the Asia	—	—	—	−0.27 (−0.30)	—	—	—
5	Area index of the Arctic vortex over the Atlantic-Europe	—	—	—	—	—	0.33 (−0.26)	—
6	Intensity index of the Arctic vortex over the Asia	—	—	—	—	—	—	0.30
7	Latitudinal position of Arctic vortex center	—	−0.28	—	—	—	—	-0.27
8	Intensity index of the Arctic vortex center	—	0.29	—	—	—	—	—
9	AO index	—	—	—	—	—	−0.29 (−0.25)	—
10	Meridional Circulation Index over Eurasia	−0.35 (−0.35)	−0.29	−0.34 (−0.36)	—	—	−0.33 (−0.26)	—
11	Latitudinal Circulation Index over Asia	—	—	—	—	—	—	0.29
12	Meridional Circulation Index over Asia	–	−0.28	—	-0.26 (-0.27)	—	−0.31 (−0.26)	—
13	W-type circulation pattern over Atlantic-Europe	—	0.28	—	—	—	0.26	—
14	E-type circulation pattern over Atlantic-Europe	—	-0.30	—	—	—	−0.32 (−0.25)	—

Note: The partial correlation coefficient is indicated in parentheses. Only the correlation coefficients that passed the 0.05 significance level test are represented in the table.

high over the North American-Atlantic, lower area of polar vortex over the Atlantic-Europe, positive phase of PT circulation over the western Pacific, and the C-type circulation dominating the Atlantic-Europe, is conducive to the transmission and stable maintenance of the trough and ridge from upstream to the downstream Qinghai, leading to more ACR.

After excluding the influence from each other of the key atmospheric circulation factors, the partial correlation coefficients of subtropical high has improved, and other's decreased. Therefore, subtropical high pressure is probably the most important circulation factor, which interacts with other circulation factors, and thus affects the ACR.

The Relationship Between ACR in Qinghai Province and Atmospheric Circulation During the Previous Period

The areas significantly correlated with PC1 in the 500hPa geopotential height field in spring are mainly located over the North American continent at middle and high latitudes, which

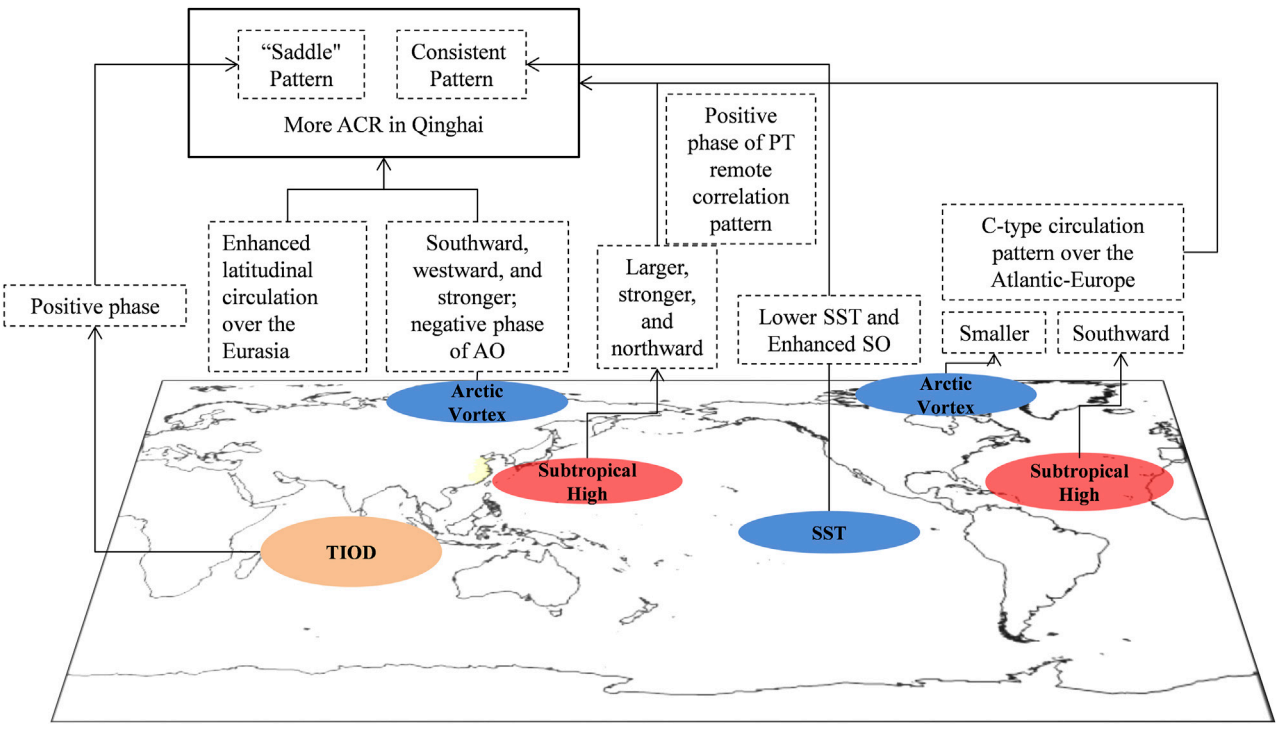

FIGURE 9 | Diagnostic model of ACR in Qinghai Province.

show significant negative correlations. By in June-July, these areas are shifted eastward and located over the northern Atlantic Ocean. In addition, the geopotential height over the Arctic in June-July shows a significant positive correlation with the EOF1 (**Figures 8A,B**).

In spring, the key areas of EOF2 in 500hPa geopotential height field are located in the Eurasia, showing a "saddle type" distribution with negative correlation. In June-July, the correlation circulation pattern is adjusted, and the areas shift to the upstream area of Qinghai Province and the Arctic, both of which show significant negative correlation (**Figures 8C,D**).

On seasonal and sub-seasonal time scales, the indications of atmospheric circulation in previous period for ACR are relatively similar. The predictable factors can be divided into four categories: subtropical high, Arctic vortex/Oscillation, Eurasian meridional/latitudinal circulation and Atlantic-Europe circulation pattern (**Table 6**). The earlier Subtropical high and Arctic vortex/Oscillation in June-July are the main factors affecting the ACR. It is favorable to more ACR under the circulation configuration in June-July like: the location of the center of the Arctic vortex is southward and strong; the area of the Arctic vortex is large in the Atlantic-Europe region and small in the Asian region; the AO shows negative phase; the subtropical high is southward and the westward extension over western Pacific; in Eurasia, the meridional circulation weaks, and the latitudinal circulation strengthens; in Atlantic-Europe, it is dominated by the latitudinal westerly circulation pattern (W-type). From the result of partial correlation analysis, different key circulation factors are interacting with each other, just like the same period.

Obviously, subtropical High, Arctic vortex, and circulation pattern over Atlantic-Eurasian are the key factors affecting on ACR in Qinghai Province. The position and intensity of subtropical high especially over west Pacific and north Indian Ocean influenced by sea-air oscillation both in Pacific Ocean and Indian Ocean will lead to anomaly of water vapor transport (Chao and Zhou, 2014; Li et al., 2014). Arctic vortex, and circulation pattern over Atlantic-Eurasian forcing by SST anomaly in Pacific Ocean and Indian Ocean (Calvo et al., 2009; Gu et al., 2017) with teleconnection wave train will lead to anomaly of clod/warm advection and the structure of atmospheric baroclinicity (Lin and Zhang, 2003).

CONCLUSION AND DISCUSSION

ACR precipitation mainly appears in the consistent type and "saddle-type" distribution across the Qinghai Province. SST and atmospheric circulation are important indicators of both seasonal and sub-seasonal rainfall of ACR. Since the ACR often occurs spanning the high summer and early autumn, the impacts on ACR from SST and atmospheric circulation vary.

In general, the significant factors for ACR include SST, Arctic vortex, subtropical high, Atlantic-Europe circulation pattern and Eurasian meridional/latitudinal circulation (**Figure 9**). The influence of oceanic factors on ACR is relatively independent, while there is an interaction between atmospheric circulation factors. In spring, the indicative signals appeared in the equatorial central eastern pacific and the tropical Indian Ocean, with the former corresponding to consistent precipitation and the latter corresponding to "saddle-type" precipitation. In terms of sub-seasonal precipitation, the tropical Indian Ocean and the equatorial central eastern pacific correspond to ACR in August and September, respectively. In the tropical Indian Ocean, its early signal can be advanced to the southern Indian Ocean in april, and it transfers to the tropical Indian Ocean in May. SST anomalies from the Pacific and Indian Oceans force different circulation patterns that can enhance meridional circulation over Europe-Asia and lead to different precipitation pattern of ACR. In June-July, the indicative signal for ACR comes from subtropical high and Arctic vortex/Oscillation. Under the north-south circulation configuration, the meridional circulation continues to be weak, and the latitudinal circulation strengthens in Eurasia, and it is dominated by the latitudinal westerly circulation pattern in Atlantic-Europe, which is favorable to more ACR in Qinghai Province.

In this work, the main patterns of ACR are extracted, and the possible impact is analyzed to explore the indication of global SST and atmospheric circulation on seasonal and sub-seasonal precipitation of ACR. This is only a basic work. The underlying mechanisms effecting on ACR of each factors are still not clear enough, and need specialized research to explore the dynamic and thermal process in the future. Besides, to carry out quantitative and refined short-term climate prediction on seasonal and sub-seasonal scales, it is necessary to further integrate the diagnostic analysis and the dynamical model, effectively revise the dynamical model using key factors from SST and atmospheric circulation, and carry out combined dynamical-statistical forecast tests (Feng et al., 2013) to improve the ability of short-term climate prediction on seasonal and sub-seasonal precipitation of ACR.

DATA AVAILABILITY STATEMENT

The original contributions presented in the study are included in the article/**Supplementary Material**, further inquiries can be directed to the corresponding author.

AUTHOR CONTRIBUTIONS

HY: writing original draft preparation. HS: providing some of the required data. YM and YY: visualization. XW and GF: review and editing. All authors contributed to the article and approved the submitted version.

FUNDING

This work was funded by the National Key Research and Development Program of China (Grant No. 2018YFA0606301), the National Natural Science Foundation of China Project (Grant Nos. 42075057 and 41875100) and Natural Science Foundation of Shanghai (Grant No. 21ZR1457600).

SUPPLEMENTARY MATERIAL

The Supplementary Material for this article can be found online at: https://www.frontiersin.org/articles/10.3389/feart.2022.801075/full#supplementary-material

REFERENCES

Calvo, N., Giorgetta, M. A., Garcia-Herrera, R., and Manzini, E. (2009). Nonlinearity of the Combined Warm ENSO and QBO Effects on the Northern Hemisphere Polar Vortex in MAECHAM5 Simulations. *J. Geophys. Res.* 114, D13109. doi:10.1029/2008JD011445

Chao, H., and Zhou, T. (2014). The Two Interannual Variability Modes of the Western north pacific Subtropical High Simulated by 28 Cmip5-Amip Models. *Clim. Dyn.* 43 (9-10), 2455–2469. doi:10.1007/s00382-014-2068-x

Cheng, P., Zhao, Q. Y., Li, J. P., and Sun, G. (2007). Analysis of Isentropic Potential Vorticity of a Continuous Rain Process in the East of Northwest China. *Arid Meteorology* 25 (1), 58–62. doi:10.3969/j.issn.1006-7639.2007.01.011

Feng, G. L., Zhao, J. H., and Zhi, R. (2013). Recent Progress on the Objective and Quantifiable Forecast of Summer Precipitation Based on Dynamical-Statistical Method. *J. Appl. Meteorol. Sci.* 24 (6), 656–665.

Fu, Y., Li, F. X., and Guo, G. (2004). Natural Disasters in Qinghai Province and Characteristics Analysis. *Earthquake Res. Plateau* 16 (4), 59–67. doi:10.3969/j.issn.1005-586X.2004.04.010

Gu, B., Zheng, Z., Feng, G., and Wang, X. (2017). Interdecadal Transition in the Relationship between the Western pacific Subtropical High and Sea Surface Temperature. *Int. J. Climatol.* 37 (5), 2667–2678. doi:10.1002/joc.4872

Kalnay, E., Kanamitsu, M., Kistler, R., Collins, W., Deaven, D., Gandin, L., et al. (1996). The NCEP/NCAR 40-year Reanalysis Project. *Bull. Amer. Meteorol. Soc.* 77 (3), 437–471. doi:10.1175/1520-0477(1996)077<0437:tnyrp>2.0.co;2

Li, W. Z., Tong, Y. Z., and Yang, Y. H. (2018). Monitoring Indicators of Continuous Rain in Qinghai: Revision and Spatial-Temporal Characteristics. *Chin. Agric. Sci. Bull.* 34 (31), 125–130.

Li, X., Zhou, W., Chen, D., Li, C., and Song, J. (2014). Water Vapor Transport and Moisture Budget over Eastern China: Remote Forcing from the Two Types of El Niño. *J. Clim.* 27 (23), 8778–8792. doi:10.1175/jcli-d-14-00049.1

Lin, S., and Zhang, K. J. (2003). Analysis of Continuous Autumn Rain in Northwest China in 2000 and 2001. *Meteorol. Monthly* 29 (2), 34–38.

Ma, Z. L. (2008). Analysis of the Weather Characteristics of Autumn Rainfall in Qinghai Province. *Qinghai Sci. Tech.* 2, 31–33. doi:10.3969/j.issn.1005-9393.2008.02.013

North, G. R., Bell, T. L., and Cahalan, R. F. (1982). Sampling Errors in the Estimation of Empirical Orthogonal Functions. *Mon. Wea Rev.* 110, 699–706.

Shi, G. S. (2003). *Natural Hazards in Qinghai Province*. Xining: Qinghai People's Press.

Shi, N. (2009). *Meteorological Statistics and Forecast*. Beijing: China Meteorological Press.

Sun, Z. B., Huang, Y. Y., and Ni, D. H. (2016). Climate and Circulation Characteristics of Continuous Autumn Rain in China. *Trans. Atmos. Sci.* 39 (4), 480–489. doi:10.13878/j.cnki.dqkxxb.20140413001

Toit, P. (2010). Doppler Radar Observation of Drop Sizes in Continuous Rain. *J. Appl. Meteorology* 6, 1082–1087.

Wei, F. Y. (2007). *Modern Statistical Diagnosis and Prediction Technology on Climate*. Beijing: China Meteorological Press.

Xiao Tiangui, T., Jin Ronghua, R., Wang Minghuan, M., and Jia Lha, fnm. (2010). in Wave energy signal features and prediction research of the continuing heavy rain process in Sichuan Basin (IEEE). doi:10.1109/mace.2010.5535482

Xu, Y. X., Dangzhou, Z. M., and Pei, S. Y. (2010). Research on Weather Forecasting Service for Continuous Rainy Weather along Qinghai Section of Qinghai-Tibet Railway. *Qinghai Sci. Tech.* 17 (5), 58–61. doi:10.3969/j.issn.1005-9393.2010.05.020

Yuan, M. K., and Yan, Y. (2017). Influence of Continuous Rainy Weather on Agriculture in Chuzhou. *Agric. Disaster Res.* 7 (4-5), 43–45. doi:10.19383/j.cnki.nyzhyj.2017.04-05.016

Conflict of Interest: The authors declare that the research was conducted in the absence of any commercial or financial relationships that could be construed as a potential conflict of interest.

frontiers in Earth Science

ORIGINAL RESEARCH
published: 04 March 2022
doi: 10.3389/feart.2022.827601

Effects of Topography and Latent Heat on the Evolution of a Mesoscale Dual-Core Southwest Vortex Over Sichuan Basin, China

Zhenzhen Wu[1,2], Haiwen Liu[3], Kelvin T. F. Chan[1,2,4], Kaijun Wu[3], Wenlong Zhang[5] and Donghai Wang[1,2]*

[1]School of Atmospheric Sciences, Sun Yat-sen University, Southern Marine Science and Engineering Guangdong Laboratory (Zhuhai), Zhuhai, China, [2]Guangdong Province Key Laboratory for Climate Change and Natural Disaster Studies, Sun Yat-sen University, Zhuhai, China, [3]Department of Aviation Meteorology, Civil Aviation University of China, Tianjin, China, [4]Key Laboratory of Tropical Atmosphere-Ocean System, Ministry of Education, Zhuhai, China, [5]Institute of Urban Meteorology, CMA, Beijing, China

The southwest vortex (SWV), a low-pressure system bringing severe rainfall in southwest China, is one of the most important synoptic systems in China. Using both the National Centers for Environmental Prediction Final (NCEP-FNL) operational global analysis dataset and the Weather Research and Forecasting (WRF) model simulation, a sophisticated SWV with dual-core structure (DCSWV) over the Sichuan Basin in 2010 was studied. The DCSWV system consisted of two cores, one near Leshan City (named "C1") and another near Langzhong City (named "C2"). The high-resolution WRF model reproduced the life cycle of the DCSWV well. The diagnostic analysis of the vorticity budget indicated that the stretching and tilting terms played important roles in the development stage of "C1", while the stretching and vertical advection of vorticity were the major contributors to the formation and development stage of "C2", which implied the importance of moisture convergence and ascending motion. Sensitivity experiments showed that the DCSWV was closely associated with the release in latent heat as well as the effect of topography. The great release in latent heat provided significantly positive feedback to the DCSWV system, which was decisive to the formation and development stages of "C2". The topography of the Tibetan Plateau and the Yun-Gui Plateau affected the location and duration of the DCSWV.

Keywords: southwest vortex, dual-core structure, numerical simulation, latent heat, topography

OPEN ACCESS

Edited by:
Sanjeev Kumar Jha,
Indian Institute of Science Education and Research, India

Reviewed by:
Chenghai Wang,
Lanzhou University, China
Devanil Choudhury,
University of Bergen, Norway

****Correspondence:***
Haiwen Liu
hwliu@cauc.edu.cn

Specialty section:
This article was submitted to Atmospheric Science, a section of the journal Frontiers in Earth Science

Received: *02 December 2021*
Accepted: *21 January 2022*
Published: *04 March 2022*

Citation:
Wu Z, Liu H, Chan KTF, Wu K, Zhang W and Wang D (2022) Effects of Topography and Latent Heat on the Evolution of a Mesoscale Dual-Core Southwest Vortex Over Sichuan Basin, China. Front. Earth Sci. 10:827601. doi: 10.3389/feart.2022.827601

INTRODUCTION

Sichuan Basin (SCB), a fertile expanse with low hills and plains almost entirely encircled by mountains, is located in the east of Tibetan Plateau (TP), west of Wu Mountain, north of Yun-Gui Plateau, and south of Daba Mountains, China (**Figure 1A**). In such complex terrain conditions, a mesoscale southwest vortex (SWV) is often observed over the SCB. Statistically, the severity of heavy precipitation caused by the SWV ranks the second in China, while precipitation from the tropical cyclones ranks the first (Wang et al., 1996). Therefore, the comprehensive understanding on the SWV is necessary, especially in the summer time.

Typically, the SWV is a cyclonic low-pressure system with significant baroclinic structures and complex temperature–humidity characteristics (Ye and Gao, 1979; Lu, 1986) between 700 and 850 hPa

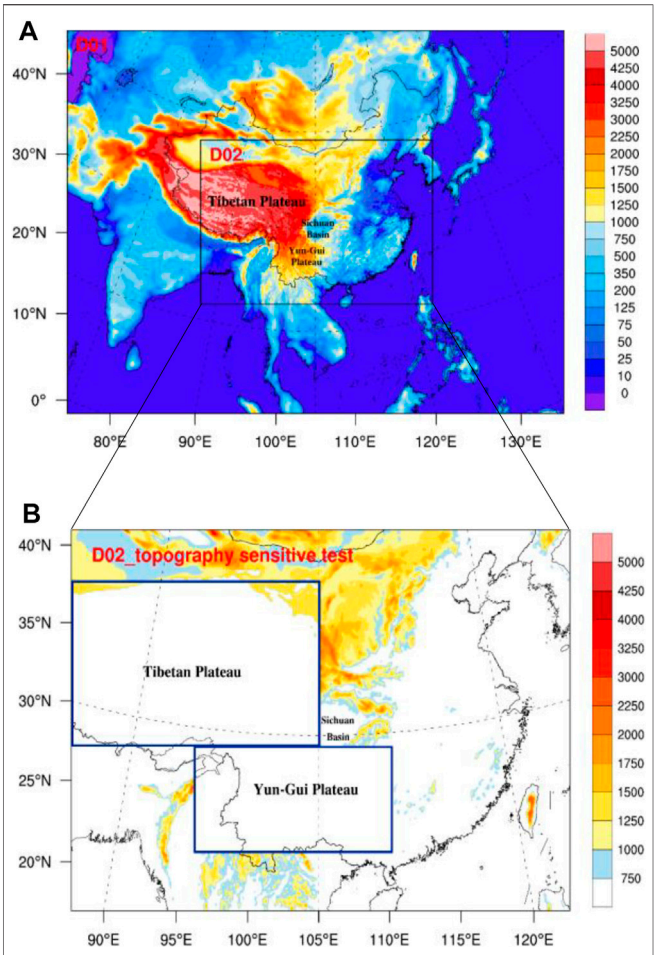

FIGURE 1 | (A) Two domains (D01–D02) used in the Weather Research and Forecasting (WRF) simulations and **(B)** the modified topography (m, shaded) for D02 in the NOTER experiment. The Tibetan Plateau, Yungui Plateau, and Sichuan Basin are marked. Two blue boxes indicate the areas of the NOTER experiment.

levels (Kuo et al., 1986; Lu, 1986). The air near the SWV is nearly moist adiabatic (Wang et al., 1993). The vorticity peaks at about 750 hPa (Feng et al., 2016). The vortex circulation in a strong SWV system is deep, which can extend up to 100 hPa (Chen et al., 1998).

With the rapid development of high-resolution reanalysis dataset, a new structure of SWV was first discovered by Zhou et al. (2017). They found that the SWV appeared with "double-yolk" or dual-core structure (DCSWV) sometimes. In other words, a big SWV embodied two small vortices. Later, Wu et al. (2018) further gave a strict definition of the DCSWV: two small coexisting vortices should be enclosed by the isohypse of the SWV, while their core centers should be within the southwest China (26–33° N, 100–108° E). Different from the conventional SWV, the DCSWV has two warm and moist centers, as well as two strong updrafts. It is accompanied by intensive precipitation centers, which brings wider rainfall range and greater influence to the regions (Zhou et al., 2017; Wu et al., 2018).

However, previous studies about the DCSWV only preliminarily revealed its structural characteristics (Zhou et al., 2017; Wu et al., 2018). The physical processes responsible for the initiation and intensification of the DCSWV are yet to be comprehensively explored. Previous studies suggested that the latent heat and topography can largely contribute to the initiation and intensification of the typical SWV (Ye and Gao, 1979; Ye, 1981; Wu and Chen, 1985; Chen and Dell'Osso, 1984; Kuo et al., 1986; Lu, 1986; Wang and Orlanski, 1987; Raymond and Jiang, 1990; Kuo et al., 1988; Fu et al., 2010; Jiang et al., 2012; Li et al., 2017). How about their roles in the DCSWV? How do they contribute to the initiation and intensification of the DCSWV? To address these, a typical DCSWV event, which occurred on July 16–17, 2010 over the SCB, is chosen, and the vorticity budget diagnostic is employed to investigate which physical processes are responsible for the initiation and intensification of the DCSWV.

The paper is organized as follows. The data and methodology are described in the *Data and methodology* section. In the *Overview of the DCSWV event on July 16–17, 2010* section, an overview of the case study based on observation is presented. The simulated evolution of the DCSWV and the possible impacts of latent heat and topography on the DCSWV is discussed in the *Modeling simulation and possible mechanisms of the evolution of the DCSWV* section. Finally, the *Summary and discussion* section gives a summary and discussion.

DATA AND METHODOLOGY

Data and model design

The 6-hourly National Centers for Environmental Prediction Final operational global analysis (NCEP-FNL) with the horizontal resolution of $1.0^{\circ} \times 1.0^{\circ}$ was used to investigate the large-scale circulation associated with the DCSWV.

The Advanced Research Weather Research and Forecasting (WRF-ARW) model Version 3.6.1 (Skamarock et al., 2008) was applied to perform model simulations. The horizontal resolutions of the outer and inner domains were 30 and 10 km, with 284 × 397 and 218 × 280 grid points, respectively. There were 30 vertical levels, and the model top was set at 50 hPa. The model domain configurations are shown in **Figure 1**. The FNL data were used as the initial and boundary conditions. In the control simulation (hereafter CTL), the following physics and parameterization schemes were employed, which had been largely used for simulating the extreme precipitation and synoptic systems near the TP (Liu et al., 2019; Qin and Zou, 2019) the WRF single-moment three-class microphysics scheme (Hong et al., 2004), the Rapid Radiative Transfer Model longwave radiation scheme (Mlawer et al., 1997), the Dudhia shortwave radiation scheme (Dudhia, 1989), the Monin–Obukhov surface layer scheme (Janjić, 2002), the Noah land surface scheme (Ek et al., 2003), and the Kain–Fritsch cumulus scheme (Alapaty et al., 2012) in both domains. The 5-h model spin-up time had been tested to be optimal for simulating the DCSWV. Therefore, all the simulations started from 12:00 UTC July 16, 2010 and continued for 30 h.

Two sensitivity experiments were designed to investigate the effects of latent heat and topography on the DCSWV. In the first experiment (NOLH), the latent heat was turned off (i.e., set "cu_physics = 0" and "no_mp_heating = 1" in the WRF

namelist), while all other progresses of physics and parameterizations remained the same as those in the CTL experiment. The second experiment (NOTER) is similar to the CTL experiment, but the terrain heights in the west of the SCB including the TP (26°–40°N, 84.5°–105°E) and the south of the SCB including the Yun-Gui Plateau (22°–30°N, 96°–111°E) were set to 500 m (**Figure 1B**).

In addition, the high-resolution CMORPH global precipitation analyses data and the Japan's second Multifunctional Transport Satellite (MTSAT-2) IR1 brightness temperature data were used to examine the convective activities, which further confirmed the existence of the DCSWV. The CMORPH precipitation data (1-hourly, $0.1^\circ \times 0.1^\circ$) combined the National Oceanic and Atmospheric Administration/Climate Prediction Center morphing technique dataset with hourly gage rainfall data from about 30,000 automatic weather stations (Pan et al., 2012). This precipitation product had been widely used in the mesoscale research field (Shen et al., 2013). The brightness temperature data (hourly, $0.05^\circ \times 0.05^\circ$) is obtained from Japan's second Multifunctional Transport Satellite (MTSAT-2) IR1 instrument (Takeuchi et al., 2007).

METHODS

The evolution of the SWV can be represented by vorticity effectively (Fu et al., 2010; Feng et al., 2020), the diagnosis of vorticity budget was used here to probe into the detailed evolution process from a single-core SWV to the DCSWV. According to Zhang (1992), the vorticity equation can be written as **Eq. 1**:

$$\underset{\text{TOT}}{\frac{\partial \zeta}{\partial t}} = -\underset{\text{HAV}}{\left[u\frac{\partial \zeta}{\partial x} + v\left(\beta + \frac{\partial \zeta}{\partial y}\right)\right]} - \underset{\text{VAV}}{\omega\frac{\partial \zeta}{\partial p}} - \underset{\text{STR}}{(f+\zeta)\nabla \cdot V} - \underset{\text{TIL}}{\left(\frac{\partial \omega}{\partial x}\frac{\partial v}{\partial p} - \frac{\partial \omega}{\partial y}\frac{\partial u}{\partial p}\right)} + \text{RES} \tag{1}$$

The local time rate of change of vorticity was abbreviated as TOT. The HAV is the horizontal advection term of the absolute vorticity, which includes relative vorticity and planetary vorticity. The VAV denotes the vertical advection term of vorticity. The STR, TIL, and RES are the stretching term, tilting term, and residual term effect due to friction, respectively. ζ is the relative vorticity, ω is the vertical velocity in the pressure coordinates, $\nabla = \frac{\partial}{\partial x}\vec{i} + \frac{\partial}{\partial y}\vec{j}$ is the horizontal gradient operator, f is the Coriolis parameter, and β is the meridional derivative of the Coriolis parameter.

Latent heat release is crucial to the generation and development of the SWV (Ye, 1981; Kuo et al., 1986; Wang and Orlanski, 1987; Kuo et al., 1988; Fu et al., 2010). To investigate the effect of the diabatic heating in the genesis process of the DCSWV from a single SWV, the atmospheric apparent heat source (Q_1) is calculated using **Eq. 2** from Yanai et al. (1973):

$$Q1 = C_p\left[\frac{\partial T}{\partial t} + V \cdot \nabla T + \left(\frac{p}{p_0}\right)^{R/C_p}\omega\frac{\partial \theta}{\partial p}\right] \tag{2}$$

where C_p is the specific heat of dry air at constant pressure, T is the temperature, V is the horizontal wind vector, p_0 is 1,000 hPa, R is the gas constant, ω is the vertical velocity in pressure coordinates, and θ is the potential temperature.

OVERVIEW OF THE SOUTHWEST VORTEX WITH DUAL-CORE STRUCTURE EVENT ON JULY 16–17, 2010

At 12:00 UTC July 16, 2010, a typical DCSWV event occurred over the SCB. This event lasted about 14 h and dissipated at 06:00 UTC July 17, 2010. The DCSWV resulted in more than 100-mm 24-hourly accumulated precipitation in 51 cities. In Bazhong City, 1.92 million people were affected, and direct economic losses were about 910 million RMB (Wang and Zhang, 2011).

To investigate the life span of the DCSWV, **Figure 2** shows the 6-hourly geopotential height and wind field using the NCEP-FNL from 12:00 UTC July 16 to 06:00 UTC July 17, 2010. At 12:00 UTC July 16 in **Figures 2A,B**, a low-pressure system within the isolines of 3,108-gpm was observed over southwest China. The center of this typical mesoscale SWV was near Leshan City (29°N, 104°E), marked as "C" in **Figure 2**. Meanwhile, a tropical low was located in the west of the South China Sea and brought southerlies wind from the ocean to the SCB. At 18:00 UTC July 16 in **Figures 2C,D**, the DCSWV appeared, which satisfied the criteria for a typical SWV reported by Lu (1986). A sub-mesoscale low-pressure vortex, marked as "C2" in **Figures 2C,D**, emerged near Langzhong City (31.5°N, 106°E). At the time, there were two vortices, "C1" and "C2", coexisting over the SCB. Both vortices were embedded by the 3,108-gpm isotypes. It was apparent that the sub-mesoscale SWV "C1" and "C2" were born from the single-core "C". Based on the criteria of Orlanski (1975), two mesoscale vortices "C1" and "C2" were regarded as the meso-β-scale vortex. The dual-core structure of SWV became more obvious at 00:00 UTC July 17 (**Figures 2E,F**). The DCSWV was mature and presented a typical double-yolk structure. It gradually moved to the northeast along with the southerly airflow, extending its influence beyond the SCB. At 06:00 UTC July 17 in **Figures 2G,H**, the dual-core structure disappeared and turned into a single-core structure. The center of the core was marked as "C3" in **Figure 2**.

The evolution of precipitation distribution associated with the DCSWV was prominent. At 12:00 UTC July 16, the precipitation center was located in the northeast of the center of SWV "C" (**Figure 3A**). At 18:00 UTC July 16, the intensity of precipitation was stronger, and there were obvious precipitation centers below the DCSWV (**Figure 3B**). Six hours later, two significant precipitation maxima (>100 mm) appeared in the west of "C1" and the east of "C2" (**Figure 3C**). Two precipitation maxima further demonstrated the existence of the DCSWV and provided better atmospheric thermal conditions. Compared with the typical SWV, the influence range of two rain belts accompanying DCSWV was wider. At the 06:00 UTC July 17, the precipitation decreased remarkably (**Figure 3D**). The rain belt shifted to the east, and the two vortices dissipated and transformed to a single-core "C3".

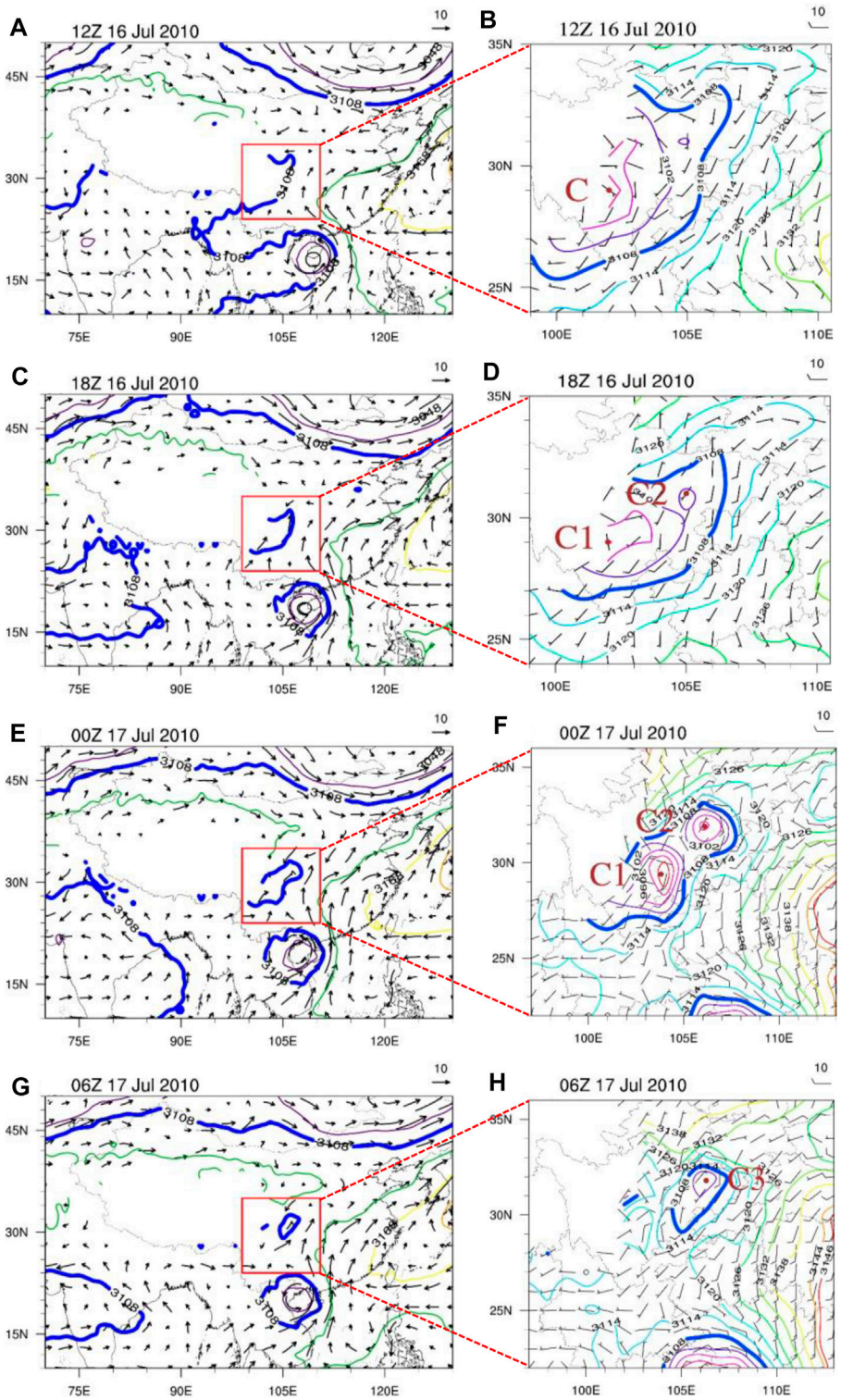

FIGURE 2 | Spatial distributions of the 700 hPa geopotential height (gpm, contours) and wind field (m s^{-1}, arrows) at **(A,B)** 12:00 UTC July 16, **(C,D)** 18:00 UTC July 16, **(E,F)** 00:00 UTC July 17, and **(G,H)** 06:00 UTC July 17. C, C1, C2, and C3 denote the southwest vortices (SWVs), and the brown dots represent their centers (the same in the following figures, if applicable).

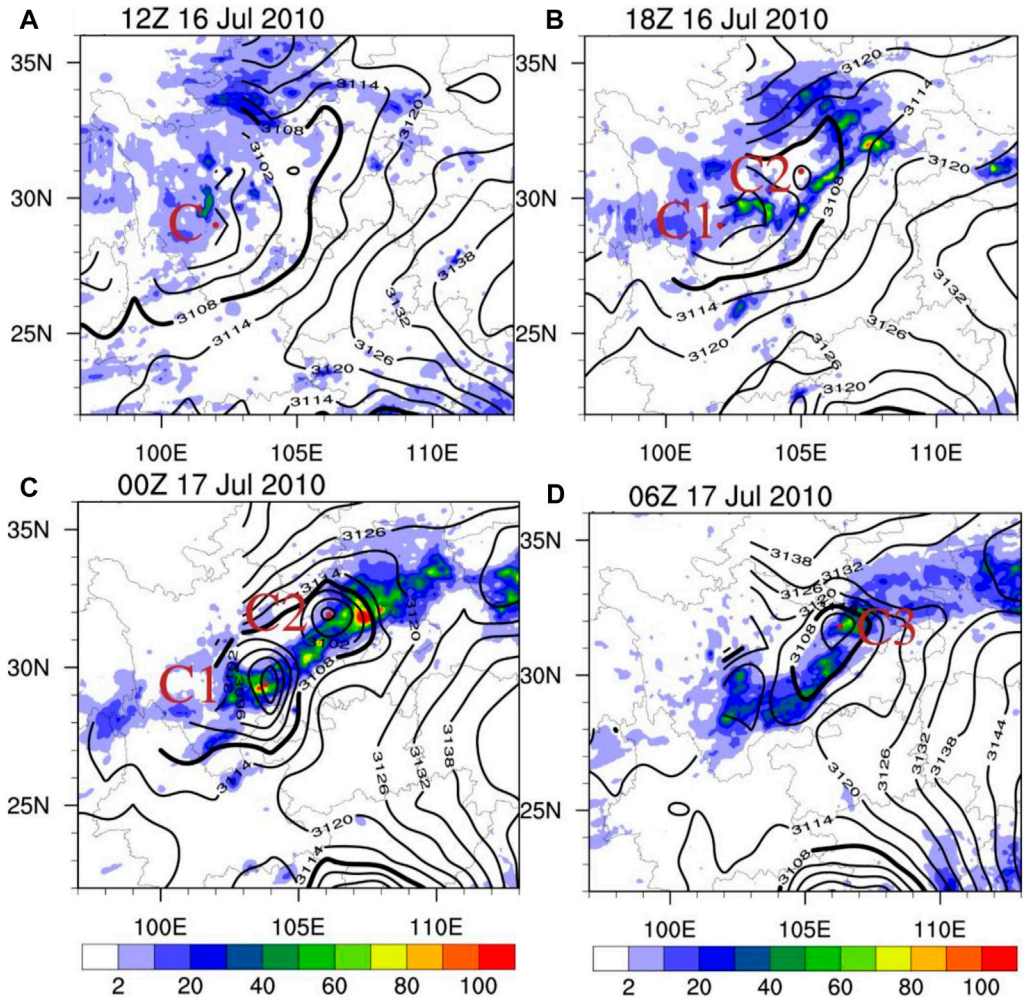

FIGURE 3 | Spatial distributions of the 700 hPa geopotential height (gpm, contours) and the pre-6-h accumulated precipitation (mm, shaded) at **(A)** 12:00 UTC July 16, **(B)** 18:00 UTC July 16, **(C)** 00:00 UTC July 17, and **(D)** 06:00 UTC July 17.

The hourly MTSAT-2 brightness temperature also indicated the evolution of the two meso-β-scale vortices (**Figure 4**). Observations showed that the organized cloud clusters were located near two meso-β-scale vortices. At 12:00 UTC July 16, the convective cloud clusters were mainly located in the western part of vortex "C" (**Figure 4A**). Six hours later, accompanying the formation of two vortices, mesoscale convective cloud clusters were observed in their eastern part (**Figure 4B**). At 00:00 UTC July 17 (**Figure 4C**), the cloud clusters were also located near two vortices. Following the eastward movement of two meso-β-scale vortices, convective cloud clusters also moved to the downstream region. The precipitation and cloud clusters, thus, both demonstrated the dual-core structure of SWV.

A planetary wave trough was observed from Lake Baikal to the SCB (not shown), which favored the formation of the SWV (Kuo et al., 1986). There was an area of high pressure over the SCB at 200 hPa (not shown), demonstrating that SWV with a dual-core structure was similar with the typical SWV, which was usually visible in the lower troposphere at 700 and 850 hPa (Kuo et al., 1986; Lu, 1986).

Figure 5 showed the vertical cross sections of the pseudoequivalent potential temperature and relative vorticity over the central points of the SWVs along the lines was shown in **Figure 4**. At 12:00–18:00 UTC July 16 (**Figures 5A, B**), the shallow positive vorticity in the lower troposphere indicated that DCSWV was a shallow weather system in the initiation stage. At 00:00 UTC July 17 (**Figure 5C**), in the mature stage, two positive relative vorticity centers were observed as the "C1" and "C2". The positive vorticity extended upward from the low level. The slightly westward-tilted "C1" was deeper than "C2", where the vorticity extended from the surface to 200 and 400 hPa, respectively. The vorticity of the two vortices both peaked at 700 hPa. Six hours later, in the dissipating stage, "C1" and "C2" transformed to "C3", which was likely the succession of "C2" (**Figure 5D**). The results of **Figure 6** agree well with **Figure 5**. Two distinct centers of upward motion were observed over "C1" and "C2" from 18:00 UTC July 16 to 00:00 UTC July 17, which extended from surface to about 100 hPa. Besides, the nearly saturated relative humidity around the "C1" and "C2" demonstrated the moist features of the DCSWV.

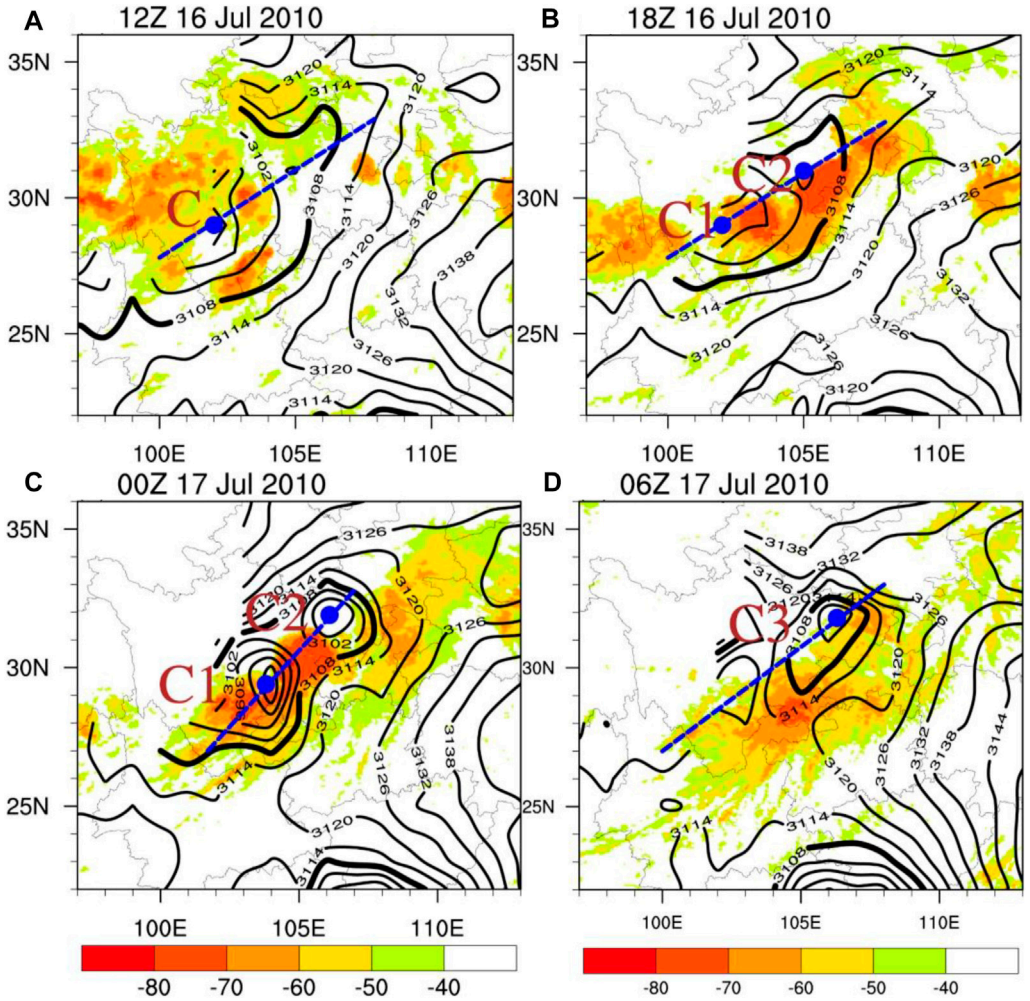

FIGURE 4 | Spatial distributions of the 700 hPa geopotential height (gpm, contours) and Japan MTSAT-2 infrared temperature (°C, shaded) at **(A)** 12:00 UTC July 16, **(B)** 18:00 UTC July 16, **(C)** 00:00 UTC July 17, and **(D)** 06:00 UTC July 17. The blue lines are used to intercept the cross sections in **Figures 5**, **6**.

MODELING SIMULATION AND POSSIBLE MECHANISMS OF THE EVOLUTION OF THE SOUTHWEST VORTEX WITH DUAL-CORE STRUCTURE

Modeling results

To quantify the capability of the WRF model in simulating the evolution of DCSWV, the FNL data were first gridded as the domain 2 of WRF model. The correlation coefficients between the WRF (simulated variables in domain 2) and the FNL data, including the 700 hPa geopotential height, U-component of wind, and V-component of wind at 18:00 UTC July 16 and 00:00 UTC 17 July 17, 2010 were calculated (**Table 1**). The correlation coefficients of the geopotential height were up to 0.87. Meanwhile, those of the U-component and the V-component of winds reached 0.83 and 0.86, respectively. All of them were statistically significant at the 99% confidence level. These indicated that the WRF simulations could well capture the evolution of DCSWV.

The evolution of the DCSWV was divided into five stages (**Figure 7**). At the first stage (16:00 UTC July 16), the single-core stage, the typical SWV, vortex "C", was enclosed by the 3,108-gpm isoline (**Figure 7A**). At the second stage (17:00 UTC July 16), the DCSWV initiation stage, the 3,108-gpm isoline extended northward, and the vortex "C2" appeared northeast of "C1". The simulated positions "C1" were basically consistent with the observation, while "C2" was located in the south of the observed "C2" (**Figure 7B**). The warm and moist southwest and southeast flows near the east of the TP led to the unstable stratification (**Figure 8B**) and upward movement (not shown) in the lower troposphere of "C1" and "C2". It was worth noting that "C1" formed at higher topography, and "C2" formed in the SCB. Whether the topography had a significant impact on the formation of "C2" will be tested in the *Topography effect* section.

At the third stage (18:00–22:00 UTC July 16), the DCSWV intensification stage (**Figures 7C, D**), a typical DCSWV was developing. Two cores were embedded in the 3,108-gpm

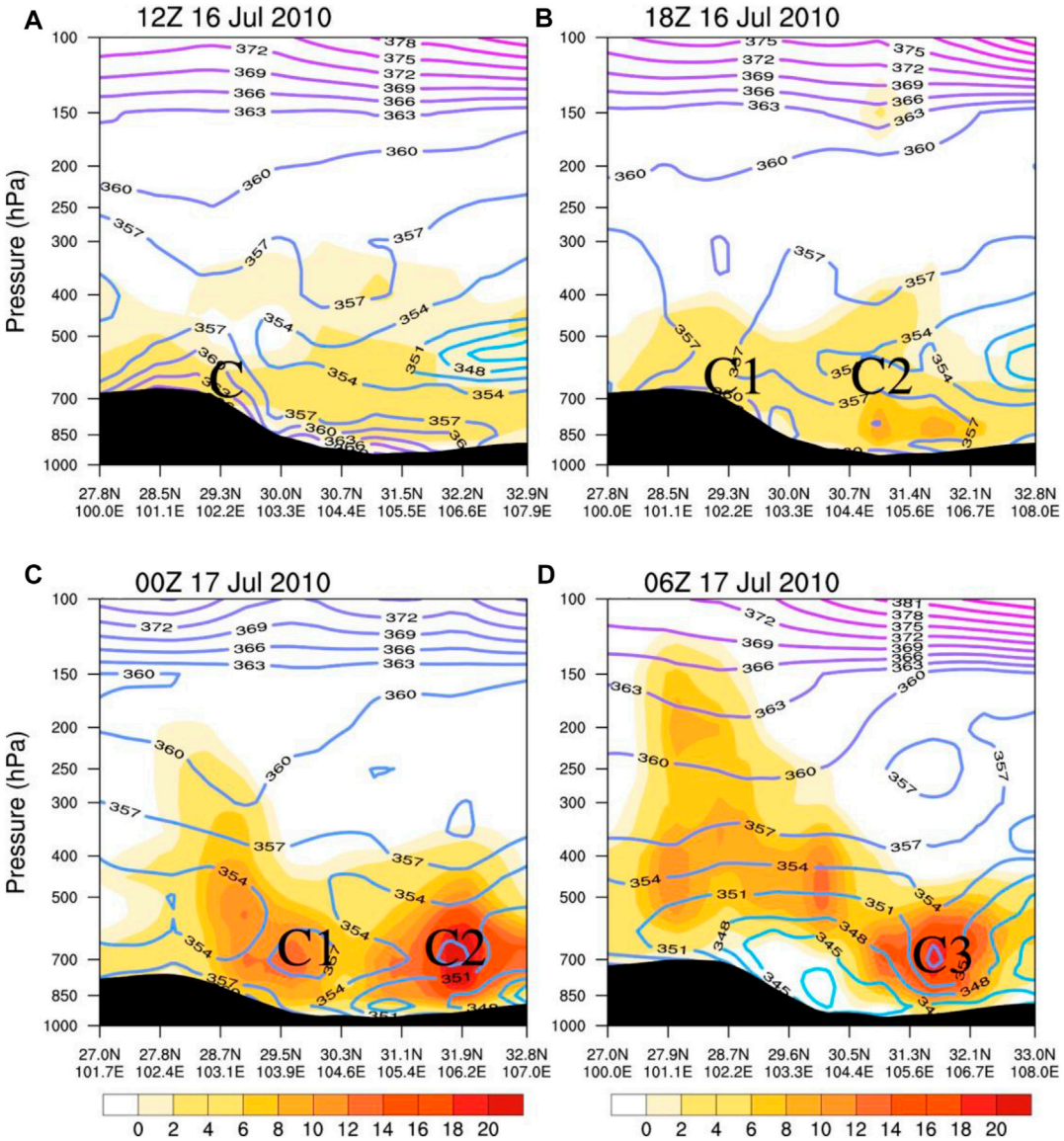

FIGURE 5 | Vertical cross sections of the pseudoequivalent potential temperature (K, contours) and relative vorticity (10^{-5} s^{-1}, shaded) at **(A)** 12:00 UTC July 16, **(B)** 18:00 UTC July 16, **(C)** 00:00 UTC July 17, and **(D)** 06:00 UTC July 17. The black areas at the bottom of the figures represent the topography (the same in the following figures).

isohypse, which was consistent with the observation (**Figure 5B**). The two obvious lower-tropospheric positive vorticity centers, as well as warm and moist conditions, facilitated the initiation and intensification of the DCSWV (**Figure 5B**, **Figures 8C,D**).

At the fourth stage (23:00 UTC July 16 to 02:00 UTC July 17), the mature stage, the structure of the DCSWV became more obvious (**Figures 7E,G**). The northeasterly to the north of DCSWV and the southwesterly to the south of DCSWV brought "C1" and "C2" closer. Two corresponding positive vorticity centers exhibited a double-yolk structure (**Figures 8E,G**).

At the fifth stage (03:00 UTC July 17 to 04:00 UTC July 17), the DCSWV entered into the decay stage. The typical pattern of two closed SWVs gradually disappeared, while the vorticity of "C2" gradually weakened at 03:00 UTC July 17 (**Figure 8H**). After 1 h, "C1" and "C2" dissipated and became a single-core vortex "C3". Only a single strong positive vorticity center was observed. In the entire process, the DCSWV lasts for about 11 h from initiation to dissipation.

Main factors of influencing the evolution of the southwest vortex with dual-core structure

Vorticity budget

Since the vorticity budget is an effective measurement to analyze the development of the SWV (Fu et al., 2014; 2017), the vorticity

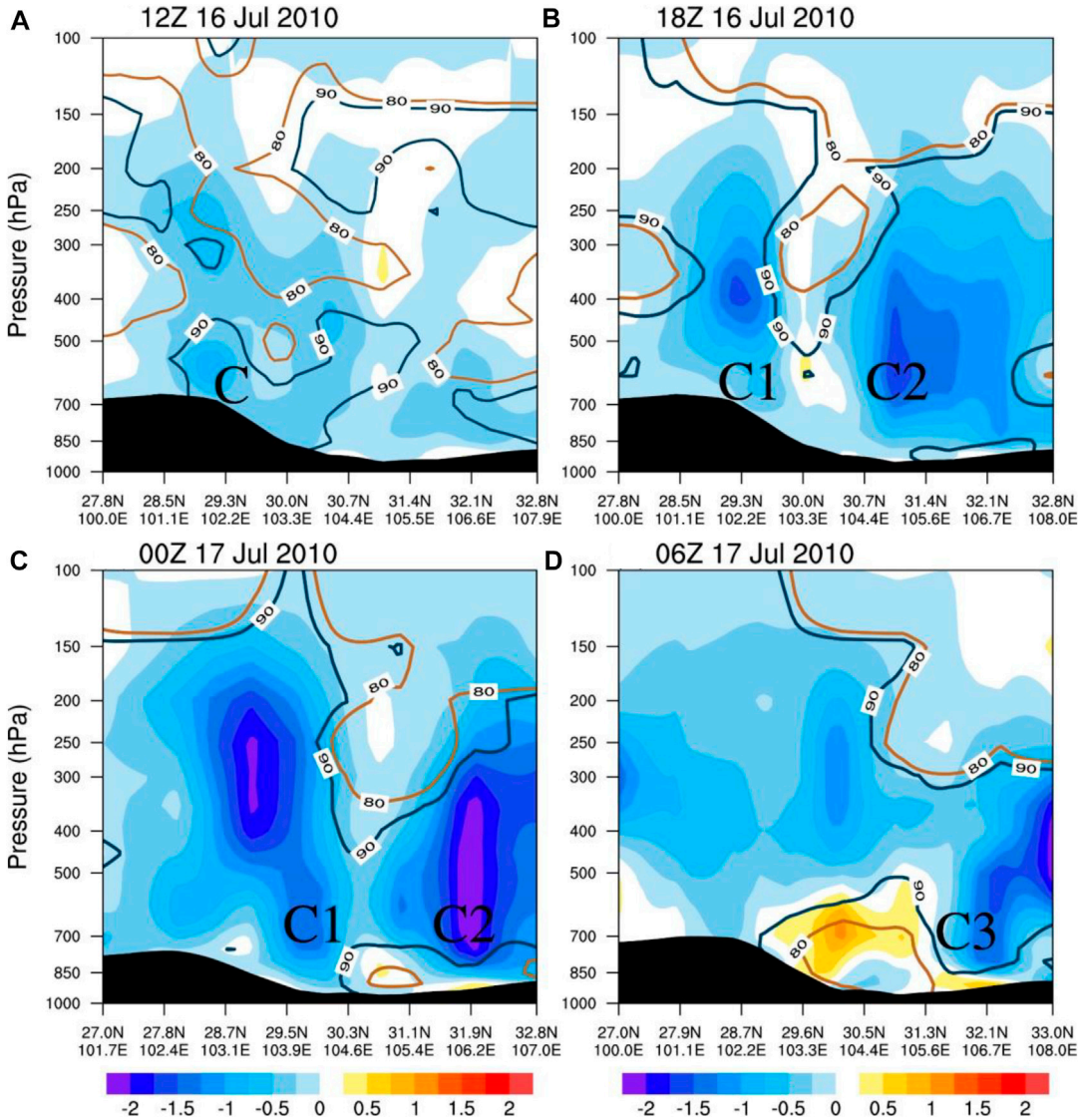

FIGURE 6 | Vertical cross-section of the vertical velocity (Pa s^{-1}, shaded) and the relative humidity (%, contours) at **(A)** 12:00 UTC July 16, **(B)** 18:00 UTC July 16, **(C)** 00:00 UTC July 17, and **(D)** 06:00 UTC July 17.

budget for the DCSWV was calculated to study the relative importance of each term in the vorticity budget equation to the DCSWV. The key region of SWVs was defined as an area within the radius of 1° from the center of the vortex. As shown in **Figure 9**, the regional averaged vorticity budgets for key regions "C", "C1", "C2", and "C3" were examined, respectively. At 16:00 UTC July 16 (the single-core stage of SWV), the moisture divergence (**Figure 10**) and vertical motion dominated the key region of "C". Under these favorable conditions, the convergence-related STR and VAV terms were the main contributions of the positive vorticity budget of "C". From 17:00 to 23:00 UTC July 16 (the formation of the DCSWV), due to intensified convection (**Figure 9C**), the convection-related TIL term transported the positive vortex from the lower troposphere to the upper level, which increased from -8.5×10^{-9} to $7.2 \times 10^{-9} s^{-2}$, acting as the second contribution of cyclonic vorticity "C1" at 700 hPa. At the same time, convergence and ascending motion intensified rapidly, while the convection around the key region of "C1" was active (**Figure 9C**). The convergence-related STR acted as the main contribution to the cyclonic vorticity of "C1" at 700 hPa, and convective-related TIL was the second contribution (**Figure 9A**). These terms resulted in the increase in the total vorticity budget (TOT). This feature suggested that the STR and TIL terms played important roles in the development of "C1". After 23:00 UTC 16 July, the "C1" within DCSWV entered the mature stage, and the HAV and TIL terms were favorable to the increase in cyclonic vorticity "C1". With the evolution of the vortex, after 01:00 UTC July 17, the HAV term increased rapidly and maintained the cyclonic vorticity in the vortex region together with the TIL

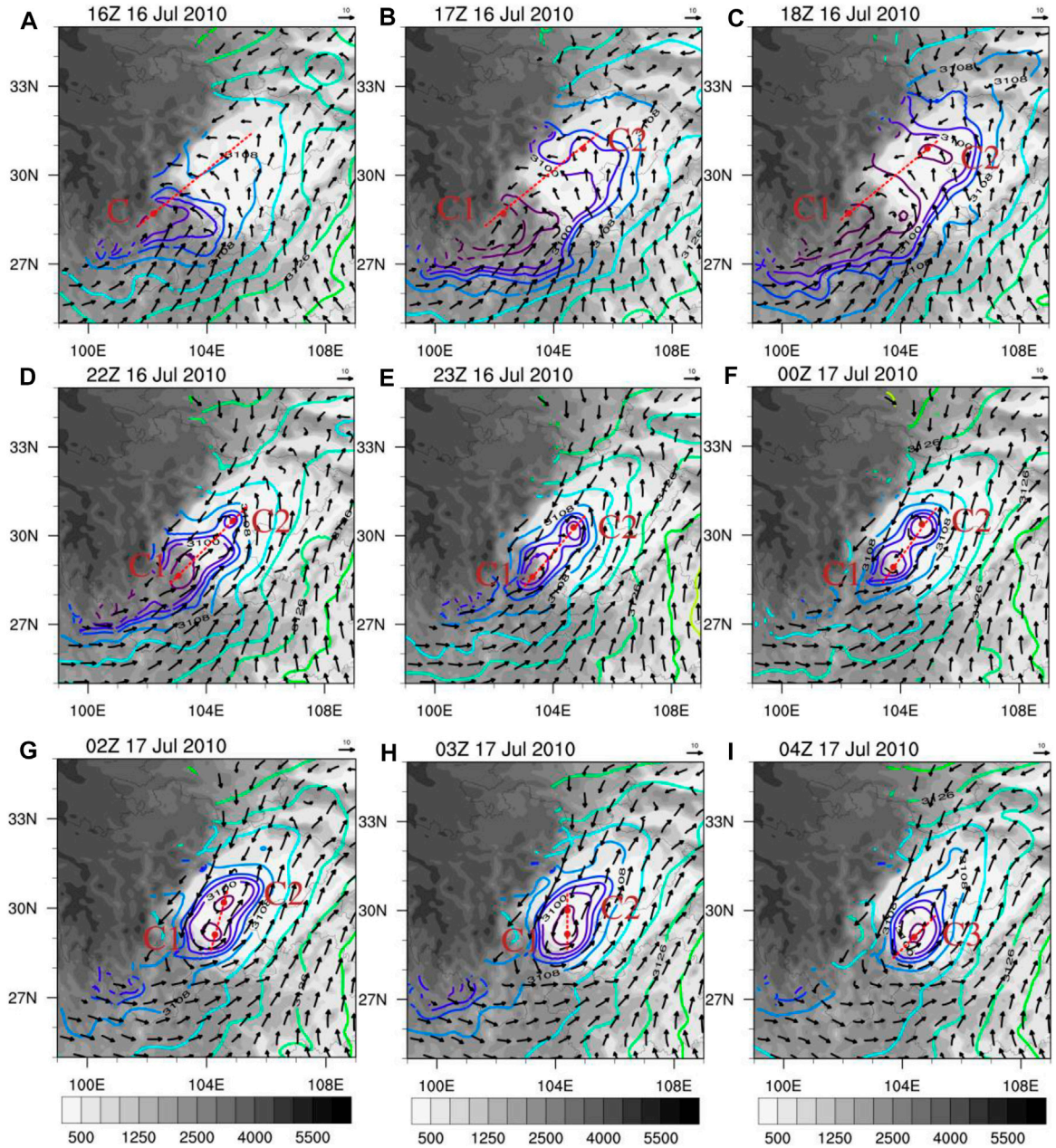

FIGURE 7 | Modeling simulated 700 hPa geopotential height (gpm, contours), wind field (m s^{-1}, arrows), and terrain height (m, shaded) from the control simulation (CTL) experiment inside Domain 02 at **(A)** 16:00 UTC July 16, **(B)** 17:00 UTC July 16, **(C)** 18:00 UTC July 16, **(D)** 22:00 UTC July 16, **(E)** 23:00 UTC July 16, **(F)** 00:00 UTC July 17, **(G)** 02:00 UTC July 17, **(H)** 03:00 UTC July 17, and **(i)** 04:00 UTC July 17. The red dots denote the centers of SWVs. The red lines indicate the transects of the cross sections in **Figure 8**.

term. At 04:00 UTC July 17, the DCSWV dissipated and transformed to "C3". Terms of HAV and TIL were the main contributions to "C3" cyclonic vorticity.

The TOTs of "C2" were smaller than those of "C1" on the whole (**Figures 9A, B**). At 16:00 UTC July 16 (the initiation stage of the DCSWV), the STR term mainly increased the cyclonic vorticity of "C2" within the key region of the DCSWV (**Figure 9B**). Moreover, the vertical upward movement was enhanced in the "C2" key region (not shown), and the term VAV became a second contributor to "C2" development. From 17:00 to 23:00 UTC July 16 (during the initiation and intensification stages of the DCSWV), the terms of STR and VAV were the main contributions to the vorticity tendency of "C2". During the DCSWV mature stage (23:00 UTC July 16 to 02:00 UTC July 17), "C2" evolved rapidly (**Figure 9B**), and its cyclonic vorticity increased because of the terms of TIL and HAV.

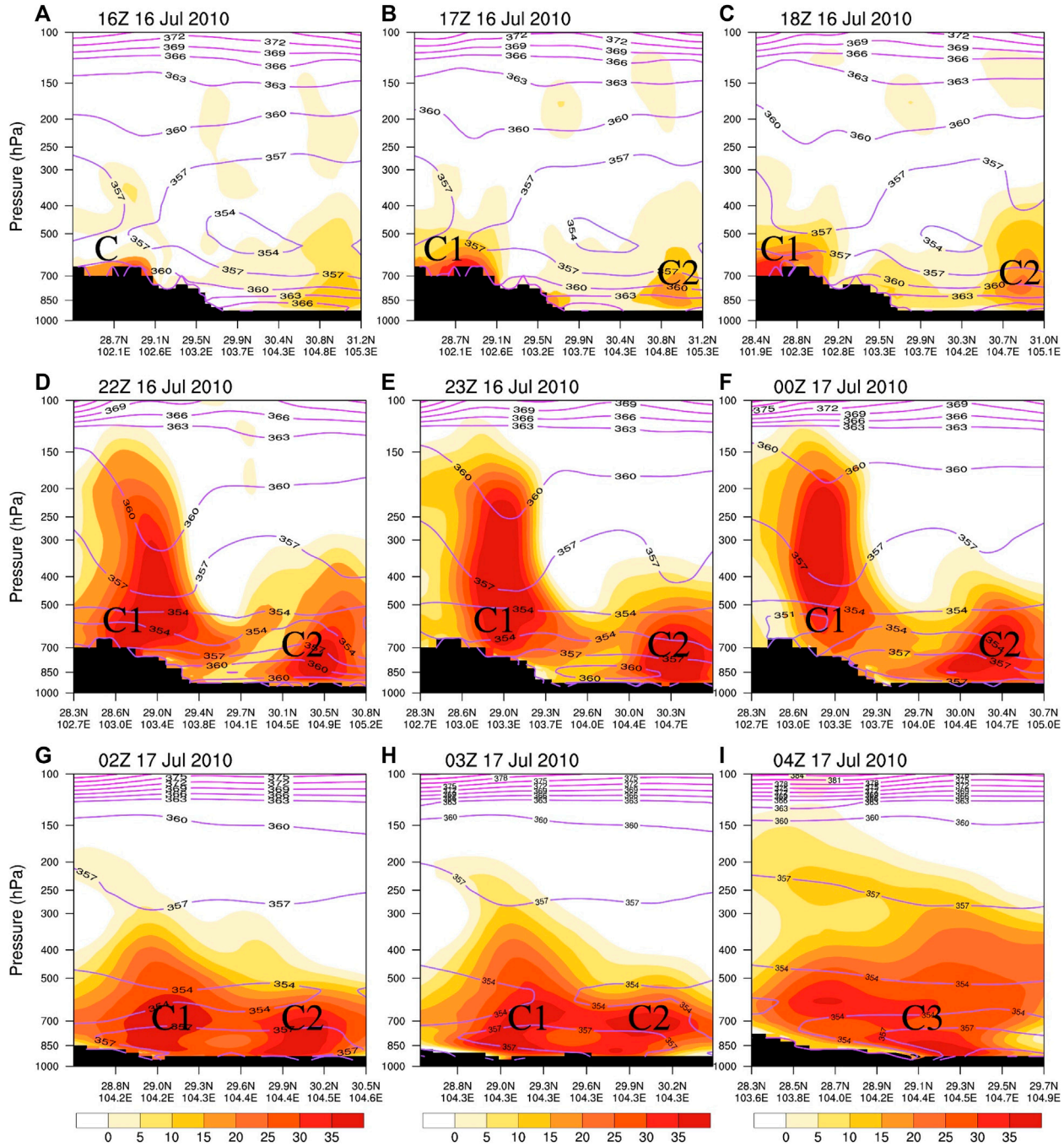

FIGURE 8 | Vertical cross sections of the pseudoequivalent potential temperature (K, contours) and relative vorticity (10^{-5} s^{-1}, shaded) from the CTL experiment at **(A)** 16:00 UTC July 16, **(B)** 17:00 UTC July 16, **(C)** 18:00 UTC July 16, **(D)** 22:00 UTC July 16 **(E)** 23:00 UTC July 16, **(F)** 00:00 UTC July 17, **(G)** 02:00 UTC July 17, **(H)** 03:00 UTC July 17, and **(I)** 04:00 UTC July 17.

After 03:00 UTC July 17, the TIL term decreased gradually, leading to the negative TOT and dissipating of "C2".

Overall, moisture convergence and vertical motion were evident within the key region of the DCSWV. As a result, the convergence-related STR and the VAV term related to ascending motion could increase the DCSWV cyclonic vorticity. However, the STR and TIL terms played important roles in the development stage of "C1", while the STR and VAV terms were the main positive contributors to the formation and development stages of "C2".

Latent heat release effect

There were obvious water vapor convergence and convection activities in the key area before the formation of the DCSWV (**Figures 9C,D**). As the previous studies suggested, latent heat

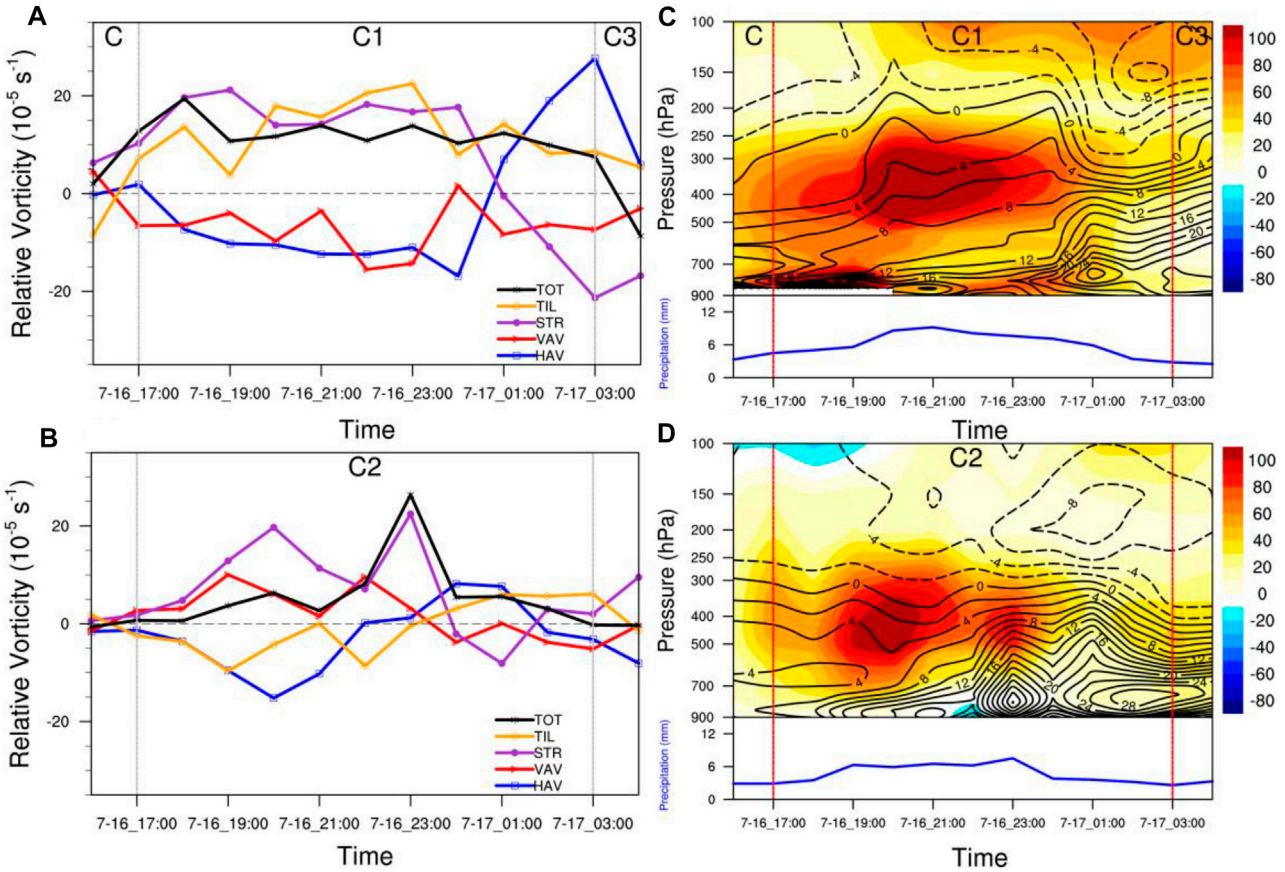

FIGURE 9 | Regionally averaged vorticity budget terms (units: 10^{-9} s^{-2}) for **(A)** C, C1, C3, and **(B)** C2 at 700 hPa, and time–pressure sections of apparent heat source Q1 (K day^{-1}, shaded), relative vorticity (10^{-5} s^{-1}, black contours), and regional mean precipitation over the key region (mm, blue line) from 16:00 UTC July 16 to 04:00 UTC July 17 in the CTL experiment for **(C)** C, C1, C3, and **(D)** C2. HAV, VAV, STR and TIL denote horizontal advection of vorticity, vertical advection of vorticity, stretching, and tilting, respectively. The local time rate of change of vorticity is abbreviated as TOT. Vertical gray solid lines mark the start and end time of the SWVs.

TABLE 1 | List of the correlation coefficients of the 700 hPa geopotential height, 700-hPa U-component of wind, and 700-hPa V-component of wind between the control simulation (CTL) run (Domain 02) data and FNL data.

Variables	18:00 UTC July 16	00:00 UTC July 17
Geopotential height	0.87	0.87
U-component of wind	0.83	0.85
V-component of wind	0.86	0.86

release can largely contribute to the formation and development of SWV (Ye, 1981; Kuo et al., 1986; Wang and Orlanski, 1987; Raymond and Jiang, 1990; Kuo et al., 1988; Fu et al., 2010; Li et al., 2017). In order to explore the influence of latent heat release on the evolution of the DCSWV, we calculated Q_1, relative vorticity, and regional mean precipitation in the key region (**Figures 9C,D**).

It is well known that water vapor flux has an important role in the release of latent heat. **Figure 10** showed the vertical integration of water vapor fluxes from 1,000 to 300 hPa by the CTL experiment. As shown in **Figure 10**, the DCSWV formed at 17:00 UTC July 16, with one water vapor channel from the South China Sea to the key area of "C1", which provided sufficient moisture to trigger convection and release lots of convective condensation latent heat. Since 19:00 UTC July 16, two southerly water vapor channels from the Bay of Bengal and the South China Sea converged and ascended over the key region of the DCSWV, which further enhanced water vapor convergence and ascending motion, releasing more latent heat to warm the lower and middle troposphere in the key region of "C1". The process increased the vorticity between 850 and 700 hPa (Raymond and Jiang, 1990), which promoted the DCSWV significantly (**Figure 9C**). The positive feedback between the enhanced latent heat and the vorticity of "C1" indicated that latent heat release played an important role in the development of "C1". After 23:00 UTC July 16, "C1" within the DCSWV reached the mature stage, with a Q_1 maximum center located in the middle and lower troposphere over the key region, which was conducive to the obvious positive vorticity center at 850–700 hPa. With the decreasing water vapor transportation from the Bay of Bengal, moisture convergence and ascending motion became weaker, leading to a weaker positive

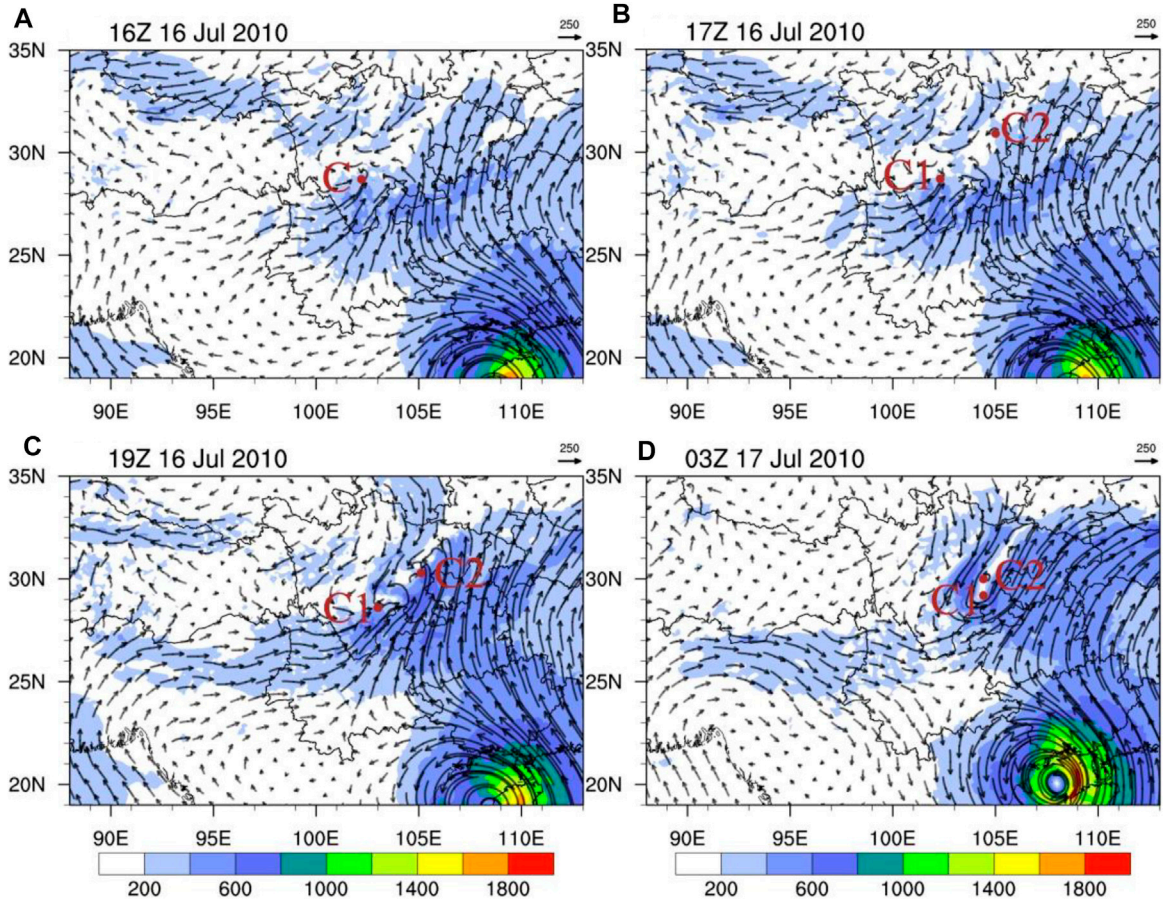

FIGURE 10 | Vertical integration of water vapor fluxes from 1,000 to 300 hPa (shadings and arrows, unit: kg m^{-1} s^{-1}) by the CTL experiment at **(A)** 16:00 UTC July 16, **(B)** 17:00 UTC July 16, **(C)** 19:00 UTC July 16, and **(D)** 03:00 UTC July 17.

vorticity. One hour later, the vortex "C1" dissipated and transformed to "C3".

Compared with "C1", Q_1 maximum over the key area of "C2" was mainly located at the 700–200 hPa (**Figures 9C,D**). Before 17:00 UTC on July 16, when "C2" had not yet formed, the key area was warm and moist (**Figure 8A**) due to the influence of the southeasterly wind. A strong upward motion also existed at the same time. These favorable physical conditions were beneficial to trigger convective activities. The associated latent heat then warmed the regional atmosphere, which was favorable to increase the vorticity in the lower troposphere and form "C2" in the DCSWV. After 23:00 UTC July 16, "C2" entered the mature stage. Similar to "C1", precipitation and Q_1 enhanced rapidly near the key area of "C2" due to the moisture transportation and accumulation from the Bay of Bengal and the South China Sea (**Figure 10**). Meanwhile, an obvious positive vorticity center appeared as the vorticity was enhanced in the lower layer. This indicated that latent heat release also played an important role in the development stage of "C2". Finally, the DCSWV dissipated at 04:00 UTC July 17 as latent heat release weakened (**Figure 9D**).

The above analyses showed that the latent heat release played an important role in the overall evolution of the DCSWV. During the evolution of DCSWV, a large amount of water vapor from the ocean converged into its key area making the lower troposphere warm and wet (**Figures 8**, **10**). These conditions, combined with the remarkable ascending motion caused by moisture convergence, could trigger convection, as well as the convective condensational latent heat release, resulting in the production of cyclonic vorticity, and the formation and development of the DCSWV. Therefore, a favorable circulation related to the DCSWV occurred through the positive feedback from the increased latent heat associated with convective activities.

To further verify the importance of latent heat release on the DCSWV, the NOLH experiment was performed, and the results were compared with CTL run. At 18:00 UTC on July 16, a shallow SWV core (marked as "C") at 700 hPa was observed over the SCB in the NOLH experiment (**Figure 11C**). The NOLH results showed weaker pseudoequivalent potential temperature and relative vorticity than those in the CTL results (not shown). Q_1 and rainfall over the key area of "C" were also weak (**Figure 12**) because the latent heat release was turned off,

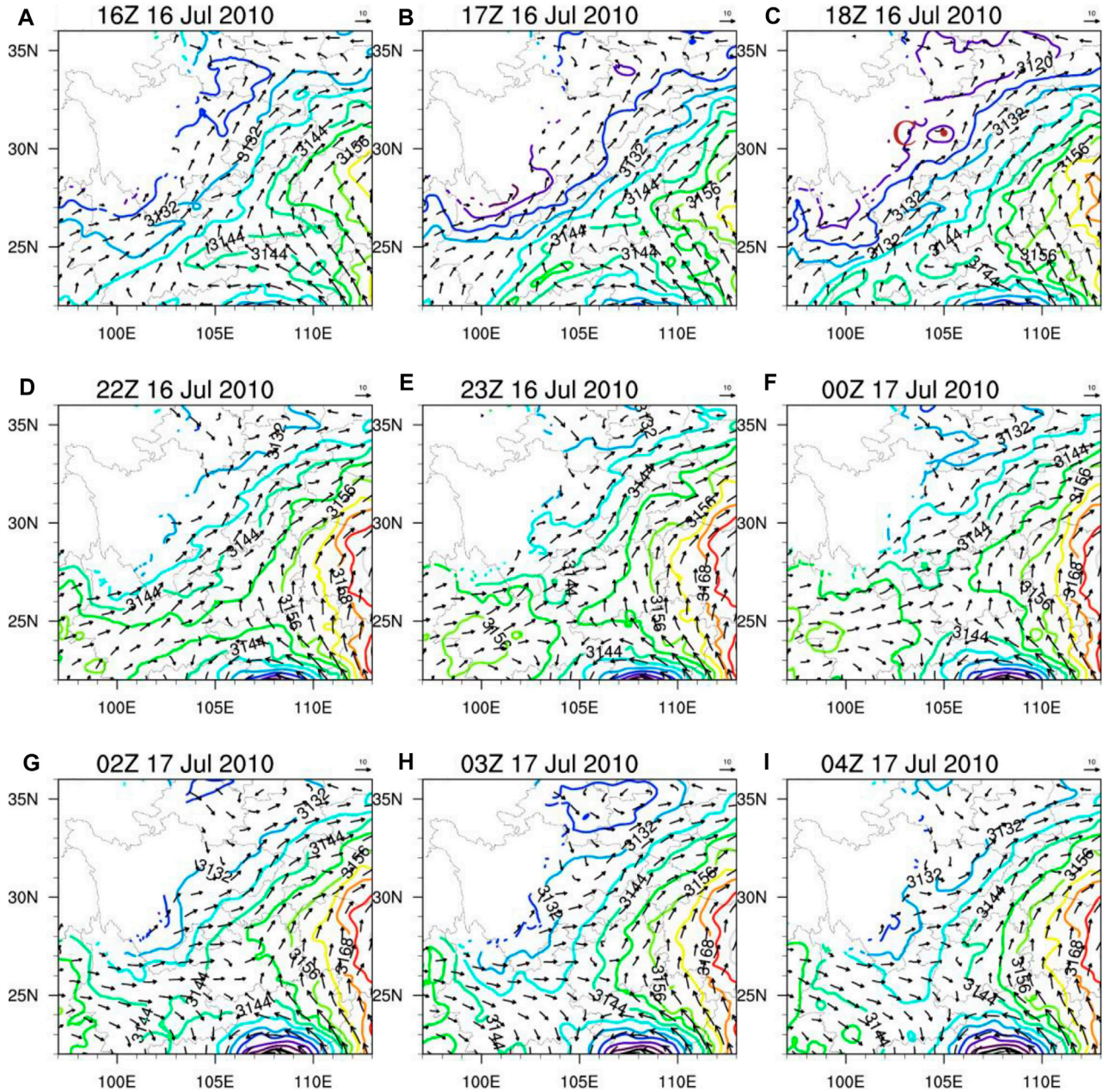

FIGURE 11 | The 700 hPa geopotential height (gpm, contours) and wind field (m s^{-1}, arrows) for the NOLH experiment at **(A)** 16:00 UTC July 16, **(B)** 17:00 UTC July 16, **(C)** 18:00 UTC July 16, **(D)** 22:00 UTC July 16 **(E)** 23:00 UTC July 16, **(F)** 00:00 UTC July 17, **(G)** 02:00 UTC July 17, **(H)** 03:00 UTC July 17, and **(i)** 04:00 UTC July 17.

which was consistent with our speculation. Moreover, a dual-core structure as the DCSWV could not be found in the NOLH experiment (**Figure 11**). It means that the positive feedback of latent heat release on the vortex disappeared, making it difficult to develop the SWV "C" and further trigger another core like "C2". With lack of positive feedback mechanism without latent heat release, DCSWV could not be formed. Therefore, the release of latent heat was the important and decisive factor in the formation and maintenance of the DCSWV.

Topography effect

Previous studies have documented that the formation and development of the SWV is influenced by the complex topography of the TP (Ye and Gao, 1979; Wu and Chen, 1985; Lu, 1986; Jiang et al., 2012). To investigate the contribution of terrain on the evolution of the DCSWV, NOTER experiment was conducted (**Figure 13**). Compared with the CTL run with topography, the NOTER experiment exhibited a similar DCSWV pattern with different location

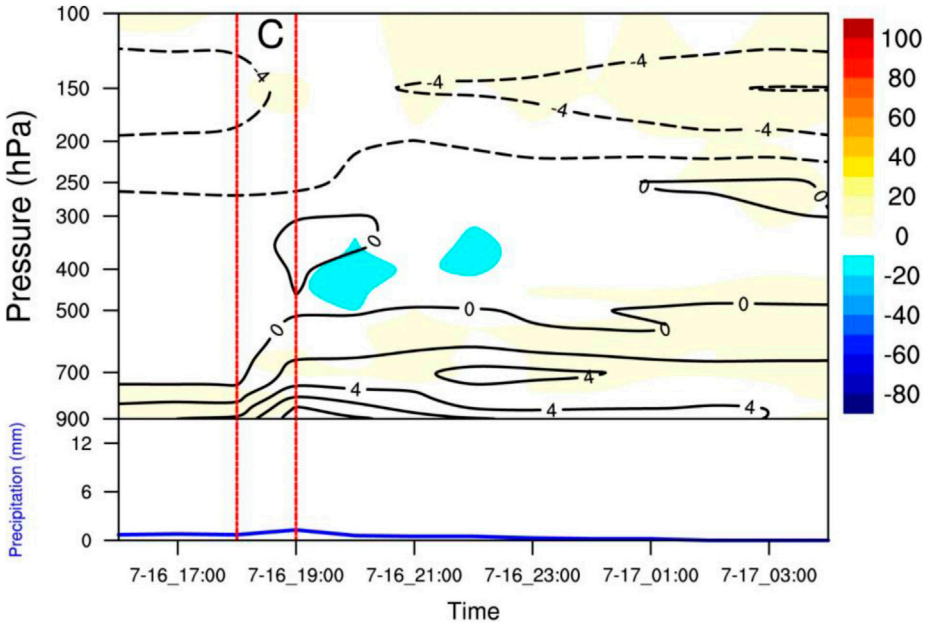

FIGURE 12 | Time–pressure sections of apparent heat source Q1 (K day^{-1}, shaded), relative vorticity (10^{-5} s^{-1}, black contours), and regional mean precipitation in the key region of C (mm, blue line) from 16:00 UTC July 16 to 04:00 UTC July 17 by the NOLH experiment.

and duration. The simulated southwesterly and southeasterly winds were stronger than those in the CTL run. The strong southerlies is the key factor to the formation of SWV (Li et al., 2017). The strong cyclonic wind shear formed because of the southwest and southeast airflow over the region where the terrain was removed. Strong convergence also occurred in the lower troposphere. Different from the CTL run, the "C1" and "C2" in the NOTER experiment appeared almost simultaneously at 19:00 UTC July 16. Moreover, the size of the DCSWV was significantly larger due to the stronger southerlies with the absence of topography influence of the TP and the Yun-Gui Plateau (**Figures 7**, **13**).

Before the generation of the DCSWV, the positive vorticity in the key region of the DCSWV was mainly contributed by the STR and VAV terms (**Figure 14A**). The intense convergence and vertical motions were conducive to the convection, which favor the associated latent heat warming the atmosphere rapidly (**Figure 14B**). As shown in **Figure 14A**, terms of VAV and HAV were the main positive contributions to the formation of the DCSWV at 20:00 UTC July 16, while HAV and TIL terms were beneficial to its maintenance until 00:00 UTC July 17. During the evolution of the DCSWV, Q_1 warmed the surrounding atmosphere in the middle and upper layers (**Figure 14B**). Compared with the CTL run (**Figures 9C,D** and **Figure 14**), the Q_1 and precipitation were weaker, and the duration of the DCSWV was shorter (lasting about 5 h) in the NOTER experiment.

To sum up, although the lateral friction in the TP and Yun-Gui Plateau were not the decisive factors for the formation of the DCSWV as latent heat, the topographical forcing and dynamical instability could influence the location, size, and duration of the DCSWV.

SUMMARY AND DISCUSSION

The DCSWV is difficult to be recognized with coarse observations, partly because its spatial and temporal scales are too small to be captured. Therefore, this study used the NCEP-FNL dataset and the WRF model to investigate and simulate the evolution of the DCSWV, as well as examine the influence of latent heat release and topography on the DCSWV. The major conclusions are summarized below:

1) The observed SWV occurred from 12:00 UTC July 16 to 06:00 UTC July 17, 2010. Two rain belts and cloud clusters were observed near the SWV "C1" and "C2", which further confirmed the presence of the DCSWV. Meanwhile, a westerly trough was observed from Lake Baikal to the SCB, which was favorable for the formation of vortexes. Besides, this DCSWV was most visible in the lower troposphere with two centers at 700 and 850 hPa, and the precipitation brought by the DCSWV had a more severe and extensive impact on the local region compared with a typical single SWV.

2) The DCSWV could be divided into five stages, with a lifetime of 11 h from gestation to dissipation. In the gestation stage of the DCSWV, the lower troposphere was warm and wet, indicating that the atmosphere was unstable. In the development and mature stage, the DCSWV had two obvious relative vorticity centers horizontally, "C1" and "C2", which was similar to the "double-yolk" structure, and it should be noted that "C1" was deeper and stronger than "C2". These two cores both had warm and moist vertical structures along with two clear centers of upward motion.

3) The vorticity budget showed that the contribution terms to the initiation and intensification of "C1" and "C2" were different. The STR and TIL terms were the main positive contributors to the

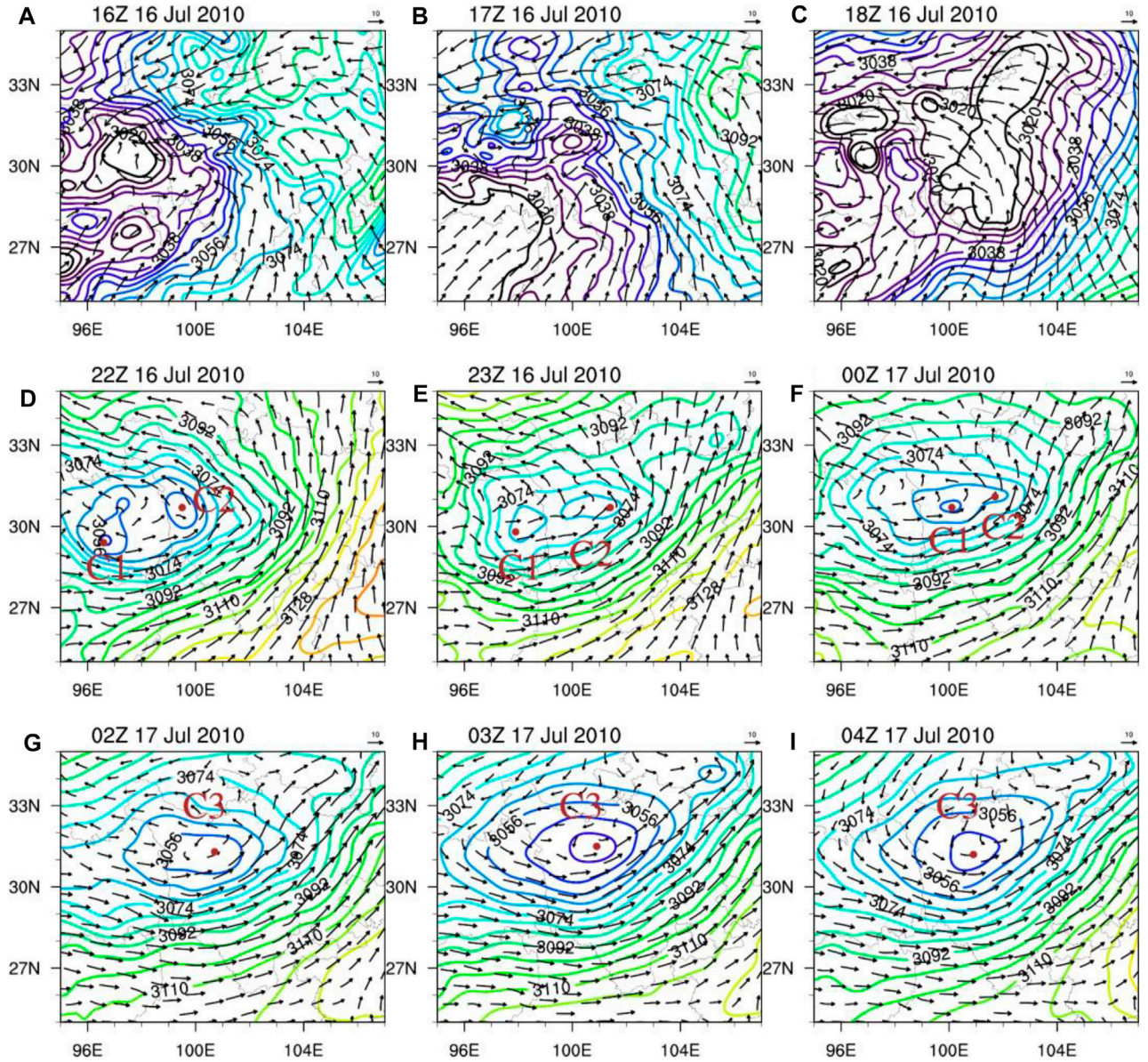

FIGURE 13 | 700 hPa geopotential height (gpm, contours) and wind field (m s^{-1}, arrows) for the NOTER experiment at **(A)** 16:00 UTC July 16, **(B)** 17:00 UTC July 16, **(C)** 18:00 UTC July 16, **(D)** 22:00 UTC July 16 **(E)** 23:00 UTC July 16, **(F)** 00:00 UTC July 17, **(G)** 02:00 UTC July 17, **(H)** 03:00 UTC July 17, and **(i)** 04:00 UTC July 17.

intensification of "C1", while the STR and VAV terms played important roles in the initiation and intensification of "C2", which implied the importance of moisture convergence and ascending motion. In fact, abundant water vapor was transported by southerlies from the Bay of Bengal and the South China Sea to the key region of the DCSWV. Abundant water vapor flux benefited the stronger moisture convergence and upward motion, which led to the release in convective latent heat that increased lower-troposphere vorticity. These thermodynamic conditions were favorable to the evolution of the DCSWV. Such positive feedback was good for the intensification stage of "C1" and decisive to the initiation and intensification stages of "C2." Furthermore, NOLH and NOTER experiments showed that topographical forcing and dynamical instability were insufficient to maintain the DCSWV without latent heat, while the TP and Yun-Gui Plateau topography could influence the location, size, and duration of the DCSWV.

This study gives details of the possible mechanism of the DCSWV using dynamic diagnosis and WRF simulation to a typical DCSWV case, which is helpful to weather forecasters to learn more about the DCSWV. Although the individual case is

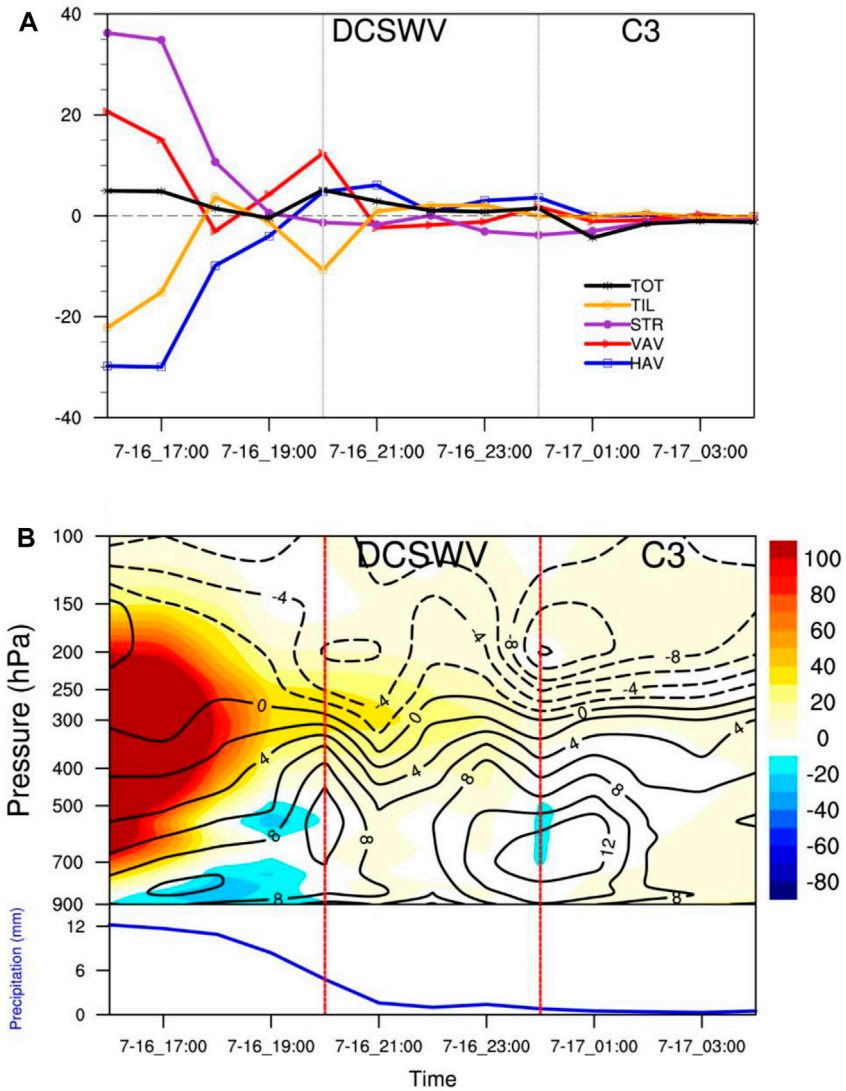

FIGURE 14 | (A) Regionally averaged vorticity budget terms (units: 10^{-9} s^{-2}) of SWVs and **(B)** time–pressure sections of apparent heat source Q1 (K day^{-1}, shaded), relative vorticity (10^{-5} s^{-1}, black contours), and regional mean precipitation within the key region (mm, blue line) from 16:00 UTC July 16 to 04:00 UTC July 17 in the NOTER experiment.

representative, the sample size is limited. Therefore, more cases of the DCSWV, as well as the wave instability and other forcing factors will be worth further study over the SCB to clarify the common physical characteristics of the DCSWV in more detail.

DATA AVAILABILITY STATEMENT

The NCEP-FNL reanalysis data were obtained from https://rda.ucar.edu/datasets/ds083.2/. The ERA5 reanalysis data were retrieved from https://www.ecmwf.int/en/forecasts/datasets/reanalysis-datasets/era5. The MTSAT-2 IR1 brightness temperature data were downloaded from http://weather.is.kochi-u.ac.jp/archive-e.html. The CMORPH global precipitation data is available at http://data.cma.cn.

AUTHOR CONTRIBUTIONS

ZW conducted the analyses. HL supervised the study. ZW, HL, KC, and KW wrote the manuscript. ZW, HL, KC, KW, and WZ contributed to the discussion of the results.

FUNDING

This work of ZW and HL was jointly supported by the National Natural Science Foundation of China (42075008), the Special Foundation for the security capacity building of China Civil Aviation Administration of China (20600822). This work of KC was jointly supported by the National Key R&D Program of China (2019YFC1510400), the National

Natural Science Foundation of China (41975052), the Innovation Group Project of the Southern Marine Science and Engineering Guangdong Laboratory (Zhuhai) (311021001), and the Guangdong Province Key Laboratory for Climate Change and Natural Disaster Studies (2020B1212060025).

REFERENCES

Alapaty, K., Herwehe, J. A., Otte, T. L., Nolte, C. G., Bullock, O. R., Mallard, M. S., et al. (2012). Introducing Subgrid-scale Cloud Feedbacks to Radiation for Regional Meteorological and Climate Modeling. *Geophys. Res. Lett.* 39, L24809. doi:10.1029/2012GL054031

Chen, S.-J., and Dell'osso, L. (1984). Numerical Prediction of the Heavy Rainfall Vortex over Eastern Asia Monsoon Region. *J. Meteorol. Soc. Jpn.* 62, 730–747. doi:10.2151/jmsj1965.62.5_730

Chen, Z.-M., Miao, Q., and Min, W.-B. (1998). A Case Analysis on Mesoscale Structure of Severe Southwest Vortex. *Q. J. Appl. Meteorology* 9, 18–27.

Dudhia, J. (1989). Numerical Study of Convection Observed during the winter Monsoon experiment Using a Mesoscale Two-Dimensional Model. *J. Atmos. Sci.* 46, 3077–3107. doi:10.1175/1520-0469(1989)046<3077:nsocod>2.0.co;2

Ek, M. B., Mitchell, K. E., Lin, Y., Rogers, E., Grunmann, P., Koren, V., et al. (2003). Implementation of Noah Land Surface Model Advances in the National Centers for Environmental Prediction Operational Mesoscale Eta Model. *J. Geophys. Res.* 108, 8851. doi:10.1029/2002JD003296

Feng, S. L., Jin, S. L., Fu, S. M., Sun, J. H., and Zhang, Y. C. (2020). Formation of a Kind of Heavy-precipitation-producing Mesoscale Vortex Around the Sichuan Basin: An Along-track Vorticity Budget Analysis. *Atmos. Sci. Lett.* 21, e949. doi:10.1002/asl2.949

Feng, X., Liu, C., Fan, G., Liu, X., and Feng, C. (2016). Climatology and Structures of Southwest Vortices in the NCEP Climate Forecast System Reanalysis. *J. Clim.* 29 (21), 7675–7701. doi:10.1175/JCLI-D-15-0813.1

Fu, S., Jian-Hua, S., Si-Xiong, Z., and Wan-Li, L. (2010). The Impact of the Eastward Propagation of Convective Systems over the Tibetan Plateau on the Southwest Vortex Formation in Summer. *Atmos. Oceanic Sci. Lett.* 3, 51–57. doi:10.1080/16742834.2010.11446836

Fu, S.-M., Sun, J.-H., Luo, Y.-L., and Zhang, Y.-C. (2017). Formation of Long-Lived Summertime Mesoscale Vortices over Central East China:Semi-Idealized Simulations Based on a 14-Year Vortex Statistic. *J. Atmos. Sci.* 74, 3955–3979. doi:10.1175/JAS-D-16-0328.1

Fu, S., Li, W., Sun, J., Zhang, J., and Zhang, Y. (2014). Universal Evolution Mechanisms and Energy Conversion Characteristics of Long-Lived Mesoscale Vortices over the Sichuan Basin. *Atmos. Sci. Lett.* 16, 127–134. doi:10.1002/asl2.533

Hong, S.-Y., Dudhia, J., and Chen, S.-H. (2004). A Revised Approach to Ice Microphysical Processes for the Bulk Parameterization of Clouds and Precipitation. *Monthly Weather Rev.* 132, 103–120. doi:10.1175/1520-0493(2004)132<0103:aratim>2.0.co;2

Janjić, Z. I. (2002). Nonsingular Implementation of the Mellor-Yamada Level 2.5 Scheme in the NCEP Meso Model. *NCEP Off. note* 437, 61.

Jiang, X., Li, Y., Zhao, X., and Koike, T. (2012). Characteristics of the Summertime Boundary Layer and Atmospheric Vertical Structure over the Sichuan basin. *J. Meteorol. Soc. Jpn.* 90, 33–54. doi:10.2151/jmsj.2012-C03

Kuo, Y.-H., Cheng, L., and Anthes, R. A. (1986). Mesoscale Analyses of the Sichuan Flood Catastrophe, 11–15 July 1981. *Monthly Weather Rev.* 114, 1984–2003. doi:10.1175/1520-0493(1986)114<1984:maotsf>2.0.co;2

Kuo, Y. H., Cheng, L., and Bao, J. W. (1988). Numerical Simulation of the 1981 Sichuan Flood. Part I: Evolution of a Mesoscale Southwest Vortex. *Monthly Weather Rev.* 116, 2481–2504. doi:10.1175/1520-0493(1988)116<2481:NSOTSF>2.0.CO;2

Li, L., Zhang, R., and Wen, M. (2017). Genesis of Southwest Vortices and its Relation to Tibetan Plateau Vortices. *Q.J.R. Meteorol. Soc.* 143, 2556–2566. doi:10.1002/qj.3106

Liu, W. G., Chen, H. S., and Yu, M. (2019). Impacts of Cumulus Convective Parameterization Schemes on Simulation of East Asian Summer Circulation and Rainfall. *Chin. J. Atmos. Sci.* 43 (1), 64–74. [in Chinese]. doi:10.3878/j.issn.1006-9895.1801.17222

Lu, J.-H. (1986). *Introduction to the Southwest Vortex (In Chinese)*. Beijing: Meteorological Press, 276.

Mlawer, E. J., Taubman, S. J., Brown, P. D., Iacono, M. J., and Clough, S. A. (1997). Radiative Transfer for Inhomogeneous Atmospheres: RRTM, a Validated Correlated-K Model for the Longwave. *J. Geophys. Res.* 102, 16663–16682. doi:10.1029/97JD00237

Orlanski, I. (1975). A Rational Subdivision of Scales for Atmospheric Processes. *Bull. Am. Meteorol. Soc.* 56, 527–530. Available at: https://www.jstor.org/stable/26216020.

Pan, Y., Shen, Y., Yu, J. J., and Zhao, P. (2012). Analysis of the Combined Gauge-Satellite Hourly Precipitation over China Based on the OI Technique. *Acta Meteorologica Sinica* 70, 1381–1389. [in Chinese].

Qin, Z., and Zou, X. (2019). Impact of AMSU-A Data Assimilation over High Terrains on QPFs Downstream of the Tibetan Plateau. *J. Meteorol. Soc. Jpn.* 97, 1137–1154. doi:10.2151/jmsj.2019-064

Raymond, D. J., and Jiang, H. (1990). A Theory for Long-Lived Mesoscale Convective Systems. *J. Atmos. Sci.* 47, 3067–3077. doi:10.1175/1520-0469(1990)047<3067:atfllm>2.0.co;2

Shen, Y., Pan, Y., Yu, J. J., Zhao, P., and Zhou, Z. J. (2013). Quality Assessment of Hourly Merged Precipitation Product over China. *Trans. Atmos. Sci.* 36, 37–46. [in Chinese]. doi:10.13878/j.cnki.dqkxxb.2013.01.005

Skamarock, W. C., Klemp, J. B., Dudhia, J., Gill, D. O., Barker, D., Duda, M. G., and Powers, J. G. (2008). A Description of the Advanced Research WRF Version 3 (Note NCAR/TN-475+STR). *University Corporation for Atmospheric Research* 113. NCAR Tech. doi:10.5065/D68S4MVH

Takeuchi, W., Nemoto, T., Kaneko, T., and Yasuoka, Y. (2007). Development of MTSAT Data Processing, Visualization and Distribution System on WWW. *J. Jpn. Soc. photogrammetry remote sensing* 46, 42–48. doi:10.4287/jsprs.46.6_42

Wang, B. (1987). Study of a Heavy Rain Vortex Formed over the Eastern Flank of the Tibetan Plateau. *Monthly weather Rev.* 115, 1370–1393. doi:10.1175/1520-0493(1987)115<1370:soahrv>2.0.co;2

Wang, M., and Zhang, Y. (2011). Diagnostic Analysis on Continual Rainstorm from July 16 to July 18, 2010. *Plateau Mountain Meteorology Res.* 31, 43–48. [in Chinese].

Wang, W., Kuo, Y.-H., and Warner, T. T. (1993). A Diabatically Driven Mesoscale Vortex in the lee of the Tibetan Plateau. *Monthly weather Rev.* 121, 2542–2561. doi:10.1175/1520-0493(1993)121<2542:addmvi>2.0.co;2

Wang, Z. S., Wang, Y., and Liang, Y. (1996). "A Numerical Simulation Study of a Heavy Rain Event Induced by a Southwest Vortex," in *Experimental, Synoptical and Dynamical Studies of Heavy Rain* (Beijing, China: China Meteorological Press), 257–267. [in Chinese].

Wu, G.-X., and Chen, S.-J. (1985). The Effect of Mechanical Forcing on the Formation of a Mesoscale Vortex. *Q.J.R. Meteorol. Soc.* 111, 1049–1070. doi:10.1002/qj.49711147009

Wu, Z. Z., Liu, H. W., and Pan, L. L. (2018). Analysis of a Binary Southwest Vortex and its Precipitation over the Sichuan basin on 4–5 August 2011. *J. Chengdu Univ. Inf. Technol.* 33, 681–687. doi:10.16836/j.cnki.jcuit.2018.06.014 [in Chinese]

Yanai, M., Esbensen, S., and Chu, J.-H. (1973). Determination of Bulk Properties of Tropical Cloud Clusters from Large-Scale Heat and Moisture Budgets. *J. Atmos. Sci.* 30, 611–627. doi:10.1175/1520-0469(1973)030<0611:dobpot>2.0.co;2

Ye, D. (1981). Some Characteristics of the Summer Circulation over the Qinghai-Xizang (Tibet) Plateau and its Neighborhood. *Bull. Amer. Meteorol. Soc.* 62, 14–19. doi:10.1175/1520-0477(1981)062<0014:scotsc>2.0.co;2

Ye, D., and Gao, Y.-X. (1979). *The Meteorology of the Qinghai-Xizang (Tibet) Plateau*. Beijing: Science Press, 278. [in Chinese].

Zhang, D.-L. (1992). The Formation of a Cooling-Induced Mesovortex in the Trailing Stratiform Region of a Midlatitude Squall Line. *Monthly weather Rev.* 120, 2763–2785. doi:10.1175/1520-0493(1992)120<2763:tfoaci>2.0.co;2

Zhou, K., Liu, H., Zhao, L., Zhu, Y., Lin, Y., Zhang, F., et al. (2017). Binary Mesovortex Structure Associated with Southwest Vortex. *Atmos. Sci. Lett.* 18, 246–252. doi:10.1002/asl.749

Conflict of Interest: The authors declare that the research was conducted in the absence of any commercial or financial relationships that could be construed as a potential conflict of interest.

Publisher's Note: All claims expressed in this article are solely those of the authors and do not necessarily represent those of their affiliated organizations, or those of the publisher, the editors, and the reviewers. Any product that may be evaluated in this article, or claim that may be made by its manufacturer, is not guaranteed nor endorsed by the publisher.

frontiers in Earth Science

ORIGINAL RESEARCH
published: 17 March 2022
doi: 10.3389/feart.2022.817084

Experiment Study of Porous Fiber Material on Infiltration and Runoff of Winter Wheat Farmland in Huaibei Plain, China

Wei Li[1,2,3], *Shanshan Liu*[3]*, *Tianling Qin*[3]*, *Shangbin Xiao*[1,2], *Chenhao Li*[3,4,5], *Xin Zhang*[3], *Kun Wang*[3] and *Sintayehu A. Abebe*[3]

[1]Engineering Research Center of Eco-Environment in Three Gorges Reservoir Region, Ministry of Education, Yichang, China, [2]College of Hydraulic and Environmental Engineering, China Three Gorges University, Yichang, China, [3]State Key Laboratory of Simulation and Regulation of Water Cycle in River Basin, China Institute of Water Resources and Hydropower Research, Beijing, China, [4]College of Resource Environment and Tourism, Capital Normal University, Beijing, China, [5]Beijing Laboratory of Water Resources Security Beijing Institute of Hydrogeology, Beijing, China

OPEN ACCESS

Edited by:
Sanjeev Kumar Jha,
Indian Institute of Science Education and Research, India

Reviewed by:
Huaiwei Sun,
Huazhong University of Science and Technology, China
Dengfeng Liu,
Xi'an University of Technology, China

***Correspondence:**
Shanshan Liu
liushanshan198705@163.com
Tianling Qin
qintl@iwhr.com

Specialty section:
This article was submitted to Hydrosphere, a section of the journal Frontiers in Earth Science

Received: 17 November 2021
Accepted: 11 January 2022
Published: 17 March 2022

Citation:
Li W, Liu S, Qin T, Xiao S, Li C, Zhang X, Wang K and Abebe SA (2022) Experiment Study of Porous Fiber Material on Infiltration and Runoff of Winter Wheat Farmland in Huaibei Plain, China. Front. Earth Sci. 10:817084. doi: 10.3389/feart.2022.817084

Drought and floods frequently occurred in the Huaibei plain, which was the main factor that restricted agricultural development. We conducted rainfall experiments, which aimed to explore the impacts of porous fiber material (PFM) on the farmland water cycle processes and soil water storage capacity. In this study, we designed two types of rainfall intensities, 4 PFM volumes, 4 growth periods of winter wheat, and a total of 8 experimental groups and 32 rainfall events to evaluate the effects. The result showed that PFM had significantly affected the soil water circulation in the grain-filling period, and the peak flow and runoff decreased maximumly compared with other periods. However, the effect of PFM on surface runoff was slighter in the fallow period, and the peak flow or runoff decreased with the PFM volumes increased (R^2 = –0.92, –0.99). In the 100 and 50 mm/h rainfall intensities, PFM decreased the average values of runoff by (55.2–59.6%) and (57.2–90.2%), reduced peak flow by (62.2–68%) and (64.2–86%), and increased the stable infiltration rate by (13.4–14.3%) and (26.6–41.3%), respectively. After the rainfall experiments ended for 1 h, the surface soil water rapidly infiltrated into PFM, which made the water-storage capacity of PFM groups higher than the control groups by 0.2–11% Vol. Subsequently, PFM increased the water-holding capacity by 0.3–2.3% Vol in the 10–70 cm depth from the heading period to the fallow period. It had a positive relationship between the PFM volumes and the average values of soil water content (R^2 = 0.8, 0.84). In general, PFM could increase infiltration, reduce runoff, and improve the water-storage capacity to alleviate soil water deficit and the risk of farmland drought and floods. It has an excellent application effect in long-duration rainfall.

Keywords: porous fiber material, infiltration, runoff, water-holding capacity, water-storage capacity

INTRODUCTION

Farmland drought and floods frequently occurred globally because the rainfall events were distributed unevenly in time and space. Meanwhile, the change of land use mode and over-development of cultivated land reduces the soil water-holding capacity and aggerates the disaster risk (Karamage et al., 2020; Winkler et al., 2021). Scholars successively studied the effect of porous materials on the water cycle of agricultural farmland (such as straw returning, biochar, and rock wool), aimed to improve the soil structure, increase water-retention capacity, and enhance risk resistance (Saffari et al., 2021; Zhao et al., 2019). Based on the above study, we assumed that the rock wool could redistribute soil water, enhance the water storage capacity, change the soil runoff, and improve the infiltration mechanism of farmland (Cai et al., 2020) (**Figure 1**). Finally, porous fiber material (PFM) reduces the occurrence of farmland drought and flood events and increases risk resistance. Therefore, we conducted extreme rainfall events to explore the impacts of rock wool materials on farmland soil infiltration, runoff, and water-holding capacity.

In the farmland water cycle processes, porosity is considered an important parameter, and it directly influences the soil water distribution and water-holding capacity. At the same time, soil porosity drives the migration of energy and materials and changes the infiltration and runoff mechanism (Helalia, 1993; Huang et al., 2021; Du et al., 2021; Wasko and Nathan, 2019). But the infiltration and runoff of farmland were complex hydrological phenomena; it was the interactive result of rainfall and soil management measures (Yu et al., 2021). Based on the above cognition, porous materials could improve the soil porosity and increase the water-absorbing capacity, water-holding capacity, and water-storage capacity (Sun et al., 2021). Some soil parameters (such as soil porosity and water conductivity) change after the porous materials are embedded in the soil, benefiting the infiltration, and effectively reducing runoff and soil erosion. The internal structural characteristics of porous materials make it easy to absorb and retain water and ultimately achieve a more effective utilization of precipitation (Li et al., 2019; Raimondi and Becciu, 2021).

At present, most scholars have explored the impacts of porous materials on the soil structure (such as the soil porosity, bulk density, water conductivity, etc.) (Humberto, 2017; Dong et al., 2019; Dunkerley, 2021) and revealed its mechanism that the probers materials were how to influence the infiltration process and soil water-holding capacity (Li et al., 2019; Ahmadi et al., 2020; Chen et al., 2020; Yang et al., 2021). Although traditional porous materials increased the infiltration and water-retaining capacity, there were the following defects: blocking soil pores, compacting soil during the application, limiting the improvement range of water-holding capacity (Pu et al., 2019; Zhang F. B. et al., 2019), which would aggravate the soil erosion of farmland in some extreme rainfall events (Werdin et al., 2021; Li et al., 2020). The

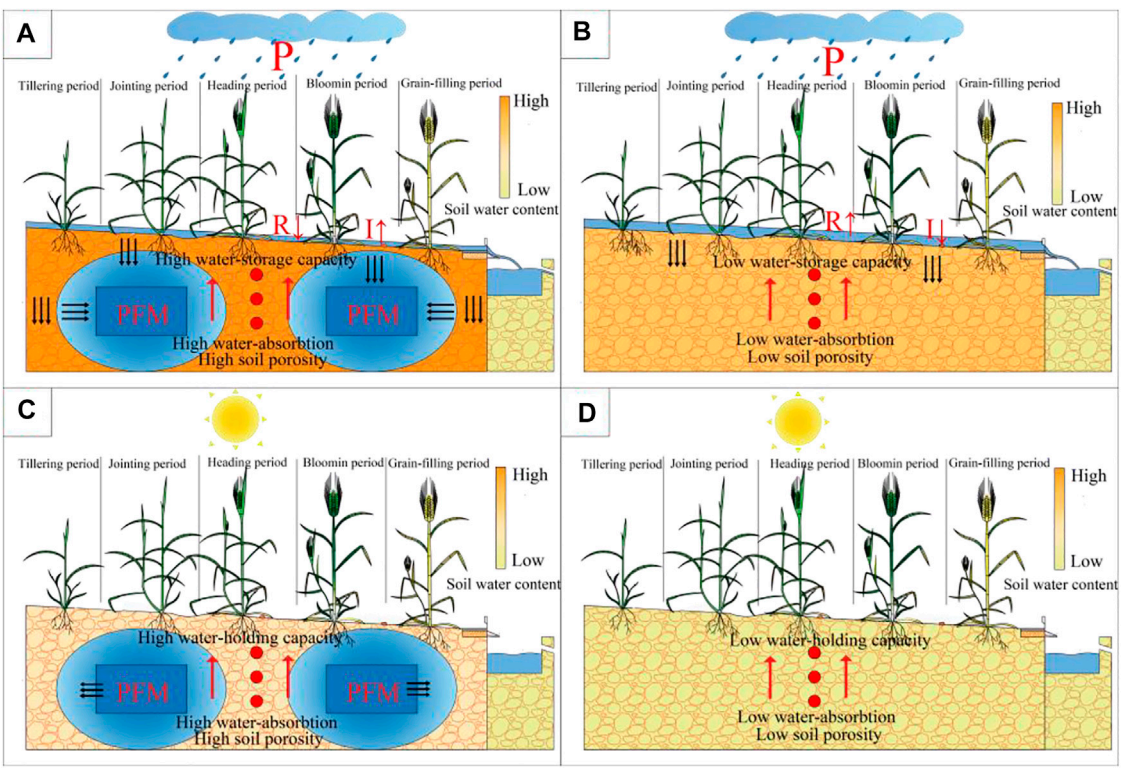

FIGURE 1 | PFM embedding in the farmland increases soil porosity, which benefits the increase of infiltration and the reduction of runoff. **(A–D)** represent the changes of soil water content in the different scenarios, respectively.

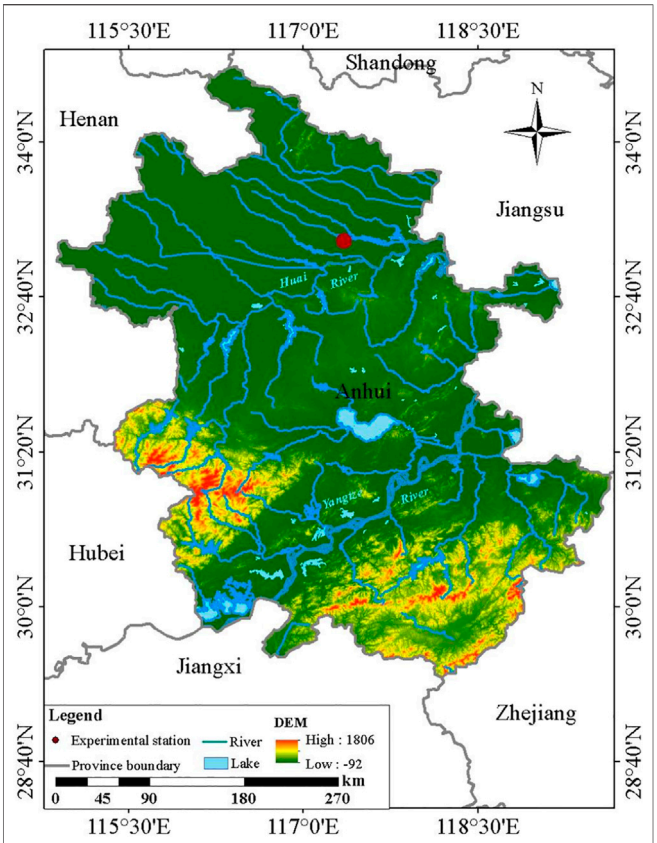

FIGURE 2 | The location of the experiment site and its terrain.

PFM is mainly composed of hydrophilic rock wool, which has stability, high porosity, pressure resistance, and water retention. PFM could quickly absorb water and drain water, which benefits the distribution of water and nutrients on the board uniformly (Bougoul and Boulard, 2006; Titouna and Bougoul, 2013; Choi and Shin, 2019). Because rock wool could regulate the proportion of water, nutrient, and gas in the plant roots' environment, it has been widely used in soilless culture (Savvas and Gruda, 2018). At the same time, the field observation experiments conducted at the woodland and farmland, which confirmed PFM had significant effects on regulating soil water distribution and increasing infiltration (Gu et al., 2020; Lv et al., 2020; Gu et al., 2021; Lv et al., 2021). The above study preliminarily proved that PFM could improve the soil water-holding capacity and had good application in preventing drought and floods disasters (De-Ville et al., 2017). However, most studies were indoor simulation tests of a single factor and a single process, which was difficult to indicate the effect of porous materials on farmland water circulation processes (Pu et al., 2019; Cai et al., 2020; Libutti et al., 2021). In addition, the study about PFM mainly focused on soilless cultivation and green roofs. However, scholars paid little attention to its influence on hydrological characteristics such as farmland soil infiltration and runoff yield processes under extreme rainfall events.

The soil in Huaibei Plain is lime concretion black soil, which has low organic matter content, heavy texture, and poor air permeability. Drought and floods frequently occurred because of the poor soil structure, which was the main factor that restricted agricultural development (Liu. et al., 2017; Bi et al., 2020; Wang et al., 2021). To solve the above problems and extend the utilization of the PFM, we explored the effect of PFM on the infiltration and runoff yield by rainfall experiments. The purposes of this paper are as follows: 1) discovering the impacts of PFM on soil infiltration and runoff; and 2) analyzing the influences of PFM on the water retention capacity of the soil.

STUDY AREA

The experiments were conducted at Wudaogou Hydrological Station (117°21′E, 33°09′N) in Bengbu City, Anhui Province, China. The hydrological station is in the Huai River Basin and Huaibei plain (**Figure 2**). The area experiences a north subtropical and warm temperate semi-humid monsoon climate zone, which is hot and rainy in summer and dry and cold in winter. According to the station data records, the annual average air and surface temperature were 14.7 and 17.9°C, respectively. The annual average precipitation was 890 mm from 1963 to 2017 in this region (Bi et al., 2020; Gou et al., 2020). The maximum rainfall intensity was about 92.4 mm/h, which occurred on June 29, 1997. The main crops include wheat, maize, peanut, soybean, and others. The soil in this region is mainly lime concretion black soil. The effective soil depth is approximately 100 cm, and the soil porosity is about 49.7%.

MATERIAL AND METHODS

Experiment Design

In this study, we set up three factors: two rainfall intensities, four PFM volumes, and four growth periods of winter wheat. Eight experimental groups were designed based on the above factors. The concrete design is shown in **Table 1**.

PFM Volume

The increased goal of soil water-holding capacity was set by 0, 5, 10, and 15%, so the PFM volumes were designed to $V_1 = 0\ m^3$, $V_2 = 1.08\ m^3$, $V_3 = 2.16\ m^3$, and $V_4 = 3.24\ m^3$, respectively. The size of PFM in A2, A3, A4 experimental plots was $0.75 \times 0.45 \times 0.4 \times 8\ m^3$ (length × width × height × block), $1.2 \times 0.45 \times 0.4 \times 10\ m^3$, and $3 \times 0.45 \times 0.4 \times 6\ m^3$, respectively (**Figure 3**), and B2, B3, B4 experimental groups were the same as A2, A3, A4 groups, respectively. PFM volumes can be expressed as (Lv et al., 2020):

$$\delta = \frac{V_1}{V_0} \times \frac{\beta_1 - \beta_0}{\beta_0} \times 100\%$$

$$V_0 = L \times D \times H$$

where δ represents the theoretical increase (%) of soil water-holding capacity; V_1 indicates the PFM volumes in different experimental plots (m^3); V_0 indicates the total volume (m^3) of the effective depth of the experimental plot; β_1 and β_2 are PFM and soil porosity (%), respectively; L, D, and H represent the

TABLE 1 | Scenarios designed and their corresponding experimental plots.

Experimental plots	PFM volume (m^3)	Rainfall intensity (mm/h)	Growth period
A1	V1	100	Heading period
B1	V1	50	
A2	V2	100	Blooming period
B2	V2	50	
A3	V3	100	Grain-filling period
B3	V3	50	
A4	V4	100	Fallow period
B4	V4	50	

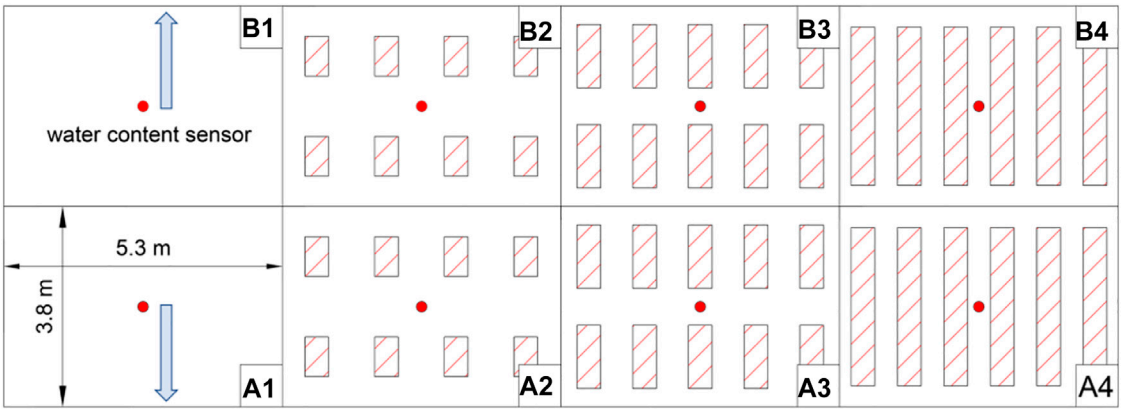

FIGURE 3 | Location of the porous-fiber module in plots and their direction of the slope. A1, A2, A3, and A4 are the experimental plots under 100 mm/h rainfall intensity; B1, B2, B3, and B4 are the experimental plots under 50 mm/h rainfall intensity; the arrow represents the direction of slope, A1~A4 plots have the same direction of the slope; B2-B4 plots are the same as the B1 plot.

length, width, and effective soil depth of the experimental plots, respectively.

Rainfall Intensity

We have referred to the annual rainfall records of the experimental station, and two rainfall intensities were set as P1 = 100 mm/h and P2 = 50 mm/h according to the Grading Standards for Rainfall of China and annual rainfall records, respectively. The rainfall amount of a single experiment was designed to be 150 mm, and the rainfall duration was set as 1.5 and 3 h, respectively.

Growth Periods

We have referred to the water requirement of winter wheat in the Huaibei area, so rainfall experiments were conducted at the heading period (3.24–3.26), the blooming period (4.14–4.17), the grain-filling period (5.8–5.10), and the fallow period (6.8–6.10), respectively. The artificial rainfall was set as the average annual rainfall amount, ensuring that winter wheat grows normally before regreening.

Experimental Plot

The size of experimental plots is 5.3 × 3.8 m^2 with a 3°slope in the north-south direction. The experimental plots and corresponding devices include a rainfall device, wind dodger, water-stop sheep, channel, rain cover, water tank, and water moisture sensor. PFM was embedded in the 30–70 cm depth. Three water sensors were buried in the 20, 40, 60 cm depth in the center of experimental plots, respectively (**Figure 1**).

Date Monitoring

We monitored the variation of soil water content at 8:00 every day. Subsequently, we started rainfall experiments when the soil water content reached 25.0 ± 2.0% Vol at a depth of 20 cm. During rainfall, we recorded the start time of runoff and measured the runoff flow rate at intervals of 5 min. After the rainfall ended, we monitored the variation of soil water content every 1 h for a total of 6 h.

Date Processing

Data were analyzed in SPSS, Excel, and Origin. The significance of the effects of the PFM on the runoff process and water-holding capacity were tested by ANOVA ($p < 0.5$). Finally, we evaluated the impact of PFM on the farmland water cycle by comparing the variation of stable infiltration rate and runoff process.

We could get the cumulative infiltration and infiltration processes according to the runoff processes when we ignored

TABLE 2 | The stable infiltration rate under different growth periods of different experimental plots and evaluation index of fitting performance.

Growth period	Group	A	R2	NSE	RE	Group	A	R2	NSE	RE
Heading period	A1	1.58	0.999	0.999	13.50%	B1	0.61	0.998	0.997	20.90%
	A2	1.58	0.999	0.999	1%	B2	0.82	0.999	0.999	6.30%
	A3	1.54	0.999	0.999	−0.40%	B3	0.77	0.999	0.999	5.40%
	A4	1.56	0.999	0.999	−0.40%	B4	0.83	0.999	0.999	3.30%
Blooming period	A1	1.23	0.999	0.996	16.30%	B1	0.49	0.997	0.993	17.30%
	A2	1.53	0.999	0.999	1.80%	B2	0.79	0.999	0.999	14.90%
	A3	1.5	0.999	0.999	1.80%	B3	0.66	0.999	0.999	3.70%
	A4	1.4	0.999	0.999	0.10%	B4	0.79	0.999	0.999	3.20%
Grain-filling period	A1	1.46	0.999	0.998	22.70%	B1	0.66	0.998	0.997	27.20%
	A2	1.65	0.999	0.999	1.70%	B2	0.83	0.999	0.999	0.80%
	A3	1.66	0.999	0.999	1.40%	B3	0.79	0.999	0.999	-0.20%
	A4	1.66	0.999	0.999	2%	B4	0.83	1	1	0%
Fallow period	A1	1.06	0.999	0.998	0.60%	B1	0.53	0.998	0.996	22%
	A2	1.34	0.999	0.999	5.30%	B2	0.59	0.999	0.998	13.20%
	A3	1.36	0.999	0.999	9.60%	B3	0.68	0.999	0.999	2.70%
	A4	1.49	0.999	0.999	4.90%	B4	0.78	0.999	0.999	8.30%

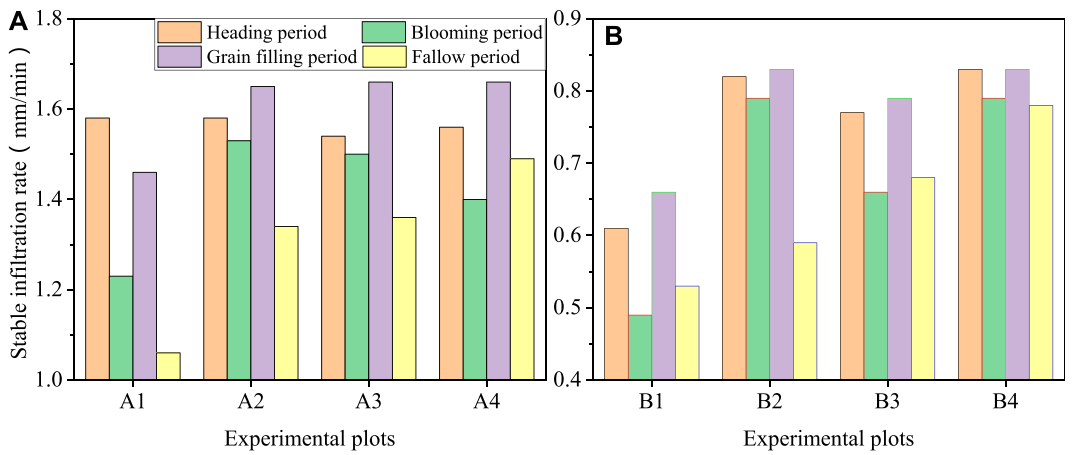

FIGURE 4 | Variations in stable infiltration rate in different rainfall intensity and growth periods. **(A)** and **(B)** in the picture represent the experimental plots under 100 and 50 mm/h rainfall intensity, respectively.

evaporation and the interception by plants. Subsequently, the soil infiltration processes of the experimental plots were fitted by the Philip model and obtained the stable infiltration rate. Finally, we used the R^2, Nash–Sutcliffe efficiency (NSE) coefficient, and relative deviation (RE) between the stable infiltration rate and the minimum infiltration rate to evaluate the performance of the Philip model (Sun et al., 2019; Duan et al., 2021).

$$I(t) = A \times t + S \times t^{0.5}$$

where $I(t)$ represents the theoretical cumulative infiltration amount during the rainfall process, mm; A represents the stable infiltration rate, mm/min; t is the rainfall time, min; S represents a parameter defined as sorptivity, mm/(min$^{0.5}$). Both A and S were determined by the least-square method.

RESULTS

PFM Increase Infiltration

The Philip model was used to fit the infiltration processes when we ignored the plant interception, the R^2 values were more than 0.997 between the stable infiltration rate and the minimum observed infiltration rate, and the Nash–Sutcliffe efficiency (NSE) coefficient values were above 0.993, and the RE values were mostly less than 10% (except the A1 and B1 groups), so the correlation was excellent (**Table 2**). In general, PFM increased the stable infiltration rate by 5.2%, 9.2%, under 100 and 50 mm/h rainfall intensity, respectively, so the PFM increased the stable infiltration rate of experimental plots (**Figure 4**).

PFM increased the stable infiltration rate. The stable infiltration rate of all PFM groups increased by 12.7–61%, compared with the

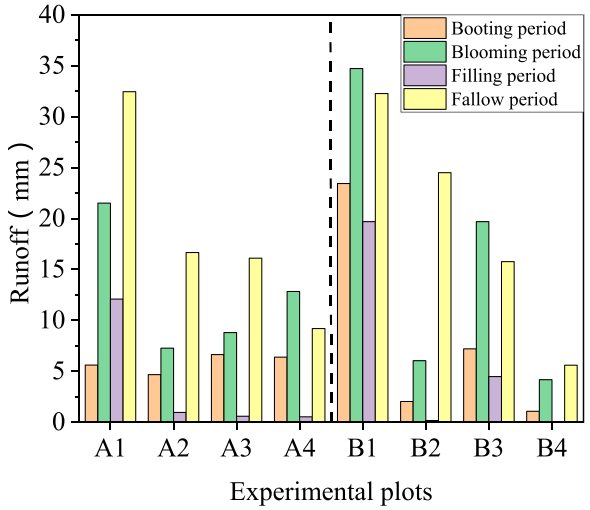

FIGURE 5 | Observed runoff in different plots and growth periods under 100 mm h^{-1} (left) and 50 mm h^{-1} (right) rainfall intensities. A1, A2, A3, and A4 are the experimental plots under 100 mm h^{-1} rainfall intensity; B1, B2, B3, and B4 are the experimental plots under 50 mm h^{-1} rainfall intensity.

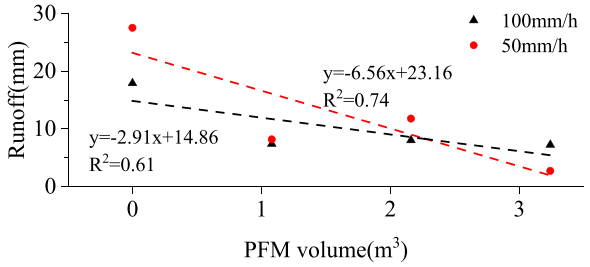

FIGURE 6 | Observed cumulative runoff in different PFM volumes under 100 mm h^{-1} and 50 mm h^{-1} rainfall intensities.

control plots, respectively (except the A1 plot in the heading stage). The minimum infiltration rate by observing increased with the PFM volumes increased too (R^2 = 0.61.0.73). In different growth periods of winter wheat, PFM significantly influenced the variation of stable infiltration rate in the fallow period, and the stable infiltration rate increased with the PFM volumes increased (R^2 = 0.87.0.99), and the stable infiltration rate of the A2, A3, and A4 plots increased by 26.6, 28.7, and 40.6%, respectively, compared with the A1 control plot. In the same way, B2, B3, and B4 groups with the PFM increased by 12.7, 29, and 48.3%, respectively, compared with the B1 control plot. But in the grain-filling period, the range of increase rate only was 13–26.8% when PFM was embedded in the soil.

Analyzing the effect of PFM on infiltration processes from the different rainfall intensities, the increased range of stable infiltration rate after PFM embedding was 13.4–14.3% compared with the A1 control plot under 100 mm/h rainfall intensity, and the stable infiltration rate of PFM experimental groups increased 26.6–41.3% under the 50 mm/h rainfall intensity, compared with the B1 control group. To sum up, we concluded that PFM has excellent applicability under low-intensity or long-duration rainfall.

PFM Decrease Runoff

In general, PFM reduced the runoff volume by 24.1–100% during the rainfall experiment, compared with the control group, respectively (except the A1 plot at the heading period). Total runoff volumes decreased with the PFM volumes increased (R^2 = 0.61.0.74) (**Figures 5**, **6**). Analyzing the impact of PFM on runoff from the growth periods, the runoff volume was the following: the fallow period > the blooming period > the heading period > the grain-filling period. PFM significantly affected runoff during the grain-filling period, and it decreased 77.2–100% at the maximum. In addition, the runoff volumes of PFM groups reduced by 24.1–82.7%, respectively, in the fallow period, compared with the control group, and it comes significantly negatively correlated with the PFM volumes (R^2 = -0.92, -0.99). In the 100 mm/h rainfall intensity, the runoff volume in A2, A3, and A4 groups reduced by 9.9–10.7 mm on average, compared with the A1 control group, respectively, and B2, B3, and B4 groups decreased (15.8–24.8) mm in 50 mm/h (**Figure 5**). PFM has a better application to reduce the runoff in low-intensity and long-duration rainfall.

PFM changes the start time of runoff, but it is not a single variation trend like delaying or moving up. Analyzing the impact of PFM on the start time of runoff from the different growth periods, the start time of runoff was the following: the fallow period < the blooming period < the heading period < the grain-filling period (**Table 3**). In the fallow period, PFM delayed the start time of runoff by 10–55 min compared to the control group (except that the B3 group was earlier than the B1 group by 5 min). In addition, the start time of runoff in the grain-filling period was delayed 27.7–42.1 min compared to other periods, respectively. In the 100 mm/h rainfall intensity, the start time of runoff was 7.5–12.5 min in advance at the PFM experimental plots, compared with the control group. But it had a different change trend under the 50 mm/h rainfall intensity; the runoff volumes of B2 and B4 groups were delayed but the B3 group was advanced, compared with the B1 group.

PFM could improve the water absorption capacity of the soil and reduce peak flow. In total, PFM reduced the peak flow by 24.8–100%, respectively (**Figures 7** and **8**), and it had a positive relationship between the peak flow and the PFM volumes (R^2 = 0.63.0.81). In different growth periods, the peak flow was as follows: the fallow period > the blooming period > the heading period > the grain-filling period. The decrease of peak flow was the largest in the grain-filling period, reaching 88.6–100%, but it was only 29.1–58.8% in the fallow period. In the different rainfall intensity, the peak flow of the A1 group was higher than the B1 group by 24.2%, and B2, B3, and B4 experimental groups increased 29.3, 51.9, and 206.4% by comparing with the A2, A3, and A4 experimental groups, respectively. In **Figure 7**, we could find that the peak flow of runoff positively correlates with the PFM volumes (R^2 = 0.63.0.81), which confirmed PFM had the practical application ability to reduce the risk of farmland flood disaster.

TABLE 3 | Start time of runoff in different experimental stages and plots.

Experimental plots	Time	A1	A2	A3	A4	B1	B2	B3	B4
Jointing period	T	55	10	20	5	20	60	15	125
	ΔT	0	−45	−35	−50	0	40	−5	105
Blooming period	T	25	10	10	15	40	55	15	55
	ΔT	0	−15	−15	−10	0	15	−25	15
Grain-filling period	T	55	55	65	50	75	140	25	—
	ΔT	0	0	10	−5	0	65	-50	—
Fallow period	T	5	15	15	20	20	30	15	75
	ΔT	0	10	10	15	0	10	-5	55
Average	T	35	22.5	27.5	22.5	38.8	71.3	17.5	85
	ΔT	0	−12.5	−7.5	−12.5	0	32.5	−21.3	46.3

T represents the start time of runoff, ΔT represents the variation between the control groups and the PFM experimental groups, — represents no runoff and water fully infiltrated into the soil.

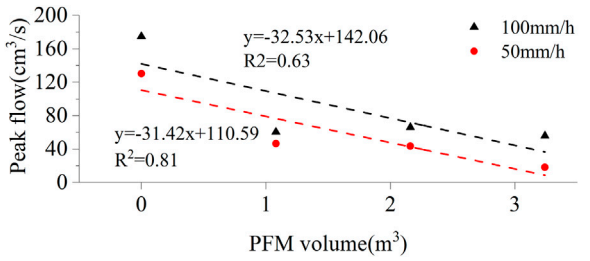

FIGURE 7 | Variation of the peak flow in different PFM volumes under 100 mm h^{-1} and 50 mm h^{-1} rainfall intensities.

PFM Increase the Soil Water-Holding Capacity

PFM could change the distribution of soil water and improve the soil water-holding capacity. In this rainfall experiment, we found that the average soil water content increased by 0.4–2.3% Vol in the 10–70 cm depth, and significantly it had a positive relationship between the soil water content with the PFM volumes (R^2 = 0.8 and 0.84, $p < 0.5$) (**Figure 9**). According to the experimental result, the variation range of soil water content by 25.2–30.9% Vol in the 10–30 cm depth ($p < 0.1$), and the average soil water content of B2 and B4 groups increased but the B3 group reduced by comparing with the B1 groups. Comparing with the 10–30 cm depth, the soil water content had a different variation trend that initially strengthened and subsequently weakened with the PFM volumes increase in the 30–50 cm depth. At the same time, A2, A3, A4, and B2, B3, B4 groups increased by (1.6–2.5% Vol) and (4.5–6.8% Vol) by comparing with the control group, respectively ($p < 0.5$). In the 50–70 cm depth, PFM reduced the soil water content by 0–2.2% Vol (except the B4 group increased by 1% Vol), and the relationship between each other passed the significance test ($p < 0.5$, except the A3 and B3 group).

The impact of PFM on soil water-holding capacity was related to the growth period of the winter wheat (**Figure 10**). The soil water content of the control groups initially decreased and lastly increased as the growth period went and reached a minimum value of 30.8% Vol in the grain-filling period. From the heading period to the fallow period, the increment of soil water content was 0–3.4% Vol in the PFM experimental groups compared with the control groups, respectively. Overall, although in the same condition, the soil water content of B2, B3, and B4 groups were lower than the A2~A4 groups by 0.5–2% Vol (except that the B4 group was higher than the A4 group in the blooming to grain-filling period), the increment of soil water content was higher than the A2, A3, and A4 groups by 0.5–2.6% Vol compared to the respective control groups, respectively.

PFM Increase the Soil Water-Storage Capacity

PFM could increase the soil water storage capacity. After the rainfall experiment ended, PFM increased the soil water content by 0.3–9.8% Vol (except that the A4 group decreased by 2.1% Vol). After rainfall ended for 6 h, the water content of PFM internal increased 0–35.1% Vol (except the B2 plot reduced by 16% Vol, compared to the B1 group), and the rising trend mainly occurred in 0~1 h (**Figure 11**). The soil water content of PFM experimental plots was higher than the control group by 0.2–11% Vol (except that A4 decreased by 1.8% Vol), respectively.

Within 6 h after the rainfall ended, the soil water infiltrated downward rapidly in the depth of 10–30 cm, and the decreased range in the PFM groups was 2.2–10.7% Vol compared with the control group. In the 30–70 cm depth of soil, soil water content decreased slower or even increased by comparing with the surface soil (**Figure 12**). In detail, PFM changed the water distribution in whole plots, and reduced the soil water content by 5.3% Vol and 2.1% Vol on average in the 10–30 cm and 30–50 cm depth of soil, respectively. Although the soil water content in PFM experimental groups had the same variable trend, the decrement was only by 1.1% Vol in the depth of 50–70 cm. So, in a short time after rainfall, the variation range of soil water content decreased with the increase of soil depth. The difference in soil water content shrank between 30 and 70 cm depth when PFM was embedded in the soil. The soil water-storage capacity improved by 0.2–11% Vol in whole plots (except the A3 group was lower than the control group by 1.8% Vol).

DISCUSSION

Porous Fiber Materials Influence the Infiltration and Runoff

The infiltration process of farmland was deeply influenced by some factors such as soil type, rainfall intensity, and initial water

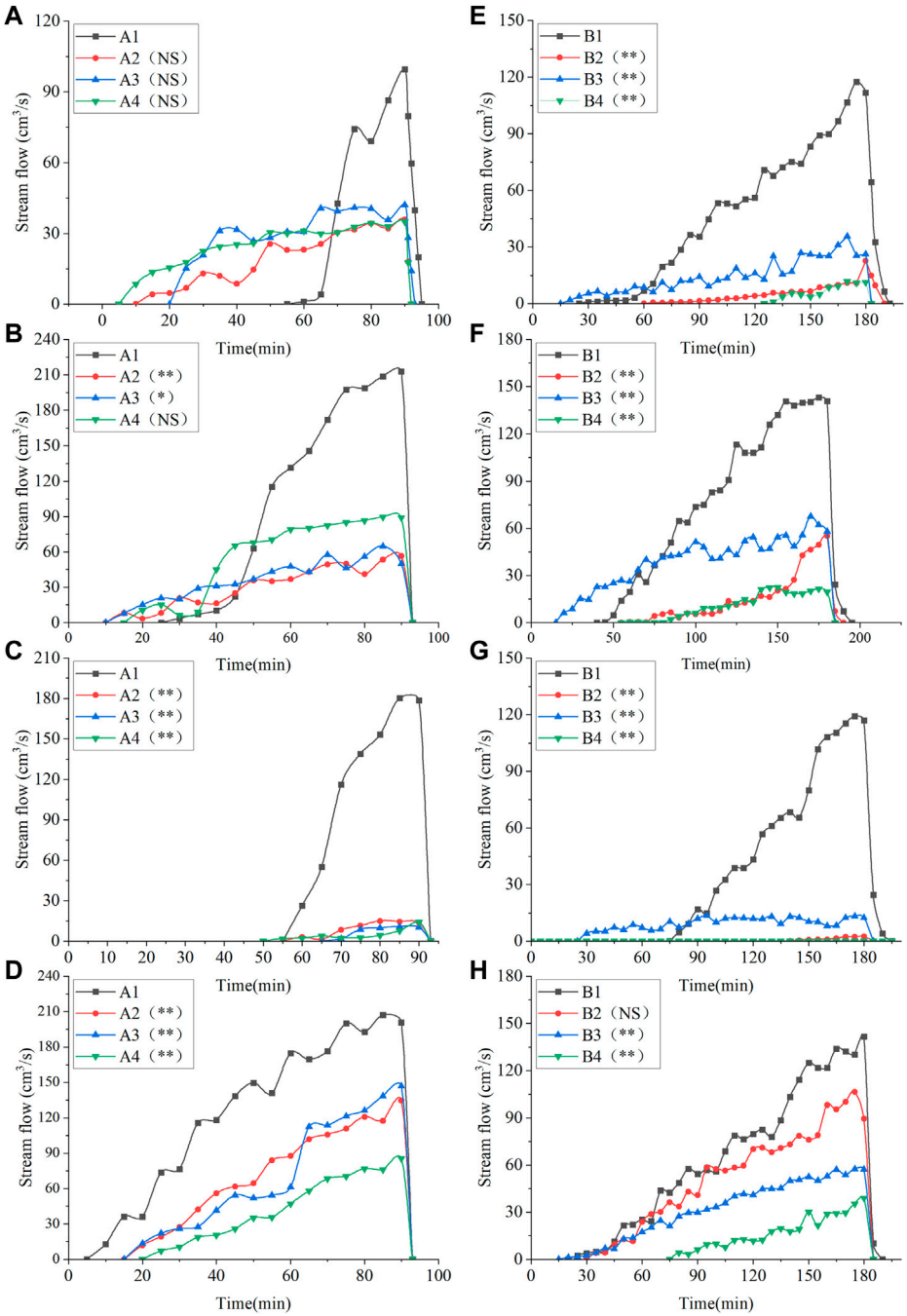

FIGURE 8 | Surface runoff process under different conditions. **(A-D)** The booting period, the blooming period, the grain-filling period, and the fallow period under 100 mm/h rainfall intensity, respectively. **(E-H)** The booting period, blooming period, grain-filling period, and fallow period under 50 mm/h rainfall intensity, respectively; * represents a significant difference in streamflow between the PFM and the control plot at $\alpha = 0.05$; ** represents significant difference between the PFM and the control plots at $\alpha = 0.01$; NS, no significant difference at $\alpha = 0.05$.

content (Humberto, 2017; Dong et al., 2019; Dunkerley, 2021). PFM increased the farmland infiltration rate, which was similar to the research results that some porous materials (such as biochar, straw, and PAM) applied in the farmland (Abrol et al., 2016; Wang et al., 2017). Porous fiber materials changed some soil physical and hydrological characteristics such as soil porosity, water conductivity, aggregate stability, and that the materials including huge pores could provide sufficient space for water storage during rainfall, which benefits the soil infiltration rate increased and reached stable infiltration faster (Gholami et al., 2019; Yu et al., 2021). In the early stage of a rainfall event, the PFM water

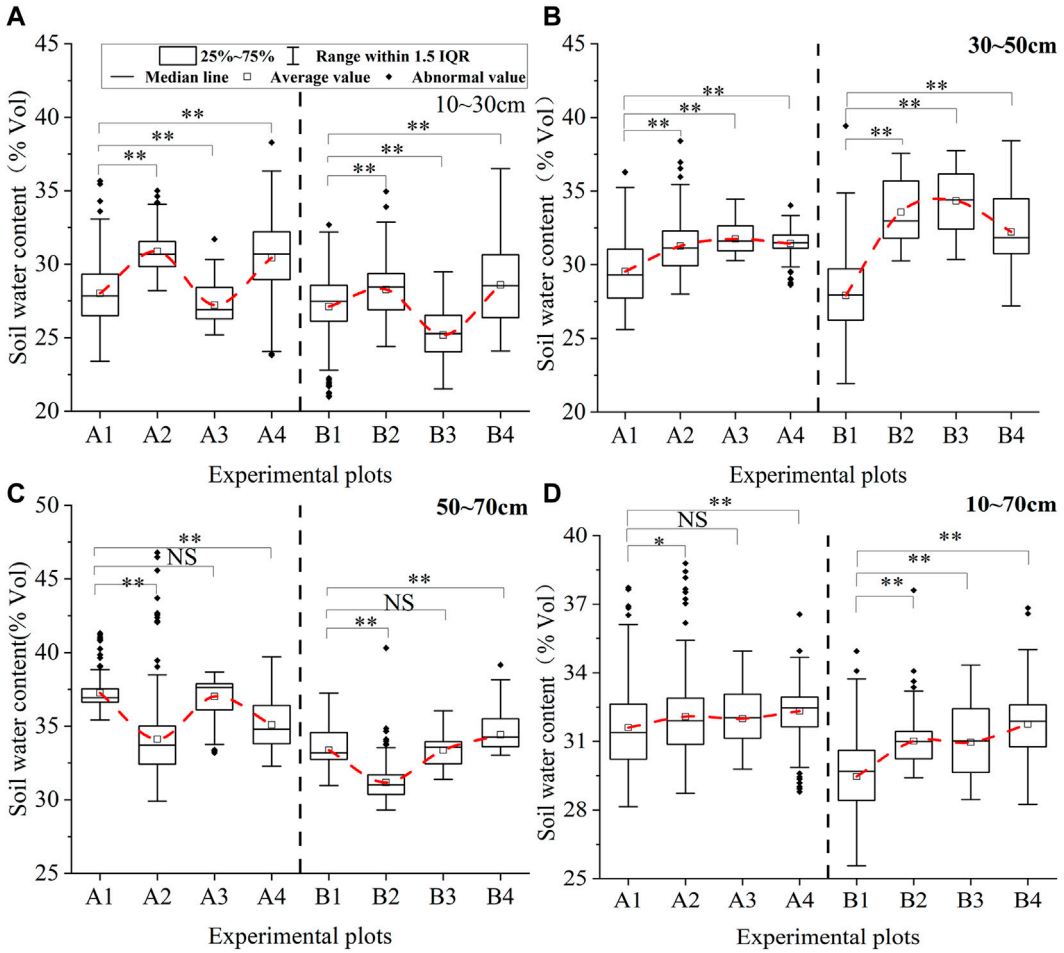

FIGURE 9 | Variations of soil water content in different depths. **(A-D)** The different depths of the soil, * represents a significant difference in streamflow between the PFM and the control plots at α = 0.05; ** represents a significant difference between the PFM and the control plots at α = 0.01; NS represents no significant difference at α = 0.05.

content was often lower than the soil water content in the same depth, which would make soil water suction in the PFM groups higher than the control groups during rain. PFM would actively absorb the free water when the soil pore saturated during the long-duration rain because the difference in potential energy, and the water absorption capacity of hydrophilic rock wool increases with the irrigation time increase, so it can enhance the effect on the infiltration process in a long duration rainfall (Lv et al., 2021). Subsequently, the infiltration rate would reach a stable value faster, which is the reason why the RE values of the control group are higher than the PFM groups.

Some researchers confirmed that green roofs filled with porous materials could reduce the runoff and the peak flow because the free water in the soil permeated into the porous materials and stored in the drainage layer during rainfall (Stovin., 2010). Similarly, porous materials should have the same advantages in the farmland, and Patrick and Vikas thought it could improve some soil structure parameters (such as porosity, texture, and particle size distribution), which benefited by reducing the surface runoff (Abrol et al., 2016; Nyambo et al., 2018; Li et al., 2019). However, biochar was easy to be washed off by runoff or block the soil pores in some extreme rainfall events, which led to the intensification of farmland floods (Peng et al., 2016). But PFM does not have the above shortcomings in practical application due to the difference in its layout mode (Yu et al., 2021). In nature, the formation and growth of surface runoff depend more on the relationship between rainfall intensity and soil infiltration rate (Zhao X. et al., 2014; Werdin et al., 2021). We have explained why the PFM could affect the infiltration process, so PFM inevitably reduced runoff when the rainfall intensity was stable.

PFM affected the starting time and processes of runoff. The effects of different PFM volumes on the start time of runoff were not a single variation trend during the rain, which was different from Zhou et al. in the biochar application (Zhou et al., 2020).

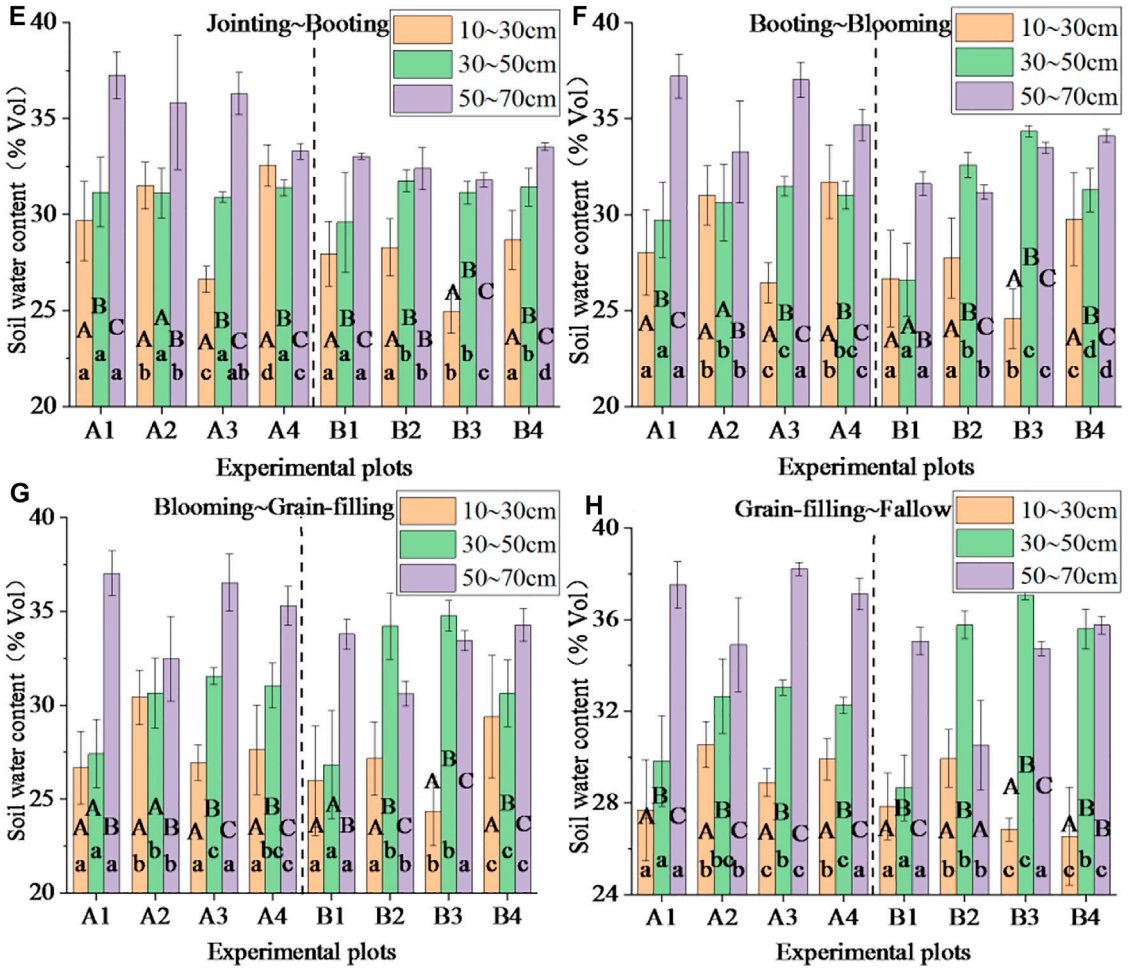

FIGURE 10 | Variations in soil water content in different growth periods and depths. **(E-H)** represent the different periods; a, b, c, d indicate the significant difference between the different depths at 0.05; **(A-C)** indicate the significant difference between different PFM volumes. PFM increases the soil water-storage capacity.

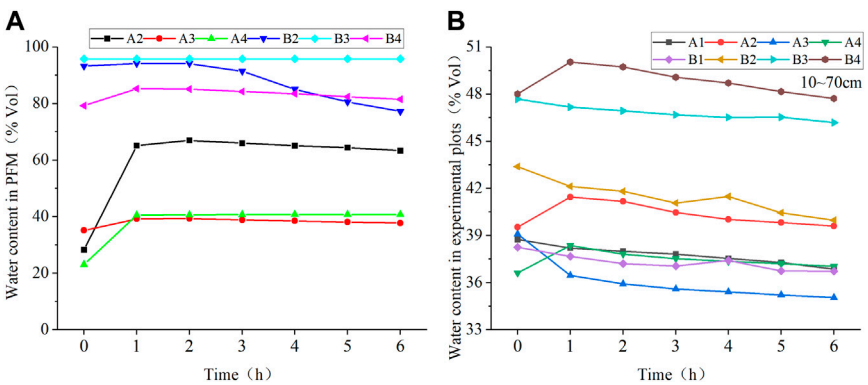

FIGURE 11 | Redistributions of soil and PFM water content in experimental plots from 1 to 6 h after rainfall (The letters **(A)** and **(B)** in the top left corner represent PFM and experimental plots, respectively.

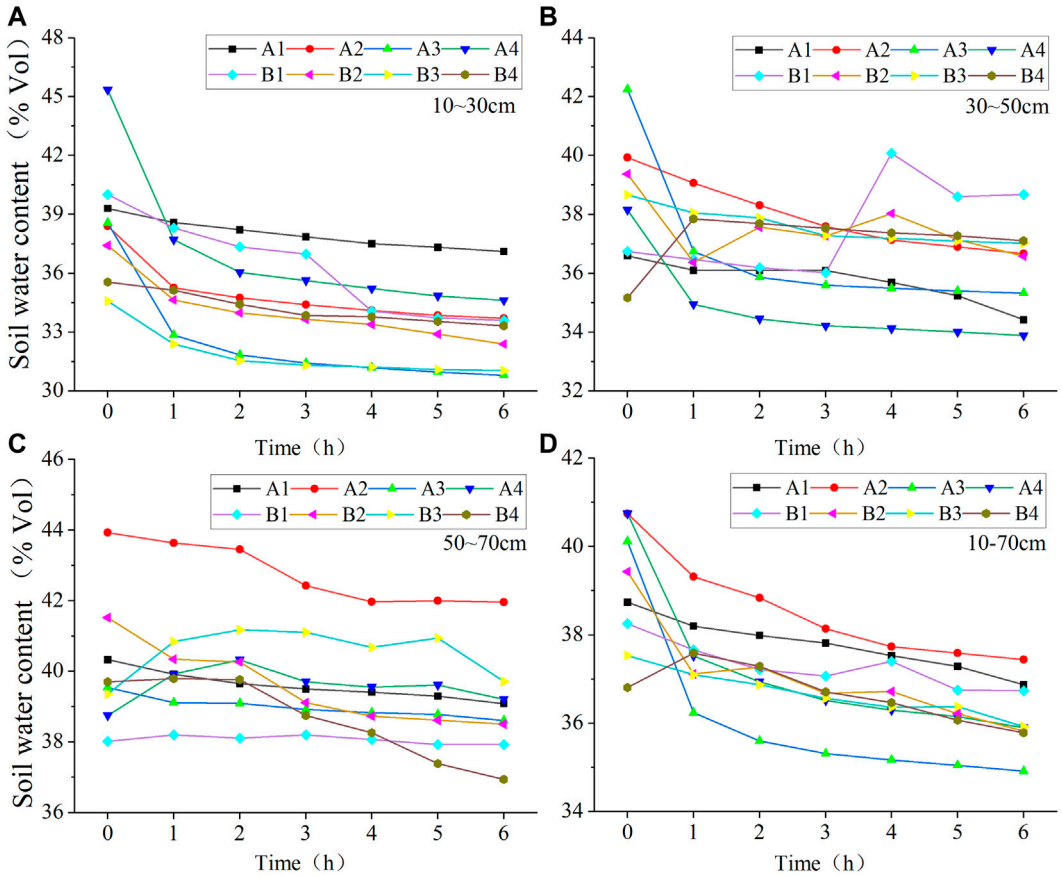

FIGURE 12 | Redistributions of soil water content in experimental plots at 10–70 cm depth from 1 to 6 h after rainfall ended (The letters **(A-D)** in the top left corner represent the different depths of soil).

The start time of runoff increased with the increase of biochar amount, this is mainly because biochar in the surface soil could absorb water and quickly respond to the infiltration processes, and delay the formation of runoff. However, PFM was difficult to respond to the formation of surface runoff in time due to the 30–70 cm depth of layout. Similarly, biochar could increase the water-holding capacity, which meant that the initial water content of the PFM groups before rainfall was higher than the control group. The porous materials have huge pores that can store water in rainfall and release water in drought, which made the soil water retain a high level, and directly affect the start time of runoff or even in advance like the B3 group (Razzaghi et al., 2020). Subsequently, surface soil water content would reach the threshold required for runoff faster, and the wetting front moved further down, finally, the surface runoff was accelerated to be formed (Song and Wang, 2019; Zhang J. L. et al., 2019; Rascon-Ramos et al., 2021), but it might be inappropriate in short-duration rain (Choi and Shin, 2019). PFM would actively absorb the free water to alleviate the flood disaster risk in long-duration rainfall after the soil water is closed to saturation, or the soil suction is less than 75 cm (Lv et al., 2021), so it has the different varied trend after the rainfall ended for 1 h under the 100 mm/h and 50 mm/h rainfall intensity. Therefore, the applicability of PFM embedding is better under continuous or long-duration rainfall (**Figure 8**).

The effect of PFM on runoff has a significant variation in the grain-filling period because the raindrops damaged the surface aggregate structure and promoted soil erosion (Ao et al., 2019; Ahmadi et al., 2020). In addition, the collapse plants absorbed a large amount of raindrops' energy and slowed down the above process. Meanwhile, winter wheat consumed large amounts of water for grouting, which made the initial soil water content lower than other periods and delayed the start time of runoff on a large scale (Zhang J. L. et al., 2019). The raindrop kinetic energy directly made soil particles separate in the fallow period, and the part of soil particle washed and taken away by runoff, another was precipitated on the soil surface to form a sealing plane, and reduced the infiltration rate and accelerated the formation and growth of runoff (Sadeghi et al., 2016; Yao et al., 2018).

The farmland runoff is usually uncertain in time and space in the natural rainfall because of the interaction of some factors such as the initial water content, rainfall intensity, and surface roughness. PFM embedding might cause a slight negative impact during short-duration rainfall. The application on farmland drainage is better in continuous rainfall events.

Porous Materials Influence the Soil Water-Holding Capacity and the Water-Storage Capacity

PFM increases the soil water-holding capacity and changes soil water distribution, the same as the results of other studies. For example, rock wool embedding in the forest land could increase the soil water content by 29.29% after a long-duration drought (Gu et al., 2020). The key to the above phenomenon was porous materials could fully absorb water during rainfall and increase soil water-storage capacity (Mollinedo et al., 2015). After the rainfall ended, soil water infiltrated, evaporated, or absorbed by the roots and gradually decreased to the unsaturated. At that time, the soil suction was much higher than PFM, which made PFM continuously release water to alleviate soil water deficit (Gu et al., 2020; Lv et al., 2021).

After the rainfall experiments, the water rapidly exchanged between the PFM and the surrounding soil on a large scale because of the various potential energy (Lv et al., 2021). The surface soil water decreased quickly, but the deep soil changed slowly. The water absorption capacity of hydrophilic rock wool increased with irrigation time (Choi and Shin, 2019). The surface and deep soil water infiltrated the PFM from vertical and horizontal directions. PFM water content increased rapidly by 0–35.1% Vol under 100 mm/h rainfall intensity after the rainfall ended for 1 h and remained stable at high levels because of the different matrix suction and the geopotential conditions (Lv et al., 2020). PFM had sufficient infiltration time under the long-duration rainfall, so it significantly has the better appliance effects under the 50 mm/h, which benefits the improvement of the soil water storage (Choi and Shin, 2019; Kołodziej et al., 2020). In general, the variation of soil moisture is an exponential downward trend during the long-dated observation. The mutations of soil water occasionally might occur after rainfall in some time because the soil exists in the heterogeneous mixture in the local area, which makes the soil hydraulic characteristics different; therefore, the B1 group rises significantly after rainfall.

PFM has evenly arranged fiber composition (one-way or cross), improving infiltration processes, and water-holding capacity. Rock wool material could naturally and continuously penetrate, buffer, and discharge rainwater and effectively achieve rainwater absorption and utilization (Wanko et al., 2016). However, the roots of winter wheat are generally short and mainly distributed in the surface soil (Nosalewicz and Lipiec, 2014; Figueroa-Bustos et al., 2018), and it is difficult to root into the PFM, so we analyzed the effect of PFM on soil water-holding capacity from the variation of soil water content. In detail, PFM steadily water to supply soil after rain and led to decreased hydraulic conductivity and increased soil water suction, further alleviating soil water deficit (Bougoul et al., 2005). In this process, the diffusion ability in vertical and horizontal directions gradually decreased from the center of the PFM embedding position to the surrounding, and shrank the gap of the soil water content in the vertical and improved the water-holding capacity (Gu et al., 2020). PFM acted as an intermediate medium to redistribute water of the surrounding in the 30–70 cm depth, which would also affect the water exchange at other depths, and adjusted the water potential difference to improve the water-holding capacity, this was similar to that PFM plays a role in regulating the root of the environment in the soilless culture (AcuA et al., 2013; Graceson et al., 2013; Narzari et al., 2017).

In summary, PFM can effectively increase soil infiltration, reduce runoff, and improve soil water storage capacity. Although porous fiber materials are currently used in soilless culture, they can adjust the proportion of water, fertilizer, and air in crop roots, which benefits plant growth well (Savvas and Gruda, 2018). In general, the expense of PFM restricted its application on a large scale at present, and the average price of a PFM ranges from ¥1,000 to ¥2,000 m^{-3}, so we can use it in intensive agriculture or economic crop planting. At the same time, we must realize that PFM cannot create water or reduce the soil water consumption of farmland. It only plays a role in enhancing soil water storage capacity to delay drought events. To effectively achieve the drought disaster risk reduction in the extremely dry years, improving the soil water content may be necessary through PFM embedding and irrigation system interaction.

CONCLUSION

PFM influences soil infiltration and water exchanging by establishing a hydraulic connection with the surrounding soil. Based on the above assumptions, we experimented with the growth period of winter wheat to explore the effects of PFM embedding on the farmland water cycle processes. The result showed that PFM could absorb a large amount of free water in saturated soil during rain. Subsequently, it increased the soil infiltration rate and reduced the runoff. After rainfall, PFM could regulate the water redistribution and improve water-holding capacity to alleviate soil water deficit. The above effects increased with the PFM volumes increased. In general, the expense of PFM restricted its application on a large scale at present, and the average price of a PFM ranges from ¥1,000 to ¥2,000 m^{-3}, so we can expand the application to intensive agriculture and economic crops in the farmland. Furthermore, we believe that PFM will have excellent application effects in soil and water conservation, sponge city, green roof, potting, etc.

DATA AVAILABILITY STATEMENT

The original contributions presented in the study are included in the article/Supplementary Material. Further inquiries can be directed to the corresponding authors.

AUTHOR CONTRIBUTIONS

WL, SL, and TQ conceived the main idea of this manuscript. SX, CL, XZ, and KW designed and performed the experiment. SA

helped to revise the manuscript. WL wrote the manuscript and all authors contributed to improving the manuscript.

FUNDING

This research was supported by the National Key Research and Development Project (Grant No. 2017YFA0605004), the National Science Fund Project for Distinguished Young Scholars (Grant No. 51725905), and the National Science Fund Project (Grant No. 52130907).

ACKNOWLEDGMENTS

We thank the reviewers for their useful comments and suggestions.

REFERENCES

Abrol, V., Ben-Hur, M., Verheijen, F. G. A., Keizer, J. J., Martins, M. A. S., Tenaw, H., et al. (2016). Biochar Effects on Soil Water Infiltration and Erosion under Seal Formation Conditions: Rainfall Simulation experiment. *J. Soils Sediments* 16, 2709–2719. doi:10.1007/s11368-016-1448-8

Acuña, R. A., Bonachela, S., Magán, J. J., Marfà, O., Hernández, J. H., and Cáceres, R. (2013). Reuse of Rockwool Slabs and Perlite Grow-Bags in a Low-Cost Greenhouse: Substrates' Physical Properties and Crop Production. *Scientia Horticulturae* 160, 139–147. doi:10.1016/j.scienta.2013.05.031

Ahmadi, S. H., Ghasemi, H., and Sepaskhah, A. R. (2020). Rice Husk Biochar Influences Runoff Features, Soil Loss, and Hydrological Behavior of a Loamy Soil in a Series of Successive Simulated Rainfall Events. *Catena* 192, 104587. doi:10.1016/j.catena.2020.104587

Ao, C., Yang, P., Zeng, W., Chen, W., Xu, Y., Xu, H., et al. (2019). Impact of Raindrop Diameter and Polyacrylamide Application on Runoff, Soil and Nitrogen Loss via Raindrop Splashing. *Geoderma* 353, 372–381. doi:10.1016/j.geoderma.2019.07.026

Bi, W., Weng, B., Yan, D., Wang, M., Wang, H., Wang, J., et al. (2020). Effects of Drought-Flood Abrupt Alternation on Phosphorus in Summer maize farmland Systems. *Geoderma* 363, 114147. doi:10.1016/j.geoderma.2019.114147

Bougoul, S., and Boulard, T. (2006). Water Dynamics in Two Rockwool Slab Growing Substrates of Contrasting Densities. *Scientia Horticulturae* 107, 399–404. doi:10.1016/j.scienta.2005.11.007

Bougoul, S., Ruy, S., de Groot, F., and Boulard, T. (2005). Hydraulic and Physical Propertiesof Stonewool Substrates in Horticulture. *Scientia Horticulturae* 104, 391–405. doi:10.1016/j.scienta.2005.01.018

Cai, W., Huang, H., Chen, P. N., Huang, X. L., and GauravPan, S. Z. (2020). Effects of Biochar from Invasive weed on Soil Erosion under Varying Compaction and Slope Conditions: Comprehensive Study Using Flume Experiments. *Biomass Convers. Biorefinery*. doi:10.1007/s13399-020-00943-3

Chen, X. A., Liang, Z. W., Zhang, Z. Y., and Zhang, L. (2020). Effects of Soil and Water Conservation Measures on Runoff and Sediment Yield in Red Soil Slope Farmland under Natural Rainfall. *Sustainability* 12, 3417. doi:10.3390/su12083417

Choi, Y. B., and Shin, J. H. (2019). Analysis of the Changes in Medium Moisture Content According to a Crop Irrigation Strategy and the Medium Properties for Precise Moisture Content Control in Rock Wool. *Hortic. Environ. Biotechnol.* 60, 337–343. doi:10.1007/s13580-019-00134-8

De-Ville, S., Menon, M., Jia, X. D., Reed, G., and Stovin, V. (2017). The Impact of green Roof Ageing on Substrate Characteristics and Hydrological Performance. *J. Hydrol.* 547, 332–344. doi:10.1016/j.jhydrol.2017.02.006

Dong, Q. G., Han, J. C., Zhang, Y., Li, N., Lei, N., Sun, Z. H., et al. (2019). Water Infiltration of Covering Soils with Different Textures and Bulk Densities in Gravelmulched Areas. *Appl. Ecol. Environ. Res.* 17, 14039–14052. doi:10.15666/aeer/1706_1403914052

Du, M. C., Zhang, J. Y., Elmahdi, A., Wang, Z. L., Yang, Q. L., Liu, H. W., et al. (2021). Variation Characteristics and Influencing Factors of Soil Moisture Content in the Lime Concretion Black Soil Region in Northern Anhui. *Water* 13, 2251. doi:10.3390/w13162251

Duan, M. L., Liu, G. H., Zhou, B. B., Chen, X. P., Wang, Q. J., Zhu, H. Y., et al. (2021). Effects of Modified Biochar on Water and Salt Distribution and Water-Stable Macro-Aggregates in Saline-Alkaline Soil. *J. Soils Sedim.* 21, 2192–2202. doi:10.1007/s11368-021-02913-2

Dunkerley, D. (2021). The Importance of Incorporating Rain Intensity Profiles in Rainfall Simulation Studies of Infiltration, Runoff Production, Soil Erosion, and Related Landsurface Processes. *J. Hydrol.* 603, 126834. doi:10.1016/j.jhydrol.2021.126834

Figueroa-Bustos, V., Palta, J. A., Chen, Y. L., and Siddique, K. H. M. (2018). Characterization of Root and Shoot Traits in Wheat Cultivars with Putative Differences in Root System Size. *Agronomy-Basel* 8, 109. doi:10.3390/agronomy8070109

Gholami, L., Karimi, N., and Kavian, A. (2019). Soil and Water Conservation Using Biochar and Various Soil Moisture in Laboratory Conditions. *Catena* 182, 104151. doi:10.1016/j.catena.2019.104151

Gou, Q. Q., Zhu, Y. H., Horton, R., Lu, H. S., Wang, Z. L., Su, J. B., et al. (2020). Effect of Climate Change on the Contribution of Groundwater to the Root Zone of winter Wheat in the Huaibei Plain of China. *Agric. Water Manage.* 240. doi:10.1016/j.agwat.2020.106292

Graceson, A., Hare, M., Monaghan, J., and Hall, N. (2013). The Water Retention Capabilities of Growing media for green Roofs. *Ecol. Eng.* 61, 328–334. doi:10.1016/j.ecoleng.2013.09.030

Gu, J. Y., Fang, W., Gao, J., Yan, S. X., Feng, G. L., Liu, C. X., et al. (2020). Improving Soil Water Retention Capacity of Economic forest Using Rock Wool in Hilly Area. *Agric. Res. Arid Areas* 38 (3), 10–18. doi:10.7606/j.issn.1000-7601.220.03.02

Gu, J. Y., Shao, S., Deng, Y. J., Yu, C. B., Chen, J. H., Qin, H., et al. (2021). Response of Growth and Physiological Indicators of Lycopersicone Sculentum to Water Stress Relieved by Rock Wool. *J. Zhejiang A&F Univ.* 38 (2), 311–319. doi:10.11833/j.issn.2095-0756.20200221

Helalia, A. M. (1993). The Relation between Soil Infiltration and Effective Porosity in Different Soils. *Agric. Water Manag.* 24, 39–47. doi:10.1016/0378-3774(93)90060-N

Huang, W., Du, J. X., Sun, H., Zhou, C. Y., Liu, Z., and Zhang, L. H. (2021). New Polymer Composites Improve Silty Clay Soil Microstructure: An Evaluation Using NMR. *Land Degradat. Devel.* 32, 3272–3281. doi:10.1002/ldr.3983

Humberto, B. C. (2017). Biochar and Soil Physical Properties. *Soil Sci. Soc. America J.* 81, 687–711. doi:10.2136/sssaj2017.01.0017

Kołodziej, B., Bryk, M., and Otremba, K. (2020). Effect of Rockwool and lignite Dust on Physical State of Rehabilitated post-mining Soil. *Soil Tillage Res.* 199, 104603. doi:10.1016/j.still.2020.104603

Li, Y. Y., Feng, G., Tewolde, H., Yang, M. Y., and Zhang, F. B. (2020). Soil, Biochar, and Nitrogen Loss to Runoff from Loess Soil Amended with Biochar under Simulated Rainfall. *J. Hydrol.* 591, 125318. doi:10.1016/j.jhydrol.2020.125318

Li, Y. Y., Zhang, F. B., Yang, M. Y., and Zhang, J. Q. (2019). Effects of Adding Biochar of Different Particle Sizes on Hydro-Erosional Processes in Small Scale Laboratory Rainfall Experiments on Cultivated Loessial Soil. *Catena* 173, 226–233. doi:10.1016/j.catena.2018.10.021

Libutti, A., Francavilla, M., and Monteleone, M. (2021). Hydrological Properties of a Clay Loam Soil as Affected by Biochar Application in a Pot Experiment. *Agronomy* 11, 489. doi:10.3390/agronomy11030489

Liu, S. M., Wang, H., Yan, D. H., Qin, T. L., Wang, Z. L., and Wang, F. X. (2017). Crop Growth Characteristics and Waterlogging Risk Analysis of Huaibei Plain in Anhui Province, China. *J. Irrigation Drainage Eng.* 143, 04017042. doi:10.1061/(ASCE)IR.1943-4774.0001219

Lv, Z. Y., Qin, T. L., Liu, S. S., Nie, H. J., Liu, F., and Wang, J. W. (2020). Porous-fiber Module Increases Infiltration and Reduces Runoff. *Agron. J.* 112, 4420–4436. doi:10.1002/agj2.20317

Lv, Z. Y., Qin, T. L., Wang, Y., Liu, S. S., Nie, H. J., and Wang, J. W. (2021). Hydraulic Properties of the Porous-Fiber Module and its Effects on Infiltration and Runoff. *Agron. J.* 113, 2913–2925. doi:10.1002/agj2.20630

Mollinedo, J., Schumacher, T. E., and Chintala, R. (2015). Influence of Feedstocks and Pyrolysis on Biochar's Capacity to Modify Soil Water Retention Characteristics. *J. Anal. Appl. Pyrolysis* 114, 100–108. doi:10.1016/j.jaap.2015.05.006

Narzari, R., Bordoloi, N., Sarma, B., Gogoi, L., Gogoi, N., Borkotoki, B., et al. (2017). Fabrication of Biochars Obtained from Valorization of Biowaste and Evaluation of its Physicochemical Properties. *Bioresour. Technol.* 242, 324–328. doi:10.1016/j.biortech.2017.04.050

Nosalewicz, A., and Lipiec, J. (2014). The Effect of Compacted Soil Layers on Vertical Root Distribution and Water Uptake by Wheat. *Plant and Soil* 375, 229–240. doi:10.1007/s11104-013-1961-0

Nyambo, P., Taeni, T., Chiduza, C., and Araya, T. (2018). Effects of Maize Residue Biochar Amendments on Soil Properties and Soil Loss on Acidic Hutton Soil. *Agronomy* 8, 256. doi:10.3390/agronomy8110256

Peng, X., Zhu, Q. H., Xie, Z. B., Darboux, F., and Holden, N. M. (2016). The Impact of Manure, Straw and Biochar Amendments on Aggregation and Erosion in a Hillslope Ultisol. *Catena* 138, 30–37. doi:10.1016/j.catena.2015.11.008

Pu, S. H., Li, G. Y., Tang, G. M., Zhang, Y. S., Xu, W. L., Li, P., et al. (2019). Effects of Biochar on Water Movement Characteristics in sandy Soil under Drip Irrigation. *J. Arid Land* 11, 740–753. doi:10.1007/s40333-019-0106-6

Raimondi, A., and Becciu, G. (2021). Performance of Green Roofs for Rainwater Control. *Water Res. Manag.* 35, 99–111. doi:10.1007/s11269-020-02712-3

Rascon-Ramos, A. E., Martinez-Salvador, M., Sosa-Perez, Gl., Villarreal-Guerrero, F., Pinedo-Alvarez, A., and Santellano-Estrada, E. (2021). Hydrological Behavior of a Semi-dry forest in Northern Mexico: Factors Controlling Surface Runoff. *Arid Land Res. Manage.* 35, 83–103. doi:10.1080/15324982.2020.1783026

Razzaghi, F., Obour, P. B., and Arthur, E. (2020). Does Biochar Improve Soil Water Retention? A Systematic Review and Meta-Analysis. *Geoderma* 361. doi:10.1016/j.geoderma.2019.114055

Sadeghi, S. H. R., Sharifi, M. E., and Khaledi, D. A. (2016). Effects of Subsequent Rainfall Events on Runoff and Soil Erosion Components from Small Plots Treated by Vinasse. *Catena* 138, 1–12. doi:10.1016/j.catena.2015.11.007

Saffari, N., Hajabbasi, M. A., Shirani, H., Mosaddeghi, M. R., and Owens, G. (2021). Influence of Corn Residue Biochar on Water Retention and Penetration Resistance in a Calcareous Sandy Loam Soil. *Geoderma* 383. doi:10.1016/j.geoderma.2020.114734

Savvas, D., and Gruda, N. (2018). Application of Soilless Culture Technologies in the Modern Greenhouse Industry – A Review. *Eur. J. Hortic. Sci.* 83, 280–293. doi:10.17660/eJHS.2018/83.5.2

Song, S., and Wang, W. (2019). Impacts of Antecedent Soil Moisture on the Rainfall-Runoff Transformation Process Based on High-Resolution Observations in Soil Tank Experiments. *Water* 11, 296. doi:10.3390/w11020296

Stovin, V. (2010). The Potential of green Roofs to Manage Urban Stormwater. *Water Environ. J.* 24, 192–199. doi:10.1111/j.1747-6593.2009.00174.x

Sun, C. X., Wang, D., Shen, X. B., Li, C. H., Liu, J., Lan, T., et al. (2021). Effects of Biochar, Compost and Straw Input on Root Exudation of Maize (Zea mays L.): From Function to Morphology. *Agricult. Ecosyst. Environ.* 308. doi:10.1016/j.agee.2020.107216

Sun, J. N., Yang, R. Y., Zhu, J. J., Zhou, C. X., Yang, M., Pan, Y. H., et al. (2019). Contrasting Effects of Corn Straw Biochar on Soil Water Infiltration and Retention at Tilled and Compacted Bulk Densities in the Yellow River Delta. *Can. J. Soil Sci.* 99, 357–366. doi:10.1139/cjss-2019-0004

Titouna, D., and Bougoul, S. (2013). Simulation Model on Water and Solute Transport in Two Types of Rockwool. *J. Plant Nutr.* 36, 429–442. doi:10.1080/01904167.2012.748063

Wang, J. F., Wang, Z. Z., Gu, F. X., Liu, H., Kang, G. Z., Feng, W., et al. (2021). Tillage and Irrigation Increase Wheat Root Systems at Deep Soil Layer and Grain Yields in Lime Concretion Black Soil. *Scientific Rep.* 11, 6394. doi:10.1038/s41598-021-85588-6

Wang, T. T., Stewart, C. E., Ma, J. B., Zheng, J. Y., and Zhang, X. C. (2017). Applicability of Five Models to Simulate Water Infiltration into Soil with Added Biochar. *J. Arid Land* 9, 701–711. doi:10.1007/s40333-017-0025-3

Wanko, A., Laurent, J., Bois, P., Mosé, R., Wagner-Kocher, C., Bahlouli, N., et al. (2016). Assessment of Rock Wool as Support Material for On-Site Sanitation: Hydrodynamic and Mechanical Characterization. *Environ. Technol.* 37, 369–380. doi:10.1080/09593330.2015.1069901

Wasko, C., and Nathan, R. (2019). The Local Dependency of Precipitation on Historical Changes in Temperature. *Clim. Change* 156, 105–120. doi:10.1007/s10584-019-02523-5

Werdin, J., Conn, R., Fletcher, T. D., Rayner, J. P., Williams, N. S. G., and Farrell, C. (2021). Biochar Particle Size and Amendment Rate Are More Important for Water Retention and Weight of green Roof Substrates Than Differences in Feedstock Type. *Ecol. Eng.* 171, 106391. doi:10.1016/j.ecoleng.2021.106391

Winkler, K., Fuchs, R., Rounsevell, M., and Herold, M. (2021). Global Land Use Changes Are Four Times Greater Than Previously Estimated. *Nat. Commun.* 12, 2501. doi:10.1038/s41467-021-22702-2

Yang, J. H., Liu, H. Q., Lei, T. W., Rahma, A. E., Liu, C. X., and Zhang, J. P. (2021). Effect of Straw-Incorporation into Farming Soil Layer on Surface Runoff under Simulated Rainfall. *Catena* 199, 105082. doi:10.1016/j.catena.2020.105082

Yao, J. J., Cheng, J. H., Zhou, Z. D., Sun, L., and Zhang, H. J. (2018). Effects of Herbaceous Vegetation Coverage and Rainfall Intensity on Splash Characteristics in Northern China. *Catena* 167, 411–421. doi:10.1016/j.catena.2018.05.019

Yu, P. F., Li, T. X., Fu, Q., Liu, D., Hou, R. J., and Zhao, H. (2021). Effect of Biochar on Soil and Water Loss on Sloping Farmland in the Black Soil Region of Northeast China during the Spring Thawing Period. *Sustainability* 13, 1460. doi:10.3390/su13031460

Zhang, F. B., Huang, C. H., Yang, M. Y., Zhang, J. Q., and Shi, W. Y. (2019). Rainfall Simulation Experiments Indicate that Biochar Addition Enhances Erosion of Loess-Derived Soils. *Land Degrad. Develop.* 30, 2272–2286. doi:10.1002/ldr.3399

Zhang, J. L., Zhou, L. L., Ma, R. M., Jia, Y. F., Yang, F., Zhou, H. Y., et al. (2019). Influence of Soil Moisture Content and Soil and Water Conservation Measures on Time to Runoff Initiation under Different Rainfall Intensities. *Catena* 182, 104172. doi:10.1016/j.catena.2019.104172

Zhao, W., Cao, T., Dou, P., Sheng, J., and Luo, M. (2019). Effect of Various Concentrations of Superabsorbent Polymers on Soil Particle-Size Distribution and Evaporation with Sand Mulching. *Sci. Rep.* 9, 3511. doi:10.1038/s41598-019-39412-x

Zhao, X., Huang, J., Gao, X., Wu, P., and Wang, J. (2014). Runoff Features of Pasture and Crop Slopes at Different Rainfall Intensities, Antecedent Moisture Contents and Gradients on the Chinese Loess Plateau: A Solution of Rainfall Simulation Experiments. *Catena* 119, 90–96. doi:10.1016/j.catena.2014.03.007

Zhou, B. B., Chen, X. P., and Henry, L. (2020). The Effect of Nano-Biochar on Soil, Water, and Nutrient Loss of a Sloping Land with Different Vegetation Covers on Loess Plateau of China. *Appl. Ecol. Environ. Res.* 18, 2845–2861. doi:10.15666/aeer/1802_28452861

Conflict of Interest: The authors declare that the research was conducted in the absence of any commercial or financial relationships that could be construed as a potential conflict of interest.

Publisher's Note: All claims expressed in this article are solely those of the authors and do not necessarily represent those of their affiliated organizations, or those of the publisher, the editors, and the reviewers. Any product that may be evaluated in this article, or claim that may be made by its manufacturer, is not guaranteed or endorsed by the publisher.

frontiers | Frontiers in Earth Science

ORIGINAL RESEARCH
published: 19 May 2022
doi: 10.3389/feart.2022.846113

Potential Use of Extreme Rainfall Forecast and Socio-Economic Data for Impact-Based Forecasting at the District Level in Northern India

*Akshay Singhal, Ashwin Raman and Sanjeev K. Jha**

Indian Institute of Science Education and Research Bhopal, Bhopal, India

Due to the increase in extreme rainfall events in India, there is an urgent need for prior communication of the expected impacts and appropriate responses in order to mitigate the losses of lives and damage to property. Extreme rainfall events cause numerous casualties, damage to property and infrastructure and vast displacement of people. Hence, the development of an approach where the rainfall forecasts are well analyzed, associated risks are identified, and the probable impacts are clearly communicated to relevant stakeholders is required. In this study, we aim to develop a framework for generating the impact-based forecasts (IBF) and associated warning matrices over the selected districts of eastern Uttar Pradesh, India, by integrating the rainfall forecasts and the socio-economic characteristics such as population, economy and agriculture. The selected districts lack proper infrastructure, have poor socio-economic conditions and have been historically prone to frequent extreme rainfall. The basic idea is to estimate the impacts that could occur over various sectors of population, economy and agriculture and suggest appropriate actions in order to mitigate the severity of the impacts. To this end, we identify the vulnerable districts based on the frequency of the number of extreme rainfall forecasts (ERFs) in the past four years (2017–2020) and the nature of socio-economic conditions. We selected three vulnerable districts based on the expected impacts, i.e., Shravasti (high category), Gorakhpur (medium category) and Jaunpur (low category) and subsequently, the corresponding IBFs are generated. Furthermore, a warning matrix is created for each district which provides updated information regarding the potential risk for a district a few days in advance. This study is significant since it identifies the different levels of potential impact over multiple sectors of society, presents a framework to generate impact-based forecasts and warnings, informs about the expected impacts, and suggests mitigation actions to reduce potential damage and losses.

Keywords: extreme rainfall, impact-based forecasting, vulnerability, hazard, NWP forecast, socio-economic, warning matrix, mitigation measures

OPEN ACCESS

Edited by:
Jorge Eduardo Teixeira Leandro, University of Siegen, Germany

Reviewed by:
A. Amarender Reddy, National Institute of Agricultural Extension Management (MANAGE), India
Ahmed Kenawy, Mansoura University, Egypt

****Correspondence:***
Sanjeev K. Jha
sanjeevj@iiserb.ac.in

Specialty section:
This article was submitted to Hydrosphere, a section of the journal Frontiers in Earth Science

Received: *30 December 2021*
Accepted: *20 April 2022*
Published: *19 May 2022*

Citation:
Singhal A, Raman A and Jha SK (2022) Potential Use of Extreme Rainfall Forecast and Socio-Economic Data for Impact-Based Forecasting at the District Level in Northern India. Front. Earth Sci. 10:846113. doi: 10.3389/feart.2022.846113

1 INTRODUCTION

India has witnessed an increase in extreme rainfall events during the summer monsoon season, which is expected to intensify in the future (Goswami et al., 2006a; Mukherjee et al., 2018; Singhal and Jha, 2021a; Singhal et al., 2022). Extreme rainfall cause damage to property and infrastructure, numerous casualties and vast displacement of people. The increase in the extreme rainfall also means an increase in the total seasonal rainfall during the monsoon season, thus leading to frequent floods (Pattanaik and Rajeevan, 2010). Floods incur huge losses of life and economy over different parts of the country. According to an estimate, floods caused due to extreme rainfall amounts to economic losses of around 3 billion USD per year in India, which is around 10% of the global economic losses (Roxy et al., 2017). In addition, they constitute the maximum share of mortality (46.1%) among all the extreme weather events in India (Ray et al., 2021). This happens despite the fact that various Quantitative precipitation Forecasts (QPFs) are available in many regions of the world, and the majority of extreme rainfall events are forecasted. The QPFs, obtained from the Numerical Weather Prediction (NWP) models, help in predicting the possible rainfall amount over a certain region a few days in advance (Froude, 2010; Verdin et al., 2016; Jha et al., 2018). In the recent decades, QPFs have shown improvement both in the quality and quantity of information (availability of lead-times) mainly due to advancement in technology, availability of real-time data and increased capability of computer simulations.

One of the main reasons for the losses in life and property despite the availability of QPFs is that the QPFs rarely include warnings about the potential impacts they may have over a certain region or over a certain population. Even if the warnings are included, they lack proper communication to the general public (Basher, 2006; Uccellini and Ten Hoeve, 2019). Several methods have been utilized for communicating the consequences of high impact weather events in the past. The methods include interviews (Bostrom et al., 2018; Tozier de la Poterie et al., 2018), surveys (Morss et al., 2018; Potter et al., 2018), experience-based decisions (Casteel, 2018; Losee and Joslyn, 2018), social media analysis (Rossi et al., 2018) etc. However, the communications are mostly based on theoretical and subjective responses of the exposed population themselves. Recently, it has been emphasized that along with the QPFs, the nature of impact which may be caused due to extreme rainfall such as area and number of people exposed, regions expected to flood, damage to trees or infrastructure must also be communicated (Pittore et al., 2017). In the same line, at the Third UN World Conference on Disaster Risk Reduction in 2015, the Sendai Framework for Disaster Risk Reduction recommended include multi-hazard early warning systems and rapid disaster risk information by 2030 (WMO, 2015). Various national and regional rainfall forecasting agencies have started issuing risk-based warnings, which include both the probability of occurrence and the degree of potential impacts arising from the extreme rainfall (Weyrich et al., 2018; Silvestro et al., 2019). Such an approach in which the forecast information is provided on the basis of the potential impact of the event is termed as Impact-Based Forecast (IBF).

IBF is an integrated framework that includes hazard, exposure and vulnerability data for identifying risks and enabling decision-making. The overall objective of IBFs is to add scientific information to severe weather warnings to promote timely response and reduce losses of lives. A more effective and user-friendly warning comprises the information regarding "What the weather will do" instead of "What the weather will be" (Kaltenberger et al., 2020). They are expected to include the specific social, economic and environmental impacts of hazard in the warning to enable people to adapt and mitigate the possible adverse consequences (WMO, 2015; Kox et al., 2018). Previous studies suggest that IBF improves the understanding of forecasts for the general public as it bridges the gap between the raw QPFs, its related warnings and potential impacts (Potter et al., 2018; Taylor et al., 2019). Moreover, it facilitates people to take timely defensive measures against the impending extreme rainfall (Casteel, 2016). However, providing IBFs can be challenging at many levels. For instance, a significant number of resources in terms of time, money and workforce is required to combine the produced weather information with the exposure and vulnerability prevalent at the ground level. Regular updates of the socio-economic status of the region must be kept so that the IBFs are consistently accurate. Socio-economic developments such as urbanization and population growth are expected to influence the exposure and vulnerability of many regions across the world, especially in hazard-prone regions (Winsemius et al., 2015; Jongman, 2018). Consequently, large datasets of socio-economic progress are required to be processed under changing scenarios for multiple sectors. Nevertheless, greater precision of QPFs, greater availability of data and lead-times (LT) provide new opportunities for enhancing IBFs (Silvestro et al., 2019).

The topic of IBF is still in its early stage and has started to gain momentum in recent years. Worldwide, few studies have explored the utility of IBFs in the case of various extreme weather hazards. For instance, Silvestro et al. (2019) used a multi-model ensemble approach to design an impact-based flash-flood probabilistic forecasting system in northwestern Italy. Sai et al. (2018) explored the use of color-codes in developing impact-based forecasts of floods among a flood-exposed community in a district of Bangladesh. Mendis (2021) developed a warning matrix as a tool of IBF to relate the risk of heavy rain hazards in Sri Lanka. Otieno et al. (2014) used a predictive model and observed satellite rainfall as a covariate to estimate flood impacts on exposed communities in a river basin of Kenya. In India, to the best of our knowledge, the potential use of QPFs and socio-economic data for IBFs is lacking. With the rise in events of extreme rainfall, there is a need to develop an approach in India where the QPFs are analyzed, associated risks are identified, and the probable impacts are estimated. Once the risks and potential impacts are identified, proper communication to local stakeholders is crucial so that the impending impacts are mitigated at the ground level (Reddy et al., 2021).

In this study, we aim to develop impact-based forecasting approach by integrating the available QPF and the local socio-economic data over the districts of the eastern part of Uttar Pradesh, India. The basic idea is to estimate the possible impacts that could be caused due to potential extreme rainfall over various social and economic sectors such as local population, marginalized groups, agriculture and economy and subsequently suggest mitigation actions. The deterministic rainfall forecast data from the National

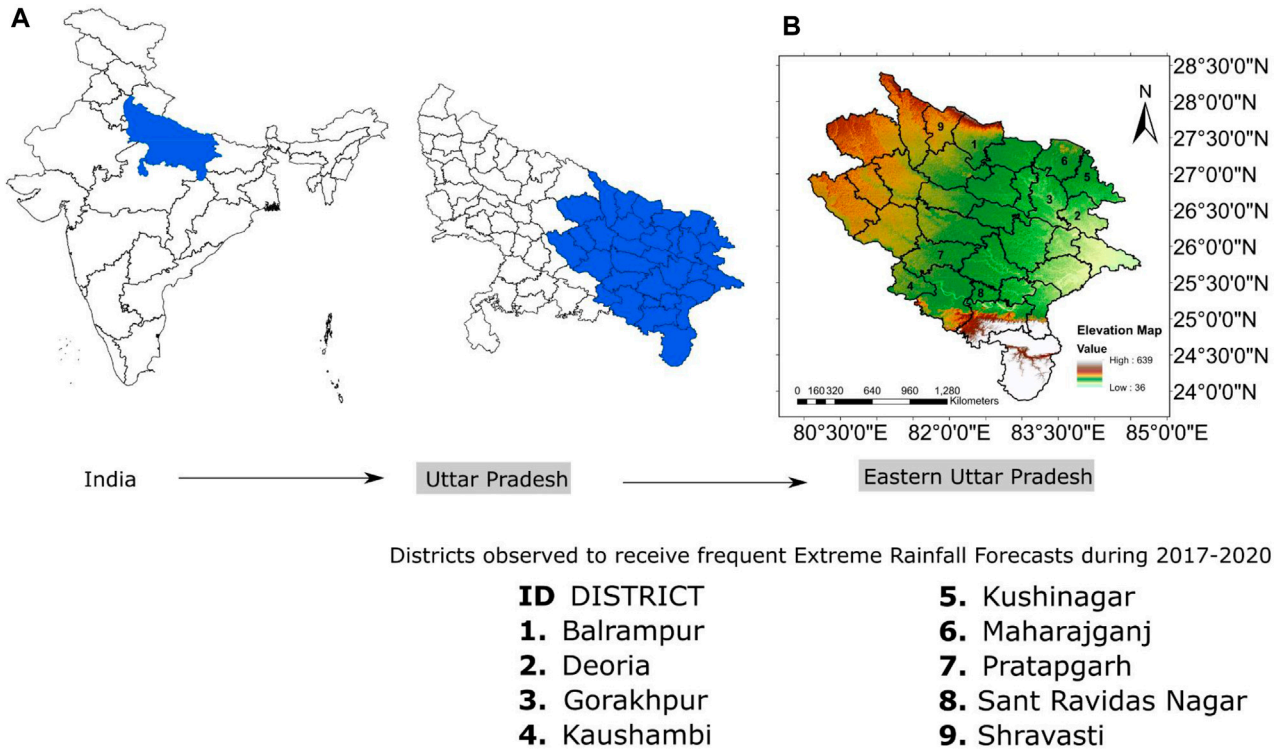

FIGURE 1 | The study area map showing **(A)** the state of Uttar Pradesh in India; **(B)** the expanded view of the districts in Uttar Pradesh (East) selected as the study area along with the names of key districts for this study which are prone to frequent extreme rainfall forecasts.

Centre for Medium-Range Weather Forecasting (NCMRWF) available for the period of 2017–2020 is used as the rainfall forecasts in the study. The socio-economic data is collected from various state and national agencies. The number of extreme rainfall events calculated for each district is correlated with the corresponding spatial maps created using the socio-economic data. The IBFs are generated on the combined basis of the frequency of the extreme rainfall and the nature of the socio-economic condition of the district. Furthermore, warning matrices are formed for the vulnerable districts, which provide information regarding the overall risk probability of a district in the case of an extreme rainfall event. This study is significant since it identifies the different levels of potential impact over multiple sectors of society and issues impact-based warnings to reduce probable damage and losses.

The rest of the paper is organized as follows. **Section 2** describes the study area and dataset. The methodology is explained in **Section 3**. Results are presented in **Section 4**. Discussions are dealt with in **Section 5**, followed by conclusions in **Section 6**.

2 STUDY AREA AND DATASET

2.1 Study Area

The study area includes thirty-two administrative districts of the eastern part of Uttar Pradesh located in the Ganga River Basin of India. **Figure 1A** shows the location of the state of Uttar Pradesh in India along with the selected districts, and **Figure 1B** shows the expanded view of the selected districts. The districts are located between 23°53′N to 28°24′N latitude and 80°30′E to 84°38′E longitude. The area is one of the most densely populated regions of India, with agriculture being the predominant source of livelihood for the majority of the population. The climate of the region is generally hot and humid, with much of the rainfall occurring during the summer monsoon season (June to September). The region has poor infrastructure, poor drainage facilities etc., due to which extreme rainfall events often lead to flash floods and waterlogging. Moreover, the presence of the Ganga River is also one of the reasons for frequent inundation of the region when heavy rainfall occurs in the upper parts of Uttarakhand. The main reason for selecting the region as our study area is that it faces a high rate of mortality of humans and livestock and annual displacement of a vast population each year due to extreme rainfall. Moreover, the socio-economic conditions of the population are generally poor with a low literacy rate. Hence, the availability of reliable forecasts along with their proper interpretation and subsequent guidelines can mitigate the losses of lives and annual displacement of a vast population.

2.2 Datasets Used

This study uses two kinds of data: 1) quantitative precipitation forecast data and 2) socio-economic data. The forecast data is obtained from the NWP model of NCMRWF, which is the premier weather forecast center of India. It provides rainfall forecasts in real-time by performing medium-range global

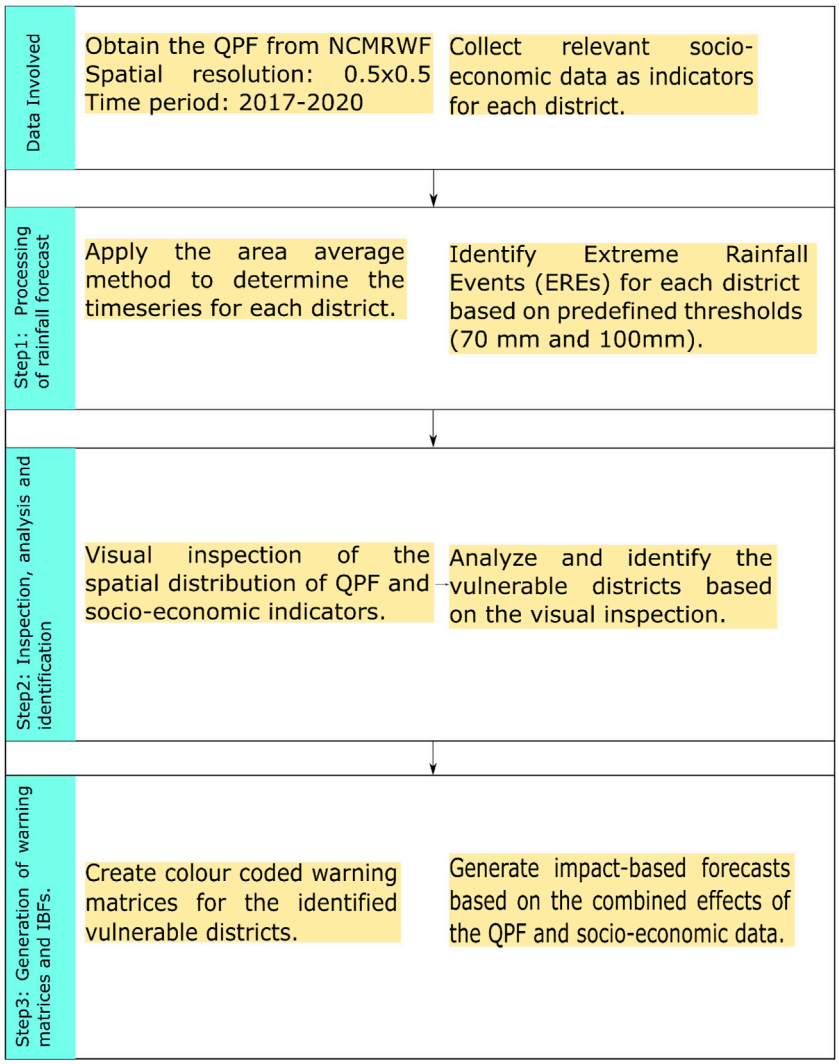

FIGURE 2 | The methodological framework applied to generate IBFs and warning matrices in the study.

assimilation. The data is downloaded from the TIGGE data portal after interpolation (at the TIGGE portal itself) at $0.5^{\circ} \times 0.5^{\circ}$ spatial grid resolution for the years 2017–2020. The temporal resolution of the data is 24 h, along with a lead time of 5 days. Moreover, various socio-economic data such as population density (total population, female population, children population), net sown area, gross domestic product (GDP), airports, percentage of population below the poverty line and number of homeless people are collected for each district. These datasets are collected from various secondary sources, such as the census handbooks of each district and primary census data. The handbooks are available at the website of the census of India (www.censusindia.gov.in).

3 METHODOLOGY

In this study, we use the integrated approach of using the QPFs (along with lead-times) and the relevant socio-economic data for generating the IBFs. The overall approach of generating the IBFs can be divided into three steps, as shown in **Figure 2**.

3.1 Processing of Rainfall Forecast

The available rainfall forecast is gridded in nature which must be calculated at the district level to make it suitable for this study. To this end, we use the method of area-weighted average to estimate the rainfall forecast in each of the districts (Jha et al., 2018; Singhal and Jha, 2021b; Singh et al., 2021). The area-weighted average method involves three steps:

(a) Estimating the area (A_i) based on the portion of the rainfall forecast grid that overlaps with the sub-district,
(b) Multiplying the area (A_i) with the rainfall forecast value (R_i) on that grid,
(c) Divide the result of area*precipitation ($\Sigma(A_i{*}R_i)$) by the value of total area ($A = \Sigma(A_i)$).

The above steps are demonstrated in **Supplementary Figure S1A** which shows the estimated area based on the portion of the rainfall forecast grid for all the districts in the study area. An expanded view of one of the districts is presented in **Supplementary Figure S1B**, in which many rainfall grids overlap. We select five grids to demonstrate the working of area-weighted average. Let us suppose that the area of overlap is estimated as A_1, A_2, ... A_5 and the rainfall forecast for each of those areas as R_1, R_2, R_3, ... R_5. In that case, the area-weighted rainfall for the district would be calculated using **Eq. 1**.

$$\text{District rainfall} = \left(P_1^* A_1 + P_2^* A_2 + P_3^* A_3 + P_4^* A_4 + P_5^* A_5\right) / \times \left(A_1 + A_2 + A_3 + A_4 + A_5\right) \quad (1)$$

Next, the obtained rainfall time-series is used to identify extreme rainfall forecasts (ERFs) for each district based on two predefined thresholds of 70 and 100 mm (Goswami et al., 2006b; Salio et al., 2015; Panda et al., 2016). The idea is to select precipitation thresholds that can cause a significant impact in the region (or any region). Generally, a rainfall of more than 70 and 100 mm per day usually will cause serious impacts in most districts of India. We select two thresholds different in magnitude to take into account the possible diversity in results. Moreover, ERFs at the three lead-times (LT_1, LT_3 and LT_5) are obtained at each of the two percentile thresholds.

Obtaining results using three lead times will allow to understand how the likelihood of probable impacts and their severity may change with an increase (or decrease) in the lead times.

3.2 Analysis and Identification of Vulnerable Districts

In this step, we plot spatial maps of the ERFs at various lead-times showing their spatial distribution in the study area (shown in **Supplementary Figure S2**). We also plot the spatial maps corresponding to the various socio-economic indicators (shown in **Supplementary Figure S3**). The idea here is to visually analyze the extent of possible impacts that could occur in a district based on the integrated effects of the magnitude of ERF and the prevalent socio-economic conditions at the ground. The combined effect determines the likelihood and severity of the impact for each district. For instance, if a district with high population density is forecasted to face extreme rainfall, the likelihood and the severity of the impact (mortality, injuries or displacement) could be much higher than that of a district with low population density. Similarly, a district having an airport facility is likely to be impacted in case of extreme rainfall more severely than a district with no airport. Subsequently, the vulnerable districts are identified to generate the warning matrices and the impact-based forecasts.

3.3 Generation of Warning Matrices and Impact-Based Forecasts

After the vulnerable districts are identified, a color-coded warning matrix is issued as an advisory for the potential impacts much before the extreme rainfall has taken place, as shown in **Supplementary Figure S4**. The advantage of such warning matrices is that they can be updated depending upon the change in risk and likelihood of impact. For instance, the 5-day lead time (LT_5; 5 days before an extreme rainfall) could advise for a "low" likelihood but "high" severity of the impact of extreme rainfall (**Supplementary Figure S4A**). In this case, the target group must be informed about the impending extreme rainfall. Subsequently, both the likelihood and impact may change for the 3-day lead time (LT_3) to "medium" (**Supplementary Figure S4B**). Then, the target group must be given appropriate warnings regarding the potential impacts. Furthermore, for the 1-day lead time (LT_1), the likelihood and impact may change to "high," meaning there is a greater possibility of the occurrence of extreme rainfall leading to severe impacts (**Supplementary Figure S4C**). Finally, an integrated warning matrix must be issued, which takes into account the warnings of all the individual matrices as shown in **Supplementary Figure S4D**. At this stage, meaningful dos and don'ts must be conveyed to the local stakeholders. Finally, impact-based forecasts must be issued in the form of a warning message for each sector which informs about the extent of the impact, its severity and possible mitigation measures.

4 RESULTS

In this section, we use the QPF from NCMRWF to determine the districts that have received the maximum ERFs (with various lead-times) during the years 2017–2020 (**Section 4.1**). Then, we evaluate the potential vulnerability of the districts using the corresponding socio-economic data of the districts (**Section 4.2**). Further, we select three days when the magnitude of forecasted rainfall in the district was highest. For each of the three days, one district is selected (belonging to different categories of impact) to generate the warning matrix and IBFs (**Section 4.3**). For brevity, we present the results using three lead times (lead times 1, 3 and 5).

4.1 Analysis of the Extreme Rainfall Forecasts

In this section, we analyze the spatial distribution of ERFs to identify the districts which have been forecasted to face the maximum number of extreme rainfall during 2017–2020 (see **Supplementary Figure S2**). **Supplementary Figures S2A–F** depicts the spatial distribution of ERFs greater than 100 and 70 mm for the LT_1, LT_3 and LT_5, respectively. Results from both the forecast thresholds show that the distribution of ERFs is quite heterogeneous over the region; however, the frequency in a few districts is higher. Using the results, we identify the districts which show a higher number of ERFs. To this end, we put a threshold on the number of ERFs issued; for instance, at least five ERFs must

TABLE 1 | Districts observed to receive frequent ERFs during 2017–2020.

District	LT_1 (100 mm)	LT_3 (100 mm)	LT_5 (100 mm)	LT_1 (70 mm)	LT_3 (70 mm)	LT_5 (70 mm)
Balrampur	4	6	3	8	12	10
Deoria	4	7	7	16	13	10
Gorakhpur	0	2	6	6	9	11
Kaushambi	2	7	7	8	10	8
Kushinagar	7	13	10	20	25	20
Maharajganj	4	10	9	15	22	20
Pratapgarh	0	7	6	2	9	9
Sant Ravidas Nagar	1	5	6	4	7	12
Shravasti	16	19	18	20	29	31

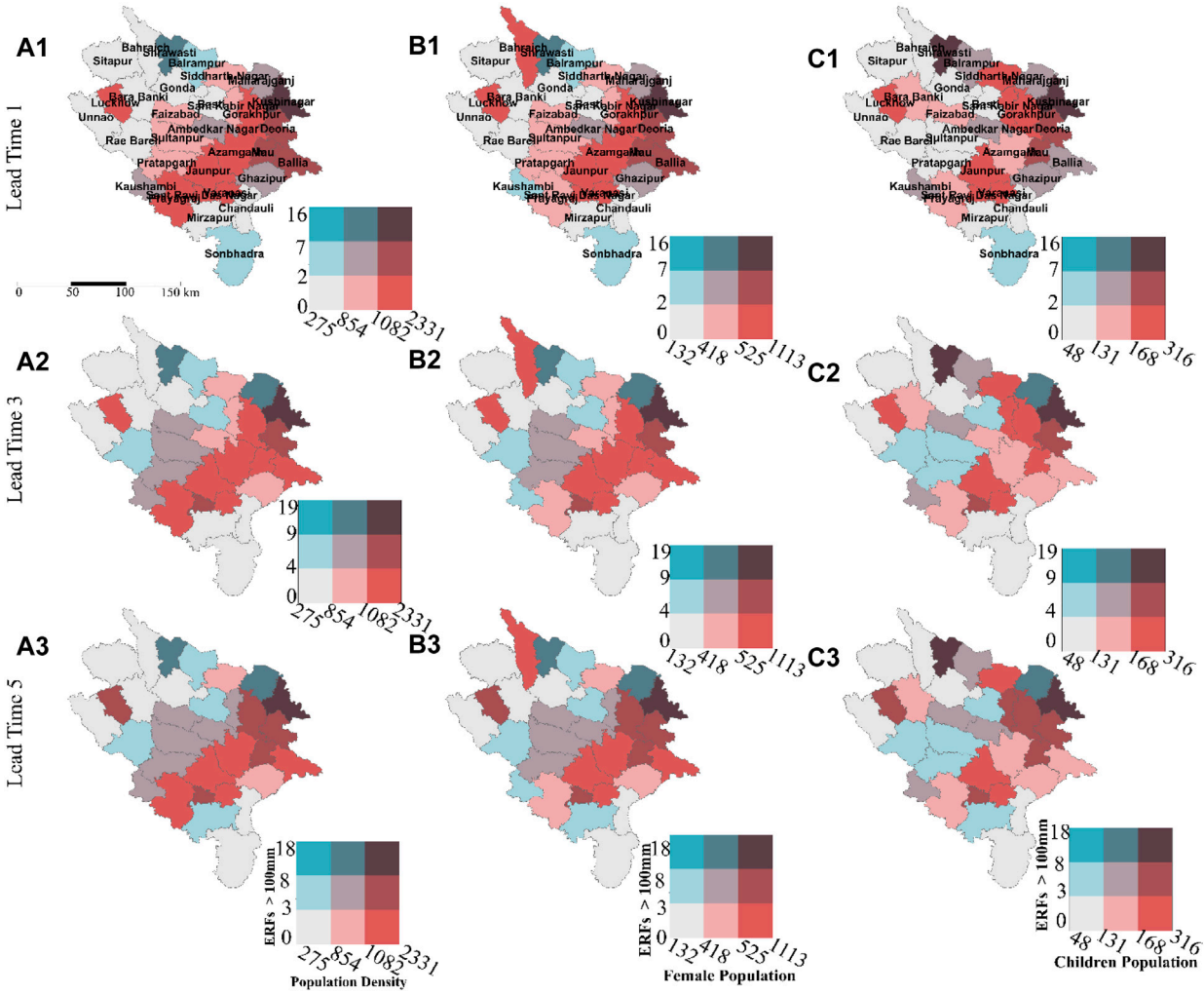

FIGURE 3 | A bivariate choropleth map showing the combined effect of the number of ERFs with the total population density (Panels **(A1–A3)**), female population density (Panels **(B1–B3)**) and children population density (Panels **(C1–C3)**) at three lead times and 100 mm threshold.

be issued above the threshold of 100 mm, and ten ERFs above the 70 mm threshold. We observe that the district Shravasti has received the maximum ERFs in the past four years, followed by Kushinagar and Maharajganj. A total of nine districts are identified whose names are listed in **Table 1**.

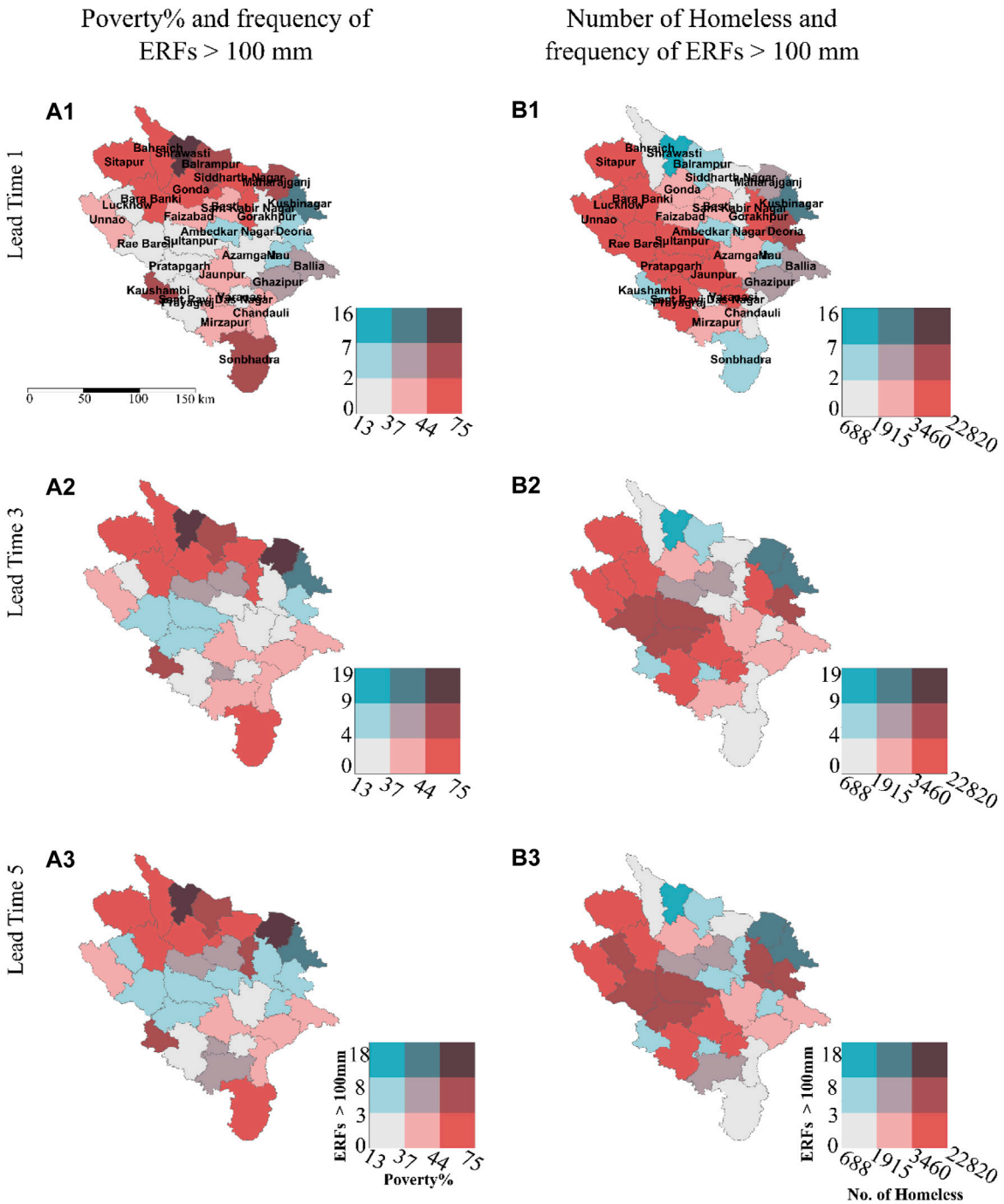

FIGURE 4 | A bivariate choropleth map showing the combined effect of the number of ERFs with the poor population (Panels **(A1–A3)**) and homeless population (Panels **(B1–B3)**) across the districts at three lead times and 100 mm threshold.

4.2 Identification and Analysis of Vulnerable Districts

In this section, we perform a combined analysis of the spatial distribution of ERFs (during 2017–2020) and the socio-economic conditions to identify the broader reasons and potential impacts over the districts in case of extreme rainfall.

4.2.1 Based on Impacts on Population

Figure 3 shows the bivariate choropleth map representing the total population density (**Figures 3A1–A3**), female population density (**Figures 3B1–B3**), and children population density (**Figures 3C1–C3**) with the number of ERFs at the 100 mm threshold for the three lead times. The aim here is to

understand the combined influence of the socio-economic characteristics and the occurrence of the ERFs on the potential impacts of respective districts. Higher population density along with a larger number of ERFs in a district would mean that a larger percentage of the population is vulnerable to adverse impacts and vice-versa. Results from LT_1 (**Figure 3A1**) shows that there exists a belt of districts from Kushinagar to Prayagraj which may face adverse impacts of extreme rainfall due to the combined effect of large population density and a large number of ERFs. Moreover, **Figures 3B1–B3** shows the spatial distribution of the adverse impacts faced by the female population among the districts. Results show that the spatial distribution is quite similar to that observed for the impacts on the total population. Further, in the case of impacts over children population (see **Figure 3C1**), the number of districts showing a high probability of impacts become less in number and are relatively scattered in distribution. Further, the results have generally been similar across all three lead times, with minor variations among the districts. The results obtained using 70 mm rainfall as the threshold is presented in **Supplementary Figure S5**. We observe that the patterns are similar to those obtained using 100 mm as the threshold. Highly vulnerable districts are located in clusters, while those which are less vulnerable are relatively scattered.

4.2.2 Based on Impacts on Marginalized Groups

Figure 4 shows the bivariate choropleth map representing the combined influence of the percentage of population below the poverty line (**Figures 4A1–A3**) and the percentage of the homeless population (**Figures 4B1–B3**) of each district along with the frequency of ERFs at the 100 mm rainfall threshold. **Figure 4A1** represents the spatial distribution of the districts where the poor population may face adverse consequences due to the extreme rainfall events for LT_1. Results from LT_1 show that a large proportion of the poor population in the northern side of the districts (district Sitapur to Maharajganj) may face adverse impacts. Moreover, we notice that a few districts in the southern part (Sonbhadra and Kaushambi) may also face negative consequences. Further, in the case of impacts over the homeless population (see **Figures 4B1–B3**), we observe a significantly larger number of vulnerable districts. Results show that the homeless population living towards the western side of the region (district Sitapur to Prayagraj) may face larger impacts in case of extreme rainfall events. However, with the increase in lead times, we find that the probability of impact in a few districts is low. Further, the results obtained using 70 mm rainfall as the threshold is presented in **Supplementary Figure S6**.

4.2.3 Based on Impacts on Agriculture and Economy

Figure 5 shows the bivariate choropleth map representing the combined influence of the net sown area (**Figures 5A1–A3**) and the amount of GDP contribution (**Figures 5B1–B3**) of each district along with the frequency of ERFs at the 100 mm rainfall threshold. Results from **Figure 5A1** show that there are multiple districts scattered across the region having relatively large net sown areas with a high probability of facing the adverse impacts of extreme rainfall for LT_1. Among them, districts such as Sitapur, Gonda and Barabanki show a high probability of impact across all three lead times. Further, in the case of GDP contribution, we find that the prominent districts which generally have a greater contribution of GDP in the region face a larger probability of impacts. For instance, **Figure 5B1** shows that the important economic centers in the region such as Faizabad, Prayagraj and Kushinagar have a larger probability of facing adverse impacts. However, the district of Lucknow (capital of the state of Uttar Pradesh) is expected to face considerably less impact. The results obtained using 70 mm rainfall as the threshold is presented in **Supplementary Figure S7**. In addition, six districts of the study area (Sultanpur, Prayagraj, Gorakhpur, Lucknow, Varanasi and Kushinagar) have the facility of airports. Of these districts, we observe that Gorakhpur and Kushinagar have frequently faced ERFs in the past years. Hence, any warning or forecast must include information about the likely delay/cancellation of flights so that the passengers may accordingly modify their travel.

4.3 Generation of Impact-Based Warnings and Forecasts

In this section, we select three days when extreme rainfall was forecasted over the majority of the districts of the study area. **Figure 6** shows the distribution of rainfall for three selected days (13th July 2019; 24th September 2020 and 25th September 2020). For each of the three days, one district is selected (belonging to a different category of impact). The selected districts are Shravasti (category-high), Gorakhpur (category-medium) and Jaunpur (category-low). More details about the three selected dates, along with the forecasted magnitude of rainfall, are presented in **Table 2**. Consequently, we generate the impact-based forecasts and the color-coded warning matrices for the districts along with appropriate actions to mitigate the potential adverse consequences.

4.3.1 Sample Impact-Based Forecast for "High" Category Impact

Table 3 shows a sample of the IBF generated for the district Shravasti under the "high" category of impact based on the magnitude of forecasted rainfall. The district is forecasted to receive extreme rainfall (with high magnitude), which puts it into the "high" category of impact. Moreover, results suggest that the income of a large percentage of the population in the district lies below the poverty line and could be highly vulnerable to an extreme rainfall event. Along with the general impacts that could occur (water-logging on streets, flooding in low-lying areas), the impacts of extreme rainfall on poor populations are also considered in the IBF. Alongside, possible responses are suggested based on the expected degree of impact.

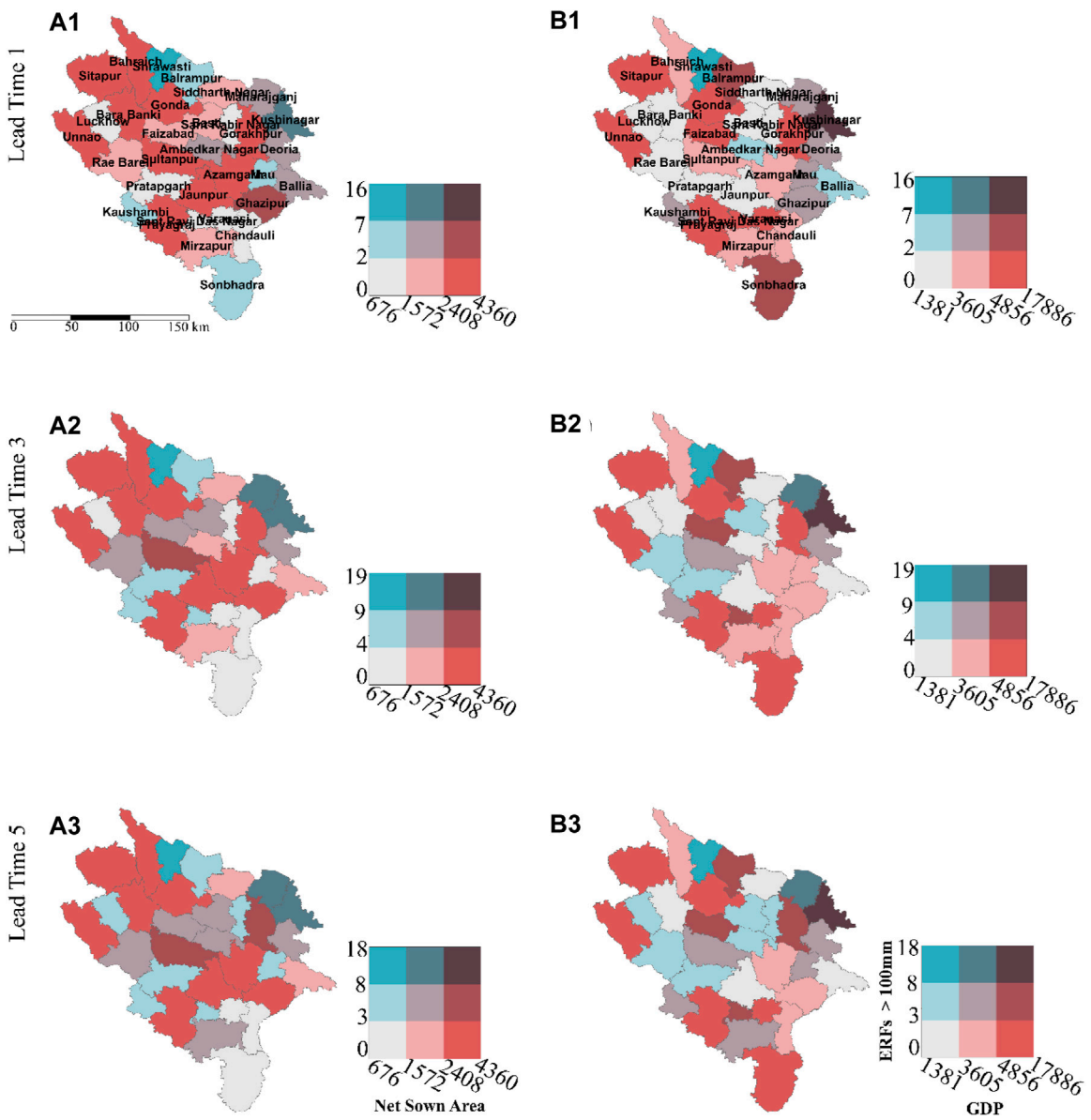

FIGURE 5 | A bivariate choropleth map showing the combined effect of the number of ERFs with net sown area (Panels **(A1–A3)**) and total GDP contribution (Panels **(B1–B3)**) across the districts at three lead times and 100 mm threshold.

4.3.2 Sample Impact-Based Forecasting for "Medium" Category Impact

A sample IBF is generated for the district of Gorakhpur under the "medium" category of impact for the date 24th September 2020, as presented in **Table 4**. A larger number of poor socio-economic parameters in the district make it more vulnerable (compared to district Shravasti) in case extreme rainfall occurs. However, in the present case, the magnitude of rainfall forecast is not as high (as in the case of Shravasti); hence the impacts are not expected to be too severe. Along with the general impacts that are expected during extreme rainfall, a large proportion of homeless people in the district are expected to be adversely impacted. Moreover, a

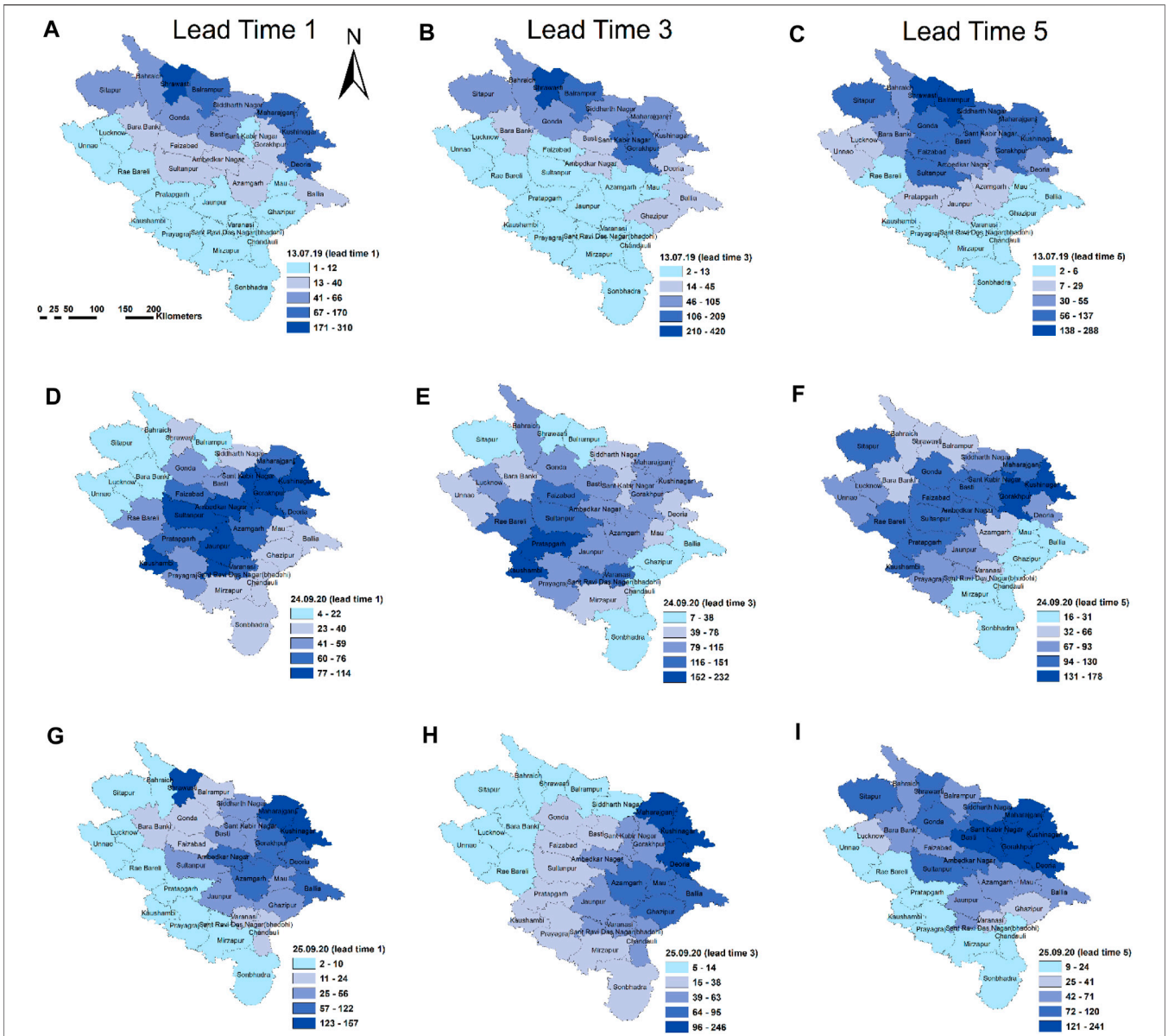

FIGURE 6 | Maps showing the spatial distribution of rainfall for three selected days. Panels **(A–C)** shows the distribution on 13th July 2019, Panels **(D–F)** on 24th September 2020 and Panels **(G–I)** on 25th September 2020 for each of the three lead times, respectively.

TABLE 2 | Details about the three dates of extreme rainfall forecast, districts selected and category of expected impact.

Date	District selected	Lead time 1 (mm)	Lead time 3 (mm)	Lead time 5 (mm)	Range of forecasts (mm)	Category of impact
13th July 2019	Shravasti	309.78	420.34	288.4	288.4–420.34	High
24th September 2020	Gorakhpur	90	91	178	90–178	Medium
25th September 2020	Jaunpur	29	62	69	29–69	Low

large percentage of the net sown area means that standing and/or harvested crops could face damage, while the facility of an airport suggests that a number of flights might get delayed during the time of heavy downpour. Possible responses/mitigation measures are suggested in **Table 4** to minimize the overall impact of the hazard.

TABLE 3 | A sample IBF generated for the district Shravasti.

Date of extreme rainfall	13th July 2019
Name of the district	Shravasti
Category of impact	High
Major socio-economic challenge	High percentage of population below the poverty line
Sample Forecast	Extreme rainfall accumulations between 288 to 420 mm are expected in the district on 13th July 2019 resulting in flooding of streets and houses in the low-lying areas
Impacts expected	• Low-lying areas of the district may face flash floods • Trees may get uprooted and fall on roads • Local colonies and unpaved roads may be flooded • Water-logging on major roads may lead to traffic congestion • High percentage of poor population in the district may face damage to kutcha (temporary) houses • Stagnant water around homes may lead to unhygienic living conditions (outbreak of mosquito-borne diseases)
Response suggested	• People must avoid unnecessary movement at least for the next 2 days • Unfamiliar roads must not be taken as there could be uncovered sinkholes and/or potholes • People having kutcha homes should be relocated to shelter homes (or permanent homes)
Color codes	Very low: no severe hazard expected / Low: be aware / Medium: be prepared / High: take action

TABLE 4 | A sample IBF generated for the district Gorakhpur.

Date of extreme rainfall	24th September 2020
Name of the district	Gorkhpur
Category of impact	Medium
Major socio-economic challenge	Significant part of population is homeless; consist of high net sown area; has the facility of airport
Sample Forecast	Extreme rainfall accumulation between 90–178 mm is expected in the district on 24th September, 2020 resulting in damage to standing/harvested crops and flooding of roads in some (low-lying) areas
Impacts expected	• Bad weather may cause flights to be delayed • High risk of mortality or injury to homeless people • Standing crops may be inundated; harvested crops may get spoilt • Water-logging on major roads may lead to traffic congestions • Stagnant water around homes may lead to unhygienic living conditions (outbreak of mosquito-borne diseases)
Response suggested	• People must avoid unnecessary movement on the day • Homeless population must take shelter under some permanent structures • Arrangements to remove excess water from the crop fields must be kept ready; harvested crops must not be kept in open
Color codes	Very low: no severe hazard expected / Low: be aware / Medium: be prepared / High: take action

4.3.3 Sample Impact-Based Forecasting for "Low" Category Impact

A sample IBF is generated for the district of Jaunpur under the "low" category of impact for the date 25th September 2020, as shown in **Table 5**. The district has a significant population that is homeless. Also, the net sown area in the district is comparatively higher. Since the magnitude of forecasted rainfall is not high (29–62 mm), minor impacts such as water-logging and inundation of crops are expected on the day. The suggested responses against the expected impacts may mitigate any adverse consequences due to the extreme rainfall.

4.3.4 Sample Warning Matrix for the Selected Districts

The corresponding sample warning matrices for the selected districts are shown in **Figure 7**. Here, the magnitude of ERF determines the severity of impact while the likelihood of occurrence increases with each lead time (given that the magnitude does not sharply decrease). In the case of the district Shravasti (**Figure 7A**), we observe that the ERF in each of the three lead-times is consistently high in magnitude (see **Table 2**). The high magnitude of ERF means that the impacts could also be 'high' in severity. Moreover, results show that the magnitude of ERF does not decrease across the three lead-times (in fact, it increases in LT_1 as compared to LT_5); hence the likelihood of the extreme rainfall is expected to increase with the lead-times. In the case of Gorakhpur (**Figure 7B**), we observe that there is a sharp decrease in the magnitude of ERF in the lead-times that follow LT_5 (see **Table 2**). This suggests that the severity of impact could be low on the actual date of the extreme rainfall, and hence, the category of impact falls to "medium" (LT_1and LT_5) from "high" (LT_5). Moreover, the likelihood of occurrence increases from "low" to "high" as the forecasts in the lead-times approach the actual day of extreme rainfall. In the case of Jaunpur, we observe that the magnitude of ERF is the lowest among the three selected districts. Also, results show that there is a sharp decrease in the magnitude in LT_5 (compared to the other two lead-times). The likelihood of the occurrence of extreme rainfall is more in LT_5 (as compared to LT_3); however, due to the sharp decrease in the magnitude, the likelihood reduces to "low" in LT_1.

4.4 Verification of the Forecast Data

In this section, we verify the occurrences of the extreme rainfall event as represented by the QPF from NCMRWF using the

TABLE 5 | A sample IBF generated for the district Jaunpur.

Date of extreme rainfall	25th September 2020
Name of the district	Jaunpur
Category of impact	Low
Major socio-economic challenge	Significant part of the population is homeless; consist of high net sown area
Sample Forecast	Extreme rainfall accumulation of 29–62 mm is expected in the district on 25th September, 2020 resulting in water-logging of streets and low-lying houses
Impacts expected	• Water-logging in some minor streets leading to increased travel times • Standing crops may be inundated; harvested crops may get spoilt • Stagnant water around homes may lead to unhygienic living conditions (outbreak of mosquito-borne diseases)
Response suggested	• Vehicles must be driven carefully without rush • Homeless population must take shelter under some permanent structures • Arrangements to remove excess water from the crop fields must be kept ready; harvested crops must not be kept in open
Color codes	Very low: no severe hazard expected / Low: be aware / Medium: be prepared / High: take action

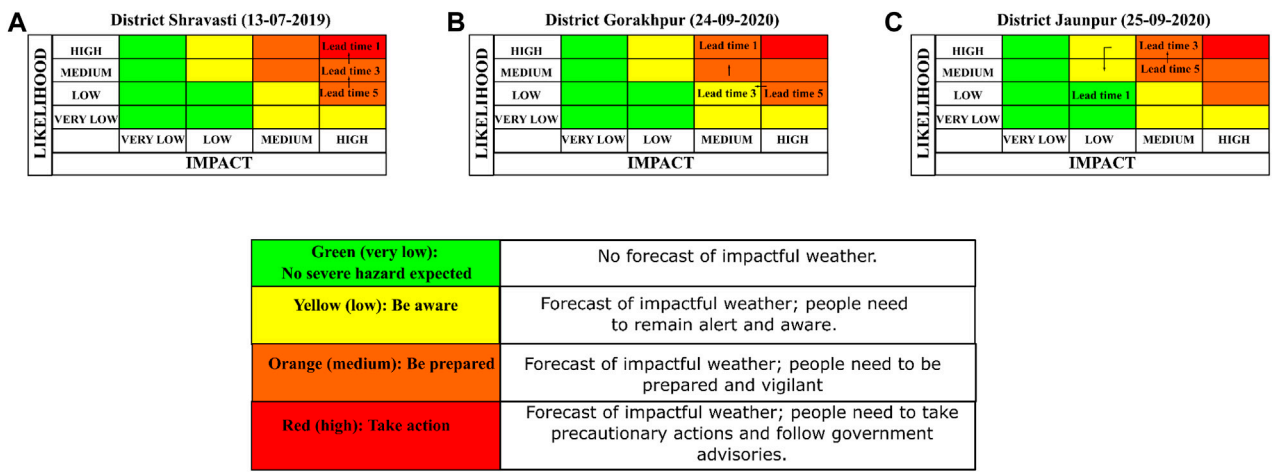

FIGURE 7 | Sample warning matrices for the selected days and the selected districts based on the rainfall magnitude of the three lead times. **(A)** shows the sample warning matrix for the district Shravasti, **(B)** shows for the district Gorakhpur while **(C)** shows it for the district Jaunpur

Integrated Multi-Satellite Retrievals for GPM (IMERG) data. IMERG is a widely used satellite-derived rainfall product used as the observation data to validate ground truth (Prakash et al., 2018; Das et al., 2022). To this end, we randomly selected four districts from the study area and plotted the time-series (by using a temporal window) of both the forecast from NCMRWF and the IMERG rainfall for a particular extreme rainfall event, as shown in **Supplementary Figure S8**. From the Figure, we observe that the ERF for the district Kushinagar coincides reasonably with the corresponding IMERG data for the first lead time (**Supplementary Figure S8A**). However, it does not coincide well with the other two lead times. Moreover, for the district, Unnao, the forecast and the observation lines match well for all the three lead times, while for the district Jaunpur, they do not match in either of the three lead times. Again, for the district Gorakhpur, the curves match well in LT_1 but fail in the other two lead times. Overall, results suggest that while the forecast data offered moderate accuracy in the study, it is still inadequate to be used by the end-users in its raw form. We suggest that post-processing methods could be applied to improve the accuracy of the forecast data before using it for operational purposes such as IBF.

5 DISCUSSION

The study focuses on an approach to generate sample warning matrices as well as IBFs for the districts of eastern Uttar Pradesh based on rainfall forecasts and socio-economic conditions. Analysis of the frequency of ERFs in the past four years (2017–2020) show that the districts located in the eastern margin (such as Shravasti, Maharajganj, Kushinagar, Deoria etc.) have been more vulnerable to events of extreme rainfall. These districts are weak in infrastructure, have poor drainage systems and consist of relatively higher population density which makes a larger population vulnerable to mortality, injuries and displacement in the case of extreme rainfall.

Specifically, we observe that Gorakhpur has a high proportion of the female population in the study area, and it has also received frequent ERFs with high magnitude. This suggests that the female

population of the district are highly exposed to extreme rainfall. In case of exposure to children population, we observe that the districts which have high children density have not been issued regular ERFs. This indicates that the children population in the region are less exposed to events of extreme rainfall in comparison to the female population. Furthermore, we find that the poor population among the districts have been highly exposed to ERFs. Population in districts such as Bahraich, Shravasti and Kaushambi are poor, and results show that these districts have been highly prone to ERFs in the past years. The concerned authorities must take into account the vulnerability of the poor population while issuing the warnings and IBFs, specifically for these districts.

In terms of impacts on agriculture and the economy, we observe that ERFs of high magnitude have been significantly issued in districts where the net sown area is large. For instance, in some districts where the severity of impact is expected to be "medium" (district Gorakhpur) or "low" (district Jaunpur), several ERFs have been issued in the past. Farmers and other stakeholders must be warned about the possible losses in case of extreme rainfall, and mitigation measures must be advised. Our results show that the GDP is high in the district of Kushinagar which is observed to be highly vulnerable to ERFs. Kushinagar is known to be a major Buddhist tourist spot and a hub of the sugar industry in Uttar Pradesh. Weather warnings and IBFs must include the possible impacts that tourists may face along with appropriate travel advisories before and during extreme rainfall occurs. Moreover, sugarcane farmers could be notified and warned of the incoming rainstorm so that their crops (standing or harvested) do not get damaged. Suitable communication must be made to industry owners and staff regarding the expected timing and duration of the extreme rainfall so that they can adjust their working hours. Furthermore, we selected three days when the ERF was highest in the study area, and one district is selected for each of those days to generate the IBF and warning matrix. The districts are purposely selected in such a way that they show varied categories of impact due to the extreme rainfall. For instance, the district Shravasti is expected to have a "high" category of impact on 13th July 2019; district Gorakhpur is expected to have a "medium" category of impact on 24th September 2020; and the district Jaunpur is expected to have "low" category of impact on 25th September 2020. Since the expected impact on the district Shravasti is "high," it means that the forecasted extreme rainfall may cause large destruction in the district. The corresponding IBFs includes all the possible implications by taking into account the socio-economic conditions of the district. Appropriate responses to all the impacted stakeholders must be conveyed. Moreover, the district Gorakhpur is under the 'medium' category, which means that the approaching extreme rainfall can cause serious impacts flooding, especially in the low-lying regions. Improper communication of mitigation responses can lead to mortalities and injuries. Furthermore, the "low" category of impact (such as in Jaunpur) is not expected to cause widespread damage. Such forecast means that the traffic (especially during the rush hour) may get congested due to waterlogging on roads. Overall, the study deals with the identification of expected impacts and appropriate communication of mitigation responses to the affected population, which is crucial to reduce the widespread destruction that may be caused by the increased events of extreme rainfall in the region.

6 CONCLUSION

The study demonstrates, for the first time, the integration of the NWP forecast and the socio-economic data to forecast the possible impacts over a region in case of an extreme rainfall event. Results show that the population in some districts, such as Shravasti and Kaushambi, are relatively poor, and the districts have been highly vulnerable to ERFs in the past years. Warnings and IBFs for these districts must include the possible impacts and responses in order to mitigate the severity of the impact. Moreover, we selected three days (with three lead-times) when the magnitude of ERF was highest in the region. For each of the three days, one district is selected to generate a sample of an IBF and warning matrix. The IBF informs about the category of impact expected on the day (either very low, low, medium or high) along with the expected impacts based on the category of impact. The magnitude of the forecast and the socio-economic condition of the district determines the extent of possible impacts. Precautionary actions are suggested to the relevant stakeholders to mitigate the adversity of the impact. Furthermore, a warning matrix is issued, which provides information regarding the "likelihood" of occurrence of the extreme rainfall and the expected severity of impact. The warning matrix is formed on the basis of estimations of rainfall in the various lead-times. Generally, the likelihood increases as the day of extreme rainfall approaches and the severity of impact are determined by the consistency in magnitude of lead time forecasts. Overall, the study provides a novel approach to generate impact-based forecasts along with warning matrices which can benefit the meteorological agencies and emergency service providers significantly to communicate crucial weather information to the local population in order to mitigate adverse impacts.

6.1 Limitations and Future Challenges

The present work aims to generate IBFs and warning matrices at the district level. Future studies may perform impact-based forecasting at more local levels such as sub-districts, following the work of Reddy et al. (2021) to provide a better understanding to policymakers and district administrators. Moreover, fine-resolution forecast datasets can be used to understand the probability and severity of impacts at the local levels. Different forecast datasets available from various NWP models and Weather Research and Forecasting (WRF) models can also be used to substantiate the findings and consequently provide reliable probabilities of impacts. Furthermore, statistical weighting methods can be used to assign weights to the socio-economic variables which may differ with each district. Several other socio-economic variables (such as the percentage of elderly

people, the road network density etc.) can also be used to broaden the scope of the study. Furthermore, post-processing of the forecast data may be explored to improve the accuracy of the forecast data (and reduce the false-alarm rate) before using it to generate IBFs.

DATA AVAILABILITY STATEMENT

The original contributions presented in the study are included in the article/**Supplementary Material**, further inquiries can be directed to the corresponding author.

AUTHOR CONTRIBUTIONS

AS: Conceptualization, data curation, formal analysis, methodology, writing-original draft, investigation, funding acquisition, validation, visualization. RA: Data curation, investigation, visualization, and formal analysis. SJ: Conceptualization, writing and editing manuscript, investigation, supervision, and funding acquisition.

FUNDING

AS acknowledges the financial support from the Department of Science and Technology, Government of India (DST/INSPIRE/03/2019/001343) (IF 190257) under the DST-INSPIRE scheme. This research was supported by the Science and Engineering Research Board (SERB), Department of Science and Technology, Government of India (project number CRG/2018/000649), awarded to SJ.

SUPPLEMENTARY MATERIAL

The Supplementary Material for this article can be found online at: https://www.frontiersin.org/articles/10.3389/feart.2022.846113/full#supplementary-material

REFERENCES

Basher, R. (2006). Global Early Warning Systems for Natural Hazards: Systematic and People-Centred. *Phil. Trans. R. Soc. A* 364, 2167–2182. doi:10.1098/RSTA.2006.1819

Bostrom, A., Morss, R., Lazo, J. K., Demuth, J., and Lazrus, H. (2018). Eyeing the Storm: How Residents of Coastal Florida See Hurricane Forecasts and Warnings. *Int. J. Disaster Risk Reduct.* 30, 105–119. Elsevier. doi:10.1016/J.IJDRR.2018.02.027

Casteel, M. A. (2018). An Empirical Assessment of Impact Based Tornado Warnings on Shelter in Place Decisions. *Int. J. Disaster Risk Reduct.* 30, 25–33. Elsevier. doi:10.1016/J.IJDRR.2018.01.036

Casteel, M. A. (2016). Communicating Increased Risk: An Empirical Investigation of the National Weather Service's Impact-Based Warnings. *Weather, Climate, and Society. Am. Meteorological Soc.* 8 (3), 219–232. doi:10.1175/WCAS-D-15-0044.1

Das, S., Jain, M. K., and Gupta, V. (2022). A Step Towards Mapping Rainfall Erosivity for India Using High-Resolution GPM Satellite Rainfall Products. *CATENA* 212, 106067. doi:10.1016/j.catena.2022.106067

Froude, L. S. R. (2010). TIGGE: Comparison of the Prediction of Northern Hemisphere Extratropical Cyclones by Different Ensemble Prediction Systems. *Weather and Forecasting. Am. Meteorological Soc.* 25 (3), 819–836. doi:10.1175/2010WAF2222326.1

Goswami, B. N., Venugopal, V., Sengupta, D., Madhusoodanan, M. S., and Xavier, P. K. (2006a). Increasing Trend of Extreme Rain Events over India in a Warming Environment. *Science* 314 (5804), 1442–1445. doi:10.1126/science.1132027

Goswami, B. N., Venugopal, V., Sengupta, D., Madhusoodanan, M. S., and Xavier, P. K. (2006b). Increasing Trend of Extreme Rain Events Over India in a Warming Environment. *Science* 314 (5804), 1442–1445. doi:10.1126/SCIENCE.1132027

Jha, S. K., Shrestha, D. L., Stadnyk, T. A., and Coulibaly, P. (2018). Evaluation of Ensemble Precipitation Forecasts Generated through Post-processing in a Canadian Catchment. *Hydrol. Earth Syst. Sci.* 22 (3), 1957–1969. doi:10.5194/hess-22-1957-2018

Jongman, B. (2018). Effective Adaptation to Rising Flood Risk. *Nat. Commun.* 9 (1), 1–3. doi:10.1038/s41467-018-04396-1

Kaltenberger, R., Schaffhauser, A., and Staudinger, M. (2020). "What the Weather Will Do" - Results of a Survey on Impact-Oriented and Impact-Based Warnings in European NMHSs. *Adv. Sci. Res.* 17, 29–38. doi:10.5194/ASR-17-29-2020

Kox, T., Lüder, C., and Gerhold, L. (2018). Anticipation and Response: Emergency Services in Severe Weather Situations in Germany. *Int. J. Disaster Risk Sci.* 9 (1), 116–128. doi:10.1007/S13753-018-0163-Z

Losee, J. E., and Joslyn, S. (2018). The Need to Trust: How Features of the Forecasted Weather Influence Forecast Trust. *Int. J. Disaster Risk Reduct.* 30, 95–104. doi:10.1016/J.IJDRR.2018.02.032

Mendis, M. M. P. (2021). "An Approach for Impact-Based Heavy Rainfall Warning, Based on the ECMWF Extreme Forecast Index and Level of Hazard Risk," in *Multi-Hazard Early Warning and Disaster Risks*. Editors D. Amaratunga, R. Haigh, and N. Dias (Cham: Springer), 543–559. doi:10.1007/978-3-030-73003-1_37

Morss, R. E., Cuite, C. L., Demuth, J. L., Hallman, W. K., and Shwom, R. L. (2018). Is Storm Surge Scary? The Influence of Hazard, Impact, and Fear-Based Messages and Individual Differences on Responses to Hurricane Risks in the USA. *Int. J. Disaster Risk Reduct.* 30, 44–58. Elsevier. doi:10.1016/J.IJDRR.2018.01.023

Mukherjee, S., Aadhar, S., Stone, D., and Mishra, V. (2018). Increase in Extreme Precipitation Events under Anthropogenic Warming in India. *Weather Clim. Extrem.* 20, 45–53. doi:10.1016/j.wace.2018.03.005

Otieno, H., Yang, J., Liu, W., and Han, D. (2014). Influence of Rain Gauge Density on Interpolation Method Selection. *J. Hydrol. Eng.* 19 (11), 04014024. doi:10.1061/(ASCE)HE.1943-5584.0000964

Panda, D. K., Panigrahi, P., Mohanty, S., Mohanty, R. K., and Sethi, R. R. (2016). The 20th Century Transitions in Basic and Extreme Monsoon Rainfall Indices in India: Comparison of the ETCCDI Indices. *Atmos. Res.* 181, 220–235. doi:10.1016/j.atmosres.2016.07.002

Pattanaik, D. R., and Rajeevan, M. (2010). Variability of Extreme Rainfall Events over India during Southwest Monsoon Season. *Met. Apps* 17 (1), 88–104. John Wiley and Sons Ltd. doi:10.1002/met.164

Pittore, M., Wieland, M., and Fleming, K. (2017). Perspectives on Global Dynamic Exposure Modelling for Geo-Risk Assessment. *Nat. Hazards* 86 (1), 7–30. doi:10.1007/S11069-016-2437-3/FIGURES/2

Potter, S. H., Kreft, P. V., Milojev, P., Noble, C., Montz, B., Dhellemmes, A., et al. (2018). The Influence of Impact-Based Severe Weather Warnings on Risk Perceptions and Intended Protective Actions. *Int. J. Disaster Risk Reduct.* 30, 34–43. doi:10.1016/J.IJDRR.2018.03.031

Prakash, S., Mitra, A. S., AghaKouchak, A., Liu, Z., Norouzi, H., and Pai, D. S. (2018). A Preliminary Assessment of GPM-based Multi-Satellite Precipitation Estimates Over a Monsoon Dominated Region. *J. Hydrol.* 556, 865–876. doi:10.1016/j.atmosres.2016.07.002

Ray, K., Giri, R. K., Ray, S. S., Dimri, A. P., and Rajeevan, M. (2021). An Assessment of Long-Term Changes in Mortalities Due to Extreme Weather Events in India: A Study of 50 years' Data, 1970-2019. *Weather Clim. Extrem.* 32, 100315. doi:10.1016/J.WACE.2021.100315

Reddy, A. A., Bhattacharya, A., Reddy, S. V., and Ricart, S. (2021). Farmers' Distress Index: An Approach for an Action Plan to Reduce Vulnerability in the Drylands of India. *Land* 10 (11), 1236. doi:10.3390/LAND10111236/S1

Rossi, C., Acerbo, F. S., Ylinen, K., Juga, I., Nurmi, P., Bosca, A., et al. (2018). Early Detection and Information Extraction for Weather-Induced Floods Using Social Media Streams. *Int. J. Disaster Risk Reduct.* 30, 145–157. doi:10.1016/J.IJDRR.2018.03.002

Roxy, M. K., Ghosh, S., Pathak, A., Athulya, R., Mujumdar, M., Murtugudde, R., et al. (2017). A Threefold Rise in Widespread Extreme Rain Events over Central India. *Nat. Commun.* 8 (1), 1–11. doi:10.1038/s41467-017-00744-9

Sai, F., Cumiskey, L., Weerts, A., Bhattacharya, B., and Haque Khan, R. (2018). Towards Impact-Based Flood Forecasting and Warning in Bangladesh: a Case Study at the Local Level in Sirajganj District. *Nat. Hazards Earth Syst. Sci. Discuss.*, 1–20. doi:10.5194/nhess-2018-26

Salio, P., Hobouchian, M. P., García Skabar, Y., and Vila, D. (2015). Evaluation of High-Resolution Satellite Precipitation Estimates over Southern South America Using a Dense Rain Gauge Network. *Atmos. Res.* 163, 146–161. Elsevier. doi:10.1016/J.ATMOSRES.2014.11.017

Silvestro, F., Rossi, L., Campo, L., Parodi, A., Fiori, E., Rudari, R., et al. (2019). Impact-based Flash-Flood Forecasting System: Sensitivity to High Resolution Numerical Weather Prediction Systems and Soil Moisture. *J. Hydrology* 572, 388–402. Elsevier. doi:10.1016/J.JHYDROL.2019.02.055

Singh, A., Tiwari, S., and Jha, S. K. (2021). Evaluation of Quantitative Precipitation Forecast in Five Indian River Basins. *Hydrological Sci. J.* 66, 2216–2231. doi:10.1080/02626667.2021.1982138

Singhal, A., Cheriyamparambil, A., and Jha, S. K. (2022). Spatial Extrapolation of Statistically Downscaled Weather Data over the Northwest Himalayas at Major Glacier Sites. *Environ. Model. Softw.* 149, 105317. Elsevier Ltd. doi:10.1016/j.envsoft.2022.105317

Singhal, A., and Jha, S. K. (2021a). An Application of Multiple-Point Statistics Downscaling Approach Over North-West Himalayas in Avalanche-Prone Areas. *Intl J. Climatol.* 42, 1902–1921. doi:10.1002/joc.7342

Singhal, A., and Jha, S. K. (2021b). Can the Approach of Vulnerability Assessment Facilitate Identification of Suitable Adaptation Models for Risk Reduction? *Int. J. Disaster Risk Reduct.* 63, 102469. Elsevier Ltd. doi:10.1016/j.ijdrr.2021.102469

Taylor, A. L., Kause, A., Summers, B., and Harrowsmith, M. (2019). Preparing for Doris: Exploring Public Responses to Impact-Based Weather Warnings in the United Kingdom. *Am. Meteorological Soc.* 11 (4), 713–729. doi:10.1175/WCAS-D-18-0132.1

Tozier de la Poterie, A. S., Jjemba, W. E., Singh, R., Coughlan de Perez, E., Costella, C. V., and Arrighi, J. (2018). Understanding the Use of 2015-2016 El Niño Forecasts in Shaping Early Humanitarian Action in Eastern and Southern Africa. *Int. J. Disaster Risk Reduct.* 30, 81–94. Elsevier. doi:10.1016/J.IJDRR.2018.02.025

Uccellini, L. W., and Ten Hoeve, J. E. (2019). Evolving the National Weather Service to Build a Weather-Ready Nation: Connecting Observations, Forecasts, and Warnings to Decision-Makers through Impact-Based Decision Support Services. *Am. Meteorological Soc.* 100 (10), 1923–1942. doi:10.1175/BAMS-D-18-0159.1

Verdin, A., Funk, C., Rajagopalan, B., and Kleiber, W. (2016). Kriging and Local Polynomial Methods for Blending Satellite-Derived and Gauge Precipitation Estimates to Support Hydrologic Early Warning Systems. *IEEE Trans. Geosci. Remote Sens.* 54 (5), 2552–2562. doi:10.1109/TGRS.2015.2502956

Weyrich, P., Scolobig, A., Bresch, D. N., and Patt, A. (2018). Effects of Impact-Based Warnings and Behavioral Recommendations for Extreme Weather Events. *Weather, Clim. Soc.* 10 (4), 781–796. doi:10.1175/WCAS-D-18-0038.1

Winsemius, H. C., Aerts, J. C. J. H., Van Beek, L. P. H., Bierkens, M. F. P., Bouwman, A., Jongman, B., et al. (2015). Global Drivers of Future River Flood Risk. *Nat. Clim. Change* 6 (4), 381–385. doi:10.1038/nclimate2893

WMO (2015). *WMO Guidelines on Multi-Hazard Impact-Based Forecast and Warning Services*Geneva: WMO

Conflict of Interest: The authors declare that the research was conducted in the absence of any commercial or financial relationships that could be construed as a potential conflict of interest.

Publisher's Note: All claims expressed in this article are solely those of the authors and do not necessarily represent those of their affiliated organizations, or those of the publisher, the editors and the reviewers. Any product that may be evaluated in this article, or claim that may be made by its manufacturer, is not guaranteed or endorsed by the publisher.

frontiers | Frontiers in Earth Science

ORIGINAL RESEARCH
published: 24 May 2022
doi: 10.3389/feart.2022.883842

A Flood Forecasting Framework Coupling a High Resolution WRF Ensemble With an Urban Hydrologic Model

Saimy Davis[1], *Likhitha Pentakota*[1], *Nikita Saptarishy*[1] *and Pradeep. P. Mujumdar*[1,2]*

[1]Interdisciplinary Centre for Water Research, Indian Institute of Science, Bangalore, India, [2]Department of Civil Engineering, Indian Institute of Science, Bangalore, India

Numerical weather prediction (NWP) models such as the Weather Research and Forecasting (WRF) model are increasingly used over the Indian region to forecast extreme rainfall events. However, studies which explore the application of high-resolution rainfall simulations obtained from the WRF model in urban hydrology are limited. In this paper, the utility of a model coupling framework to predict urban floods is explored through the case study of Bangalore city in India. This framework is used to simulate multiple extreme events that occurred over the city for the monsoons of years 2020 and 2021. To address the uncertainty from the WRF model, a 12-member convection permitting ensemble is used. Model configurations using Kain Fritsch and WSM6 parameterization schemes could simulate the spatial and temporal pattern of the selected event. The city is easily flooded with rainfall events above a threshold of 60 mm/day and to capture the response of the urban catchment, the Personal Computer Storm Water Management Model (PCSWMM) is used in this study. Flood forecasts are created using the outputs from the WRF ensemble and the Global Forecasting System (GFS). The high temporal and spatial resolution of the rainfall forecasts (<4 km at 15-min intervals), has proved critical in reproducing the urban flood event. The flood forecasts created using the WRF ensemble indicate that flooding and water levels are comparable to the observed whereas the GFS underestimates these to a large extent. Thus, the coupled WRF–PCSWMM modelling framework is found effective in forecasting flood events over an Indian city.

Keywords: WRF, flood forecasting, PCSWMM, urban flooding, extreme events, NWP, prediction, high resolution

OPEN ACCESS

Edited by:
Sanjeev Kumar Jha,
Indian Institute of Science Education and Research, India

Reviewed by:
Kuldeep Sharma,
Meteorological Service Singapore, Singapore
Meenu Ramadas,
Indian Institute of Technology Bhubaneswar, India

***Correspondence:**
Pradeep. P. Mujumdar
pradeep@iisc.ac.in

Specialty section:
This article was submitted to Hydrosphere, a section of the journal Frontiers in Earth Science

Received: *25 February 2022*
Accepted: *06 May 2022*
Published: *24 May 2022*

Citation:
Davis S, Pentakota L, Saptarishy N and Mujumdar PP (2022) A Flood Forecasting Framework Coupling a High Resolution WRF Ensemble With an Urban Hydrologic Model. Front. Earth Sci. 10:883842. doi: 10.3389/feart.2022.883842

INTRODUCTION

The sixth assessment report of the Intergovernmental Panel on Climate Change (IPCC) observes that human-induced warming is increasing at 0.2°C per decade which will lead to an inevitable increase of 1.5°C in the global temperature (Allen et al., 2018). This would imply a substantial increase in the occurrence/intensity of extreme events which is evident from the rising numbers of extreme events in cities. (Shastri et al., 2015; Paul et al., 2016; Paul et al., 2018; Roxy et al., 2017). Floods in the rapidly urbanising India have devastating effects on the property due to the unplanned growth of its cities. The problem of urban flooding is critical because of the fast responses of these catchments to extreme rainfall and shorter times of concentration, (Awol et al., 2021). High intensity rainfall events and

inadequate storm water infrastructure, results in a huge amount of flood runoff in cities in a short period of time (Mondal and Mujumdar, 2015; Rupa and Mujumdar, 2019). Implementation of traditional structural flood mitigation measures such as detention ponds, levees, pump-sump systems, and culverts is difficult to execute in densely populated urban areas. With the inevitable increase in urban floods in the near future, the World Meteorological Organization (WMO) encourages a shift to non-structural measures such as real time flood forecasting and early warning systems to minimize flood impact (World Meteorological Organization, 2011). The Hydromet Alliance group launched at the United Nations Framework Convention on Climate Change (UNFCCC) Conference of the Parties in 2019 (COP 25) focuses on the development of reliable weather, climate, and hydrological (hydromet) services which will help in the installation of early warning systems (Houmann, 2016) worldwide.

Numerical weather prediction (NWP) models represent the atmosphere as a dynamic fluid and solve for its behaviour through the use of mechanics and thermodynamics and play an important role in early warning systems. Regional Climate Models (RCMs) (which are also NWP models) are used to resolve region specific weather patterns using real time weather data available at a coarse resolution from global NWP models. A dynamic downscaling approach is used to generate forecasts that can provide reliable information at a scale that resolves local interactions between topography and synoptic phenomena, which then can be applied in hydrologic models (Thayyen et al., 2013; Patel et al., 2019).

The Weather Research and Forecasting (WRF) model, a commonly used RCM, has been used in several studies over the Indian region to simulate extreme rainfall events (Sahoo et al., 2014; Chawla and Mujumdar, 2015; Chevuturi et al., 2015; Chawla et al., 2018; Mohandas et al., 2020; Kadaverugu et al., 2021; Kirthiga et al., 2021). Rainfall being a result of many atmospheric processes over different scales, is the most difficult process to be captured by the WRF model. Uncertainty in initial and boundary conditions, physics schemes, and sensitivity of the model concerning configuration of the domain size and grid spacing are the main contributing factors to the model performance (Arnold et al., 2012; Liu et al., 2012; Sun et al., 2014). Although many studies have shown that the best combination of physics schemes can be determined for a region, it is difficult to identify the characteristics of future rainfall events as the current rise in global temperature has led to unprecedented changes (Tian et al., 2017). In order to consider the uncertainties associated with the selection of physics schemes, it is a commonly accepted practice to generate an ensemble with multiple model runs (Ji et al., 2012). An ensemble generated using a combination of WRF model setups with a grid resolution less than 4 km is referred to as a convection permitting ensemble. This resolution limits the errors from the physics scheme that parameterizes the convective process and improves interactions between different processes of the WRF model (Clark et al., 2016).

With increasing computational power, there is an increase in the resolution of products from NWP models. Outputs from the Global Forecasting System (GFS, an operational weather forecast model), are currently available at a high resolution of 25 km as compared to the earlier resolutions of 100 and 50 km. Few studies in the Indian region have explored the utility of such NWP products for hydrological modelling of river basins. Singh et al. (2021) compared different NWP products at a common grid of 0.5° to evaluate the hydrological parameters in five major river basins in India. Goswami et al. (2018) used a NWP product at 17 km resolution over the Narmada basin during the southwest monsoon period and found that the rainfall estimates had location specific biases. Studies outside India have demonstrated the success of flood models coupled with weather forecast models like WRF in forecasting floods in urban catchments (Sikder et al., 2019). Real time prediction of the urban flood was demonstrated for Milano, Italy, by Ravazzani et al. (2016) where the WRF model was coupled with a spatially distributed rainfall-runoff model. A study on Can Tho city in Vietnam indicates the effects of urbanization on the local precipitation using the WRF model coupled with a land use model (Huong and Pathirana, 2011). Over the Indian region similar studies have been conducted over river basins.

Dhote et al. (2018) used WRF model output for forecasting a heavy rainfall event 3 days prior to its occurrence over the North-Western Himalayas. Asghar et al. (2019) compared the applications of WRF forecast against the GCM products and concluded that the WRF model outputs perform better over the transboundary Chenab River. Coupling of high-resolution hydrologic models with WRF model outputs reduce uncertainties associated with the localization of rainfall driven flood responses in catchments with complex terrain and short response time (Yucel et al., 2015). Flood forecasting systems have been developed for the coastal cities of Mumbai and Chennai by coupling WRF forecasts with the integrated MIKE 11, MIKE 21, and MIKE FLOOD model (Ghosh et al., 2019; Ghosh et al., 2022). There are no such studies conducted for inland catchments with complex topography with hydrology governed by lakes which acts as storage structures. An experiment is designed to examine the additional value in improving flood forecasts by using the WRF model as compared to using the coarser resolution NWP products (like GFS) over Bangalore city in India. A loosely coupled modelling framework is used for the experiment with rainfall forecasts from the WRF ensemble being fed into the PCSWMM hydrological model to create flood forecasts.

Bangalore city has faced an increase in severe flood events over the last decade due to an increase in rainfall intensities, an increase in developed areas, and the associated changes in the land surface properties (Mujumdar et al., 2021). Research groups in the CSIR-4PI [Council of Scientific and Industrial Research (CSIR) Fourth Paradigm Institute] have worked on the generation of high resolution rainfall forecasts from the WRF model over Bangalore city and at a ward scale over Karnataka (Rakesh et al., 2015; Rakesh et al., 2021; Mohapatra et al., 2017; Sahoo et al., 2020b; Bhimala et al., 2021). An ensemble of WRF Forecasts is developed for the Bangalore city in this paper and is used in the hydrologic model to create flood forecasts at storm water drains. Forecasts generated 6 h prior to the event are fed into a detailed hydrological model, the Personal Computer Storm Water Management Model (PCSWMM), built using high resolution datasets. The specific objectives of the study are: evaluation of rainfall forecasts from a convection permitting

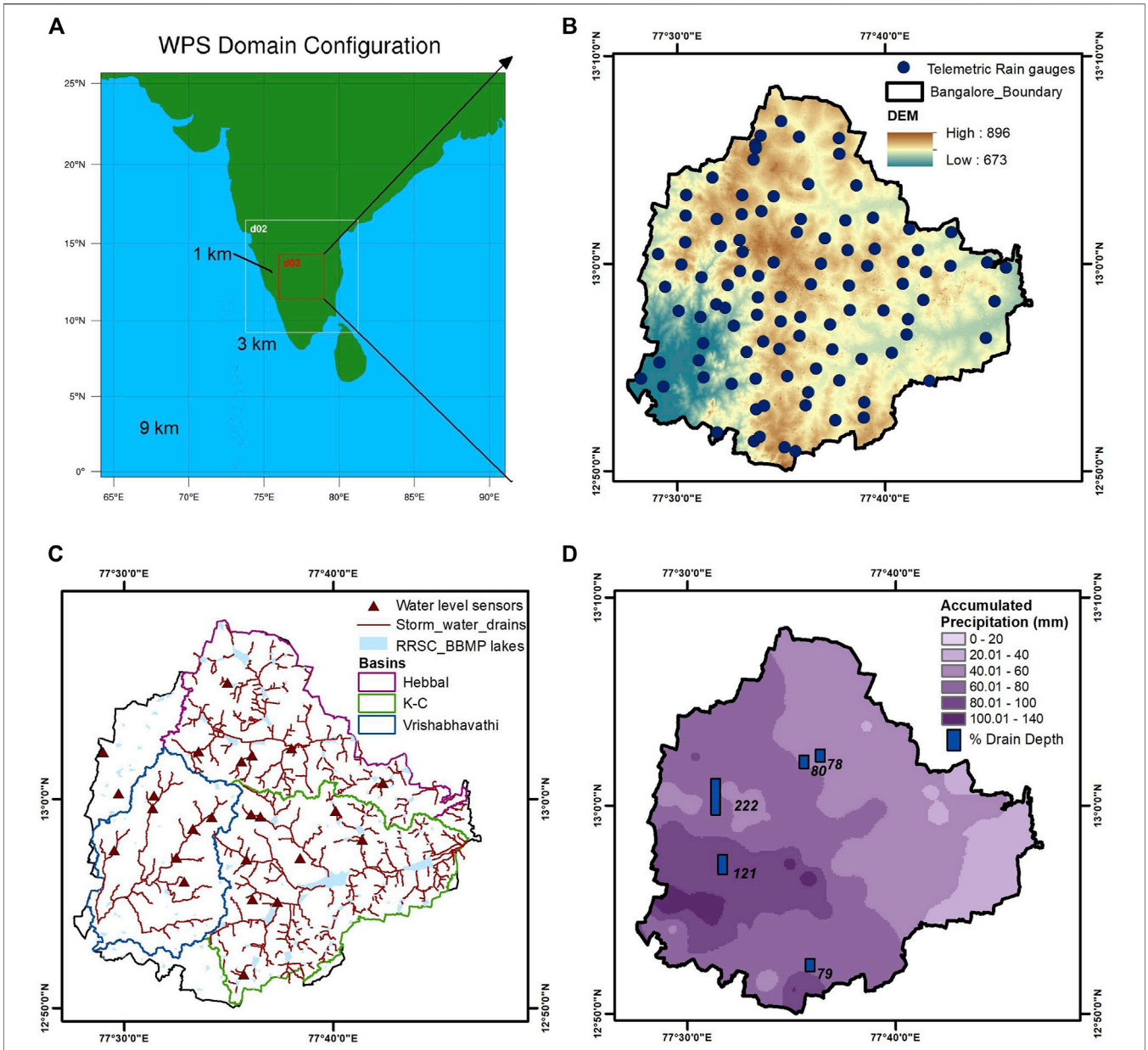

FIGURE 1 | Study area and data used for development, calibration and validation of WRF and PCSWMM models. **(A–D)**, WRF model domain configuration used for simulating extreme rainfall events over Bangalore city **(A)**, Location of automatic rain gauges overlain over the digital elevation model (DEM) **(B)**, Location of water level sensors with storm water drainage network, valley boundaries and lakes used for the development of the hydrological model **(C)** and Spatial map of observed rainfall for 20–21 October 2020 heavy rainfall event along with observed water levels represented as the percentage of flow depth with respect to drain depth **(D)**.

WRF ensemble and assessment of flood forecasts from the hydrological model using the WRF ensemble output. The outputs from the WRF model are evaluated against the output from the GFS, which is used for forcing the WRF model. In this paper, we evaluate the skill of a WRF ensemble (developed using multiple physics parameterization schemes) to capture the spatial and temporal distribution of the heavy rainfall event and the consequent urban flooding. The best performing ensemble members are identified using error indices and a subset of the initial ensemble is fed into the detailed PCSWMM model developed over Bangalore city. The calibrated and validated flood model is then used to obtain flood forecasts for inputs from the WRF ensemble and the GFS output.

DATA AND METHODS

Study Area

Bangalore city is geographically located between 12.75°N-13.17°N and longitude 77.42°E–77.75°E, covering 709 km^2. The

administrative boundary of the Bruhat Bengaluru Mahanagara Palike (BBMP), a city level governing body is selected for demarcating the study area. **Figure 1A** shows the location of the study area within the atmospheric model. The city is located at the southern part of the Deccan plateau and the elevation ranges from 896 to 673 m (MSL) towards the south west Bangalore. The natural topography divides the city into three outwardly draining watersheds—Hebbal (HB) valley, Koramangala-Chellaghatta (KC) valley, and Vrishabhavathi (VV) valley. The undulating terrain facilitates creation of a large number of lakes across the city (188 lakes approx.), which are interconnected through natural drains. **Figures 1B,C** show the high-resolution datasets used in the flood model development. The region receives rainfall from both south-west (from June to September) and north-east (from October to December) monsoon. The extreme precipitation events over Bangalore city have high spatial variability. The spatial distribution of the rainfall observed for the extreme event considered for the study is shown in **Figure 1D**. The extreme rainfall threshold over Bangalore city is identified as 60 mm/day (Mohapatra et al., 2017). It was observed that about 55% of rain gauge stations recorded rainfall more than 60 mm and the heavy rainfall was mainly localized to Vrishabhavathi valley region. The maximum values from critical water level sensors are expressed in terms of drain depth as shown in **Figure 1D**.

Description of the Atmospheric Model

The atmospheric model used in the study is the WRF model which is used widely over the Indian region for creating short range rainfall forecasts. The WRF model version 3.6 (Skamarock et al., 2008) creates high resolution weather forecasts for a specific region. The dynamic core of the model solves the compressible non-hydrostatic Euler equations and the physical processes, which cannot be resolved to the model grid are represented empirically using parameterization schemes. The initial and boundary conditions required for the WRF model are generated from the Global Forecast System (GFS) which is a global weather forecast model maintained by the National Centre for Environmental Prediction (NCEP, 2015). The three hourly forecasts of climate variables at a horizontal resolution of $0.25^{\circ} \times 0.25^{\circ}$ are given as an input to the model.

Description of the Hydrological Model

An urban flood model is useful in the assessment, study, and forecasting of flood conditions for reliable flood mitigation measures (Qi et al., 2021). In this study, the flood model used is the PCSWMM model (based on the United States Environmental Protection Agency's SWMM5 model), which is a dynamic rainfall runoff model designed to simulate single and long-term events specifically for urban areas (Rossman, 2005; CHI, 2020). PCSWMM provides tools for 1D and 2D analysis of rainfall runoff process and also has the ability to model storm water source technologies (low impact development) to manage water quality and quantity. It facilitates modelling with the implementation of graphical user interface and GIS (Geographic Information System) enabled tools which make visualization and processing easier. PCSWMM can represent natural systems in urban regions as it can incorporate lakes and tanks using the storage unit feature. The model accounts for the hydrological processes that produce runoff from the urban catchments which include time-varying rainfall, evaporation, infiltration and helps in modelling the generation and transportation of runoff through a system of pipes, channels, and storage structures. The flowchart of the PCSWMM model methodology is shown in **Supplementary Figure S1**. The choice of hydrological modelling platform depends on the hydrological characteristics of the study areas and the data available. Bangalore is an inland catchment with a complex terrain with around 244 lakes acting as storage structures within the city and flooding is monitored *via* the water level in the storm water drains which were constructed based on the natural drainage within the city. The PCSWMM model is most suitable for modelling urban catchments with fast responses and connections between lakes and storm water drains. Hence, the PCSWMM modelling platform has been used for the study.

Coupling of Atmospheric and Hydrologic Model

WRF and PCSWMM models are one-way coupled with the rainfall forecasts from the high-resolution grid of the atmospheric model being forced into the hydrologic model to generate flood forecasts at predefined locations within the city. The forcing conditions which are generated at 18 UTC prior to the day of the event are selected for the model run. The coupled model cycle (as shown in **Figure 2**) is completed before 06 UTC of the event date.

On test runs using different initial conditions, it is observed that the forecast boundary condition generated closest to the event gives a significantly improved result. After running the model, the rainfall variable is extracted from the WRF model grid at a high spatial and temporal resolution. A script using NCAR Command Language (NCL) and NetCDF Operators (NCO) commands are used to convert the coordinates and to extract time series files corresponding to grids nearest to the locations of the stations with the observed Automatic Rain Gauge (ARG) network (National Centers for Environmental Prediction, 2019; Zender, 2008; Zender, 2014). The time series of the rainfall forecast is provided as an input to the rain gauge locations using a Matlab code (Matlab, 2010). The spatial distribution of rainfall from these rain gauges within the sub-catchments are specified in the PCSWMM model using the Thiessen polygon (Akhter and Hewa, 2016) weighted method. After simulation, the flood model forecasts water levels at sensor locations distributed in the storm water drain network. **Figure 2** shows the broad framework of model coupling.

Experiment Design Using the WRF Model

The WRF model comprises of three nested domains, with the outermost domain of 9 km resolution covering the Indian region with the adjacent oceans, the intermediate domain covering the southern part of India at a resolution of 3 km, and the innermost domain centered over the city of Bangalore with a resolution of 1 km as shown in **Figure 1A**. The WRF model takes 12 h to

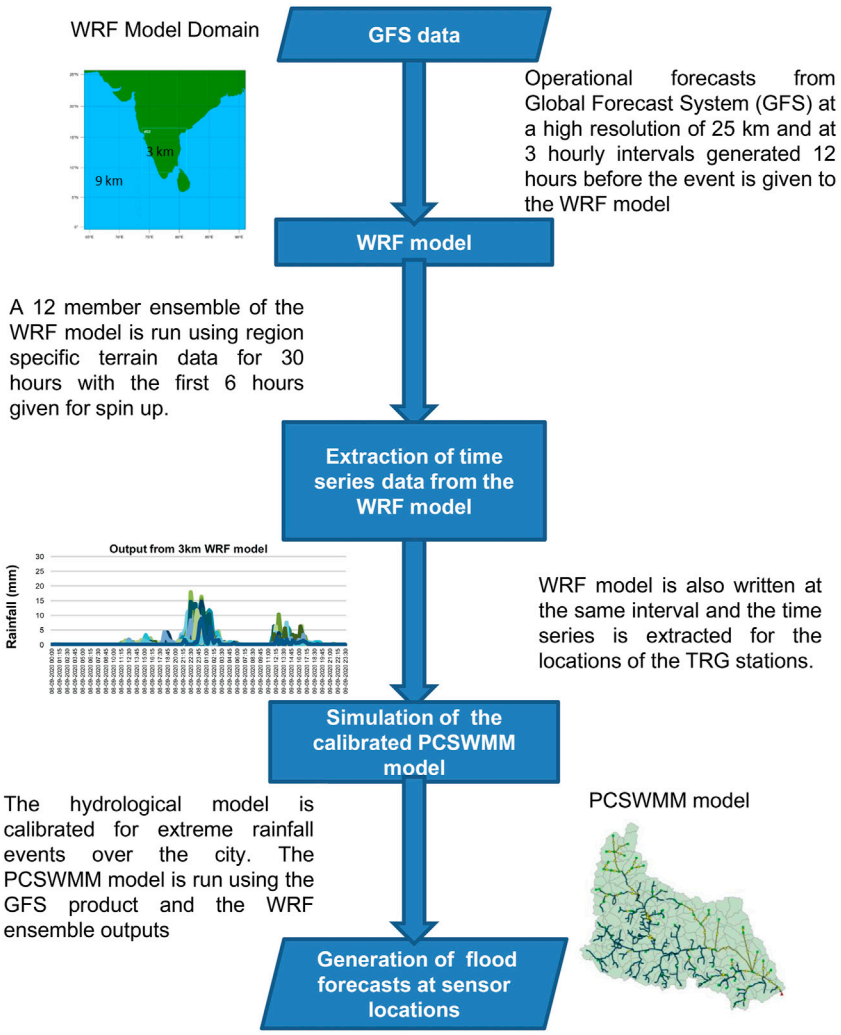

FIGURE 2 | Flowchart representing the methodology of coupling of the atmospheric and hydrologic model. Operational GFS data is used to run the WRF model to generate high resolution rainfall forecasts. The data corresponding to the locations of the observed network is extracted and given as an input to the PCSWMM flood model to forecast water levels at critical sensor locations.

TABLE 1 | WRF model configuration and physics scheme.

	Domain 1	Domain 2	Domain 3
Horizontal grid	9 km	3 km	1 km
Time steps	45 s	15 s	5 s
Number of grids	325	271	325
Vertical levels	38 terrain-following sigma (σ) coordinates		
Shortwave radiation	Dudhia (Dudhia, 1989)		
Longwave radiation	Rapid radiative transfer model (Mlawer et al., 1997)		
Land surface model	Thermal diffusion model (Dudhia, 1996)		
Planetary boundary layer	Boulac (Bougeault and Lacarrere, 1989)		
Urban surface physics	Single layer urban canopy model (Chen et al., 2011)		
Land use	Advanced wide field sensor (AWiFS) (Gharai, 2018)		
Topography	Shuttle radar topography mission V3 (Farr et al., 2007)		

complete 30 h of simulation. Therefore, the forecast conditions generated by the Global Forecast Model (GFS) at 18 UTC the previous day is selected for the event. The model configuration used here has 38 vertical levels and the model top is kept at a constant pressure surface of 50 hPa. The details of the WRF model configuration are shown in **Table 1**.

The land use land cover dataset in the United States Geological Survey (USGS) set of static data comprising of albedo, green fraction, land use land cover is replaced with a recent version of the dataset from the Indian Space Research Organization (ISRO) (2018-2019). The LULC data generated by the National Remote Sensing Centre (NRSC), ISRO, was derived from the Indian satellite IRS-P6, Advanced Wide Field Sensor (AWiFS) and is compatible with WRF pre-processing system. Many studies have demonstrated the improvement in the model outcomes, using this dataset over the Indian region (Kar et al., 2014; Sahoo et al., 2020a; Gupta et al., 2021), and also over the Bangalore region (Sahoo et al., 2020b). Navale and Singh (2020), Golzio et al. (2021) have demonstrated the significant impact of variation in topography on the fine scale pattern of rainfall generated by the WRF model over complex topography. The default topography dataset is the Global Multi-resolution Terrain Elevation Data (GMTED) (Danielson and Gesch, 2011) which has a resolution of 900 m (30 s).

This is replaced with the latest version of the Shuttle Radar Topography Mission (SRTM) dataset made available by the National Aeronautics and Space Administration (NASA). The NASA SRTM version 3 is a recently released version of the high resolution 30 m SRTM data which was void-filled using the GMTED 2010 data and the Advanced Spaceborne Thermal Emission and Reflection Radiometer (ASTER) Global Digital Elevation Model Version 3.

An ensemble of forecast scenarios is generated using a combination of convective and microphysics parameterization schemes that were used in the past studies over Bangalore city (Mohapatra et al., 2017; Bhimala et al., 2021; Rakesh et al., 2021; Sarkar and Himesh, 2021). The city having a complex terrain, may benefit from the high-resolution simulations as demonstrated by earlier studies. The simulations are carried out for each ensemble member, for 30 h and the model outcomes are recorded at a 15-min interval. The first 6 h are treated as spin-up and the 24 h corresponding to the rainfall event are used for analysis.

Studies have shown that certain processes that contribute to convection can only be captured when the resolution of the numerical model is below 2 km (Iriza et al., 2016). To understand this in detail, the rainfall forecasts obtained from both the domains—3 and 1 km are used in the study. It is also observed in the experimental test runs that different physics parameterization scheme combinations simulated the heavy rainfall event at both resolutions. The most commonly used convective parameterization schemes are the Kain Fritsch and the Betts Miller Janjic (BMJ) scheme. Kain Fritsch is a scheme that uses the Convective Available Potential Energy (CAPE) removal method to detect the onset of convection (Kain and Fritsch, 1993; Kain, 2004). BMJ scheme is an adjustment type scheme that generates deep and shallow convection (Janjić, 1994). The Grell Freitas scheme is a recently added convective scheme to the WRF model and has shown good performance over the Cauvery catchment region in Karnataka (Sarkar and Himesh, 2021). The three convective parameterization schemes chosen are based on the previous work done over Bangalore city by CSIR-4PI (Mohapatra et al., 2017; Bhimala et al., 2021; Rakesh et al., 2021; Sarkar and Himesh, 2021).

The microphysics (MP) scheme is responsible for heat and moisture flux within the atmosphere and gives the surface resolved rainfall. The WRF Single-Moment 6-class scheme (WSM6) is a scheme with ice, snow, and graupel processes suitable for high-resolution simulations. The WRF Double-Moment 6-class scheme (WDM6), has been developed by adding a double-moment treatment for the warm-rain process into the WSM6 scheme. Mohapatra et al. (2017) compared simulations of the WRF model for localised and non-localised urban extreme rainfall events over Bangalore city. The study concludes that the WRF model has a tendency to underestimate the magnitude of non-localized or uniformly distributed heavy rainfall events. This has been attributed to the incorrect treatment of cloud droplet size by the WSM6 scheme and the study suggests using the WDM6 scheme, as it has a better representation of physical processes.

Combinations using two microphysics schemes, three convective parameterization schemes, and two different resolutions result in a 12-member ensemble. The details of the ensemble are given in **Table 2**. In order to quantify the additional value provided by the rainfall forecasts from the WRF ensemble, the rainfall variable from the GFS is extracted. The time series for the locations of the ARG network is extracted from the corresponding grids of the GFS. The hydrological model is forced using the rainfall values from both the GFS and the WRF ensemble.

Calibration and Validation of the PCSWMM Model

The development of the flood model for Bangalore city is completed using high density storm water drainage network, lakes data, and ARG network as shown in **Figures 1B,C**. The digital elevation model of 10 m resolution (as shown in **Figure 1B**) is procured from the National Remote Sensing Centre (NRSC), India. The details of the administrative boundaries and lakes used in the model are provided by Bruhat Bengaluru Mahanagara Palike (BBMP) and Regional Remote Sensing Centre (RRSC) (Hebbar et al., 2018) as shown in **Figure 1C**. The percentage imperviousness of sub-catchments is calculated using the Land Use Land Cover (LULC) map for the year 2020 provided by the Bengaluru Development Authority (BDA). The details of the input data to the PCSWMM model are given in **Supplementary Table S1**. The datasets for the model setup., viz., nodes, drains, storage tanks, ARG locations, and sub-catchments are processed, connected and imported from ArcGIS (version 10.3) to PCSWMM. The runoff is computed at the sub-catchment level after accounting for various losses and the flow from the sub-catchment outlets is routed kinematically through storm water drainage channels. More details on urban flood

TABLE 2 | List of physics combinations for the 12-member WRF ensemble.

S. no.	Scenario name	Microphysics parameterization scheme	Cumulus parameterization scheme	Resolution (km)
1	WSM6KF3	WSM6	Kain Fritsch	3
2	WSM6KF1	WSM6	Kain Fritsch	1
3	WSM6GF3	WSM6	Grell Freitas	3
4	WSM6GF1	WSM6	Grell Freitas	1
5	WSM6BMJ3	WSM6	Betts Miller Janjic	3
6	WSM6BMJ1	WSM6	Betts Miller Janjic	1
7	WDM6KF3	WDM6	Kain Fritsch	3
8	WDM6KF1	WDM6	Kain Fritsch	1
9	WDM6GF3	WDM6	Grell Freitas	3
10	WDM6GF1	WDM6	Grell Freitas	1
11	WDM6BMJ3	WDM6	Betts Miller Janjic	3
12	WDM6BMJ1	WDM6	Betts Miller Janjic	1

model development for Bangalore city are given in Mujumdar et al. (2021).

The three valleys are independent of each other with different outlet points and in their response to rainfall events. Hence the valleys are calibrated and validated separately for different rainfall events. The observed water level data at some sensors because of blockage to the flow, shows fluctuations and rise in water depth irrespective of rainfall. The water level sensors are selected for calibration and validation based on the availability of the observed water level data with no unaccounted flow and continuity of the data in the time period. The PCSWMM model developed over Bangalore city is calibrated using a recent heavy rainfall event that occurred on 8, 9 September 2020 (**Supplementary Figure S2A**).

The model output is verified against water level data at a high temporal resolution of 15 min. The parameters considered for the calibration of the model include sub-catchment properties which are width, Manning's roughness coefficient, and percentage imperviousness, properties of the storm water network, viz., the slope and roughness coefficient of the conduits. The model is further validated for a heavy rainfall event on 5, 6 November, 2020 (**Supplementary Figure S2B**). Calibration and validation of the model is demonstrated here for a sensor located in the Hebbal valley, a catchment towards the northern side of Bangalore city. The performance indices for the calibration and validation of the model are as shown in **Supplementary Table S2**. The model is seen to perform well and is used to generate flood water levels for the rainfall forecasts from the WRF model ensemble and the GFS.

Event Description

Bangalore city receives rainfall from both south-west (from June to September) and north-east (from October to December) monsoon. The model coupling framework discussed (**Figure 2**), is used to simulate extreme events over the region for the monsoons of years 2020 and 2021(**Supplementary Figures S3–S6**). An extreme rainfall event that occurred on 20 and 21 October 2020, is selected for a detailed demonstration of this framework. The spatial pattern of this particular event had spatial characteristics similar to the mean return levels of annual maximum precipitation with a 10-years return period (**Supplementary Figure S7**).

TABLE 3 | Contingency table for the calculation of categorical indices.

Model/Observed	Rain (R)	No rain (N)
Rain (R)	RR (Hits)	RN (False alarms)
No Rain (N)	NR (Misses)	NN (Correct negatives)

The southwest monsoon in the year 2020 was prolonged due to unseasonal weather systems that occurred in the Arabian sea and the Bay of Bengal (IMD, 2020). The onset of the north east monsoon season was delayed by 3 weeks. The heavy rainfall event marked the end of the southwest monsoon of 2020 over Bangalore city. This event occurred between the depression over the Arabian Sea (17–19 October 2020) and the depression over Bay of Bengal (22–24 October 2020).

The city received heavy rainfall throughout on 20 and 21 October 2020 and a daily rainfall maximum of 124.5 mm was observed at Kengeri station in Raja Rajeshwari Nagar located in the Vrishabhavathi valley (**Supplementary Figure S8**). In the event of a flood, water levels at the sensors that exceed 75% of the drain depth are assumed to be critical as per the alert system followed by the urban flood model during flooding (Mujumdar et al., 2021). The five sensors which were identified as critical at the time of the observed event is then selected and studied here. The maximum water level from these sensors is expressed in terms of the percentage of drain depth which shows the level of water relative to the drain depth at each location. The details of the water level sensors such as location, depth of drain, and observed water level data for the 20–21 October 2020 event at critical sensors (>75% drain depth) are given in **Supplementary Table S3** (**Supplementary Figure S9**).

Performance Indices for Rainfall Forecasts

The skill of the WRF model presented here is evaluated by comparing the simulated and observed rainfall at a high resolution of 15 min. The performance indices are used to analyze spatial and temporal errors across the observational network. To calculate categorical indices, the variable values are considered in a non-probabilistic manner. Categorical statistics are computed from the elements in the contingency

table (Wilks, 2006) as shown in **Table 3**. Hits refer specifically to those grids which show rainfall. For a sample threshold value of 40–60 mm, the values are calculated accordingly. If the observed grid is showing a value between 40 and 60 mm and the corresponding model grid is showing a value in the same range, it is a Hit.

If the model grid is showing a value lesser than 40 mm it is a Miss. If the model grid is showing a value greater than 60 mm it is a false alarm. If the value in the observed grid doesn't fall within this range and the same is calculated for the model grid, then it is a correct negative.

The Critical Success Index (CSI), also known as the Threat Score, describes the overall skill of the simulation relative to the observation. The CSI value ranges from 0 to 1, where 0 indicates no skill and 1 indicates perfect skill. It measures the fraction of observed and forecast events that were correctly predicted. It does not distinguish the source of the forecast error. It is described as shown in **Eq. 1**.

$$\mathbf{CSI} = \frac{\mathbf{hits}}{(\mathbf{hits} + \mathbf{misses} + \mathbf{false\ alarms})} \quad (1)$$

Some additional indices that are calculated using the contingency table are accuracy, bias score (BS), probability of detection (POD) and Hiedke Skill Score (HSS) the details of which are provided in the supplementary document (**Supplementary Table S4**).

The categorical indices are obtained based on the spatial distribution patterns from the observed rainfall. Continuous and categorical indices are calculated in comparison with the observed data and the ensemble members performing better are identified. The rainfall time series for each station is provided as an input to the PCSWMM model and the model is run with the best performing subset of the WRF ensemble. The 3-h time series from the GFS were also given as an input to the PCSWMM model. The water levels at various locations are compared and analyzed for performance evaluation against the observed data.

RESULTS AND DISCUSSSION

The performance of the WRF ensemble is assessed for the selected event using categorical indices. The best performing members are then selected as a subset and used in hydrological modelling. The additional value from the high resolution WRF model output (3 and 1 km at 15 min intervals) as compared to the GFS data (25 km at three hourly intervals) is quantified in this section.

Verification of Spatial Distribution

gridded data is plotted using the ArcGIS software after accumulating rainfall, 08:30 a.m. to 21 October 08:30 a.m. 2020 (ESRI, 2020). It can be observed that the microphysics scheme plays a significant role in the amount of rainfall simulated from **Figure 3**. Scenarios using the WSM6 scheme (**Figures 3A–F**) have forecasted a higher quantity of rainfall as compared to those with WDM6 (**Figures 3G–L**). The single-moment microphysics scheme predicts the total mass concentration of hydrometeors (liquid or solid water particles that may be suspended or fall through the atmosphere) whereas double moment schemes include the prediction of total number concentration (number of particles per volume). Cloud Condensation Nuclei (CCN) and number concentration are the two additional variables predicted in the double moment scheme. This scheme is selected because it has a better physical representation of the processes. However, some studies have shown that in certain regions the simulation of CCN has resulted in an overall decrease in the rainfall quantity (Li et al., 2008). Also, the performance of the double moment scheme is dependent on the accuracy of a large number of microphysics processes than the single moment scheme (Lim and Hong, 2010).

The convective parameterization (CP) scheme details the sub-grid processes associated with convective clouds and operates only on individual columns where the scheme is triggered and provides the convective component of rainfall. Among the convective schemes selected for the study, Kain Fritsch gives better spatial representation in comparison to the observed rainfall (**Figures 3A,D,G,K**). The location of the event is well simulated by the Kain Fritsch scheme across domains and microphysics schemes.

The comparison of results for 1 and 3 km shows no significant pattern to determine the better performance among the two domains. The 1 km domain performs better for the WSM6 microphysics scheme whereas, the 3 km domain performs better for the WDM6 scheme. A similar observation was made in a comparison study by the Korean Meteorological Agency which observes that both WSM6 and WDM6 underestimate convective events in spite of WDM6 predicting realistic rain drop size and relative humidity due to a dependence on grid resolution (Min et al., 2015). However, for a combination of certain physics schemes - WSM6KF (**Figures 3A,D**) and WDM6GF (**Figures 3H,K**), both the domains offer a fair representation of the spatial pattern. More events need to be considered in order to understand the combined impact of grid resolution and microphysics schemes. Out of the 12 forecast scenarios, 10 indicate the occurrence of a heavy rainfall event for the given time period within the city (**Figures 3A–I,K**).

Categorical Indices

The categorical indices are calculated for the 12 simulations created for the heavy rainfall event that occurred on 20–21 October 2020. For each simulation, the indices are calculated for different rainfall thresholds—20, 40, 60, 80, 100, and 140 mm as shown in **Supplementary Figures S10A,B**. Capturing the location of the rainfall, plays an important role in flood forecast and therefore the ensemble members which capture the location of the rainfall range gives higher CSI values. For example, the rainfall in the range of 40–60 mm lies in the central part of the city and the members WSM6GF1, WSM6BMJ3, and WSM6KF1 capture it with the highest CSI values (**Supplementary Figure S10B**). The heavy rainfall range (>60 mm) for this event occurs towards the south western side of Bangalore city, and although there is a general underestimation from the ensemble, some scenarios, viz., WSM6KF3, WSM6KF1, and WDM6KF3 predict the location accurately (**Figures 3A,D,J**).

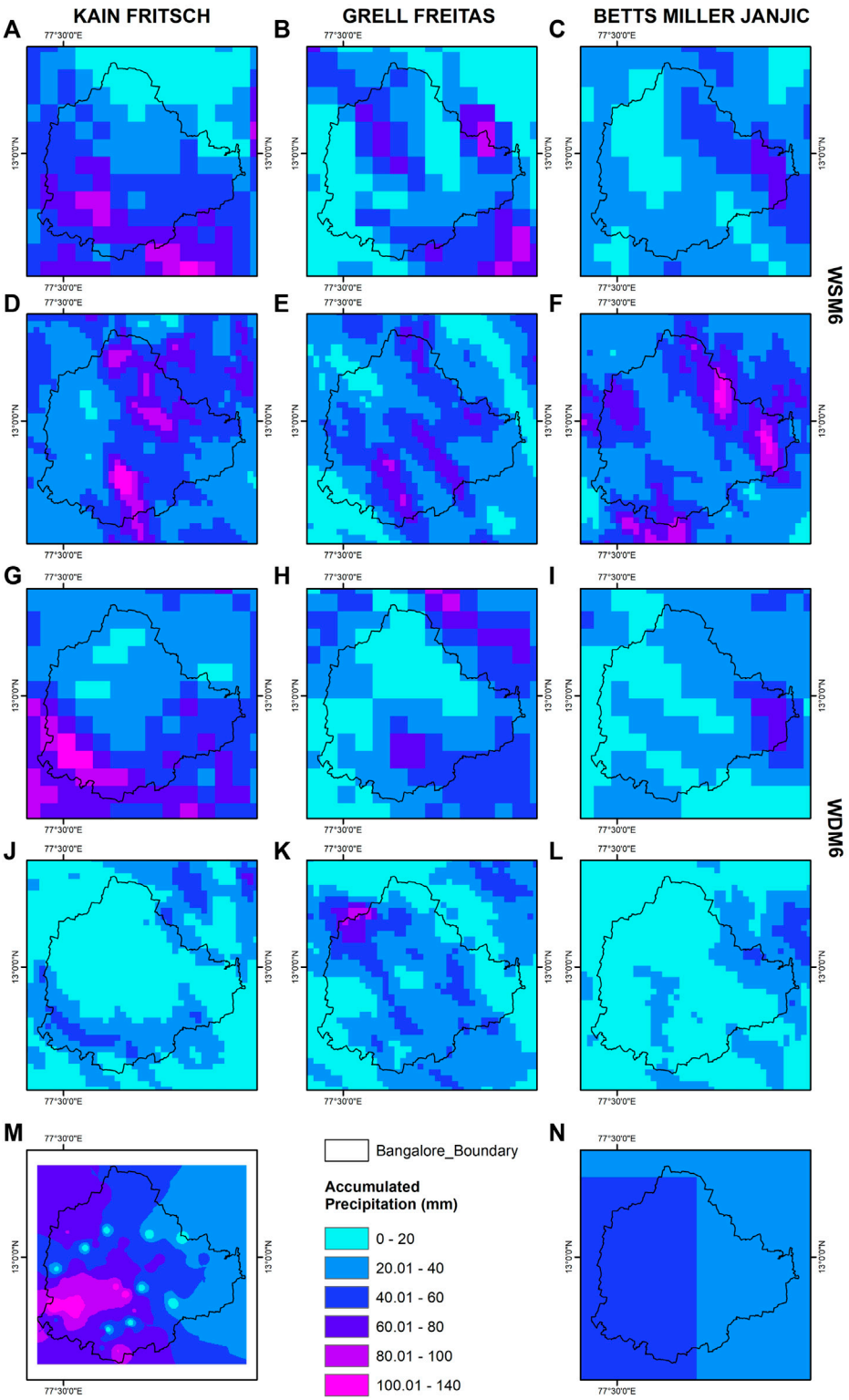

FIGURE 3 | Spatial distribution of 24 h accumulated rainfall (mm) from WRF ensemble, Global Forecast System (GFS) data and observed rainfall. **(A–N)**, Spatial distribution of 24 h accumulated rainfall (mm) from WRF ensemble simulations WSM6KF3 **(A)**, WSM6GF3 **(B)**, WSM6BMJ3 **(C)**, WSM6KF1 **(D)**, WSM6GF1 **(E)**, WSM6BMJ1 **(F)**, WDM6KF3 **(G)**, WDM6GF3 **(H)**, WDM6BMJ3 **(I)**, WDM6KF1 **(J)**, WDM6GF1 **(K)**, WDM6BMJ1 **(L)**, the Global Forecast System (GFS) data **(N)**, and observed **(M)**, over the Bangalore city for the period 0300 UTC 20 October to 0300 UTC 21 October 2020. The heavy rainfall quantities (>60 mm/day) is well represented by the WRF ensemble and it can be seen from **(A–L)** that the extreme rainfall pattern is reflected in the WRF ensemble output as compared to the GFS. The three columns correspond to the three convective parameterization schemes selected for the study—Kain Fritsch, Grell Freitas, and Betts Miller Janjic. The first two rows show the results from WSM6 microphysics schemes and the next two rows present the results from WDM6.

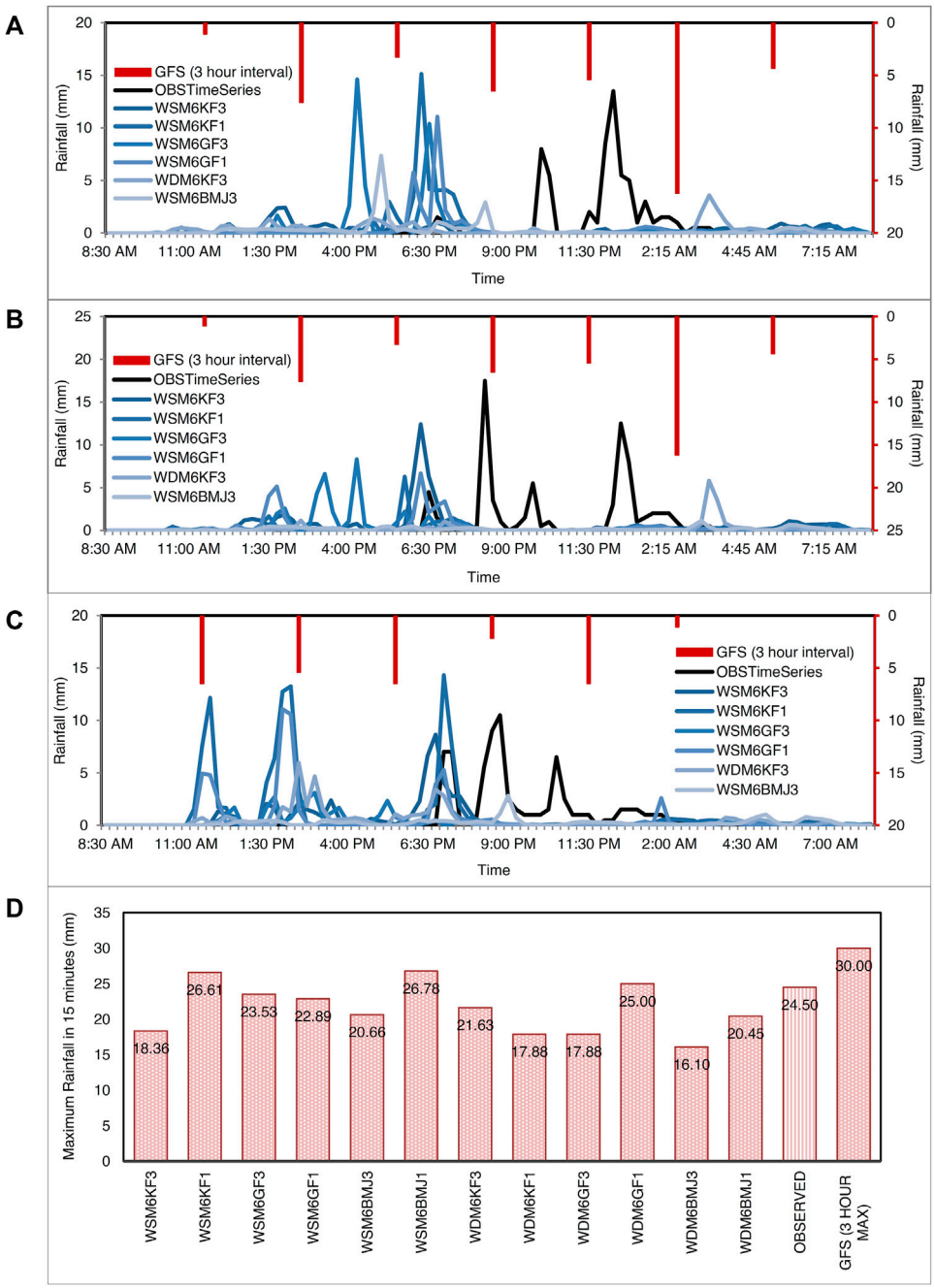

FIGURE 4 | Comparison of rainfall time series from the selected forecast scenarios for rain gauge locations. **(A–C)**, Comparison of rainfall time series from the WRF forecasts, GFS forecasts and Observed rainfall for ARG locations in Koramangala-Chellaghatta valley **(A)**, Vrishabhavathi valley **(B)**, and Hebbal valley **(C)**. **(D)**, Comparison of 15-min maximum rainfall from each member of the ensemble with the 15-min maximum value from observed ARG network. The WRF ensemble is able to capture the intensities of the event as compared to the GFS.

The WSM6KF3 configuration of the WRF ensemble is also validated across four heavy rainfall events from the monsoons of 2020 and 2021—September 8–9, October 20–21 for the year 2020 and November 4–5, October 11–12 for the year 2021. The spatial verification and categorical metrics calculated across these events for different rainfall thresholds are included in the supplementary material (**Supplementary Figures S3–S6, S11**; **Supplementary Tables S4, S5**). On an average, the model setup has a better performance than a random/chance forecast for a rainfall threshold of 60 mm as can be seen by the positive value of Hiedke Skill Score (**Supplementary Figure S11**). Based on the spatial distribution of rainfall and categorical indices, the ensemble members with better model performance are identified and used in the flood forecast

model. The members identified to be given as an input to the hydrological models are—WSM6KF3, WSM6KF1, WSM6GF3, WSM6GF1, WDM6KF3, and WSM6BMJ3. The time series of this subset is further verified at locations adjacent to the critical water level sensors in the hydrological model.

Verification of Temporal Distribution

The 15-min time series data corresponding to the automatic rain gauges is extracted from the above-mentioned WRF ensemble subset and is provided as an input to the PCSWMM model. The time series for six ensemble members at three critical locations (one representative of each valley) are examined here as shown in **Figure 4**. The GFS data extracted for the location is also shown in **Figure 4**. It can be seen for all valleys, that the 15-min maximum value of the observed time series is captured.

For Koramangala-Chellaghatta (KC) valley, maximum values and the temporal patterns of rainfall at 15 min are captured by the ensemble member, for Vrishabhavathi (VV) valley the patterns are captured with lesser intensity and in Hebbal valley, a slight overestimation is noted as shown in **Figures 4A–C**. The GFS data (red bar graphs shown on the inverted axis in **Figures 4A–C**) consistently underestimates the daily rainfall value at all three locations and the timing of the peak occurs after the rainfall event at some locations.

The WRF model is able to capture the intensities of the rainfall albeit with a temporal shift. This could be due to the fact that the single layer urban canopy physics option used may not capture the heat exchanges that happen within the city. Opting for a multi-layer urban canopy model and incorporating detailed representation of urban land use classes in future studies may improve the timing of the prediction (Holt and Pullen, 2007; Salamanca et al., 2011; Jandaghian and Berardi, 2020). The WRF model output is captured at every 15 min as against the 3-h time interval of the input GFS data. The 15-min maximum value for the rainfall forecast from each WRF ensemble member is compared against the observed data. Even the lower performing members of the ensemble, WDM6KF1, and WDM6BMJ1 based on the spatial verification shown in **Figures 3K,L** have captured a maximum value of 17.88 and 25 mm respectively, as compared to the observed value of 24 mm.

Most ensemble members capture the 15-min maxima with a variation of not more than 10 mm. This implies that irrespective of the spatial and temporal displacements of the simulated rainfall, the maximum intensity is fairly well captured by the WRF model ensemble. The maximum from the GFS is 30 mm in a 3-h interval which is very low in comparison to the values from the WRF ensemble. From this section, it can be concluded that three hourly rainfall forecasts from GFS fail to capture the temporal variability and intensity of the observed rainfall.

Comparison of PCSWMM Model Output

The WRF ensemble members are selected based on their ability to simulate the spatial distribution and location of heavy rainfall (>60 mm/day), and the forecasted rainfall is given as inputs to the hydrological model. Prediction of water levels in urban flooding situations requires accurate sub-hourly intensity/values of rainfall to be given as an input to the flood models. The data extracted at rain gauge locations from the nearest grids in the WRF model is given as input to the PCSWMM model. The spatial plot of the PCSWMM input data is shown in **Figure 5**. The spatial distribution of rainfall is improved by downscaling the GFS data as visible in **Figures 5A–H** in terms of extent and intensity, and similar improvement can be observed for water level forecasts.

The critical water level sensors in Vrishabhavathi, Koramangala-Chellaghatta, and Hebbal valley are selected for the analysis based on the observed water level depth during the storm event (>75% of drain depth). The plots also show the outputs from PCSWMM for these sensor locations across Bangalore city (**Figures 5A–G**) and the peak water level depths at those locations are expressed in terms of the percentage of the drain depth covered. The PCSWMM model simulation outputs for the three hourly rainfall time series from the GFS data are also shown in **Figure 5G**.

The spatial distribution of the rainfall forecasts has a significant impact on the water level peak forecasts as can be seen from **Figures 5A–F**. For Koramangala-Chellaghatta and Hebbal valley, the WRF model forecasts are performing better than the GFS data forecasts. For the critical sensors in Vrishabhavathi valley, which had the highest recorded water levels (exceeds the drain depth by 122 and 21%), the values are underestimated by both the WRF ensemble and GFS data. The flood model responds well to all sources of rainfall input (Observed, WRF ensemble, and GFS data) and the variation in the water level correlates with rainfall intensities. The error in predicting the location of the heavy rainfall threshold (above 60 mm/day) impacts the forecasts of the flooding locations from the hydrological model.

It can be observed that water level peaks are being captured at certain locations in spite of a general underestimation in the rainfall forecasts. This can be attributed to the fact that the sub hourly rainfall intensity which is a strong indicator of the extremity of the event is captured to a larger extent by the WRF downscaled forecasts. It can be observed in **Figure 4C** that the 15-min maximum rainfall from observed sensors which is 24 mm is fairly captured by all members of the ensemble.

A spatial shift in the simulated rainfall can be observed in certain ensemble members towards the southern side of Bangalore (shown **Figures 5C,D**), which is reflected in the simulated water depths. The spatial distribution of rainfall has improved to a greater extent using the WRF ensemble forecasts, Also, the forecasted water levels are closer to the observed data and higher than the GFS data forecasts.

Verification of Flood Forecasts From PCSWMM

The high spatial and temporal intensity of the urban flood that occurred following the heavy rainfall event on 20–21 October 2020 is captured fairly by the PCSWMM model. The observed rainfall data from the ARGs is given as an input and the flood model output (Input_ARG_Rainfall) is compared with the water level sensor data and flood forecast values from the WRF

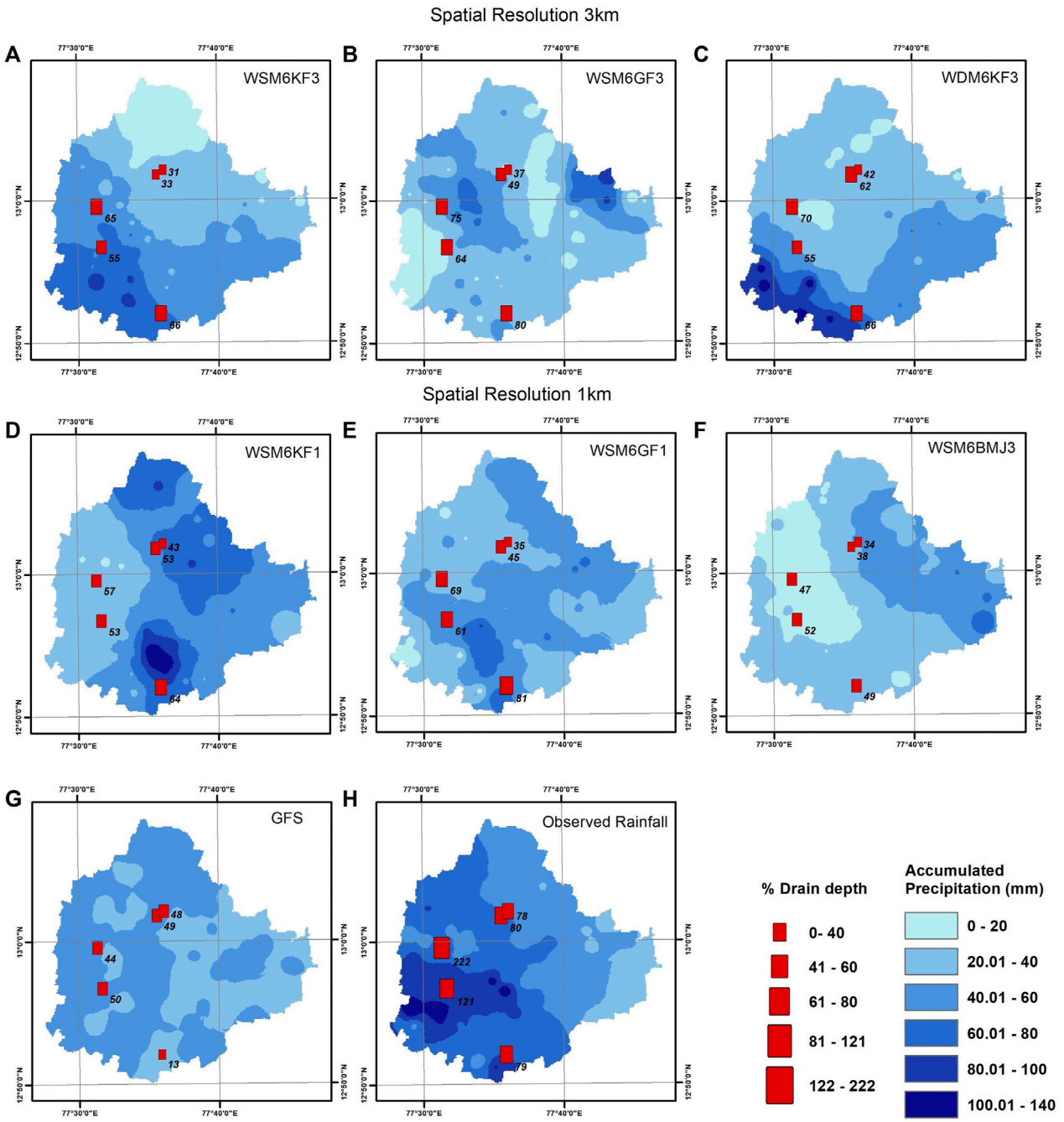

FIGURE 5 | Rainfall forecasts from WRF ensemble members and GFS forecast and the corresponding water level forecasts. **(A–F)**, Spatial variability in rainfall and corresponding flood forecasts from WRF ensemble member WSM6KF3 **(A)**, WSM6GF3 **(B)**, WDM6KF3 **(C)**, WSM6KF1 **(D)**, WSM6GF1 **(E)**, WSM6BMJ3 **(F)**, **(G,H)** Spatial variation in rainfall and corresponding flood forecasts from GFS **(G)**, and Observed ARGs **(H)**. The red boxes indicate the forecasted water levels at critical locations by the model represented as percentage of drain depth occupied by water. The water level forecasts show similarity with the observed water levels which are better than the forecasts using GFS.

ensemble and GFS data as shown in **Figures 6A,B**. It can be observed from **Figure 6A** the water level forecast from the WRF ensemble provides a good indication of high water levels and shows a high variability when compared with forecasts from the GFS data as shown in **Figures 6A,B**. Similar result can be observed for sensors in Vrishabhavathi valley (**Supplementary Table S6**). From extensive field visits and ground scenario comparisons, it is observed that certain obstructions in the form of debris from sewage flow, including solid waste and tree/plant growth, cause the water in the storm water drains to

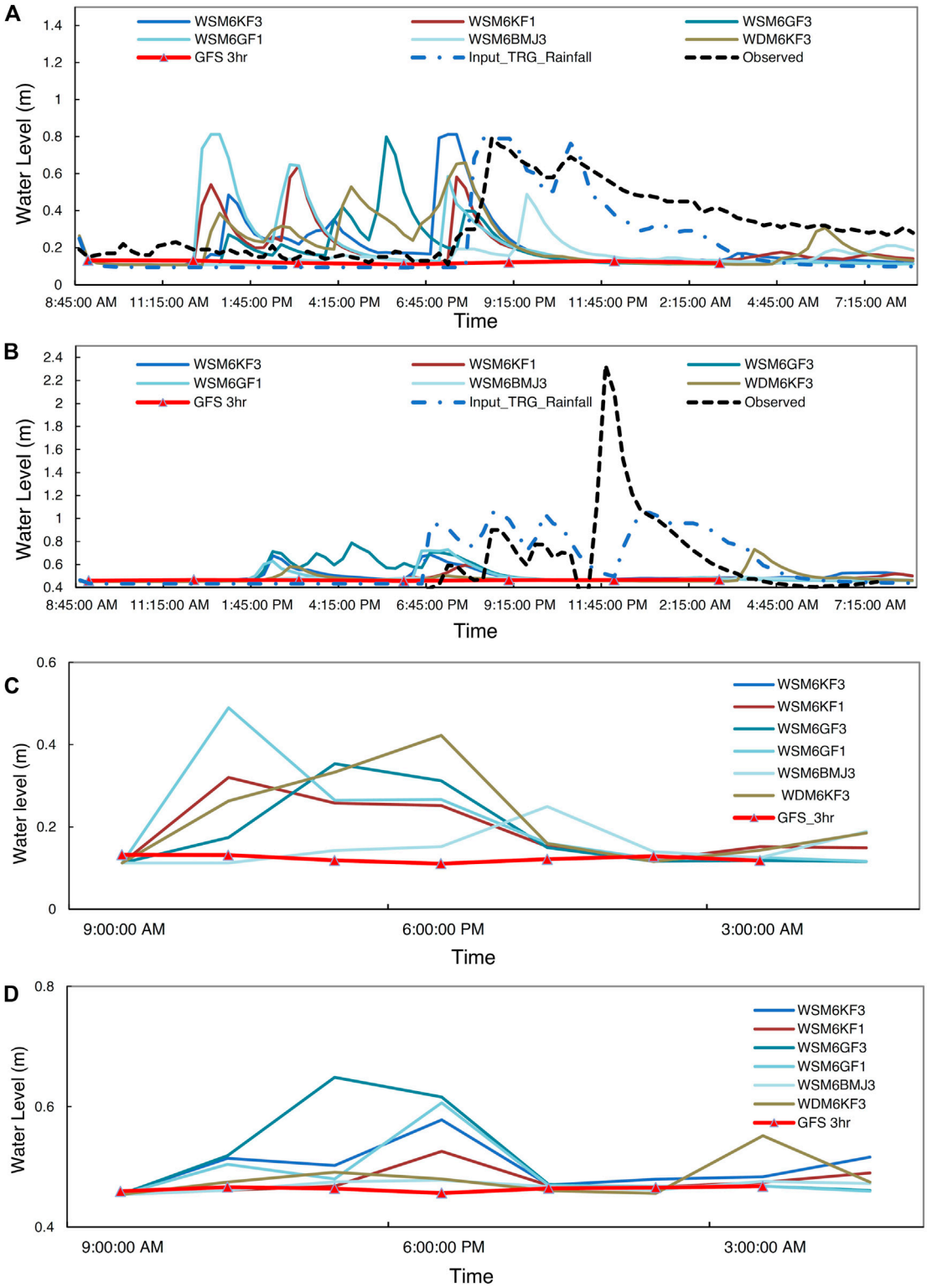

FIGURE 6 | Comparison of water level at critical water level sensor locations. **(A,B)**, Comparison of forecasted water level using WRF ensemble forecasts, GFS forecasts and observed rainfall with observed water levels at water level sensor location in Vrishabhavathi valley **(A)** and Koramangala-Chellaghatta valley **(B)** at 15-min interval. The water level is captured fairly using WRF forecasts than GFS forecasts. **(C,D)**, comparison of forecasted water levels from WRF ensemble members(3 h averaged) and GFS forecasts at three hourly intervals at water level sensor location in Vrishabhavathi valley **(C)**, and Koramangala-Chellaghatta valley **(D)**.

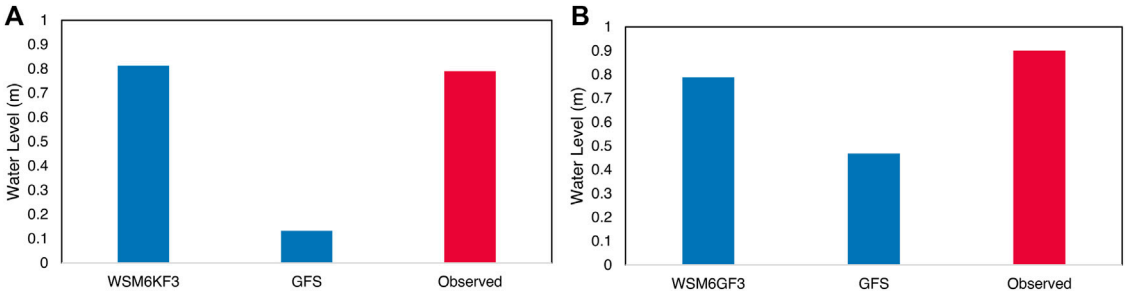

FIGURE 7 | Comparison of maximum water level at critical water level sensor locations. **(A,B)**, Comparison of water level between maximum value from WRF ensemble forecast, GFS forecast and observed data at sensor location in Koramangala-Chellaghatta valley **(A)**, and Vrishabhavathi valley **(B)**. The bias between the WRF ensemble and the GFS is 0.68 and 0.32 m. The flood maximum value is predicted by the WRF ensemble at both locations.

rise resulting in outliers in the observed water level sensors data as shown in **Figure 6B**. It can be seen from **Figure 6B**, that the flood forecast is not able to capture the peak value (2.2 m) which maybe a result of external factors and not the rainfall event. Excluding the outlier value, the maximum water level (0.9 m) is reflected in the flood forecasts generated using the WRF ensemble.

Based on observations made for Vrishabhavathi Valley, it can be observed from **Supplementary Table S6**, that the model performs well in predicting water level peaks for all valleys. As shown in **Supplementary Table S6**, 50 and 16.7% of the ensemble members indicate flooding (>75% drain depth) for Koramangala-Chellagatta and Vrishabhavathi valley respectively which is useful for early warning and disaster preparedness. The average percentage drain depth obtained from the flood forecast using WRF ensemble is 63 and 70 for Vrishabhavathi and Koramangala-Chellagatta valley, respectively.

The WRF forced PCSWMM model output was further averaged to 3 h to match with the resolution of the GFS data The results shown in **Figures 6C,D**, indicate that the WRF ensemble captures the variability with a slight underestimation in the flood peak. Flooding in urban areas is majorly caused by high-intensity short duration rainfall which leads to saturation of the available pervious area and overwhelming of the drainage capacity. When using the forecast from the GFS data as rainfall input, with an interval of 3 h most of the rainfall infiltrates and the soil is not saturated enough to produce an overland flow that can contribute to an increase in the water level. This results in the water levels remaining unchanged throughout the hydrological model run (**Figure 6**). The high-resolution rainfall forecasts from the WRF ensemble produce the flood peaks more effectively than the GFS data as shown in **Figure 7**. The hydrological model simulation when forced with global forecast at 3-h intervals, is not able to accurately represent the hydrology specially of an urban area and thus highly underestimates the flood magnitude.

CONCLUSION

The rising number of extreme events in Indian cities is a serious concern with the high population density and unplanned growth, making them suffer huge economic losses in the aftermath of such an event. As per the recent IPCC reports, the increase in the global temperature is bound to bring about unprecedented changes which cannot be predicted by analyzing historical data. The impact of recent urban floods highlights the requirement for the development of a high-resolution flood forecasting system for Indian cities. The nature of the urban flood demands a system built using high resolution data to capture the sub-hourly intensities occurring for short durations, as, such rainfall events are known to cause extensive damage. The city of Bangalore has a high-density network of automatic rain gauges and water level sensors. The data is made available at a 15-min temporal resolution; hence the city is used as a case study to evaluate a real time flood forecasting system. In this context, the real time forecast data at a resolution of 25 km from the Global Forecast System model—is used to as a boundary condition to drive the WRF model. As Bangalore covers an area of 765 km^2, climate data at 25 km maybe insufficient to resolve interactions with local topography and adequately forecast convective systems that may cause extreme rainfall events and urban flooding as a consequence. Hence, a popularly used RCM, the WRF model, is used to dynamically downscale real time climate information to a high resolution of 3 and 1 km. As WRF model outputs contain some uncertainty associated with the complexity of the rainfall generation process, a combination of 12 model configurations, with different physics schemes are used for the experiment.

The PCSWMM modelling platform is used to study the urban hydrology, using high resolution datasets to obtain water level observations in open channel drains. The model was calibrated, validated, and run for real time scenarios and have been able to effectively capture the points of flooding for the selected extreme events. This urban flood model is used for flood forecasting by using rainfall data from the WRF model and GFS data. The additional value brought about by using the WRF model is evaluated by comparing the flood forecasts from GFS data with the observed.

The present study reveals that the high-resolution WRF model is able to provide additional value in terms of characteristics of the rainfall pattern and sufficient variability in the water level pattern as compared to the 25 km GFS data. The accumulated rainfall and its location are found to be sensitive to the choice of convective

and microphysics parameterization schemes. Model simulated rainfall is noted to be closer to the observed rainfall in the case when the microphysics scheme is WSM6 and the convective parameterization scheme is Kain Fritsch.

Ten out of the twelve members of the WRF ensemble, forecast an extreme rainfall event within the city. The GFS data shows a rainfall event but fails to capture any rainfall above 60 mm/day which is the threshold for flooding in Bangalore city (Mohapatra et al., 2017). Six out of twelve members are successful in capturing the location and spatial distribution of the event and are used as an input for the calibrated PCSWMM model (**Supplementary Figure S2**).

The spatial and temporal resolution of the rainfall input plays an important role in the urban flood event analysis. The dense spatial and temporal network used for verification of the performance of the forecasting framework is a novelty of the work. It can be seen that the flood model outputs using the WRF ensemble data have more variability as compared to the runs using the GFS data as an input. The inability to capture the extreme rainfall features and the coarse temporal resolution of the GFS data has caused the water level output to be both spatially and temporally unvaried. The WRF ensemble aids in the model performance for flood forecasts with the ensemble water level peaks being much closer to the observed than GFS data (**Figure 7**). The flood peak appears 6–8 h in advance as compared to the observed which may be due to inadequate representation of urban heat island effect within the model (Paul et al., 2018).

The study demonstrates the first ever integrated application of a high-resolution numerical weather model coupled with a detailed hydrological model to capture a recent urban flood event over an Indian city. The urban catchment considered for the study is a lake based inland catchment and can serve as a model for other cities with similar urban hydrology. While the Bangalore city is a highly gauged or data rich study area that facilitates urban flood forecasting studies, the study framework can be adaptable for any city by giving inputs that reflect extreme rainfall events. The best performing member of the modelling framework (WSM6KF3) has been tested for various events and the performance across events have been included in the supplementary section for the sake of brevity (**Supplementary Figures S3–S6, S11**, **Supplementary Tables S4, S5**). The WSM6KF3 member has been tested for four heavy rainfall events from the monsoons of 2020 and 2021—September 8, 9; October 20, 21; 2020: November 4, 5; October 10, 11; 2021. The combined categorical indices have been added to the supplementary material (**Supplementary Figure S11**). On an average, the model setup has a better performance than a random/chance forecast for rainfall threshold above 60 mm as can be seen by the positive value of Hiedke Skill Score (**Supplementary Figure S11A**).

The WRF model ensemble is being improved continuously to reduce inconsistencies and errors in the initial conditions. The current physics ensemble selected for the study needs to be calibrated further in order to develop an ensemble with each member equally likely to predict a convective storm one to 3 days in advance. The accuracy of the ensemble can be further improved by assimilation of the observed network data. The one-way coupled framework has certain limitations as the feedback of surface hydrology variables such as lateral water flow and soil moisture to the atmospheric model are not considered. The lack of a two-way feedback mechanism also leads to the separation of the rainfall process from the land surface hydrological processes.

The modelling framework is designed to generate short range forecasts for the city of Bangalore. Continuous assessment of the operational runs of this framework can be used to develop medium range and long-range flood forecasts. Operational forecasts from the flood forecasting framework aids in building climate resilience for the city if and when these urban feedbacks are considered into regional planning processes (Gonzalez et al., 2021). The accuracy of the modelling framework can be further improved to include future sources of climate data—localised climate zones, data assimilation, higher resolution LULC and DEM. It can also be utilised for future climate scenarios if uncertainties from corresponding future land use land cover prediction datasets that will be used in the hydrological models is quantified.

DATA AVAILABILITY STATEMENT

The data analyzed in this study is subject to the following licenses/restrictions: High resolution observation data provided by the Karnataka State Natural Disaster Monitoring Center is available on request basis and is not publicly accessible. Data provided by local government bodies are classified and is not available on a public platform. Requests to access these datasets should be directed to Director, KSNDMC, Government of Karnataka (E-mail: director@ksndmc.org).

AUTHOR CONTRIBUTIONS

PM designed the concept, edited and proofread the manuscript. SD carried out the development, pre-processing and simulation of WRF model, post-processing of WRF results and writing manuscript. NS and LP worked on development, simulation and data analysis of hydrological model, post-processing of WRF results, preparation of results, editing and formatting manuscript.

FUNDING

Ministry of Electronics and Information Technology (MeITy), under the National Supercomputing Mission program of Government of India, through the following project: "Urban Modelling: Development of Multi-sectorial Simulation Lab and Science-Based Decision Support Framework to Address Urban Environment Issues" (Sanction Number MeitY/R&D/HPC/2(1)/2014).

ACKNOWLEDGMENTS

The authors acknowledge the financial support from Centre for Development of Advanced Computing (CDAC), on behalf of the Ministry of Electronics and Information Technology (MeITy), under the National Supercomputing Mission program of Government of India, through the following project: "Urban Modelling: Development of Multi-sectorial Simulation Lab and Science-Based Decision Support Framework to Address Urban Environment Issues" (Sanction Number MeitY/R&D/HPC/2(1)/2014). The authors would like to thank the Karnataka State Natural Disaster Monitoring Centre (KSNDMC), Bruhat Bengaluru Mahanagara Palike (BBMP), Bengaluru Development Authority (BDA), National Remote Sensing Centre (NRSC), Regional Remote Sensing Centre (RRSC), India Meteorological Department (IMD), and, National Aeronautics and Space Administration (NASA), for providing the high-resolution data used in this study. The authors are thankful to Pankaj Dey for his help in proofreading the manuscript.

SUPPLEMENTARY MATERIAL

The Supplementary Material for this article can be found online at: https://www.frontiersin.org/articles/10.3389/feart.2022.883842/full#supplementary-material

REFERENCES

Akhter, M., and Hewa, G. (2016). The Use of PCSWMM for Assessing the Impacts of Land Use Changes on Hydrological Responses and Performance of WSUD in Managing the Impacts at Myponga Catchment, South Australia. *Water* 8, 511. doi:10.3390/w8110511

Allen, M. R., Dube, O. P., Solecki, W., Aragón-Durand, F., Cramer, W., Humphreys, S., et al. (2018). Framing and Context. In: *Global Warming of 1.5°C. An IPCC Special Report on the Impacts of Global Warming of 1.5°C above Pre-industrial Levels and Related Global Greenhouse Gas Emission Pathways, in the Context of Strengthening the Global Response to the Threat of Climate Change, Sustainable Development, and Efforts to Eradicate Poverty*. Editors V. Masson-Delmotte, P. Zhai, H.-O. Pörtner, D. Roberts, J. Skea, P.R. Shukla, et al. IPCC. https://www.ipcc.ch/site/assets/uploads/sites/2/2019/06/SR15_Full_Report_High_Res.pdf.

Arnold, D., Morton, D., Schicker, I., Seibert, P., Rotach, M. W., Horvath, K., et al. (2012). Issues in High-Resolution Atmospheric Modeling in Complex Topography - the HiRCoT Workshop. *Hrvat. Meteoroloski Cas.* 47 (47), 3–11. https://meteo.boku.ac.at/report/BOKU-Met_Report_21_online.pdf.

Asghar, M. R., Ushiyama, T., Riaz, M., and Miyamoto, M. (2019). Flood and Inundation Forecasting in the Sparsely Gauged Transboundary Chenab River Basin Using Satellite Rain and Coupling Meteorological and Hydrological Models. *J. Hydrometeorol.* 20 (12), 2315–2330. doi:10.1175/JHM-D-18-0226.1

Awol, F. S., Coulibaly, P., and Tsanis, I. (2021). Identification of Combined Hydrological Models and Numerical Weather Predictions for Enhanced Flood Forecasting in a Semiurban Watershed. *J. Hydrol. Eng.* 26 (1), 04020057. doi:10.1061/(asce)he.1943-5584.0002018

Bhimala, K. R., Gouda, K. C., and Himesh, S. (2021). Evaluating the Spatial Distribution of WRF-Simulated Rainfall, 2-m Air Temperature, and 2-m Relative Humidity over the Urban Region of Bangalore, India. *Pure Appl. Geophys.* 178 (3), 1105–1120. doi:10.1007/s00024-021-02676-4

Bougeault, P., and Lacarrere, P. (1989). Parameterization of Orography-Induced Turbulence in a Mesobeta-Scale. *Mon. Weather Rev.* 117, 1872–1890.

Chawla, I., and Mujumdar, P. P. (2015). Isolating the Impacts of Land Use and Climate Change on Streamflow. *Hydrol. Earth Syst. Sci.* 19, 3633–3651. doi:10.5194/hess-19-3633-2015

Chawla, I., Osuri, K. K., Mujumdar, P. P., and Niyogi, D. (2018). Assessment of the Weather Research and Forecasting (WRF) Model for Simulation of Extreme Rainfall Events in the Upper Ganga Basin. *Hydrol. Earth Syst. Sci.* 22, 1095–1117. doi:10.5194/hess-22-1095-2018

Chen, F., Kusaka, H., Bornstein, R., Ching, J., Grimmond, C. S. B., Grossman-Clarke, S., et al. (2011). The Integrated WRF/Urban Modelling System: Development, Evaluation, and Applications to Urban Environmental Problems. *Int. J. Climatol.* 31 (2), 273–288. doi:10.1002/joc.2158

Chevuturi, A., Dimri, A. P., Das, S., Kumar, A., and Niyogi, D. (2015). Numerical Simulation of an Intense Precipitation Event over Rudraprayag in the Central Himalayas during 13-14 September 2012. *J. Earth Syst. Sci.* 124, 1545–1561. doi:10.1007/s12040-015-0622-5

CHI (Computational Hydraulics International) (2020). *PCSWMM Professional 2D Version: 7.3.3095, Guelph, Ontario, Canada*. [Online]. Available: www.chiwater.com (Accessed August 08, 2021).

Clark, P., Roberts, N., Lean, H., Ballard, S. P., and Charlton-Perez, C. (2016). Convection-permitting Models: A Step-Change in Rainfall Forecasting. *Mater. Apps.* 23 (2), 165–181. doi:10.1002/met.1538

Danielson, J. J., and Gesch, D. B. (2011). "Global Multi-Resolution Terrain Elevation Data 2010 (GMTED2010)," in *Open-File Report*. doi:10.3133/ofr20111073

Dhote, P. R., Thakur, P. K., Aggarwal, S. P., Sharma, V. C., Garg, V., Nikam, B. R., et al. (2018). Experimental Flood Early Warning System in Parts of Beas Basin Using Integration of Weather Forecasting, Hydrological and Hydrodynamic Models. *Int. Arch. Photogramm. Remote Sens. Spat. Inf. Sci.* XLII-5 (5), 221–225. doi:10.5194/isprs-archives-XLII-5-221-2018

Dudhia, J. (1989). Numerical Study of Convection Observed During the Winter Monsoon Experiment Using a Mesoscale Two-Dimensional Model. *J. Atmos. Sci.* 46, 3077–3107.

ESRI (2020). *ArcGIS Desktop: Release 10*. Redlands, CA: Environmental Systems Research Institute.

Evans, J. P., Ekström, M., and Ji, F. (2012). Evaluating the Performance of a WRF Physics Ensemble over South-East Australia. *Clim. Dyn.* 39, 1241–1258. doi:10.1007/s00382-011-1244-5

Farr, T. G., Rosen, P. A., Caro, E., Crippen, R., Duren, R., Hensley, S., et al. (2007). The Shuttle Radar Topography Mission. *Rev. Geophys.* 45 (2). doi:10.1029/2005RG000183

Gharai, B. (2014). IRS-P6 AWiFS Derived Gridded Land Use/Land Cover Data Compatible to Mesoscale Models (MM5 and WRF) over Indian Region. NRSC Technical Document No. NRSC-ECSA-ACSG-OCT-2014-TR-651, 1–11. Available at: http://bhuvan.nrsc.gov.in.

Ghosh, M., Karmakar, S., and Ghosh, S. (2022). "Flood Modelling for an Urban Indian Catchment: Challenges and Way Forward," in *Climate Change and Water Security. Lecture Notes in Civil Engineering*. Editors S. Kolathayar, A. Mondal, and S. C. Chian (Singapore: Springer), Vol. 178, 51–62. doi:10.1007/978-981-16-5501-2_5

Ghosh, S., Karmarkar, S., Saha, A., Mohanty, M. P., and Ali, S. (2019). Development of India's First Integrated Expert Urban Flood Forecasting System for Chennai. *Curr. Sci.* 117 (5), 741–745. doi:10.18520/cs2Fv1172Fi52F741-745

Golzio, A., Ferrarese, S., Cassardo, C., Diolaiuti, G. A., and Pelfini, M. (2021). Land-Use Improvements in the Weather Research and Forecasting Model over Complex Mountainous Terrain and Comparison of Different Grid Sizes. *Boundary-Layer Meteorol.* 180 (2), 319–351. doi:10.1007/s10546-021-00617-1

González, J. E., Ramamurthy, P., Bornstein, R. D., Chen, F., Bou-Zeid, E. R., Ghandehari, M., et al. (2021). Urban Climate and Resiliency: A Synthesis Report of State of the Art and Future Research Directions. *Urban Clim.* 38, 100858–100955. 2212. doi:10.1016/j.uclim.2021.100858

Goswami, S. B., Bal, P. K., and Mitra, A. K. (2018). Use of Rainfall Forecast from a High-Resolution Global NWP Model in a Hydrological Stream Flow Model

over Narmada River Basin during Monsoon. *Model. Earth Syst. Environ.* 4 (3), 1029–1040. doi:10.1007/s40808-018-0436-y

Gupta, K., PushplataLalitha, A., Lalitha, A., Ghosh Dastidar, P., Malleswara Rao, J., Thakur, P., et al. (2021). Modeling Seasonal Variation in Urban Weather in Sub-tropical Region of Delhi. *J. Indian Soc. Remote Sens.* 49 (2), 193–213. doi:10.1007/s12524-020-01198-1

Hebbar, R., Raj, U., Raj, K. G., Garg, S., Sagar, G. V., et al. (2018). *Spatio-Temporal Analysis of Lakes of Bengaluru (S-TALAB). Regional Remote Sensing Centre, NRSC, Bangalore*. NRSC Technical Document No. NRSC-RC-RRSCBANG-JUL-2018-TR-1176-V2.0.

Holt, T., and Pullen, J. (2007). Urban Canopy Modeling of the New York City Metropolitan Area: A Comparison and Validation of Single- and Multilayer Parameterizations. *Mon. weather Rev.* 135 (5), 1906–1930. doi:10.1175/MWR3372.1

Houmann, L. D. (2016). The Power of Partnership. *Healthc. Exec.* 31 (2), 64–67.

Huong, H. T. L., and Pathirana, A. (2011). Urbanization and Climate Change Impacts on Future Urban Flooding in Can Tho City, Vietnam. *Hydrol. Earth Syst. Sci.* 17, 379–394. doi:10.5194/hess-17-379-2013

India Meteorological Department (2020). Monthly Weather Review for the Month of Oct, 2020. Available at: https://internal.imd.gov.in/press_release/20201105_pr_926.pdf.

Iriza, A., Dumitrache, R. C., Lupascu, A., and Stefan, S. (2016). Studies Regarding the Quality of Numerical Weather Forecasts of the WRF Model Integrated at High-Resolutions for the Romanian Territory. *Atm* 29 (1), 11–21. doi:10.20937/ATM.2016.29.01.02

Jandaghian, Z., and Berardi, U. (2020). Comparing Urban Canopy Models for Microclimate Simulations in Weather Research and Forecasting Models. *Sustain. Cities Soc.* 55, 102025–106707. doi:10.1016/j.scs.2020.102025

Janjić, Z. I. (1994). The Step-Mountain Eta Coordinate Model: Further Developments of the Convection, Viscous Sublayer, and Turbulence Closure Schemes. *Mon. Weather Rev.* 122 (5), 927–945. doi:10.1175/1520-0493(1994)122<0927:TSMECM>2.0.CO;2

Kadaverugu, R., Matli, C., and Biniwale, R. (2021). Suitability of WRF Model for Simulating Meteorological Variables in Rural, Semi-urban and Urban Environments of Central India. *Meteorol. Atmos. Phys.* 133 (4), 1379–1393. doi:10.1007/s00703-021-00816-y

Kain, J. S., and Fritsch, J. M. (1993). "Convective Parameterization for Mesoscale Models: The Kain-Fritsch Scheme," in *The Representation of Cumulus Convection in Numerical Models. Meteorological Monographs*. Editors K. A. Emanuel and D. J. Raymond (Boston, MA: American Meteorological Society), 165–170. doi:10.1007/978-1-935704-13-3_16

Kain, J. S. (2004). The Kain-Fritsch Convective Parameterization: An Update. *J. Appl. Meteor.* 43 (1), 170–181. doi:10.1175/1520-0450(2004)043<0170:tkcpau>2.0.co;2

Kar, S. C., Mali, P., and Routray, A. (2014). Impact of Land Surface Processes on the South Asian Monsoon Simulations Using WRF Modeling System. *Pure Appl. Geophys.* 171 (9), 2461–2484. doi:10.1007/s00024-014-0834-7

Kirthiga, S. M., Narasimhan, B., and Balaji, C. (2021). A Multi-Physics Ensemble Approach for Short-Term Precipitation Forecasts at Convective Permitting Scales Based on Sensitivity Experiments over Southern Parts of Peninsular India. *J. Earth Syst. Sci.* 130 (2). doi:10.1007/s12040-021-01556-8

Li, G., Wang, Y., and Zhang, R. (2008). Implementation of a Two-Moment Bulk Microphysics Scheme to the WRF Model to Investigate Aerosol-Cloud Interaction. *J. Geophys. Res.* 113 (D15). doi:10.1029/2007JD009361

Lim, K.-S. S., and Hong, S.-Y. (2010). Development of an Effective Double-Moment Cloud Microphysics Scheme with Prognostic Cloud Condensation Nuclei (CCN) for Weather and Climate Models. *Mon. Weather Rev.* 138 (5), 1587–1612. doi:10.1175/2009MWR2968.1

Liu, J., Bray, M., and Han, D. (2012). Sensitivity of the Weather Research and Forecasting (WRF) Model to Downscaling Ratios and Storm Types in Rainfall Simulation. *Hydrol. Process.* 26 (20), 3012–3031. doi:10.1002/hyp.8247

matlab (2010). *Version 7.10.0 (R2010a*. Natick, Massachusetts: The MathWorks Inc.

Min, K.-H., Choo, S., Lee, D., and Lee, G. (2015). Evaluation of WRF Cloud Microphysics Schemes Using Radar Observations. *Weather Forecast.* 30 (6), 1571–1589. doi:10.1175/WAF-D-14-00095.1

Mlawer, E. J., Taubman, S. J., Brown, P. D., Iacono, M. J., and Clough, S. A. (1997). Radiative Transfer for Inhomogeneous Atmospheres: RRTM, A Validated Correlated-K Model for the Longwave. *J. Geophys. Res. Atmos.* 102 (14), 16663–16682. doi:10.1029/97jd00237

Mohandas, S., Francis, T., Singh, V., Jayakumar, A., George, J. P., Sandeep, A., et al. (2020). NWP Perspective of the Extreme Precipitation and Flood Event in Kerala (India) during August 2018. *Dyn. Atmos. Oceans.* 91 (August 2019), 101158. doi:10.1016/j.dynatmoce.2020.101158

Mohapatra, G. N., Rakesh, V., and Ramesh, K. V. (2017). Urban Extreme Rainfall Events: Categorical Skill of WRF Model Simulations for Localized and Non-localized Events. *Q.J.R. Meteorol. Soc.* 143 (707), 2340–2351. doi:10.1002/qj.3087

Mondal, A., and Mujumdar, P. P. (2015). Regional Hydrological Impacts of Climate Change: Implications for Water Management in India. *Proc. IAHS.* 366, 34–43. doi:10.5194/piahs-366-34-2015

Mujumdar, P. P., Mohan Kumar, M. S., Sreenivasa Reddy, G. S., Avinash, S., Chawla, I., Kaushika, G. S., et al. (2021). Development of an Urban Flood Model for Bengaluru City, Karnataka, India. *Curr. Sci.* 120 (9), 1441–1448. doi:10.18520/cs/v120/i9/1441-1448

National Centers for Environmental Prediction (2015). National Weather Service/NOAA/U.S. Department of Commerce, *NCEP GFS 0.25 Degree Global Forecast Grids Historical Archive*. Research Data Archive at the National Center for Atmospheric Research, Computational and Information Systems Laboratory. (Accessed January 27, 2021) Boulder, CO. doi:10.5065/D65D8PWK

Navale, A., and Singh, C. (2020). Topographic Sensitivity of WRF-Simulated Rainfall Patterns over the North West Himalayan Region. *Atmos. Res.* 242, 105003. doi:10.1016/j.atmosres.2020.105003

Patel, P., Ghosh, S., Kaginalkar, A., Islam, S., and Karmakar, S. (2019). Performance Evaluation of WRF for Extreme Flood Forecasts in a Coastal Urban Environment. *Atmos. Res.* 223 (March), 39–48. doi:10.1016/j.atmosres.2019.03.005

Paul, S., Ghosh, S., Oglesby, R., Pathak, A., and Chandrasekharan, A. (2016). Weakening of Indian Summer Monsoon Rainfall due to Changes in Land Use Land Cover. *Nat. Publ. Group* 1–10. doi:10.1038/srep32177

Paul, S., Ghosh, S., Mathew, M., Devanand, A., Karmakar, S., and Niyogi, D. (2018). Increased Spatial Variability and Intensification of Extreme Monsoon Rainfall Due to Urbanization. *Sci. Rep.* 8 (1), 3918. doi:10.1038/s41598-018-22322-9

Qi, W., Ma, C., Xu, H., Chen, Z., Zhao, K., and Han, H. (2021). A Review on Applications of Urban Flood Models in Flood Mitigation Strategies. *Nat. Hazards* 108 (1), 31–62. doi:10.1007/s11069-021-04715-8

Rakesh, V., Goswami, P., and Prakash, V. S. (2015). Evaluation of High Resolution Rainfall Forecasts over Karnataka for the 2011 Southwest and Northeast Monsoon Seasons. *Mater. Apps.* 22 (1), 37–47. doi:10.1002/met.1438

Rakesh, V., Mohapatra, G. N., and Bankar, A. (2021). Historical Extreme Rainfall over the Bangalore City, India, on 14 and 15 August 2017: Skill of Sub-kilometer Forecasts from WRF Model. *Meteorol. Atmos. Phys.* 133, 1057–1074. doi:10.1007/s00703-021-00794-1

Ravazzani, G., Amengual, A., Ceppi, A., Homar, V., Romero, R., Lombardi, G., et al. (2016). Potentialities of Ensemble Strategies for Flood Forecasting over the Milano Urban Area. *J. Hydrology.* 539. doi:10.1016/j.jhydrol.2016.05.023

Rossman, L. A. (2015). *Storm Water Management Model User's Manual Version 5.0*. Washington, DC: U.S. Environmental Protection Agency. Available at: https://www.epa.gov/water-research/storm-water-management-model-swmm-version-51-users-manual.

Roxy, M. K., Ghosh, S., Pathak, A., Athulya, R., Mujumdar, M., Murtugudde, R., et al. (2017). A Threefold Rise in Widespread Extreme Rain Events Over Central India. *Nat. Commun.* 8, 708. doi:10.1038/s41467-017-00744-9

Rupa, C., and Mujumdar, P. P. (2018). Quantification of Uncertainty in Spatial Return Levels of Urban Precipitation Extremes. *J. Hydrol. Eng.* 23 (1), 04017053. doi:10.1061/(ASCE)HE.1943-5584.0001583

Rupa, C., and Mujumdar, P. P. (2019). Flood Modelling: Recent Indian Contributions. *Proc. Indian Nation. Sci. Acad.* 85 (4), 705–722. doi:10.16943/ptinsa/2019/49648

Sahoo, S. K., Ajilesh, P. P., Gouda, K. C., and Himesh S, S. (2020a). Impact of Land-Use Changes on the Genesis and Evolution of Extreme Rainfall Event: a Case Study over Uttarakhand, India. *Theor. Appl. Climatol.* 140 (3), 915–926. doi:10.1007/s00704-020-03129-z

Sahoo, S. K., Gouda, K. C., Himesh, S., Mohapatra, G. N., and Goswami, P. (2014). *Simulation of Extreme Rainfall Event over Himalayan Region Using WRF*

Model. Darmstadt, Germany: The Climate Symposium, October, 2014). doi:10.13140/RG.2.1.1180.5921

Sahoo, S. K., Himesh, S., and Gouda, K. C. (2020b). Impact of Urbanization on Heavy Rainfall Events: A Case Study over the Megacity of Bengaluru, India. *Pure Appl. Geophys.* 177 (12), 6029–6049. doi:10.1007/s00024-020-02624-8

Salamanca, F., Martilli, A., Tewari, M., and Chen, F. (2011). A Study of the Urban Boundary Layer Using Different Urban Parameterizations and High-Resolution Urban Canopy Parameters with WRF. *J. Appl. Meteorology Climatol.* 50 (5), 1107–1128. doi:10.1175/2010JAMC2538.1

Sarkar, S., and Himesh, S. (2021). Evaluation of the Skill of a Fully-Coupled Atmospheric-Hydrological Model in Simulating Extreme Hydrometeorological Event: A Case Study over Cauvery River Catchment. *Pure Appl. Geophys.* 178 (3), 1063–1086. doi:10.1007/s00024-021-02684-4

Sikder, Md . S., Ahmad, S., Hossain, F., Gebregiorgis, A., and Lee, H. (2019). Case Study: Rapid Urban Inundation Forecasting Technique Based on Quantitative Precipitation Forecast for Houston and Harris County Flood Control District. *J. Hydrologic Eng.* 28. doi:10.1061/(ASCE)HE.1943-5584.0001807

Singh, A., Tiwari, S., and Jha, S. K. (2021). Evaluation of Quantitative Precipitation Forecast in Five Indian River Basins. *Hydrological Sci. J.* 66 (15), 2216–2231. doi:10.1080/02626667.2021.1982138

Shastri, H., Paul, S., Ghosh, S., and Karmakar, S. (2015). Impacts of Urbanization On Indian Summer Monsoon Rainfall Extremes. *J. Geophys. Res.* 120 (2), 496–516. doi:10.1002/2014JD022061

Skamarock, W. C., Klemp, J. B., Dudhi, J., Gill, D. O., Barker, D. M., Duda, M. G., et al. (2008). A Description of the Advanced Research WRF Version 3. *Tech. Rep.*, 113. doi:10.5065/D6DZ069T

Sun, J., Xue, M., Wilson, J. W., Zawadzki, I., Ballard, S. P., Onvlee-Hooimeyer, J., et al. (2014). Use of Nwp for Nowcasting Convective Precipitation: Recent Progress and Challenges. *Bull. Am. Meteorological Soc.* 95 (3), 409–426. doi:10.1175/BAMS-D-11-00263.1

Thayyen, R. J., Dimri, A. P., Kumar, P., and Agnihotri, G. (2013). Study of Cloudburst and Flash Floods Around Leh, India, During August 4-6, 2010. *Nat. Hazards* 65 (3), 2175–2204. doi:10.1007/s11069-012-0464-2

The NCAR Command Language (2019). Version 6.6.2. Boulder, Colorado: UCAR/NCAR/CISL/TDD. Software. doi:10.5065/D6WD3XH5

Tian, J., Liu, J., Yan, D., Li, C., and Yu, F. (2017). Numerical Rainfall Simulation with Different Spatial and Temporal Evenness by Using a WRF Multiphysics Ensemble. *Nat. Hazards Earth Syst. Sci.* 17 (4), 563–579. doi:10.5194/nhess-17-563-2017

Wilks, D. S. (2006). "Statistical Methods in the Atmospheric Sciences," in *International Geophysics Series*, 2nd ed. 91. Burlington: Elsevier Academic Press, 627.

World Meteorological Organization (2011). *Manual on Flood Forecasting and Warning-WMO-No. 1072*. Geneva. Available at: https://library.wmo.int/index.php?lvl=notice_display&id=5841#.YoKHQ-hBxPb.

Yucel, I., Onen, A., Yilmaz, K. K., and Gochis, D. J. (2015). Calibration and Evaluation of a Flood Forecasting System: Utility of Numerical Weather Prediction Model, Data Assimilation and Satellite-Based Rainfall. *J. Hydrology.* 523, 0022–1694. 49-66. doi:10.1016/j.jhydrol.2015.01.042

Zender, C. S. (2008). Analysis of Self-Describing Gridded Geoscience Data with netCDF Operators (NCO). *Environ. Model. Softw.* 23 (10), 1338–1342. doi:10.1016/j.envsoft.2008.03.004

Zender, C. S. (2014). *netCDF Operator (NCO) User Guide*. Version 4.4.3. Available from: http://nco.sf.net/nco.pdf.

Conflict of Interest: The authors declare that the research was conducted in the absence of any commercial or financial relationships that could be construed as a potential conflict of interest.

Publisher's Note: All claims expressed in this article are solely those of the authors and do not necessarily represent those of their affiliated organizations, or those of the publisher, the editors and the reviewers. Any product that may be evaluated in this article, or claim that may be made by its manufacturer, is not guaranteed or endorsed by the publisher.

frontiers | Frontiers in Earth Science

ORIGINAL RESEARCH
published: 03 June 2022
doi: 10.3389/feart.2022.908869

Quantitative Precipitation Estimation Model Integrating Meteorological and Geographical Factors at Multiple Spatial Scales

Wei Tian[1,2]*, *Kailing Shen*[1,2]*, *Lei Yi*[1,2], *Lixia Zhang*[3], *Yang Feng*[3] and *Shiwei Chen*[4]

[1]School of Computer Science and Software, Nanjing University of Information Science and Technology, Nanjing, China, [2]Engineering Research Center of Digital Forensics, Ministry of Education, Nanjing University of Information Science and Technology, Nanjing, China, [3]Shijiazhuang Meteorological Bureau, Shijiazhuang, China, [4]School of Automation, Nanjing University of Information Science and Technology, Nanjing, China

OPEN ACCESS

Edited by:
Sanjeev Kumar Jha,
Indian Institute of Science Education and Research, India

Reviewed by:
Caihong Hu,
Zhengzhou University, China
Serena Ceola,
University of Bologna, Italy

***Correspondence:**
Wei Tian
tw@nuist.edu.cn
Kailing Shen
skling@nuist.edu.cn

Specialty section:
This article was submitted to Atmospheric Science, a section of the journal Frontiers in Earth Science

Received: 31 March 2022
Accepted: 18 May 2022
Published: 03 June 2022

Citation:
Tian W, Shen K, Yi L, Zhang L, Feng Y and Chen S (2022) Quantitative Precipitation Estimation Model Integrating Meteorological and Geographical Factors at Multiple Spatial Scales. Front. Earth Sci. 10:908869. doi: 10.3389/feart.2022.908869

Heavy precipitation tends to cause mountain torrents, urban waterlogging and other disasters. It poses a serious threat to people's life and property safety. Therefore, real-time quantitative precipitation estimation is especially important to keep track of precipitation changes and reduce negative impacts. However, high-resolution and high-accuracy quantitative precipitation estimation is a challenging task due to the complex spatial and temporal variability of microphysics in precipitation processes. Previous studies have focused only on small-scale radar reflectivity factors above rain gauges and did not pay enough attention to the contribution of covariates to model performance. Meteorological and geographical factors play an important role in rain process, so these factors are taken into account during our research. In this study, a quantitative precipitation estimation model that can employ multi-scale radar reflectivity factors and fuse meteorological and geographical factors is proposed to further improve precipitation accuracy. In addition, we propose the muti-scale self-attention (MS-SA) module that can further utilize information at multiple spatial scales to improve the accurate precipitation estimation. The proposed model reduced the root mean square error of precipitation estimation by 83.8% compared to the conventional Z-R relationship that correlates the rainfall and radar reflectivity factors, i.e., $Z = aR^b$, and by 43.7, 24.6, and 22.7% compared to the back propagation neural network (BPNN), convolutional neural network (CNN), and convolutional neural network with the addition of meteorological factors and geographical factors as covariates in the proposed model, respectively. Therefore, we can conclude that multi-scale radar reflectivity factors fused with meteorological and geographical factors can produce more accurate precipitation estimation.

Keywords: precipitation estimation, weather radar, deep learning, multi-scale, meteorological factors, geographical factors

INTRODUCTION

Rainfall is a fundamental part of the natural water cycle and is necessary for the continuation of all life in nature. In recent years, as global warming has intensified, the atmosphere contains higher levels of water vapor and the frequency and intensity of heavy precipitation events have increased significantly (Groisman et al., 2005; Cremonini and Tiranti, 2018; Giang, 2021; Zhao et al., 2021). This inevitably leads to natural disasters such as floods and has many indirect negative effects on human social activities such as transportation and agriculture (Iwashima and Yamamoto, 1993; Ramos et al., 2005; Sun and Huang, 2011; Lee et al., 2014; Wu J. et al., 2020; Paxton et al., 2021). Therefore, quantitative precipitation estimation (QPE) based on weather radar with high spatial and temporal resolution can be of great help for decision makers to make timely and correct decisions with great reference value, which in turn also plays an important role in mitigating urban flash floods and warning extreme weather (Morin and Gabella, 2007; Germann et al., 2009; Chen and Chandrasekar, 2015; Gou et al., 2018; Lu et al., 2019). Real-time and high-precision QPE is also continuously studied by meteorologists as an important topic (Sadeghi et al., 2019; Wu H. et al., 2020). Rain gauges are a direct means of measuring rainfall and their measurements are often used in QPE as a label for the ground truth value at a fixed location. However, rain gauge networks suffer from low spatial density, uneven distribution, inconsistent historical recording periods, and high costs in the task of measuring the depth of precipitation in a certain area (Fan et al., 2021). Therefore, rainfall measurements in a certain region based only on rain gauges are not spatially representative. Weather radar, as an indirect means of measuring rainfall, is commonly used to observe the spatial structure characteristics of microscopic particles in the high-dimensional space of precipitation and rainfall fields. Furthermore, in the business of Radar Quantitative Precipitation Estimation (RQPE), weather radar has the advantages of high spatial and temporal resolution, wide geographical coverage, and real-time data transmission (Berne and Krajewski, 2013; Tian et al., 2020). It should be noted that its performance depends on the physical model of the raindrop size distribution and the relationship established by the radar parameters and the physical model. Thus, due to the above-mentioned advantages of radar, and the nature of the spatial distribution of the radar network, it is able to count and model extreme weather and the natural hazards it causes on both spatial and temporal scales. This compensates for the deficiencies of the rain gauge network (Yang et al., 2004; Delrieu et al., 2009; Germann et al., 2009). However, estimating precipitation by radar is a complex process, which is mainly caused by the complex spatiotemporal motion and variation of microscopic particles in the precipitation process, as well as the poor measurement accuracy due to multiple error sources in the radar measurement process (Berne and Krajewski, 2013; Chen et al., 2019). The traditional quantitative precipitation estimation (QPE) algorithm uses the relationship between weather radar echo intensity and rainfall intensity, i.e., the Z-R relationship where Z is the radar echo intensity, R is the rainfall intensity, to invert the rainfall amount of a rainfall field (Legates, 2000; Rosenfeld and Ulbrich, 2003; Barros and Prat, 2009). The empirical coefficients a and b in the Z-R relationship are influenced by many environmental factors, such as weather conditions, geography, etc. It is fundamentally influenced by the spectral characteristics of raindrop size. Therefore, the range and environment to which a fixed Z-R relationship can be adapted is greatly limited. The same Z-R relationship can produce great errors in different areas, especially in mountainous areas and under strong convective weather. Previous studies have mainly focused on increasing the accuracy of the Z-R relationship and trying to break out of this dilemma. Alfieri et al. (2010) considered the Z-R relationship to be closely related to time and they improved it to be constantly updated with time. Specially, they took all available Z-R relationship pairs for each time step to correct the parameters and then adjusted the power law equation to convert the radar reflectivity factor measurements into rainfall rates. Wu et al. (2018) suggested that the echo top height can reflect the stage of storm development and the intensity of precipitation system. Therefore, a new dynamic Z-R relationship for RQPE was established using echo top-height classification, and better performance was obtained in comparison experiments with different seasonal precipitation events. However, although previous studies have considered the effects of independent time and space on the Z-R relationship and calibrated it, or dynamically adjusted the empirical coefficients a, b by grouping reflectivity and precipitation, none of them have addressed the essential problem of the Z-R relationship. The Z-R relationship, as an ideal model that is difficult to satisfy, cannot capture the spatial and temporal variability in the rainfall process well, and because of the Z-R relationship generally operates on independent lattice points and does not take into account the spatial correlation between regions. It is difficult to meet the demand of the meteorological community for high-quality QPE. All these dilemmas have been solved in our study, and the model proposed in our study can be more adaptable to the complex geographical and climatic environments. In addition, our model can provide more accurate precipitation estimation than the Z-R relationship and its derivative methods.

The rapid development of machine learning, especially deep learning in recent years has advanced the research of QPE in the meteorological community (Teschl et al., 2006; Gagne et al., 2014; Kühnlein et al., 2014; Sorooshian et al., 2016; Beusch et al., 2018; Chen et al., 2020; Min et al., 2020; Zhang et al., 2020; Wu et al., 2021). In the era of big data, machine learning has great potential for parsing the underlying patterns of huge data without assuming any physical relationships. And deep learning, with the powerful learning ability of deep neural networks for complex nonlinear relationships in nature, has broadened the applicable field of machine learning and realized numerous applications. In addition, deep neural networks have powerful adaptive and fault-tolerant capabilities. Therefore, the deep neural network is a new option for improving the accuracy of QPE (Wu et al., 2021). Shin et al. (2019) evaluated the applicability of random forests, stochastic gradient augmentation models, and extreme learning machine methods to QPE and used multivariate

combinations as inputs. The results show that the approach based on machine learning performs better than the model with Z-R relationship and resolves the time lag between the radar data and ground observations, and the accuracy is improved by an appropriate combination of multiple input variables. The overall performance of their proposed three models is 8.18 mm/h, 8.38 mm/h, 7.91 mm/h for root mean square error (RMSE) values, respectively. Sivasubramaniam et al. (2018) developed a nonparametric prediction model, the K-nearest neighbor regression estimator, and demonstrated that the inclusion of air temperature as an additional covariate for model significantly improved prediction results in cold air with an improvement of 15% in RMSE compared to radar precipitation rate as a single predictor in model. Chen et al. (2019) designed a two-stage neural network for estimating precipitation intensity and inversion of satellite radar profiles, respectively. They demonstrated that the machine learning approach can better detect changes in precipitation microphysical processes. Moreover, Chen et al. (2020) also proposed a data fusion framework based on a multilayer perceptron model with machine learning. The results indicate that the machine learning model is more flexible and can fuse multiple data sources. In addition, the data fusion framework can better capture precipitation intensity. However, although the previous studies used covariate or multiple data sources fusion models proved the validity, they considered only in one dimensional space and did not use two-dimensional data. In other words, they ignored the role of the spatial structure of variables on rainfall estimation during the rainfall process.

In addition to using traditional machine learning methods, Sadeghi et al. (2020) used a U-Net convolutional architecture with infrared information and geographic information as input to verify that adding latitude and longitude information to infrared information can improve real-time precipitation estimation. Then, for RMSE, mean absolute error (MAE) and correlation coefficient (CC), their models were more accurate in summer (winter) than the comparison model, i.e., PERSIANN-CCS (Hong et al., 2007), by 20% (10%), 21% (16%) and 140% (38%), respectively. Wu H. et al. (2020) analyzed the advantages and disadvantages of rainfall gauges and satellite products in rainfall operations. Moreover, they used deep learning methods to model the spatial and temporal correlations of these two sensors. Their CNN-LSTM model provides more accurate rainfall estimates. Specifically, their model outperformed the comparative models (CNN, LSTM, and MLP) with a 17.0 and 14.0% reduction in RMSE and MAE, respectively, and an increase in correlation coefficient from 0.66 to 0.72. It demonstrates the importance of capturing the spatiotemporal correlation of precipitation. A multi-model, multi-task precipitation estimation depth model was proposed by Moraux et al. (2019). The model uses an encoder-decoder as the main framework, and combines multiple modalities and multiple scales in a multitasking manner to suppress the respective errors and improve accuracy. More specifically, it estimates precipitation amount with a MAE of 0.605 mm/h and a RMSE of 1.625 mm/h for instantaneous rates. Furthermore, Moraux et al. (2021) also investigated combining different precipitation measurement modes to improve the accuracy of QPE. They combined well the inputs of three modes, rainfall gauge, radar and infrared satellite imagery, on the basis of the original model and obtained the best accuracy. The results show that RMSE decreases to 1.488 mm/h for rainfall estimates. Then, they demonstrate that building deep learning methods on basis of traditional methods is highly promising in the field of meteorology. Previous deep learning-based approaches have demonstrated the effectiveness of deep learning models in rainfall estimation operations. In addition, multiple sources of two-dimensional data were widely adopted as model inputs. However, considering that the input features can intermingle with information unrelated to rainfall, their model lacks the ability to adaptively adjust the proportion of weights to the features. In our study, we achieve a non-uniform distribution of weights and combine multi-scale information through a multi-scale self-attention module.

Previous studies have focused only on radar reflectivity factors at small-scales, while rainfall is the result of the interaction of complex weather systems at multiple scales (Zhang M. et al., 2021). Inspired by this, we believe that large scale radar reflectivity factors can also provide valid information for rainfall estimation, so we adopt multi-scale rainfall field information as the observations for the model, i.e., covering different ranges of rainfall fields centered on the rainfall collection points. In addition, although previous studies have used additional inputs as covariates, such as temperature (Sivasubramaniam et al., 2018). However, they ignored the influence of the spatial structural characteristics of the covariates on rainfall, so we used meteorological and geographic factors in two dimensions as covariates to establish their association with rainfall at the spatial scale. Finally, we also designed a multi-scale self-attention module, which helps our model to focus on factors that contribute to rainfall estimation and suppress noise. To the best of our knowledge, this has not been considered in previous studies, and our study demonstrates the effectiveness of this module. However, the process of this study also has some shortcomings. Since the radar detection process is affected by ground clutter, biological clutter, etc., the preprocessing scheme used in this study may not completely eliminate the influence of clutter, and this problem will be gradually improved in future studies.

In summary, a multi-scale neural network is built in this study to improve the accuracy of QPE by employing rain gauge and weather radar, with rain gauge data as labels, high spatial and temporal resolution radar data as the main input, and meteorological factors and elevation as covariates. The more accurate the quantitative rainfall estimates are, the better they can help meteorologists in their deeper study of weather systems and assist relevant managers in making more precise and timely warnings to minimize damage caused by natural disasters. The structure of this paper is presented as follows. "DATA AND METHODOLOGY" describes the data areas sampled and the detailed processing of the data set, as well as our specific scheme design, design ideas, evaluation metrics and information criteria. The "RESULTS" section discusses our experimental results and

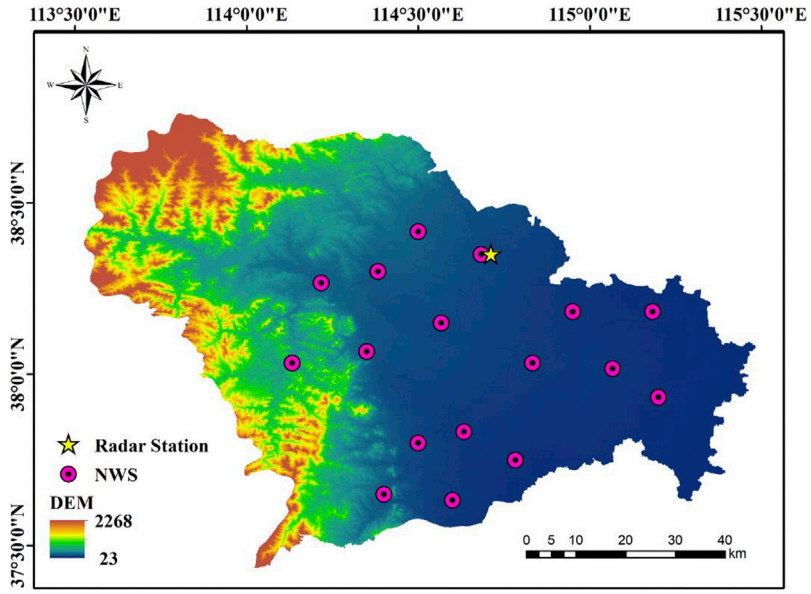

FIGURE 1 | Elevation map of Shijiazhuang city. The map shows the distribution of radar stations (yellow pentagons) and 17 NWSs (pink circles) and the extent of our study area.

conclusions. Finally, we summarize our work in "CONCLUSION" section.

DATA AND METHODOLOGY

Data and Preprocessing

The data were obtained from the Shijiazhuang Meteorological Station Z9311 Doppler Weather Radar and 17 National Weather Stations (NWSs) from June to September 2017 to 2019. The Shijiazhuang domain spans two geomorphic units, the North China Plain and the Taihang Mountains, with a complex topography of elevated terrain in the west and flat terrain in the east. The climate is characterized by an uneven spatial and temporal distribution of rainfall, with significant seasonal and regional differences in the trend of precipitation, and a rainy season mostly in summer. The Doppler Weather Radar completes a body sweep every 6 min to obtain the radar reflectivity factors and the corresponding latitude and longitude for nine different elevation angles in all directions, with a volumetric sweep of VCP21. The NWSs record minute-by-minute meteorological elements, including barometric pressure, temperature, humidity, rainfall and other data. The study area was taken from longitude 113.5°–115.5° and latitude 37.0°–39.0°. The study area and NWSs are shown in **Figure 1**.

This study is an estimation of precipitation with radar reflectivity factors as the main input and meteorological and geographical factors as covariates, where temperature e and humidity are used for meteorological factors and elevation is used for geographical factors. Since the radar detection process is influenced by clutter and the radar reflectivity factors of a single elevation angle cannot completely express the real situation of cloud masses in a certain range, we use combined reflectivity. Furthermore, as the radar reflectivity factors of low elevation angles are more closely related to the precipitation, the combined reflectivity factors with maximum radar reflectivity factors of 0.49°, 1.40°, and 2.38° elevation angles are considered. In addition, we calculate the average reflectivity intensity of all radar echo images and sort them from smallest to largest, take the average reflectivity intensity of the smallest 0.1% number of radar echo images as background noise, and denoise the remaining radar echo images to some extent. The radar reflectivity factors need to be matched with the precipitation amount. Considering the delay of precipitation, the sum of the precipitation amount 6 min after the current moment is taken as the rainfall label of this moment. According to the first law of geography (Wasko et al., 2013), the correlation between the neighboring grids and the grid to be estimated decays with increasing distance, so the spatial matching of the radar reflectivity factors and precipitation is performed based on the latitude and longitude of the NWSs, and the grid points closest to the NWSs are selected as the center of the reflectivity. Specifically, considering that the radar reflectivity factors closer to the NWSs are more correlated with the precipitation values and the completeness of rainfall field information at long distances, multi-scale information is fed into our network.

Finally, as shown in **Figure 2**, the radar reflectivity factors centered at the NWSs in the ranges of 50 km, 25 km, 12.5 km are taken as the input radar reflectivity factors. The spatial resolution of the radar reflectivity factors is 0.005°, i.e., the grid points are 0.5 km away from each other, and the temporal resolution is 6 min. For the meteorological factors used in this study, temperature and humidity are used as covariates. Considering that the temporal resolution of the radar reflectivity factors is

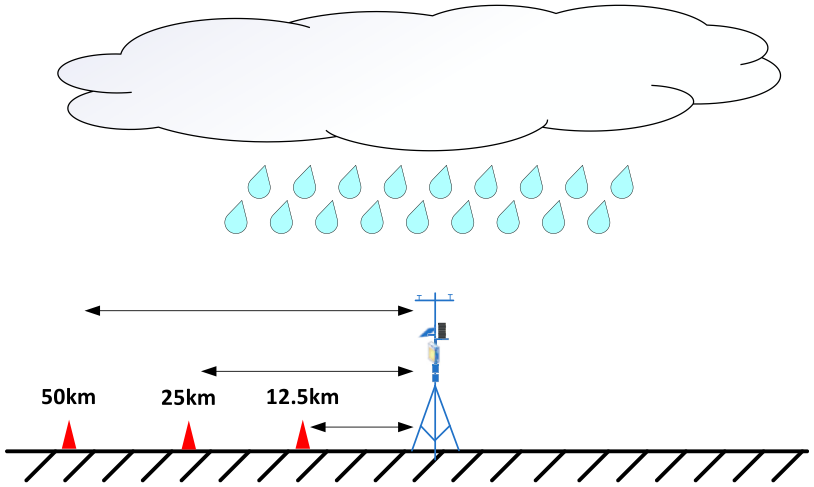

FIGURE 2 | The graph of the weather station in the figure represents the NWS, and the three red triangles represent the boundaries of the sampling ranges for the small-scale input, the medium-scale input, and the large-scale input. The sampling area is a rectangular area centered on the NWS at a horizontal resolution of 0.005°.

6 min, while the temporal resolution of the meteorological elements is 1 min. Therefore, a temporal matching operation is performed on both data by taking the average of the meteorological factors for a total of 6 min above and below the current moment as the value of the current moment. Specifically, the meteorological factors in the range are interpolated according to the spherical model using Ordinary Kriging interpolation based on the meteorological factor data from the NWSs, and then temporally and spatially matched with the radar reflectivity factors, which are jointly used as inputs. The detail process of Kriging is as follows (Oliver and Webster, 1990):

$$E = \sum_{i=1}^{n} \lambda_i z(x_i) \tag{1}$$

where E is the estimation of meteorological factors in certain areas, λ_i is the proportion of weights for each sampling point and $z(x_i)$ is the data of the real meteorological factors recorded at the sampling sites. The sampling sites in this experiment are NWSs.

Geographical and topographical factors are constant influencing factors of rainfall (Liu et al., 2018; Sadeghi et al., 2020; Sønderby et al., 2020). Therefore, according to the digit elevation model of Shijiazhuang city, the elevation values in grid form are obtained according to the spatial resolution of 0.005°, and then the spatial matching operation is performed to cut multi-scale with the NWSs as the center.

To evaluate the model more accurately, we divided the data set into a training set and a test set in a ratio of 8:2. The training set is used to help the model fit the relationship between the radar reflectivity factors and precipitation, and the test set is used to verify their relationship. For the partitioning of the dataset, random partitioning will lead to an uneven spatial and temporal distribution of the dataset. Therefore, the data set is classified according to the latitude and longitude coordinates of the NWSs and the month. Finally, they are randomly divided into training and test sets in the ratio of 8:2.

Methodology

Baseline Model

Traditional methods usually rely on converting the radar reflectivity factors to rainfall through a nonlinear relationship between the radar echo intensity and rainfall intensity (Z-R relationship). Models based on the Z-R relationship are also widely used in QPE models. The specific equation for the Z-R relationship is:

$$Z = aR^b \tag{2}$$

where Z is the radar echo intensity, R is the rainfall intensity, and a and b are the empirical coefficients. The Z-R relationship is mainly influenced by the spectral characteristics of the rainfall. In addition, the Z-R relationship is influenced by many factors such as geography, meteorological conditions, and hydrology. Parameters a and b will be adjusted to suit different conditions according to these factors (Tian et al., 2020).

Therefore, according to the equation of the relationship between radar reflectivity factor and its physical quantity $dBZ = 10\lg Z$, the Z-R relationship is rewritten as:

$$\lg R = \frac{1}{10b} dBZ - \frac{1}{b} \lg a \tag{3}$$

Then, we fit the values of the parameters a, b using a linear regression model. Finally, the value of a takes the value of 1.91 and the value of b takes the value of 0.578.

Model Architecture

It is well known that precipitation is a complex process, which is closely related to meteorological factors and influenced by geographical factors. Therefore, only considering the radar reflectivity factors cannot accurately fit the relationship with precipitation intensity, and the inclusion of covariates is particularly important. In this study, meteorological factors (temperature and humidity) and geographical factors

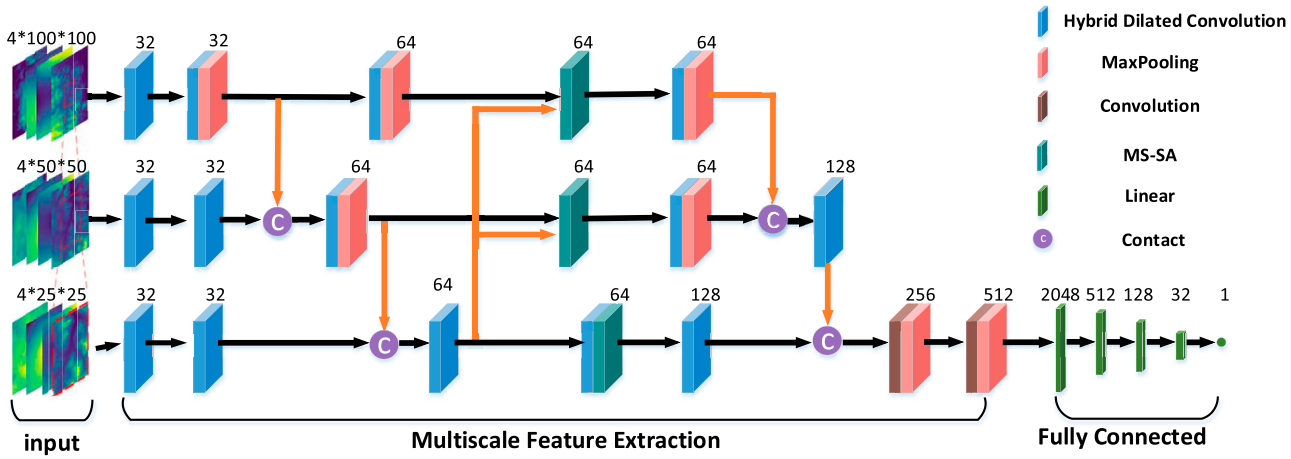

FIGURE 3 | The MS-FCVNet model receives information input from three scales, undergoes multi-scale feature extraction and fusion, and finally outputs the predicted values through a fully connected layer.

(elevation) are mainly used as covariates. In addition, an attention mechanism among multiple scales is introduced in this study. With this mechanism, the module not only focuses on the most relevant influences near the site, but also takes into account the spatial variability on a large scale to produce more accurate estimation.

In contrast to the single-scale input of the model in previous studies, our model called MS-FCVNet uses a multi-scale input centered on NWSs. In detail, small-scale images have a small sensory field, focusing on the variation in details of rainfall fields around the station. Large-scale images have a wide range of sensory fields, focusing on the overall spatial structure of weather conditions. And Medium-scale images mainly play a transitional effect, linking the spatial information of large scale and small scale, and providing the necessary spatial change information. In terms of model structure, the model includes Hybrid Dilated Convolution (HDC), pooling layer, fully connected layer, and multi-scale self-attention modules (MS-SA). The model structure is shown in **Figure 3**, and the details of the modules and their specific functions will be explained in detail below.

Hybrid Dilated Convolution

HDC consists of a number of dilated convolutions (Wang et al., 2018a). Dilated convolution mainly involves adding empty holes, i.e., zero pixels, to the feature mapping of the convolution kernel for the purpose of expanding the receptive field. Ordinary convolution generally achieves the purpose of expanding the receptive field by adding a pooling layer, which leads to the loss of detailed information. Compared to ordinary convolution, dilated convolution can improve the resolution of the sampled image without increasing the number of parameters to achieve dense feature extraction in deep CNNs. For an ordinary convolution kernel of size K, the corresponding dilated convolution kernel size is $K + (K-1)*(R-1)$, where R is the dilation rate when we sample the feature map. Taking the two-dimensional dilated convolution as an example, the process can be expressed as the following equation:

$$\begin{cases} \mathrm{f}_{i,j}^{[l]} = \sum_{m=0}^{S-1}\sum_{n=0}^{S-1} w_{m,n}^{[l]} x_{(m-S//2)*r+i,(n-S//2)*r+j}^{[l-1]} + b^{[l]} \\ x_{i,j}^{[l]} = g\left(f_{i,j}^{[l]}\right) \end{cases} \tag{4}$$

where f is the feature points extracted from the convolution kernel after the convolution operation, S is the length of the convolution kernel, and w is the weight of the convolution kernel. x is the position of the sampled points, b is the bias, and g is the activation function. However, simply stacking the dilated convolutions will lead to a grid effect, i.e., the pixel points on the sampled final feature map will view the information of the original feature map in the form of a grid. This will lead to discontinuities in local information, weakening spatial correlation and not conducive to capturing the spatial information of the image. Therefore, HDC is used to build the network in this study. Specifically, different dilation rates are used for several phase-consecutive dilation convolution kernels in HDC. The main purpose is to compensate for the holes caused by a series of convolutions, so that the pixel points of the sampled feature map can sample a complete region of the original feature map. For a number of N convolution layers, the convolution kernel size of each layer is K, and its void rate is $[r1, r2, \ldots, rn]$, and its maximum dilation rate needs to satisfy the following equation:

$$M_i = \max[M_{i+1} - 2r_i, M_{i+1} - 2(M_{i+1} - r_i), r_i] \tag{5}$$

where r_i is the dilation rate of layer i and M_i is the maximum dilation rate of layer i. With HDC, it can achieve a wider field of perception without losing local information and capture more global information. **Figure 4** shows the specific configuration of our HDC, where we take 1, 3, and 5 as consecutive dilation rates.

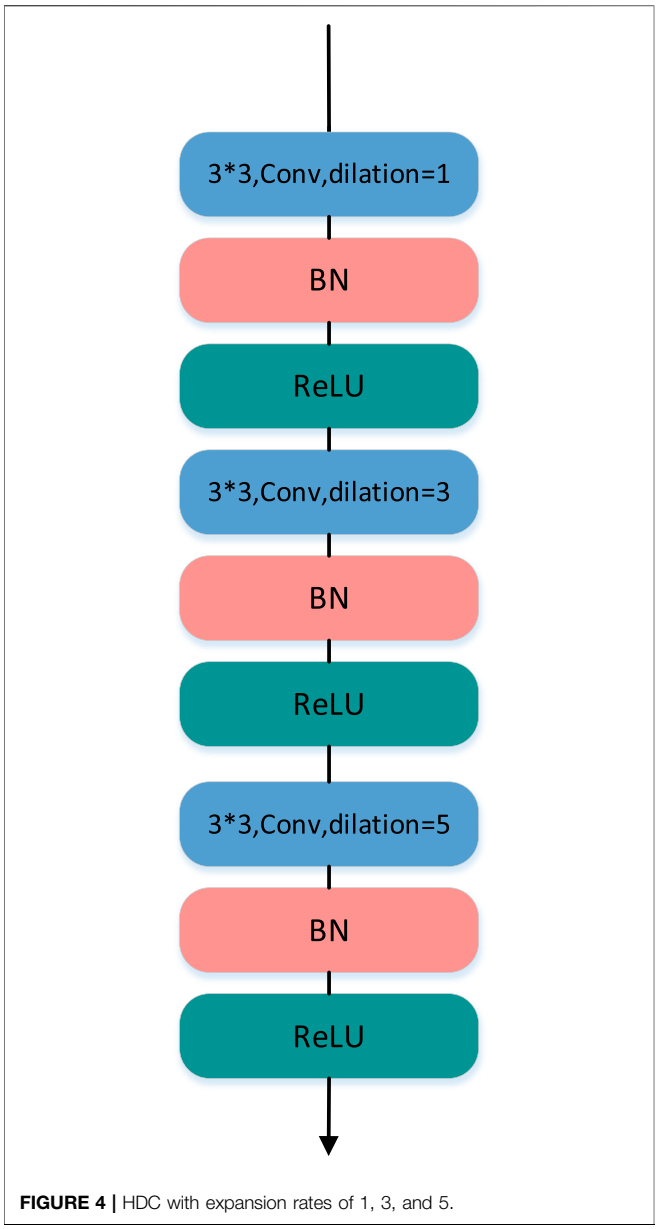

FIGURE 4 | HDC with expansion rates of 1, 3, and 5.

Multi-Scale Self-Attention Modules

In our study, we consider that the large-scale radar reflectivity factors will contain more complete meteorological information, such as the overall condition of the cloud mass and the meteorological conditions near the site will be much more important compared to the distant ones. To balance the consideration of large-scale images and small-scale images centered on the site, we design the MS-SA. Its model structure is shown in **Figure 5**.

The design of MS-SA is based on the non-local block module. The essence of the non-local block module is to capture the global spatio-temporal characteristics for each pixel point on the image, assign different weights, and finally aggregate them at each location to enrich the spatio-temporal characteristics (Wang et al., 2018b). The input is x_i, $i \in S^{m*n}$. S^{m*n} is the set of all pixel points in the image, if the input is spatio-temporal sequence then $i \in S^{t*m*n}$. The default input in this paper is the image. *conv_K*, *conv_Q*, *conv_V* are three different feature mappings, and we use 1*1 convolution operation to implement them in the model. The result of the input after *conv_K*, *conv_Q*, i.e., the Key module and Query module are multiplied to get the global pixel similarity score between any two pixels in the global pixel, which is expressed as $f_{i,j} = (W_Q * x_i)^T * (W_k * x_j)$. The expression can be simplified as $f = Q^T * K$. The similarity score is then transformed into the weight score of the global information for each pixel point by the softmax function. The output of each location is represented by z_i, which is the weighted sum of the global information.

$$z_i = W_z\left(\frac{1}{C(x)}\sum_{j=1}^{m*n} f_{i,j} * V\left(x_j\right)\right) + x_i \tag{6}$$

i is the index of the input and output points, j is the index of the global sampling points, $C(x)$ is the normalization factor, and W_z is the weight fraction of the global location with respect to location i. V is also a mapping operation on the input, i.e., the Value module, and multiplying the two results is the input of each location after non-equal distribution of weights. The addition of the input as the residual term in the formula can make the non-local block module more stable.

To take full advantage of the multi-scale input of the model, MS-SA receives two inputs, i.e., a small-scale feature map x_M and a large-scale feature map x_L. The small-scale feature map with feature mapping *conv_Q* is used as the Query module, and the large-scale feature map with feature mapping *conv_K* and *conv_V* is used as the Key and Value modules. Multiplying the Query module and Key module is the x_M and x_L pixel-by-pixel similarity scoring matrix $G_{i,j} = (W_Q * (x_M)_i)^T * (W_K * (x_L)_j)$. Each row of the similarity matrix is the similarity score of each position of x_M relative to all positions of x_L, and each column of the matrix is each position of x_M. After the softmax function, the elements in x_L that are similar to x_M will be given higher weights. These elements, after a series of previous convolution operations, will gather more spatial information that is not originally available in the small-scale relative to the elements of x_M, especially the edge positions. It can also be interpreted as allowing the small-scale range near the site to learn the spatial information of the wider region and gather in the center. It not only takes into account the spatial information of the larger area but also emphasizes the key information of the small area near the site. As **Figure 6** shows the evaluation process of similarity between multiple scales, the spatial information of the central region of the large-scale image has higher similarity with the spatial information of the small-scale image compared with the spatial information of the remaining location regions in the large-scale image. This is because the small-scale image is cropped from the central region of the large-scale image. The feature map processed by the multi-scale attention mechanism not only takes into account the spatial information of large regions but also emphasizes the key information of small regions near the site. The output of each position is

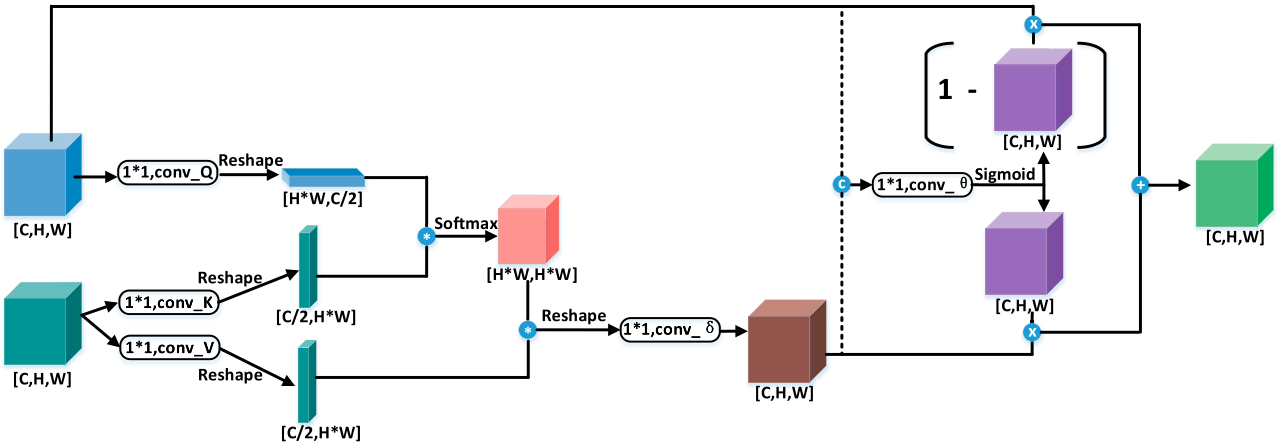

FIGURE 5 | The model receives inputs at two different scales and undergoes different convolution operations to generate the Query block, Key block and Value block, respectively. The weighted feature maps are generated by the Query and Key modules, and then multiplied with the Value module to generate the attention-passed feature maps. Finally, the final feature map is generated by mask branching.

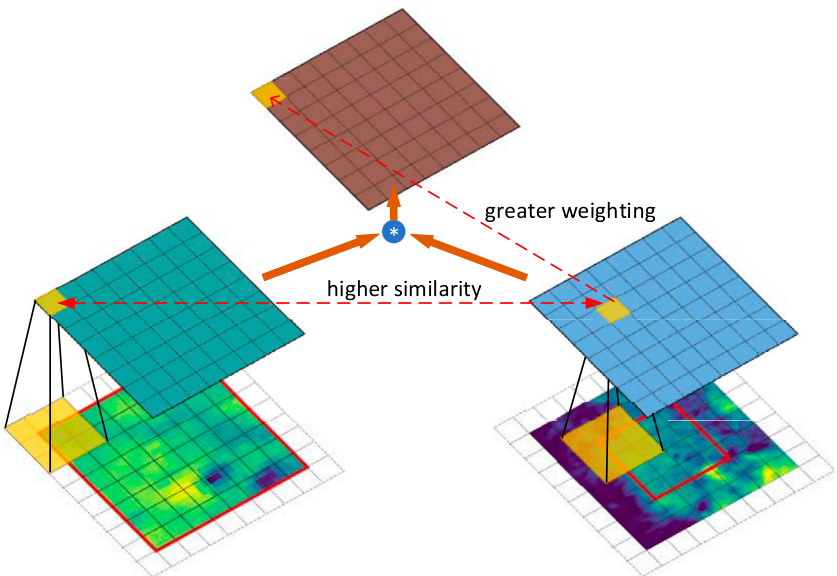

FIGURE 6 | The center region of the large-scale image (right) is convolved with respect to the upper left corner region of the small-scale image (left) and the upper left corner region of the small-scale image for similarity scoring. Since the small-scale image is cropped from the large-scale image, the same parts are given more weight in the similarity evaluation by the attention mechanism.

represented by z_i, which is the result of a preliminary fusion of small-scale and large-scale information:

$$z_i = W_z\left(\frac{1}{C(x)}\sum_{j=1}^{m*n} G_{i,j} * V\left((x_L)_j\right)\right) \tag{7}$$

To make the module more stable, the inputs are often connected at the end of the model as a shortcut. However, since there are features on an image that are beneficial for precipitation estimation and features that are not useful for precipitation estimation, a simple summation does not effectively utilize the features that are beneficial for precipitation estimation. Therefore, the model needs to have the ability to adaptively assign weights to each location. To solve this problem, we design a feature fusion module as a mask branch. Combining the input x_M and the output z in the channel direction after aggregating large-scale spatial information, learning spatial information by convolution operation, then feature mapping and adjusting the number of channels by convolution *conv_θ* with a convolution kernel size of 1, and finally activation by sigmoid function to be used as the assigned weights ζ.

$$R_i = \zeta * z_i + (1-\zeta) * (x_M)_i \tag{8}$$

Fully Connected Layer

The role of the fully-connected layer is to map the distributed high-level features extracted by the model to the target space. Each element of each layer in the fully connected layer is associated with all elements of the previous layer and has a strong fitting capability. The final layer of the fully connected layer outputs the predicted rainfall estimates.

Pooling Layer

The pooling layer mainly plays the role of reducing the dimensionality of the input feature vectors in this study. Pooling is divided into average pooling and maximum pooling, and we use maximum pooling.

$$y_{i,j}^{[l+1]} = \max_{1\le m\le f, 1\le n\le f} \left(x_{m,n}^{[l]}\right) \tag{9}$$

m, n are the coordinates of the pixel points of the convolution kernel, x is the position of the sampled points in the lth layer, and y is the result of the feature extraction in the $(l+1)th$ layer.

Loss Function

In the training process, the loss function we use is a weighted combination of mean square error (MSE) and mean absolute error (MAE). The specific reason is that in experiments, MSE is usually used as the loss function because MSE can better reflect the error between the true and predicted values. However, in QPE, anomalous values are inevitably generated due to strong convective weather and the influence of clutter. In addition to this, there is the problem of skewed distribution of rainfall data. If a single MSE is used as a loss function, it will cause the model to trend towards underestimating the evaluation of rainfall in heavy rainfall situations, as well as paying more attention to the anomalous values. The specific equation is:

$$Loss = a * MSE + b * MAE \tag{10}$$

where a, b are the weight parameters of MSE and MAE. After a series of experiments, we take the case where a is 1 and b is 10 to achieve the best training effect. In addition to this, during the training process, we use the gradient descent method to update the errors and get the optimal results based on the analysis of the experimental results in the time and space dimensions. Finally, the model has a learning rate of 0.0001, a batch size of 8, a training epoch of 100, and an optimization algorithm using Adam.

Evaluation Metrics

$$RMSE = \sqrt{\frac{1}{N}\sum_{i=1}^{N}(G_i - R_i)^2} \tag{11}$$

$$MAE = \frac{1}{N}\sum_{i=1}^{N}|G_i - R_i| \tag{12}$$

$$CC = \frac{\sum_{i=1}^{N}(G_i - \bar{G}_i)(R_i - \bar{R}_i)}{\sqrt{\sum_{i=1}^{N}(G_i - \bar{G}_i)^2}\sqrt{\sum_{i=1}^{N}(R_i - \bar{R}_i)^2}} \tag{13}$$

where N is the number of samples in the dataset, G is the ground truth value, and R is the model estimation. $\bar{G}$ is the mean of the ground truth value and $\bar{R}$ is the mean of the model estimation. The goal of our study is to make the larger the CC value, the smaller the values of $RMSE$ and MAE, which represent the excellence of the model.

Information Criteria

In addition, Since we will compare different models with different input variables and parameters in the **RESULTS** section, we use the Akaike information criterion (AIC) and the Bayesian information criterion (BIC) (Akaike, 1974; Burnham and Anderson, 2016; Kuha, 2016) which are typically penalized likelihood criteria used to compare non-nested models and can be used to measure the complexity and fit of individual models.

AIC is defined as:

$$\mathrm{AIC} = -2\ln\mathcal{L} + 2k \tag{14}$$

where $\mathcal{L}$ is the maximum likelihood of the model and k is the number of parameters required to fit the model to the nonlinear relationship.

BIC is defined as:

$$\mathrm{BIC} = -2ln\mathcal{L} + k\ln N \tag{15}$$

where the parameters $\mathcal{L}$ and k are defined in the same way as in the above equation. The parameter N is the number of samples used for the fit.

The AIC mainly depends on the accuracy of the first model and the number of parameters of the second model. When the number of parameters of the models used for comparison is similar, the higher the accuracy of the model, the lower the AIC value. When the difference in the accuracy of the models used for comparison is small, the simpler the model structure is, the lower the AIC value is. Therefore, the lower the AIC, the better the model performance. BIC additionally takes into account the sample size.

RESULTS

In this study, to show the superiority of MS-FCVNet, we compare it with the baseline model (Z-R model), the BPNN network (Rongrui and Chandrasekar, 1997), the CNN (1) network (Tian et al., 2020), and the CNN (2) network. It is worth noting that CNN (1) and CNN (2) have the same network structure, the only difference between them is the input to the network. We only use radar reflectivity factors as input for CNN (1). In contrast, we not only use single radar reflectivity factors as input, but also multivariate inputs for CNN (2). In detail, it takes the radar reflectivity factors as the main variable and temperature, humidity and elevation as covariates, in order to make the inputs

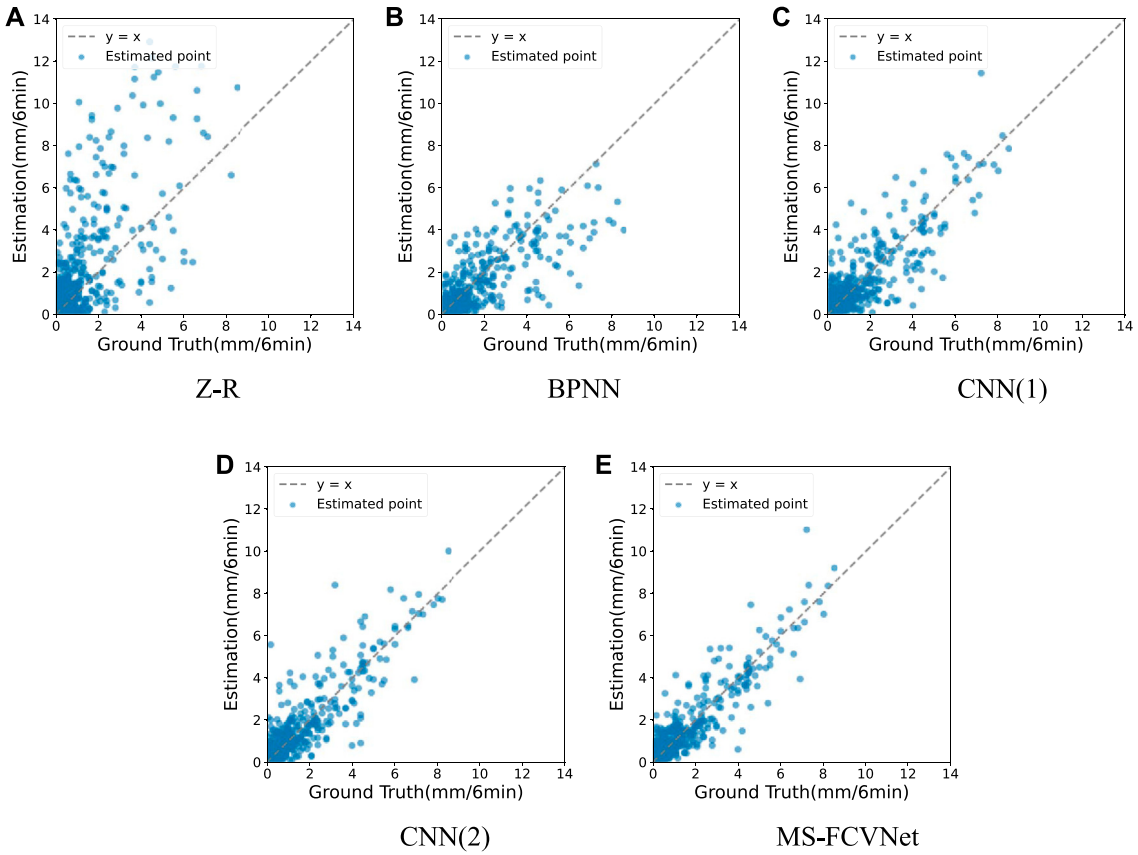

FIGURE 7 | Distribution of model **(A)** Z-R relationship, **(B)** BPNN, **(C)** CNN (1), **(D)** CNN (2) and **(E)** MS-FCVNet estimation in the test set relative to the ground truth value.

of the models used for comparison closer to MS-FCVNet and to make the differences in the experimental results more dependent on the enhancement brought by our model structure itself.

Figure 7 shows the distribution of the predicted values of the models relative to the ground truth value. The horizontal axis of each graph is the ground truth value and the vertical axis is the estimated rainfall value predicted by the model. The more accurate the model predicts, the more the dots in the graph are clustered on the $y = x$ axis. **Figure 7A** shows the distribution of the predicted values of the Z-R relationship. It is obvious that the distribution is very scattered, so it expresses that the predicted values of Z-R relationship differs significantly from the ground truth value and the traditional method does not fit the relationship between radar reflectivity factors and rainfall well compared to the deep learning method. Among the deep learning methods, as shown in **Figure 7B**, the distribution of the estimation predicted by BPNN performed more concentration compared to Z-R relationship, which proves the effectiveness of deep learning in fitting the radar reflectivity factors to the rainfall. In contrast, **Figures 7C,D** display that the performance of the BPNN is slightly less than that of the two CNN networks, which shows that rainfall has a strong spatial correlation, and the CNN captures this spatial structure that is ignored by the BPNN. For both CNN networks, **Figure 7D** reveals that the CNN (2) network that adds temperature, humidity and elevation as covariates gives more accurate rainfall values than CNN (1) which simply uses the radar reflectivity factors as input, indicating the correlation between rainfall and meteorological and geographic environments. Finally, **Figure 7E** shows that our proposed model can predict the rainfall that are more concentrated and closer to the $y = x$ axis, i.e., closer to the ground truth value than other models and proves the superiority of our model.

Table 1 shows the comparison of the Z-R, BPNN, CNN (1), CNN (2) and MS-FCVNet under the same evaluation metrics and information criteria. The first column of the table is the names of models. The second to the fifth columns of the table are the inputs to the model, which are the radar reflectivity factors, temperature, humidity, and elevation, respectively. The sixth column shows the selection of MS-SA moudle. The last five columns are the evaluation metrics RMSE, MAE, CC and information criteria AIC, BIC. Their specific meanings have been discussed in **Evaluation Metrics** Chapter and **Information Criteria** Chapter respectively. Lower RMSE, MAE values and higher CC values represent better performance of the model. The lower the AIC,BIC, the better the model can balance model complexity and accuracy. The experimental results show that the RMSE and MAE values of Z-R are higher and the CC values

TABLE 1 | The scores of Z-R, BPNN, CNN (1), CNN (2) and MS-FCVNet under evaluation metrics RMSE, MAE, CC at the 6-minute scale and information criteria AIC, BIC. The bold text is the optimal level of the evaluation index.

Model	dBZ	T	H	E	MS-SA	RMSE	MAE	CC	AIC(10^3)	BIC
Z-R	√					2.63	0.840	0.722	/	/
BPNN	√					0.640	0.289	0.748	46575.980	105250.350
CNN (1)	√					0.562	0.264	0.766	40443.567	89458.270
CNN (2)	√	√	√	√		0.549	0.249	0.796	40443.501	89392.440
MS-FVNet	√					0.463	0.220	0.819	44151.519	98218.340
	√	√				0.459	0.211	0.842	44153.220	98195.361
	√		√			0.458	0.219	0.836	44153.220	98195.361
	√			√		0.451	0.212	0.841	44153.171	98146.272
	√	√	√			0.461	0.225	0.821	44154.961	98213.429
	√	√		√		0.446	0.206	0.830	44154.863	98114.503
	√		√	√		0.453	0.207	0.846	44154.891	98192.792
	√	√	√	√		0.454	0.209	0.847	44156.648	98176.199
	√				√	0.482	0.240	0.823	45992.660	102961.961
	√	√			√	0.442	0.209	0.838	45994.136	102714.731
	√		√		√	0.449	0.207	0.840	45994.187	102765.799
	√			√	√	0.463	0.218	0.841	45994.271	102849.361
	√	√	√		√	0.461	0.205	0.844	45995.985	102840.107
	√	√		√	√	0.448	0.207	0.843	45995.901	102755.734
	√		√	√	√	0.446	0.211	0.838	45995.887	102741.181
	√	√	√	√	√	**0.424**	**0.201**	**0.861**	**40223.388**	**87141.007**

are lower, indicating that the fixed Z-R are more restricted and the predicted values are more different from the ground truth value. Considering that deep neural networks and simple linear regression, i.e., the computational process of Z-R relationship, are not comparable in terms of the number of parameters, the AIC, BIC of the Z-R relationship is not considered. The RMSE and MAE values of BPNN are lower than those of Z-R relationship, indicating that the estimation values of BPNN are closer to the ground truth and more concentrated in distribution. In addition, the CC values of BPNN are higher than the Z-R relationship, indicating that the predicted values of BPNN are more correlated with the rainfall. However, compared to the result of the CNN networks which shown in the 4th and 5th rows of the table, the performance of the BPNN is lower than the CNN networks. CNN can capture the spatial information of rainfall fields that BPNN cannot learn and the results demonstrate the influence of spatial correlation in the rainfall process on rainfall estimation and the correctness of using two-dimensional data input in our model. Comparing CNN (1) and CNN (2) networks, CNN (2), i.e., CNN network with covariates, has lower RMSE, MAE and higher CC than CNN (1). It indicates that the rainfall estimates of CNN network with covariates are more accurate and the necessity of the covariates during the precipitation estimation. The focus is on the ablation experiments of MS-FCVNet, i.e., rows 6th to 21st of **Table 1**. We consider the individual and combined cases of covariate inputs to the model and the changes brought by the addition of MS-SA to the network. Rows 6th to 9th in the table indicate the performance of the model is improved when adding temperature, humidity, and elevation as covariates alone, which is consistent with the findings of other researchers (Shu et al., 2007; Zhang Y. et al., 2021), indicating the relevance of meteorological factors, geographic factors, and precipitation. As shown in rows 10th to 13th of **Table 1**, when the combination of temperature, humidity and elevation were entered as covariates, the model performed better in some pairings than when they were added separately. It demonstrates that the interconnection of meteorological and geographical factors had an enhancing effect on the correct estimation of the model by adverse or noisy factors of rainfall. Row 14th of the table demonstrates that our model with the addition of the MS-SA module, there is a deterioration in the performance of our model with the radar reflectivity factors alone as an input compared to the model without the addition of the MS-SA module. This may be because, in the absence of covariate constraints, more features with less correlation with precipitation are extracted from the large-scale radar reflectivity factors. And the MS-SA module condenses the features extracted at large-scales into small-scales, which leads the model to focus on more features that are not conducive to precipitation estimation and has a bad effect on the estimation of rainfall. In contrast, the pairing with the MS-SA module produced better performance when meteorological factors were available as covariates. When elevation alone is added as a covariate, as shown in row 17th, the model performance is worse than that without the MS-SA module. The possible reason is that the addition of elevation makes the model more sensitive to areas with complex terrain, such as near stations in the southwestern region of Shijiazhuang, while the aggregation characteristics of the MS-SA module would make the model more insensitive to precipitation characteristics in flat terrain in the eastern region, and without the meteorological factors, the model will be even less effective. **Figure 8** shows the comparison of RMSE values, MAE values and CC values for the model with and without MS-SA, using only geography as a fixed covariate. We selected the three most southwestern sites 53693, 53698, 53795 and the three most northeastern sites 53699, 54621, 54701 for comparison experiments to test our conjecture. **Figure 8A**

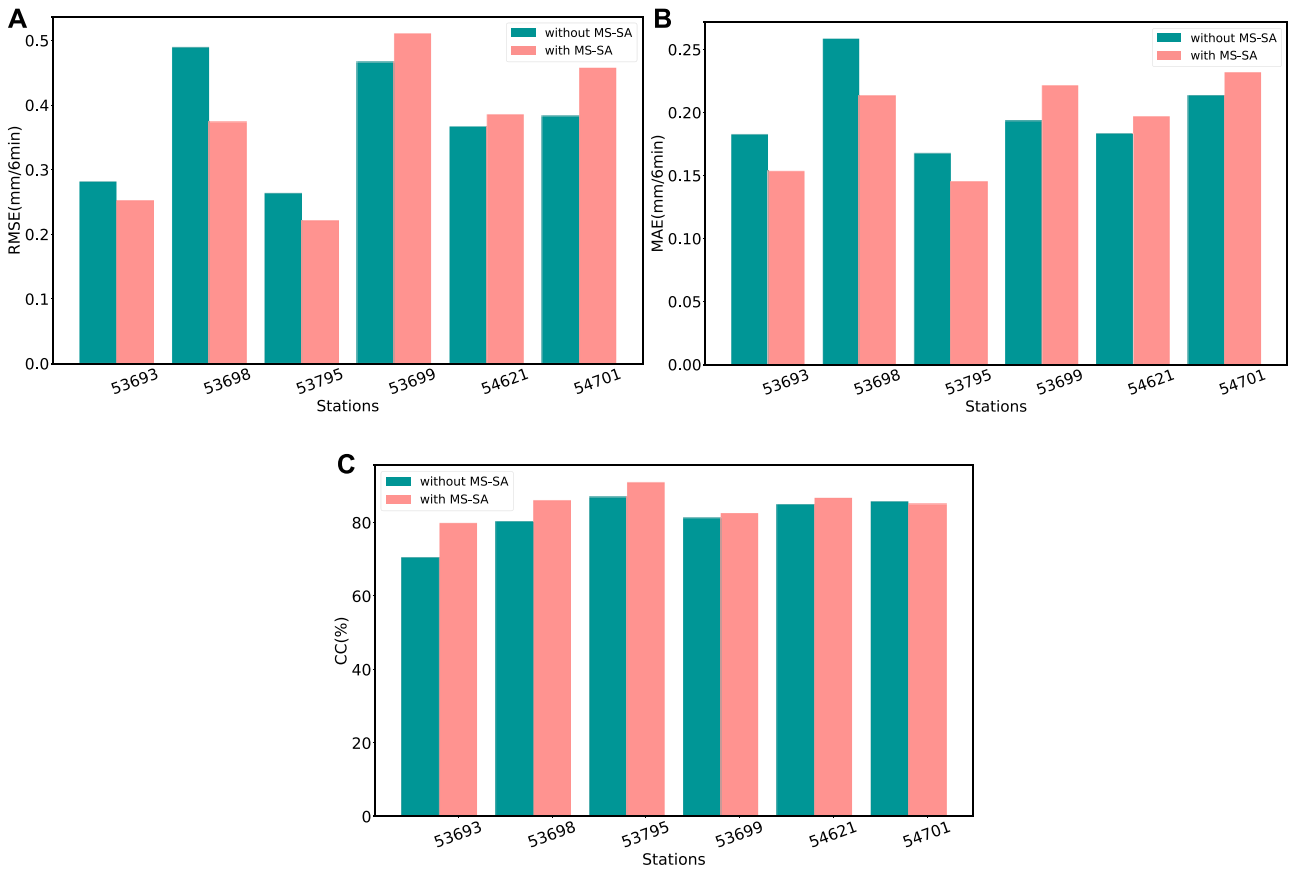

FIGURE 8 | Model incorporation of elevation and MS-SA modules for **(A)** RMSE scores, **(B)** MAE scores **(C)** CC scores at the southwestern Shijiazhuang NWSs 53693, 53698, 53795 and the northeastern NWSs 53699, 54621, 54701.

shows the lower RMSE values of the model with MS-SA added in the more complex topography in the southwest, and the lower RMSE values of the model without MS-SA in the plain area in the northeast. We can find that with the inclusion of the MS-SA module, the maximum overestimation of precipitation estimation by the model can be reduced in regions with complex topography, and the minimum underestimation of precipitation estimation can be mitigated. It is shown in **Figure 8B** that the inclusion of the MS-SA module in the model reduces the overall degree of error for areas with complex topography. From **Figure 8C**, it can be understood that model which includes the MS-SA module usually correlate with the true value of rainfall to a greater extent than the model without the MS-SA module. This is consistent with our hypothesis. Compared with Z-R relations, BPNN, CNN (1) and CNN (2), our model performs best with temperature, humidity, and elevation as covariates and with the addition of the MS-SA module. In addition, the RMSE is reduced by 8.42%, the MAE is reduced by 8.63%, and the CC is improved by 3.41% compared to the case without the inclusion of any covariates as well as the MS-SA module. According to the comparison of AIC and BIC of all compared models, it can be found that the AIC and BIC values of CNN (1) and CNN (2) are lower than those of BPNN, which indicates that BPNN stacking too many fully connected layers sacrifices the complexity of the model, but does not improve the accuracy too much. In addition, although our model performs well under most combination of input variables and MS-SA modules relative to the normal CNN networks, i.e., CNN (1),CNN (2) under other evaluation metrics, it sacrifices too much model complexity, which leads to high AIC,BIC. Finally, only the MS-FCVNet with the addition of temperature, humidity, and elevation as covariates and MS-SA has lower AIC, BIC than the other comparison models, indicating that our final model sacrifices model complexity but brings greater accuracy improvement. It is worth mentioning that the performance improvement of MS-FCVNet over the CNN model with the inclusion of meteorological factors and geographical factors is significant, which demonstrates the superiority of our model structure.

Figure 9 shows the performance of MS-FCVNet and the comparison model at 17 NWSs, 6-min scales, respectively. The horizontal axis of **Figure 9** represents the 17 NWSs, and the vertical axis shows the three evaluation metrics RMSE, MAE, and CC. Considering that the coefficients a, b in the Z-R relation have a small adaptation range and are influenced by geographic environment and weather conditions, we use different empirical coefficients a, b for the experiments located at 17

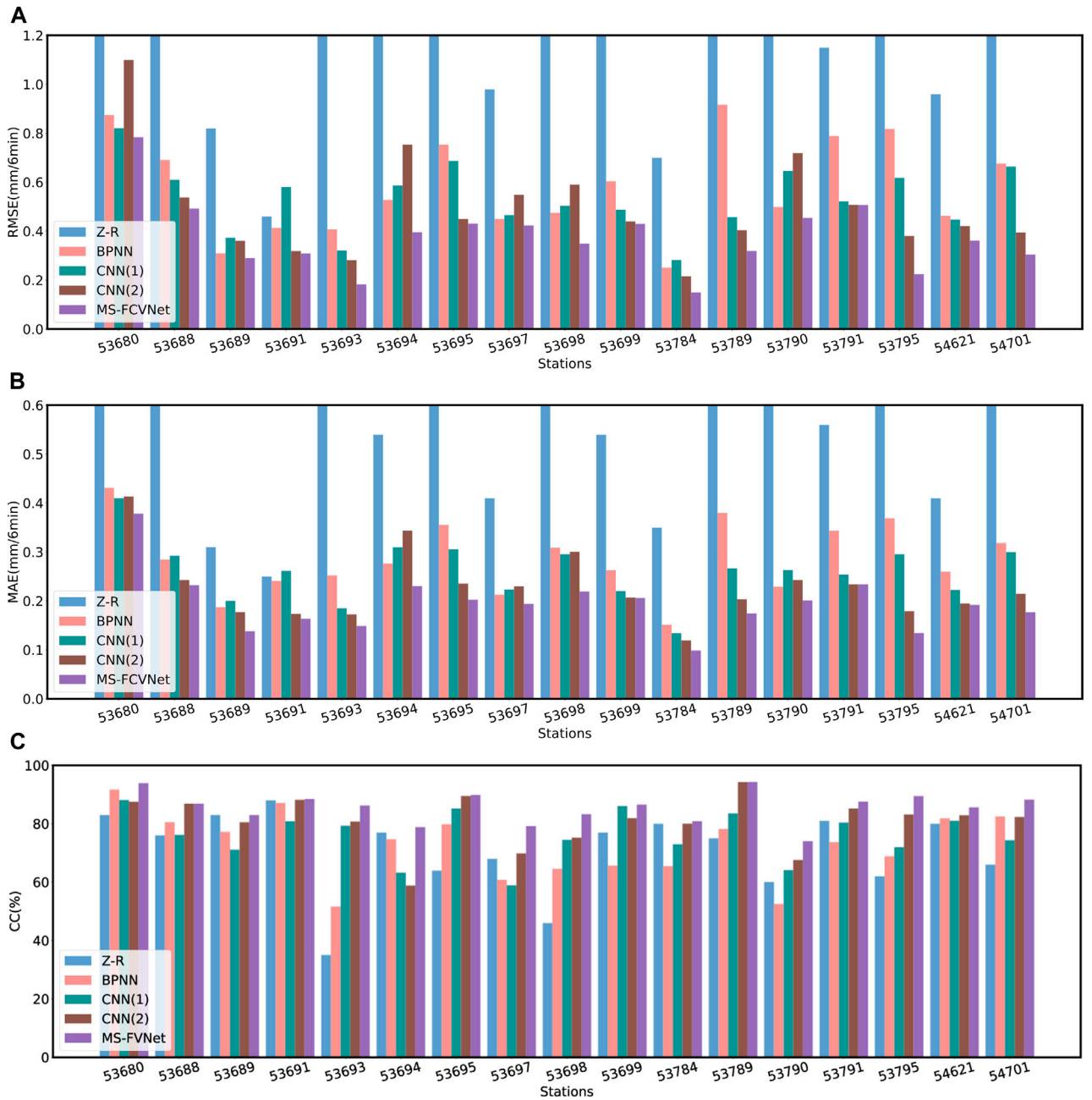

FIGURE 9 | MS-FCVNet scores for **(A)** RMSE, **(B)** MAE, **(C)** CC at 17 NWSs.

NWSs. From **Figure 9A**, we can see that the RMSE of Z-R relationship is less stable and has larger errors compared to other machine learning and deep learning algorithms. The BPNN, although better than the Z-R relationship in RMSE evaluation, still generally performs worse than the CNN network that can capture the spatial structure features on each NWS. The RMSE values of CNN (1) and CNN (2) networks have unbalanced performance levels across sites. MS-FCVNet performs optimally on each NWS with a stable RMSE values between 0.1 mm/6 min and 0.8 mm/6 min, which shows that MS-FCVNet overestimates and underestimates the rainfall to a much lesser extent than the other methods. **Figure 9B** shows the evaluation of MAE values for each model at each station, which is generally consistent with the results of RMSE values. The MAE values of MS-FCVNet are stable between 0.1 mm/6 min and 0.4 mm/6 min. Although the MAE values are high at station 53680, they are still lower than the other methods at this station, indicating that MS-FCVNet is lower than the other methods in terms of overall error. **Figure 9C**

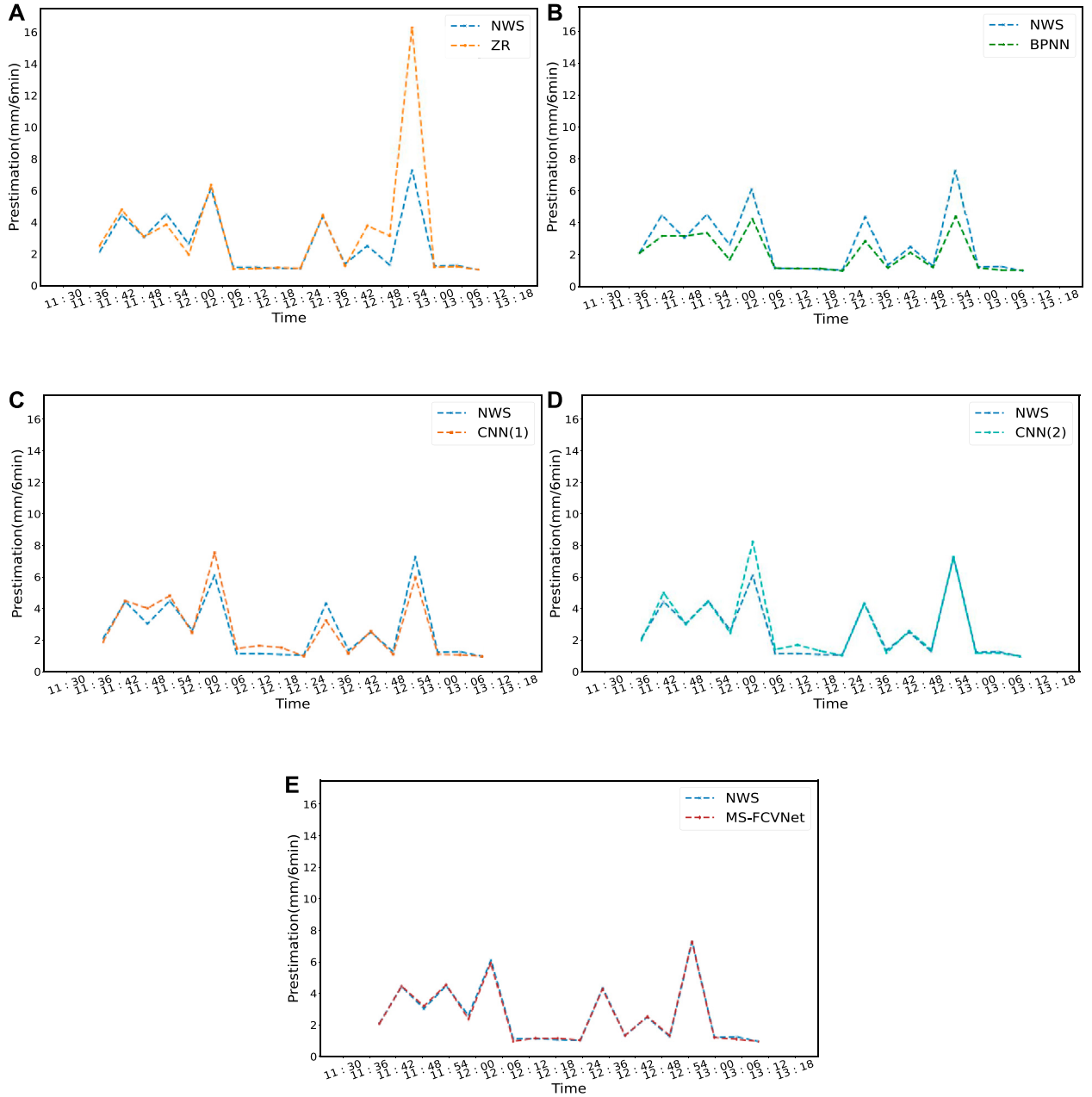

FIGURE 10 | Estimated values of models **(A)** Z-R relationship, **(B)** BPNN, **(C)** CNN (1), **(D)** CNN (2), **(E)** MS-FCVNet versus ground truth for the rainfall period from 11:30 to 13:18 on 12 August 2018.

shows the performance of the model in terms of correlation coefficient. The CC values of MS-FCVNet ranges from 74 to 93%, and although there are some fluctuations in the evaluation of the CC at each station, it is still generally better than other methods, indicating the strong correlation between the estimated value of MS-FCVNet and the real value of precipitation.

The performance of the model in strong convective weather is also an indicator that many studies have focused on (Zhang et al., 2020). **Figure 10** shows the time series line plot of the model and the true rainfall values for the NWS during a period of heavy rainfall on 12 August 2018. The horizontal coordinate is time and the vertical coordinate is the estimated and true rainfall of the model. Both the Z-R relationship and the BPNN have severe overestimated and underestimated performance in the time series. The Z-R relationship produces a positive deviation of 10 mm/6 min in the rainfall prediction at 13:00 on 12 August 2018, which severely overestimates the rainfall value, indicating the inaccuracy of the Z-R relationship in prediction during heavy rainfall. The rainfall estimate of BPNN reaches a negative deviation of 3.2 mm/6 min at the 13:00 moment on 12 August

2018, and differs significantly from the true value at all other moments, with an average deviation of 0.63 mm/6 min. The overestimation and underestimation of rainfall values predicted by the CNN (1) network are smaller than those of the Z-R relationship and the BPNN, but the bias values are still higher than those of the CNN (2) network at most moments, which demonstrates the effectiveness of the model's inclusion of covariates in reducing the bias values. The rainfall estimates of the MS-FCVNet network are close to those of the CNN (2) network. Although there are overestimates and underestimates, but overall, the estimation of MS-FCVNet are closer to the true values than the CNN network. Specifically, the positive deviation of our model's predicted values relative to the true rainfall values does not exceed 0.19 mm/6 min and the negative deviation does not exceed 0.25 mm/6 min.

CONCLUSION

In this study, we use deep learning techniques to demonstrate the effectiveness of multi-scale radar reflectivity factors, as well as meteorological and geographic factors as covariates in QPE. In addition, we developed an MS-SA module for better combining factors that favor precipitation estimation in the multi-scale, with some suppression of unfavorable factors. In particular, we have the following innovations and conclusion:

- Multi-scale deep learning networks are able to make accurate prediction of rainfall. Compared with deep learning networks with single-scale inputs, the large-scale feature maps in multi-scale can learn the complete rainfall field information over a wide region that also have an impact on rainfall gauges, and in addition, the small-scale feature maps can learn spatial information with stronger correlation with precipitation near the rainfall gauges. Therefore, multi-scale inputs can provide more accurate predictions for QPE.
- Temperature, humidity, and elevation as covariates can improve the QPE accuracy. Precipitation is a complex process, and there are many factors affecting precipitation, including meteorological and geographic factors. In addition, the spatial correlation of meteorological and geographic factors is considered to strengthen the spatial modeling capability of the model. In this study, two-dimensional meteorological and geographical factors were used as covariates to capture their spatial characteristics, and the validity was experimentally demonstrated.
- The multi-scale self-attentive module MS-SA is a new module we propose to better integrate factors that favor precipitation estimation in different scales and suppress irrelevant factors. It also can integrate covariates with radar reflectivity to constrain each other, reduce errors and make more accurate precipitation estimation. The experimental results further demonstrate the importance of multi-scale integration.
- The experimental results show that MS-FCVNet has a RMSE of 0.424 mm per 6 min for precipitation estimation, which is the best performance among Z-R, BPNN, CNN with only radar reflectivity factors as input and CNN with covariates involved, and maintains good performance in different geographical locations as well as time series.

The method proposed in this paper, especially the MS-SA module, is not lightweight enough and requires higher computational effort than the general method, which is also a future research direction. However, in general, our proposed model offers the possibility of more accurate estimation for QPE in operations.

DATA AVAILABILITY STATEMENT

The original contributions presented in the study are included in the article/supplementary material, further inquiries can be directed to the corresponding authors.

AUTHOR CONTRIBUTIONS

KS designed the experiments and performed the experiment. LZ and YF prepared the data. SC and LY guide the experiment. WT led the writing of the manuscript. All authors discussed the analysis and results and contributed to the manuscript.

FUNDING

This research was supported by the National Natural Science Foundation of China (Grant number 42175157 and 41875027), the National Key Research and Development Program of China (Grant number 2021YFE0116900) and the Shijiazhuang Meteorological Bureau (Grant No. SJZQXJHT 2019-45).

ACKNOWLEDGMENTS

The authors acknowledge Shijiazhuang City for providing Doppler radar data and weather station data.

REFERENCES

Akaike, H. (1974). A New Look at the Statistical Model Identification. *IEEE Trans. Autom. Contr.* 19 (6), 716–723. doi:10.1109/tac.1974.1100705

Alfieri, L., Claps, P., and Laio, F. (2010). Time-dependent Z-R Relationships for Estimating Rainfall Fields from Radar Measurements. *Nat. Hazards Earth Syst. Sci.* 10 (1), 149–158. doi:10.5194/nhess-10-149-2010

Barros, A. P., and Prat, O. P. (2009). Exploring the Transient Behavior of Z–R Relationships: Implications for Radar Rainfall Estimation. *J. Appl. Meteorol. Climatol.* 48 (10), 2127–2143. doi:10.1175/2009jamc2165.1

Berne, A., and Krajewski, W. F. (2013). Radar for Hydrology: Unfulfilled Promise or Unrecognized Potential? *Adv. Water Resour.* 51, 357–366. doi:10.1016/j.advwatres.2012.05.005

Beusch, L., Foresti, L., Gabella, M., and Hamann, U. (2018). Satellite-Based Rainfall Retrieval: From Generalized Linear Models to

Artificial Neural Networks. *Remote Sens.* 10 (6), 939. doi:10.3390/rs10060939

Burnham, K. P., and Anderson, D. R. (2016). Multimodel Inference. *Sociol. Methods Res.* 33 (2), 261–304. doi:10.1177/0049124104268644

Chen, H., Chandrasekar, V., Cifelli, R., and Xie, P. (2020). A Machine Learning System for Precipitation Estimation Using Satellite and Ground Radar Network Observations. *IEEE Trans. Geosci. Remote Sens.* 58 (2), 982–994. doi:10.1109/tgrs.2019.2942280

Chen, H., Chandrasekar, V., Tan, H., and Cifelli, R. (2019). Rainfall Estimation from Ground Radar and TRMM Precipitation Radar Using Hybrid Deep Neural Networks. *Geophys. Res. Lett.* 46 (17-18), 10669–10678. doi:10.1029/2019gl084771

Chen, H., and Chandrasekar, V. (2015). The Quantitative Precipitation Estimation System for Dallas–Fort Worth (DFW) Urban Remote Sensing Network. *J. Hydrol.* 531, 259–271. doi:10.1016/j.jhydrol.2015.05.040

Cremonini, R., and Tiranti, D. (2018). The Weather Radar Observations Applied to Shallow Landslides Prediction: A Case Study from North-Western Italy. *Front. Earth Sci.* 6. doi:10.3389/feart.2018.00134

Delrieu, G., Braud, I., Berne, A., Borga, M., Boudevillain, B., Fabry, F., et al. (2009). Weather Radar and Hydrology. *Adv. Water Resour.* 32 (7), 969–974. doi:10.1016/j.advwatres.2009.03.006

Fan, Z., Li, W., Jiang, Q., Sun, W., Wen, J., and Gao, J. (2021). A Comparative Study of Four Merging Approaches for Regional Precipitation Estimation. *IEEE Access* 9, 33625–33637. doi:10.1109/access.2021.3057057

Gagne, D. J., McGovern, A., and Xue, M. (2014). Machine Learning Enhancement of Storm-Scale Ensemble Probabilistic Quantitative Precipitation Forecasts. *Weather Forecast.* 29 (4), 1024–1043. doi:10.1175/waf-d-13-00108.1

Germann, U., Berenguer, M., Sempere-Torres, D., and Zappa, M. (2009). REAL-Ensemble Radar Precipitation Estimation for Hydrology in a Mountainous Region. *Q.J.R. Meteorol. Soc.* 135 (639), 445–456. doi:10.1002/qj.375

Giang, P. Q. (2021). Prediction of the Variability of Changes in the Intensity and Frequency of Climate Change Reinforced Multi-Day Extreme Precipitation in the North-Central Vietnam Using General Circulation Models and Generalized Extreme Value Distribution Method. *Front. Earth Sci.* 8. doi:10.3389/feart.2020.601666

Gou, Y., Ma, Y., Chen, H., and Wen, Y. (2018). Radar-derived Quantitative Precipitation Estimation in Complex Terrain over the Eastern Tibetan Plateau. *Atmos. Res.* 203, 286–297. doi:10.1016/j.atmosres.2017.12.017

Groisman, P. Y., Knight, R. W., Easterling, D. R., Karl, T. R., Hegerl, G. C., and Razuvaev, V. N. (2005). Trends in Intense Precipitation in the Climate Record. *J. Clim.* 18 (9), 1326–1350. doi:10.1175/jcli3339.1

Hong, Y., Gochis, D., Cheng, J.-t., Hsu, K.-l., and Sorooshian, S. (2007). Evaluation of PERSIANN-CCS Rainfall Measurement Using the NAME Event Rain Gauge Network. *J. Hydrometeorol.* 8 (3), 469–482. doi:10.1175/jhm574.1

Iwashima, T., and Yamamoto, R. (1993). NOTES AND CORRESPONDENCE : A Statistical Analysis of the Extreme Events : Long-Term Trend of Heavy Daily Precipitation. *J. Meteorol. Soc. Jpn.* 71 (5), 637–640. doi:10.2151/jmsj1965.71.5_637

Kuha, J. (2016). AIC and BIC. *Sociol. Methods Res.* 33 (2), 188–229. doi:10.1177/0049124103262065

Kühnlein, M., Appelhans, T., Thies, B., and Nauß, T. (2014). Precipitation Estimates from MSG SEVIRI Daytime, Nighttime, and Twilight Data with Random Forests. *J. Appl. Meteorol. Climatol.* 53 (11), 2457–2480. doi:10.1175/jamc-d-14-0082.1

Lee, T., Shin, J., Park, T., and Lee, D. (2014). Basin Rotation Method for Analyzing the Directional Influence of Moving Storms on Basin Response. *Stoch. Environ. Res. Risk Assess.* 29 (1), 251–263. doi:10.1007/s00477-014-0870-y

Legates, D. (2000). Real-Time Calibration of Radar Precipitation Estimates. *Prof. Geogr.* 52 (2), 235–246. doi:10.1111/0033-0124.00221

Liu, W., Zhang, Q., Fu, Z., Chen, X., and Li, H. (2018). Analysis and Estimation of Geographical and Topographic Influencing Factors for Precipitation Distribution over Complex Terrains: A Case of the Northeast Slope of the Qinghai–Tibet Plateau. *Atmosphere* 9 (9), 349. doi:10.3390/atmos9090349

Lu, Y., Jiang, S., Ren, L., Zhang, L., Wang, M., Liu, R., et al. (2019). Spatial and Temporal Variability in Precipitation Concentration over Mainland China, 1961–2017. *Water* 11 (5), 881. doi:10.3390/w11050881

Min, X., Ma, Z., Xu, J., He, K., Wang, Z., Huang, Q., et al. (2020). Spatially Downscaling IMERG at Daily Scale Using Machine Learning Approaches Over Zhejiang, Southeastern China. *Front. Earth Sci.* 8. doi:10.3389/feart.2020.00146

Moraux, A., Dewitte, S., Cornelis, B., and Munteanu, A. (2021). A Deep Learning Multimodal Method for Precipitation Estimation. *Remote Sens.* 13 (16), 3278. doi:10.3390/rs13163278

Moraux, A., Dewitte, S., Cornelis, B., and Munteanu, A. (2019). Deep Learning for Precipitation Estimation from Satellite and Rain Gauges Measurements. *Remote Sens.* 11 (21), 2463. doi:10.3390/rs11212463

Morin, E., and Gabella, M. (2007). Radar-Based Quantitative Precipitation Estimation over Mediterranean and Dry Climate Regimes. *J. Geophys. Res.* 112 (D20). doi:10.1029/2006jd008206

Oliver, M. A., and Webster, R. (1990). Kriging: a Method of Interpolation for Geographical Information Systems. *Int. J. Geogr. Inf. Syst.* 4 (3), 313–332. doi:10.1080/02693799008941549

Paxton, A., Schoof, J. T., Ford, T. W., and Remo, J. W. F. (2021). Extreme Precipitation in the Great Lakes Region: Trend Estimation and Relation with Large-Scale Circulation and Humidity. *Front. Water* 3. doi:10.3389/frwa.2021.782847

Ramos, M. H., Creutin, J.-D., and Leblois, E. (2005). Visualization of Storm Severity. *J. Hydrol.* 315 (1-4), 295–307. doi:10.1016/j.jhydrol.2005.04.007

Rongrui, X., and Chandrasekar, V. (1997). Development of a Neural Network Based Algorithm for Rainfall Estimation from Radar Observations. *IEEE Trans. Geosci. Remote Sens.* 35 (1), 160–171. doi:10.1109/36.551944

Rosenfeld, D., and Ulbrich, C. W. (2003). Cloud Microphysical Properties, Processes, and Rainfall Estimation Opportunities. *Radar Atmos. Sci. A Collect. Essays Honor David Atlas, Meteorol. Monogr.* 30, 237–258. doi:10.1007/978-1-878220-36-3_10

Sadeghi, M., Asanjan, A. A., Faridzad, M., Nguyen, P., Hsu, K., Sorooshian, S., et al. (2019). PERSIANN-CNN: Precipitation Estimation from Remotely Sensed Information Using Artificial Neural Networks–Convolutional Neural Networks. *J. Hydrometeorol.* 20 (12), 2273–2289. doi:10.1175/jhm-d-19-0110.1

Sadeghi, M., Nguyen, P., Hsu, K., and Sorooshian, S. (2020). Improving Near Real-Time Precipitation Estimation Using a U-Net Convolutional Neural Network and Geographical Information. *Environ. Model. Softw.* 134, 104856. doi:10.1016/j.envsoft.2020.104856

Shin, J.-Y., Ro, Y., Cha, J.-W., Kim, K.-R., and Ha, J.-C. (2019). Assessing the Applicability of Random Forest, Stochastic Gradient Boosted Model, and Extreme Learning Machine Methods to the Quantitative Precipitation Estimation of the Radar Data: A Case Study to Gwangdeoksan Radar, South Korea, in 2018. *Adv. Meteorol.* 2019, 1–17. doi:10.1155/2019/6542410

Shu, S.-J., Wang, Y., and Xiong, A.-Y. (2007). Estimation and Analysis for Geographic and Orographic Influences on Precipitation Distribution in China. *Chin. J. Geophys.* 50 (6), 1482–1493. doi:10.1002/cjg2.1168

Sivasubramaniam, K., Sharma, A., and Alfredsen, K. (2018). Estimating Radar Precipitation in Cold Climates: the Role of Air Temperature within a Non-parametric Framework. *Hydrol. Earth Syst. Sci.* 22 (12), 6533–6546. doi:10.5194/hess-22-6533-2018

Sønderby, C. K., Espeholt, L., Heek, J., Dehghani, M., Oliver, A., Salimans, T., et al. (2020). *Metnet: A Neural Weather Model for Precipitation Forecasting*. ArXiv, abs/2003.12140.

Sorooshian, S., Hsu, K., Gao, X., Tao, Y., and Ihler, A. (2016). A Deep Neural Network Modeling Framework to Reduce Bias in Satellite Precipitation Products. *J. Hydrometeorol.* 17 (3), 931–945. doi:10.1175/jhm-d-15-0075.1

Sun, W., and Huang, Y. (2011). Global Warming over the Period 1961-2008 Did Not Increase High-Temperature Stress but Did Reduce Low-Temperature Stress in Irrigated Rice across China. *Agric. For. Meteorol.* 151 (9), 1193–1201. doi:10.1016/j.agrformet.2011.04.009

Teschl, R., Randeu, W. L., and Teschl, F. (2006). "Weather Radar Estimates of Rainfall Adjusted to Rain Gauge Measurements Using Neural Networks," in The 2006 IEEE international joint conference on neural network proceedings. doi:10.1109/IJCNN.2006.247242

Tian, W., Yi, L., Liu, W., Huang, W., Ma, G., and Zhang, Y. (2020). Ground Radar Precipitation Estimation with Deep Learning Approaches in Meteorological Private Cloud. *J. Cloud Comp.* 9 (1). doi:10.1186/s13677-020-00167-w

Wang, P., Chen, P., Ye, Y., Ding, L., and Cottrell, G. (2018a). "Understanding Convolution for Semantic Segmentation," in IEEE Winter Conference on Applications of Computer Vision (WACV), 1451–1460. doi:10.1109/wacv.2018.00163

Wang, X., Girshick, R., Gupta, A., and He, K. (2018b). "Non-Local_Neural_Networks," in IEEE/CVF Conference on Computer Vision and Pattern Recognition, 7794–7803. doi:10.1109/CVPR.2018.00813

Wasko, C., Sharma, A., and Rasmussen, P. (2013). Improved Spatial Prediction: A Combinatorial Approach. *Water Resour. Res.* 49 (7), 3927–3935. doi:10.1002/wrcr.20290

Wu, H., Yang, Q., Liu, J., and Wang, G. (2020a). A Spatiotemporal Deep Fusion Model for Merging Satellite and Gauge Precipitation in China. *J. Hydrol.* 584, 124664. doi:10.1016/j.jhydrol.2020.124664

Wu, J., Han, Z., Xu, Y., Zhou, B., and Gao, X. (2020b). Changes in Extreme Climate Events in China under 1.5 °C–4 °C Global Warming Targets: Projections Using an Ensemble of Regional Climate Model Simulations. *J. Geophys. Res. Atmos.* 125 (2), 106. doi:10.1029/2019jd031057

Wu, W., Zou, H., Shan, J., and Wu, S. (2018). A Dynamical Z-R Relationship for Precipitation Estimation Based on Radar Echo-Top Height Classification. *Adv. Meteorol.* 2018, 1–11. doi:10.1155/2018/8202031

Wu, Y., Tang, Y., Yang, X., Zhang, W., and Zhang, G. (2021). Graph Convolutional Regression Networks for Quantitative Precipitation Estimation. *IEEE Geosci. Remote Sens. Lett.* 18 (7), 1124–1128. doi:10.1109/lgrs.2020.2994087

Yang, D., Koike, T., and Tanizawa, H. (2004). Application of a Distributed Hydrological Model and Weather Radar Observations for Flood Management in the Upper Tone River of Japan. *Hydrol. Process.* 18 (16), 3119–3132. doi:10.1002/hyp.5752

Zhang, C., Wang, H., Zeng, J., Ma, L., and Guan, L. (2020). Short-Term Dynamic Radar Quantitative Precipitation Estimation Based on Wavelet Transform and Support Vector Machine. *J. Meteorol. Res.* 34 (2), 413–426. doi:10.1007/s13351-020-9036-7

Zhang, M., Li, W., Bi, X., Zong, L., Zhang, Y., and Yang, Y. (2021a). Synergistic Modulations of Large-Scale Synoptic Patterns and Local-Scale Urbanization Effects on Summer Rainfall in South China. *Front. Clim.* 3. doi:10.3389/fclim.2021.771772

Zhang, Y., Chen, S., Tian, W., and Chen, S. (2021b). Radar Reflectivity and Meteorological Factors Merging-Based Precipitation Estimation Neural Network. *Earth Space Sci.* 8 (10). doi:10.1029/2021ea001811

Zhao, R., Chen, B., and Xu, X. (2021). Intensified Moisture Sources of Heavy Precipitation Events Contributed to Interannual Trend in Precipitation Over the Three-Rivers-Headwater Region in China. *Front. Earth Sci.* 9. doi:10.3389/feart.2021.674037

Conflict of Interest: The authors declare that the research was conducted in the absence of any commercial or financial relationships that could be construed as a potential conflict of interest.

Publisher's Note: All claims expressed in this article are solely those of the authors and do not necessarily represent those of their affiliated organizations, or those of the publisher, the editors and the reviewers. Any product that may be evaluated in this article, or claim that may be made by its manufacturer, is not guaranteed or endorsed by the publisher.

frontiers | Frontiers in Earth Science

ORIGINAL RESEARCH
published: 04 July 2022
doi: 10.3389/feart.2022.881579

Impact of Water Vapor on the Development of a Supercell Over Eastern China

Hao Wang[1]*, *Zeyong Hu*[1], *Peng Liu*[2] and *Feimin Zhang*[2]

[1]Northwest Institute of Eco-Environment and Resources, University of Chinese Academy of Sciences, Chinese Academy of Sciences, Lanzhou, China, [2]Key Laboratory of Climate Resource Development and Disaster Prevention of Gansu Province, College of Atmospheric Sciences, Lanzhou, China

In this study, the impact of water vapor on the improvement of precipitation simulation in a supercell event over eastern China is investigated by assimilating lightning data into the weather research and forecast (WRF) three-dimensional variational system. The results indicate that the vertical distribution of vapor plays a crucial role in convection precipitation simulation. The WRF alone fails to capture the vertical distribution of vapor, especially at higher altitudes, and vapor simulation is often weak in WRF. Assimilation of lightning data enhances the range and intensity of precipitation forecasts; assimilation of pseudo water vapor transformed from lightning data improves the convection intensification and updraft height of supercells by rectifying the vertical moisture profile. Lightning data assimilation can efficiently compensate for the paucity of observations during supercell growth, and the benefits of lightning data assimilation are concentrated in areas where lightning data is accessible. Further, the importance of microscale water vapor variations, which can be well represented by assimilating pseudo-water vapor, in representing the supercell's range and intensity is highlighted.

Keywords: supercell forecast, lightning, data assimilation, pseudo water vapor, modelling

OPEN ACCESS

Edited by:
Sanjeev Kumar Jha,
Indian Institute of Science Education and Research, Bhopal, India

Reviewed by:
Yoav Yosef Yair,
Interdisciplinary Center Herzliya, Israel
Ying Wang,
Nanjing University of Information Science and Technology, China
Zhiqiang Cui,
Chinese Academy of Meteorological Sciences, China

***Correspondence:**
Hao Wang
wanghao214@mails.ucas.ac.cn

Specialty section:
This article was submitted to Atmospheric Science, a section of the journal Frontiers in Earth Science

Received: *22 February 2022*
Accepted: *13 June 2022*
Published: *04 July 2022*

Citation:
Wang H, Hu Z, Liu P and Zhang F (2022) Impact of Water Vapor on the Development of a Supercell Over Eastern China. Front. Earth Sci. 10:881579. doi: 10.3389/feart.2022.881579

1 INTRODUCTION

Supercells are strong convective storms with deep and continuous rotating updrafts (Davies-Jones, 2015), accompanied by high-impact weather, such as strong winds, local rainstorms, hails, downbursts, and even tornadoes (Thompson et al., 2003; Bluestein et al., 2019; van Den Broeke 2020; Montopoli et al., 2021), which can cause loss to life and property. Despite major advances in numerical weather prediction, supercell forecast remains challenging due to their local, abrupt, high-intensity, small-scale, fast moving speed, brief lifetime, and other characteristics. It is challenging to comprehend the occurrence and evolution of supercells and increase the forecasting performance.

In the current stage, because of the insufficient physical details of mesoscale weather, especially for cumulus-scale processes, as well as the limitation of model resolution and parameterization, assimilation of different types of observation data to improve the model's initial conditions is a primary approach for improving the mesoscale weather system forecast performance. In general, radar data, which can capture finer features of mesoscale weather, are assimilated into the model to improve mesoscale weather simulation and forecasting in operating systems and can be applied to nowcasting systems (Yang et al., 2012). Assimilating satellite data can effectively improve the prediction performance of the general circulation models (Bauer et al., 2015). However, conventional observations have coarse spatial and temporal resolutions and are influenced by clouds and aerosols;

radar observations generally represent local information in a lower atmosphere and are easily influenced by terrain height; satellite radiances are assimilated in the models as their contributions to the forecast improvement are generally better for atmospheric temperature than for precipitation, and the associated effects are limited to the lower atmosphere owing to their source being the upper atmosphere. Therefore, for supercells with shorter (several hours) lifecycle convection systems, how to achieve maximum improvement effects by data assimilation needs to be further explored in both technical and theoretical aspects.

Lightning can identify areas of deep, mixed-phase convection because it is an important phenomenon that occurs within thunderstorm clouds (Mansell et al., 2007). Studies have indicated that assimilating lightning data is a promising approach to improve forecasts of severe convective precipitation events. For instance, based on an empirical lightning-convective rainfall relationship, Pessi and Businger (2009) showed that the assimilation of lightning data generally improved the simulation of the evolution of a winter storm. Lightning data assimilation can reproduce the observed cold pools during forecast initialization (Mansell et al., 2010). The results of Fierro et al. (2012) showed that the assimilation of lightning data can significantly improve the forecast of tornado outbreaks with respect to the timing and structures of convection (Qie et al., 2014). showed that the representation of convection is markedly improved when lightning data are assimilated.

Lightning data are non-conventional observations; they are generally assimilated into a model by transforming them into other model variables, such as temperature and moisture. Studies have suggested that lightning data can be assimilated into a model by transforming the data into vertical velocity (e.g., Gan et al., 2021), proxy radar reflectivity (e.g., Yang et al., 2015; Chen et al., 2020), ice-phase particles or graupel content (e.g., Allen et al., 2016; Wang et al., 2018; Chen et al., 2019; Kong et al., 2020), and rainfall. The relationship between lightning and model variables

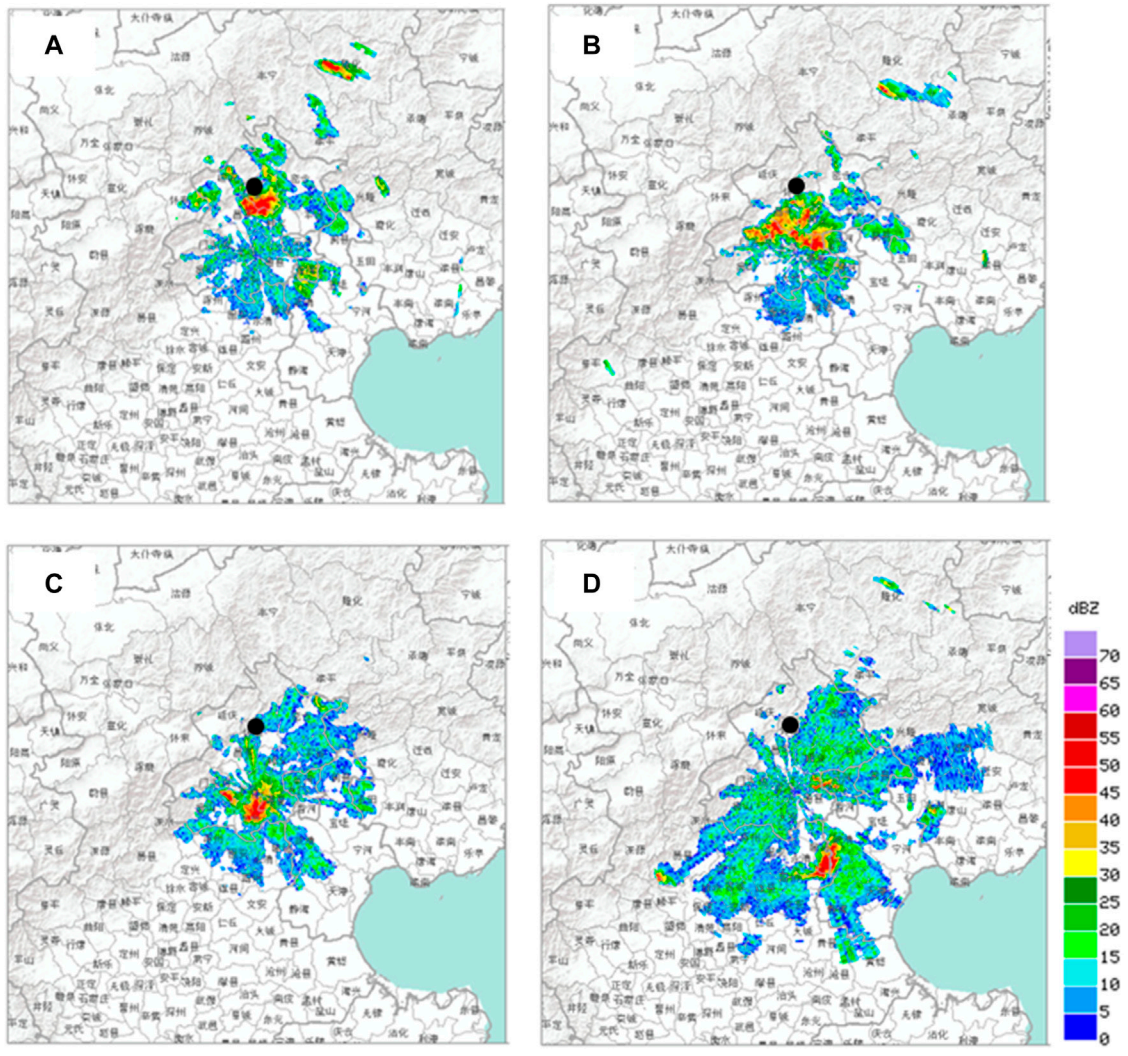

FIGURE 1 | Observed radar reflectivity (unit: dBZ) at **(A)** 1000 UTC, **(B)** 1100 UTC, **(C)** 1200 UTC, and **(D)** 1300 UTC on 9 August 2021.

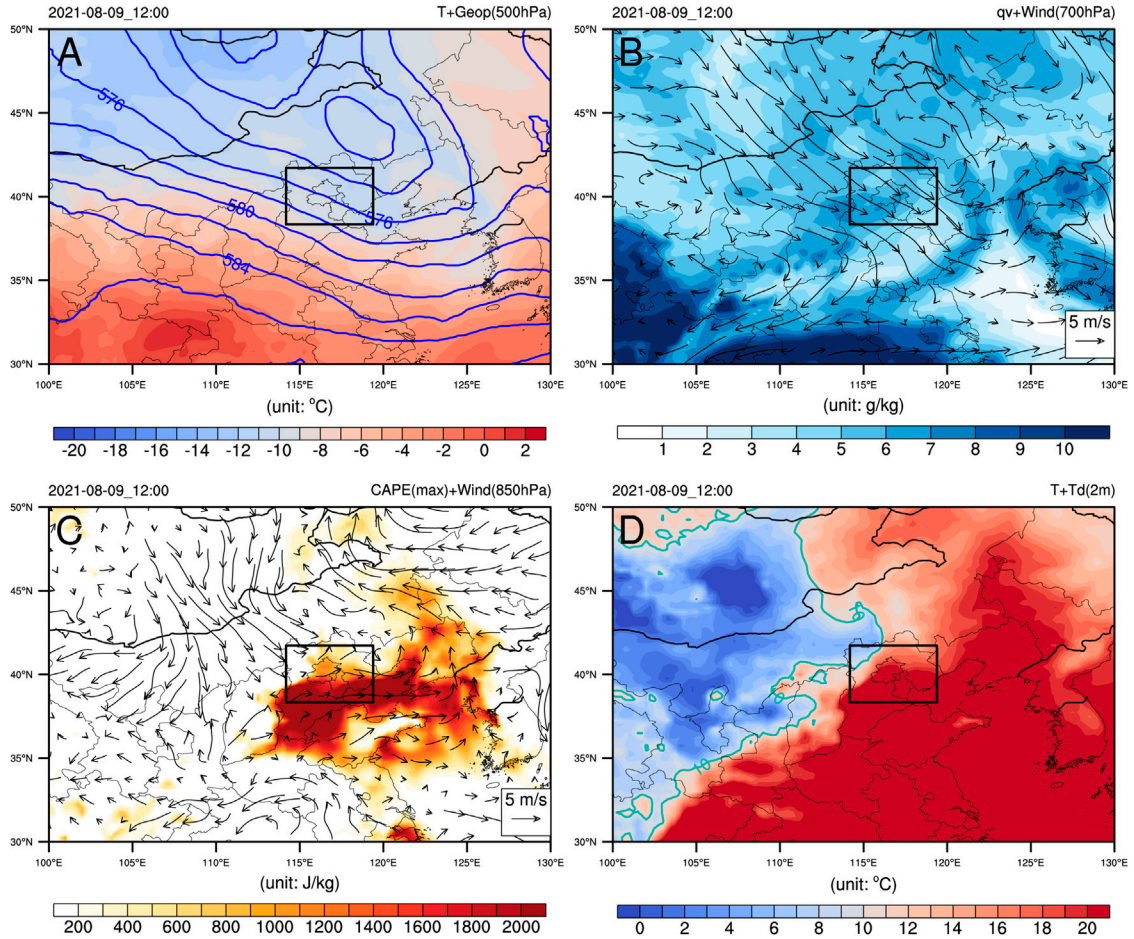

FIGURE 2 | Background of general circulation of supercell at 1200 UTC 9 August in terms of **(A)** geopotential height (blue contours, unit: gpm) and temperature (shaded colors, unit: °C) at 500 hPa, **(B)** specific humidity (shaded colors, unit: g kg^{-1}) and wind (vectors, unit: m s^{-1}) at 750 hPa, **(C)** convective available potential energy (shaded colors, unit: J kg^{-1}) and near-surface wind (vectors, unit: m s^{-1}), and **(D)** near-surface temperature (shaded color, unit: °C) and dew temperature (green contours, unit: °C). The black box denotes the regions where the supercell was active.

is not universal and is sensitive to storm location and climatic state. When vertical velocity, proxy radar reflectivity are used as a proxy variable of lightning, they are easily influenced by local climate and convective intensity, thus may not suitable for lightning data assimilation.

In general, the assimilation of lightning data has a shorter impact time on the forecast because it lacks the adjustment for the water vapor environment. Our recent results suggest that lightning data can be transformed into pseudo water vapor observations (Liu et al., 2021a; Liu et al., 2021b) and has been proven to be a potential approach to improve the forecast performance of convection. Therefore, investigating the water vapor characteristics of convective system by assimilating lightning data with the correct vapor condition could be a potential approach to improve supercell forecasts. The Lightning Mapping Imager (LMI) onboard FengYun-4A (FY-4A) geostationary satellites continuously measures the total lightning activity on high spatial and temporal resolution (Yang et al., 2017). LMI is able to effectively detect lightning events that occur during severe convective events over China (Liu et al., 2020; Chen et al., 2021).

In this study, the lightning data were assimilated into the weather research and forecasting (WRF) model by transforming it into pseudo water vapor observations to reproduce supercell precipitation. The impact and mechanism of lightning data assimilation were also investigated, focusing on the effects of water vapor on the forecast improvement of supercells. We primarily addressed two issues: 1) what changes in water vapor in supercells after lightning data assimilation? Second, what is the mechanism for the improvement of the representation of the supercell? Understanding these issues can be beneficial for deepening our understanding of convection processes.

Two numerical experiments were conducted on a supercell event in eastern China. The next section introduces the model, data, and experimental design as well as gives an overview of a supercell event. The validation of the lightning data assimilation against observations is presented in **Section 3**. The impact of

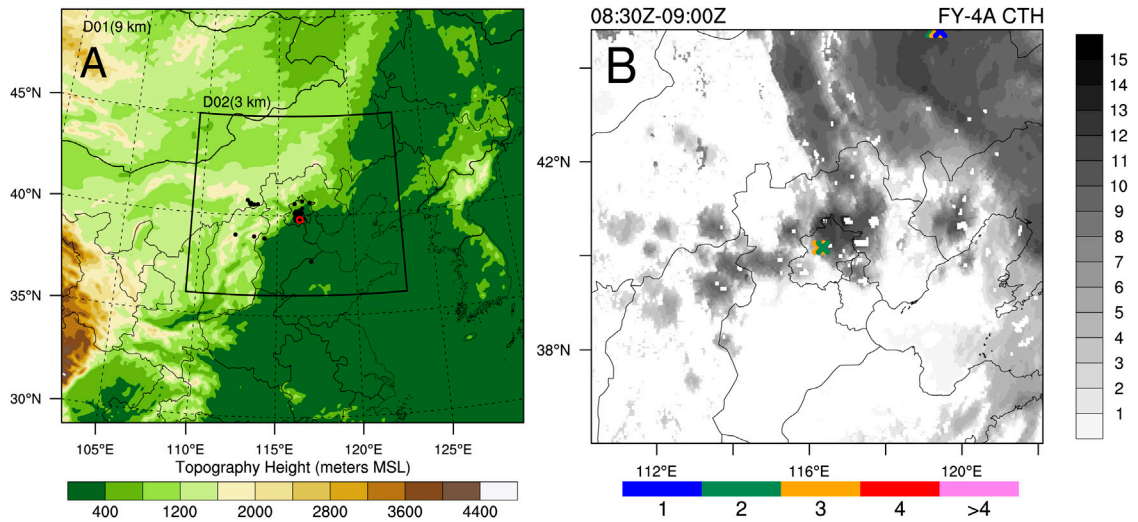

FIGURE 3 | (A) Configuration of the two nested weather research and forecasting (WRF) simulation domains in Lambert conformal projection, and the terrain height (shaded colors, unit: m). **(B)** The accumulated lightning frequency (colored cross signs) from 0,830 to 0900 UTC 9 August and the height of cloud top (gray shaded colors, unit: km). The black and red dots in panel **(A)** represent *in-situ* observed surface and sounding stations.

lightning data assimilation on the forecast is discussed in **Section 4**. The concluding remarks are presented in the final section.

2 INTRODUCTION OF WEATHER, DATA, AND METHODS

2.1 Overview of the Supercell Case

The supercell case selected in this study occurred near Beijing City in eastern China, which was active from 1000 UTC to 1300 UTC on 9 August 2021, with a maximum wind speed of 21 m s^{-1} and a maximum gust of 29 m s^{-1}, accompanied by heavy rainfall (over 30 mm h^{-1}) and hail. The strongest precipitation occurred at 1200 UTC, with an *in situ* observed maximum hourly precipitation of 34.4 mm. **Figure 1** shows the evolution of radar reflectivity from 1000 UTC to 1300 UTC. Results show that this was a typical supercell weather case, with the characteristics of high intensity (the strongest echo lasts for 50 dBZ), high speed (speed of approximately 30 km h^{-1}), and a small range (the range of echo intensity exceeding 45 dBZ is approximately 30 km), and it moved from north to south.

Figure 2 shows the synoptic weather situation at 1200 UTC on August 9, when the supercell was the strongest. The supercell occurred at a trough extending to the southeast at 500 hPa, with obvious cold advection (**Figure 2A**). At 750 hPa (**Figure 2B**), a cyclonic vortex is active in the supercell's northeastern direction, facilitating the passage of warm, moist air from southern China and maintaining unstable stratification. The near-surface data showed that (**Figures 2C,D**), in the region of Beijing city, cold dry air from the northwest and warm moist air from the southeast met, promoting the accumulation of convective unstable energy with high convective available potential energy.

2.2 Model, Data, and Experiment Design

An advanced research version of the weather research and forecasting (WRF ARW) model (Skamarock et al., 2008) version 4.2 was employed to simulate this case. Two domains in a two-way nested procedure were used, with grid spacing of 9 and 3 km (**Figure 3A**), and the innermost domain covers the main activity region of this supercell. A terrain-following (η) vertical coordinate system was adopted in this study, including 50 vertical levels. The physical parameterization scheme includes the Kain-Fritsch cumulus scheme (Kain 2004; for the "d01" domain only); the rapid radiative transfer model (Iacono et al., 2008) for longwave radiation and the Dudhia scheme for shortwave radiation; the Noah land surface scheme (Chen and Dudhia 2001); the ACM2 planetary boundary layer scheme (Pleim 2007); and the revised fifth Mesoscale Model (MM5) surface layer scheme (Jiménez et al., 2012).

The initial and boundary conditions were derived from the Global Forecast System (GFS), with a temporal resolution of 3 h and a horizontal resolution of 0.25° × 0.25°. Observations used in this study include atmospheric soundings, LMI lightning data from the FY-4A geostationary satellite, *in-situ* observed precipitation, and radar reflectivity image products. The data were obtained from the China Meteorological Administration (CMA). The ERA5 reanalysis data were used to analyze the synoptic weather conditions, as shown in **Figure 2**. Note that the simulation and observation data were interpolated at the same grid resolution during the comparison.

The "control" experiment (referred as CTL) simulates from 0600 UTC 9 August to 1200 UTC 9 August 2021 without any data assimilation, whereas the "lightning data assimilation" experiment (referred as LDA) simulates pseudo water vapor created from FY-4A lightning data. In the lightning data assimilation experiment, assimilation was performed only in the innermost domain. The pseudo-water vapor between the lifting condensation level (LCL)

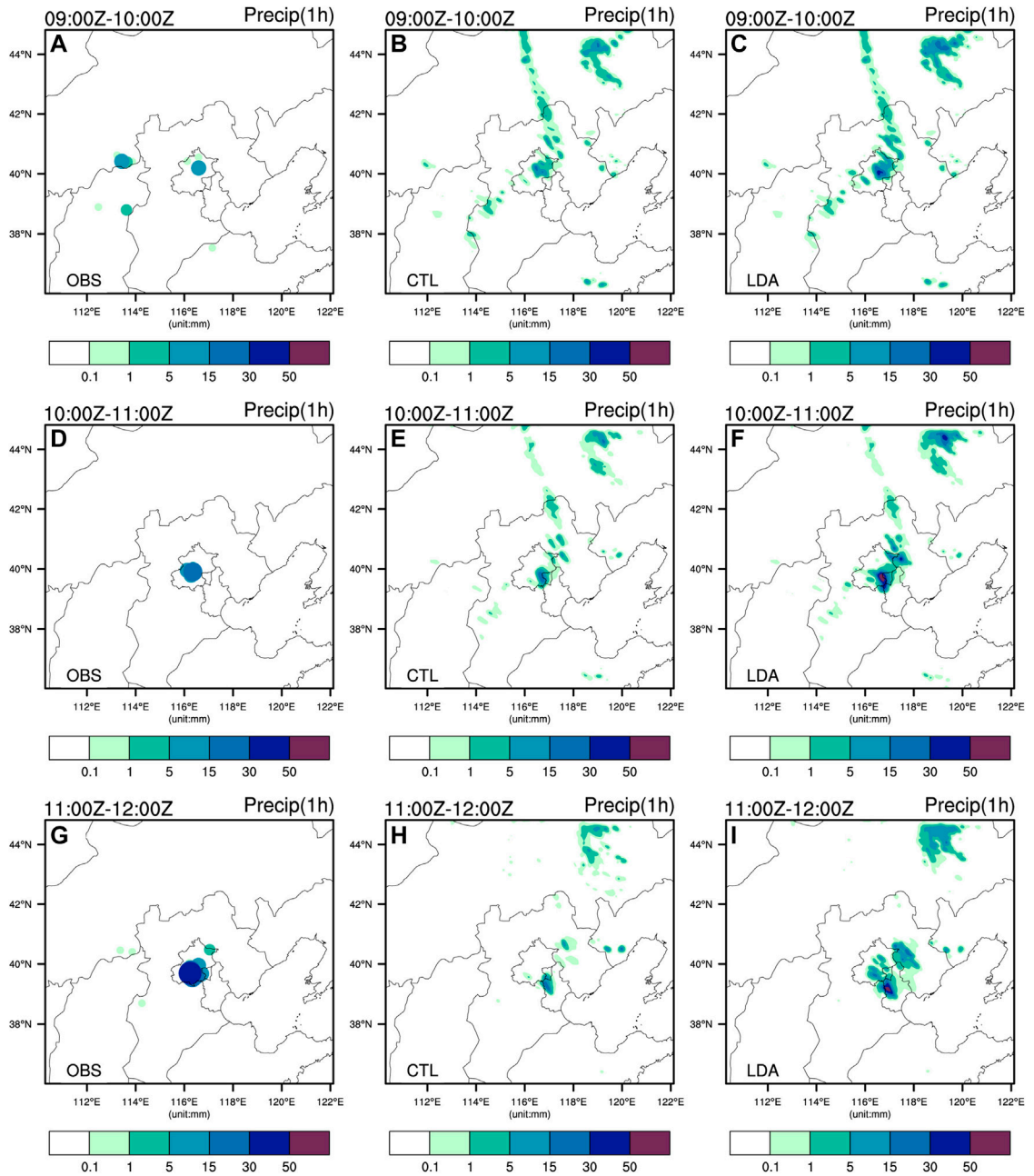

FIGURE 4 | Hourly precipitation from **(A–C)** 0,900 to 1000 UTC **(D–f)** 1,000 to 1100 UTC, and **(G–I)** 1,100 to 1200 UTC in **(A,D,G)** observations **(B,E,H)** control experiments, and **(C,F,I)** assimilation experiment.

and cloud top was first derived from the lightning frequency and then assimilated using the three-dimensional variational (3DVAR) system. The lightning frequency accumulated over 30 min from 0,830 to 0900 UTC. In the assimilation widow, when the observed lightning frequency per grid cell exceeds zero, then the relative humidity of the column in the background field less than 90% will be adjusted to 90%. The adjusted relative humidity field constitutes a three-dimensional pseudo-water vapor observation (Liu et al., 2020). The assimilation window was set from 0,830 to 0900 UTC, and the first 3 h were regarded as the model spin-up period and thus excluded.

Figure 3B shows the accumulated lightning frequency in the assimilation window from 0,830 to 0900 UTC, as well as the height of the cloud top derived from the FY-4A satellite. The data from FY-4A satellite indicated that the supercell is accompanied by vigorous convection, with a mean cloud top above 15 km. More importantly, several lightning events within the supercell were captured using the FY-4A satellite. Because atmospheric sounding data are only available at 0000 UTC and 1200 UTC, lightning data effectively compensates for the lack of observation during this time period and may be useful in improving the model's initial conditions.

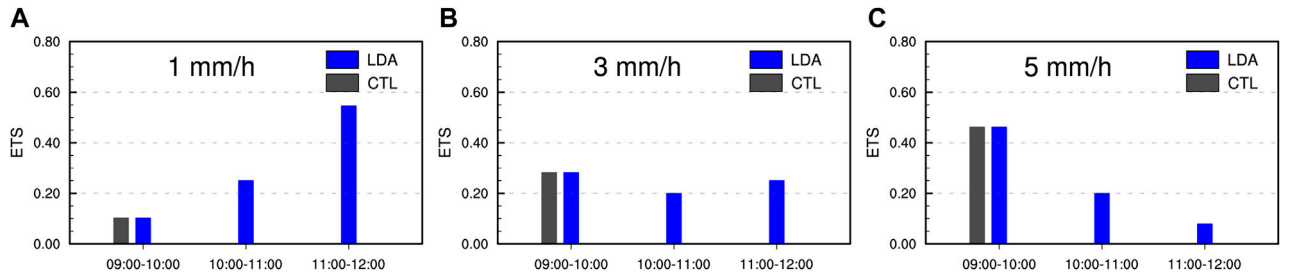

FIGURE 5 | Comparison of equitable threat score (ETS) for hourly precipitation between different experiment at the threshold of **(A)** 1 mm, **(B)** 3 mm, and **(C)** 5 mm. The gray and blue bars indicate control experiment and assimilation experiment, respectively.

TABLE 1 | Forecast skill scores of accumulative precipitation forecast at different thresholds for the control experiment (CTL) and the lightning assimilation experiment (LDA), respectively.

Precipitation threshold	Period (UTC)	POD		FAR		FBI	
		CTL	LDA	CTL	LDA	CTL	LDA
1.00 mm/h	09:00–10:00	0.17	0.17	0.00	0.00	0.17	0.17
	10:00–11:00	0.00	0.50	1.00	0.00	0.00	0.50
	11:00–12:00	0.00	0.82	1.00	0.00	0.00	0.82
3.00 mm/h	09:00–10:00	0.33	0.33	0.00	0.00	0.33	0.33
	10:00–11:00	0.00	0.33	1.00	0.00	0.00	0.33
	11:00–12:00	0.00	0.50	1.00	0.00	0.00	0.50
5.00 mm/h	09:00–10:00	0.50	0.50	0.00	0.00	0.50	0.50
	10:00–11:00	0.00	0.33	1.00	0.00	0.00	0.33
	11:00–12:00	0.00	0.33	1.00	0.25	0.00	0.44

The prediction performance of supercell precipitation is evaluated using forecast skill scores, including equitable threat score (ETS), the probability of detection (POD), false alarm ratio (FAR), and frequency bias (FBI) (Clark et al., 2010). The forecast skill scores are computed by hits (correct forecast of an event), misses (observed but not forecast event), false alarms (forecast but not observed event), and correct negatives (correct forecast of nonevent). Forecast skill scores are defined as follows:

$$\mathrm{ETS} = \frac{\mathrm{hits} - \mathrm{chance}}{\mathrm{hits} + \mathrm{misses} + \mathrm{false\ alarms} - \mathrm{chance}} \tag{1}$$

$$\mathrm{POD} = \frac{\mathrm{hits}}{\mathrm{hits} + \mathrm{misses}} \tag{2}$$

$$\mathrm{FAR} = \frac{\mathrm{false\ alarms}}{\mathrm{hits} + \mathrm{false\ alarms}} \tag{3}$$

$$\mathrm{FBI} = \frac{\mathrm{hits} + \mathrm{false\ alarms}}{\mathrm{hits} + \mathrm{misses}} \tag{4}$$

where,

$$\mathrm{chance} = \frac{(\mathrm{hits} + \mathrm{misses}) \cdot (\mathrm{hits} + \mathrm{false\ alarms})}{\mathrm{hits} + \mathrm{misses} + \mathrm{false\ alarms} + \mathrm{correct\ negatives}} \tag{5}$$

The larger ETS, POD and smaller FAR, the better of the forecast skills. ETS = 1, POD = 1 and FAR = 0 indicate a perfect forecast, while ETS = 0, POD = 0 and FAR = 1 stand for no forecast skill. FBI >1 indicates wet bias and FBI <1 indicates dry bias.

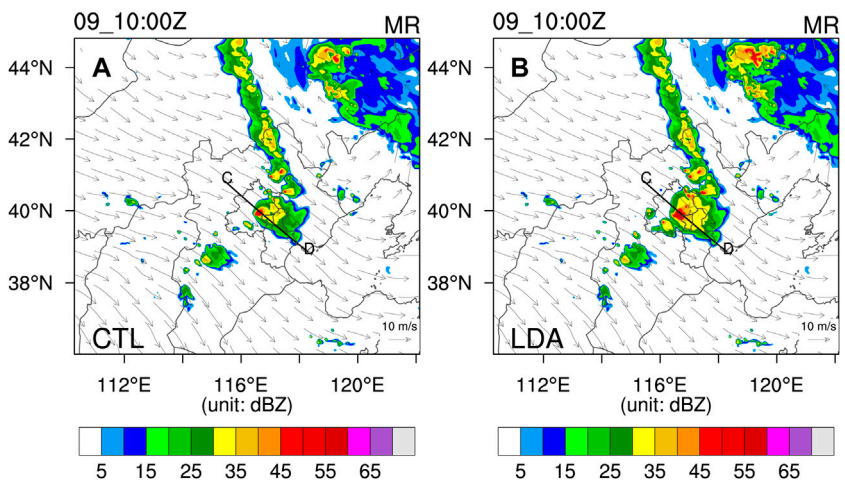

FIGURE 6 | Comparison of radar reflectivity (shaded color, unit: dBZ) and wind at 5 km above ground level (vectors, unit: m s^{-1}) at 1200 UTC 9 August between **(A)** control experiment and **(B)** assimilation experiment. The black line will be used for cross-section in **Figures 9C,D**.

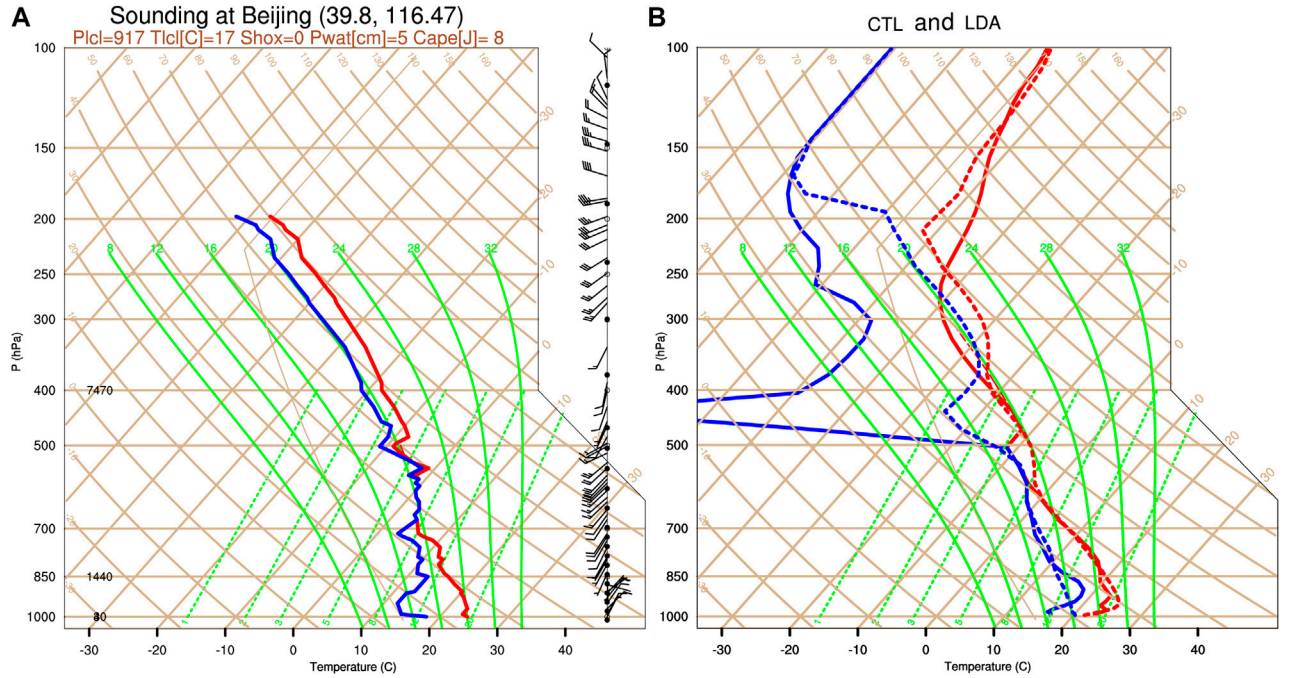

FIGURE 7 | Comparison of *in-situ* soundings at 1200 UTC 9 August between **(A)** observations and **(B)** simulations. The solid and dash lines in panel **(B)** represents control experiment and assimilation experiment, respectively.

TABLE 2 | The root mean squared error (RMSE) of temperature and relative humidity in control experiment (CTL) and lightning data assimilation experiment (LDA).

	RMSE (T, °C)	RMSE (RH, %)
CTL	3.79	36.54
LDA	3.01	15.12

TABLE 3 | Comparison of pressure of lifting condensational level (P_{LCL}, unit: hPa) and convective available potential energy (CAPE, unit: J kg^{-1}) between *in-situ* sounding and simulations of control experiment (CTL) and lightning data assimilation experiment (LDA).

	P_{LCL} (hPa)	CAPE (J kg^{-1})
Obs	917	8
CTL	902	134
LDA	950	39

3 RESULTS

3.1 Improvement in Supercell and Its Precipitation Forecast by Assimilating Lightning Data

To evaluate the supercell and its precipitation forecast improvement by assimilating lightning data, **Figure 4** compares the spatial distribution of hourly precipitation between simulations and observations at 0,900–1000 UTC, 1,000–1100 UTC, and 1,100–1200 UTC. The observation result shows that the observed hourly precipitation gradually strengthened from 0,900 UTC–1200 UTC in Beijing City (**Figures 4A,D,G**). Although the control-run accurately predicted the position of the observed maximum precipitation, the precipitation was underestimated (**Figures 4B,E,H**). The maximum precipitation, precipitation range, and their evolution are better portrayed and are closer to observations with the incorporation of lightning data (**Figures 4C,F,I**), implying that by incorporating lightning data into the model, the model's performance at simulating supercell precipitation can be improved.

Figure 5 depicts the performance of the precipitation forecast following lightning data assimilation using an ETS. **Table 1** compares the forecast skill scores of POD, FAR and FBI between the CTL experiment and LDA experiment. The result indicates that although the forecast performances were comparable between the two experiments during 0,900–1000 UTC, the control run achieved no forecast skill at different thresholds during 1,000–1100 UTC and 1,100–1200 UTC. With the assimilation of lightning data, the ETS and POD becomes larger at almost all times of the respective threshold, the FAR becomes smaller and FBI closes 1, indicating that lightning data assimilation outperforms the control run. Moreover, the forecast improvement of lightning data assimilation is most obvious for the 1 mm threshold, followed by the 3 and 5 mm thresholds.

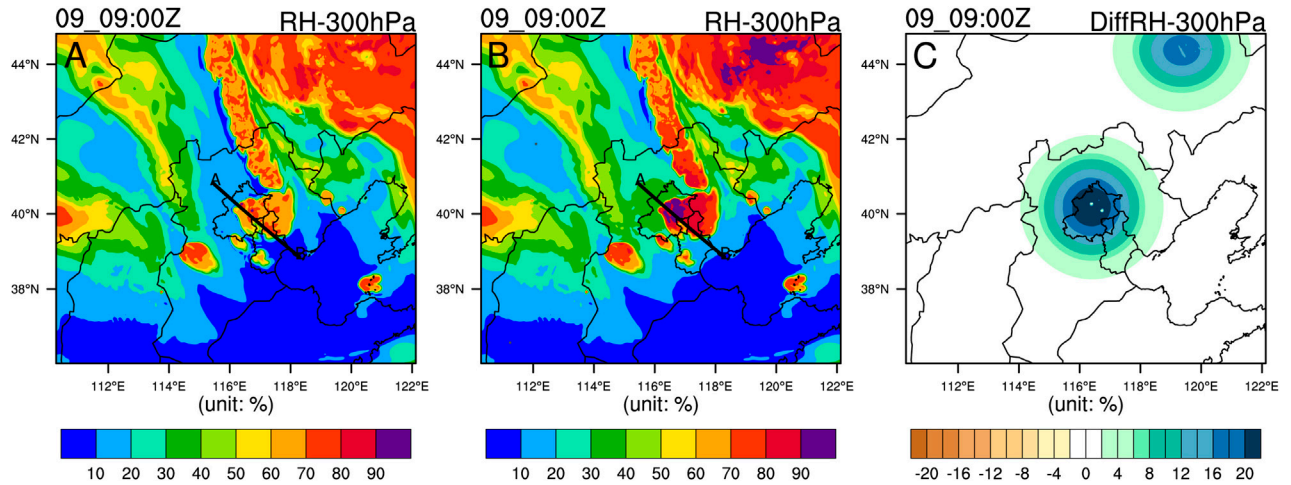

FIGURE 8 | Comparison of relative humidity (unit: %) at 300 hPa at 0900 UTC 9 August between **(A)** control experiment, **(B)** assimilation experiment, and **(C)** differences between control experiment and assimilation experiment. The solid lines represent cross-section in **Figures 9A,B**.

Furthermore, **Figure 6** compares the simulated radar reflectivity between the two experiments at 1200 UTC 9 August when the observed supercell convection was the strongest. The result shows that the two simulations accurately simulated the location of the observed radar reflectivity (**Figure 1C**), and the simulated wind fields are similar to the ERA5 reanalysis. Compared to the control experiment, the simulated radar reflectivity with the assimilation of lightning data has a bigger extent and intensity, which is closer to observations made. In addition, the forecast improvement is positioned mainly within the supercell itself, indicating that the range of influence of lightning data assimilation is limited.

3.2 Mechanism of Improving Supercell by Assimilating Lightning Data

The above results indicate that compared to the control run, the assimilation of lightning data evidently improves the range and intensity of the precipitation simulation. Due to satellite-based lightning data is transformed to pseudo water vapor in the assimilation experiment, which means that assimilation of lightning data presumably has a direct impact on moisture conditions.

To better understand the causes of improvement in the supercell event simulation, **Figure 7** compares the skew-T sounding results at 1200 UTC 9 August between observations and simulations. The observed result shows that (**Figure 7A**) a shear line is obvious in the lower atmosphere, where northeastlies exist below 850 hPa and southwestlies exist in a higher atmosphere, providing suitable dynamic conditions for the development of supercells. In addition, the atmosphere between 700 hPa and 500 hPa was almost saturated, suggesting that precipitation formed mainly in these layers. It is also notable that the dew depression (temperature *minus* dew temperature) is small above 500 hPa, suggesting that clouds are vigorous in higher atmosphere. A comparison of the simulation results in **Figure 7B** indicates that the assimilation of the lightning data improves the representation of the thermodynamic structure of the entire atmosphere when the supercell is active. Noticeable improvement is evident, especially in atmospheres above 500 hPa, where the simulated dry bias in the control run is alleviated by the incorporting lightning data. **Figure 7** also indicates that the most pronounced simulation discrepancies between the two experiments are the thermodynamic structures in the upper troposphere. The assimilation of lightning data reduces the RMSE of temperature and relative humidity (**Table 2**). The assimilation of lightning data results in a wetter environment at higher altitudes, which encourages the formation of precipitation.

Further comparison of the convective quantities in **Table 3** also indicates that, assimilation of lightning data produces weaker convective available potential energy (CAPE) and lower lifting condensation level (LCL) that are closer to observations.

To further examine the improvement in moisture in the supercell by assimilating lightning data, **Figure 8** compares the spatial distribution of relative humidity at 300 hPa between the control and assimilation experiments. The results indicate that assimilating lightning data amplifies the range and intensity of humidity in the vicinity of the supercell center (Beijing City). In addition, changes in the assimilation experiment are located within the supercell itself (**Figure 8C**), indicating that assimilating pseudo-water vapor can increase the water vapor content in the supercell.

Furthermore, the vertical cross-section of the simulated relative humidity and radar reflectivity between the control and assimilation experiments (**Figure 9**) indicates that the simulated relative humidity and radar reflectivity are very similar below 6 km; however, the assimilation of lightning data produces a more humid atmosphere and stronger radar reflectivity above 6 km. In general, the cumulonimbus top is approximately 12–15 km, which illustrates that this supercell is

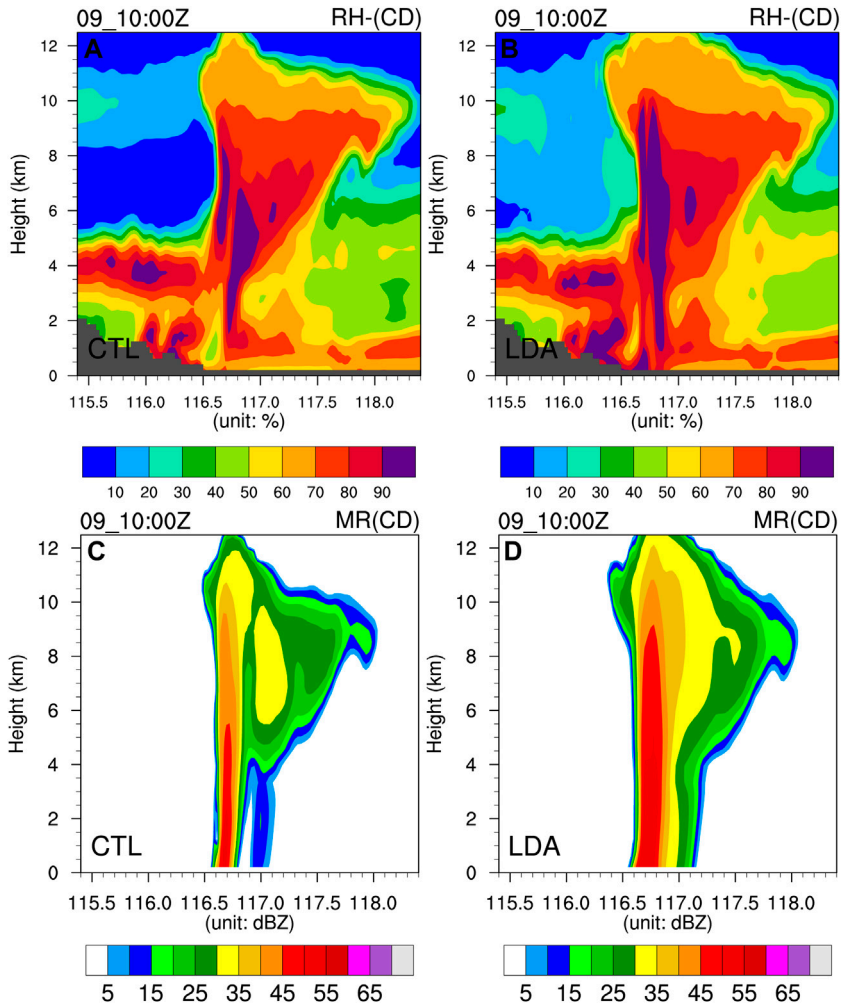

FIGURE 9 | Height vs. position cross-section of **(A,B)** relative humidity (unit: %) and **(C,D)** radar reflectivity (unit: dBZ) at 1000 UTC 9 August in **(A,C)** control experiment and **(B,D)** assimilation experiment.

high and deep, while control experiment simulates a lower supercell height, and assimilation improves the supercell's convection height. Observational studies have indicated that the maximum cumulus cloud base in eastern China can reach up to approximately 2,500 m in summer (Liu et al., 2016), implying that lightning data assimilation changes the thermodynamic profile in the whole cumulonimbus, i.e., it improves the supercell vertical structure and intensity.

A comparison of **Figure 7–9** indicates that the simulation improvement of the supercell by assimilating lightning data occurs in the higher troposphere, and the simulation improvement of moisture is most distinct, which improves the convection intensity and updraft height. In other words, pseudo-water vapor assimilation improves the simulation of convection intensity and updraft height by enhancing the water vapor content and vertical distribution, especially in the upper part of the supercell, which is more favorable for convection development due to near-saturated water vapor conditions.

4 DISCUSSION

Currently, either ground-based or satellite-based lightning observation systems, mainly observe the location of lightning and the intensity of discharge radiation. Therefore, lightning observations, which are not model variables, are difficult to assimilate directly into numerical models. A suitable lightning proxy variable is crucial for the assimilation of lightning observations. Studies have indicated that vertical velocity (Gan et al., 2021), ice-phase particles or graupel content (Qie et al., 2014), and proxy radar reflectivity (Wang et al., 2014; Chen et al., 2020) can be used as lightning proxy variable for lightning assimilation. Papadopoulos et al. (2005) and Mansell et al. (2007) used lightning data to adjust the water vapor content in convective parameterization scheme to active convection. However, this lightning data assimilation method relies on convective parameterization scheme, and is not applicable to convective-scale assimilation. Based on a Nudging method, an empirical formula was proposed to increase the water vapor content at the location of lightning occurrence (Fierro et al., 2015, 2016; Federico et al., 2019; Torcasio et al.,

2021); although this is also an effective way to improve model's moisture field, however, uncertainties exist because of the empirical formula is not suitable for different climatic state and convective intensities. Results of our study indicate that, assimilating lightning data by transforming it to pseudo-water vapor within clouds is an effective approach to improve supercell prediction. Specifically, it is emphasized that suitable water vapor conditions in upper atmosphere are also important for convective system development. In theory, when water vapor is used as a lightning proxy variable, it requires a relative longer spin-up period because of the initialization of convection through the physical parameterization scheme, which can be seen in the limited improvement of lightning data assimilation in the first forecasting hour.

The framework proposed in this study is expected to be useful for understanding the role of water vapor in the upper atmosphere in the development of a supercell. Although the findings of this study are based on only one case study, when compared to the findings of other studies, it is affirmative that assimilating lightning data can distinctly improve the water vapor in convections. Long-term verification or additional cases are undoubtedly required to acquire more reliable results. Besides, assimilation of water vapor in combination with other proxy variables (vertical velocity, ice-phase particles, etc.) could be the potential way to improve supercell simulation.

5 CONCLUSION

Based on the assimilation of lightning data derived from FY-4A satellite, this study investigates the potential benefit of water vapor characteristics and their associated changes in convective scale event (supercell). Furthermore, the mechanism of improving supercell simulation by assimilation was also investigated. The major results are summarized as follows:

The mesoscale model generally fails to reproduce precipitation during convection events. In this case, the vertical distribution of water vapor has prominent biases in both its intensity and location. These biases can be rectified by assimilating lightning data if they are readily transformed into pseudo water vapor. Therefore, assimilating lightning data has potential benefits for convection forecasting in the numerical weather prediction.

Forecast improvement of supercells by assimilating satellite-based lightning data is most prominent for thermodynamic profiles in the atmospheres above 3 km (700 hPa), with the maximum improvement above 7 km (400 hPa). In particular, the improvement in the moisture profile is most distinct, which means that lightning data can effectively detect the bottom of convective clouds, assimilation of satellite data can improve the vertical profile of the convective system, and improve the forecasting of the supercell accordingly.

Satellite-based lightning data offers abundant moisture information. Assimilation of lightning data can considerably improve the range and intensity of convective scale precipitation simulations. These improvements are obvious in regions where lightning data are available, demonstrating that the effects of lightning data assimilation are localized.

In the early stage of a thunderstorm, lightning can be detected by satellite. In our case, the lightning data is assimilated when supercell was developing; therefore, assimilating lightning data by transforming lightning to pseudo-water vapor is a potential approach for improving the forecast of convective weather events from its genesis stage to strongest stage, such as supercells. The forecast improvement is closely related to the improvement of water vapor content and its vertical distribution, which implies that moisture in the upper level of a convection event is important, and assimilating lightning data by transforming it into pseudo water vapor observation can rectify the moisture bias in the upper level.

DATA AVAILABILITY STATEMENT

The raw data supporting the conclusions of this article will be made available by the authors, without undue reservation.

AUTHOR CONTRIBUTIONS

HW designed the experiment, conducted the analysis and wrote the initial manuscript; ZH discussed and contributed to the idea; PL processed the data and figures; FZ improved the manuscript.

FUNDING

This study is supported by the Natural Science Foundation of Gansu Province of China (Nos. 20JR10RA654 and 20JR5RA309), and the Fundamental Research Funds for the Central Universities (lzujbky-2021-kb24).

ACKNOWLEDGMENTS

Authors are grateful for efforts by the National Center for Atmospheric Research (NCAR) in making the community research version of the WRF model available on the public website. Computational support by Supercomputing Center of Lanzhou University is also appreciated.

REFERENCES

Allen, B. J., Mansell, E. R., Dowell, D. C., and Deierling, W. (2016). Assimilation of Pseudo-GLM Data Using the Ensemble Kalman Filter. *Mon. Wea. Rev.* 144, 3465–3486. doi:10.1175/mwr-d-16-0117.1

Bauer, P., Thorpe, A., and Brunet, G. (2015). The Quiet Revolution of Numerical Weather Prediction. *Nature* 525, 47–55. doi:10.1038/nature14956

Bluestein, H. B., Thiem, K. J., Snyder, J. C., and Houser, J. B. (2019). Tornadogenesis and Early Tornado Evolution in the El Reno, Oklahoma, Supercell on 31 May 2013. *Mon. Wea. Rev.* 147, 2045–2066. doi:10.1175/mwr-d-18-0338.1

Bouttier, F., and Kelly, G. (2001). Observing-system Experiments in the ECMWF 4D-Var Data Assimilation System. *Q.J R. Met. Soc.* 127 (574), 1469–1488. doi:10.1002/qj.49712757419

Chen, F., and Dudhia, J. (2001). Coupling an Advanced Land Surface-Hydrology Model with the Penn State-NCAR MM5 Modeling System. Part I: Model

Implementation and Sensitivity. *Mon. Wea. Rev.* 129, 569–585. doi:10.1175/1520-0493(2001)129<0569:caalsh>2.0.co;2

Chen, Y., Yu, Z., Han, W., He, J., and Chen, M. (2020). Case Study of a Retrieval Method of 3D Proxy Reflectivity from FY-4A Lightning Data and its Impact on the Assimilation and Forecasting for Severe Rainfall Storms. *Remote Sens.* 12, 1165. doi:10.3390/rs12071165

Chen, Z., Qie, X., Liu, D., and Xiong, Y. (2019). Lightning Data Assimilation with Comprehensively Nudging Water Contents at Cloud-Resolving Scale Using WRF Model. *Atmos. Res.* 221, 72–87. doi:10.1016/j.atmosres.2019.02.001

Chen, Z., Qie, X., Sun, J., Xiao, X., Zhang, Y., Cao, D., et al. (2021). Evaluation of Fengyun-4A Lightning Mapping Imager (LMI) Performance during Multiple Convective Episodes over Beijing. *Remote Sens.* 13, 1746. doi:10.3390/rs13091746

Clark, A. J., Gallus, W. A., Jr, and Weisman, M. L. (2010). Neighborhood-Based Verification of Precipitation Forecasts from Convection-Allowing NCAR WRF Model Simulations and the Operational Nam. *Weather Forecast.* 25 (5), 1495–1509. doi:10.1175/2010waf2222404.1

Davies-Jones, R. (2015). A Review of Supercell and Tornado Dynamics. *Atmos. Res.* 158-159, 274–291. doi:10.1016/j.atmosres.2014.04.007

Dudhia, J. (1989). Numerical Study of Convection Observed during the Winter Monsoon Experiment Using a Mesoscale Two-Dimensional Model. *J. Atmos. Sci.* 46, 3077–3107. doi:10.1175/1520-0469(1989)046<3077:nsocod>2.0.co;2

Federico, S., Torcasio, R. C., Avolio, E., Caumont, O., Montopoli, M., Baldini, L., et al. (2019). The Impact of Lightning and Radar Reflectivity Factor Data Assimilation on the Very Short-Term Rainfall Forecasts of RAMS@ISAC: Application to Two Case Studies in Italy. *Nat. Hazards Earth Syst. Sci.* 19 (8), 1839–1864. doi:10.5194/nhess-19-1839-2019

Fierro, A. O., Clark, A. J., Mansell, E. R., MacGorman, D. R., Dembek, S. R., and Ziegler, C. L. (2015). Impact of Storm-Scale Lightning Data Assimilation on WRF-ARW Precipitation Forecasts during the 2013 Warm Season over the Contiguous United States. *Weather Rev.* 143, 757–777. doi:10.1175/mwr-d-14-00183.1

Fierro, A. O., Gao, J., Ziegler, C. L., Calhoun, K. M., Mansell, E. R., and MacGorman, D. R. (2016). Assimilation of Flash Extent Data in the Variational Framework at Convection-Allowing Scales: Proof-Of-Concept and Evaluation for the Short-Term Forecast of the 24 May 2011 Tornado Outbreak. *Mon. Wea. Rev.* 144, 4373–4393. doi:10.1175/mwr-d-16-0053.1

Fierro, A. O., Mansell, E. R., Ziegler, C. L., and MacGorman, D. R. (2012). Application of a Lightning Data Assimilation Technique in the WRF-ARW Model at Cloud-Resolving Scales for the Tornado Outbreak of 24 May 2011. *Mon. Weather Rev.* 140, 2609–2627. doi:10.1175/mwr-d-11-00299.1

Gan, R., Yang, Y., Qiu, X., Wang, R., Qiu, X., and Zhu, L. (2021). Assimilation of the Maximum Vertical Velocity Converted from Total Lightning Data through the EnSRF Method. *J. Geophys. Res. Atmos.* 126, e2020JD034300. doi:10.1029/2020jd034300

Jiménez, A. P., Dudhia, J., Gonzalez-Rouco, J. F., Navarro, J., Juan, P., and Garcia-Bustamante, E. (2012). A Revised Scheme for the WRF Surface Layer Formulation. *Mon. Wea. Rev.* 140, 898–918. doi:10.1175/MWR-D-11-00056.1

Kain, J. S. (2004). The Kain-Fritsch Convective Parameterization: An Update. *J. Appl. Meteor.* 43, 170–181. doi:10.1175/1520-0450(2004)043<0170:tkcpau>2.0.co;2

Kong, R., Xue, M., Fierro, A. O., Jung, Y., Liu, C., Mansell, E. R., et al. (2020). Assimilation of GOES-R Geostationary Lightning Mapper Flash Extent Density Data in GSI EnKF for the Analysis and Short-Term Forecast of a Mesoscale Convective System. *Mon. Weather Rev.* 148, 2111–2133. doi:10.1175/mwr-d-19-0192.1

Liu, P., Yang, Y., Gao, J., Wang, Y., and Wang, C. (2020). An Approach for Assimilating FY4 Lightning and Cloud Top Height Data Using 3DVAR. *Front. Earth Sci.* 8, 288. doi:10.3389/feart.2020.00288

Liu, P., Yang, Y., Lai, A., Wang, Y., Fierro, A. O., Gao, J., et al. (2021a). Assimilating FY-4A Lightning and Radar Data for Improving Short-Term Forecasts of a High-Impact Convective Event with a Dual-Resolution Hybrid 3DEnVAR Method. *Remote Sens.* 13, 3090. doi:10.3390/rs13163090

Liu, P., Yang, Y., Xin, Y., and Wang, C. (2021b). Impact of Lightning Data Assimilation on Forecasts of a Leeward Slope Precipitation Event in the Western Margin of the Junggar Basin. *Remote Sens.* 13, 3584. doi:10.3390/rs13183584

Liu, X. M., Zhang, M. J., Wang, S. J., Zhao, P. P., Wang, J., and Zhou, P. P. (2016). Estimation and Analysis of Precipitation Cloud Base Height in China. *Meteoro. Mon.* 42 (9), 1135. doi:10.7519/j.issn.1000-0526.2016.09.011

Liu, Y., Wang, H., Li, Z., and Wang, Z. (2021). A Verification of the Lightning Detection Data from FY-4A LMI as Compared with ADTD-2. *Atmos. Res.* 248, 105163. doi:10.1016/j.atmosres.2020.105163

Mansell, E. R., Ziegler, C. L., and MacGorman, D. R. (2007). A Lightning Data Assimilation Technique for Mesoscale Forecast Models. *Mon. Wea. Rev.* 135, 1732–1748. doi:10.1175/mwr3387.1

Montopoli, M., Picciotti, E., and Baldini, L. (2021). Gazing inside a Giant-Hail-Bearing Mediterranean Supercell by Dual-Polarization Doppler Weather Radar. *Atmos. Res.* 264, 105852. doi:10.1016/j.atmosres.2021.105852

Papadopoulos, A., Chronis, T. G., and Anagnostou, E. N. (2005). Improving Convective Precipitation Forecasting through Assimilation of Regional Lightning Measurements in a Mesoscale Model. *Mon. Weather Rev.* 133, 1961–1977. doi:10.1175/mwr2957.1

Pessi, A. T., and Businger, S. (2009). The Impact of Lightning Data Assimilation on a Winter Storm Simulation over the North Pacific Ocean. *Mon. Wea. Rev.* 137 (10), 3177–3195. doi:10.1175/2009mwr2765.1

Pleim, J. E. (2007). A Combined Local and Nonlocal Closure Model for the Atmospheric Boundary Layer. Part I: Model Description and Testing. *J. Appl. Meteor. Climatol.* 46, 1383–1395. doi:10.1175/jam2539.1

Qie, X., Zhu, R., Yuan, T., Wu, X., Li, W., and Liu, D. (2014). Application of Total-Lightning Data Assimilation in a Mesoscale Convective System Based on the WRF Model. *Atmos. Res.* 145-146, 255–266. doi:10.1016/j.atmosres.2014.04.012

Skamarock, W. C., Klemp, J. B., Dudhia, J., Grill, D. O., Barker, D. M., Duda, M. G., et al. (2008). *A Description of the Advanced Research WRF Version 3*. Boulder, Colorado, USA: NCAR. NCAR/TN-475+STR.125.

Thompson, R. L., Edwards, R., Hart, J. A., Elmore, K. L., and Markowski, P. (2003). Close Proximity Soundings within Supercell Environments Obtained from the Rapid Update Cycle. *Wea. Forecast.* 18, 1243–1261. doi:10.1175/1520-0434(2003)018<1243:cpswse>2.0.co;2

Torcasio, R. C., Federico, S., Comellas Prat, A., Panegrossi, G., D'Adderio, L. P., and Dietrich, S. (2021). Impact of Lightning Data Assimilation on the Short-Term Precipitation Forecast over the Central Mediterranean Sea. *Remote Sens.* 13, 682. doi:10.3390/rs13040682

Van Den Broeke, M. (2020). Disdrometer, Polarimetric Radar, and Condensation Nuclei Observations of Supercell and Multicell Storms on 11 June 2018 in Eastern Nebraska. *Atmosphere* 11, 770. doi:10.3390/atmos11070770

Wang, H., Liu, Y., Zhao, T., Liu, Y., Xu, M., Shen, S., et al. (2018). Continuous Assimilation of Lightning Data Using Time-Lagged Ensembles for a Convection-Allowing Numerical Weather Prediction Model. *J. Geophys. Res. Atmos.* 123, 9652–9673. doi:10.1029/2018jd028494

Wang, Y., Yang, Y., and Wang, C. (2014). Improving Forecasting of Strong Convection by Assimilating Cloud-To-Ground Lightning Data Using the Physical Initialization Method. *Atmos. Res.* 150, 31–41. doi:10.1016/j.atmosres.2014.06.017

Yang, J., Zhang, Z., Wei, C., Lu, F., and Guo, Q. (2017). Introducing the New Generation of Chinese Geostationary Weather Satellites, Fengyun-4. *Bull. Am. Meteorol. Soc.* 98, 1637–1658. doi:10.1175/bams-d-16-0065.1

Yang, Y., Wang, Y., and Zhu, K. (2015). Assimilation of Chinese Doppler Radar and Lightning Data Using WRF-GSI: A Case Study of Mesoscale Convective System. *Adv. Meteorol.* 2015, 763919. doi:10.1155/2015/763919

Conflict of Interest: The authors declare that the research was conducted in the absence of any commercial or financial relationships that could be construed as a potential conflict of interest.

Publisher's Note: All claims expressed in this article are solely those of the authors and do not necessarily represent those of their affiliated organizations, or those of the publisher, the editors and the reviewers. Any product that may be evaluated in this article, or claim that may be made by its manufacturer, is not guaranteed or endorsed by the publisher.

frontiers | Frontiers in Earth Science

ORIGINAL RESEARCH
published: 04 July 2022
doi: 10.3389/feart.2022.917069

Precipitation Trends Analysis Using Gridded Dynamic Sampling Zones: Case Study Yangtze Delta Megalopolis

Xiaolong Liu[1,2,3], *Dafang Fu*[1,2]*, *Chris Zevenbergen*[3,4]*, *Meixiu Yu*[5] and *Alagarasan Jagadeesh Kumar*[6]

[1]School of Civil Engineering, Southeast University, Nanjing, China, [2]Southeast University-Monash University Joint Research Centre for Future Cities, Suzhou, China, [3]Department of Coastal and Urban Risk and Resilience, IHE Delft Institute for Water Education, Delft, Netherlands, [4]Department of Urbanism, Faculty of Architecture and the Built Environment, Delft University of Technology, Delft, Netherlands, [5]College of Hydrology and Water Resources, Hohai University, Nanjing, China, [6]School of Chemistry and Chemical Engineering, Jiangsu University, Zhenjiang, China

OPEN ACCESS

Edited by:
Sanjeev Kumar Jha,
Indian Institute of Science Education and Research, Bhopal, India

Reviewed by:
José Pedro Matos,
Stucky SA, Switzerland
Haibo Yang,
Zhengzhou University, China

***Correspondence:**
Dafang Fu
fdf@seu.edu.cn
Chris Zevenbergen
c.zevenbergen@un-ihe.org

Specialty section:
This article was submitted to Environmental Informatics and Remote Sensing, a section of the journal Frontiers in Earth Science

Received: 10 April 2022
Accepted: 13 June 2022
Published: 04 July 2022

Citation:
Liu X, Fu D, Zevenbergen C, Yu M and Kumar AJ (2022) Precipitation Trends Analysis Using Gridded Dynamic Sampling Zones: Case Study Yangtze Delta Megalopolis. Front. Earth Sci. 10:917069. doi: 10.3389/feart.2022.917069

As a result of the fast growth of remote sensing and data assimilation technology, many global land use land cover (LULC) and climate reanalysis data sets have been used to advance our understanding of climate and environmental change. This paper investigates the precipitation variations of the Yangtze Delta Megalopolis by using precipitation reanalysis data under conditions of dynamic urban sprawl. Compared with current precipitation characteristic analyses, which are often based on a limited number of ground rainfall stations, the approach followed in this study comprises a grid-based statistical method using large sets of samples with a uniform distribution and a same representative grid area. This novel approach of dynamic sampling is applied in this study to overcome the temporal and spatial inconsistency of stationary sampling. This approach allows to examine the impact of urbanization on regional precipitation characteristics. The Yangtze Delta Megalopolis (YDM) region, one of the most developed regions in China, was selected as a case study to evaluate the impact of urbanization on subsequent precipitation features. The results reveal that the annual total precipitation (TP) and the maximum daily precipitation (MDP) in both urban and non-urban areas of the YDM region generally have increased during the past 30 years. Hence, the region has become increasingly humid. Extrema of annual MDP and TP show obvious spatial characteristics, in which most maxima are located in the southern part of YDM while minima are more concentrated in the northern part. This newly developed approach has potentials for application in studies where underlying surface features exhibit rapid alterations. The findings of this case study provide relevant information for planning and design of regional water resources management, flood risk management, and planning of the urban drainage system of the YDM region.

Keywords: trend analysis, urbanization, land use change, statistical dynamic sampling, precipitation, climate change, Yangtze Delta megalopolis

INTRODUCTION

The impact of climate change and associated anthropogenic activities on the alteration of the urban hydrological regime and meteorological characteristics are an emerging and challenging subject of current urban hydrological research. The World Bank reported that the global air temperature in the middle of this century will rise by 2°C and reach 4°C by the end of the century, compared to the pre-industrial level in the 18th century (Potsdam Institute for Climate Impact Research and Climate Analytics, 2013). This will lead to an increase in the frequency and intensity of extreme rainfall, heat waves, and consequently, of droughts and floods. There is scientific consensus attributing global warming and more frequent climate extremes to human activities (IPCC et al., 2013a; IPCC et al., 2021b; Zhang et al., 2022). In the past 100 years (1908–2007), the climate change pattern observed in China was similar to the global one (Ding et al., 2006). Its average surface temperature increased by 1.1°C, slightly higher than the global average for the same period. The average annual rainfall showed an upward trend in the past 50 years, especially in the middle and lower reaches of the Yangtze River basin and the southeast of China. Both the frequency and intensity of climate extreme events have increased (Zhang et al., 2022; Ding et al., 2006; The State Council Information Office of the People's Republic of China, 2008; National Development and Reform Commission (NDRC), 2013).

Since the 1980s, China's economy has grown sharply, and the level of urbanization has risen drastically (Liu et al., 2021). The nominal gross domestic product (GDP) expanded 274 times from 367.87 billion CNY in 1978 to 100.88 trillion CNY in 2020, while the urban population percentage climbed from 17.92 to 63.89%. Although the level of urbanization is a critical indicator of social and economic development, the rapid urbanization in the last two decades has triggered a series of social-ecological-environmental processes, resulting amongst others into the occurrence of urban rain islands, urban heat islands, urban dust domes, and urban canyon effects (Central Committee of the Communist Party of China (CPC), 2014; Ding, 2018; Zhang et al., 2014). Compared with natural vegetation coverage, the urban heat island effect and dust cover effect aggravate variations in the regional spatial distribution of rainfall, resulting in a marked increase in rainfall peaks in built zones and downwind areas (Shepherd, 2005; Goddard Space Flight Center, 2012). The increase of impervious surfaces reduces evapotranspiration and infiltration, shortens the time of concentration, and increases the runoff coefficient (Zhang et al., 2014; Schueler, 1995; Federal Interagency Stream Restoration Working Group (FISRWG), 1989; Fletcher et al., 2013; Zhao et al., 2013; He et al., 2003). The changes of urbanization to the underlying surface have exacerbated the occurrence of extreme rainfalls, floods, and droughts (Research Council, 2008; Yu et al., 2014).

The Yangtze River Delta (YRD) has experienced rapid urbanization in the past decades and has become one of the most developed regions in China, forming the world-renowned Yangtze Delta Megalopolis (YDM) (Fang, 2019; Yu et al., 2021). While rapid development brought prosperity to the YDM, it also caused drawbacks challenging its livability, such as foggy haze (Meng et al., 2015; Liu et al., 2020), heat waves (Huang et al., 2008; Huang and Lu, 2015), and heavy precipitation (Fu et al., 2017; Ding, 2018). In the past decade, the intensity and frequency of extreme rainfall events and the resulting flood disasters exceeded the stationary reference standards for both urban drainage and flood control systems in the region (Wang et al., 2015; Xu et al., 2019; Xu et al., 2020). Extreme rainfall and snow destroy infrastructure services such as housing, transportation, communications, and electricity, threatening city safety. The impact of urbanization on regional and extreme rainfall has received extensive attention. Most of the studies on the impact of urbanization on urban rainfall are based on ground rain gauge stations (**Table 1**). The statistical rigor and hence the effectiveness of the methods applied are dependent on the availability of reliable and representative urban precipitation data. These are often limited as they require a dense gauge station network to achieve true urban coverage. In addition, these studies rarely consider urbanization as a dynamic phenomenon influencing the environment of the observation sites, such as a change of the underlying surface conditions due to urban densification and expansion. This hinders the exploration of the temporal variation of rainfall characteristics, which makes such an analysis inconsistent in time and space.

It is common practice to examine the temporal and spatial distribution of urban precipitation using precipitation data from visible ground weather stations. Hu (2015) examined the characteristics of rainstorm-induced hazards in Beijing City and the effect of urbanization based on precipitation data derived from 20 precipitation gauge stations. Using precipitation data from 170 precipitation stations of Shanghai City, Chow and Chang (1984) plotted the isohyets of average annual precipitation, average wet season precipitation, and average dry season precipitation to analyze the relationship between precipitation distribution and city development. Significant urban rainfall islands were detected in the central region of Shanghai City based on the hourly precipitation of 11 precipitation stations by Ding (2018), who found that the maximum hourly precipitation occurred in the city center and gradually decreased from the city center to the suburbs. Fang et al. (2012) analyzed the daily precipitation at Baoshan Station in Shanghai and showed that the number of rainy days gradually decreased from 1971 to 2010, whilst the intensity and frequency of short-duration rainfall increased. The domain size, number of precipitation stations, and average density of research concentrating on differences in urban precipitation at different spatial scales are shown in **Table 1**. By dividing the domain area by the number of precipitation stations, the average density of precipitation stations was computed. The spatial scale of the study areas varied widely, ranging from cities to countries, natural river basins to the worldwide river system. Station network density ranged from 10.91 km^2 per station to 51,612.9 km^2 per station, with an average of 7,182.56 km^2 per station. Some scholars were overly optimistic in their assessment of site precipitation trends as regional trends, while others cautioned that site precipitation characteristics merely represent gauge station precipitation trends (Fang et al., 2012; Şen, 2014). The spatial distribution

TABLE 1 | Summary of the characteristics of the case study on precipitation.

Author	Study area	Size of the area (km^2)	Number of stations	Density of stations (area in km^2 per station)
Hu (2015)	Beijing City	16,410	20	820.5
Chow and Chang (1984)	Shanghai City	6,340.5	170	37.3
Ding (2018)	Shanghai City	6,340.5	11	576.41
Fang et al. (2012)	Shanghai City	6,340.5	1	6,340.5
Chen et al. (2016)	Nanjing City	6,587.02	71	92.77
Deng (2017)	Hefei City	7,266	9	807.33
Gao et al. (2016)	Jiangsu Province	107,200	68	1,576.47
Wang et al. (2003)	Zhejiang Province	105,500	63	1,674.6
Luo et al. (2020)	Anhui Province	140,100	81	1,729.63
Su et al. (2021)	Yunan Province	394,100	125	3,152.8
Yang et al. (2014)	Taihu Lake Basin	36,895	27	1,366.48
Han et al. (2015a), Han et al. (2015b)	Yangtze River Delta	95,400	16	5,962.5
Sang et al. (2013)	Yangtze River Delta	210,700	58	3,632.76
Wang et al. (2016)	Yangtze River Delta	95,400	24	3,975
Cao et al. (2018)	Yangtze River Delta	99,600	56	1,778.57
Pei et al. (2018)	Yangtze River Delta	104,985	16	6,561.56
Wang et al. (2020)	Yangtze River Delta	95,400	14	6,814.29
Yu et al. (2022)	Yangtze River Delta	301,700	126	2,394.44
Becker et al. (2006)	Yangtze River Basin	1,800,000	36	50,000
Li et al. (2015), Zhang et al. (2016))	Mainland China	9,600,000	186	51,612.9
Yu et al. (2007)	Mainland China	9,600,000	588	16,326.53
Yu et al. (2014)	Mainland China	9,600,000	752	12,765.96
Zhou et al. (2008)	China	9,600,000	626	15,335.46
Huff (1975)	St. Louis area	5,500	225	24.44
Burian and Shepherd (2005)	Houston metropolitan area	3,350	53	63.21
Diem and Mote (2005)	Atlanta metropolitan area	101,788	30	3,392.93
Hand and Shepherd (2009)	Oklahoma City	5,625	14	401.79
Daniels et al. (2016)	Dutch West Coast	5,300	60	88.33
Caloiero et al. (2018)	Southern Italy	85,000	129	658.91
Paul et al. (2018)	Mumbai City	600	55	10.91
Westra et al. (2013)	Globe	149,000,000	8,326	17,895.75

of precipitation stations employed in most research was excessively sparse when compared to the World Meteorological Organization's (WMO) suggested minimum densities of precipitation stations (10–20 km^2 per station in urban areas) (World Meteorological Organization, 2008a; Chacon-Hurtado et al., 2017). When the density of precipitation stations is excessively high, the results of statistical analysis may be equivocal according to the large sample principle of statistical analysis, which states that the larger the sample size, the more they tend to their true value.

In a study spanning several decades, it is not uncommon that initially non-urban areas, or upwind/downwind zones, gradually become urban areas as a result of urban expansion. As a result, the weather stations in these shifting areas have transitioned from rural to urban stations. Many studies have used the existing underlying surface to differentiate between urban and non-urban areas when detecting precipitation trends without taking into account the passive changes in the site background environment generated by urbanization: for example, in Hu (2015), Hand and Shepherd (2009), Chen et al. (2016), and Kishtawal et al. (2010). Some researchers have noted that when cities grow, the classification of certain weather stations changes from non-urban to urban. To assess the impact of small and fragmented urban areas on precipitation along the Dutch West coast, Daniels et al. (2016) used land use data and geostrophic wind direction with a record length of 59 years for every 10 years to dynamically divide precipitation sites into rural and urban categories. By using remotely sensed image analysis, Zhang et al. (2021) discovered that land use and anthropogenic heat flow produced by urbanization had a considerable impact on the consistency of surface weather station data. Yu et al. (2022) identified urban and rural stations by using a method that combined a circular buffer and the percentage of urban area within the buffer to explore the shift pathways of the light and heavy precipitation associated with urbanization in the Yangtze River Delta region. Due to the availability of LULC data, there was no extra station identification for precipitation before 1980 and after 2015. In addition, the categories of stations were considered static in a few analyses, for example, the case analyzing the effect on sample size. Once the category of a rain gauge station being affected by urban expansion alters, it is often accompanied by a modification of the features of the domain that the rain station represents. This may lead to a loss of consistency in the rainfall data observed before and after the change (Dahmen and Hall, 1990; World Meteorological Organization, 2008b). If a trend analysis is performed directly on those precipitation stations while ignoring the change in their categories, the applicability of the precipitation characteristic data will be considerably reduced.

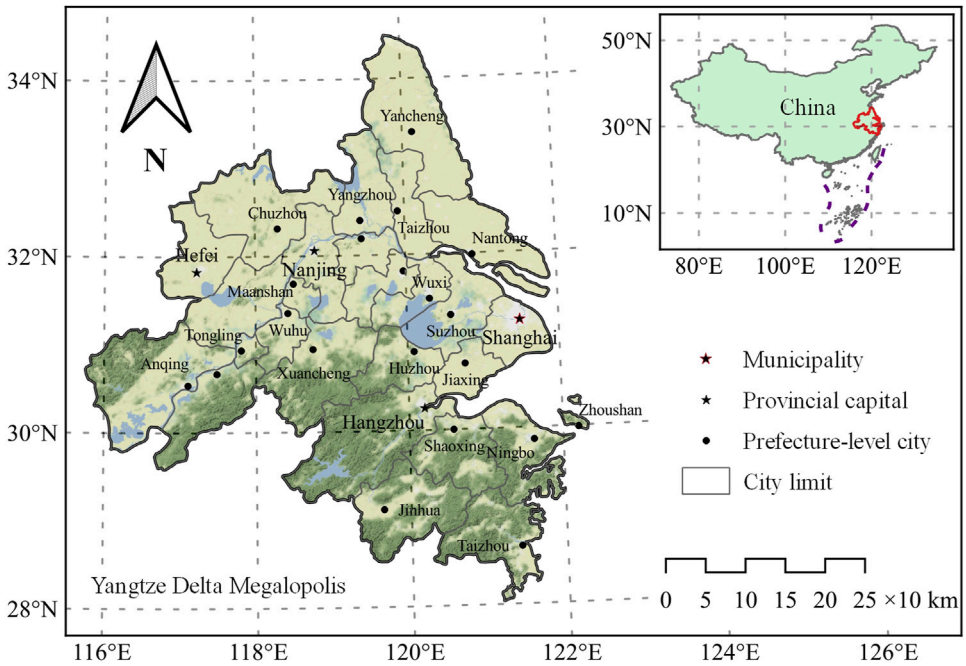

FIGURE 1 | The study area of the Yangtze Delta Megalopolis, China. Terrain tiles by Stamen Design (Terrain Classic Contributors, 2021) are used as a background.

The purpose of this study is to describe and demonstrate a novel method based on a statistical analysis of remotely sensed data sets to overcome the sampling sufficiency challenge in rainfall trend analysis in terms of size and representativeness which acknowledges the dynamic nature of the surface area due to urbanization. The YDM region was selected as a case study as it experienced rapid expansion of its built area and frequent heavy precipitation events in recent decades.

STUDY AREA AND DATA

The Yangtze River Delta is one of the most developed regions in China. The growth rate of its economic and urban development is ahead of the national average (Yu et al., 2021). The "Development Plan for the Yangtze Delta Megalopolis" was issued by the Chinese central government as one of the national strategies in 2016, in order to strengthen the coordination and cooperation in cross-city/regional development and enhance the international competitiveness of Chinese cities. The Yangtze Delta Megalopolis, located downstream of the Yangtze River Basin, has a land area of approximately 2.12 $\times 10^5$ km^2, and accommodates 26 cities, i.e. Shanghai, nine cities in Jiangsu Province (Nanjing, Wuxi, Changzhou, Suzhou, Nantong, Yancheng, Yangzhou, Zhenjiang, and Taizhou), eight cities in Zhejiang Province (Hangzhou, Ningbo, Jiaxing, Huzhou, Shaoxing, Jinhua, Zhoushan, and Taizhou), and eight cities in Anhui Province (Hefei, Wuhu, Maanshan, Tongling, Anqing, Chuzhou, Chizhou and Xuancheng) (**Figure 1**) (National Development and Reform Commission of the People's Republic of China (NDRC), 2016). At the end of 2019, its registered population had reached 132.6 million, accounting for 9.47% of China's population and 1.73% of the global population. Its nominal GDP in 2019 was 19.71 trillion CNY, accounting for 19.98% of China's GDP and 3.55% of the global GDP, respectively.

Climate Hazards Group InfraRed Precipitation with Station data (CHIRPS) was jointly released by the University of California, Santa Barbara (UCSB) Climate Hazards Center and the United States Agency for International Development (USAID) in 2015 (Funk et al., 2015). This data set is based on the fusion of ground station and satellite-based remotely sensed data. Ranging from 1981 to near-present, it completely covers the YDM with a resolution of 0.05°×0.05° (approximately 5.6 km at the equator, less than 5 km in the YDM). Bai et al. (2018) assessed the accuracy of CHIRPS compared with rain gauges over mainland China and concluded that CHIRPS had a better performance in rainy areas than in arid or semi-arid areas. Tang et al. (2019) conducted a series of hydrological simulations using the Soil and Water Assessment Tool (SWAT) forced with different precipitation products in the Lancang River Basin. CHIRPS performed well in both the whole basin and sub-basins on the daily and monthly scales. Catholic University of Louvain (UCLouvain) has produced Global Land Cover (ESA-CCI-LC), a global land cover data product based on data obtained from the European Space Agency's (ESA) Climate Change Initiative (CCI) (Defourny et al., 2017; Copernicus Climate Change Service, 2020; European Space Agency (ESA), 2015). With a horizontal resolution of 300 m and a time resolution of a year, this data collection follows the land cover categorization system (LCCS) defined by the United Nations (UN) Food and Agriculture

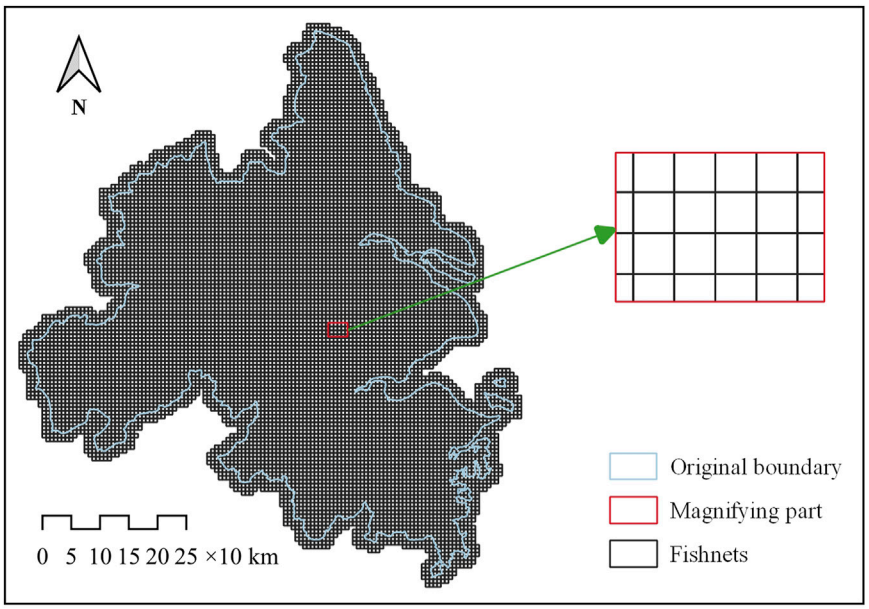

FIGURE 2 | Fishnets in the YDM.

Organization (FAO) (Gregorio and Jansen, 2000). On the premise of ensuring the availability of data in the YDM region, and after comparing the time series lengths and temporal and spatial resolution of the current available precipitation/land cover data, the CHIRPS data set as the daily precipitation data source was selected for this study. This allowed taking advantage of the high spatial resolution of 5 km as well as the long time coverage from 1981 to the present. ESA-CCI-LC was chosen as the basic land cover data in this study since it has a horizontal resolution of 300 m and a yearly time resolution from 1992 to the present.

METHODOLOGY

Generation of Dynamic Regions

The original boundary of the YDM was extended about 10 km outwards. Then, the extended YDM was divided into grids with the same size and location as the land use and precipitation data grids. The spatial coordinate reference system (CRS) used for grid creation was EPSG:32650; the affine transformation was set by defining the limits (west, south, east, north), length, and width, with parameters of 340,000, 3,065,000, 1,060,000, 3,875,000, 5,000, and 5,000, respectively. In the study area YDM, a total of 9,698 effective grids with a horizontal resolution of 5 km × 5 km were created (**Figure 2**). The gridding method provides the advantages of a large sample size, uniform distribution, and the same cell area, as shown in **Figure 2**.

To compare the impact of urbanization on regional precipitation, the ESA-CCI-LC data set was binarized/converted into land use maps with two classes of urban/built-up and non-urban/built-up based on the class value of the land cover being equal to 190 or not (190 for urban areas). All grids of the urban/built-up class were designated as urban region, the others were deemed non-urban region in the YDM region (**Supplementary Figure S1**). To ensure that the land use maps matched the precipitation data grid, they were resampled at a horizontal resolution of 5 km × 5 km. **Supplementary Figure S1** depicts the 2020 binarized land use map.

The annual land use maps for urban and non-urban regions from 1992 to 2020 were generalized by the binarization approach to characterize the evolution dynamics of urbanization. After binarization, the grid number of urban and non-urban regions was counted year by year using the land use map. **Figure 3** presents the trend of the grid number over time. **Supplementary Figure S2** depicts the temporal and spatial distributions of urban construction in the YDM from 1995 to 2015.

Statistics of Precipitation

Using the yearly MDP as an example, the following statistical approach was developed for the above-mentioned year-by-year change of the gridded precipitation. Assuming that the dynamic area has n grids in the x^{th} year, the following matrix can be used to express all of the precipitation sample values for that year:

$$P^{x}_{daily,cell} = \begin{bmatrix} p_{1,1} & p_{1,2} & \cdots & p_{1,j} & \cdots & p_{1,n} \\ p_{2,1} & p_{2,2} & \cdots & p_{2,j} & \cdots & p_{2,n} \\ \vdots & \vdots & \ddots & \vdots & \ddots & \vdots \\ p_{i,1} & p_{i,2} & \cdots & p_{i,j} & \cdots & p_{i,n} \\ \vdots & \vdots & \ddots & \vdots & \ddots & \vdots \\ p_{m,1} & p_{m,2} & \cdots & p_{m,j} & \cdots & p_{m,n} \end{bmatrix} \quad (1)$$

where $p_{i,j}$ is the precipitation of the j^{th} grid on the i^{th} day of the x^{th} year, in millimeters; m is the total number of days in a year, which is 365 for an average year and 366 for a leap year.

The first statistic was taken on the above matrix P_x by extracting the maximum value of each column. These maxima represent the annual MDP of each grid in the x^{th} year, which can be expressed as the vector:

$$\boldsymbol{P}^{x}_{max,cell} = \left\{ \boldsymbol{p}_{max,1}, \boldsymbol{p}_{max,2}, \ldots, \boldsymbol{p}_{max,j}, \ldots, \boldsymbol{p}_{max,n} \right\} \quad (2)$$

where $p_{max,j}$ is the annual MDP of the j^{th} grid the x^{th} year, in millimeters. The extraction was conducted using the Google Earth Engine platform, the outputs of which were exported locally for subsequent use (Gorelick et al., 2017).

Then, in $P^{x}_{max,cell}$, the 0 values were removed as they represent a cell without precipitation, and the second statistic can be performed on the remaining. A variety of characteristic values can be chosen, such as the maximum value, the average value, the median, and so on, to meet specific demands. In this study the maximum, 75th percentile, 50th percentile (median), 25th percentile, and minimum as characteristic values, have been used which are recorded as $P^{x}_{max,max}$, $P^{x}_{max,75\%}$, $P^{x}_{max,50\%}$, $P^{x}_{max,25\%}$, and $P^{x}_{max,min}$, respectively.

Assuming t – the total number of years, the time series of the characteristic values of the MDP can be constructed as follows:

$$\begin{cases} \boldsymbol{P}_{max,max} = \left\{ \boldsymbol{P}^{1}_{max,max}, \boldsymbol{P}^{2}_{max,max}, \ldots, \boldsymbol{P}^{x}_{max,max}, \ldots, \boldsymbol{P}^{t}_{max,max} \right\} \\ \boldsymbol{P}_{max,75\%} = \left\{ \boldsymbol{P}^{1}_{max,75\%}, \boldsymbol{P}^{2}_{max,75\%}, \ldots, \boldsymbol{P}^{x}_{max,75\%}, \ldots, \boldsymbol{P}^{t}_{max,75\%} \right\} \\ \boldsymbol{P}_{max,50\%} = \left\{ \boldsymbol{P}^{1}_{max,50\%}, \boldsymbol{P}^{2}_{max,50\%}, \ldots, \boldsymbol{P}^{x}_{max,50\%}, \ldots, \boldsymbol{P}^{t}_{max,50\%} \right\} \\ \boldsymbol{P}_{max,25\%} = \left\{ \boldsymbol{P}^{1}_{max,25\%}, \boldsymbol{P}^{2}_{max,25\%}, \ldots, \boldsymbol{P}^{x}_{max,25\%}, \ldots, \boldsymbol{P}^{t}_{max,25\%} \right\} \\ \boldsymbol{P}_{max,min} = \left\{ \boldsymbol{P}^{1}_{max,min}, \boldsymbol{P}^{2}_{max,min}, \ldots, \boldsymbol{P}^{x}_{max,min}, \ldots, \boldsymbol{P}^{t}_{max,min} \right\} \end{cases} \quad (3)$$

Taking out the *max*:

$$\begin{cases} \boldsymbol{P}_{max} = \left\{ \boldsymbol{P}^{1}_{max}, \boldsymbol{P}^{2}_{max}, \ldots, \boldsymbol{P}^{x}_{max}, \ldots, \boldsymbol{P}^{t}_{max} \right\} \\ \boldsymbol{P}_{75\%} = \left\{ \boldsymbol{P}^{1}_{75\%}, \boldsymbol{P}^{2}_{75\%}, \ldots, \boldsymbol{P}^{x}_{75\%}, \ldots, \boldsymbol{P}^{t}_{75\%} \right\} \\ \boldsymbol{P}_{50\%} = \left\{ \boldsymbol{P}^{1}_{50\%}, \boldsymbol{P}^{2}_{50\%}, \ldots, \boldsymbol{P}^{x}_{50\%}, \ldots, \boldsymbol{P}^{t}_{50\%} \right\} \\ \boldsymbol{P}_{25\%} = \left\{ \boldsymbol{P}^{1}_{25\%}, \boldsymbol{P}^{2}_{25\%}, \ldots, \boldsymbol{P}^{x}_{25\%}, \ldots, \boldsymbol{P}^{t}_{25\%} \right\} \\ \boldsymbol{P}_{min} = \left\{ \boldsymbol{P}^{1}_{min}, \boldsymbol{P}^{2}_{min}, \ldots, \boldsymbol{P}^{x}_{min}, \ldots, \boldsymbol{P}^{t}_{min} \right\} \end{cases} \quad (4)$$

The time series constructed above has been used to conduct a precipitation trend analysis by adopting a probabilistic analysis strategy with percentile statistics (Stensrud and Yussouf, 2007; Du and Chen, 2010; IPCC, 2021b). Meanwhile, a decadal average was performed to smooth out the fluctuations of the yearly statistics and highlight their trends (Akrami et al., 2014). To investigate the linear correlation for the time series between urban and non-urban regions, the Pearson correlation coefficient (PCC) and corresponding significance p-value were calculated by using the linregress function provided by the SciPy library (Taylor, 1990; Virtanen et al., 2020). The overall agreement was quantified using modified Kling-Gupta efficiency (KGE) (Gupta et al., 2009; Kling et al., 2012). The Mann-Kendall test supported by pyMannKendall was implemented to determine the trends of statistics (Yue and Wang, 2004; Hussain and Mahmud, 2019).

The statistical method comparable to annual MAP was made for finding total annual precipitation. Here, in **Eq. 2** *max* was substituted to calculate the sum precipitation on a grid,

$$\boldsymbol{P}^{x}_{sum,cell} = \left\{ \boldsymbol{p}_{sum,1}, \boldsymbol{p}_{sum,2}, \ldots, \boldsymbol{p}_{sum,j}, \ldots, \boldsymbol{p}_{sum,n} \right\} \quad (5)$$

where $p_{sum,j}$ is the total annual precipitation of the j^{th} grid in the x^{th} year, in millimeters.

RESULTS AND DISCUSSION

Annual Maximum Daily Precipitation

As shown in **Figure 3**, the number of sampling grids exhibit a gradual increase in the urban region over time with a decrease in the non-urban region. It is to be expected that an expansion of the sampling regions will result in higher maxima and lower minima

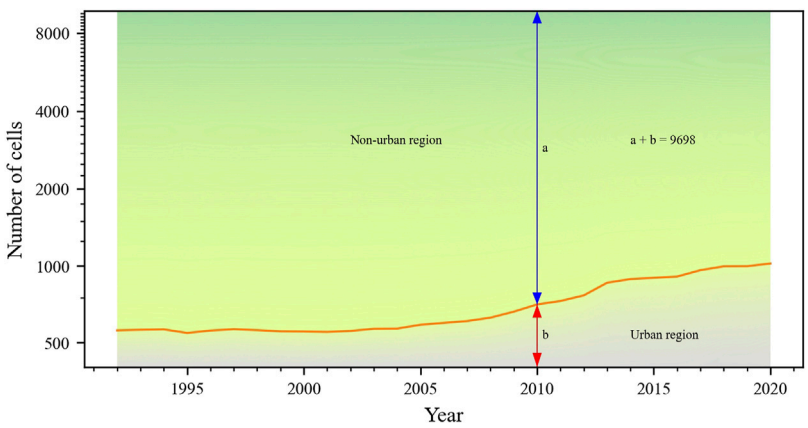

FIGURE 3 | Temporal variations of the sampling grid number for urban and non-urban regions in the YDM. The sum of the grid numbers of urban region and non-urban region always equals to 9,698.

TABLE 2 | The MK trend test for annual MDP in different percentiles of the YDM from 1992 to 2020.

Region	Metric	Minimum	25%	Medium	75%	Maximum
Urban (changing)	MK value	3.240	4.062	3.512	3.205	3.120
	p-value	$p < 0.01$	$p < 0.001$	$p < 0.001$	$p < 0.01$	$p < 0.01$
Urban (unchanged)	MK value	5.360	5.138	4.016	3.789	2.874
	p-value	$p < 0.001$	$p < 0.001$	$p < 0.001$	$p < 0.001$	$p < 0.01$
Non-urban (changing)	MK value	6.700	4.418	4.357	3.655	1.948
	p-value	$p < 0.001$	$p < 0.001$	$p < 0.001$	$p < 0.001$	$p \geq 0.05$
Non-urban (unchanged)	MK value	6.700	4.319	4.281	3.690	1.948
	p-value	$p < 0.001$	$p < 0.001$	$p < 0.001$	$p < 0.001$	$p \geq 0.05$

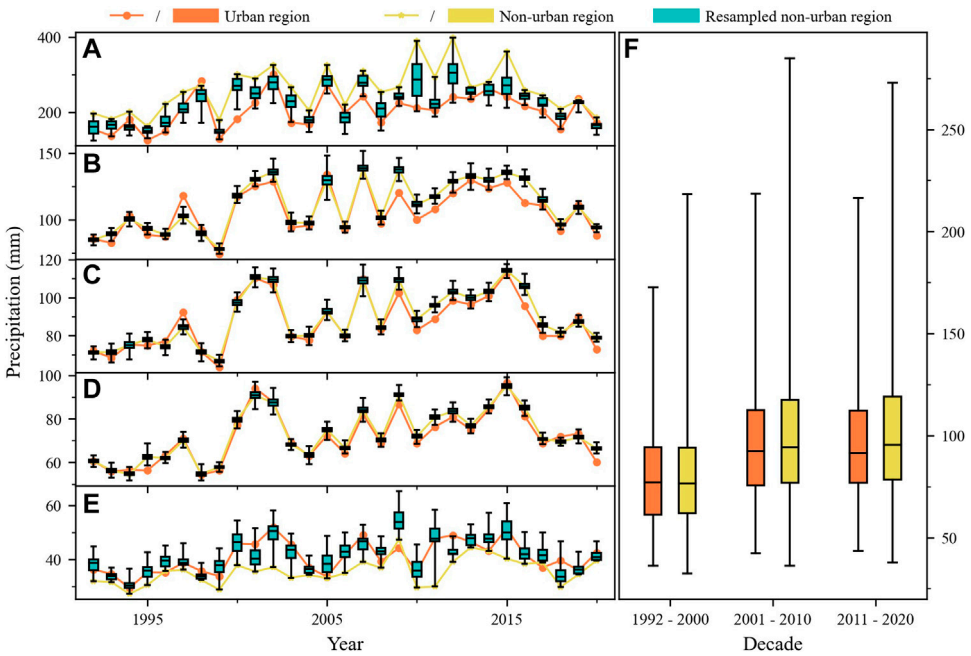

FIGURE 4 | The annual MDP in the YDM from 1992 to 2020. **(A)** maximum, **(B)** 75th percentile, **(C)** median, **(D)** 25th percentile, and **(E)** minimum represent the yearly changes. The boxplot of decadal averages is shown in **(F)**.

of daily precipitation than the unchanged sampling cells. To investigate how a change in sample size for the urban region affects the results, we compared the precipitation statistics for the expanding and unchanged urban regions using grids from 1992 to 2020. It follows from the results that these effects are too small (fall within the noise range) to be of particular concern for MDP in the urban regions before 2010 (**Supplementary Figure S3**). The interquartile ranges show a minor shift downwards from 2010 to 2020. These shifts are also quantitatively reflected in the MK values (**Table 2**). The effects of the reduced sampling cells are negligible in the non-urban regions (**Supplementary Figure S4**). Kling-Gupta efficiency coefficient (KGE) values reveal a similar pattern of all five quantiles of the annual MDP between the changing urban and non-urban regions and their unchanging parts, with values greater than 0.902 (**Supplementary Table S1**). In addition, the difference in sample size between urban and non-urban regions may also affect the results. We resampled an equal number of sampling cells from the non-urban region, equivalent to the number of sampling cells in the urban region, and extracted its five-number summary. After repeating 1,000 times, we found that the difference between the urban region and resampled non-urban regions was positively related to the difference between the urban and non-urban regions (**Figures 4A–E**). The extreme values of MDP amplified/decreased by the large sampling cells in the non-urban region. This amplification/decrease complicates an analysis of the relationship of precipitation extremes between the urban and non-urban regions, especially minima. As for the other three quartiles, they show great stability, irrespective of the sample size. Although the sample size matters, the difference in sample size disturbed the extrema of MDP slightly as well as strengthened the interquartile law under the context of a large sample strategy adopted in this study. Previous studies were hindered due to the limited number of ground stations and their representativeness (Sang et al., 2013; Han et al., 2015a; Han et al., 2015b; Wang et al., 2016; Cao et al., 2018; Pei et al., 2018; Wang et al., 2020; Yu et al., 2022). This limitation

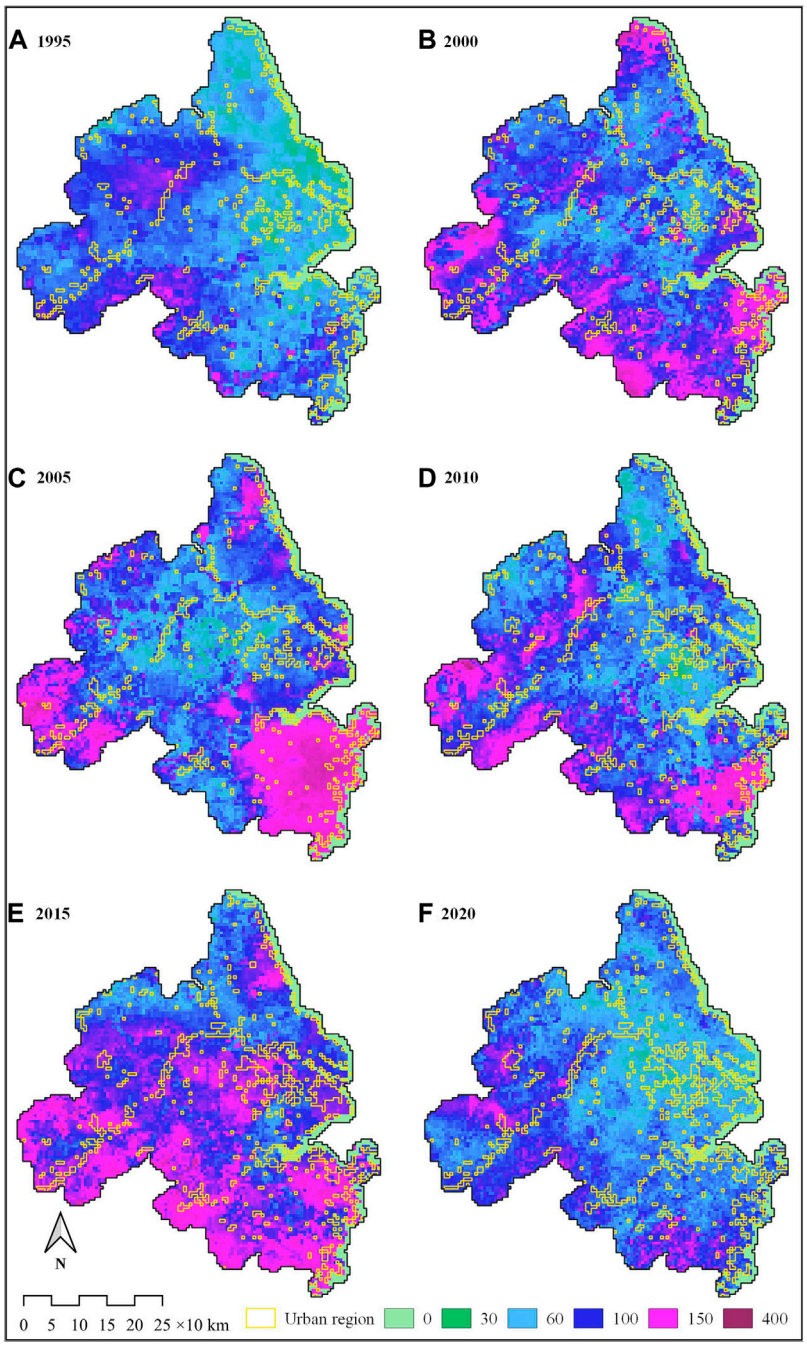

FIGURE 5 | The distribution of annual MDP in the YDM at quinquennial intervals from 1995 to 2020.

exacerbated after applying complex category identification of these stations (Diem and Mote, 2005; Yu et al., 2022). High-resolution reanalysis data such as CHIRPS provides a promising solution.

The distribution of MDP has recognizable spatial characteristics within each year interval, but there is no unified feature between the years (**Figure 5**). However, **Figures 6A,B** depict that most of the maxima of MDP are located south of 31°N and most of the minima are located north of 31°N for both urban and non-urban regions, which may be related to topography and landform (**Supplementary Figure S7**). This is in line with observations of more heavy precipitation in the southern part of YRD reported in previous work (Sang et al., 2013; Han et al., 2015a; Wang et al., 2016).

Figures 4A–E show that the five quantiles of the yearly MDP increased to varying degrees in both the urban and non-urban regions. The percentiles of 25, 50, and 75% exhibit stable

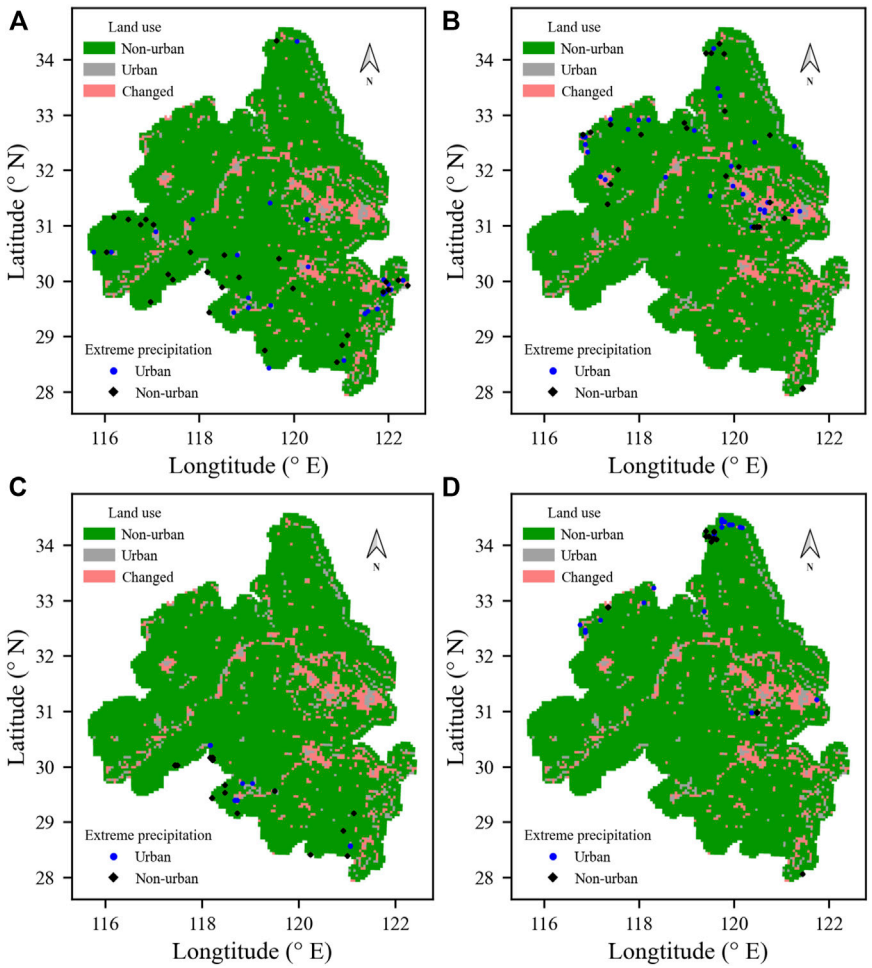

FIGURE 6 | The distribution of yearly precipitation extrema in the YDM from 1995 to 2020 for **(A)** maxima of MDP, **(B)** minima of MDP, **(C)** maxima of TP, and **(D)** minima of TP.

characteristics, ignoring the complexities of extrema that are influenced by the differences in sampling cells between urban and non-urban regions. All six time series in the MK trend test revealed a significant increasing trend, with five out of six (25% quantile and median of the annual MDP in the urban region and the 25%, median, and 75% in the non-urban region) meeting the significance level of 0.001 (**Table 2**). The distribution of difference for 10-year period averages of annual MDP in the YDM between the 1990s and 2010s is illustrated in **Figure 7**. In the past three decades, most cells have experienced an increase in annual MTP of decadal average. This increasing trend is uniform and significant for both urban and non-urban regions. If the non-urban region that is relatively less affected by human activities is regarded as a baseline, this explicitly indicates that the YDM climate change may be playing a dominant role in the trend variations of annual extreme precipitation. However, the yearly MDP in the YDM's urban region is rising which may lead to a growing risk of urban flooding (Yu et al., 2022). This is in line with the observed increase in the frequency of flooding of many urban areas in recent years, as well as the higher economic losses caused by floods in the YDM. **Figure 8** depicts a significant rise in economic losses due to urban flooding in the YDM region from 2006 to 2020 (Ministry of Water Resources of the People's Republic of China (MWR), 2021). In addition, these results differ from previous studies on the impact of urbanization on hourly precipitation, which have shown a correlation between rapid urbanization and more extreme precipitation events (sub-daily) in urban areas (Liang and Ding, 2017; Ding, 2018; Jiang et al., 2020; Wang et al., 2021). In the comparison of these studies, this may be affected by data sources (station-/ non-station- based and the number of stations), statistic methods, and sizes and locations of case domains. And/or, it may be recommended that there are critical temporal resolutions greater than 3 h and less than 24 h in YDM, which separate these rules.

The Pearson correlation coefficient (PCC) and its *p*-value, as well as the Kling-Gupta efficiency coefficient (KGE) were used to assess the correlation between annual MDP of various quantiles across the urban and non-urban regions (**Table 3**). The line plots fluctuate similarly in the five quantiles of annual MDP in the urban and non-urban regions (**Figures 4A–E**), with values of

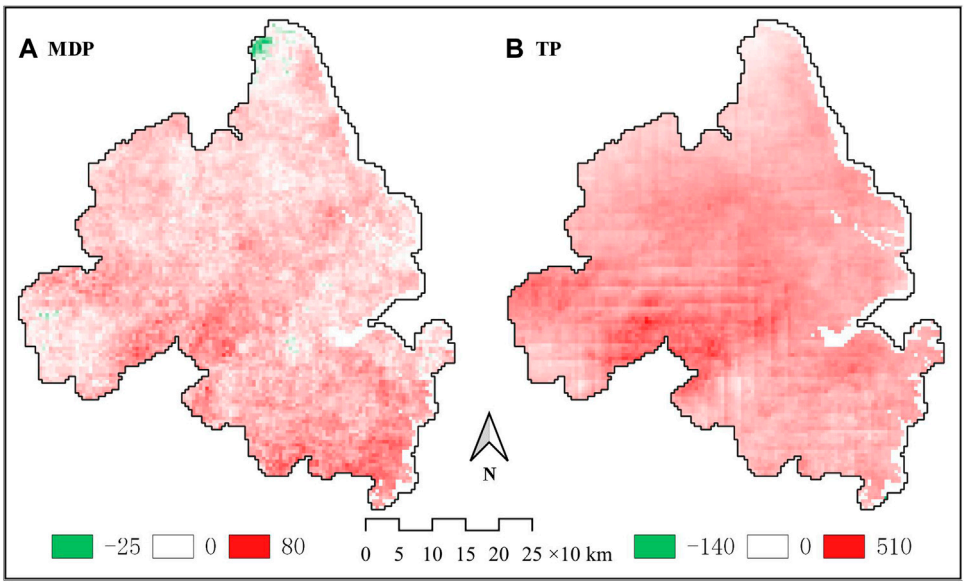

FIGURE 7 | The distribution of precipitation difference for 10-year period averages in the YDM between the 1990s and 2010s for **(A)** MDP and **(B)** TP.

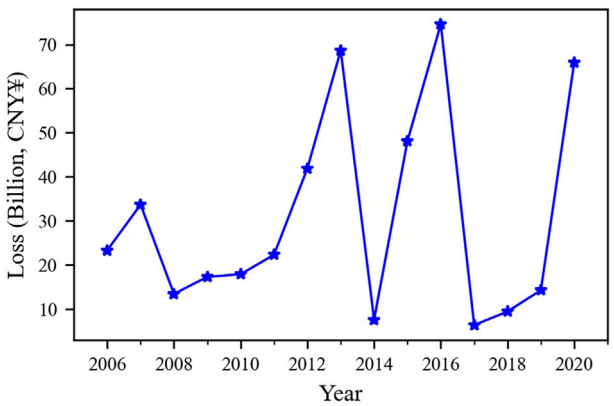

FIGURE 8 | Historical flood loss in Jiang-Zhe-Hu-Wan region. Jiang, Zhe, Hu, and Wan are the abbreviations of Jiangsu Province, Zhejiang Province, Shanghai City, and Anhui province, respectively.

TABLE 3 | Correlation and fitting of the annual MDP in different percentiles between urban and non-urban regions of the YDM during 1992–2020.

Metric	Minimum	25%	Medium	75%	Maximum
PCC	0.588	0.978	0.967	0.939	0.703
p-value	<0.001	<0.001	<0.001	<0.001	<0.001
KGE	0.563	0.964	0.959	0.922	0.592

PCC and KGE lying between 0.588–0.978 and 0.563–0.964, respectively (**Table 3**). The non-urban region has a significantly lower annual MDP than the urban region for the lowest, whereas the other quantiles in the non-urban region are generally higher than the urban region, with the maximum being the most significant. In both urban and non-urban regions, the 75th percentile, median, and 25th percentile of annual MDP are very close, and their PCC and KGE values are both above 0.9. According to the findings, there is a significant positive correlation between annual MDP in urban and non-urban areas, with the correlation in the middle three quantiles being significantly stronger than the correlation in the extreme quantiles. The yearly MDP of the urban region matches well with the non-urban region, with the middle three quantiles showing a better fit than the extreme quantiles. The yearly MDP fluctuation features in urban and non-urban locations are similar, with no significant differences, according to the strong correlation coefficients and satisfactory fitting methods.

The box plot's interdecadal variations reveal a gradual increase in the 10-year period averages of annual MDP in both urban and non-urban areas from the 1990s to the 2010s (**Figure 4F**). Except for the lowest percentile, non-urban regions' yearly MDP percentiles are greater than those in urban areas. Using the median as an example, in the 1990s, the decadal averages in urban and non-urban regions are nearly identical (76.99 and 76.61 mm), but in the 2010s, the averages grow to 91.53 and 95.53 mm, respectively, with percentage increases of 18.89 and 24.70%. Comparing the MK values of the 25th percentile, median, and 75th percentile in **Table 2**, the increase of the values in the non-urban region are greater than those in the urban region. Regardless of the impact of the sample size, this may be due to land cover and atmospheric humidity changes caused by urban expansion and human activities. Lu et al. (2019) found that the increase in the recurrence levels of annual MDP of non-urban stations is higher than that of urban stations considering the urbanized impacts. The non-urban areas with woodland, rainfed croplands, and grassland as the main underlying surface, which are the dominant land covers of precipitationsheds, may provide more

TABLE 4 | The MK trend test for annual TP in different percentiles of the YDM during 1992–2020.

Region	Metric	Minimum	25%	Medium	75%	Maximum
Urban (changing)	MK value	5.468	7.890	4.878	2.294	2.862
	p-value	$p < 0.001$	$p < 0.001$	$p < 0.001$	$p < 0.05$	$p < 0.01$
Urban (unchanged)	MK value	6.426	8.359	5.605	2.950	2.122
	p-value	$p < 0.001$	$p < 0.001$	$p < 0.001$	$p < 0.01$	$p < 0.05$
Non-urban (changing)	MK value	6.484	10.090	4.995	3.350	2.591
	p-value	$p < 0.001$	$p < 0.001$	$p < 0.001$	$p < 0.001$	$p < 0.01$
Non-urban (unchanged)	MK value	6.484	9.749	4.587	3.140	2.583
	p-value	$p < 0.001$	$p < 0.001$	$p < 0.001$	$p < 0.01$	$p < 0.01$

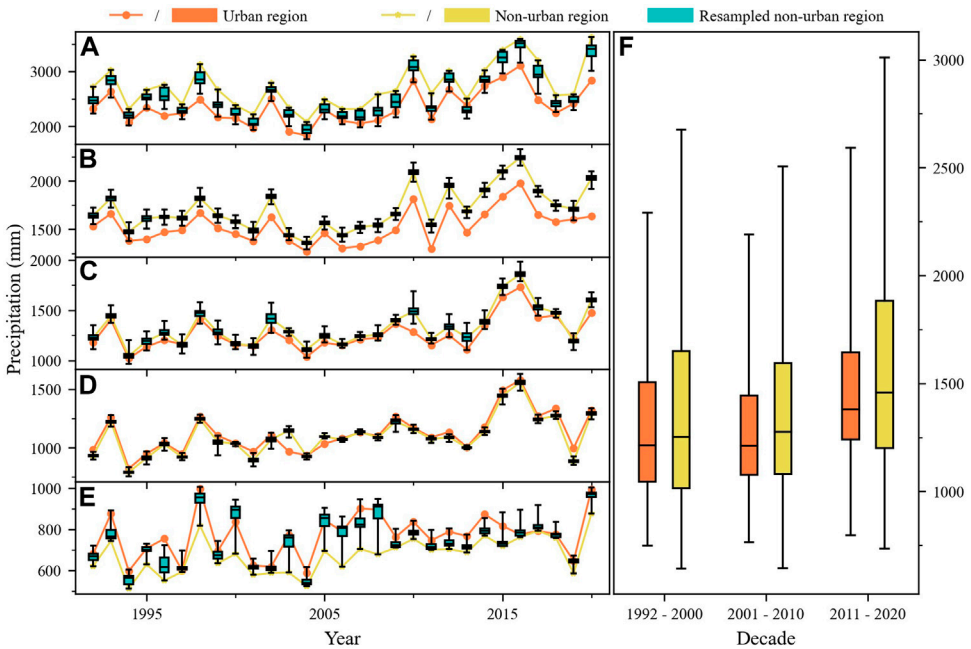

FIGURE 9 | The annual TP from 1992 to 2020 in the YDM. Yearly fluctuations of **(A)** maximum, **(B)** 75th percentile, **(C)** median, **(D)** 25th percentile, and **(E)** minimum. **(F)** boxplot of decadal averages.

favorable conditions for the generation of stronger heavy precipitation or heavier rainstorm centers at a daily scale (Keys et al., 2012). However, evapotranspiration is weakened in urban areas due to the loss of green vegetation. In comparison with the natural ground cover, the evapotranspiration decreases from 40 to 30% of the precipitation as the impervious surface area increases in urban areas (Federal Interagency Stream Restoration Working Group (FISRWG), 1989; Ellison et al., 2017). This process will result in a drop of atmospheric water vapor content, so the precipitation possibly decreases in the precipitationshed's sink zone (Keys et al., 2012; Luo and Lau, 2019).

Annual Total Precipitation

An estimate of the impact of sample size changes on TP was conducted. **Supplementary Figure S6** shows that the quantiles of TP for the decreasing non-urban regions are almost the same as those extracted from the unchanged region. The good fit reflected by these KGEs close to 1 are presented in **Supplementary Table S1**. **Supplementary Figure S5** depicts that in the growing urban regions with more sampling cells the ranges of TP have expanded in certain years resulting from an increase of their extremes compared to the unchanged urban region. The interquartile ranges are a little bit narrowed due to the downward shift in the upper quartiles in the 2010s. Compared to the unchanged urban region, the MK values for percentiles of 25, 50, and 75% in the changing urban regions decrease as well (**Table 4**). Considering the large difference in sample size between non-urban and urban regions, **Figures 9A–E** reflect that this difference has little effect on the 25th percentile, median, and 75th percentile. There is a significant influence on most extrema, but the relative magnitude of TP extrema in urban and non-urban areas is rarely affected. Similar to annual MDP, impacts of sample size changes on annual TP are very

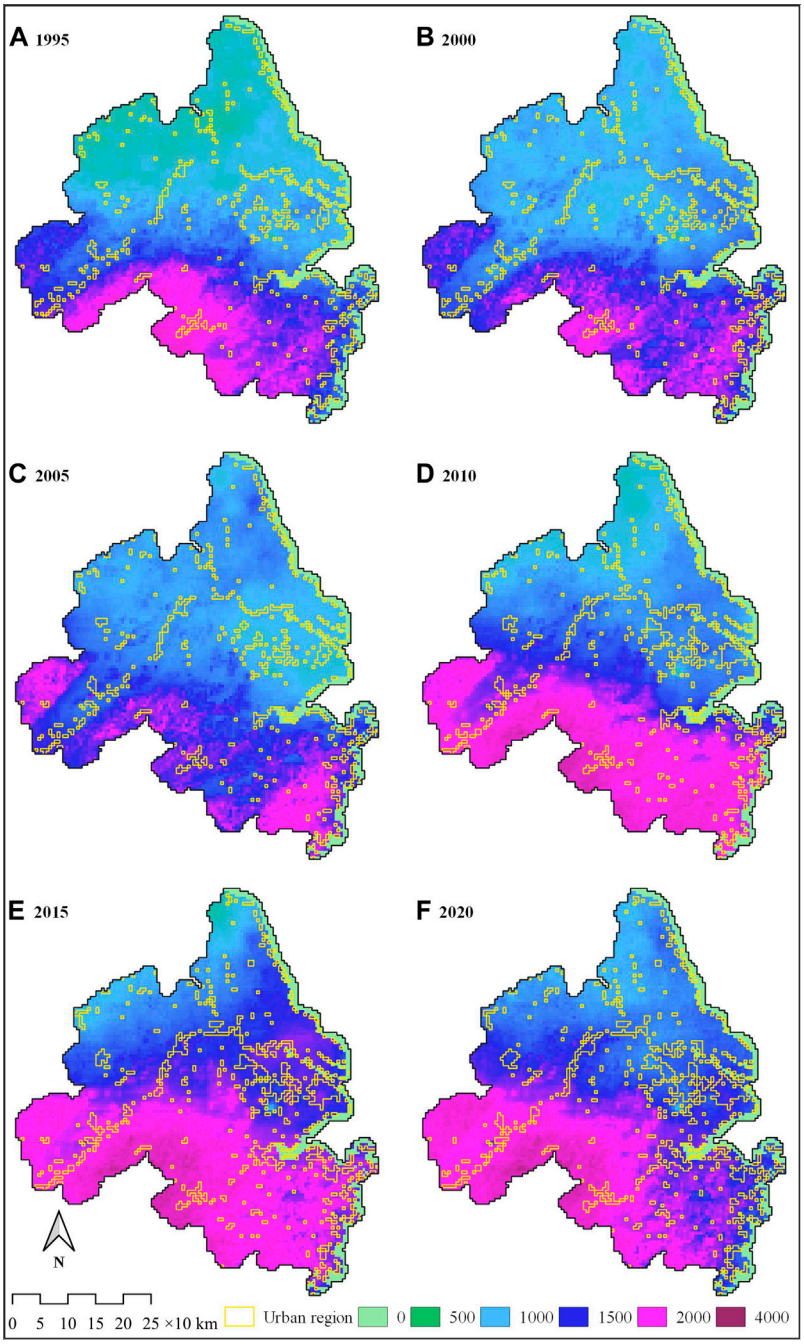

FIGURE 10 | The distribution of annual TP in the YDM at quinquennial intervals from 1995 to 2020.

limited, in contrast, the characteristics in the interquartile ranges are pretty stable under the large sample strategy.

Figure 10 depicts the spatial characteristics of the coordinated increase in annual TP from northern to southern of the YDM, which is valid for all years. They coincide with the contour map of the average annual precipitation released by the Ministry of Water Resources (Bureau of Hydrology, Ministry of Water Resources and Nanjing Hydraulic Research Institute, 2006). A similar spatial distribution of average annual precipitation was obtained using TRMM 3B43 (Cao et al., 2018). Compared with annual MDP, the extrema of annual TP are more obviously concentrated in a certain small area. The maxima gather in the southern part and most minima are crowded into the northern part. The annual summary consolidates the spatial features and eliminates the randomness of daily precipitation.

TABLE 5 | Correlation and fitting of the annual TP in different percentiles between urban and non-urban regions of the YDM during 1992–2020.

Metrics	Minimum	25%	Medium	75%	Maximum
PCC	0.821	0.960	0.970	0.961	0.925
p-value	<0.001	<0.001	<0.001	<0.001	<0.001
KGE	0.772	0.954	0.885	0.809	0.789

The five quantiles of the annual TP increase to varying degrees in both the urban and non-urban regions, as shown in **Figures 9A–E**. A significant rising trend is observed of the MK values of the lower, median, and upper quartiles of annual TP in both urban and non-urban regions. Except for the upper quartile in rural areas, the other five time series have a confidence level of 99.9% (**Table 4**). Of the 10 years averages, all sampling grids in YDM have witnessed the growth of TP from the 1990s to the 2010s (**Figure 10**). The observed rising trend in the annual TP in the YDM region reveals that regional water resources are more abundant in the 2010s than in the 1990s, as stated in China's "National Assessment Report on Climate Change" (Lin et al., 2006). The significant increase in the amount of water resources in the YDM region will aid in resolving the contradictions between rapid economic development and rising water demands from industrial production, domestic water and ecological water requirements in urban areas, and rainfed agriculture water needs in non-urban areas.

The line charts fluctuate similarly in the five quantiles of annual TP in the urban and non-urban regions (**Figures 9A–E**). They are highly correlated and have a good fit with PCC and KGE of the middle three quartiles that are greater than or equal to 0.960 and 0.809, respectively (**Table 5**). Combined with the increasing trend, high correlation, and good agreement between urban and non-urban regions, climate change has impacted these features in the YDM.

The box plot's interdecadal changes reveal that yearly TP in urban and non-urban areas grows from the 1990s to the 2010s, after remaining relatively consistent during the 1990s and 2000s (**Figure 9F**). Except for the lowest percentile, the non-urban percentiles of the annual TP are greater than the urban percentiles. Using the median as an example, from 1990 to 2010, the decadal averages of annual TP in urban and non-urban regions grows from 1,214.39 mm and 1,251.09 mm to 1,379.18 mm and 1,456.61 mm, with increases of 13.57 and 16.43%, respectively. MK values of the 25th percentile, median, and 75th percentile of annual TP in the non-urban region are greater than those in the urban region. This is similar to the annual MDP with a slightly smaller difference between urban and non-urban regions. The non-urban region, with woods, rainfed croplands, and grassland as the primary land uses of precipitationsheds, is more likely to provide more favorable formation conditions for large-scale precipitation than the urban region.

CONCLUSION

This study provides a statistical method using grid-based precipitation characteristics to demonstrate a novel approach of dynamic sampling area to effectively address the limited representative space of ground precipitation sites in dynamic urban areas. The temporal and spatial inconsistency of static sampling, which is caused by urban growth, has effectively been addressed by this novel approach resulting in figures which are based on hundreds of thousands of sampling grids. In non-urban areas, the density of their fundamental data has surpassed the WMO suggested density, while in urban areas, it is very close to the required value (World Meteorological Organization, 2008a; Chacon-Hurtado et al., 2017). The statistics gathered by the newly created approach in this study are more in line with the requirements of large samples for statistical analysis as compared to traditional site-based research. What's more, this method is flexible in the sense that the resolution of the reanalyzed product can be adjusted according to requirements.

Applying the foregoing methodologies for the analysis of precipitation features and trends in the YDM region revealed that:

(i) In the context of the large-sample strategy, the spatiotemporal changes of the sampling cells interfere with the limited extrema and have little effect on the laws within the interquartile ranges in the YDM.
(ii) The annual TP and MDP in the YDM region's urban and non-urban areas both show a considerable upward trend, mainly due to climate change. They demonstrate that the region's water supplies are expanding and that the risk of urban waterlogging is increasing.
(iii) Most maxima of annual MDP and TP are located in the south of YDM, while the minima are located in the north. Geographical differences affect the spatial distribution characteristics of precipitation in the YDM.
(iv) The increase in annual MDP and TP in the non-urban regions is greater than in the urban regions. It indicates that the land cover categories woods, grassland, and rainfed agricultural land may play a positive role in the formation of precipitationsheds' sink zones.

Despite the rapid improvement of precipitation reanalysis products, their spatial and temporal resolution remains a limitation. Both horizontal and temporal resolution of existing products are insufficient for a more precise and accurate analysis of precipitation characteristics in urban areas.

To improve the current study, future work should concentrate on the following aspects:

(i) The impact of urbanization on its downwind areas. The contribution of the influence of urbanization at a scale of a megalopolis on precipitation on its downwind areas to the precipitation of non-urban areas needs further investigation.
(ii) Due to a lack of attribution analysis of precipitation change, it is difficult to differentiate between the increase of precipitation in the YDM region which is affected by anthropogenic activities and by global climate change. Therefore, an attribution analysis

based on a statistical or deterministic study still needs to be considered in future work.

DATA AVAILABILITY STATEMENT

The binarized land use images with a resolution of 5 km, as well as the extracted time series of percentile statistics in the YDM from 1992 to 2020, are available on Zenodo with a doi of https://doi.org/10.5281/zenodo.6640436 and are free to use and distribute under the CC BY 4.0 license.

AUTHOR CONTRIBUTIONS

Conceptualization, XL; methodology, XL; software, XL; validation, XL; formal analysis, XL; investigation, XL; resources, XL; data curation, XL; writing—original draft preparation, XL and MY; writing—review and editing, CZ, AK, and MY; visualization, XL; supervision, DF and CZ; project administration, DF; funding acquisition, DF and MY. All authors have read and agreed to the published version of the manuscript.

FUNDING

This research was funded by the National Key R&D Program of China (2018YFC0809904) and National Natural Science Foundation of China (51909058).

ACKNOWLEDGMENTS

Many thanks to Python community, Google Earth Engine, and QGIS. Land cover images from 1992 to 2020 in the YDM courtesy of the European Space Agency. The original boundary of the YDM courtesy of OpenStreetMap. Terrain tiles used as background in **Figure 1** courtesy of Stamen Design. CHIRPS courtesy of UC Santa Barbara and USAID.

SUPPLEMENTARY MATERIAL

The Supplementary Material for this article can be found online at: https://www.frontiersin.org/articles/10.3389/feart.2022.917069/full#supplementary-material

REFERENCES

Akrami, S. A., El-Shafie, A., Naseri, M., and Santos, C. A. G. (2014). Rainfall Data Analyzing Using Moving Average (MA) Model and Wavelet Multi-Resolution Intelligent Model for Noise Evaluation to Improve the Forecasting Accuracy. *Neural Comput. Appl.* 25 (7), 1853–1861. Dec 1. doi:10.1007/s00521-014-1675-0

Bai, L., Shi, C., Li, L., Yang, Y., and Wu, J. (2018). Accuracy of CHIRPS Satellite-Rainfall Products over Mainland China. *Remote Sens.* 10 (3), 362. Feb 26. doi:10.3390/rs10030362

Becker, S., Gemmer, M., and Jiang, T. (2006). Spatiotemporal Analysis of Precipitation Trends in the Yangtze River Catchment. *Stoch. Environ. Res. Ris. Assess.* 20 (6), 435–444. Sep 1. doi:10.1007/s00477-006-0036-7

Bureau of Hydrology, Ministry of Water Resources and Nanjing Hydraulic Research Institute (2006). *Atlas of Statistical Parameters of Rainstorm in China*. Beijing, CN: China Water Conservancy and Hydropower Press.

Burian, S. J., and Shepherd, J. M. (2005). Effect of Urbanization on the Diurnal Rainfall Pattern in Houston. *Hydrol. Process.* 19 (5), 1089–1103. Mar 30. doi:10.1002/hyp.5647

Caloiero, T., Coscarelli, R., and Ferrari, E. (2018). Application of the Innovative Trend Analysis Method for the Trend Analysis of Rainfall Anomalies in Southern Italy. *Water Resour. Manage* 32 (15), 4971–4983. Dec 1. doi:10.1007/s11269-018-2117-z

Cao, Y., Zhang, W., and Wang, W. (2018). Evaluation of TRMM 3B43 Data over the Yangtze River Delta of China. *Sci. Rep.* 8 (1), 5290. doi:10.1038/s41598-018-23603-z

Central Committee of the Communist Party of China (CPC) (2014). *State Council. National New-type Urbanization Plan (2014-2020)*. [Internet]. Beijing, China: Xinhua News Agency. Available from: http://www.gov.cn/gongbao/content/2014/content_2644805.htm ([cited 2021 Nov 30].

Chacon-Hurtado, J. C., Alfonso, L., and Solomatine, D. P. (2017). Rainfall and Streamflow Sensor Network Design: a Review of Applications, Classification, and a Proposed Framework. *Hydrol. Earth Syst. Sci.* 21 (6), 3071–3091. Jun 28. doi:10.5194/hess-21-3071-2017

Chen, S., Yin, D., Li, Y., Sun, Y., and Li, C. (2016). Analysis of Differences of Rainfall between Urban and Rural Regions in Nanjing. *J. Meteorol. Environ.* 32 (6), 27–33. doi:10.3969/j.issn.1673-503X.2016.06.004

Chow, S. D., and Chang, C. (1984). Shanghai Urban Influences on Humidity and Precipitation Distribution. *GeoJournal* 8 (3), 201–204. Apr 1. doi:10.1007/bf00446468

Copernicus Climate Change Service (2020). "Product User Guide and Specification: ICDR Land Cover 2016 to 2019,". [Internet]Report No. 2018/C3S_312b_Lot5_VITO/SC1, 38. UCLouvain and Brockmann Consult GMBHAugAvailable from: https://datastore.copernicus-climate.eu/documents/satellite-land-cover/D3.3.12-v1.3_PUGS_ICDR_LC_v2.1.x_PRODUCTS_v1.3.pdf (Accessed April 25, 2019).

Dahmen, E. R., and Hall, M. J. (1990). *Screening of Hydrological Data: Tests for Stationarity and Relative Consistency*. Wageningen, NL: ILRI publication.

Daniels, E. E., Lenderink, G., Hutjes, R. W. A., and Holtslag, A. A. M. (2016). Observed Urban Effects on Precipitation along the Dutch West Coast. *Int. J. Climatol.* 36 (4), 2111–2119. Mar 30. doi:10.1002/joc.4458

Defourny, P., Lamarche, C., Bontemps, S., De Maet, T., Van Bogaert, E., Moreau, I., et al. (2017). "Land Cover CCI Product User Guide Version 2.0,". Report No. CCI-LC_PUGv2, 105. UCLouvain, Brockmann Consult GMBH and Gamma RSAprAvailable at: https://maps.elie.ucl.ac.be/CCI/viewer/download/ESACCI-LC-Ph2-PUGv2_2.0.pdf (Accessed September 14, 2015).

Deng, Z. (2017). On Temporal and Spatial Variation Characteristic of Precipitation in Hefei City from 1963 to 2012. *J. Jiangsu Second Norm. Univ. Nat. Sci.* 33 (6), 25–29+124. Jun. http://xb.jssnu.edu.cn/

Diem, J. E., and Mote, T. L. (2005). Interepochal Changes in Summer Precipitation in the Southeastern United States: Evidence of Possible Urban Effects Near Atlanta, Georgia. *J. Appl. Meteorol.* 44 (5), 717–730. May 1. doi:10.1175/jam2221.1

Ding, Y., Ren, G., Shi, G., Gong, P., Zheng, X., Zhai, P., et al. (2006). National Assessment Report of Climate Change (I): Climate Change in China and its Future Trend. *Adv. Clim. Change Res.* 02 (01), 3–8. doi:10.3969/j.issn.1673-1719.2007.z1.001

Ding, Y. (2018). Impact of Climate Change and Urbanization on Extreme Rainstorms in China's Megacities. *China Flood Drought Manag.* 28 (02), 1–2. http://www.cfdm.cn

Du, J., and Chen, J. (2010). The Corner Stone in Facilitating the Transition from Deterministic to Probabilistic Forecasts-Ensemble Forecasting and Its Impact on Numerical Weather Prediction. *Meteorol. Mon.* 36 (11), 1–11. doi:10.7519/j.issn.1000-0526.2010.11.001

Ellison, D., Morris, C. E., Locatelli, B., Sheil, D., Cohen, J., Murdiyarso, D., et al. (2017). Trees, Forests and Water: Cool Insights for a Hot World. *Glob. Environ. Change* 43, 51–61. Mar 1. doi:10.1016/j.gloenvcha.2017.01.002

European Space Agency (ESA). ESA CCI Land Cover Website [Internet]. 2021. Available from: http://www.esa-landcover-cci.org/ (Accessed April 8, 2021)

Fang, C. (2019). The Basic Law of the Formation and Expansion in Urban Agglomerations. *J. Geogr. Sci.* 29 (10), 1699–1712. Oct 1. doi:10.1007/s11442-019-1686-y

Fang, G., Gao, Y., Xu, L., Hu, L., and Zhang, S. (2012). Analysis of Precipitation Change and the Characteristics of Disaster Rainfalls in Shanghai. *Resour. Environ. Yangtze Basin* 21 (10), 1270–1273. http://yangtzebasin.whlib.ac.cn

Federal Interagency Stream Restoration Working Group (FISRWG) (1989). *Stream Corridor Restoration: Principles, Processes, and Practices*. [Internet]. Washington, DC, USA: Federal Interagency Stream Restoration Working Group, 637. Available from: https://www.nrcs.usda.gov/wps/portal/nrcs/detailfull/national/water/manage/restoration/?cid=stelprdb1043244 ([cited 2019 Oct 3]).

Fletcher, T. D., Andrieu, H., and Hamel, P. (2013). Understanding, Management and Modelling of Urban Hydrology and its Consequences for Receiving Waters: A State of the Art. *Adv. Water Resour.* 51, 261–279. doi:10.1016/j.advwatres.2012.09.001

Fu, D., Tang, D., and Levy, G. (2017). The Impacts of 2008 Snowstorm in China on the Ecological Environments in the Northern South China Sea. *Geomatics, Nat. Hazards Risk* 8 (2), 1034–1053. Dec 15. doi:10.1080/19475705.2017.1292559

Funk, C., Peterson, P., Landsfeld, M., Pedreros, D., Verdin, J., Shukla, S., et al. (2015). The Climate Hazards Infrared Precipitation with Stations-A New Environmental Record for Monitoring Extremes. *Sci. Data* 2 (1), 150066. Dec 8. doi:10.1038/sdata.2015.66

Gao, F., Liu, H., Yang, J., and Liu, W. (2016). Analysis and Comparison on Plum Rain Characteristics within Yangtze-Huaihe Region and South Jiangsu Area. *Water Resour. Hydropower Eng.* 47 (09), 1–4+10. doi:10.13928/j.cnki.wrahe.2016.09.001

Goddard Space Flight Center (2012). *NASA Satellite Confirms Urban Heat Islands Increase Rainfall Around Cities*. [Internet]. Greenbelt, MD: National Aeronautics and Space Administration (NASA). Available from: https://svs.gsfc.nasa.gov/stories/urban_rain_20020618 ([cited 2022 Jan 10].

Gorelick, N., Hancher, M., Dixon, M., Ilyushchenko, S., Thau, D., and Moore, R. (2017). Google Earth Engine: Planetary-Scale Geospatial Analysis for Everyone. *Remote Sens. Environ.* 202, 18–27. Jul 6. doi:10.1016/j.rse.2017.06.031

Gregorio, A. D., and Jansen, L. J. M. (2000). *Land Cover Classification System (LCCS)*. [Internet]. Rome, Italy: Food and Agriculture Organization of the United Nations. Available from: http://www.fao.org/3/x0596e/x0596e00.htm ([cited 2021 Apr 7]).

Gupta, H. V., Kling, H., Yilmaz, K. K., and Martinez, G. F. (2009). Decomposition of the Mean Squared Error and NSE Performance Criteria: Implications for Improving Hydrological Modelling. *J. Hydrol.* 377 (1), 80–91. Oct 20. doi:10.1016/j.jhydrol.2009.08.003

Han, L., Xu, Y., Pan, G., Deng, X., Hu, C., Xu, H., et al. (2015a). Changing Properties of Precipitation Extremes in the Urban Areas, Yangtze River Delta, China, during 1957-2013. *Nat. Hazards* 79 (1), 437–454. Oct 1. doi:10.1007/s11069-015-1850-3

Han, L., Xu, Y., Yang, L., and Deng, X. (2015b). Changing Structure of Precipitation Evolution during 1957-2013 in Yangtze River Delta, China. *Stoch. Environ. Res. Risk Assess.* 29 (8), 2201–2212. Dec 1. doi:10.1007/s00477-015-1034-4

Hand, L. M., and Shepherd, J. M. (2009). An Investigation of Warm-Season Spatial Rainfall Variability in Oklahoma City: Possible Linkages to Urbanization and Prevailing Wind. *J. Appl. Meteorol. Climatol.* 48 (2), 251–269. Feb 1. doi:10.1175/2008jamc2036.1

He, B., Chen, C., Zhou, N., and Xu, S. (2003). Urbanized Area Runoff Coefficient and its Application. *Shanghai Environ. Sci.* 22 (7), 472–475. https://mall.cnki.net/magazine/magalist/SHHJ.htm

Hu, H. (2015). Spatiotemporal Characteristics of Rainstorm-Induced Hazards Modified by Urbanization in Beijing. *J. Appl. Meteorol. Climatol.* 54 (7), 1496–1509. Jul 1. doi:10.1175/jamc-d-14-0267.1

Huang, L., Zhao, D., Wang, J., Zhu, J., and Li, J. (2008). Scale Impacts of Land Cover and Vegetation Corridors on Urban Thermal Behavior in Nanjing, China. *Theor. Appl. Climatol.* 94 (3–4), 241–257. doi:10.1007/s00704-007-0359-4

Huang, Q., and Lu, Y. (2015). The Effect of Urban Heat Island on Climate Warming in the Yangtze River Delta Urban Agglomeration in China. *Ijerph* 12 (8), 8773–8789. Aug. doi:10.3390/ijerph120808773

Huff, F. A. (1975). Urban Effects on the Distribution of Heavy Convective Rainfall. *Water Resour. Res.* 11 (6), 889–896. Dec. doi:10.1029/wr011i006p00889

Hussain, M., and Mahmud, I. (2019). pyMannKendall: a python Package for Non Parametric Mann Kendall Family of Trend Tests. *Joss* 4 (39), 1556. Jul 25. doi:10.21105/joss.01556

Jiang, X., Luo, Y., Zhang, D.-L., and Wu, M. (2020). Urbanization Enhanced Summertime Extreme Hourly Precipitation over the Yangtze River Delta. *J. Clim.* 33 (13), 5809–5826. Jul 1. doi:10.1175/jcli-d-19-0884.1

Keys, P. W., van der Ent, R. J., Gordon, L. J., Hoff, H., Nikoli, R., and Savenije, H. H. G. (2012). Analyzing Precipitationsheds to Understand the Vulnerability of Rainfall Dependent Regions. *Biogeosciences* 9 (2), 733–746. Feb 10. doi:10.5194/bg-9-733-2012

Kishtawal, C. M., Niyogi, D., Tewari, M., Pielke, R. A., and Shepherd, J. M. (2010). Urbanization Signature in the Observed Heavy Rainfall Climatology over India. *Int. J. Climatol.* 30 (13), 1908–1916. Nov 15. doi:10.1002/joc.2044

Kling, H., Fuchs, M., and Paulin, M. (2012). Runoff Conditions in the Upper Danube Basin under an Ensemble of Climate Change Scenarios. *J. Hydrology* 424-425, 264–277. Mar 6. doi:10.1016/j.jhydrol.2012.01.011

Li, J., Wang, W., Che, W., Liu, C., and Zhao, Y. (2015). Explanation of Sponge City Development Technical Guide: Regional Division for Total Rainfall Runoff Volume Capture Target. *China Water Wastewater* 31 (8), 6–12. doi:10.19853/j.zgjsps.1000-4602.2015.08.002

Liang, P., and Ding, Y. (2017). The Long-Term Variation of Extreme Heavy Precipitation and its Link to Urbanization Effects in Shanghai during 1916-2014. *Adv. Atmos. Sci.* 34 (3), 321–334. Mar 1. doi:10.1007/s00376-016-6120-0

Lin, E., Xu, Y., Jiang, J., Li, Y., Yang, X., Zhang, J., et al. (2006). National Assessment Report of Climate Change (II): Climate Change Impacts and Adaptation. *Adv. Clim. Change Res.* 02 (02), 51–56. Mar 30. doi:10.3969/j.issn.1673-1719.2006.02.001

Liu, A., Wang, H., Cui, Y., Shen, L., Yin, Y., Wu, Z., et al. (2020). Characteristics of Aerosol during a Severe Haze-Fog Episode in the Yangtze River Delta: Particle Size Distribution, Chemical Composition, and Optical Properties. *Atmosphere* 11 (1), 56. Jan. doi:10.3390/atmos11010056

Liu, X., Fu, D., Zevenbergen, C., Busker, T., and Yu, M. (2021). Assessing Sponge Cities Performance at City Scale Using Remotely Sensed LULC Changes: Case Study Nanjing. *Remote Sens.* 13 (4), 580. doi:10.3390/rs13040580

Lu, M., Xu, Y., Shan, N., Wang, Q., Yuan, J., and Wang, J. (2019). Effect of Urbanisation on Extreme Precipitation Based on Nonstationary Models in the Yangtze River Delta Metropolitan Region. *Sci. Total Environ.* 673, 64–73. Jul 10. doi:10.1016/j.scitotenv.2019.03.413

Luo, M., and Lau, N. C. (2019). Urban Expansion and Drying Climate in an Urban Agglomeration of East China. *Geophys. Res. Lett.* 46 (12), 6868–6877. doi:10.1029/2019gl082736

Luo, X., Yang, B., Zhang, Y., Wang, C., and Yao, Y. (2020). Distribution Characteristics of Minute Rainfall Rate in Anhui Province. *Chin. J. Radio Sci.* 35 (6), 908–913. doi:10.13443/j.cjors.2020103001

IPCC (2021b). "Summary for Policymakers. [Internet] in *Climate Change 2021: The Physical Science Basis Contribution of Working Group I to the Sixth Assessment Report of the Intergovernmental Panel on Climate Change*. Editors V. Masson-Delmotte, P. Zhai, A. Pirani, S. L. Connors, C. Péan, S. Berger, et al. (Cambridge, United Kingdom and New York, NY, USA: Cambridge University Press). Available from: https://www.ipcc.ch/report/sixth-assessment-report-working-group-i/.

IPCC (2013a). [Internet] Editors T. F. Stocker, D. Qin, G-K. Plattner, M. M. B. Tignor, S. K. Allen, J. Boschung, et al. (Cambridge, United Kingdom and New York, NY: Cambridge University Press), 1535. Available from: https://www.ipcc.ch/report/ar5/wg1/.*Climate Change 2013: The Physical Science Basis*.

Meng, Q., Fan, S., He, J., Zhang, J., Sun, Y., Zhang, Y., et al. (2015). Particle Size Distribution and Characteristics of Polycyclic Aromatic Hydrocarbons during a Heavy Haze Episode in Nanjing, China. *Particuology* 18, 127–134. Feb 1. doi:10.1016/j.partic.2014.03.010

Ministry of Water Resources of the People's Republic of China (MWR) (2021). *Bulletin of Flood and Drought Disaster in China*. [Internet]. Beijing, CN: China Water Power Press. Available from: http://www.mwr.gov.cn/sj/.

National Development and Reform Commission (NDRC) (2013). Ministry of Finance (MOF) Ministry of Housing and Urban-Rural Development (MOHURD) Ministry of Transport (MOT) Ministry of Water Resources (MWR) Ministry of Agriculture (MOA). [Internet]Report No. FGQH-2013-2252. Beijing, CN: National Strategy for Climate Change Adaptation. Available from: https://www.ndrc.gov.cn/xxgk/zcfb/tz/201312/t20131209_963985.html?code=&state=123 ([cited 2021 Nov 24]Accessed Nov 24, 2021).

National Development and Reform Commission of the People's Republic of China (NDRC) (2016). Ministry of Housing and Urban-Rural Development of the People's Republic of China (MOHURD) The Plan for the Development of the Yangtze Delta Megalopolis [Internet]. Beijing 57. Report No.: FGGH-2016-1176. Available from: https://www.ndrc.gov.cn/xxgk/zcfb/ghwb/201606/t20160603_962187.html (Aceessed Jun).

Paul, S., Ghosh, S., Mathew, M., Devanand, A., Karmakar, S., and Niyogi, D. (2018). Increased Spatial Variability and Intensification of Extreme Monsoon Rainfall Due to Urbanization. *Sci. Rep.* 8 (1), 3918. Mar 2. doi:10.1038/s41598-018-22322-9

Pei, F., Wu, C., Liu, X., Hu, Z., Xia, Y., Liu, L.-A., et al. (2018). Detection and Attribution of Extreme Precipitation Changes from 1961 to 2012 in the Yangtze River Delta in China. *CATENA* 169, 183–194. Oct 1. doi:10.1016/j.catena.2018.05.038

Potsdam Institute for Climate Impact Research and Climate Analytics (2013). *Turn Down the Heat: Climate Extremes, Regional Impacts and the Case for Resilience*. [Internet]. Washington, DC, USA: World Bank. Available from: http://hdl.handle.net/10986/14000.

Research Council, National (2008). *Urban Stormwater Management in the United States*. Washington, DC, USA: National Research Council, 1–529.

Sang, Y.-F., Wang, Z., Li, Z., Liu, C., and Liu, X. (2013). Investigation into the Daily Precipitation Variability in the Yangtze River Delta, China. *Hydrol. Process.* 27 (2), 175–185. doi:10.1002/hyp.9202

Schueler, T. R. (1995). The Importance of Imperviousness. *Watershed Prot. Tech.* 1 (3), 100–111. https://owl.cwp.org/mdocs-posts/elc_pwp1/

Şen, Z. (2014). Trend Identification Simulation and Application. *J. Hydrol. Eng.* 19 (3), 635–642. doi:10.1061/(ASCE)HE.1943-5584.0000811

Shepherd, J. M. (2005). A Review of Current Investigations of Urban-Induced Rainfall and Recommendations for the Future. *Earth Interact.* 9 (12), 1–27. Jul 1. doi:10.1175/ei156.1

Stensrud, D. J., and Yussouf, N. (2007). Reliable Probabilistic Quantitative Precipitation Forecasts from a Short-Range Ensemble Forecasting System. *Weather Forecast* 22 (1), 3–17. Feb 1. doi:10.1175/waf968.1

Su, J., Zhang, W., Song, J., and Xu, A. (2021). Study on Spatio-Temporal Distribution of Hourly Precipitation in Yunnan Province. *Meteorol. Mon.* 47 (02), 133–142. doi:10.7519/j.issn.1000-0526.2021.02.001

Tang, X., Zhang, J., Wang, G., Yang, Q., Yang, Y., Guan, T., et al. (2019). Evaluating Suitability of Multiple Precipitation Products for the Lancang River Basin. *Chin. Geogr. Sci.* 29 (1), 37–57. Feb 1. doi:10.1007/s11769-019-1015-5

Taylor, R. (1990). Interpretation of the Correlation Coefficient: A Basic Review. *J. Diagnostic Med. Sonogr.* 6 (1), 35–39. Jan 1. doi:10.1177/875647939000600106

Terrain Classic Contributors (2021). China: Yangtze Delta Megalopolis. 119°56′15.84″E, 31°07′0795″N, zoom level 8. Map tiles by Stamen Design, under CC BY 3.0. Data by OpenStreetMap, under ODbL. [Internet]. Available from: https://github.com/stamen/terrain-classic ([cited 2021 Dec 8].

The State Council Information Office of the People's Republic of China (2008). *Responding to Climate Change: China's Policies and Actions*. [Internet]. Beijing, China: Xinhua News Agency. Available from: http://www.gov.cn/zwgk/2008-10/29/content_1134378.htm ([cited 2021 Oct 28].

Virtanen, P., Gommers, R., Oliphant, T. E., Haberland, M., Reddy, T., Cournapeau, D., et al. (2020). SciPy 1.0: Fundamental Algorithms for Scientific Computing in Python. *Nat. Methods* 17 (3), 261–272. Mar. doi:10.1038/s41592-019-0686-2

Wang, J., Wang, J., Wei, C., Hua, Z., Xu, Y., and Yin, P. (2015). Study on Urban Rainwater Utilization Modes in Jiangsu Province. *China Water Resour.* 15, 31–33+40. doi:10.3969/j.issn.1000-1123.2015.15.011

Wang, J., Chen, F., Doan, Q.-V., and Xu, Y. (2021). Exploring the Effect of Urbanization on Hourly Extreme Rainfall over Yangtze River Delta of China. *Urban Clim.* 36, 100781. Mar 1. doi:10.1016/j.uclim.2021.100781

Wang, W., Hu, B., Teng, W., and Zhuang, X. (2003). Analysis of Main Meteorological Conditions and Characteristics of Summer Drought in Zhejiang Province. *J. Zhejiang Meteorol.* 24 (1), 21–25. doi:10.3969/j.issn.1004-5953.2003.01.006

Wang, Y., Xu, Y., Lei, C., Li, G., Han, L., Song, S., et al. (2016). Spatio-temporal Characteristics of Precipitation and Dryness/wetness in Yangtze River Delta, Eastern China, during 1960-2012. *Atmos. Res.* 172-173, 196–205. May 15. doi:10.1016/j.atmosres.2016.01.008

Wang, Y., Xu, Y., Tabari, H., Wang, J., Wang, Q., Song, S., et al. (2020). Innovative Trend Analysis of Annual and Seasonal Rainfall in the Yangtze River Delta, Eastern China. *Atmos. Res.* 231, 104673. Jan 1. doi:10.1016/j.atmosres.2019.104673

Westra, S., Alexander, L. V., and Zwiers, F. W. (2013). Global Increasing Trends in Annual Maximum Daily Precipitation. *J. Clim.* 26 (11), 3904–3918. Jun 1. doi:10.1175/jcli-d-12-00502.1

World Meteorological Organization (2008a). "Data Processing and Quality Control,". [Internet] in *Guide to Hydrological Practices: Hydrology - from Measurement to Hydrological Information*. 6th ed. (Geneva, Switzerland: WMO), 1. Available from: http://www.whycos.org/hwrp/guide/index.php.

World Meteorological Organization (2008b). "Methods of Observation,". [Internet] in *Guide to Hydrological Practices: Hydrology - from Measurement to Hydrological Information*. 6th ed. (Geneva, Switzerland: WMO), 1. Available from: http://www.whycos.org/hwrp/guide/index.php.

Xu, T., Liu, K., Shan, Y., and He, S. (2019). Flood Situation Analysis and Strategy Research on Hangjiahu Area. *China Rural. Water Hydropower* (02), 123–125. doi:10.3969/j.issn.1007-2284.2019.02.025

Xu, Z., Ren, M., Cheng, T., and Chen, H. (2020). Managing Urban Floods: the Urban Water Cycle Is the Foundation; the Unified Management of River Basins Is the Fundamental. *China Flood Drought Manag.* 30 (04), 20–24. doi:10.16867/j.issn.1673-9264.2019119

Yang, M.-n., Xu, Y.-p., Pan, G.-b., and Han, L.-f. (2014). Impacts of Urbanization on Precipitation in Taihu Lake Basin, China. *J. Hydrol. Eng.* 19 (4), 739–746. Apr 1. doi:10.1061/(asce)he.1943-5584.0000852

Yu, M., Li, Q., Hayes, M. J., Svoboda, M. D., and Heim, R. R. (2014). Are Droughts Becoming More Frequent or Severe in China Based on the Standardized Precipitation Evapotranspiration Index: 1951-2010? *Int. J. Climatol.* 34, 545–558. doi:10.1002/joc.3701

Yu, R., Zhou, T., Xiong, A., Zhu, Y., and Li, J. (2007). Diurnal Variations of Summer Precipitation over Contiguous China. *Geophys. Res. Lett.* 34. Jan 1Available from. doi:10.1029/2006GL028129

Yu, X., Gu, X., Kong, D., Zhang, Q., Cao, Q., Slater, L. J., et al. (2022). Asymmetrical Shift Toward Less Light and More Heavy Precipitation in an Urban Agglomeration of East China: Intensification by Urbanization. *Geophys Res. Lett.* 49 (4), e2021GL097046. doi:10.1029/2021gl097046

Yu, Z., Chen, L., Li, L., Zhang, T., Yuan, L., Liu, R., et al. (2021). Spatiotemporal Characterization of the Urban Expansion Patterns in the Yangtze River Delta Region. *Remote Sens.* 13 (21), 4484. Jan. doi:10.3390/rs13214484

Yue, S., and Wang, C. (2004). The Mann-Kendall Test Modified by Effective Sample Size to Detect Trend in Serially Correlated Hydrological Series. *Water Resour. Manag.* 18 (3), 201–218. Jun 1. doi:10.1023/b:warm.0000043140.61082.60

Zhang, J., Song, X., Wang, G., He, R., and Wang, X. (2014). Development and Challenges of Urban Hydrology in a Changing Environment: Ⅰ: Hydrological Response to Urbanization. *Adv. Water Sci.* 25 (04), 594–605. doi:10.14042/j.cnki.32.1309.2014.04.020

Zhang, J., Zhou, T., and Jin, J. (2022). What Can the Water Sector Do to Achieve China's Dual Carbon Target. *Hydro-Sci Eng.* (1), 1–8. doi:10.12170/20210927006

Zhang, K., Che, W., Zhang, W., and Zhao, Y. (2016). Discussion about Initial Runoff and Volume Capture Ratio of Annual Rainfall. *Water Sci. Technol.* 74 (8), 1764–1772. doi:10.2166/wst.2016.307

Zhang, Y., Ning, G., Chen, S., and Yang, Y. (2021). Impact of Rapid Urban Sprawl on the Local Meteorological Observational Environment Based on Remote Sensing Images and GIS Technology. *Remote Sens.* 13 (13), 2624. Jan. doi:10.3390/rs13132624

Zhao, A., Zhu, X., Shi, P., and Pan, Y. (2013). Review on Hydrological Response to Urbanization at Home and Abroad. *J. China Hydrol.* 33 (05), 16–22. doi:10.3969/j.issn.1000-0852.2013.05.004

Zhou, T., Yu, R., Chen, H., Dai, A., and Pan, Y. (2008). Summer Precipitation Frequency, Intensity, and Diurnal Cycle over China: A Comparison of Satellite Data with Rain Gauge Observations. *J. Clim.* 21 (16), 3997–4010. Aug 15. doi:10.1175/2008jcli2028.1

Conflict of Interest: The authors declare that the research was conducted in the absence of any commercial or financial relationships that could be construed as a potential conflict of interest.

Publisher's Note: All claims expressed in this article are solely those of the authors and do not necessarily represent those of their affiliated organizations, or those of the publisher, the editors and the reviewers. Any product that may be evaluated in this article, or claim that may be made by its manufacturer, is not guaranteed or endorsed by the publisher.

frontiers | Frontiers in Earth Science

TYPE Original Research
PUBLISHED 25 July 2022
DOI 10.3389/feart.2022.915954

OPEN ACCESS

EDITED BY
Sanjeev Kumar Jha,
Indian Institute of Science Education and Research, India

REVIEWED BY
Chenghai Wang,
Lanzhou University, China
Devanil Choudhury,
University of Bergen, Norway

*CORRESPONDENCE
GuoPing Li,
liguoping@cuit.edu.cn

SPECIALTY SECTION
This article was submitted to Atmospheric Science, a section of the journal Frontiers in Earth Science

RECEIVED 08 April 2022
ACCEPTED 27 June 2022
PUBLISHED 25 July 2022

CITATION
Dong Y, Li G, Jiang X and Wang Y (2022), The characteristics and formation mechanism of double-band radar echoes formed by a severe rainfall occurred in the Sichuan Basin under the background of two vortices coupling. *Front. Earth Sci.* 10:915954. doi: 10.3389/feart.2022.915954

The characteristics and formation mechanism of double-band radar echoes formed by a severe rainfall occurred in the Sichuan Basin under the background of two vortices coupling

YuanChang Dong[1], GuoPing Li[2,3]*, XingWen Jiang[1] and YuanCheng Wang[4]

[1]Institute of Plateau Meteorology, China Meteorological Administration (CMA)/ Heavy Rain and Drought-Flood Disaster in Plateau and Basin Key Laboratory of Sichuan Province, Chengdu, China, [2]School of Atmospheric Sciences, Chengdu University of Information Technology, Chengdu, China, [3]Collaborative Innovation Center on Forecast and Evaluation of Meteorological Disasters, Nanjing University of Information Science and Technology, Nanjing, China, [4]Chengdu Academy of Environment Sciences, Chengdu, China

During 29–30 UTC June 2013, a severe rainfall event with a long and narrow region of strong precipitation occurred in the central of the Sichuan Basin (SCB). Under the combined influence of a Tibetan Plateau vortex (TPV) and a southwest vortex (SWV), two banded strong radar echoes existed and developed simultaneously over the SCB. The analysis reveals that the vertical wind shear (VWS) caused by the circulations of the TPV and the SWV was the dominant factor of the formation and development of the radar echoes over the SCB. During the coupling period of the two vortices, the SWV provided abundant water vapor at the middle and lower levels over the SCB and the updrafts of the two vortices break through that formed deep convection, which made the precipitation in the SCB reach the maximum intensity. The enhancement of horizontal vorticity caused by the baroclinicity and the secondary circulation related to the two vortices created conditions for the formation of the double-band radar echoes. The matching degree of water vapor and heating conditions accompanying the circulation of the two vortices could affect the developments of convective storms and precipitation.

KEYWORDS

the Tibetan plateau vortex, the southwest vortex, coupling, vertical wind shear, radar echoes

1 Introduction

The formation and development of Tibetan plateau vortices and southwest vortices (TPSWVs), as well as the rainstorms and flood disasters caused by them, have always been an important topic concerned by meteorologists. Tao (1980) earlier revealed that typhoons, fronts, and cyclonic vortices (mainly the Tibetan Plateau vortices (TPVs) and the southwest vortices (SVWs) (Xiao et al., 2017)) moving eastward from the Tibetan Plateau and its downstream areas were the main triggering systems of extreme heavy precipitation events in China. TPSWVs might cause high-impact and severe weather events, such as heavy rains, thunderstorms, and windstorms over the Sichuan Basin (SCB) and its surrounding areas (Luo et al., 1993; Qian and Jiao, 1997). After years of research, many aspects about TPSWVs have been recognized, including the weather situation of rainstorms caused by the TPVs (Gao and Yu, 2017), water vapor conditions of TPSWVs (Pan et al., 2011; Yue and Li, 2016), the role of Mesoscale Convective Systems (MCSs) in the rainstorms caused by SVWs (Hu et al., 2014), the role of Tibet plateau shear line in the formation of the rainstorms caused by SVWs (Hao et al., 2016), and the energy budget of TPVs (Dong and Li, 2015; Fu et al., 2015). The Tibetan plateau vortex (TPV) and the southwest vortex (SWV) usually developed independently, but there were also weather events in which they appeared simultaneously over the SCB or its surrounding areas. Chen et al. (2004) and Zhao and Wang (2010) studied the interaction mechanism when the two vortices appeared simultaneously and pointed out that the coupling of the two vortices was an important inducement to trigger heavy precipitation in the SCB. Zhou et al. (2014) used radar mosaic reflectivity data to analyze the characteristics of radar echoes in the SCB under the influence of a TPV and a SWV, which helped us to further understand the relationship between the two vortices and the formation and development of mesoscale convective systems.

Heavy rains are the main meteorological disaster caused by TPVs or SVWs. Over the course of about 50 years of research, meteorologists tried lots of methods including theoretical derivation (Yeh and Gao, 1979), weather analysis (Huang et al., 2010; Zhao et al., 2011), numerical simulation (Liu and Li, 2014), multi-source data (Du et al., 2013; Li and Deng, 2013; Ni et al., 2017), and multi-diagnosis (Huang et al., 2011; Song and Li, 2016) to establish the relationships between the development of the two vortices and heavy rains in order to make breakthroughs in the prediction of related heavy precipitation. Precipitation regions caused by TPVs or SVWs were more frequent on the east or southeast side of the vortex (Li et al., 2015). Jiang et al. (2014) and Yang et al. (2017) found that heavy rains mostly appeared in the right front side of the forward direction of the vortex center mainly because the positive vorticity advection transported by the vortex to this region stimulated the upward motion of the airflow. However, in the actual forecast, the uncertainty of the region and intensity of precipitation caused by a vortex is great. The main reason for this situation is that we do not know enough about the relationships between the occurrence and development of the two vortices and the convective systems in their circulation. Chen et al. (2011) established the connection between MCSs and a SWV by using a numerical simulation method, which promoted our understanding of the interaction between the SWV and MCSs. Nevertheless, little is known about how the variation of convective intensity, distribution characteristics, and development are related to the TPSWVs.

The strong convective precipitations caused by the TPSWVs are closely related to the development of mesoscale convective systems in the circulation of the two vortices. In recent years, with the development of the new generation weather radar network of China Meteorological Administration (CMA), we have made lots

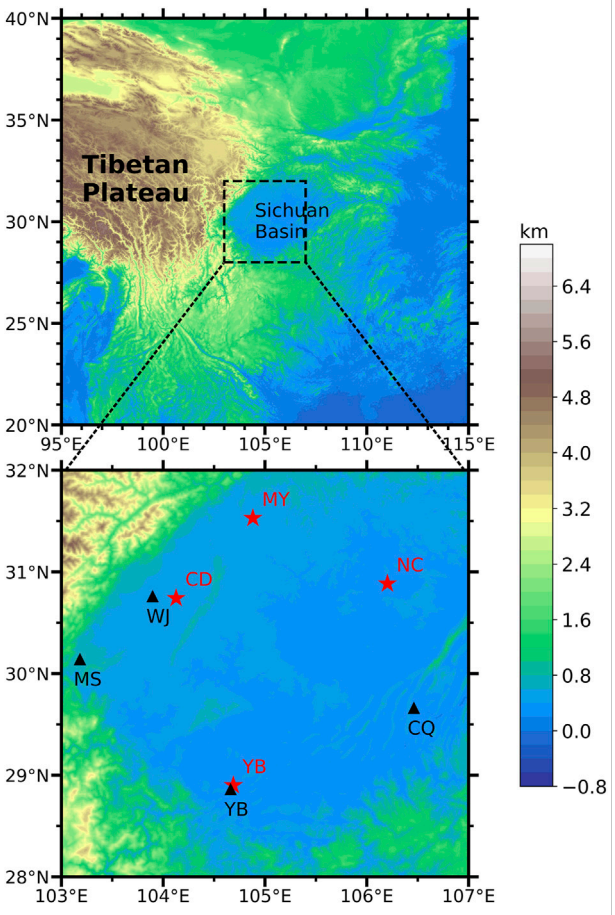

FIGURE 1
Observations used in this study and the topographic feature of the SCB and its surrounding areas. The location of the sounding sites (WJ, MS, YB, and CQ) is marked by the black triangles. The locations of selected ground-based S-band Doppler radar sites (MY, CD, YB, and NC) are marked by the red asterisks. The locations of AWS sites are too many (about 1,500 sites) to be marked. The area highlighted by the dotted box is the DWCPO.

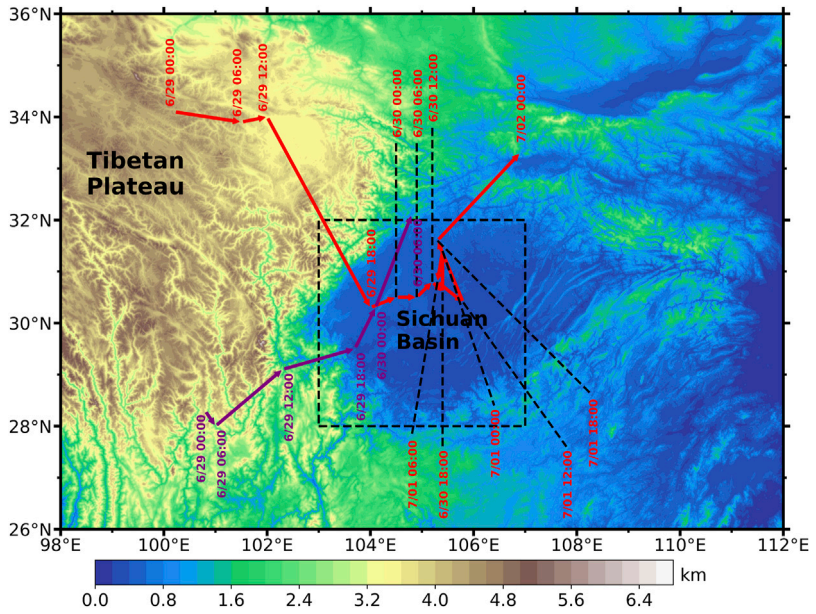

FIGURE 2
Topographic feature of the SCB and its surroundings and motion path of the two vortices (the red arrows represent the TPV motion path at 500 hPa and the purple arrows represent the SWV motion path at 700 hPa). The area highlighted by the dotted box indicates the DWCPO.

of achievements in the study of mesoscale convective systems. In many research conclusions, it has become a consensus that environmental vertical wind shear (VWS) plays an important role in the occurrence and development of convective systems. Zhang et al. (2012) believed that among the environmental elements conducive to the occurrence of convective systems, the convective available potential energy (CAPE) only needed to reach moderate intensity, but large deep VWS was required. Klemp (1987) used numerical simulation methods to verify that VWS was the main source of vorticity in the early stage of convective systems development, and also the important dynamic factors for the splitting and renewal of convective storms during the middle and late development periods.

Previous studies have pointed out the distribution of precipitation region and given the mechanism explanation when the SWV or the TPV developed alone. As introduced above, precipitation regions influenced by the SWV or the TPV were closely related to its circulation. However, when the two vortices were coupled, the intensity and distribution of precipitation would change significantly. Considering that the interaction of the circulations of the vortices during the coupling period might be an important factor leading to the change of precipitation region and the development of MCSs was closely related to the enhancement of rainfall intensity, the relationship between the two vortices and convective systems was established by VWS based on a strong precipitation event over the SCB, and the effects of the atmospheric dynamic and thermodynamic fields of the two vortices and terrain were investigated. The aim of our work is to reveal the new characteristics of the location of precipitation region when the two vortices were coupled and the mechanism that causes such new characteristics. The results will provide reference for the prediction of strong precipitation of the two vortices. The data and methods utilized in this work are introduced in Section 2. The relationships between the two vortices' circulations and the convective storms over the SCB are analyzed in Section 3. In Section 4, we analyze the new characteristics, formation and development mechanism, and fine radar echo structures of precipitation related to the two vortices. A summary and discussion are given in Section 5.

2 Data and methods

The data used and their functions mainly include:

1) The geographical location and motion path of the two vortices and the characteristic of the winds, temperature, and humidity were analyzed by using the ERA5 reanalysis hourly data (Hersbach et al., 2020) with a horizontal resolution of 0.5°*0.5° during June–July 2013.

2) The structure and variation of radar echoes were analyzed by using the radar mosaic reflectivity (RMR) data and the radar mosaic combination reflectivity (RMCR) data with a horizontal resolution of 1 km*1 km and 6 min temporal interval. The RMR data were derived from raw data observed by four CMA operational S-band (10 cm) Doppler radars located at Mianyang (MY), Chengdu (CD), Nanchong (NC), and Yibin

(YB) (Figure 1) during 28–30 UTC June 2013. The RMR data could make up for the limitation of single radar detection range (Xiao and Liu, 2006) and improve the data quality in the complex terrain area so that it is more suitable for the analysis and research of mesoscale weather systems in a larger spatio-temporal range.

3) The intensity and distribution of precipitation were studied by using the data observed by the automatic weather system (AWS) with more than 1,500 stations in SCB and its surrounding areas during 28–30 UTC June 2013.

4) The data observed by sounding sites located at Wenjiang (WJ), Mingshan (MS), YB, and Chongqin (CQ) (Figure 1) on 29 UTC June 2013 were used to analyze the atmospheric stratification for the formation and development of the convective systems over the SCB. The intensive observation experiment of the southwest vortex in Sichuan Province was conducted by the Institute of Plateau Meteorology from late June to early August.

VWS is an important condition for the formation and development of mesoscale convective systems. The main activity heights of TPVs and SVWs are 500 hPa and 700 hPa, respectively. The change of the position of the two vortices can form VWS zones with different intensity and distribution over the SCB. Therefore, the magnitude of VWS is an important connection between the development of the two vortices and the formation and development of convective systems over the SCB.

$$VWSV_1 = \left|\vec{V}_{500} - \vec{V}_{700}\right|, \quad (1)$$

$$VWSV_2 = \left|\vec{V}_{400} - \vec{V}_{850}\right|, \quad (2)$$

where $VWSV_1$ and $VWSV_2$ are the magnitude of the VWS vector of 500–700 hPa and 400–850 hPa, respectively (unit: m/s), and $\vec{V}$ is the wind vector.

$VWSV_1$ and $VWSV_2$ were used to measure the influence of the two vortices on the magnitude and distribution of VWS and the depth of VWS over the domain where convection and precipitation occurred (DWCPO). As can be seen from Figure 1, DWCPO is a sub-region of the SCB.

3 Influence of the two vortices' circulations on the occurrence and development of convection over the SCB

3.1 Overview of the two vortices

At 0000 UTC 29 June 2013, the TPV was generated in Gande County, Guoluo Tibetan Autonomous Prefecture, Qinghai Province. Meanwhile, the SWV was generated in Daocheng County, Ganzi Prefecture, Sichuan Province. After the formation of the two vortices, they moved towards the SCB. In the following 12 h, the positions of the two vortices experienced a process of rapid proximity from distance to coupling of their circulations over the SCB. At 1800 UTC 29 June, the intensity of the SWV gradually weakened and disappeared in the northern part of the SCB 12 h later. Compared with the SWV, the TPV stayed over the SCB for a long time. The center of the TPV entered the SCB at 1800 UTC 30 June and kept wandering in the central and northern part of the SCB. In the following 48 h, its position moved less, and disappeared to the northern part of the SCB at 0000 UTC 2 July (Figure 2). Considering the research focus of this paper and the integrity of observation data, the research period was determined as the period of simultaneous existence of the two vortices (from 0000 UTC 28 June to 0600 UTC 30 June 2013).

3.2 Influence of the two vortices' development on VWS over the SCB

From June to July, southerly winds prevailed at 700 hPa and westerly winds prevailed at 500 hPa over the SCB and its surrounding areas, and there was a cyclonic transition from northerly winds to southerly winds over the SCB (figures omitted). Therefore, an obvious region of VWS was formed in the central and western parts of the SCB, with a magnitude of about 7.5 m/s. When the VWS reached a certain intensity, it would become a favorable factor for genesis of convective systems over the SCB.

At 0000 UTC 29 June 2013, the TPV was initially generated, and the westerly airflow to the south of the TPV center was obviously strengthened. The westerly winds showed cyclonic transition from the west side to the east of the SCB at 500 hPa. The direction of the changed winds tended to be consistent with the direction of the southerly winds at 700 hPa, which was not conducive to the enhancement of $VWSV_1$ over the SCB (Figure 3B). Hence, the increase of $VWSV_1$ over the DWCPO was mainly due to the increase of wind velocity at 500 hPa and 700 hPa. At 0000 UTC 29 June, the centers of the two vortices moved to 102°E. At this time, winds at 500 hPa did not increase significantly over the DWCPO, but the cyclonic shift of winds direction moved east to 106°E, which made the $VWSV_1$ over the DWCPO was significantly strengthened only by the larger angle of the wind vectors between 500 hPa and 700 hPa. The maximum $VWSV_1$ increased to about 12.5 m/s, and the region with large value of the $VWSV_1$ showed an obvious north-south distribution (Figure 3C). At 1200 UTC 29 June, the centers of the two vortices moved rapidly toward the SCB, and the circulation fields of the two vortices tended to be coupled, resulting in the gradual decrease of $VWSV_1$ over the DWCPO (Figure 3D).

Based on the formation time and position changes of the two vortices, the research period could be divided into stages I, II, and III, as indicated in Figure 4. In stage I, before the two vortices

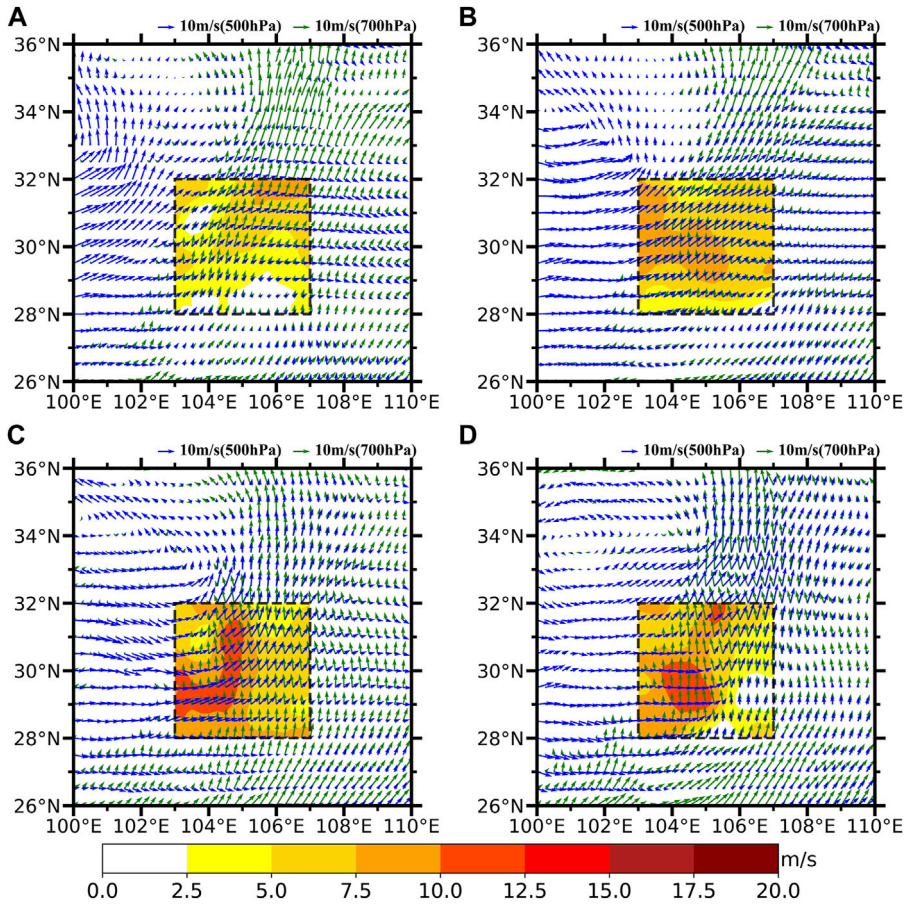

FIGURE 3
(A–D) Horizontal winds (m/s; the blue vectors represent winds at 500 hPa and the green vectors represent winds at 700 hPa) and VWSV1 (m/s; color shading) over the DWCPO from 1800 UTC 28 June to 1200 UTC 29 June 2013 at 6-h intervals. The inserted boxes (dotted boxes) indicate the DWCPO.

generated, large average $VWSV_2$ and small average $VWSV_1$ were observed over DWCPO (from 0000 UTC 28 June to 0000 UTC 29 June 2013). The two vortices moved towards the SCB, and the VWS over the DWCPO was gradually strengthened due to the change of the position of the two vortices in stage II (from 0000 UTC 29 June to 1200 UTC 29 June 2013). Convective systems over the DWCPO developed rapidly during the period from two vortices coupling to decoupling in stage III (from 1200 UTC 29 June to 0600 UTC 30 June 2013).

The average $VWSV_1$ over the DWCPO ranges from 7 m/s to 8.5 m/s in stage I (Figure 4), which was close to the average value of June and July. The average $VWSV_2$ was about 14 m/s, much larger than the average $VWSV_1$. At the early phases of the two vortices, the distance between the centers of the two vortices was about 600 km (in stage II). As the two vortices moved slowly, the distance between the two vortices became smaller. The cyclonic shear zone of westerly winds over the DWCPO moved eastward due to the movement of the TPV at 500 hPa, and the angle of wind vectors between 700 hPa and 500 hPa layers increased, resulting in a rapid increase of the average $VWSV_1$ over the DWCPO from 2100 UTC 28 June to 1200 UTC 29 June 2013. Meanwhile, both the average $VWSV_1$ and the average $VWSV_2$ had an increasing trend, and the VWS of the whole atmosphere was relatively consistent. The deep VWS created good conditions for the occurrence of convection over the DWCPO. As the distance between the two vortices rapidly approached, the circulations of the two vortices tended to be coupled, which was the main reason for the rapid decline of the average $VWSV_1$ and the average $VWSV_2$ in stage III.

3.3 Influence of VWS on the development of precipitation echoes

As can be seen from Figure 3, at 1200 UTC 29 June 2013, the $VWSV_1$ over the DWCPO reached its maximum with the

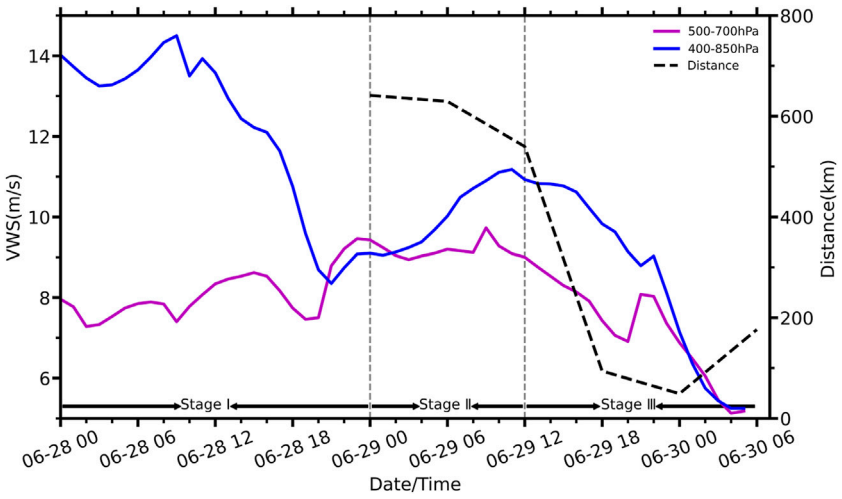

FIGURE 4
Time series of average VWSV1(m/s; purple solid line) and average VWSV2(m/s; blue solid line) over the DWCPO from 0000 UTC 28 June to 0600 UTC 30 June 2013 at 1-h intervals and the horizontal distance (km; black dotted line) between the centers of the two vortices from 0000 UTC 29 June to 0600 UTC 30 June 2013 at 6-h intervals. The time windows of stages I, II, and III are also marked.

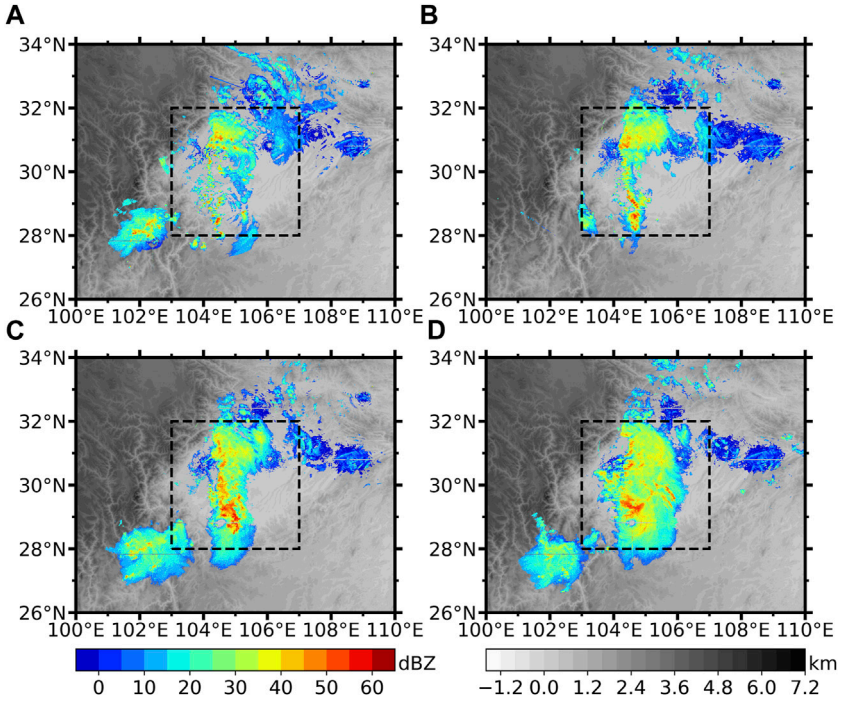

FIGURE 5
(A–D) RMCR (dBZ; color shading) from 1130 to 1730 UTC 29 June 2013 at 2-h intervals and topographic feature (km; gray shading). The inserted boxes (dotted boxes) indicate the DWCPO.

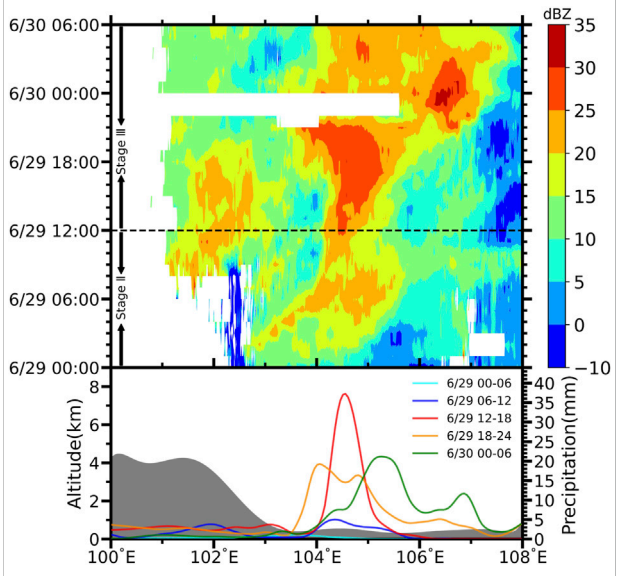

FIGURE 6
Temporal variation of the average RMCR (dBZ; color shading) from 0000 UTC 29 June to 0600 UTC 30 June 2013 at 1-h intervals and the average accumulated precipitation in 6-h (mm; color lines) observed by AWS in the SCB. The gray shading in the lower portion indicates the topography of the SCB and its surroundings along the 30°N.

changes of the positions of the two vortices, and the strong VWS region presented an obvious north-south zonal distribution. In the following hours, the VWS gradually weakened, the zonal distribution gradually disappeared, and the large value center was mainly in the southern part of the SCB. The above distribution characteristics and intensity changes of $VWSV_1$ were highly consistent with the development of radar echoes over the DWCPO during this period (Figure 5). At 1130 UTC 29 June 2013, radar echoes began to form over the DWCPO, and the radar echoes presented a north-south zonal distribution from the northern part of Yunnan province to the central part of Sichuan Province near 105°E, corresponding to the large value belt of $VWSV_1$. About 15 convective storms developed at the same time, with the scale less than 50 km and the central intensity generally exceeding 50 dBZ (Figure 5A). About 2 hours later, the relatively dispersed convective cells gradually joined into one piece, presenting an obvious north-south zonal distribution feature (Figure 5B). During this period, the intensity and scale of the convective cells increased continuously. With the weakening of the strong VWS over the DWCPO and the retention of the large value center in the southern part of the SCB, the strong radar echoes mainly developed in the southern part of the SCB, and the area of the strong echoes gradually exceeds that in the central and northern part of the SCB (Figure 5C). It is worth mentioning that with the weakening of the zonal feature of *VWSV1*, the zonal feature of the strong radar echoes over the SCB also gradually disappeared, and the strong echoes diffused to the east of the SCB (Figure 5D). In conclusion, VWS was an important condition for the occurrence and development of convective storms over the SCB and had a good indication for the intensity and distribution of radar echoes.

4 Characteristics of convective storms and precipitation over/in the SCB under the interaction of the two vortices

4.1 Spatial and temporal distribution of convection and precipitation

The change of position of the two vortices created good VWS conditions for the occurrence of convective storms over the SCB in stage II. During the following 6 h after 1200 UTC 29 June were the period of the strongest convective storms and precipitation over/in the SCB.

As shown in Figure 6, in stage II, the intensity of radar echoes over the SCB was weak, with the meridian average intensity generally lower than 25 dBZ, and the east-west scale of the echoes was small. With the passage of time, the radar echoes over the SCB gradually moved eastward, with a small change in intensity but a significant increase in zonal scale. Since the development of convective storms was closely related to the magnitude of VWS, although the circulations of the two vortices had affected the weather in the SCB, the development of convective storms over the SCB was generally weak because the intensity of $VWSV_1$ had not reached its maximum.

The center of strong precipitation was mainly concentrated near 102°E and 104.5°E from 0600 to 1200 UTC 29 June 2013, and the meridional average 6-h accumulated precipitation was less than 5 mm. The accumulated precipitation value from 0000 to 0600 UTC 29 June was negligible. In stage III, the changes of radar echoes and precipitation characteristics over/in the SCB could be divided into three phases. The early phase was from 1,200 to 1800 UTC 29 June. During this phase, due to the maximum VWS over the SCB, the convective storms developed rapidly, and the mean meridian RMCR reached about 35 dBZ between 104° and 105°E. The region of strong radar echoes increased rapidly, and the east-west position moved less. At the same time, the precipitation intensity reached its peak, and the meridian average accumulated precipitation between 104° and 105°E was about 40 mm over a 6-h period. The middle phase was from 1800 to 2400 UTC 29 June. In this phase, with the weakening of $VWSV_1$ over the SCB and the gradual disappearance of zonal distribution characteristics, the concentrated strong north-south echoes' region over the SCB began to develop eastward. As this strong echo region was not strictly along the south-to-north direction, no obvious double strong echoes' structure could be seen in Figure 6, but an obvious

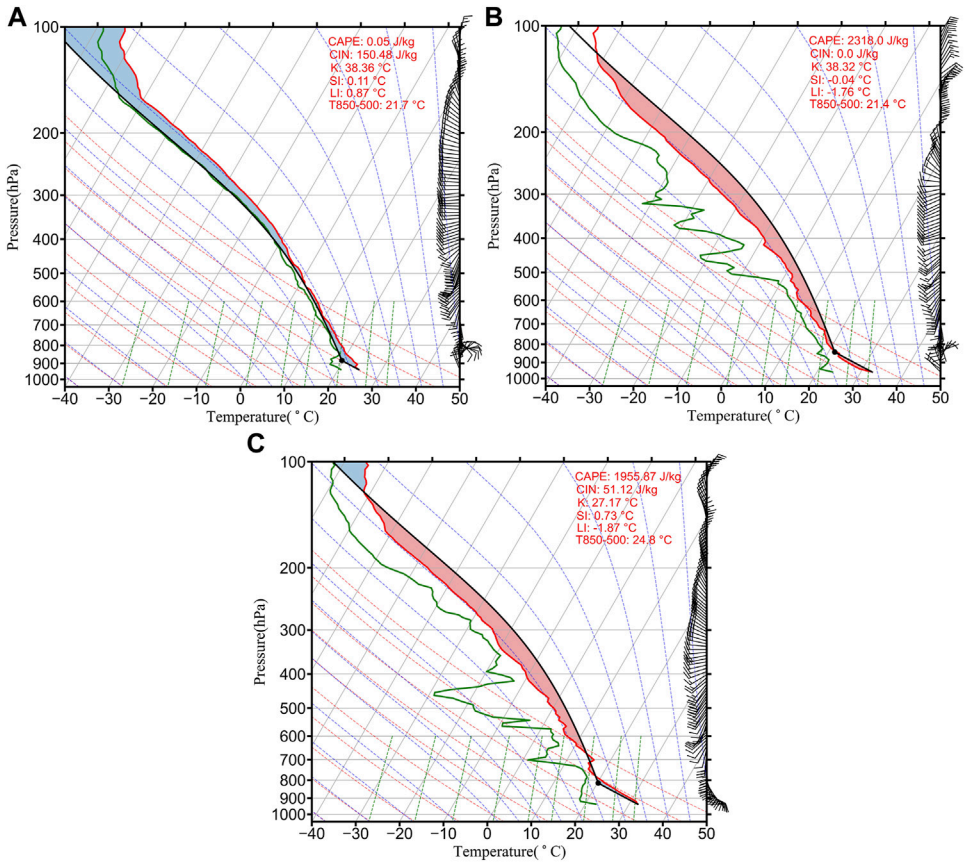

FIGURE 7
Skew T-logp diagrams over **(A)** the WJ site, **(B)** the YB site, and **(C)** the CQ site at 1200 UTC 29 June 2013.

bimodal structure can be seen in the precipitation curve during this phase (yellow curve in Figure 6). The maximum value of precipitation was obviously weaker than the previous period. The late phase was from 0000 to 0600 UTC 30 June. During this phase, the precipitation in the SCB was mainly controlled by the TPV as the SWV moved northward. Although the precipitation bimodal structure still existed, the precipitation intensity weakened significantly. In Section 4.3, the suppression effect of the TPV on convection will be discussed in detail. This suppression effect made radar echoes stratification appear in certain areas of the SCB and precipitation intensity decreased significantly.

4.2 Mechanism of double-band radar echoes formation and its relationship with precipitation in the SCB

Hydrostatic instability, water vapor in lower atmosphere, convective triggering conditions, and VWS are the four main factors for the occurrence of severe convective weather events. As can be seen from Figure 7, at 1200 UTC 29 June, the hydrostatic instability at the WJ site was the highest. Convection inhibition (CIN for short) played a dominant role from 900 hPa to 100 hPa and CAPE only 8.89 J/kg. K-index, SI-index, $T_{850\text{-}500}$, and other convective indexes were not prominent, and the situation at the MS site with similar location was similar (figures omitted). The CAPE at the YB site located at the southern end of the convective zone reached 1,641.98 J/kg, while CIN was only about 40 J/kg because it was in the strong convective region. At the same time, K-index, SI-index, and $T_{850\text{-}500}$ showed that the atmospheric stratification at the YB site were very conducive to the occurrence and development of convective storms. The CAPE at the CQ site was even higher than YB, reaching 1955.87 J/kg, which provided good environmental conditions for the development of radar echoes moving eastward over the SCB during the middle and late phases of stage III. In conclusion, strong convection occurred and developed in the middle of the SCB due to both strong VWS and unstable atmospheric stratification.

Among the four factors that influenced the occurrence of strong convection, the water vapor at low levels and VWS were closely related to the development of the two vortices, while the

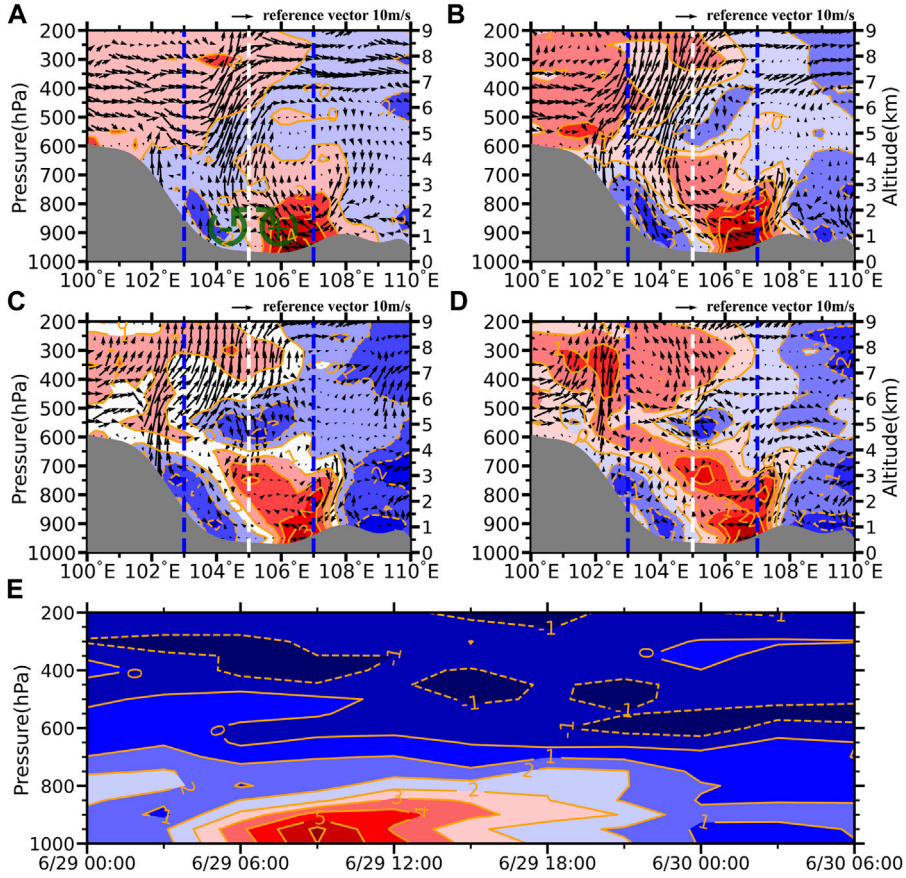

FIGURE 8
Vertical cross section of wind vectors (combined zonal wind and tenfold vertical velocity) and temperature space anomaly (K; color shading) along the 30°N. The gray shading indicates the topography along the 30°N. Heuristic diagrams (green curved vectors) indicating horizontal vorticity (+ and -) are also marked. The two blue dotted lines indicate the east and west boundary of the DWCPO. The white dotted line divided the DWCPO to the east and west regions. **(A)** 1200 UTC 29 June 2013, **(B)** 1500 UTC 29 June 2013, **(C)**1800 UTC 29 June 2013, and **(D)** 0000 UTC 30 June 2013. **(E)**Vertical cross section of the difference of temperature anomalies between the east and west regions of the DWCPO from 0000 UTC 29 June to 1500 UTC 29 June 2013 at 1-h intervals.

trigger condition and atmospheric stratification were related to the spatial thermal environment of the SCB.

As the night fell on June 29, the temperature of the near surface layer of the SCB was lower in the west and higher in the east due to the different radiation cooling. According to the temperature anomaly field (Figure 8), at the same altitude, the maximum temperature difference in the east–west temperature anomaly centers of the SCB was 6 K. The boundary between positive and negative values of near-surface temperature anomalies was just near 105°E, which was consistent with the region where double-band echoes occurred (Figures 5A–C). At 1200 UTC 29 June, the center of SWV was located in the southwest of the SCB, while the center of TPV was still in the northeast of the plateau and did not move into the SCB. At this time, the airflow movement in the middle and lower layers of the SCB were mainly influenced by the circulation of the SWV, leading to the prevailing easterly airflows below 800 hPa in the eastern part of the SCB. The airflows showed obvious upward movement in the central part of the SCB, and the strong part of its ascending branch was located near 105°E (Figure 8A).

The convergence of warm and cold airflow near the surface layer and strong upward movement were good trigger conditions for the occurrence of convection. In combination with unstable atmospheric stratification, abundant water vapor in the lower layer, and deep VWS, all conditions for the occurrence of strong convection near 105°E over the SCB were available. In the following 6 h, with the enhancement of radiative cooling in the western mountains of the SCB, the confrontation between the cold and warm air near 105°E was maintained, and with the coupling effect of the two vortices moving into the SCB, the vertical movement of the atmosphere over the SCB developed particularly deep (Figures 8B,C). At 0000 UTC 30 June, the confrontation of near-surface temperature and the development of deep convection over the SCB disappeared gradually due to

solar radiation and the weakening of the SWV. It is worth mentioning that by comparing the circulation over the SCB dominated by the SWV (Figure 8A) and that dominated by the TPV (Figure 8D), it can be found that the strong vertical movement over the SCB under the influence of the SWV is mainly below 600 hPa, while above 500 hPa under the influence of the TPV.

The westerly winds above 500 hPa on the south side of the TPV cooled and descended in the eastern part of the SCB, while the easterly winds below 700 hPa on the north side of the SWV heated and rose in the central part of the SCB, forming an obvious secondary circulation over the SCB in coordination with deep VWS. Before the two vortices coupled, the secondary circulation was particularly obvious, which shows an obvious horizontal vortex tube rotating clockwise over the SCB (Figure 8A). Klemp (1987) pointed out that the horizontal vortex tube tilted by the updraft rising and the vorticity couplet formed were an important dynamic mechanism for the generation and development of convective storms. It was also the main reason for the formation of many mesoscale convective cell cores in the north-south zonal convective systems over the SCB.

In order to reveal the role of the secondary circulation, we analyze the vertical and horizontal vorticity associated with the secondary circulation.

$$\frac{\partial \zeta}{\partial t} = M+N+P+R+S, \tag{3}$$

$$M = -\left[u\frac{\partial \zeta}{\partial x}+v\left(\beta+\frac{\partial \zeta}{\partial y}\right)\right], \tag{4}$$

$$N = -\omega\frac{\partial \zeta}{\partial p}, \tag{5}$$

$$P = -(\zeta+f)\nabla\cdot\vec{V}, \tag{6}$$

$$R = -\left(\frac{\partial \omega}{\partial x}\frac{\partial v}{\partial p}-\frac{\partial \omega}{\partial y}\frac{\partial u}{\partial p}\right). \tag{7}$$

From the first to the last term on the right (Eq. 3) are the horizontal advection term (M), vertical advection term (N), horizontal divergence term (P), tilting term (R), and friction term (S), respectively.

After magnitude analysis, the horizontal vorticity of the P-coordinate system can be simplified into the following formula (Eq. 8, 9):

$$\zeta_x = \frac{\partial w}{\partial y}+\frac{pg}{R_dT}\frac{\partial v}{\partial p}\propto\frac{\partial v}{\partial p}, \tag{8}$$

$$\zeta_y = -\frac{\partial w}{\partial x}-\frac{pg}{R_dT}\frac{\partial u}{\partial p}\propto-\frac{\partial u}{\partial p}. \tag{9}$$

ζ_y is the main horizontal vorticity over the DWCPO during the gradual coupling process (Figure 9). The positive region of ζ_y experienced a process from strengthening up to weakening subsidence from 0600 UTC 29 June to 0000 UTC 30 June (Figures 9A1–D1). When the secondary circulation was strong, the positive horizontal vorticity below 600 hPa had obvious convergence uploading characteristics and the vortex tube uploading was unidirectional (Figure 9B1), which indicated that the circulation of the SWV could actively affect the TPV, while the TPV had no obvious influence on the SWV.

The north-south vortex tubes caused by the secondary circulation tilted under the action of updraft, resulting in the transformation of horizontal vorticity to vertical vorticity. It could be seen from Figures 9A2–D2 that the large value distribution of R was consistent with that of ζ_y and the large value of ζ_y was mainly distributed in the central and western regions of the DWCPO at 0600 UTC 29 June (Figure 9A2). At the same time, the large value region of R presented an obvious north-south zonal distribution, which was consistent with the distribution characteristics of strong radar echo in this period. The distribution of ζ_y had little change at 1200 UTC 29 June (Figure 9B2), but the large value region of R presents a double-band distribution structure similar to the strong radar echoes. Based on Figure 9A2 and Figure 9B2, it was found that the formation of the double-band structure of radar echoes was closely related to the distribution of the R value.

It was worth noting that the ζ_y positive region near 800 hPa had two significant high value centers at 0600 UTC 29 June (Figure 9A1). After 6 h, the two large value centers strengthened and connected (Figure 9B1). Considering that the transformation from horizontal vorticity to vertical vorticity could enhance the local convection intensity, the distribution characteristics of the ζ_y positive value may be the key factor for the development of strong echo region from single-band distribution to double-band distribution.

With the proximity of the two vortices, the intensity of ζ_y and R over the DWCPO region gradually weakened (Figure 9C2–D2), which was consistent with the weakening of the intensity of the secondary circulation in this period.

Due to the relatively fixed location of the large value region of VWS formed by the circulations of the two vortices, the occurrence and development region of strong convection over the SCB was relatively fixed too. In terms of precipitation, it was a long and narrow heavy precipitation belt from YB in the south to MY in the north. The north-south scale of the heavy precipitation belt was more than 300 km, but its east-west width was only about 50 km (Figures 10A1–D1).

After the generation of the first band echo formed by the rain area seen on radar, many convective cells with a scale less than 10 km were gradually formed not far from its east side, and these convective cells gradually connect north and south to form a new band echo (Figures 10A2–D2). Generally, after a convective storm developed to the mature phase, the colder air at mid-levels would pass through the updraft region and descended, which resulted in strengthening the strength of the near-surface cold pool at the back of the mature storm, then cutting off the warm and wet air in the middle and lower layers of the old convective storm, and triggering a new one at the front of the

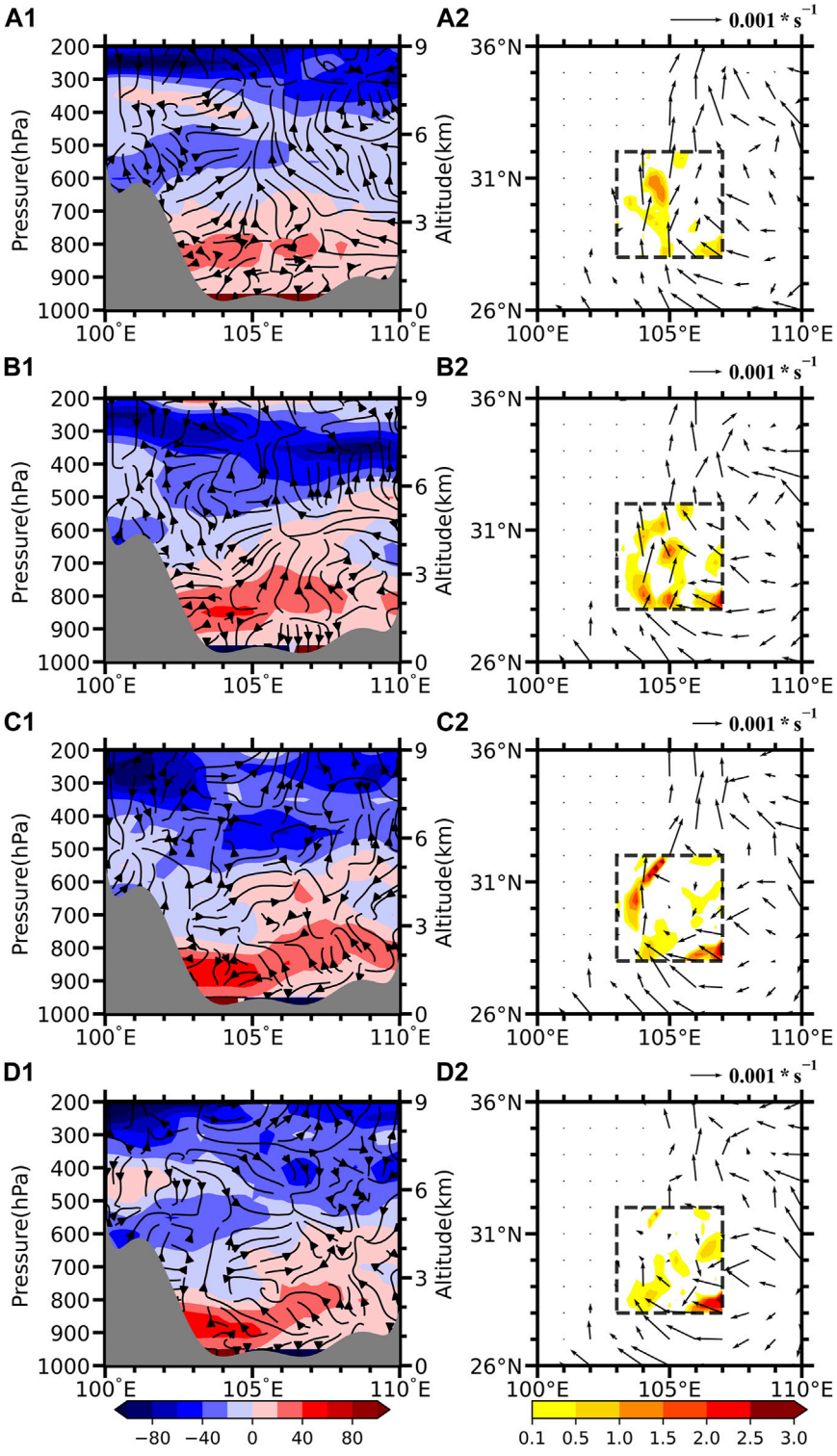

FIGURE 9
(A1–D1) Vertical cross section of vorticity vectors (combined ζ_y and tenfold vertical vorticity) and the zonal mean (28°N-32°N) of ζ_y ($10^{-3}s^{-1}$; color shading) from 0600 UTC 29 June to 0000 UTC 30 June 2013 at 6-h intervals. The gray shading indicates the zonal mean (28°N-32°N) of the topography. **(A2–D2)** Horizontal vorticity ($10^{-3}s^{-1}$; vector) and the positive tilting term ($10^{-8}s^{-2}$; color shading) over the DWCPO from 0600 UTC 29 June to 0000 UTC 30 June 2013 at 6-h intervals.

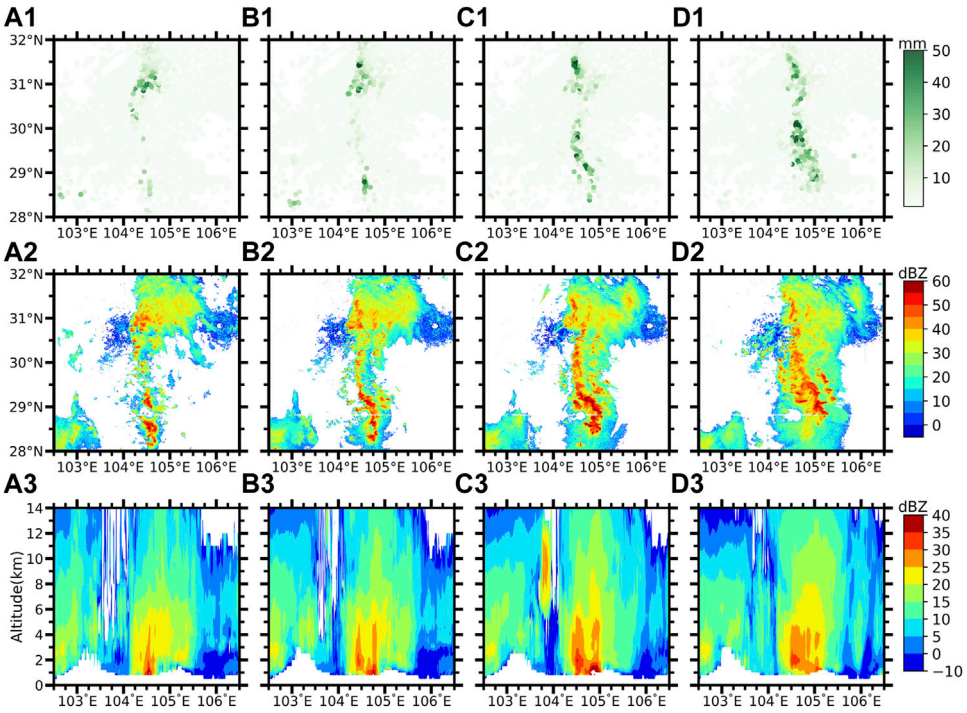

FIGURE 10
(A1–D1) Precipitation intensity in the DWCPO (mm/hour, color dots) from 1200 UTC 29 June to 1500 UTC 29 June 2013 at 1-h intervals. **(A2–D2)** As in **(A1–D1)** but for the RMCR (dBZ; color shading). **(A3–D3)** Vertical cross section of the mean meridional RMR (dBZ; color shading) from 1200 UTC 29 June to 1500 UTC 29 June 2013 at 1-h intervals.

surface cold pool. This is the main mechanism for the alternation of old and new convective storms (Rotunno et al., 1988). In contrast, there was a double-band echoes in which old and new convective storms coexist over the SCB.

Therefore, we believe that the main reasons for the coexistence of double-band radar echoes are as follows:

1) The formation and coexistence of the double-band radar echoes mainly occurred in the early phase of stage III, when the VWS over the SCB reached the maximum, and then the two vortices coupled over the SCB. The strong updraft near the centers of the two vortices ran through the 700–500 hPa layers, making the updraft over the SCB extend from the near surface to 200 hPa. The updraft was dominant, leading to the weakening of horizontal motion of parcels in the vicinity of the convective cell, which enabled almost all the CAPE of the environment east of the old cell to be converted to kinetic energy of vertical motion, enabling the rapid development of the new cell.

2) From the simplified equation of vorticity in the x–z plane obtained by ignoring geostrophic deflection force (Eq. (10), Houze (1993)), it can be seen that the change of vorticity is mainly generated only baroclinically and is redistributed by advection in the x–z plane. As can be seen from Figures 8A–C, the temperature difference between the east and west sides of the near-surface region where convection storms occurred over the SCB leaded to the enhancement of baroclinicity, which resulted in the enhancement of horizontal vorticity of the airflows (Figure 8A). This was balanced by the clockwise vertical shear caused by the secondary circulation near the surface so that the parcels at the front of the convective storm had no predisposition toward either negative or positive vorticity, thus forming a new convective storm in the front of the old one. Rotunno et al. (1988) called it the “optimal” mode of air parcels’ movement in convective regions.

$$\xi_t = -B_x - u\xi_x - \omega\xi_z, \tag{10}$$

where ξ_t represents the time variation of vorticity, B_x is the baroclinic generation term of horizontal vorticity, and $u\xi_x$ and $\omega\xi_z$ are vorticity advection terms in x and z directions, respectively.

ξ_t caused by baroclinicity was closely related to the temperature difference. We divided the DWCPO into east and west regions along 105°E and used the difference of temperature anomalies between the east and west regions (DTAEW) to measure the baroclinicity. As shown in Figure 8E, the large DTAEW mainly occurred at 6–15 on June 29, which was consistent with the formation of double-band echoes. In the vertical direction, the large center of the DTAEW mainly appeared in the near-surface layer (950 hPa) and slowly moved up to 800 hPa over time, which was consistent with

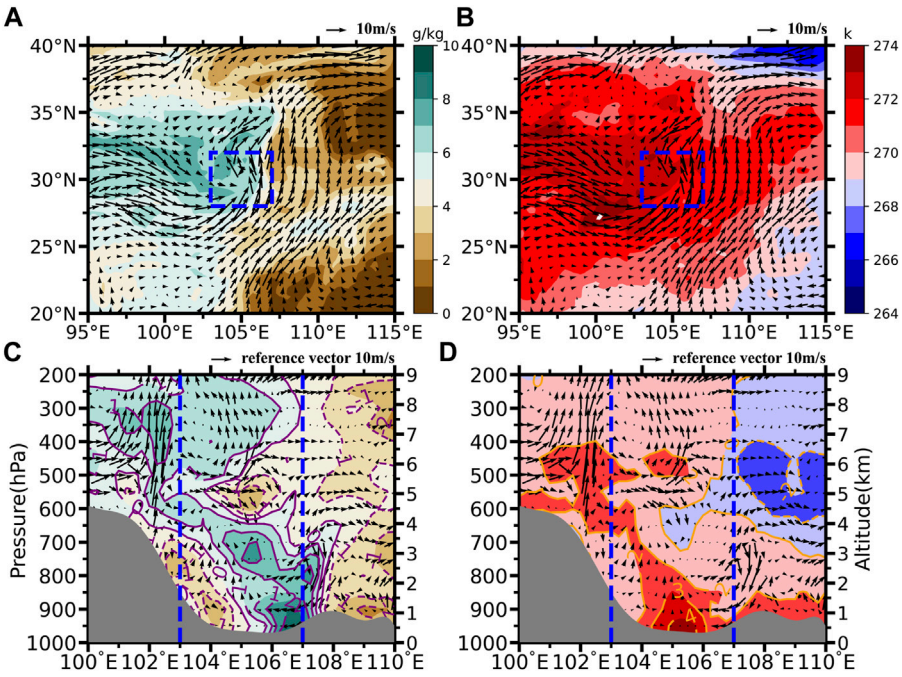

FIGURE 11
(A) Horizontal winds (m/s; vectors) and specific humidity (g/kg; color shading) obtained from ERA5 at 500 hPa at 1900 UTC 29 June 2013. The inserted boxes (blue dotted boxes) indicate the DWCPO. **(B)** As in **(A)** but for horizontal winds (m/s; vectors) and temperature (K; color shading). **(C)** Vertical cross section of wind vectors (combined zonal wind and tenfold vertical velocity) and space anomaly of specific humidity (g/kg; color shading) along the 29°N. The gray shading indicates the topography along the 29°N. The two blue dotted lines indicate the east and west boundary of the DWCPO. **(D)** As in **(C)** but for wind vectors (combined zonal wind and tenfold vertical velocity) and space anomaly of temperature (g/kg; color shading).

the upward movement of the large center of the temperature anomaly in the eastern part of the SCB. From 1200 UTC 29 June, the intensity of the secondary circulation and the DTA near the surface decreased synchronously; with the weakening of the DTAEW and the secondary circulation, the double-band signature of the radar echoes disappeared too.

3) As shown in Figures 8A–C, due to reasons such as the terrain of SCB, the eastern front of the colder airflows to the west of 105°E had been relatively fixed, coupled with a strong upward motion when the two vortices coupling made it hard for the colder airflows at mid-levels to pass through the updraft area and descend to strengthen the cold pool. The old convective storm continued to develop because the warm and moist airflows at the lower level would not be cut off by the cold pool. As shown in Figures 10A3–D3, the new convective storm was independently generated about 20 km to the east of the old one, and there was an obvious boundary between the two strong echoes formed by the old and new convective storms.

Different from the old band echo, the new band echo had a relatively short lifetime, weak intensity, and faster moving speed, resulting in small local accumulated precipitation. This explained why there was no obvious double-band distribution of accumulated precipitation in the same period of time (Figures 10A1–D1).

4.3 Formation conditions and characteristics of radar echoes stratification

At 1700 UTC 29 June, the east-west width of the strong echo over the SCB increased rapidly (Figure 5D), and the intensity gradually weakened. The main reason for this phenomenon was that the position of the SWV at 700 hPa was north and its intensity was weakened, which weakened the strong VWS over the SCB and the deep updraft caused by the coupling of the two vortices. However, the TPV was still strong at this time. From the perspective of specific humidity and temperature in the TPV circulation, the part of the circulation to the west of the center of the TPV was wetter and warmer than the part to the east of the center of the TPV because it was closer to the Tibetan plateau. According to Figures 11A,B, the humidity (temperature) of the part east of the center of the TPV was about 2 g/kg (2 k) lower than that of the part west of the center of the TPV. The southerly winds to the south of the TPV at 500 hPa brought the cold and dry airflows around the vortex circulation into the center of the TPV. The dry-cold advection formed an obvious dry-cold layer wedged into the TPV circulation between 600 hPa and 500 hPa (Figures 11C,D). Due to the existence of this cold and dry layer,

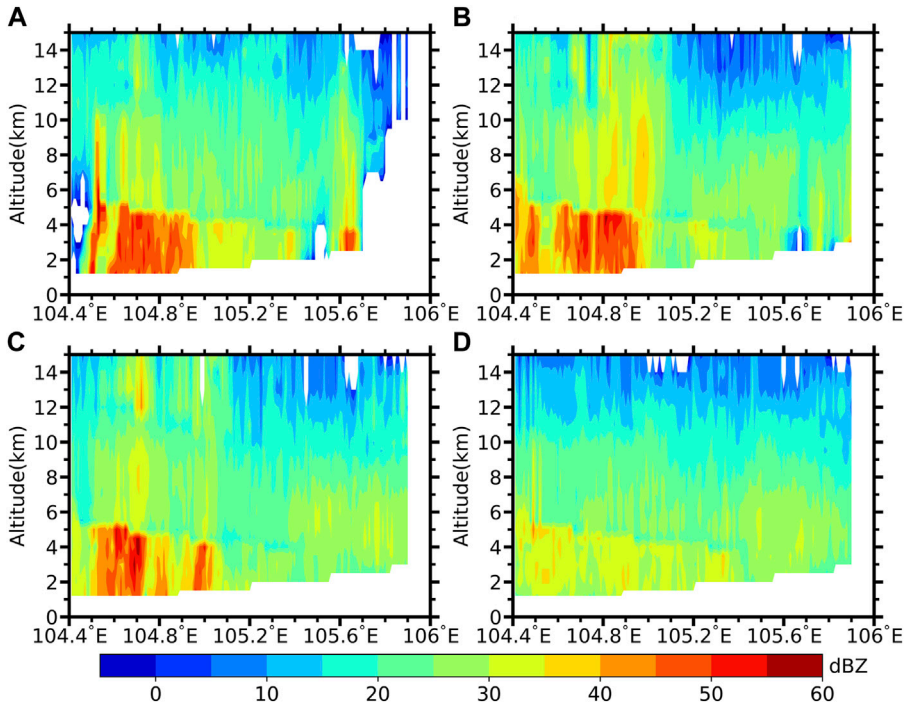

FIGURE 12
(A–D) Vertical cross section of RMR (dBZ; color shading) along 29°N from 1600 to 1900 UTC 29 June 2013 at 1-h intervals.

there were obvious stratification of specific humidity and air temperature over the southern part of the SCB. The boundary between the warm and wet layer in the upper part and the warm and wet layer in the lower part was just between 600 hPa and 500 hPa.

The stratification of temperature and specific humidity was the main reason for the stratification of radar echoes over the SCB in the vertical direction. During this period, the SWV was located to the north of the SCB and gradually weakened and disappeared. From the southern section of the SCB (29°N), the easterly winds and the vertical motion dominated by the SWV in the lower layer were very weak. The temperature and humidity field and circulation field dominated by the TPV over the SCB were mainly characterized by temperature and humidity stratification and strong vertical motion mainly concentrated at levels above 500 hPa (Figures 11C,D). The formation of these features requires the weakening and the northward movement of the SWV. If the SWV was strong, the deep and strong upward motion when the two vortices were coupled would rapidly transport the warm and wet airflows in the lower layer to the middle and high layers, and it was difficult to establish the stratification phenomenon of specific humidity and temperature. In addition, the strong VWS and easterly winds would limit the convective storms over the SCB to a relatively fixed area, and it was difficult to form the stratification phenomenon of radar echoes. Therefore, only when the TPV dominated the SCB, it was beneficial to establish the stratified structure of temperature and humidity over the SCB.

At 1600 UTC 29 June, the double-band echoes over the SCB gradually widened and moved eastward, especially for the strong echoes region in the south of the SCB (Figure 5C). The air temperature near 500 hPa over the SCB was significantly lower than the surrounding area, and the cooling air and downdraft would inhibit the development of convection below 500 hPa, which was consistent with the research conclusion of Qiu et al. (2015). As shown in Figure 12A, the top height of strong echoes between 104.4° and 105°E in the southern part of the SCB was about 5 km (500–600 hPa), which was consistent with the boundary of temperature and humidity stratification (Figure 11C). The updraft dominated by the TPV combined with the relatively warm and humid air resulted in condensation of water vapor above 500 hPa, which resulted in enhanced radar echoes. In combination with the strong radar echoes restricted by dry and cold air at the middle and low levels, radar echo stratification was formed (Figures 12A–D).

The temperature and humidity stratification caused by the TPV was mainly concentrated in the east region of its center, so the suppression effect of the TPV on the strong radar echoes at middle and low levels mainly occurred in this region. As shown in Figure 12A, near 104.5°E, strong echoes could develop from

surface to altitude of up to 10 km, but the phenomenon of "cutting" of echoes by temperature and humidity stratification became particularly obvious in the area east of 104.5°E. In the middle and late phases of stage III, the phenomenon of echo stratification would continue to exist (Figures 12B–D). The strong easterly echoes were continuously suppressed by the stratification of temperature and humidity, and the intensity gradually decreased (Figure 12D).

The existence of echo stratification indicated that the development height of convection might be limited. As a result, the precipitation intensity in the SCB was obviously lower than that in the early phase of stage III. The echo over the SCB dominated by the TPV was larger in area, weaker in intensity, and faster in movement. Meanwhile, the stratification of temperature and humidity and the cold air descending east of the vortex center limited the height of echoes development in this region. Therefore, the intensity of precipitation in the SCB dominated by the TPV weakened significantly after the SWV weakened and disappeared.

5 Summary and discussion

Based on ERA5 re-analysis data, RMR/RMCR data, radiosonde data, and precipitation from AWS observations, we analyzed a special severe precipitation event in the SCB on 29 and 30 UTC June 2013 under the background that the TPV and the SWV coupling. The main conclusions are as follows:

1) The changes of the positions of the two vortices could cause strong VWS over the SCB. Strong VWS was a necessary condition for the development of convective storms over the SCB. The intensity and distribution characteristics of VWS dominated the development and distribution of convective storms and precipitation over/in the SCB to some extent.

2) The vorticity associated with the secondary circulation caused by the two vortices was positive. The negative vorticity caused by baroclinicity just neutralizes the positive vorticity at low level of the SCB so that as the parcel rose above the boundary layer, it had no predisposition toward either negative or positive vorticity, and it thus rose vertically. Combined with the relatively fixed boundary between cold and warm air masses, the old and new convective storms could exist and develop simultaneously, and finally formed the double-band echoes seen on radar.

3) The dry and cold advection on the east side of the vortex center made the temperature and humidity over the SCB form a stratified structure when the TPV dominated the circulation over the SCB. The colder air, downdraft, and the hydrothermal stratification structure in the east of the vortex center inhibit the convection in the middle and lower layers so that the radar echoes formed an obvious stratified structure in the corresponding regions.

4) The precipitation was strongest in the SCB mainly when the two vortices couple. During this period, water vapor was transported over the SCB by the SWV and converged to the vortex center, and the deep convection caused by the coupling of the two vortices was conducive to the development of strong precipitation. The TPV dominated the precipitation in the SCB after the two vortices decoupled, and would suppress the convective height in some regions, which made the rainfall area expand, but the precipitation intensity decreases significantly.

It is rare for the SWV and TPV to appear over the SCB and its surrounding areas at the same time, but the coupling of the two vortices is very easy to cause extreme heavy precipitation events. Different from the weather process related to the SWV or TPV alone, it is extremely difficult to forecast the precipitation area caused by the vortex under the interaction of the two vortices, because the heavy precipitation does not occur in the usual area (southeast to the vortex center). Cheng et al. (2016) explained the cause of the distribution of the precipitation area related to the two vortices from the perspective of frontogenesis. This paper further revealed the relationship between the two vortices and the convective systems to explain the formation mechanism of the precipitation area.

Because the two vortices usually need to cooperate with other weather systems to cause a strong precipitation process, it is necessary to study the role of the two vortices in a heavy precipitation process. In particular, how the developments of the two vortices affect the occurrence and development of mesoscale convective systems that can produce heavy rainfall deserves further study.

VWS plays an important role in the development of tropical cyclone (TC). Li (1990) earlier revealed that VWS in the lower troposphere had an inhibitory effect on the generation of tropical cyclones (TCs), and the magnitude of this inhibitory effect might be correlated with the strength of VWS (Zeng et al., 2006; Fu et al., 2019). Both the TPV and the SWV have a warm-core structure similar to TC. In particular, the TPV has been proved to have dynamic and thermal structures similar to tropical cyclone-like vortices (Li and Yang, 1998). Therefore, the effect of VWS on the two vortices may be similar to that of TCs. The difference is that both the southwest vortex and the plateau vortex are shallow systems (the vertical thickness is only 2–3 km). Therefore, the effect of VWS at different heights on shallow systems needs further study. At the same time, in the period of the two vortices coupling, the VWS is small because the circulation of the two vortices tends to be consistent. How the smaller VWS affects the development of low vortexes in the period of the two vortices coupling requires further research in the future.

As this study dealt with one event, the mechanism of the two vortices and the relationship between the vortices and the convective system revealed in this paper may not be necessarily applicable to other similar events. We need to analyze more similar weather processes in future work to reveal the general and special laws of heavy rainfall under the background of coupling of two vortices.

Data availability statement

The datasets presented in this study can be found in online repositories. The names of the repository/repositories and accession number(s) can be found below: 1) https://cds.climate.copernicus.eu/cdsapp#!/dataset/reanalysis-era5-single-levels?tab=overview. 2) http://10.194.89.55/cimissapiweb/apidataclassdefine_list.action.

Author contributions

YD and GL contributed to the conception and design of the research. XJ and YW organized the database and performed the statistical analysis. YD drew the figures and wrote the manuscript. All authors contributed to manuscript revision and read and approved the submitted version.

Funding

This work was jointly sponsored by the National Natural Science Foundation of China (Grant Nos. 91937301 and 42175002), the Science and Technology Development Foundation of Heavy Rain and Drought-Flood Disasters in Plateau and Basin Key Laboratory of Sichuan Province (Grant No. SCQXKJQN201712) and the Innovation Team Fund of Southwest Regional Meteorological Center, China Meteorological Administration (Grant No. XNQYCXTD-202202) provided part of the data collection fees and open access publication fees for the research.

Conflict of interest

The authors declare that the research was conducted in the absence of any commercial or financial relationships that could be construed as a potential conflict of interest.

Publisher's note

All claims expressed in this article are solely those of the authors and do not necessarily represent those of their affiliated organizations, or those of the publisher, the editors, and the reviewers. Any product that may be evaluated in this article, or claim that may be made by its manufacturer, is not guaranteed or endorsed by the publisher.

References

Chen, T., Zhang, F.-H., and Duan, Y.-H. (2011). A study of relationship between a southwest vortex and the mesoscale convective systems during the severe "6.12" rainstorm event in Guangxi province. *Acta Meteorol. Sin.* 69 (3), 472–485. (in Chinese). doi:10.11676/qxxb2011.041

Chen, Z.-M., Min, W.-B., Miao, Q., and He, G.-B. (2004). A case study on coupling interaction between Plateau and southwest vortexes. *Plateau Meteorol.* 23 (1), 75–80. (in Chinese). doi:10.3321/j.issn:1000-0534.2004.01.011

Cheng, X. -L., Li, Y. -Q., and Xu, L. (2016). An analysis of an extreme rainstorm caused by the interaction of the Tibetan plateau vortex and the southwest China vortex from an intensive observation. *Meteorol. Atmos. Phys.* 128, 373–399. doi:10.1007/s00703-015-0420-2

Dong, Y.-C., and Li, G.-P. (2015). The structure and precipitation characteristics of typical Tibetan Plateau vortices as revealed by energy analysis. *Chin. J. Atmos. Sci.* 39 (6), 1136–1148. (in Chinese). doi:10.3878/j.issn.1006-9895.1502.14263

Du, Q., Qin, D.-Y., and Zhang, P. (2013). Observation and analysis of a southwest vortex rainstorm in southern China using FY-2 satellite data. *Meteor Mon.* 39 (7), 821–831. (in Chinese). doi:10.7519/j.issn.1000-0526.2013.07.003

Fu, H., Wang, Y.-Q., Riemer, M., and Li, Q. (2019). Effect of unidirectional vertical wind shear on tropical cyclone intensity change-lower-layer shear versus upper-layer shear. *J. Geophys. Res. Atmos.* 124 (12), 6265–6282. doi:10.1029/2019jd030586

Fu, S.-M., Li, W.-L., Sun, J.-H., Zhang, J., and Zhang, Y. (2015). Universal evolution mechanisms and energy conversion characteristics of long-lived mesoscale vortices over the Sichuan Basin. *Atmos. Sci. Lett.* 16 (2), 127–134. doi:10.1002/asl2.533

Gao, W.-L., and Yu, S.-H. (2017). Analyses on mean circulation field of the plateau low vortex moving out of Tibetan Plateau. *Plateau Meteorol.* 26 (1), 206–212. (in Chinese). doi:10.1002/jrs.1570

Hao, L.-P., Zhou, J., and Kang, L. (2016). Weather analyses and numerical study of Southwest China vortex and its induced heavy rainfall. *Plateau Meteorol.* 35 (5), 1182–1190. (in Chinese). doi:10.7522/j.issn.1000-0534.2015.00046

Hersbach, H., Bell, B., Berrisford, P., Hirahara, S., Horányi, A., Muñoz-Sabater, J., et al. (2020). The ERA5 global reanalysis. *Q. J. R. Meteorol. Soc.* 146 (730), 1999–2049. doi:10.1002/qj.3803

Houze, R. A. (1993). "Atmospheric dynamics," in *Cloud dynamics*, Amsterdam: Academic Press, 31.

Hu, Z.-H., Li, G.-P., Guan, C.-G., and Wang, H.-L. (2014). Diagnostic analysis of mesoscale convective systems influence on sustained rainstorm caused by southwest vortex. *Plateau Meteorol.* 33 (1), 116–129. (in Chinese). doi:10.7522/j.issn.1000-0534.2013.00002

Huang, C.-H., Gu, Q.-Y., Li, G.-P., and Chen, G.-X. (2010). Mechanism analysis of Plateau vortex moving east trigger rainstorm in Sichuan Basin. *Plateau Meteorol.* 29 (4), 832–839. (in Chinese).

Huang, C.-H., Li, G.-P., Niu, J.-L., Luo, L., and Zhang, W. (2011). Moist helicity analysis of a heavy rainstorm in Sichuan Basin induced by plateau vortex moving eastward. *Plateau Meteorol.* 30 (6), 1427–1434. (in Chinese).

Jiang, L.-J., Li, G.-P., Mu, L., and Kong, L. (2014). Structural analysis of heavy precipitation caused by southwest vortex based on TRMM data. *Plateau Meteorol.* 33 (3), 607–614. (in Chinese). doi:10.7522/j.issn.1000-0534.2013.00094

Klemp, J. B. (1987). Dynamics of tornadic thunderstorms. *Annu. Rev. Fluid Mech.* 19, 369–402. doi:10.1146/annurev.fl.19.010187.002101

Li, C.-Y. (1990). Influences of sensible heating and vertical wind shear on subtropical CISK disturbance. *Chin. J. Atmos. Sci.* 14 (2), 173–180. (in Chinese). doi:10.3878/j.issn.1006-9895.1990.02.05

Li, C., Li, Y.-Q., and Jiang, X.-W. (2015). Statistical characteristics of the inter-monthly variation of the Sichuan Basin vortex and the distribution of daily precipitation. *Chin. J. Atmos. Sci.* 39 (6), 1191–1203. (in Chinese). doi:10.3878/j.issn.1006-9895.1502.14270

Li, G.-P., and Yang, X.-Y. (1998). Effects of the thermal forcing on nonlinear internal inertia gravitational waves in the atmosphere. *Chin. J. Atmos. Sci.* 22 (5), 791–797. (in Chinese). doi:10.3878/j.issn.1006-9895.1998.05.14

Li, G., and Deng, J. (2013). Atmospheric water monitoring by using ground-based GPS during heavy rains produced by TPV and SWV. *Adv. Meteorology* 2013 (4), 1–12. doi:10.1155/2013/793957

Liu, X.-R., and Li, G.-P. (2014). Numerical simulation and potential vorticity diagnosis of an eastward moving southwest vortex. *Plateau*

Meteorol. 33 (5), 1204–1216. (in Chinese). doi:10.7522/j.issn.1000-0534.2013.00151

Luo, S.-W., He, M.-L., and Liu, X.-D. (1993). Study on summer vortex over qinghai-xizang (Tibetan) plateau. *Sci. China (Series B)* 23 (7), 778–784. (in Chinese). doi:10.1360/zb1993-23-7-778

Ni, C.-C., Li, G.-P., and Xiong, X.-Z. (2017). Analysis of a vortex precipitation event over Southwest China Using AIRS and *in situ* measurements. *Adv. Atmos. Sci.* 34 (4), 559–570. doi:10.1007/s00376-016-5262-4

Pan, Y., Li, J., and Yu, R.-C. (2011). Climatic characteristics of the spatial structure of the eastward-moving southwest vortex. *Clim. Environ. Res.* 16 (1), 60–70. (in Chinese). doi:10.3878/j.issn.1006-9585.2011.01.06

Qian, Z.-G., and Jiao, Y.-J. (1997). Advances and problems on Qinghai-Xizang Plateau meteorology research. *Adv. Earth Sci.* 12 (3), 207–216. (in Chinese). doi:10.11867/j.issn.1001-8166.1997.03.0207

Qiu, J.-Y., Li, G.-P., and Hao, L.-P. (2015). Diagnostic analysis of potential vorticity on a heavy rain in Sichuan Basin under interaction between Plateau Vortex and southwest vortex. *Plateau Meteorol.* 34 (6), 1556–1565. (in Chinese). doi:10.7522/j.issn.1000-0534.2014.00117

Rotunno, R., Klemp, J. B., and Weisman, M. L. (1988). A theory for strong, long-lived squall lines. *J. Atmos. Sci.* 45, 463–485. doi:10.1175/1520-0469(1988)045<0463:ATFSLL>2.0.CO;2

Song, W.-W., and Li, G.-P. (2016). Analysis and application of the two type vorticity vectors on a heavy rainfall in Sichuan Basin. *Plateau Meteorol.* 35 (6), 1464–1475. (in Chinese). doi:10.7522/j.issn.1000-0534.2015.00115

Tao, S.-Y. (1980). *Rainstorms in China*. Beijing: Science Press. (in Chinese).

Xiao, D.-X., Yang, K.-Q., and Yu, X.-D. (2017). Characteristics analyses of extreme rainstorm events in Sichuan Basin. *Meteorol. Mon.* 43 (10), 1165–1175. (in Chinese). doi:10.7519/j.issn.1000-0526.2017.10.001

Xiao, Y.-J., and Liu, L.-P. (2006). Study of methods for interpolating data from weather radar network to 3-D grid and mosaics. *Acta Meteorol. Sin.* 64 (5), 647–657. (in Chinese). doi:10.11676/qxxb2006.063

Yang, K.-Q., Lu, P., and Zhang, L. (2017). Analyses of heavy rainstorm in warm sector under the influence of the low-pressure system of qinghai-xizang plateau. *J. Trop. Meteorology* 33 (03), 415–425. (in Chinese). doi:10.16032/j.issn.1004-4965.2017.03.012

Yeh, T., and Gao, Y.-X. (1979). *Meteorology of the qinghai–xizang plateau*. Beijing: Science Press, 278pp. (in Chinese)

Yue, J., and Li, G.-P. (2016). Study on the moisture source of rainstorms in Sichuan Basin by the Lagrangian method. *J. Trop. Meteorology* 32 (2), 256–264. (in Chinese). doi:10.16032/j.issn.1004-4965.2016.02.012

Zeng, Z.-H., Chen, L.-S., Wang, Y.-Q., and Gao, Z.-Q. (2006). A numerical simulation study of super Typhoon Saomei intensity and structure changes. *Acta Meteorol. Sin.* 67 (5), 750–763. (in Chinese). doi:10.11676/qxxb2009.075

Zhang, Y.-P., Yu, X.-D., Wu, Z., Liang, J.-P., and Lv, L.-Y. (2012). Analysis of the two tornado events during a process of regional torrential rain. *Acta Meteorol. Sin.* 70 (5), 961–973. (in Chinese). doi:10.11676/qxxb2012.081

Zhao, D.-J., Jiang, Y.-H., and Li, Y. (2011). Diagnostic analysis and numerical simulation of a torrential rainstorm process caused southwestern low vortex. *Plateau Meteorol.* 30 (5), 1158–1169. CNKI:SUN:GYQX.0.2011-05-002(in Chinese).

Zhao, Y.-C., and Wang, Y.-H. (2010). A case study on plateau vortex inducing southwest vortex and producing extremely heavy rain. *Plateau Meteorol.* 29 (4), 819–831. (in Chinese). doi:10.16082/j.cnki.issn.1001-4578.2016.01.017

Zhou, M., Liu, L.-P., and Wang, H.-Y. (2014). Analysis of the echo structure and its evolution as shown in a severe precipitation event caused by the plateau vortex and the southwest vortex. *Acta Meteorol. Sin.* 72 (3), 554–569. (in Chinese). doi:10.11676/qxxb2014.029

frontiers | Frontiers in Earth Science

TYPE Review
PUBLISHED 25 August 2022
DOI 10.3389/feart.2022.823090

OPEN ACCESS

EDITED BY
Liguang Wu,
Fudan University, China

REVIEWED BY
Suman Paul,
Sidho Kanho Birsha University, India
Eric Hendricks,
National Center for Atmospheric Research (UCAR), United States
Raghavendra Ashrit,
National Centre for Medium Range Weather Forecasting, India

*CORRESPONDENCE
Pankaj Kumar,
kumarp@iiserb.ac.in

SPECIALTY SECTION
This article was submitted to Atmospheric Science, a section of the journal Frontiers in Earth Science

RECEIVED 29 November 2021
ACCEPTED 21 July 2022
PUBLISHED 25 August 2022

CITATION
Tiwari G, Kumar P and Tiwari P (2022), The appraisal of tropical cyclones in the North Indian Ocean: An overview of different approaches and the involvement of Earth's components. *Front. Earth Sci.* 10:823090. doi: 10.3389/feart.2022.823090

The appraisal of tropical cyclones in the North Indian Ocean: An overview of different approaches and the involvement of Earth's components

Gaurav Tiwari[1], Pankaj Kumar[1]* and Pooja Tiwari[2]

[1]Department of Earth and Environmental Sciences, Indian Institute of Science Education and Research Bhopal, Bhopal, India, [2]Helmholtz-Zentrum Hereon Institute, Geesthacht, Germany

This study aims to provide a comprehensive and balanced assessment of recent scientific studies on the evolution, temporal variability and prediction of tropical cyclones (TCs), focusing on the North Indian Ocean (NIO). The involvement of earth's components in TC genesis and intensification has been elaborated in a confined way. The advancement of multidisciplinary approaches for comprehending the TCs is highlighted after a brief description of the involvement of oceanic, atmospheric, and land surface processes. Only a few studies illustrate how land surface plays a role in TC intensification; however, the role of latent heat flow, moisture, and convection in cyclogenesis is well documented. Despite two to 3 decades of advancement and significant development in forecasting techniques and satellite products, the prediction of TC's intensity, dissipation, track, and landfall remains a challenge. The most noticeable improvements in NIO TC's prediction have been achieved in the last couple of decades when concord techniques are utilized, especially the data assimilation methods and dynamical coupled atmosphere-ocean regional models. Through diverse methodologies, algorithms, parameterization, *in-situ* observational data, data mining, boundary layer, and surface fluxes, significant research has been done to increase the skills of standalone atmospheric models and air-sea coupled models. However, some crucial issues still exist, and it is suggested that they should be addressed in future studies.

KEYWORDS

tropical cyclone, north indian ocean, track, intensity, numerical weather prediction

1 Introduction

Tropical cyclone (TC) is a broad term for a non-frontal synoptic scale low-pressure system that develops over the warm tropical oceans with organized convective processes (Wang and Wu, 2004). Upper ocean heat content (UOHC) and sea surface temperature (SST) are primary oceanic components that make favourable conditions for convection,

TABLE 1 North Indian Ocean tropical cyclone intensity scale by IMD based on 3-min average maximum sustained wind speed.

Category		Maximum Sustained wind Speed
Depression	D	31–50 km/h
Deep Depression	DD	51–62 km/h
Cyclonic Storm	CS	63–88 km/h
Severe Cyclonic Storm	SCS	89–117 km/h
Very Severe Cyclonic Storm	VSCS	118–165 km/h
Extremely Severe Cyclonic Storm	ESCS	166–220 km/h
Super Cyclonic Storm	SuCS	>220 km/h

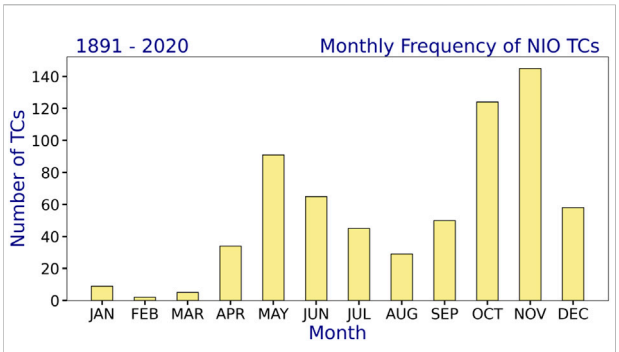

FIGURE 1
Annual cycle of NIO TCs frequency from 1891 to 2020 using IMD data.

which results in the development of a low-pressure area (Tiwari et al., 2021). TCs have a horizontal scale of hundreds to thousand kilometres extending throughout the troposphere's height (Wang et al., 2012). TCs are demarcated by different names in various oceanic basins such as "typhoon" (Western Pacific), "hurricane" (Atlantic and Eastern Pacific), and "tropical cyclone" (north Indian Ocean). The World Meteorological Organization and India Meteorological Department (IMD) have classified the TCs over the north Indian Ocean (NIO) with 3-min maximum sustained wind (MSW) speed (Table 1); however, the criterion for MSW differs for different regions. A low-pressure area with MSW 31–50 km/h is characterized as depression followed by deep depression (51–62 kmph), cyclonic storm (CS, 63–88 km/h), severe cyclonic storm (SCS, 89–117 km/h), etc. (Table 1).

The NIO, with a coastline of ~7,516 km, is accountable for 6–8% of TCs that develop over the globe dominated by the Bay of Bengal (BoB) (Das et al., 2014; Espejo et al., 2016; Mohapatra, 2016; Gupta et al., 2019; Mohanty et al., 2019). The NIO shows a bimodal distribution of TCs activities over the BoB and Arabian Sea (ARB) basins. The primary peak lies in the post-monsoon season (October-December) and another in the pre-monsoon season, i.e., April-June. The trend of the propagation of NIO TCs is northwestwards. Therefore, most of the BoB TCs cause devastation on the eastern coast of India (Gupta et al., 2019; Nadimpalli et al., 2021). Since the last decade, an increase in the frequency of pre-monsoon intense ARB TCs have been observed, and they mostly showed north-eastward propagation (Sriver, 2011; Wang et al., 2012). Thus, it is crucial to understand the synoptic and mesoscale circulations that help in the TC genesis and evolution.

Usually, the TC activities in the BoB are approximately four times higher than in the ARB (Deshpande et al., 2021). However, recent studies have reported an increasing trend of very intense ARB TCs in the changing climate scenario due to the rise in the ARB SST (Sriver, 2011; Wang et al., 2012; Gupta et al., 2019). Deshpande et al. (2021) observed a significant change in the frequency, duration, and intensity of the ARB and BoB CS and VSCS during 1982–2019. The frequency of ARB CS has increased by 52% in the recent epoch (2001–2019), whereas the frequency of BoB CS showed a decrease in the same period. The year 2019 was the most active period for NIO, with 5 TCs in the ARB and three in the BoB (Deshpande et al., 2021). Figure 1 demonstrates the monthly frequency of NIO TCs taken from the IMD data for a period of 130 years (1891–2020). 49.8% of the NIO TCs were formed in the post-monsoon season, while 28.9% were in the pre-monsoon season. The overall contribution of these 6 months was approximately 80%.

Figure 2 depicts the decadal frequency and trend of NIO TCs for three seasons: March-May (MAM), June-September (JJAS), and October-December (OND), as well as the annual period from 1891 to 2020. The MAM TCs (Figure 2A) has declined slightly, with a trend value of −0.004 and an average of 10 TCs each decade. Above a 90% confidence level, the Mann-Kendal test confirms that the trend is not significant. With a mean of 14.5 TCs per decade, JJAS (Figure 2B) has shown a significant decreasing trend (above 90% confidence level). However, with an average of 25.2 TCs each decade, the OND season has shown an increasing trend (not significant at 90% confidence level) (Figure 2C). With a trend value of −0.159 and 50.5 TCs per decade, yearly NIO TCs have demonstrated a decreasing trend (not significant above 90% confidence level) (Figure 2D).

Furthermore, Figure 3 shows the decadal frequency of ARB TCs for the same seasons and duration as Figure 2. 34 TCs were identified for the MAM season, with a slightly declining trend from 1891 to 2020. In the JJAS and OND seasons, 39 and 59 TCs were formed with an increasing trend, showing a ratio of 1: 1.74 for the ARB and OND seasons. In the recent 2 decades (2001–10 and 2011–20), the number of ARB TCs for OND has more than doubled. Over the last 4 decades, the frequency of yearly TCs has monotonically increased, with an overall increasing trend.

Mondal et al. (2021) examined the characteristics of BoB TCs from 1982 to 2020 in the context of the El Nino Southern Oscillation (ENSO). They reported that TC activities have increased during ENSO years, with some shifts in their genesis locations. The majority of the TCs were developed

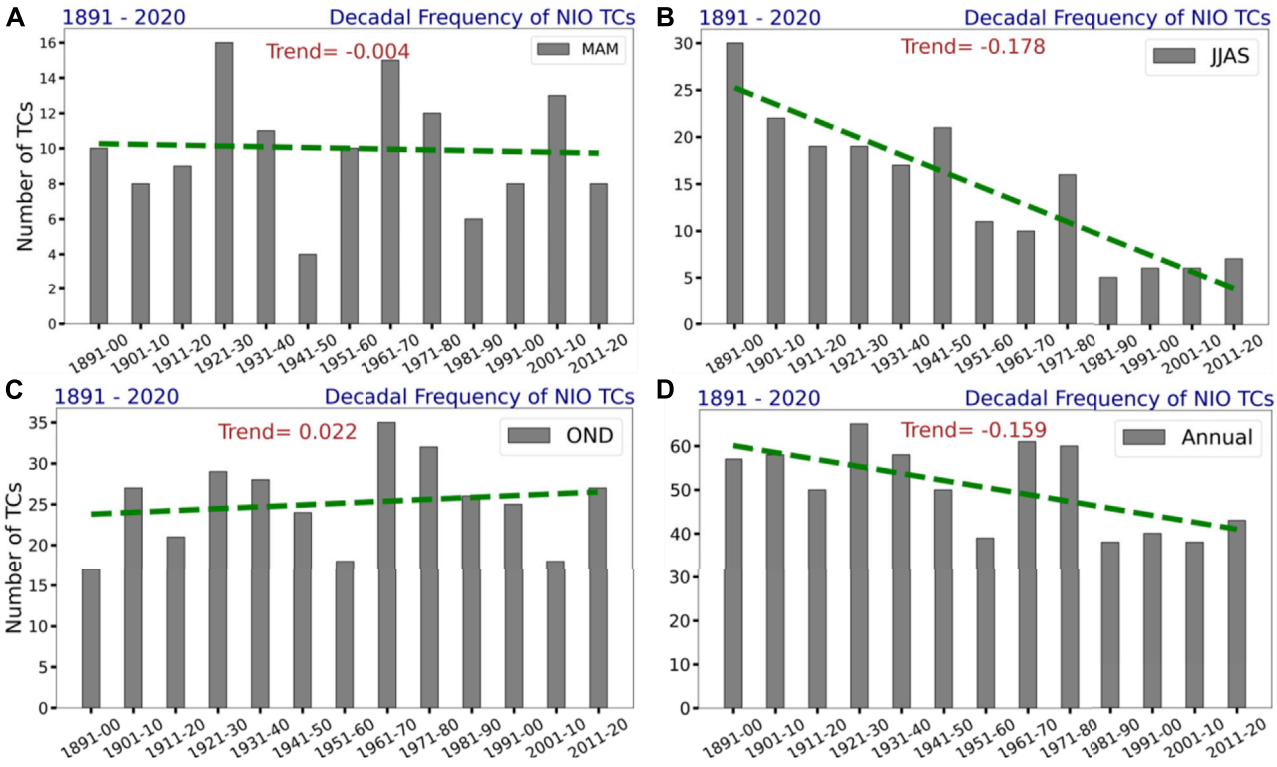

FIGURE 2
Decadal frequency of NIO TCs and their trends during 1891–2020 for the seasons **(A)** MAM, **(B)** JJAS, **(C)** OND, and **(D)** Annual.

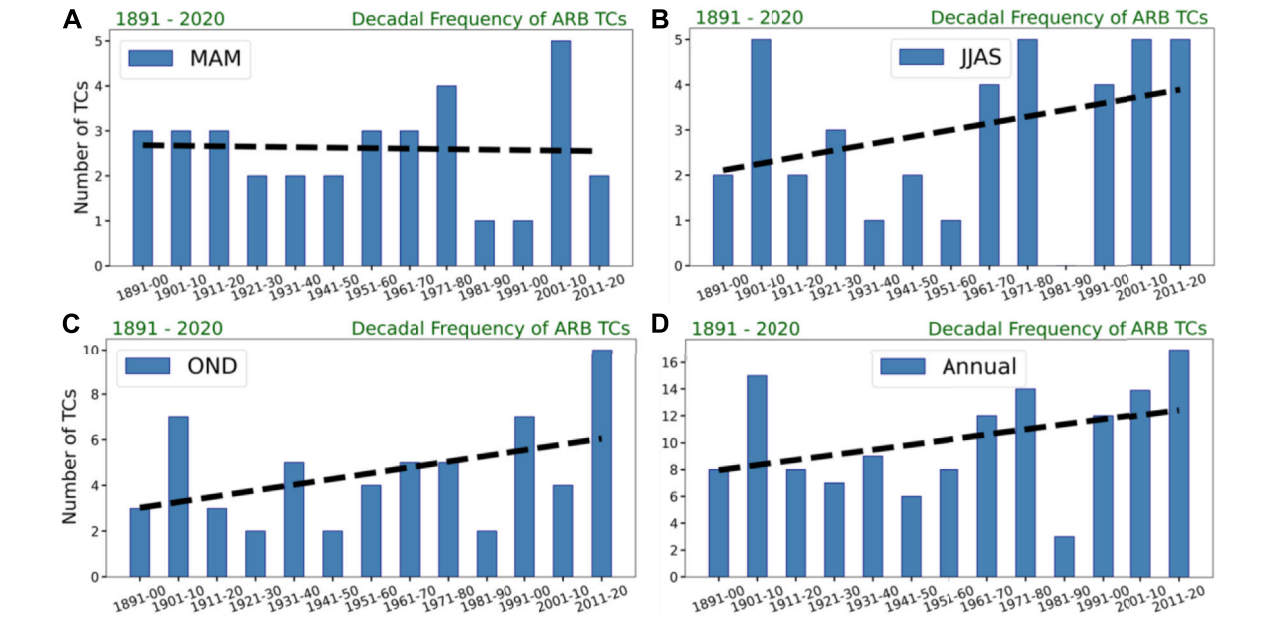

FIGURE 3
Decadal frequency of ARB TCs during 1891–2020 for the seasons **(A)** MAM, **(B)** JJAS, **(C)** OND, and **(D)** Annual.

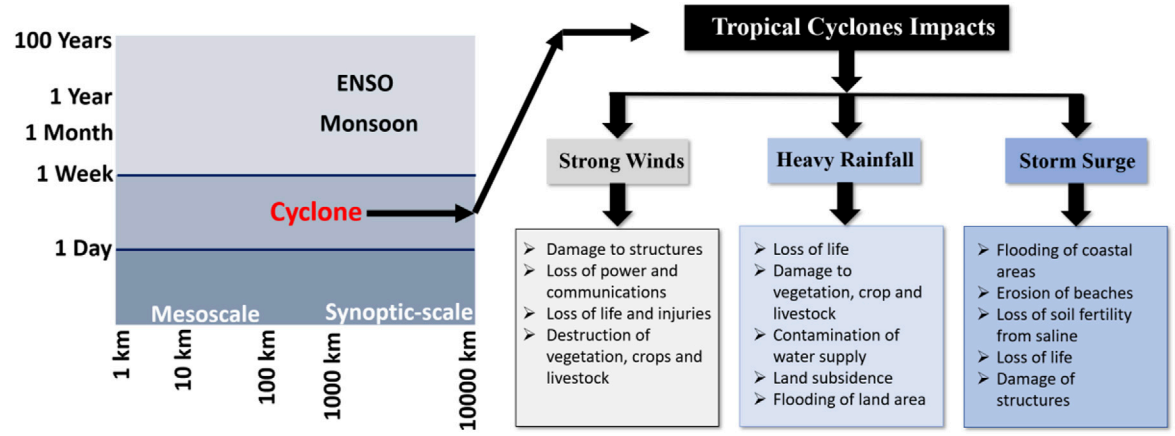

FIGURE 4
Various characteristics of a TC those can make severe impacts on lives and property.

between 5° and 15°N. During La Nina (El Nino) conditions, almost two-thirds of TCs were headed eastward (westward). The TCs of La Nina years were found to have a longer lifespan than those of El Nino. La Nina years had an average of 8.92 annual TC days, which was twice as many as El Nino years (4.51 days).

In recent years, studies have been carried out to understand the dynamics and thermodynamics of TCs', physics of the numerical weather prediction (NWP) models including boundary layer parameterizations, and vortex initialization to improve the TC forecast eventually to prevent devastations and huge losses. The intense TCs cause unfair losses of lives, infrastructure, and agriculture, especially near the coastal region (Figure 4). Therefore, it cannot be ignored that with the advancement in the TC forecast, there will be a significant reduction in the loss of lives. Few recent perfidious TCs like Amphan (2020), Fani (2019), Hudhud (2014), and Phailin (2013), due to very to extremely severe intensity, resulting in a loss of $6-7 billion. It extended the space of forecast improvement to the numerical models and forecasting community (Gupta et al., 2019).

In this review article, following with the Introduction, the authors provide an overview of the role of earth's components associated with TC genesis and intensification in section 2. Section 3 focuses on multidisciplinary approaches to study the TC. Revolution in NIO TCs prediction in the satellite era is discussed in section 4. Concluding remarks are given in the last section.

2 Earth's components and cyclogenesis

A TC is a very complex phenomenon resulting from the steady-state changes in the composite environment. A low-pressure area develops over the ocean and concentrates into depression and deep depression with favourable conditions intensifying into a TC expanding in the troposphere. Usually, after the landfall, it again concentrates into a depression (Chauhan et al., 2021). Therefore, analysis of all the environmental components contributing to TC activities would be helpful to develop a better understanding of the TC formation and precisely forecast its characteristics such as intensity, eye formation, track, landfall, heavy rainfall, storm surge, etc.

2.1 Role of ocean

A warm ocean with a low-pressure system is the niche for the formation of TCs. However, the thermal gradient of the NIO consisting of BoB and ARB gives rise to many furious TCs. Several studies have been done to understand the dynamics and thermodynamics of the ocean involved in the TCs' formation (Webster et al., 2005). In addition, there are studies done in the past to understand the impact of TC on the BoB region. The findings from the studies confirm the rise in the NIO SST (Tiwari et al., 2021). Mishra et al. (2020) reported a strong role of ARB warming on increasing weather extremes. In addition to this, a study by Mohanty et al. (2012) confirms the role of SST in increasing the number of SCS in the ARB. Also, there are recent studies done so far to understand the ocean's role in TC formation and its activities. For example, Prakash and Pant (2017) studied the dominant role of mixed layer heat budget in TC genesis. The study's findings confirmed the reduction in the magnitude and diurnal periodicity of the net surface heat fluxes interconnected with the cloud cover during the cyclone. On the other hand, Patwardhan and Bhalme (2001) and Jadhav and Munot (2009) identified a significant decrease in the trend of

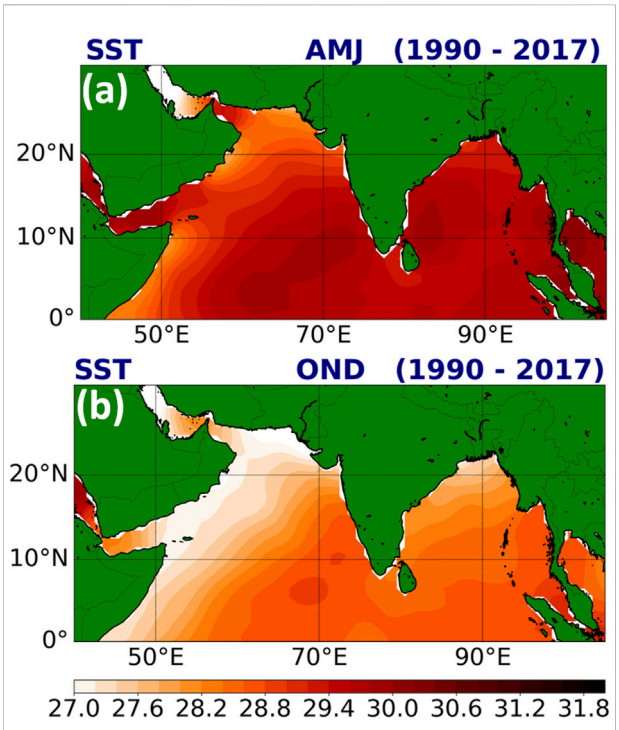

FIGURE 5
The mean SST (°C) over the NIO during 1990–2017 for **(A)** April-June (AMJ) and **(B)** October-December (OND). The SST data was obtained from Hadley Centre Global Sea Ice and Sea Surface Temperature dataset.

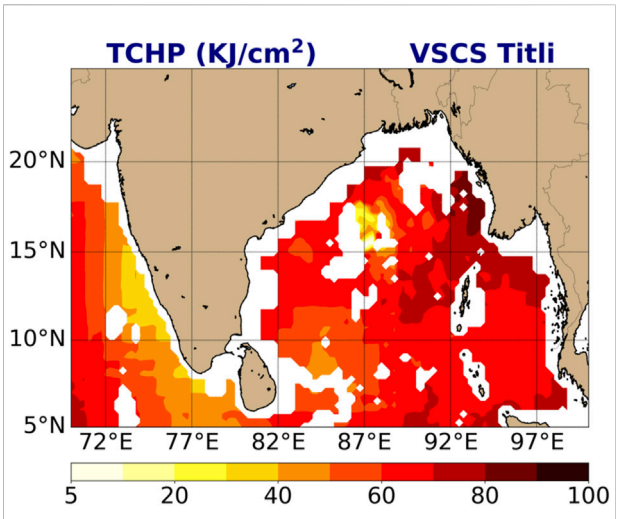

FIGURE 6
Spatial distribution of tropical cyclone heat potential (KJ/cm^2) over the BoB valid for 10 October 2018 during the life of a very severe cyclonic storm Titli. The data was obtained from the National Remote Sensing Centre- Indian Space Research Organisation, India.

TC frequency seasonally despite increasing SST in recent decades. Therefore, to simulate the accurate TC obtaining a realistic SST is a big challenge to researchers. However, there are studies conducted to do sensitivity experiments of models to get realistic SST. SST obtained through satellite corresponds to TC (Mandal and Mohanty, 2010; Mohanty et al., 2019). While few contrasting studies (Demaria and Kalpana, 1994) reveal that SST has a relatively less impact on the intensification and propagation of TC after the formation. Bhatla et al. (2020) mentioned that global warming had increased the upper troposphere temperature and also the SST. This rise in SST could be a reason for intense TCs (Chauhan et al., 2021). Another study by Frank and Young (2007) also confirmed the role of SST in the formation and increased intensity of TC.

A 28-years (1990–2017) mean SST in the pre-monsoon (AMJ) and post-monsoon (OND) seasons over the NIO has been shown in Figures 5A,B using the Hadley Centre Global Sea Ice and Sea Surface Temperature (HadISST) data. The pre-monsoon season is associated with boreal summer, and thus the SST in this season was relatively high (Figure 5A). Southeast ARB was warmer than other regions, and most of the intense ARB TCs formed over this region. Due to the Indian Summer Monsoon Rainfall season from June to September, the SST during the post-monsoon becomes low but sufficient to conceive TCs (Figure 5B). Central to south-east BoB was comparatively warm, and most of the intense BoB TCs developed over this region.

Other oceanic subsurface parameters play a vital role in modifying the TCs genesis and other characteristics. Tropical Cyclone Heat Potential (TCHP), currents, and eddies over the warm oceans help in the TC's rapid intensification (RI). Moreover, a trace of eddies formation near TC tracks could assess the RI phase (Jangir et al., 2020). Lin et al. (2013) also mentioned the role of TCHP and eddy currents in the TC's RI. A spatial demonstration of TCHP over the BoB during the life of VSCS Titli is shown in Figure 6. A cyclonic system like VSCS Titli that encounter the TCHP and eddy currents are more disastrous during the landfall and further inland progression. Mawren and Reason (2017) and Patnaik et al. (2014) also mentioned the contribution of eddies in the TC intensification over the NIO. In addition, there are sparse studies carried out using the oceanic numerical models to understand and forecast the TC. For example, Das et al. (2014) used Princeton Ocean Model (POM) to study the thermodynamics of oceans over BoB.

2.2 Role of atmosphere

TC is always a concern for meteorologists because it results from synoptic and mesoscale interactions accompanied by other natural phenomena like strong winds, heavy rainfall, and storm surge. Likewise, ocean components other essential factors of the weather system that contribute to the formation of TCs are Coriolis force, vorticity, low vertical wind shear, moisture and

moist convection. Moreover, in tropical regions, moist convection dominates the process of transporting mass, energy, and momentum through the atmosphere (Kumar et al., 2017). Albert et al. (2022) reported a 0.58 correlation between power dissipation index (PDI) and SCS category TCs from 1979 to 2019. They also found that relative humidity at 600 hPa, positive relative vorticity at 850 hPa, and reduced outgoing longwave radiation at 500 hPa have significantly contributed to the NIO's increased TC frequency. Balaji et al. (2018) used the accumulated cyclone energy (ACE) metric to analyze TC activities over the NIO from 1981 to 2014 and observed an increasing trend in recent years. SST, UOHC, atmospheric water vapour, and the genesis potential index (GPI) were all strongly associated with the growth and variability of ACE. According to Duan et al. (2021), the lower and middle troposphere's relative humidity and vertical wind shear are the two key contributors to TC genesis. The combination of these two variables drives the bimodal seasonal cycle of TCs' in both the ARB and the BoB. Tiwari et al. (2021) investigated the characteristics of post-monsoon season TCs' over the BoB from 1979 to 2018 using various metrices such as ACE and PDI. They also used correlation and principal component analysis on the VSCS, SCS, and CS category TCs, taking into account SST, vertical wind shear, MSW, minimum sea level pressure (MSLP), relative vorticity, and specific rainwater content, among other parameters and revealed that relative vorticity is the most influential among all the controlling elements that impact the final intensity of the BoB TCs'. A study by Chan (2005) explained the importance of the baroclinic process in the TC. However, the energy and heat transfer through convection modifies the temperature gradient and vertical wind shear (Osuri et al., 2010). Again, the representation of dynamical changes in the NWP model is a big challenge. However, this has been further improved with satellite products that help to develop the better initial vortex position and structure of TC in the NWP models.

Further to confirm the data dependencies for position and structure of TC, Courtney et al. (2019) used different best-track datasets from IMD and Joint Typhoon Warning Center (JTWC) to analyze the intensity of VSCS Hudhud. They found different results with both the dataset as underestimation in one and overestimation in other due to different criteria of sources for MSW. Mohanty et al. (2020) portray the impact of dry air intrusion on the ESCS Fani caused by asymmetric wind. This dry air significantly impacts the vortex initialization that affects the structure, landfall, and TC intensity. However, few studies focused on improving the vortex initialization by using better satellite and reanalysis data (Nadimpalli, 2020a; Nadimpalli, 2020b). In addition to SST, atmospheric high temperature and diabatic heating also plays a dominant role in the evolution of the intensity and determining the track of TC (Singh and Bhaskaran, 2020). Henceforth, many studies confirmed the direct correlation between seasonal changes and TC formation. Therefore, the NIO favours the formation of more intense BoB TCs in the post-monsoon season and less frequent but intense ARB TCs in the pre-monsoon season (Nadimpalli et al., 2021).

2.3 Role of land surface

The land is a sink for TCs, and they get energetic when crossing the lands (Pattanayak and Mohanty, 2010). Advancements in data assimilation techniques have improved the forecast skills of the NWP models in wide ranges during pre- and post-monsoon seasons. Also, land surface features have helped to enhance the mesoscale features such as drying, precipitation, and deep convection. It further helps in better representation of Land Surface Models (LSM), Land use and Land Cover (LULC), soil moisture and other parameters (Osuri et al., 2017). Raju et al. (2011) progressively showed the importance of land data assimilation in improving the TC's intensity prediction through better representation of boundary layer flux exchange. Rajesh et al. (2017) confirmed the same conclusion of the role of the land surface in mesoscale moist convection. Scholarly articles indicate the inland role in a TC, whereas the "Brown Ocean" concept was also introduced, indicating the role of wetland in mimicking the ocean to fuel moisture to the TC intensification over the many regions across the world (Andersen and Shepherd, 2017). Nair et al. (2019) reported the role of LULC change, soil moisture, heat flux in the intensification of TC over land. Mohanty et al. (2001) mentioned in the Indian Ocean Experiment (INDOEX) that deep offshore plume-like structure resulting from diurnal variability and topography heterogeneity plays a vital role in modulating the local and large-scale circulation patterns. Chang et al. (2009) have signified the role of soil condition before the storm in predicting the landfalling storm. Kishtawal et al. (2012) analyzed the role of change in soil bulk density and change in land features over the decay of the TCs and post-landfall intensity changes. However, there are very few studies to evaluate the role of land in TC's intensification and weakening. Also, the forecast of accurate landfall and post-landfall intensification is a question of debate. Henceforth, many studies suggested the use of improved land force parameters for better prediction of TCs (Mohanty et al., 2001; Corsaro and Toumi, 2017; Rajesh et al., 2017).

3 Multidisciplinary approaches addressing the cyclones

3.1 Numerical modelling (standalone models)

In numerical models of the earth's climate system and mesoscale weather events, the atmosphere, ocean, land, and

TABLE 2 Details on the weather and climate models in brief.

Types of numerical models	Example	Major purposes
Numerical weather prediction models	Weather Research and Forecasting (WRF) model, Hurricane Weather Research and Forecasting (HWRF) model	Real-time prediction of cyclones over the various oceans
Regional climate models (RCMs)	Conformal Cubic Atmospheric Model (CCAM) from Commonwealth Scientific and Industrial Research Organisation, RegCM from International Centre for Theoretical Physics, REMO model from Max Planck Institute for Meteorology, etc.	o Simulation of regional climate using the global climate model's output as input to a high-resolution (fine grids) climate model o RCMs encompass a larger number of atmospheric, oceanic, and land elements than weather models
Global climate models (GCMs)	Norwegian Earth System Model (NorESM1-M), GFDL Earth System Model Version 4.1 (GFDL-ESM 4.1) from Geophysical Fluid Dynamics Laboratory, Canadian Earth System Model (CanESM2), etc.	o GCMs can be used to produce climate projections o Provide data for RCM's input forcings.

cryosphere, among other elements, are mathematically represented. One of the best examples of such models is NWP models, which have been the mainstay of operational weather prediction for the last 2 decades or so. As new modelling algorithms, parameterization schemes, and faster computing resources become available, NWP is a complex and specialized field that is constantly evolving. The NWP models cover both hydrostatic and non-hydrostatic assumptions. The conservation of momentum, conservation of mass, conservation of energy, the first law of thermodynamics, equation of state, and the relationship among pressure, temperature, and density are all addressed in the fundamental governing equations of NWP models, and some of them are shown below:

$$\frac{dV}{dt} + fk \times V = -\nabla \emptyset + \frac{\sigma}{Ps}\frac{\partial \emptyset}{\partial \sigma}\nabla Ps + F \quad (1)$$

$$\nabla.(Ps\,V) + \frac{\partial}{\partial \sigma}(Ps\,\sigma) + \frac{\partial Ps}{\partial t} = 0 \quad (2)$$

$$\frac{\partial \emptyset}{\partial \sigma} = -\frac{RT}{\sigma} \quad (3)$$

Eq. 1, 2, and 3 are the horizontal momentum equation, continuity equation, and hydrostatic equation, respectively. Here, V is the horizontal wind velocity, Ps is the surface pressure, T is the temperature, and σ, $\emptyset$ are the diagnostic fields.

Thus, a set of partial differential equations that explain the dynamic and thermodynamic processes in the earth's atmosphere are used to generate the prediction or forecast. The equation set and model performance are highly influenced by the horizontal and vertical grid structure, initial and boundary conditions, and model domain.

There are various numerical models with different resolutions for predicting and projecting TCs worldwide, including NWP models, regional climate models (RCMs), and global climate models (GCMs) (Table 2). However, due to inaccurate vortex initialization of TCs, incomplete representation of complex physical processes, error in parameterization, and coarse resolution of the models, there are biases in the predictions of TC intensity, genesis and landfall that are still a challenge for forecasters (Chen et al., 2020). Osuri et al. (2012) performed numerical experiments to improve the TC intensity prediction by assimilating satellite-derived wind data. Further research improves uncertainty in the NWP system in predicting heavy rainfall associated with TC through Doppler Weather Radar (DWR) data assimilation (Mohanty et al., 2014). An example of TC simulation using the WRF model is provided in Figure 7. Simulated MSLP (Figure 7A) and surface wind at 10-m height (Figure 7B) during a VSCS Titli (2018) over the BoB was captured well by the model that shows the model's potential to predict the TC's over the region.

The prediction skill of the NWP model is highly reliable on the exactness of the initial state of the atmosphere. The conventional measurements like Sonde, Pilot, Profiler, Airep, Buoy, Ship, etc., have benefited the weather predictions, including the tropical belt but to a lesser extent (Guerbette et al., 2016). However, space-borne sensors provide continuous data at a high spatiotemporal resolution over sparse areas, mainly oceans. TCs are one of the deadliest natural hazards over the tropical regions to predict in terms of location and intensity to mitigate the devastation (Kumar and Shukla, 2019). The forecasting of severe weather events highly depends on moisture distribution and pre-convection environment transportation (Sieglaff et al., 2009). Though various conventional and satellite observations are routinely assimilated in the NWP model to produce a precise estimate of the initial model state (Montmerle et al., 2007), the use of satellite radiances perform an important role in the present operational data assimilation system (Kelly and Thépaut, 2007; Zupanski, 2013).

Due to a notable diversity in the observations, the Earth system modelling and its evaluation using satellite data have become challenging. Previous studies suggested that assimilation of clear-sky or cloud-cleared radiance assimilation from Microwave (MW) and Infrared (IR) sensors have improved the temperature and moisture analysis (Madhulatha et al., 2018). Zou et al. (2013) assimilated the Advanced Technology

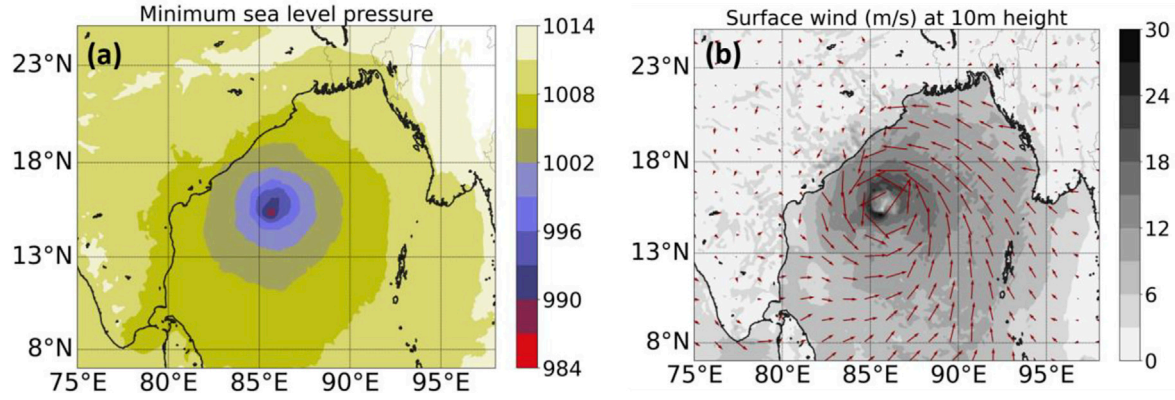

FIGURE 7
Spatial distribution of **(A)** MSLP and **(B)** 10-m surface wind during the life of cyclone Titli (2018) over the ARB using the high-resolution WRF model.

TABLE 3 Advantages and disadvantages of different methods over one another.

Approaches	Strength	Weakness	Best suited for
Numerical modelling	Provides a reliable confidence on real-time TCs' prediction	Large computational resources require for the numerical simulations	Operational forecasting, e.g., real-time prediction of TCs' at IMD
Coupled models	Provide a better understanding of oceanic surface and sub-surface processes involved in cyclogenesis, which the standalone atmospheric models do not provide	Substantial requirement of computational resources and computation time.	Cyclone related research and study of various parameters like tropical cyclone heat potential
Statistical approach	Relatively less computational resources require	Less confidence on medium-range weather forecasting	Probabilistic analysis of cyclones
Machine learning methods	○ Relatively less computational resources require ○ Useful to address the complexity involved between TC predictors, which the statistical methods get failed to resolve	Less confidence on cyclone prediction compared to numerical modelling approach	Probabilistic study and projection of cyclones
Observational datasets	Provide best possible records of meteorological parameters	○ Data is rarely available over the remote locations ○ Inconsistency in data continuity ○ Association of instrumental error	Play critical role in the real-time prediction of cyclones

Microwave Sounder (ATMS) radiances in the HWRF model to analyze its influence on track and intensity forecasts. They suggested a consistently positive impact on model predictions. The accuracy in predicting severe weather events by numerical models can be further improved by incorporating precipitation and cloud affected radiances from MW sensors (Madhulatha et al., 2018). In practice, it is difficult to separate the effect of cloud and precipitation in the temperature and moisture observations, therefore the assimilation of such data in the NWP models is still a significant challenge (Kumar and Shukla, 2019).

In the assimilation of clear-sky radiances, a large amount of information is discarded due to the non-linearity of the system, spatial and temporal discontinuity of the clouds and precipitation, and limitations in the model dynamics. Also, most of the data assimilation techniques forcefully transform the nonlinear processes into the linearized form (Ohring and Bauer, 2011; Kumar and Shukla, 2019). To avoid these difficulties to some extent, many agencies use the clear-sky IR/MW radiance in operational forecasts (Madhulatha et al., 2018). As a result, the clear sky radiance from different MW sensors has shown a positive impact on the NWP model forecasts.

Ice and precipitation-affected radiances have a massive potential to improve accuracy (Ohring and Bauer, 2011; Zupanski, 2013; Kumar and Shukla, 2019). Modification in observation thinning and quality control allowed Zhu et al. (2016) to assimilate all-sky satellite radiances in the Grid-point Statistical Interpolation (GSI) analysis system and evaluate the outputs over the clear-sky approach. The

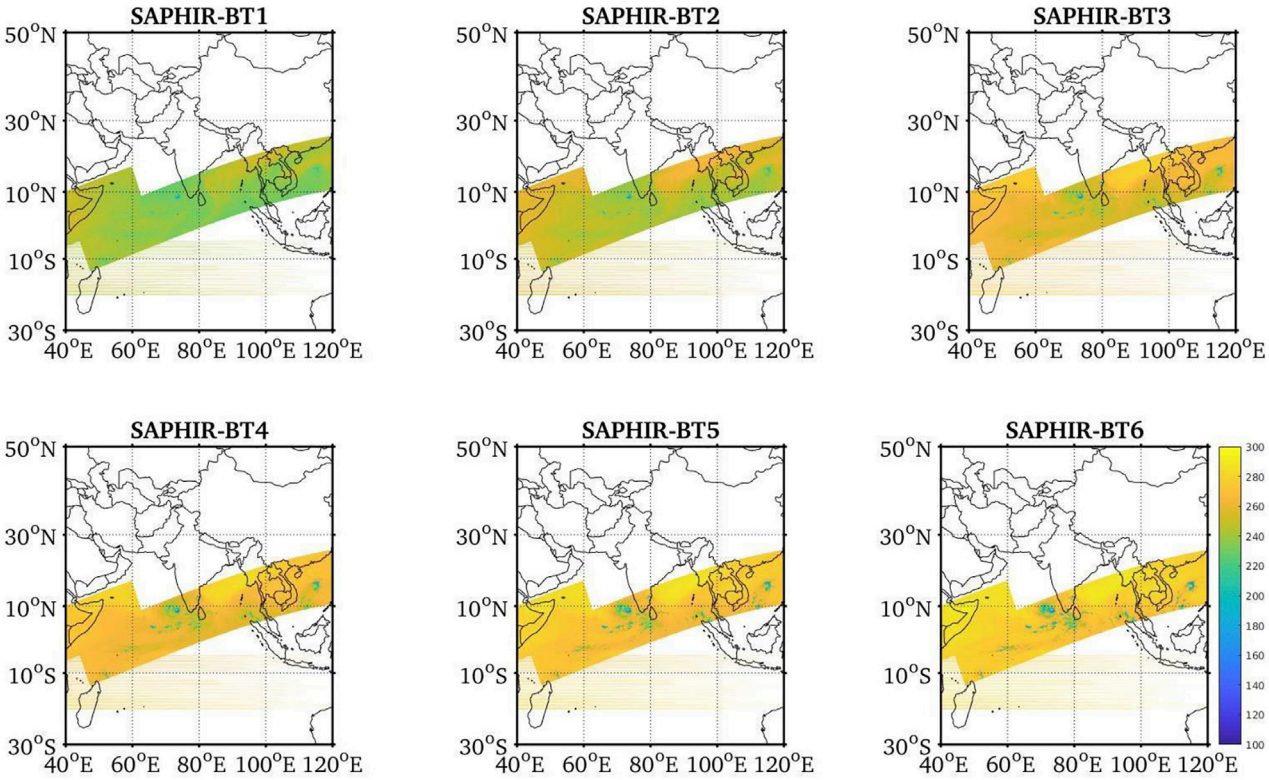

FIGURE 8
An overview of the brightness temperature dataset obtained from the 6-channels of SAPHIR, Megha-Tropiques satellite during the life of a very severe cyclonic storm Ockhi (29 November 2017–6 December 2017) over the NIO.

all-sky assimilation system provided more realistic brightness temperature (TB) results and cloud water analysis increments. Yang et al. (2016) analyzed the impact of clear-sky and all-sky AMSR2 radiances in predicting Hurricane Sandy. All-sky AMSR2 assimilation experiment showed the improved forecast of MSLP, cloud distribution, and warm-core structure compared to clear-sky radiance because more precipitation/cloud-affected data was assimilated through all-sky radiance around hurricane core areas. Assimilation of MW radiometers measured radiances in cloudy and rainy areas has shown recent progress in the humidity analysis (Yang et al., 2016; Zhu et al., 2016). Previously, Guerbette et al. (2016) showed the sensitivity of the Sondeur Atmosphérique du Profil d'Humidité Intertropicale par Radiométrie (SAPHIR) sounder within cloud systems to solid precipitating hydrometeors. Singh et al. (2013) compared the NWP model simulated radiances from SAPHIR using input profiles retrieved from Atmospheric Infra-Red Sounder (AIRS) data and radiosonde profiles. Singh et al. (2013) found good agreement between SAPHIR and Microwave Humidity Sounder (MHS) TB. A representation of SAPHIR TB during the cyclone Ockhi (2017) over the NIO is also demonstrated in Figure 8.

3.1.1 A NIO TC simulation instance with standalone WRF model

We have performed the simulation of TC Titli (2018) over the BoB basin of NIO using the WRF model. The initial and boundary conditions were taken from the "final analysis" product of the National Centers for Environmental Prediction (NCEP). The model simulation was started at 00 UTC on 9 October 2018, for a period of 120 h, and the results were compared to the "best-track" data from the IMD. The model simulation of cyclone Titli's genesis point was southwest of the observed location. The simulated storm crossed the observed track three to four times within the first 24 h (Figure 9). Then it proceeded continually on the left side of the observed track and made landfall on India's east coast about 6 h later, to the southwest of the actual landfall region. Further, we evaluated the mean absolute error in simulated TC's track (Figure 10A) and intensity errors (in terms of MSW; Figure 10B) to the IMD best-track data (Figure 10). The model performed excellently for the first 24 h, with a track error of less than 50 km (Figure 10A). However, the model began to exhibit substantial errors

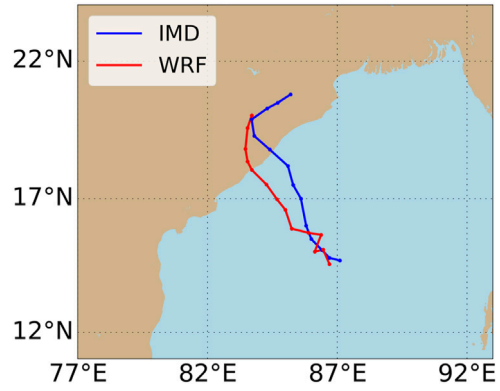

FIGURE 9
Observed (IMD best-track) and simulated (WRF) tracks of TC Titli (2018) over the NIO initialized at 00 UTC 2018–10-09 using the input forcings from the NCEP 1° × 1° final analysis product.

(more than 100 km) after 30 h of lead time and continued to do so until the simulation was completed. Similarly, the model produced a reasonably good intensity simulation with a 1-day lead time (Figure 10B). The model showed a relatively large error (underprediction) at 30 and 36 h and an overestimation in the TC's intensity simulation from 42 h onwards. Except for a few steps, the intensity error was less than or close to five hPa. In general, the model has demonstrated the ability to address the characteristics of NIO TC, while improved techniques such as 4DVar data assimilation can produce more accurate results.

The performance of the WRF model over the NIO is analogous to those of other basins. For example, Islam et al. (2015) reproduced Typhoon Haiyan's track movement and strength over the West Pacific Ocean. The model performed well in the track simulation, but it significantly underestimated the intensity simulation. Tiwari et al. (2019) used the WRF model to simulate super typhoon Maysak over the Northwest Pacific Ocean, and the model provided reasonable results compared to observations.

3.2 Coupled models (two-way or three-way)

It is noticed that atmosphere, ocean, and land all together have a role in the TC genesis through the exchange of fluxes that ultimately affect TC intensification and track changes. Moreover, it is confirmed by Mohanty et al. (2001) that land-air-sea interaction has a significant impact on the regional circulation pattern. There is a developed strong feedback teleconnection, interaction and feedback between the regional and global scale features. Recent research mentioned the importance of the air-sea interface for intensity prediction. Following the same, there are many studies over the influence of air-sea interaction on TC physical activity and its simulation. It is well established that air-sea moisture difference and surface entropy flux increase the intensity and hence destructiveness. Single standalone models used for the TC forecasts are more biased and inaccurate due to the unrealistic feedback in the model. Such static SST is provided in the NWP models, with a high probability of biases in the results (Bender and Ginis, 2000; Bender et al., 2007). Henceforth, coupled models emerged as a helping tool to the modelling community in improving the predictability skills of the model. Many studies have been done so far to test the predicting skills of coupled ocean-atmosphere models over NIO and other oceans. For example, the sensitivity experiment of the HWRF-POM/HYCOM coupled ocean-atmosphere model was conducted to demonstrate the predicting skills of these widely used regional models (Mohanty et al., 2019). Another study using WRF-ROMS demonstrated the benefits of a coupled atmosphere-ocean model for obtaining realistic simulations of atmospheric and oceanic parameters under the extreme weather conditions associated with a very intense cyclone such as TC Phailin (Prakash and Pant, 2017). There are more studies observed using coupling between ocean-atmosphere but three ways coupled models are significantly less explored. However, few studies demonstrated the usefulness of the inclusion of realistic land surface features has the potential to improve the predicting skills of models.

3.3 Statistical approach

Studies show that using a statistical approach is a challenge. The statistical models and methods have limitations in TC prediction beyond 24 h over a heterogeneous environment like NIO (Mohanty and Gupta, 1997; Gupta, 2006). However, these methods are not far behind in contributing to the improvement in TC forecast. Statistical approaches are used to correct the data, fill the gaps for data, bias correction, downscaling, and many more ways to explore the correlation between environmental drivers and TC activity. A study was conducted by Lee et al. (2020) using the statistical downscaling approach to investigate the TC's frequency, and the result indicates that future TCs will be more devastating (more intense). Data used in NWP models is always a hindrance in the TC forecast. Statistical approaches help improve the quality of input data for initial and boundary conditions and post-processing.

3.4 Machine learning methods

Orthodox statistical models often fail to address the nonlinear and complex relationship between TC predictors (Demaria et al., 2005; Lee et al., 2015; Wang et al., 2015). To

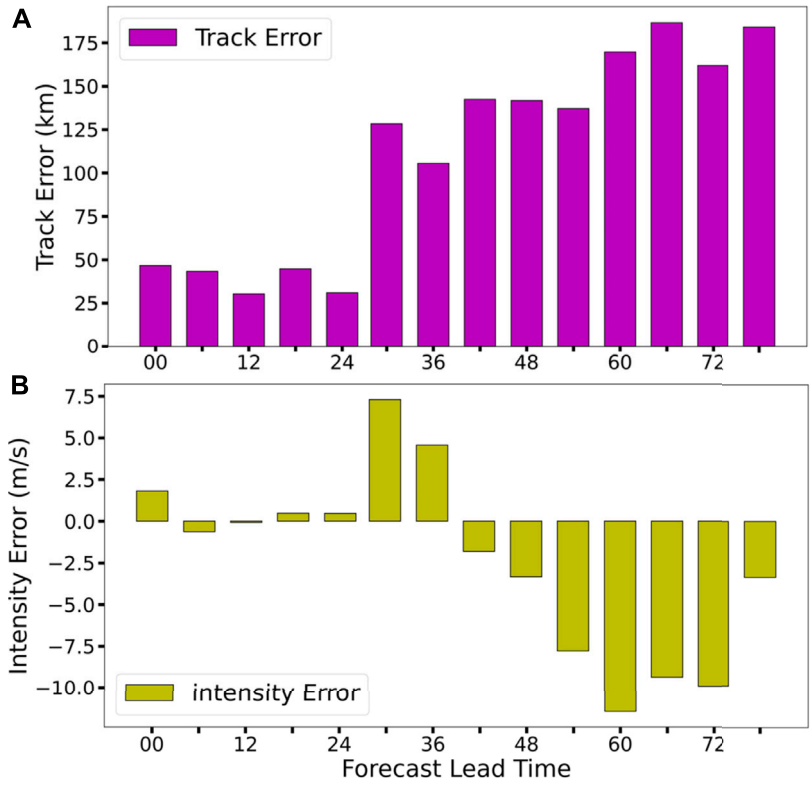

FIGURE 10
6-hourly **(A)** track error (km) and **(B)** intensity error (m/s) in terms of MSW for the simulation of TC Titli initialized at 00 UTC 2018–10-09 using WRF model. The outputs are validated against the IMD best-track data.

solve such challenges, the concept of machine learning is being used to explore the observational datasets to improve the TCs forecast skills (Chen et al., 2020). It also helps to improve the uncertainties in the NWP models by enhancing the pre-processing, i.e., refining the initial condition of a model through data assimilation techniques. Artificial intelligence, a part of machine learning, is a new development to the current century. According to their applications, we can divide the machine learning algorithms into three categories: feature selection, clustering, and regression (Chen et al., 2020). Richman et al. (2017) applied the support vector regression (SVR) method to an initial predictor pool to reduce the TC seasonal prediction errors. Alemany et al. (2019) proposed a fully connected recurrent neural network to predict the TCs trajectory. Their method successfully predicted the hurricane's track up to 120 h with reduced error.

3.5 Observational datasets

Once the TC approaches the land, the automatic weather station (AWS) and conventional observations such as sonde, pilot, profiler, airep, buoy, ship, and doppler weather radar data are relevant for TC prediction. Because conventional observations over the ocean are unavailable, satellite data are being used and have shown to be significant for studying and understanding TC characteristics (Jaiswal et al., 2017). Microwave scatterometers have been effective in studying cyclogenesis in its early phases (Sharp et al., 2002). The use of a sea-winds scatterometer has been valuable in understanding tropical disturbances (Sharp et al., 2002; Li et al., 2003). Jaiswal and Kishtawal (2011) and Jaiswal et al. (2013) applied the scatterometer derived surface wind. They used a wind pattern matching based technique that relied on the availability of a cyclonic disturbance during the satellite overpass.

Apart from conventional observations, the reanalysis products from the European Centre for Medium-Range Weather Forecasts (ERA-I, ERA-40, and ERA-5, and others), National Centers for Environmental Prediction—National Center for Atmospheric Research, Modern-Era Retrospective Analysis for Research and Applications, etc., are widely used in many kinds of literature to study the TCs, such as Evan et al. (2006); Balaji et al. (2018); Duan et al. (2021); Tiwari et al. (2021); Ranji et al. (2022); etc.

3.6 Intercomparison of strength and weakness of various approaches

The numerical modelling approach is demarcated as best suited for operational forecasting; however, the coupled models are best to perform the cyclone related research (Table 3).

3.7 Performance comparison of various approaches

The simulation of cyclone Phailin induced storm surge and inundation was carried out by means of ADvanced CIRCulation (ADCIRC) model by Kumar et al. (2015). Phailin made landfall on 12 October 2013 at Odisha (east coast of India). Within a few days of landfall, the model-simulated inundation extent corresponded closely with field surveys at Ganjam, Odisha. Furthermore, the model nicely simulated the temporal evolution of the surge residual based on measurements from a tide gauge in Paradip. However, the model slightly underestimated the magnitude compared to observations, which might be attributed to the model's paucity of wave setup and uncertainty in wind and pressure parameters. More or less a similar kind of study was performed by Murty et al. (2014) by implementing a coupled wave + surge hydrodynamic modeling system to simulate storm surge caused by cyclone Phailin. The coupled model setup provides a realistic representation of the dynamic interaction of currents, waves, tides, and wind, which is important for operational forecasts.

Saxby et al. (2021) compared the performance of a regional convection-permitting atmosphere-ocean coupled model, i.e., the Met Office Unified Model atmosphere-only configuration and three-dimensional dynamical ocean model for the simulations of BoB TCs. Results showed that the atmosphere-only configuration produced stronger TCs than the coupled configuration; however, both model configurations reasonably represented the TC dynamics. Sahoo et al. (2019) evaluated the impact of cyclone Phailin's strong winds and heavy rainfall on the power distribution network. The data from the tailored WRF model was found to be highly effective in managing power distribution and transmission networks in electric power grids. A thorough inspection of the results reveals that the atmospheric model fared well to capture power line tripping time. This study's overall knowledge offers a greater scope for developing a framework for efficient power network planning operations, resource allocation, and disaster preparedness. Kumar et al. (2017) evaluated the WRF model with nested domains (horizontal resolutions of 27 and 9 km for outer and inner domains, respectively) to simulate cyclone Phailin. Compared to the domain-1 simulation, the cyclone's intensity was well simulated in domain-2. In the domain-2 simulation, the average root mean square error and standard deviations of surface wind and MSLP were significantly lower. The track of cyclone Phailin was also well demonstrated by domain-2 simulation with respect to IMD best-track observation.

4 Current status of the NIO cyclones prediction

Many studies in recent years have shown remarkable advances in NIO cyclones' track prediction; nonetheless, intensity prediction and rapid intensity prediction remain a crucial challenge for researchers and the scientific community. This section discusses the literature on the current status of NIO TCs, covering characteristics such as genesis, track, intensification, landfall, rainfall, and so on.

4.1 Status of cyclones genesis, track, intensification, and RI

For NIO cyclones real-time prediction, the IMD in New Delhi introduced some in-house global and limited area NWP models (Mohapatra et al., 2014, Mohapatra et al., 2013; Mohanty et al., 2015; Nadimpalli et al., 2020a). IMD employed the Quasi-Lagrangian model as a TC operational model with a coarser resolution and only 16 vertical levels in the twenty-first century's first decade. Under the auspices of the 'Forecast Demonstration Project of Landfalling TCs,' some prestigious research centres and academic institutes in India also provide real-time TC forecasts to IMD for official usage (Mohapatra et al., 2011; Nadimpalli et al., 2020a). Since 2007, some operational centres have adopted the WRF model for real-time TC prediction. Adapting such mesoscale models like WRF and HWRF for the NIO region has been a significant development in recent years. Some works of literature such as Kanase and Salvekar (2015); Mahala et al. (2021); Osuri et al. (2012); Pattanayak et al. (2012a), and Raju et al. (2011) conducted dedicated simulations to determine the optimal parameterization scheme set up within the WRF model for the NIO region. The WRF model was used by Osuri et al. (2013) to simulate 17 NIO TCs. The TCs movement had an eastward and sluggish bias. Track errors ranged from 113 to 375 km with a model resolution of 27 km. Pattanayak et al. (2012b) and Mohanty et al. (2013) found better results with the HWRF model for TCs' track prediction and improved intensity prediction over the BoB. Nadimpalli et al. (2020a) evaluated the forecasts from WRF and HWRF models in a quasi-operational setup for 10 BoB TCs from 2013 to 2017. Both models performed well for forecasts up to 30 h; however, HWRF generated more accurate results for longer forecasts.

Vinodhkumar et al. (2022) studied the climatology of NIO cyclone RI behaviour from 1990 to 2019. If the MSW speed of a cyclone increases by 15.4 m/s or greater in 24 h, it is classified as RI. During the time period given above, 46 NIO cyclones had the RI

feature, with a considerable increase beginning in the year 2000. The post-monsoon season proved more favourable for RI TCs. While around 70% of RI TCs migrated north-westward or westward, eastern states of India (Tamil Nadu, and Andhra Pradesh) are more vulnerable to RI TCs. A possible cause behind the increase in the RI TCs over the NIO could be the higher moisture and SST over the cyclogenesis locations than the non-RI TCs (Nadimpalli et al., 2021). Munsi et al. (2021) used the WRF model to perform three-dimensional variational-Ensemble Kalman Filter data assimilation for three cyclones over the NIO: Fani, Ockhi, and Luban. To investigate the RI of these TCs, upper-air observations, radiometer wind, and radiance data were assimilated. In all cases, the model framework correctly simulated the RI.

4.2 Status of cyclones landfall and rainfall

Osuri et al. (2013) reported the WRF model to be more efficient in predicting the landfall location than the other attributes. Govindankutty et al. (2010) showed a positive impact of assimilating the conventional and Doppler weather radar radial wind assimilation on the intensity and rainfall distribution of NIO TCs. Sandeep et al. (2017) assimilated the Doppler weather radar wind profiles in the 3DVar and Hybrid 3DVar mode and found a minimal improvement in the TC's zonal and meridional winds simulation. Gopalakrishnan and Chandrasekar (2018) performed the assimilation of satellite-derived winds, satellite radiance, and conventional observations with 3DVar and four-dimensional variational (4DVar) mode for the first time over the NIO for 4 TCs. The 4DVar experiments revealed better results than 3DVar in terms of track and intensity and rainfall prediction.

5 Conclusion

This study has provided the literature review on the climatology and recent progress in the tropical cyclone (TC) prediction over the North Indian Ocean (NIO) along with various methods to study them. Although the authors have tried to include as many aspects as possible, some studies could have been missed because of the rapid advancement of this research area. Several important facets of TC have been discussed, including the earth's components and multidisciplinary approaches for TC prediction. In recent years, a rise in the NIO sea surface temperature, especially in the Arabian Sea, has been a primary factor for the genesis of highly intense TCs. Along with SST, vertical profiles of tropical cyclone heat potential in the ocean also affect the TC formation and intensification. A direct correlation of TC frequency with seasonal changes successfully claims the genesis of intense Arabian Sea (Bay of Bengal) TCs in the pre-monsoon (post-monsoon) season. At India Meteorological Department in New Delhi, operational forecasting of the NIO TCs is mainly being done by numerical modelling systems, including Weather Research and Forecasting and Hurricane Weather Research Forecasting models. Recent studies have shown significant improvements in TCs prediction with the assimilations of remote sensing observations. However, the improvement in the intensity and rapid intensity prediction of NIO cyclones is still of major concern. There is sufficient literature on three-dimensional variational (3DVar) data assimilations; very few studies on four-dimensional variational (4DVar) data assimilations over the NIO region are available. Being a more accurate technique, further scientific development with the 4DVar data assimilation method for NIO TCs prediction is on high priority in the present scenario.

Author contributions

All authors listed have made a substantial, direct, and intellectual contribution to the work and approved it for publication.

Funding

The first author is thankful to the Department of Science and Technology, Government of India, for giving the DST-INSPIRE research fellowship, registration number IF160165. Indian Institute of Science Education and Research (IISER) Bhopal has provided the research facilities and lab environment. PK acknowledges funding from the Science and Engineering Research Board (SERB), Department of Science and Technology (DST), Government of India, Grant Number CRG/2021/001227.

Conflict of interest

The authors declare that the research was conducted in the absence of any commercial or financial relationships that could be construed as a potential conflict of interest.

Publisher's note

References

Albert, J., Krishnan, A., Bhaskaran, P. K., and Singh, K. S. (2022). Role and influence of key atmospheric parameters in large-scale environmental flow associated with tropical cyclogenesis and ENSO in the North Indian Ocean basin. *Clim. Dyn.* 58, 17–34. doi:10.1007/s00382-021-05885-8

Alemany, S., Beltran, J., Perez, A., and Ganzfried, S. (2019). "Predicting hurricane trajectories using a recurrent neural network," in The Thirty-Third AAAI Conference on Artificial Intelligence, Hilton Hawaiian Village, Honolulu, Hawaii, USA, Jan 27–Feb 1, 2019.

Andersen, T., and Shepherd, M. (2017). "Inland tropical cyclones and the "Brown ocean" concept," in *Hurricanes and climate change*. Editors J. Collins and K. Walsh (Cham: Springer). doi:10.1007/978-3-319-47594-3_5

Balaji, M., Chakraborty, A., and Mandal, M. (2018). Changes in tropical cyclone activity in north Indian Ocean during satellite era (1981–2014). *Int. J. Climatol.* 38, 2819–2837. doi:10.1002/joc.5463

Bender, M. A., and Ginis, I. (2000). Real-case simulations of hurricane–ocean interaction using A high-resolution coupled model: Effects on hurricane intensity. *Mon. Weather Rev.* 128, 917–946. doi:10.1175/1520-0493(2000)128<0917:rcsoho>2.0.co;2

Bender, M. A., Tuleya, R., Thomas, B., and Marchok, T. (2007). The operational GFDL coupled hurricane–ocean prediction system and a summary of its performance. *Mon. Weather Rev.* 135, 3965–3989. doi:10.1175/2007mwr2032.1

Bhatla, R., Raj, R., Mall, R. K., and Shivani (2020). "Tropical cyclones over the north Indian ocean in changing climate," in *Techniques for disaster risk management and mitigation*. Editors P. K. Srivastava, S. K. Singh, U. C. Mohanty, and T. Murty. 1st ed. (Hoboken, New Jersey, United States: Wiley), 63–76. doi:10.1002/9781119359203.ch5

Chan, J. C. L. (2005). The physics of tropical cyclone motion. *Annu. Rev. Fluid Mech.* 37, 99–128. doi:10.1146/annurev.fluid.37.061903.175702

Chang, H.-I., Niyogi, D., Kumar, A., Kishtawal, C. M., Dudhia, J., Chen, F., et al. (2009). Possible relation between land surface feedback and the post-landfall structure of monsoon depressions: Land surface and monsoon depressions. *Geophys. Res. Lett.* 36, 1–6. doi:10.1029/2009GL037781

Chauhan, A., Singh, R. P., Dash, P., and Kumar, R. (2021). Impact of tropical cyclone "Fani" on land, ocean, atmospheric and meteorological parameters. *Mar. Pollut. Bull.* 162, 111844. doi:10.1016/j.marpolbul.2020.111844

Chen, R., Zhang, W., and Wang, X. (2020). Machine learning in tropical cyclone forecast modeling: A review. *Atmosphere* 11, 676. doi:10.3390/atmos11070676

Corsaro, C. M., and Toumi, R. (2017). A self-weakening mechanism for tropical cyclones. *Q. J. R. Meteorol. Soc.* 143, 2585–2599. doi:10.1002/qj.3109

Courtney, J. B., Langlade, S., Sampson, C. R., Knaff, J. A., Birchard, T., Barlow, S., et al. (2019). Operational perspectives on tropical cyclone intensity change Part 1: Recent advances in intensity guidance. *Trop. Cyclone Res. Rev.* 8, 123–133. doi:10.1016/j.tcrr.2019.10.002

Das, Y., Mohanty, U. C., Jain, I., Subba Rao, M., and Murty, A. S. N. (2014). Modeling on the aspects of thermal response of Bay of bengal to tropical cyclone TC05B 1999 using Princeton Ocean model (POM): Preliminary results. *Am. J. Model. Optim.* 2, 47–59. doi:10.12691/ajmo-2-2-2

Demaria, M., and Kaplan, J. (1994). A statistical hurricane intensity prediction scheme (SHIPS) for the atlantic basin. *Wea. Forecast.* 9, 209–220. doi:10.1175/1520-0434(1994)009<0209:aships>2.0.co;2

Demaria, M., Mainelli, M., Shay, L. K., Knaff, J. A., and Kaplan, J. (2005). Further improvements to the statistical hurricane intensity prediction scheme (SHIPS). *Weather Forecast.* 20, 531–543. doi:10.1175/waf862.1

Deshpande, M., Singh, V. K., Ganadhi, M. K., Roxy, M. K., Emmanuel, R., and Kumar, U. (2021). Changing status of tropical cyclones over the north Indian Ocean. *Clim. Dyn.* 57, 3545–3567. doi:10.1007/s00382-021-05880-z

Duan, W., Yuan, J., Duan, X., and Feng, D. (2021). Seasonal variation of tropical cyclone genesis and the related large-scale environments: Comparison between the Bay of bengal and Arabian Sea sub-basins. *Atmosphere* 12, 1593. doi:10.3390/atmos12121593

Espejo, A., Mendez, F. J., Diez, J., Medina, R., and Al-Yahyai, S. (2016). Seasonal probabilistic forecasting of tropical cyclone activity in the North Indian Ocean: Forecasting tropical cyclone activity. *J. Flood Risk Manag.* 9, 379–389. doi:10.1111/jfr3.12197

Frank, W. M., and Young, G. S. (2007). The interannual variability of tropical cyclones. *Mon. Weather Rev.* 135, 3587–3598. doi:10.1175/mwr3435.1

Gopalakrishnan, D., and Chandrasekar, A. (2018). On the improved predictive skill of WRF model with regional 4DVar initialization: A study with north Indian Ocean tropical cyclones. *IEEE Trans. Geosci. Remote Sens.* 56, 3350–3357. doi:10.1109/tgrs.2018.2798623

Govindankutty, M., Chandrasekar, A., and Pradan, D. (2010). Impact of 3DVAR assimilation of Doppler Weather Radar wind data and IMD observation for the prediction of a tropical cyclone. *Int. J. Remote Sens.* 31, 6327–6345. doi:10.1080/01431160903413689

Guerbette, J., Mahfouf, J. F., and Plu, M. (2016). Towards the assimilation of all-sky microwave radiances from the SAPHIR humidity sounder in a limited area NWP model over tropical regions. *Tellus A Dyn. Meteorology Oceanogr.* 68, 28620. doi:10.3402/tellusa.v68.28620

Gupta, A. (2006). Current status of Tropical Cyclone track prediction techniques and forecast errors. *Mausam* 57, 151–158. doi:10.54302/mausam.v57i1.464

Gupta, S., Jain, I., Johari, P., and Lal, M. (2019). "Impact of climate change on tropical cyclones frequency and intensity on Indian coasts," in Proceedings of International Conference on Remote Sensing for Disaster Management, Visakhapatnam, India, October 11–13, 2017. Editors P. J. Rao, K. N. Rao, and S. Kubo (Springer International Publishing), 359–365. doi:10.1007/978-3-319-77276-9_32

Islam, T., Srivastava, P. K., Rico-Ramirez, M. A., Dai, Q., Gupta, M., and Singh, S. K. (2015). Tracking a tropical cyclone through WRF–ARW simulation and sensitivity of model physics. *Nat. Hazards (Dordr).* 76, 1473–1495. doi:10.1007/s11069-014-1494-8

Jadhav, S. K., and Munot, A. A. (2009). Warming SST of Bay of Bengal and decrease in formation of cyclonic disturbances over the Indian region during southwest monsoon season. *Theor. Appl. Climatol.* 96, 327–336. doi:10.1007/s00704-008-0043-3

Jaiswal, N., Kishtawal, C. M., and Pal, P. K. (2013). Prediction of tropical cyclogenesis in North Indian Ocean using Oceansat-2 scatterometer (OSCAT) winds. *Meteorol. Atmos. Phys.* 119, 137–149. doi:10.1007/s00703-012-0230-8

Jaiswal, N., Kishtawal, C. M., and Pal, P. K. (2017). "Tropical cyclogenesis prediction in the north Indian ocean during 2013 using OSCAT derived surface wind observations," in *Tropical cyclone activity over the north Indian ocean*. Editors M. Mohapatra, B. Bandyopadhyay, and L. Rathore (Cham: Springer). doi:10.1007/978-3-319-40576-6_14

Jaiswal, N., and Kishtawal, C. M. (2011). Prediction of tropical cyclogenesis using scatterometer data. *IEEE Trans. Geosci. Remote Sens.* 49, 4904–4909. doi:10.1109/tgrs.2011.2153862

Jangir, B., Swain, D., and Ghose, S. K. (2020). Influence of eddies and tropical cyclone heat potential on intensity changes of tropical cyclones in the North Indian Ocean. *Adv. Space Res.* 68, 773–786. S0273117720300296. doi:10.1016/j.asr.2020.01.011

Kanase, R. D., and Salvekar, P. S. (2015). Effect of physical parameterization schemes on track and intensity of cyclone LAILA using WRF model. *Asia. Pac. J. Atmos. Sci.* 51, 205–227. doi:10.1007/s13143-015-0071-8

Kelly, G., and Thépaut, J. N. (2007). Evaluation of the impact of the space component of the global observing system through observing system experiments. *ECMWF Newsl.* 113, 16–28.

Kishtawal, C. M., Niyogi, D., Kumar, A., Bozeman, M. L., and Kellner, O. (2012). Sensitivity of inland decay of North Atlantic tropical cyclones to soil parameters. *Nat. Hazards (Dordr).* 63, 1527–1542. doi:10.1007/s11069-011-0015-2

Kumar, P., and Shukla, M. V. (2019). Assimilating INSAT-3D thermal infrared window imager observation with the particle filter: A case study for vardah cyclone. *J. Geophys. Res. Atmos.* 124, 1897–1911. doi:10.1029/2018jd028827

Kumar, S., Routray, A., Tiwari, G., Chauhan, R., and Jain, I. (2017). "Simulation of tropical cyclone 'Phailin' using WRF modeling system," in *Tropical cyclone activity over the north Indian ocean*. Editors M. Mohapatra, B. K. Bandyopadhyay, and L. S. Rathore (Midtown Manhattan, New York: Springer International Publishing), 307–316. doi:10.1007/978-3-319-40576-6_21

Kumar, T. S., Murty, P. L. N., Kumar, M. P., Kumar, M. K., Padmanabham, J., Kumar, N. K., et al. (2015). Modeling storm surge and its associated inland inundation extent due to very severe cyclonic storm Phailin. *Mar. Geod.* 38 (4), 345–360. doi:10.1080/01490419.2015.1053640

Lee, C.-Y., Camargo, S. J., Sobel, A. H., and Tippett, M. K. (2020). Statistical–dynamical downscaling projections of tropical cyclone activity in a warming climate: Two diverging genesis scenarios. *J. Clim.* 33, 4815–4834. doi:10.1175/JCLI-D-19-0452.1

Lee, C. Y., Tippett, M. K., Camargo, S. J., and Sobel, A. H. (2015). Probabilistic multiple linear regression modeling for tropical cyclone intensity. *Mon. Weather Rev.* 143, 933–954. doi:10.1175/mwr-d-14-00171.1

Li, T., Fu, B., Ge, X., Wang, B., and Peng, M. (2003). Satellite data analysis and numerical simulation of tropical cyclone formation. *Geophys. Res. Lett.* 30, 2122. doi:10.1029/2003gl018556

Lin, I.-I., Goni, G. J., Knaff, J. A., Forbes, C., and Ali, M. M. (2013). Ocean heat content for tropical cyclone intensity forecasting and its impact on storm surge. *Nat. Hazards (Dordr).* 66, 1481–1500. doi:10.1007/s11069-012-0214-5

Madhulatha, A., Rajeevan, M., Bhowmik, S. R., and Das, A. K. (2018). Impact of assimilation of conventional and satellite radiance GTS observations on simulation of mesoscale convective system over Southeast India using WRF-3DVar. *Pure Appl. Geophys.* 175, 479–500. doi:10.1007/s00024-017-1689-5

Mahala, B. K., Mohanty, P. K., Xalxo, K. L., Routray, A., and Misra, S. K. (2021). Impact of WRF parameterization schemes on track and intensity of extremely severe cyclonic storm "Fani. *Pure Appl. Geophys.* 178, 245–268. doi:10.1007/s00024-020-02629-3

Mandal, M., and Mohanty, U. C. (2010). Simulation of severe land-falling Bay of bengal cyclones during 1995–1999 using mesoscale model MM5. *Mar. Geod.* 33, 315–337. doi:10.1080/01490419.2010.518070

Mawren, D., and Reason, C. J. C. (2017). Variability of upper-ocean characteristics and tropical cyclones in the South West Indian Ocean. *J. Geophys. Res. Oceans* 122, 2012–2028. doi:10.1002/2016JC012028

Mishra, A. K., Dwivedi, S., Di Sante, F., and Coppola, E. (2020). Thermodynamical properties associated with the Indian summer monsoon rainfall using a regional climate model. *Theor. Appl. Climatol.* 141, 587–599. doi:10.1007/s00704-020-03237-w

Mohanty, S., Nadimpalli, R., Mohanty, U. C., Mohapatra, M., Sharma, A., Das, A. K., et al. (2020). Quasi-operational forecast guidance of extremely severe cyclonic storm Fani over the Bay of Bengal using high-resolution mesoscale models. *Meteorol. Atmos. Phys.* 133, 331–348. doi:10.1007/s00703-020-00751-4

Mohanty, U. C., and Gupta, A. (1997). Deterministic methods for prediction of Tropical Cyclone tracks. *Mausam* 48, 257–272. doi:10.54302/mausam.v48i2.4008

Mohanty, U. C., Nadimpalli, R., Mohanty, S., and Osuri, K. K. (2019). Recent advancements in prediction of tropical cyclone track over north Indian Ocean basin. *Mausam* 70, 57–70. doi:10.54302/mausam.v70i1.167

Mohanty, U. C., Niyogi, D., Raman, S., and Sarkar, A. (2001). Numerical study of the role of land-air-sea interactions for the northeasterly monsoon circulations over Indian Ocean during INDOEX. *Curr. Sci.* 80, 60–68.

Mohanty, U. C., Osuri, K. K., and Pattanayak, S. (2013). A study on high resolution mesoscale modeling systems for simulation of tropical cyclones over the Bay of Bengal. *Mausam* 64, 117–134. doi:10.54302/mausam.v64i1.661

Mohanty, U. C., Osuri, K. K., and Pattanayak, S. (2014). "Mesoscale modelling for tropical cyclone forecasting over the north Indian ocean," in *Monitoring and prediction of tropical cyclones in the Indian ocean and climate change*. Editors U. C. Mohanty, M. Mohapatra, O. P. Singh, B. K. Bandyopadhyay, and L. S. Rathore (Dordrecht, Netherlands: Springer Netherlands), 274–286. doi:10.1007/978-94-007-7720-0_24

Mohanty, U. C., Osuri, K. K., Pattanayak, S., and Sinha, P. (2012). An observational perspective on tropical cyclone activity over Indian seas in a warming environment. *Nat. Hazards (Dordr).* 63, 1319–1335. doi:10.1007/s11069-011-9810-z

Mohanty, U. C., Osuri, K. K., Tallapragada, V., Marks, F. D., Pattanayak, S., Mohapatra, M., et al. (2015). A great escape from the Bay of bengal "super sapphire–phailin" tropical cyclone: A case of improved weather forecast and societal response for disaster mitigation. *Earth Interact.* 19, 1–11. doi:10.1175/EI-D-14-0032.1

Mohapatra, M., Bandyopadhyay, B. K., and Tyagi, A. (2014). "Status and plans for operational tropical cyclone forecasting and warning systems in the north Indian ocean region," in *Monitoring and prediction of tropical cyclones in the Indian ocean and climate change*. Editors U. C. Mohanty, M. Mohapatra, O. P. Singh, B. K. Bandyopadhyay, and L. S. Rathore (Dordrecht: Springer).

Mohapatra, M. (2011). *Forecast demonstration project (FDP) for improving track, intensity and landfall of Bay of Bengal tropical cyclones implementation of pilot phase, 2010- a report*. New Delhi: IMD.

Mohapatra, M. (2016). "Monitoring and forecasting of tropical cyclones over north Indian ocean," in *Advanced numerical modeling and data assimilation techniques for tropical cyclone prediction*. Editors U. C. Mohanty and S. G. Gopalakrishnan (Dordrecht, Netherlands: Springer Netherlands), 409–447. doi:10.5822/978-94-024-0896-6_16

Mohapatra, M., Sikka, D. R., Bandyopadhyay, B. K., and Tyagi, A. (2013). Outcomes and challenges of forecast demonstration project (FDP) on landfalling cyclones over the Bay of Bengal. *Mausam* 64, 1–12. doi:10.54302/mausam.v64i1.650

Mondal, M., Biswas, A., Haldar, S., Mandal, S., Bhattacharya, S., and Paul, S. (2021). Spatio-temporal behaviours of tropical cyclones over the Bay of bengal basin in last five decades, *Trop. Cyclone Res. Rev.*, 11, 1–15. doi.org/doi:10.1016/j.tcrr.2021.11.004

Montmerle, T., Rabier, F., and Fischer, C. (2007). Relative impact of polar-orbiting and geostationary satellite radiances in the Aladin/France numerical weather prediction system. *Q. J. R. Meteorol. Soc.* 133, 655–671. doi:10.1002/qj.34

Munsi, M., Kesarkar, A., Bhate, J., Panchal, A., Singh, K., Kutty, G., et al. (2021). Rapidly intensified, long duration North Indian Ocean tropical cyclones: Mesoscale downscaling and validation. *Atmos. Res.* 259, 105678. doi:10.1016/j.atmosres.2021.105678

Murty, P. L. N., Sandhya, K. G., Bhaskaran, P. K., Jose, F., Gayathri, R., Nair, T. M. B., et al. (2014). A coupled hydrodynamic modeling system for PHAILIN cyclone in the Bay of Bengal. *Coast. Eng.* 93, 71–81. doi:10.1016/j.coastaleng.2014.08.006

Nadimpalli, R., Mohanty, S., Pathak, N., Osuri, K. K., Mohanty, U. C., and Chatterjee, S. (2021). Understanding the characteristics of rapid intensity changes of tropical cyclones over north Indian ocean. *SN Appl. Sci.* 3, 68. doi:10.1007/s42452-020-03995-2

Nadimpalli, R., Osuri, K. K., Mohanty, U. C., Das, A. K., Kumar, A., Sil, S., et al. (2020a). Forecasting tropical cyclones in the Bay of Bengal using quasi-operational WRF and HWRF modeling systems: An assessment study. *Meteorol. Atmos. Phys.* 132, 1–17. doi:10.1007/s00703-019-00669-6

Nadimpalli, R., Srivastava, A., Prasad, V. S., Osuri, K. K., Das, A. K., Mohanty, U. C., et al. (2020b). Impact of INSAT-3D/3DR radiance data assimilation in predicting tropical cyclone Titli over the Bay of bengal. *IEEE Trans. Geosci. Remote Sens.* 58, 6945–6957. doi:10.1109/TGRS.2020.2978211

Nair, U. S., Rappin, E., Foshee, E., Smith, W., Pielke, R. A., Mahmood, R., et al. (2019). Influence of land cover and soil moisture based Brown ocean effect on an extreme rainfall event from a Louisiana gulf coast tropical system. *Sci. Rep.* 9, 17136. doi:10.1038/s41598-019-53031-6

Ohring, G., and Bauer, P. (2011). The use of cloud and precipitation observations in data assimilation (CPDA). *Q. J. R. Meteorol. Soc.* 137, 1933. doi:10.1002/qj.946

Osuri, K. K., Mohanty, U. C., Routray, A., Kulkarni, M. A., and Mohapatra, M. (2012). Customization of WRF-ARW model with physical parameterization schemes for the simulation of tropical cyclones over North Indian Ocean. *Nat. Hazards (Dordr).* 63, 1337–1359. doi:10.1007/s11069-011-9862-0

Osuri, K. K., Mohanty, U. C., Routray, A., Mohapatra, M., and Niyogi, D. (2013). Real-time track prediction of tropical cyclones over the north Indian ocean using the ARW model. *J. Appl. Meteorology Climatol.* 52, 2476–2492. doi:10.1175/jamc-d-12-0313.1

Osuri, K. K., Nadimpalli, R., Mohanty, U. C., Chen, F., Rajeevan, M., and Niyogi, D. (2017). Improved prediction of severe thunderstorms over the Indian Monsoon region using high-resolution soil moisture and temperature initialization. *Sci. Rep.* 7, 41377. doi:10.1038/srep41377

Osuri, K. K., Routray, A., Mohanty, U. C., and Kulkarni, M. A. (2010). "Simulation of tropical cyclones over Indian seas: Data impact study using WRF-var assimilation system," in *Indian Ocean tropical cyclones and climate change*. Editor Y. Charabi (Dordrecht, Netherlands: Springer Netherlands), 115–124. doi:10.1007/978-90-481-3109-9_15

Patnaik, K. V. K. R. K., Maneesha, K., Sadhuram, Y., Prasad, K. V. S. R., Ramana Murty, T. V., and Brahmananda Rao, V. (2014). East India Coastal Current induced eddies and their interaction with tropical storms over Bay of Bengal. *J. Operational Oceanogr.* 7, 58–68. doi:10.1080/1755876X.2014.11020153

Pattanayak, S., Mohanty, U. C., and Gopalakrishnan, S. G. (2012b). Simulation of very severe cyclone mala over Bay of bengal with HWRF modeling system. *Nat. Hazards* 63, 1413–1437. doi:10.1007/s11069-011-9863-z

Pattanayak, S., Mohanty, U. C., and Osuri, K. K. (2012a). Impact of parameterization of physical processes on simulation of track and intensity of tropical cyclone nargis (2008) with WRF-NMM model. *Sci. World J.*, 2012, 1–18. doi:10.1100/2012/671437

Pattanayak, S., and Mohanty, U. C. (2010). "Simulation of track and intensity of gonu and sidr with WRF-NMM modeling system," in *Indian Ocean tropical cyclones and climate change*. Editor Y. Charabi (Dordrecht, Netherlands: Springer Netherlands), 83–89. doi:10.1007/978-90-481-3109-9_12

Patwardhan, S. K., and Bhalme, H. N. (2001). A study of cyclonic disturbances over India and the adjacent ocean. *Int. J. Climatol.* 2, 527–534. doi:10.1002/joc.615

Prakash, K. R., and Pant, V. (2017). Upper oceanic response to tropical cyclone Phailin in the Bay of Bengal using a coupled atmosphere-ocean model. *Ocean. Dyn.* 67, 51–64. doi:10.1007/s10236-016-1020-5

Rajesh, P. V., Pattnaik, S., Mohanty, U. C., Rai, D., Baisya, H., and Pandey, P. C. (2017). Land surface sensitivity of monsoon depressions formed over Bay of Bengal using improved high-resolution land state. *Dyn. Atmos. Oceans* 80, 155–172. doi:10.1016/j.dynatmoce.2017.10.007

Raju, P. V. S., Potty, J., and Mohanty, U. C. (2011). Sensitivity of physical parameterizations on prediction of tropical cyclone Nargis over the Bay of Bengal using WRF model. *Meteorol. Atmos. Phys.* 113, 125–137. doi:10.1007/s00703-011-0151-y

Ranji, Z., Zarifsanayei, A. R., Cartwright, N., and Soltanpour, M. (2022). Climate change impacts on tropical cyclones of the Arabian Sea: Projections and uncertainty investigations. *Int. J. Climatol.* 1, 21. doi:10.1002/joc.7523

Richman, M. B., Leslie, L. M., Ramsay, H. A., and Klotzbach, P. J. (2017). Reducing tropical cyclone prediction errors using machine learning approaches. *Procedia Comput. Sci.* 114, 314–323. doi:10.1016/j.procs.2017.09.048

Sahoo, B., Bhaskaran, P. K., and Pradhan, A. K. (2019). Application of weather forecasting model WRF for operational electric power network management-a case study for Phailin cyclone. *Theor. Appl. Climatol.* 137, 871–891. doi:10.1007/s00704-018-2639-6

Sandeep, A., Prasad, V. S., and Johny, C. J. (2017). Quality and impact of Indian Doppler weather radar wind profiles: A diagnostic study. *Pure Appl. Geophys.* 174, 2847–2862. doi:10.1007/s00024-017-1544-8

Saxby, J., Crook, J., Peatman, S., Birch, C., Schwendike, J., Valdivieso da Costa, M., et al. (2021). Simulations of Bay of Bengal tropical cyclones in a regional convection-permitting atmosphere–ocean coupled model. Weather Clim. Dynam. Discuss. [preprint], in review, doi:10.5194/wcd-2021-46

Sharp, R. J., Bourassa, M. A., and Brien, J. J. O. (2002). Early detection of tropical cyclones using seawinds-derived vorticity. *Bull. Am. Meteorol. Soc.* 83, 879–889. doi:10.1175/1520-0477(2002)083<0879:edotcu>2.3.co;2

Sieglaff, J. M., Schmit, T. J., Menzel, W. P., and Ackerman, S. A. (2009). Inferring convective weather characteristics with geostationary high spectral resolution IR window measurements: A look into the future. *J. Atmos. Ocean. Technol.* 26, 1527–1541. doi:10.1175/2009jtecha1210.1

Singh, K. S., and Bhaskaran, P. K. (2020). Prediction of landfalling Bay of bengal cyclones during 2013 using the high-resolution weather research and forecasting model. *Meteorol. Appl.* 27. doi:10.1002/met.1850

Singh, R., Ojha, S. P., Kishtawal, C. M., and Pal, P. K. (2013). Quality assessment and assimilation of Megha-Tropiques SAPHIR radiances into WRF assimilation system. *J. Geophys. Res. Atmos.* 118, 6957–6969. doi:10.1002/jgrd.50502

Sriver, R. L. (2011). Man-made cyclones. *Nature* 479, 50–51. doi:10.1038/479050a

Tiwari, G., Kumar, S., Routray, A., Panda, J., and Jain, I. (2019). A high-resolution mesoscale model approach to reproduce super typhoon Maysak (2015) over northwestern Pacific ocean. *Earth Syst. Environ.* 3, 101–112. doi:10.1007/s41748-019-00086-0

Tiwari, G., Rameshan, A., Kumar, P., Javed, A., and Mishra, A. K. (2021). Understanding the post-monsoon tropical cyclone variability and trend over the Bay of Bengal during the satellite era. *Q. J. R. Meteorol. Soc.* 148, 1–14. doi:10.1002/qj.4189

Vinodhkumar, B., Busireddy, N. K. R., Ankur, K., Nadimpalli, R., and Osuri, K. K. (2022). On occurrence of rapid intensification and rainfall changes in tropical cyclones over the North Indian Ocean. *Int. J. Climatol.* 42, 714–726. doi:10.1002/joc.7268

Wang, B., Xu, S., and Wu, L. (2012). Intensified Arabian Sea tropical storms. *Nature* 489, E1–E2. doi:10.1038/nature11470

Wang, Y., Rao, Y., Tan, Z. M., and Schönemann, D. (2015). A statistical analysis of the effects of vertical wind shear on tropical cyclone intensity change over the western north pacific. *Mon. Weather Rev.* 143, 3434–3453. doi:10.1175/mwr-d-15-0049.1

Wang, Y., and Wu, C.-C. (2004). Current understanding of tropical cyclone structure and intensity changes? A review. *Meteorol. Atmos. Phys.* 87, 257–278. doi:10.1007/s00703-003-0055-6

Webster, P. J., Holland, G. J., Curry, J. A., and Chang, H.-R. (2005). Changes in tropical cyclone number, duration, and intensity in a warming environment. *Science* 309, 1844–1846. doi:10.1126/science.1116448

Yang, C., Liu, Z., Bresch, J., Rizvi, S. R., Huang, X. Y., and Min, J. (2016). AMSR2 all-sky radiance assimilation and its impact on the analysis and forecast of Hurricane Sandy with a limited-area data assimilation system. *Tellus A Dyn. Meteorology Oceanogr.* 68, 30917. doi:10.3402/tellusa.v68.30917

Zhu, Y., Liu, E., Mahajan, R., Thomas, C., Groff, D., Van Delst, P., et al. (2016). All-sky microwave radiance assimilation in NCEP's GSI analysis system. *Mon. Weather Rev.* 144, 4709–4735. doi:10.1175/mwr-d-15-0445.1

Zou, X., Weng, F., Zhang, B., Lin, L., Qin, Z., and Tallapragada, V. (2013). Impacts of assimilation of ATMS data in HWRF on track and intensity forecasts of 2012 four landfall hurricanes. *J. Geophys. Res. Atmos.* 118, 11–558. doi:10.1002/2013jd020405

Zupanski, M. (2013). "All-sky satellite radiance data assimilation: Methodology and challenges," in *Data assimilation for atmospheric, oceanic and hydrologic applications* (Berlin, Heidelberg: Springer), II, 465–488.

frontiers | Frontiers in Earth Science

TYPE Original Research
PUBLISHED 30 August 2022
DOI 10.3389/feart.2022.847317

OPEN ACCESS

EDITED BY
Sanjeev Kumar Jha,
Indian Institute of Science Education and Research, India

REVIEWED BY
Junqiang Yao,
China Meteorological Administration, China
Chenghai Wang,
Lanzhou University, China

*CORRESPONDENCE
Shuping Ma,
mashuping@mail.iap.ac.cn

SPECIALTY SECTION
This article was submitted to Atmospheric Science, a section of the journal Frontiers in Earth Science

RECEIVED 02 January 2022
ACCEPTED 01 August 2022
PUBLISHED 30 August 2022

CITATION
Cao J, Ma S and Ran L (2022), Comparative analysis of two flow decomposition approaches and their applications in diagnosing water vapor in extreme precipitation events over Xinjiang province, China.
Front. Earth Sci. 10:847317.
doi: 10.3389/feart.2022.847317

Comparative analysis of two flow decomposition approaches and their applications in diagnosing water vapor in extreme precipitation events over Xinjiang province, China

Jie Cao[1], Shuping Ma[2,3]* and Lingkun Ran[3]

[1]Key Laboratory of Meteorological Disaster, Ministry of Education and Collaborative Innovation Center on Forecast and Evaluation of Meteorological Disasters, Nanjing University of Information Science and Technology, Nanjing, China, [2]School of Geography and Planning, Ningxia University, Yinchuan, China, [3]Institute of Atmospheric Physics, Chinese Academy of Sciences, Beijing, China

Water vapor flux divergence under the terrain-following coordinate system is decomposed into slow and fast manifolds with the adoption of the Barnes filter method and the synoptic approach based on the Helmholtz theorem in this study. The performances and applications of both methods are evaluated in precipitating events over the Xinjiang province in China when traditional analysis fails to capture the evolutions of extreme precipitations caused by multi-scale systems and complicated terrains. A blizzard with a short duration under weak moisture environments and a persistent torrential rainfall event with abundant water vapor in the summer are selected as test examples for comparative analysis of the relationships between water vapor divergence and precipitation characteristics with the adoptions of both traditional synoptic diagnosis and two decomposition methods. It is found that divergent areas of the total water vapor flux divergence at the middle and high levels are blocked by false convergence at the low levels as the precipitation weakens in both cases, which leads to the failure of traditional synoptic diagnoses. Meanwhile, the two decomposition methods can provide superior indicators for extreme precipitation, especially before rainfall decreases or terminates. The synoptic approach performs better than the Barnes filter method as the latter sharply decreases in accuracy as the complexity of the flow fields and moisture conditions increase. Remedies for relieving this problem are proposed before being used for further applications.

KEYWORDS

extreme precipitation, flow decomposition, Helmholtz theorem, Barnes filter, moisture flux divergence

1 Introduction

The recently published IPCC AR6 report presents a full and systematic evaluation of extreme weather events. It shows that severe precipitation increases 7% in intensity when the temperature increases 1°. Furthermore, the variability of torrential rainfall events is studied and seen well-related to global climate warming in the form of non-linear processes (IPCC, 2021; Zhang et al., 2021). Compared to regions at the same latitudes, Central Asia is more sensitive to global climate change for its complicated terrains and unevenly distributed hydrological sources (Yin et al., 2014; Li et al., 2015; Hu et al., 2016; Jiang et al., 2020). Featuring in scarce precipitation, Central Asia is experiencing an increase in the occurrence of extreme rainfall and has been vulnerable to extreme precipitation in recent years (Deng et al., 2014; Huang et al., 2014, 2015; Hu et al., 2014, 2017; Malsy et al., 2015; Zhao et al., 2016; Zhang et al., 2017). Increased extreme precipitation may help solve the limited water availability problem, but introduce floods and secondary disasters (Knapp and Coauthrs., 2008) at the same time. Severe droughts and floods threaten human lives and constructions of the Silk Road Economic Belt. Xinjiang province, the key area of the Silk Road Economic Belt, has suffered 45 local rainstorms and floods every year in average for the past 10 years (Wang and Wang, 2021). Apart from complicated terrains and soil types, dominant weather systems of different scales are also responsible for the sudden and extreme precipitations in both summer and winter (Ma et al., 2021). Anomalous precipitation is directly related to the moisture supply and can be represented by water vapor transport which is well studied and widely used globally or over East Asia (Ding, 1994; Trenberth et al., 1995; Zhou and Yu, 2005; Gao et al., 2017, 2021; Qin et al., 2021). Hu et al. (2021) studied the water vapor transport of the summer half-year from 1979 to 2018, the results showed that water vapor from the North Atlantic Ocean, Europe, and the Mediterranean Sea contributes to northern Xinjiang's extreme precipitation, while water vapor from the Arabian Sea, the Arabian Peninsula, and the Indian Peninsula contribute to extreme precipitation over southern Xinjiang. By far, a detailed comprehension of the relationship between water vapor transport by different scales of motions and extreme precipitation over the Xinjiang province is deficient and should be an issue of considerable urgency.

Multi-scale flows coexist in the real atmosphere. In other words, real weather events can be seen as a combination of slow manifolds and fast ones from the perspective of phase space (Leith, 1980; Lorenz, 1980, 1986; Daley, 1991). Slow manifolds follow basic physical principles with high predictability, while fast ones contain randomness and thus are hard to forecast. However, the fast manifold motions and their interaction with slow ones are the direct reason for the initiation of most severe weather events. For climatic studies, the slow manifold covers systems of planetary scale and large-scale ones (Hasselmann, 1976). Most climate numerical models are constructed by eliminating fast manifolds which coexist as perturbations over the slow ones. For synoptic studies, the slow manifold serves as the background for the fast one which includes flows of sub-synoptic, mesoscale, and convective scales. There are three types of approaches to decompose slow and fast manifolds which are: the statistical method (Seager et al., 2010), synoptic analysis, and dynamic one. Barnes filter (Barnes, 1973) is a classical statistical method which has been broadly used in diagnosing typhoons, cyclones, and Meiyu fronts (Doswell, 1977; Gomis and Alonso, 1990; Xu et al., 2017; Xue et al., 2018; Zou et al., 2018; Ma et al., 2021), the mathematical procedure is direct and efficient, but the physical basis is not solid, especially for a specific case study. The synoptic analysis approach is based on the Helmholtz theorem by decomposing horizontal velocity into rotational and divergent flow components (Hawkins and Rosenthal, 1965; Dimego and Bosart, 1982; Ullah et al., 2020, 2021). The latter is the fast manifold which is directly linked to vertical motions and is responsible for severe weather. Applications of this physically solid method are wide in both atmospheric and oceanic motions. However, the accuracy and efficiency for mesoscale diagnosis in a limited domain limits this method in climatic or large-scale applications (Renfrew et al., 1997). Xu et al. (2011) designed an integral method with the adoption of Green's function for limited areas of arbitrary shapes. The dynamic analysis approach approximates primitive equations to different extents and can be divided into geostrophic and balanced types (Allen, 1991; Xu, 1992). This is the most solid physical approach but at the same time is extremely complicated for numerical computations. High resolution dataset outputs from mesoscale models add difficulties to the applications of the dynamic analysis approach.

The intensity of the net water vapor advection or water vapor flux divergence in the lower troposphere is the core factor to judge the precipitation intensity, which is also the key factor in the analysis and forecast of large-scale rainstorm (Sun, 2017), therefore, water vapor flux divergence is critical in a rainstorm, and many case studies have confirmed the effectiveness of its decomposed components (Zhou and Zhang., 2016; Ma et al., 2022; Wu et al., 2022). Ma et al. (2022) analyzed the decomposition of water vapor flux divergence and its application to a Blizzard event over Ili Valley in Central Asia from 30 Nov to 1 Dec, 2018. Cao et al. (2022b) analyzed the decomposed components' application to rainstorms caused by Typhoon Rumbia in 2018, and Wu et al. (2022) researched persistent extreme precipitation events in the post-flood season over Hainan Island from 16 to 18 Oct, 2020. The results of those cases showed that the decomposed water vapor flux divergence can better interpret which components play more important roles during extreme precipitation. This is useful for further applications in rainfall predictions. The main purpose of this study is to decompose water vapor flux divergence with the Barnes filter and synoptic methods in different precipitation events to see their performances when traditional analysis fails to identify the evolution of extreme

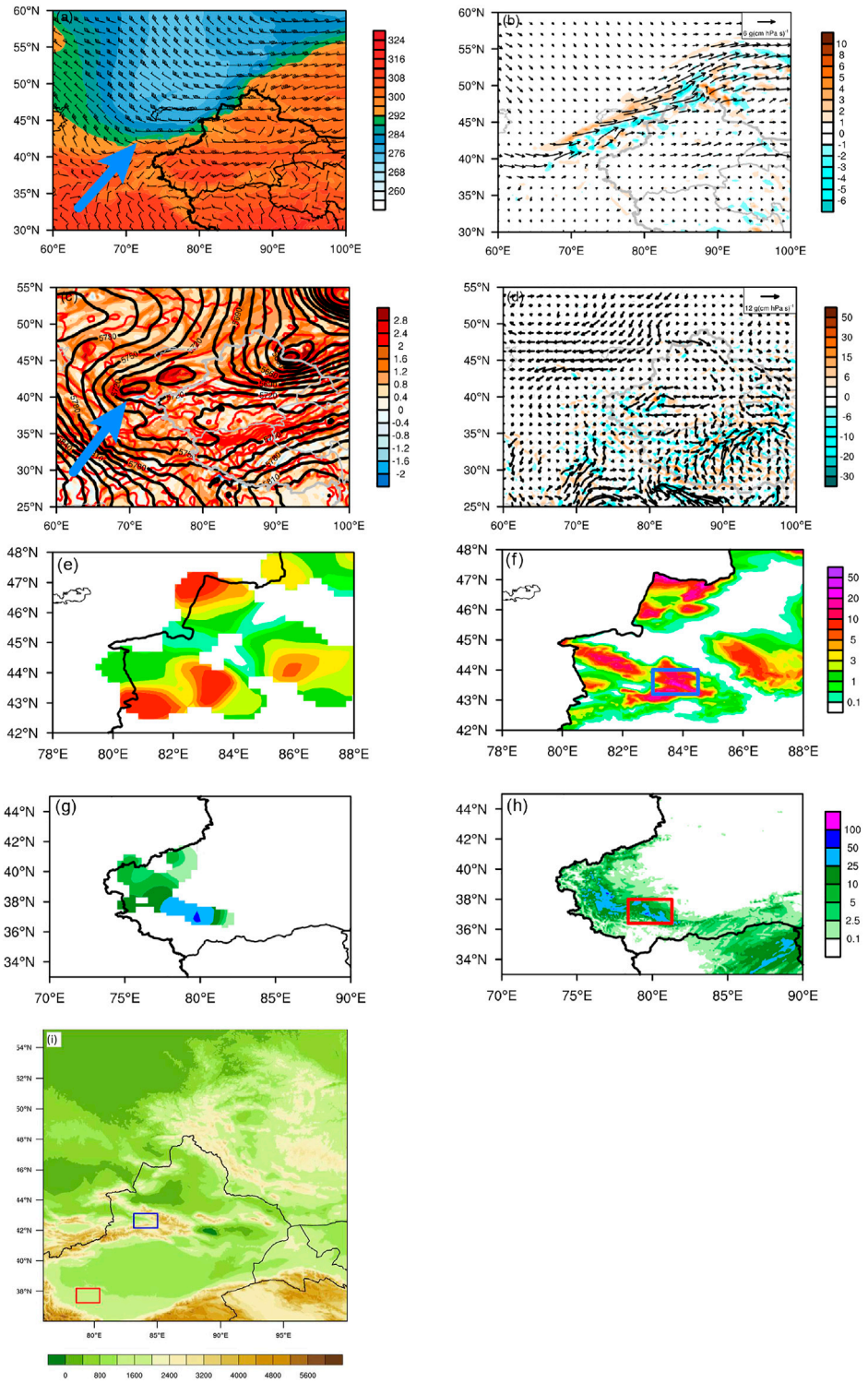

FIGURE 1
(A) Wind vector and equivalent temperature (shaded, units: (K) and **(B)** water vapor flux (vector, unit: g cm^{-1} hPa^{-1} s^{-1}) and its divergence (shaded, unit: 10^{-7} g cm^{-2} hPa^{-1} s^{-1}) at 700 hPa at 12 UTC 30 November 2018, **(C)** geopotential (solid contours, unit: gpm), temperature (dashed contours, unit: K), and relative vorticity (shaded, unit: 10^{-4} s^{-1}) at 500 hPa and **(D)** water vapor flux (vector, unit: g cm^{-1} hPa^{-1} s^{-1}) and its divergence (shaded, unit: 10^{-7} g cm^{-2} hPa^{-1} s^{-1}) at 850 hPa at 00UTC on 15 Jun, 2021. Twelve hour-accumulated observed rainfall **(E)** and simulated results **(F)** at 00UTC on 1 Dec, 2018. **(G)** and **(H)** are the same as (E) and (F) correspondingly except for at 00UTC on 16 June, 2021. Units are mm. **(I)** Terrain heights in the unit of m. The blue and red rectangular regions in Figures 1F,H are the target domains for the following analysis.

precipitations over the Xinjiang province. Quantitative comparisons of these two methods in two severe precipitations distinct in synoptic and hydrological backgrounds, terrain heights ranging from 500 m to 4,000 m, and durations are performed with the hope to seize useful information for severe precipitation forecasts from decomposed manifolds. The traditional synoptic analysis and numerical configurations for the two real cases are presented in Section 2, followed with brief derivations of these two decomposition approaches. In Section 3, the decomposed slow manifolds by the Barnes filter and synoptic methods are analyzed compared to the original water vapor flux divergence and to each other. Further decomposition of the moisture parameter is carried out with the hope to seize the dominant signal for precipitations. Conclusions and short discussions are presented in Section 4.

2 Methodology

2.1 Observational analysis

From 0000 UTC on November 30 to 0000 UTC on December 2, 2018, the passage of cold front over the Ili River Valley with complicated plains, mountains, and valleys (blue domain in Figure 1I) in northern Xinjiang triggered a blizzard of short duration. The Ili River Valley is under the control of the warm and humid southwest airflow in front of the trough at 700 hPa (Figure 1A). There is a weak west water vapor channel at 700 hPa (Figure 1B), which transports water vapor from Lake Balkhash to the Ili River Valley. However, the negative Q^{all} areas are small, and it is distributed alternately with the stronger divergence. Seen from the Q^{all} pattern, it is not favorable for severe precipitation in the near future.

From 0000 UTC on June 15 to 0000 UTC on June 15, 2021, a persistent torrential rainfall event occurs in the Hotan Region of southern Xinjiang with flat lands (red domain Figure 1I). The Central Asia vortex is the dominant large-scale system at 500 hPa (Figure 1C). The easterly and northerly water vapor channels transport moisture flux from the Arctic Ocean and the Siberian marshes to the southern Xinjiang basin through the gap between the Altay Mountains and the Tianshan Mountains and it is blocked by the Kunlun Mountains in the south. There is visible Q^{all} in the Hotan area (Figure 1D). Abundant moisture exists in this summer case, but negative Q^{all} centers are not closely correlated to rainfall belts.

In a short conclusion, the winter case is characterized with a cold front and weak moisture flux, while the summer case is with the Central Asia vortex and abundant moisture.

2.2 Modeling system and configuration

Numerical simulations for the two events are performed by using the Weather Research and Forecasting modeling system (Skamarock et al., 2008). The background field and lateral boundary conditions of the rainfall process are the European Centre for Medium-Range Weather Forecasts (ECMWF) ERA5 hourly data with the horizontal resolution of 0.25°×0.25°. Physical parameterization schemes adopted in the two simulations are described in Table 1. Seen from the similarity of the pattern and intensity of the precipitation in both cases in Figures 1E–H, the two simulations reproduced the two events well. Validity of the other parameters are performed and described in our previous study (Ma et al., 2021).

2.3 Flow decomposition approaches

2.3.1 Barnes filter

The Barnes band-pass filter is constructed on the basis of the Barnes objective analysis scheme (Maddox, 1980) and is used to smooth parameters such as geopotential height and wind fields (Xu et al., 2017; Xue et al., 2018). First, each grid point is assigned a first-guess value

$$A_G(i,j) = \sum_{k=1}^{k=N} w_k A_k \Big/ \sum_{k=1}^{k=N} w_k \tag{1.1}$$

where $w_k = \exp(-r_k^2/4c)$ is the weight function, r_k is the distance between the station kth and the grid (i, j) and c is a prescribed constant. Second, the first-guess field is corrected according to

$$A(i,j) = A_G(i,j) + \sum_{k=1}^{k=N} w_k' E_n \Big/ \sum_{k=1}^{k=N} w_n' \tag{1.2}$$

where $E_k = A_k - A_{Gk}$ is the difference (or error) between the observation and first-guess field at the station kth and $w_n' = \exp(-r_k^2/4c\lambda)$ with $0 < \lambda < 1$.

The horizontal velocity field $\mathbf{v}$ and specific humidity q can thus be partitioned into mean and disturbed components, respectively, expressed in Eqs. 1.3, 1.4. Selecting filter parameters $c_1 = 270$, $c_2 = 400$, $g_1 = 0.3$, $g_2 = 0.4$ in the winter case, the reciprocal of the maximum response difference r is 3.6, the filter parameters $c_1 = 310$, $c_2 = 840$, $g_1 = 0.3$, $g_2 = 0.4$ are selected in the summer case, and the maximum response difference reciprocal r is 1.95. The response functions for the summer and winter cases are calculated and depicted in Figure 2.

$$\mathbf{v} = \bar{\mathbf{v}} + \mathbf{v}' \tag{1.3}$$

$$q = \bar{q} + q' \tag{1.4}$$

2.3.2 Synoptic decomposition method based on the Helmholtz theorem

According the Helmholtz theorem, a horizontal velocity field $\mathbf{v}$ can be partitioned into rotational and divergent components represented by stream function ψ and velocity potential χ, respectively, as follows:

TABLE 1 Model scheme settings.

Physical scheme	Winter snowfall event	Summer rainfall event
cloud microphysics scheme	Thompson (Thompson et al., 2004)	WRF Single-Moment 6-class scheme (Hong and Lim, 2006)
longwave and shortwave radiation scheme	RRTMG, RRTMG (Iacono et al., 2008)	RRTMG, RRTMG (Iacono et al., 2008)
planetary boundary layer scheme	Yonsei University scheme (Hong et al., 2006)	Yonsei University scheme (Hong et al., 2006)
surface layer scheme	Mellor-Yamada-Janjic (Eta) TKE scheme (Janjić, 1994)	MM5 similarity (Jiménez et al., 2012)
land-surface processes	Noah Land Surface Model (Chen and Dudhia, 2001)	Noah Land Surface Model (Chen and Dudhia, 2001)

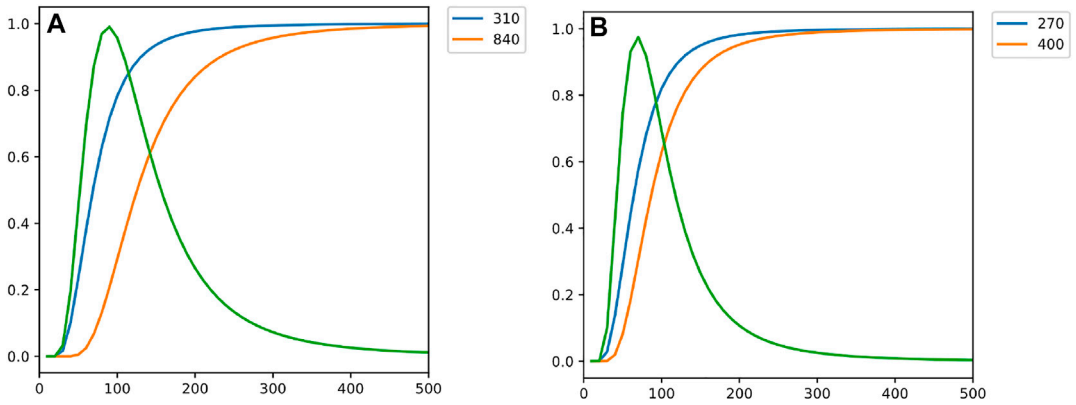

FIGURE 2
The band-pass filter response functions of **(A)** rainfall in 2021 and **(B)** snowstorm in 2018. The orange line and blue line are for the low-pass filters used to define te bandpass filter represented by the green line, the numbers in the upper right corner of the figure represent filter parameters.

$$\mathbf{v} = \mathbf{v_r} + \mathbf{v_d} \tag{2.1}$$

$$\mathbf{v_r} = \mathbf{k} \times \nabla\psi \tag{2.2}$$

$$\mathbf{v_d} = \nabla\chi, \tag{2.3}$$

where $\mathbf{k}$ is the unit vector in the vertical direction and ∇ is the horizontal gradient operator. There are analytical solutions for Eqs. 2.1, 2.2, 2.3 in unlimited domains or global situations. But for the limited domain, the accurate solutions are thoroughly studied for decades (Sangster, 1960; Lynch, 1989; Chen and Kuo, 1992a, 1992b; Xu et al., 2011). Recently a hybrid method is designed and applied for computing the stream function and velocity potential for complex flow fields over mesoscale domains (Cao et al., 2022a), and it is adopted in the following calculation.

2.3.3 Decomposition of water vapor flux divergence

Water vapor flux divergence under the terrain-following coordinate system (denoted by Q^{all}), and its three components: flow divergence, moisture convection term by non-divergent or slow manifold, and moisture convection term by divergent or fast manifold (denoted as Q^{div}, Q^{S}, and Q^{F}, respectively) are re-derived as:

$$\begin{aligned} Q^{all} &= \nabla\cdot(q\mathbf{v})\big|_p = (\partial_x qu)\big|_p + (\partial_y qv)\big|_\eta - \left[(\partial_p qu)(\partial_x p)\big|_\eta \right. \\ &\quad \left. + (\partial_p qv)(\partial_y p)\big|_\eta\right] \end{aligned} \tag{3.1}$$

$$\begin{aligned} Q^{div} &= (q\nabla\cdot\mathbf{v})\big|_p = q\partial_x u\big|_\eta + q\partial_y v|\eta - q\left[(\partial_p u)(\partial_x p)\big|_\eta \right. \\ &\quad \left. + (\partial_p v)(\partial_y p)\big|_\eta\right] \end{aligned} \tag{3.2}$$

$$\begin{aligned} Q^{S} &= (\mathbf{v}^S\cdot\nabla q)\big|_\eta \\ &= u^S\partial_x q\big|_\eta + v^S\partial_y q\big|_\eta - u^S(\partial_p q)(\partial_x p)\big|_\eta - v^S(\partial_p q)(\partial_y p)\big|_\eta \end{aligned} \tag{3.3}$$

$$\begin{aligned} Q^{F} &= (\mathbf{v}^F\cdot\nabla q)\big|_p \\ &= u^F\partial_x q\big|_\eta + v^F\partial_y q\big|_\eta - u^F(\partial_p q)(\partial_x p)\big|_\eta - v^F(\partial_p q)(\partial_y p)\big|_\eta \end{aligned} \tag{3.4}$$

Here, $\mathbf{v} \equiv (u, v)$ is the horizontal velocity field, q is specific humidity, with S denoting slow manifold, F denoting fast manifold in the superscript, x, y, and p denoting the partial derivatives in the x, y, and p directions, respectively, and subscript η denoting the terrain-following coordinate system. The subscript B in Q_B^S and Q_B^F represents the Barnes filter, H in Q_H^S and Q_H^F represents synoptic decomposition based on the Helmholtz theorem. The following chain rules (Gerrity, 1972) are used in the aforementioned derivation:

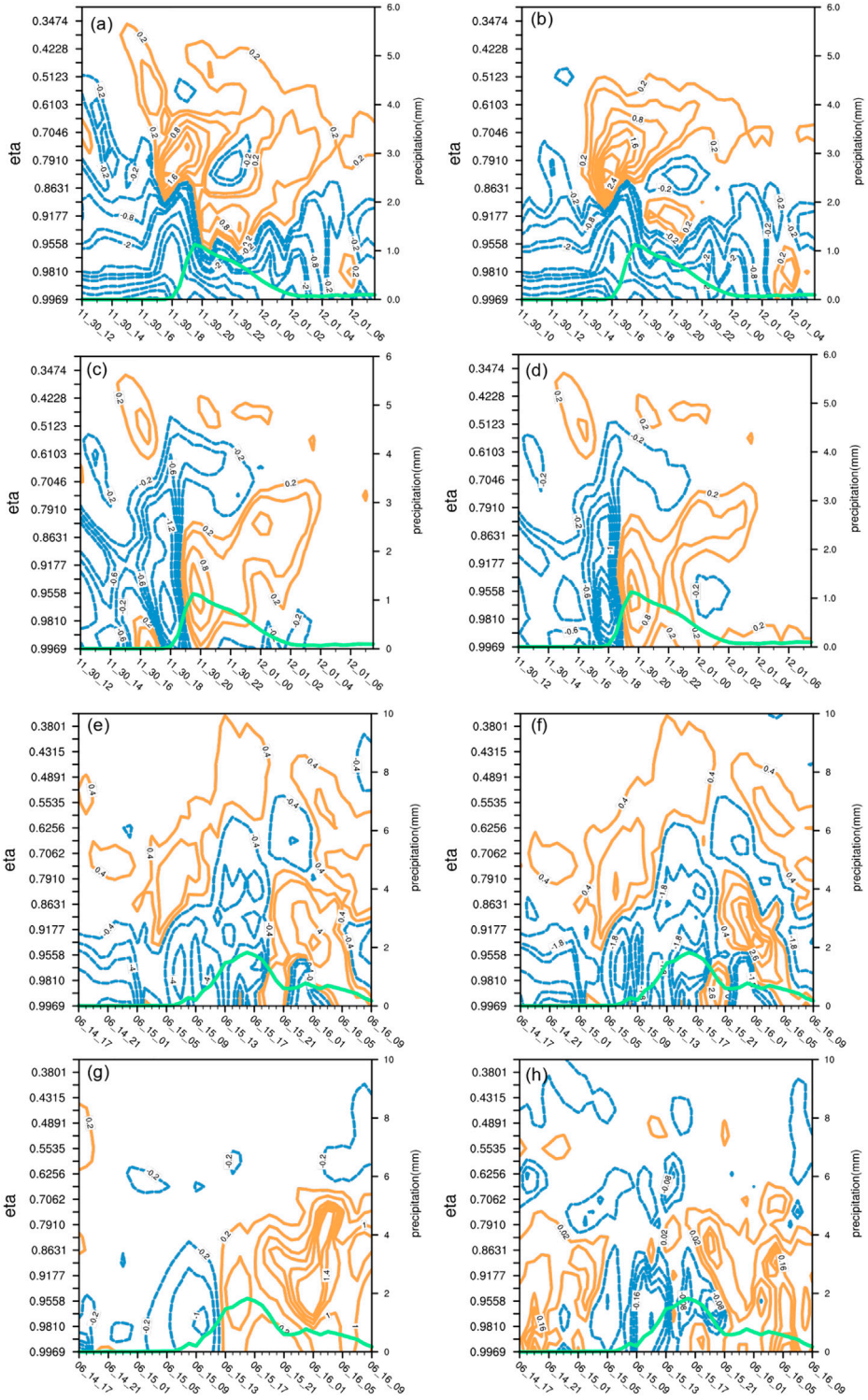

FIGURE 3
Domain averaged **(A)** Q^{all}, **(B)** Q^{div}, **(C)** Q_B^S and **(D)** Q_H^S in the unit of 10−7 g cm−2 hPa−1 s−1 in the winter case from 1200UTC 30 November to 0730 UTC 1 December with the target domain marked by a blue rectangular region in Figure 1F. **(E–H)** are the same except for the summer case from 1700UTC 14 to 0900UTC 16 June with the target domain marked by a red rectangular region in Figure 1H. The green curves represent the 30-min accumulated precipitation (right y-axis, units: mm).

$$\partial_p A = \left(\partial_\eta A\right)\left(\partial_p \eta\right) \tag{3.5}$$

$$\left(\partial_s A\right)\big|_\eta = \left(\partial_s A\right)\big|_p + \left(\partial_p A\right)\left(\partial_s p\right)\big|_\eta \tag{3.6}$$

Here, A represents any variable. The subscript *s* represents the horizontal direction (x or y).

3 Moisture flux divergence analysis

Q^{div} shares similar quantities and evolving patterns with Q^{all} at all levels. However, neither of them presents divergent signals before the precipitation weakens. In winter snowstorms of short durations, the divergence regions at the middle levels seen in Q^{all} (Figure 3A) are blocked by large convergence at the middle and low levels (Figure 3B). In the summer case with persistent rainfall, divergent signals presented by Q^{all} (Figure 3E) show up after the precipitation reaches its maximum, and the divergence is weaker in Q^{div} (Figure 3F). Large convergent regions in Q^{all} and Q^{div} are also blocked at the middle levels as rainfall ends. Therefore, though occupying the largest magnitude in Q^{all}, Q^{div} fails to identify the weakening or ceasing of precipitation in both torrential events.

In both winter and summer events presented in Figure 3, Q^{div} (Figures 3B,F) shares the evolving patterns as Q^{all} (Figures 3A,E) at all levels with dominant quantities compared to the other two components. However, neither of them in both events discloses the divergent signals before precipitation weakens, as shown by the green curves. To be specific, the large divergent regions of Q^{all} (Figure 3A) after 20 UTC Nov. 30 above the middle levels are blocked by large convergent areas at lower levels which have resulted from negative values in Q^{div} (Figure 3B). Meanwhile, the convergent signals presented by Q^{all} (Figure 3E) and Q^{div} (Figure 3F) still occupy low and middle levels over the target domain for around 6 h after the precipitation reaches its maximum. Furthermore, as the rainfall ends, there is still large convergent Q^{div} transporting downward which contradicts with the precipitating characteristics. Therefore, though occupying the largest magnitude in Q^{all}, Q^{div} fails to identify the weakening or ceasing of precipitation in both torrential events.

Q_B^S in both events (Figures 3C,G) present strong convergence as precipitation increases, and abruptly change to divergence before precipitation weakens. Q_H^S (Figures 3D,H) performs slightly better compared to Q_B^S (Figures 3C,G) in both the winter event with uniform divergence at lower levels since 20 UTC Nov. 30, and the summer event with small convergent areas before rainfall increases since 21 UTC June 15. As a short conclusion, the decomposed Q^S by both the Barnes filter and synoptic methods are useful for depicting the precipitating evolutions during the winter and summer events, while the latter performs better.

However, the accuracy between the reconstructed velocity and the initial one in winter is much lower than the summer case mainly due to the fact that the wind field is more complicated in the short duration snowstorm. The deviations of the reconstructed zonal and meridional wind component by the synoptic method and Barnes filter to their corresponding initial one over the target domain are investigated. In the winter, meridional differences by the synoptic method (Figure 4A) keep a uniform vertical distribution with a small magnitude of the same order as in the summer, while those by the Barnes filter (Figure 4B) are tremendously amplified with maximum centers after a snowstorm. Zonal differences by the synoptic method (Figure 4C) show a uniform distribution vertically, while those by the Barnes filter (Figure 4D) with the same magnitude but increase evidently as the rainfall intensifies in the summer. The power spectral density of the vertical velocity in the summer event (Figure 4F) is evidently less complicated than that in the winter (Figure 4E) event. Therefore, the capability for accurately reconstructing the complex flow field may be a reason for the better performance of the synoptic method over the Barnes filter in both summer and winter events.

Another possible reason for the worse situation by the Barnes filter in the winter event may due to the less abundance but more variable moisture. The moisture is thus decomposed by the Barnes filter with the same response function in Figure 1B to further decompose q into slow and fast manifold components as follows:

$$q = q^{\mathrm{m}} + \mathrm{q}' \tag{4.1}$$

Substituting Eq. 4.1 into Eq. 3.3 leads to:

$$Q_B^S = \left(\mathbf{v}^S \cdot \nabla q\right)_B = Q_B^{Sm} + Q_B^{Sd} + Q_B^{Fm}$$

$$Q_B^{Sm} = u^S \partial_x q^m\big|_\eta + v^S \partial_y q^m\big|_\eta - u^S\left(\partial_p q^m\right)\left(\partial_x p\right)\big|_\eta - v^S\left(\partial_p q^m\right)\left(\partial_y p\right)\big|_\eta$$

$$Q_B^{Sd} = u^S \partial_x q^d\big|_\eta + v^S \partial_y q^d\big|_\eta - u^S\left(\partial_p q^d\right)\left(\partial_x p\right)\big|_\eta - v^S\left(\partial_p q^d\right)\left(\partial_y p\right)\big|_\eta$$

$$Q_B^{Fm} = u^F \partial_x q^m\big|_\eta + v^F \partial_y q^m\big|_\eta - u^F\left(\partial_p q^m\right)\left(\partial_x p\right)\big|_\eta - v^F\left(\partial_p q^m\right)\left(\partial_y p\right)\big|_\eta$$

Here, the subscript B denotes the Barnes filter, the superscript m denotes mean, and d denotes disturbance. Q_B^S is the moisture convection term by non-divergent or slow manifold based on the Barnes filter, Q_B^{Sm} is the mean component of the moisture convection term by non-divergent or slow manifold based on the Barnes filter, Q_B^{Sd} is the disturbed component of the moisture convection term by non-divergent or slow manifold based on the Barnes filter, Q_B^{Fm} is the mean component of the moisture convection term by divergent or fast manifold based on the Barnes filter.

Compared to the weak convergence in Q_B^S (Figure 3C) when a snowstorm weakens, the decomposed mean component of Q_B^{Sm} (Figure 5A) keeps uniform divergence as precipitation ceases. It can be seen from Q_B^{Sd} (Figure 5B) that the false convergence signal is resulted from *q*'. This can

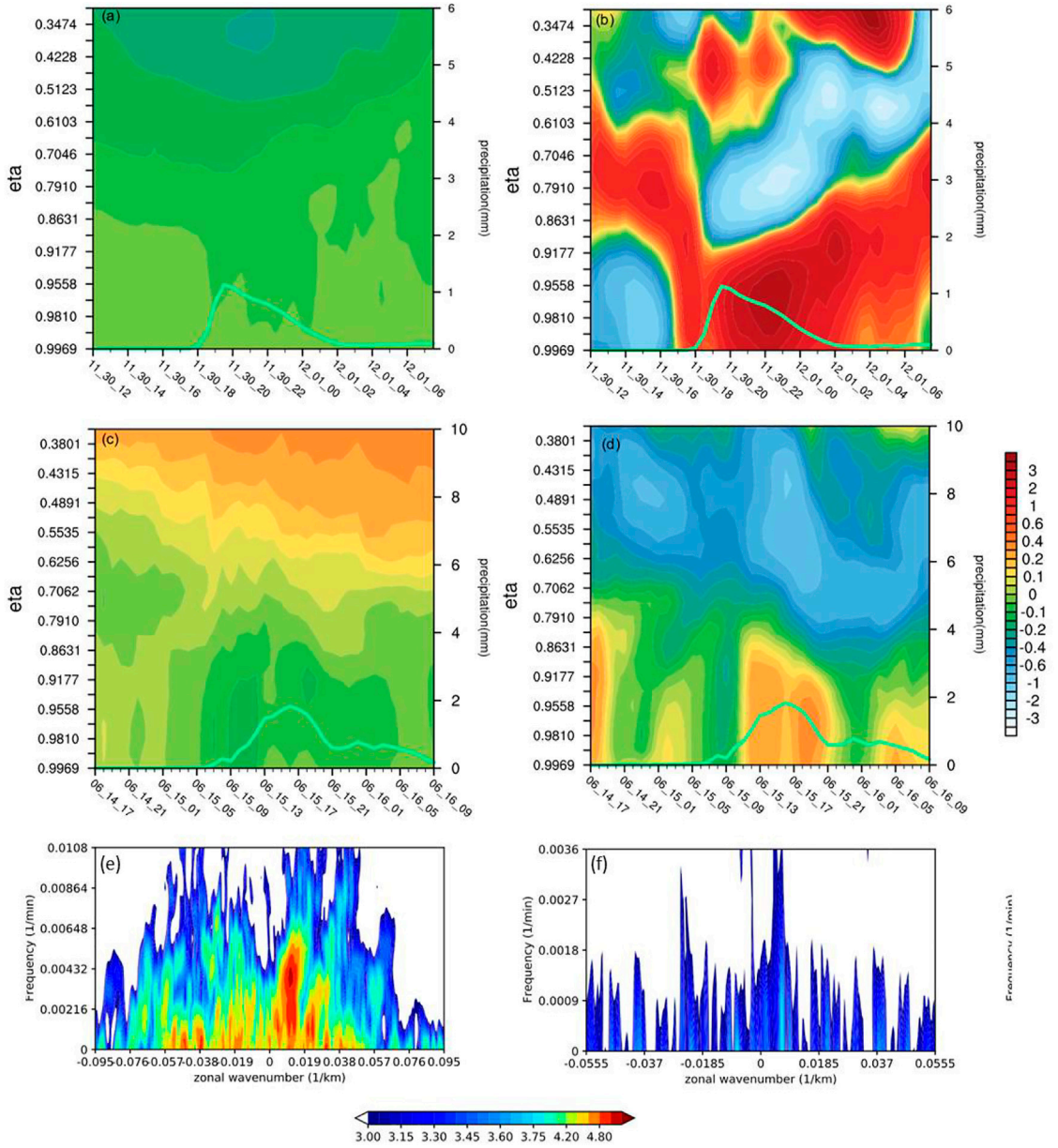

FIGURE 4
Domain averaged meridional wind residual by using **(A)** the synoptic method, **(B)** the Barnes filter in winter case, zonal wind residual by using **(C)** the synoptic method, and **(D)** the Barnes filter in summer case. The target domains are marked by blue and red rectangular regions in Figures 1F,H, respectively. Unit is m s^{-1}. Power spectral density of the vertical velocity at the height of 12 km **(E)** along 44.5°N in the winter case, and **(F)** 37.2°N in the summer case. Unit is $m^2 \cdot s^{-2}$.

be seen vividly in the distributions of q (Figure 5E) and its decomposed components (Figures 5F,G). However, both Q_B^{Sm} and Q_B^{Sd} in the summer event remain uniformly divergent as precipitation ceases and convergent as it increases, as shown in Figures 5C,D with q and its components keeping the same signals (Figs. omitted). This proves the necessity of further decomposing q especially for the winter event with complicated flow patterns.

4 Conclusion and discussions

In the research of extreme precipitation climate events, the method of decomposing the influence of water vapor flux divergence (Q^{all}) into climatic and large-scale systems has been mature. For extreme precipitation weather events, similar ideas are adopted to separate the influence of synoptic and sub-synoptic scale weather systems represented by slow and fast

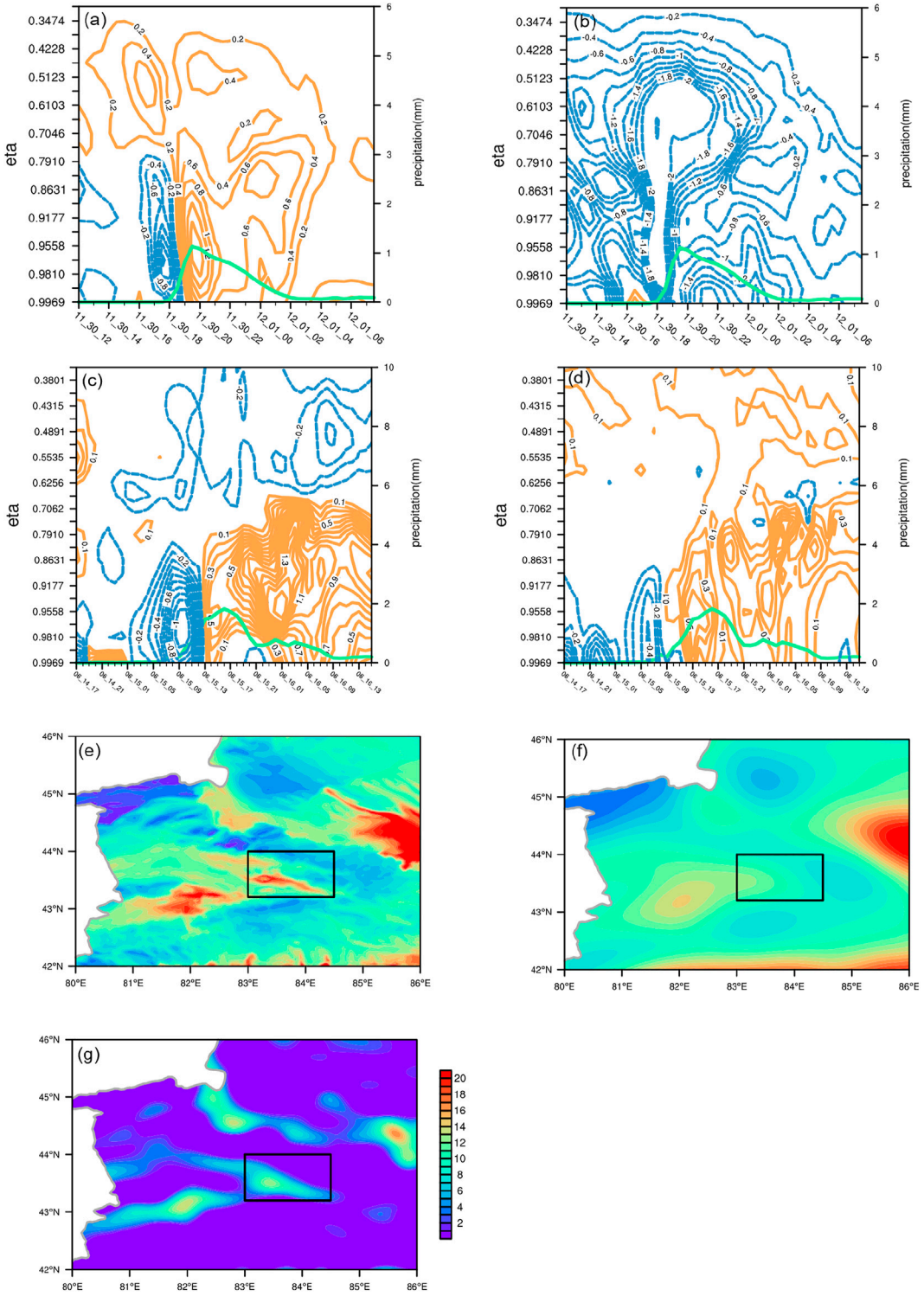

FIGURE 5
Domain averaged **(A)** Q_B^{Sm}, **(B)** Q_B^{Sd} in the unit of 10^{-7} g cm^{-2} hPa^{-1} s^{-1}, **(E)** q, **(F)** q^m, and **(G)** q' at η=0.9558 (shaded, unit: 10^{-4} kg kg^{-1}) at 2330 UTC on 30 Nov in winter case. Domain averaged **(C)** Q_H^{Sm}, **(D)** Q_H^{Sd} in the unit of 10^{-7} g cm^{-2} hPa^{-1} s^{-1} in summer case.

manifolds, respectively, in this study with the purpose to better forecast precipitation.

The statistical Barnes filter method and the synoptic decomposition approach are adopted by dividing Q^{all} under the terrain-following coordinate system into three components, i.e., Q^{div}, Q^{S}, and Q^{F}. These components represent flow divergence, moisture convection term by slow and fast manifolds. A blizzard process with a short duration and weak moisture and a persistent rainstorm event with abundant water vapor are investigated with both traditional synoptic analysis and decomposition methods. The main results are as follows:

(1) Q^{div}, which is directly related to the convergence and divergence of the large-scale velocity field, always occupies the biggest magnitude in Q^{all}. During the periods of intensification and weakening of extreme precipitation events, Q^{all} at the middle and lower levels converges which contradicts to the ceasing of the precipitation. Vertical distributions that show the divergent signals of mid-to-high-level Q^{all} are blocked at the middle and high levels.
(2) Although Q^{S}, which represents specific humidity transportation by large-scale motions, only accounts for 10% in Q^{all}, visible divergent regions at the middle and low levels can be seen before precipitation weakens.
(3) In the persistent rainfall event, Q^{S} obtained by the Barnes filter and synoptic method show similar temporal and spatial evolutions better than Q^{all}. In the short-term snowfall event, Q^{S} obtained by the Barnes filter presents a false convergence signal when the snow is about to end. There are two possible reasons for this deficiency. One is the evident low accuracy of reconstructed flow field by the Barnes filter which may be caused by the complexity of the original velocity field. The other reason is the increased discrete error introduced by differentiating weak moisture. By further decomposing specific humidity into its mean and disturbance components, the latter problem is partially relived.

The two decomposition methods can provide superior indicators for the prediction of extreme precipitation weather events, especially the decrease and termination of precipitation. However, the accuracy of the Barnes filter method is more related to the complexity of flow fields as well as the moisture conditions. In the future, this research will combine these two scale decomposition methods with high-resolution numerical models, and carry out research on other material transport and aggregation such as dust in other parts of the earth.

Data availability statement

The raw data supporting the conclusions of this article will be made available by the authors, without undue reservation.

Author contributions

The JC and SM analyzed and wrote the article, and the LR is responsible for the simulation of extreme precipitation cases.

Funding

This work was supported by the National Natural Science Foundation of China Grants 91937301 and 41875074, the Second Tibetan Plateau Comprehensive Scientific Expedition 2019QZKK0104, the Startup Foundation for Introducing Talent of NUIST 2022r004, and the National Key Scientific and Technological Infrastructure Project “EarthLab”.

Acknowledgments

The authors are thankful to the anonymous reviewers for their comments and suggestions on the original manuscript that improved the structures and presentations of the results. The authors are thankful to Drs. Xin XU and Shaofeng HUA for providing the codes of the Barnes filter. The computing for this project was performed at the Supercomputing Center for Education and Research at the University of Oklahoma (OU), United States.

Conflict of interest

The authors declare that the research was conducted in the absence of any commercial or financial relationships that could be construed as a potential conflict of interest.

Publisher’s note

References

Allen, J. (1991). Balanced equations based on momentum equations with global invariants of potential enstrophy and energy. *J. Phys. Oceanogr.* 21, 265–276. doi:10.1175/1520-0485(1991)021<0265

Barnes, S. (1973). Mesoscale objective map analysis using weighted time series observations. *NOAA Tech. Memo. ERL NSSL-* 62, 60.

Cao, J., Xu, Q., Ma, S., and Chen, H. (2022a). Hybrid methods for computing streamfunction and velocity potential for complex flow fields over mesoscale domains. *Adv. Atmos. Sci.* 39, 1417–1431. doi:10.1007/s00376-021-1280-y

Cao, J., Zhou, G., Liu, L., Zhao, W., and Yan, Y. (2022b). Kinetic energy budget analyses among different quadrants during typhoon recurvature: A case study of Typhoon Rumbia (2018). *Atmos. Res.* 278, 106319. doi:10.1016/j.atmosres.2022.106319

Chen, F., and Dudhia, J. (2001). Coupling an advanced land-surface/hydrology model with the Penn State/NCAR MM5 modeling system. Part I: Model description and implementation. *Mon. Wea. Rev.* 129, 569–585. doi:10.1175/1520-0493(2001)129%3C0569

Chen, Q., and Kuo, Y. (1992b). A consistency condition for wind-field reconstruction in a limited area and a harmonic-cosine series expansion. *Mon. Wea. Rev.* 120, 2653–2670. doi:10.1175/1520-0493(1992)120<2653:ACCFWF>2.0.CO;2

Chen, Q., and Kuo, Y. (1992a). A harmonic-sine series expansion and its application to the partitioning and reconstruction problem in a limited area. *Mon. Wea. Rev.* 120, 91–112. doi:10.1175/1520-0493

Daley, R. (1991). *Atmospheric data analysis*. Cambridge: Cambridge University Press, 457.

Deng, H., Chen, Y., Shi, X., Li, W., Wang, H., Zhang, S., et al. (2014). Dynamics of temperature and precipitation extremes and their spatial variation in the arid region of northwest China. *Atmos. Res.* 138, 346–355. doi:10.1016/j.atmosres.2013.12.001

Dimego, G., and Bosart, L. (1982). The transformation of tropical storms Agnes into an extratropical cyclone, Part I: The observed fields and vertical motion computations. *Mon. Wea. Rev.* 110, 385–411. doi:10.1175/1520-0493

Ding, Y. H. (1994). *Monsoons over China*. New York: Springer, 90.

Doswell, C. (1977). Obtaining meteorologically significant surface divergence fields through the filtering property of objective analysis. *Mon. Wea. Rev.* 105, 885–892. doi:10.1175/1520-0493

Gao, S., Mao, J., Zhang, W., Zhang, F., and Shen, X. (2021). Atmospheric moisture shapes increasing tropical cyclone precipitation in southern China over the past four decades. *Environ. Res. Lett.* 16, 034004. doi:10.1088/1748-9326/abd78a

Gao, S., Zhai, S., Chen, B., and Li, T. (2017). Water budget and intensity change of tropical cyclones over the western North pacific. *Mon. Weather Rev.* 145, 3009–3023. doi:10.1175/mwr-d-17-0033.1

Gerrity, J. (1972). The potential vorticity theorem in general s-coordinates. *Natl. Meteorol. Cent. Off. Note* 76, 5.

Gomis, D., and Alonso, S. (1990). Diagnosis of a cyclogenetic event in the western Mediterranean using an objective technique for scale separation. *Mon. Wea. Rev.* 118, 723–736. doi:10.1175/1520-0493(1990)118<0723:DOACEI>2.0

Hasselmann, K. (1976). Stochastic climate models, Part I: Theory. *Tellus* 28, 473–485. doi:10.1111/j.2153-3490.1976.tb00696.x

Hawkins, H. F., and Rosenthal, S. L. (1965). On the computation of stream functions from the wind field. *Mon. Wea. Rev.* 93, 245–252. doi:10.1175/1520-0493(1965)093<0245:OTCOSF>2.3

Hong, S. Y., and Lim, J. O. J. (2006). The WRF single-moment 6-class microphysics scheme (WSM6). *J. Korean Meteor. Soc.* 42, 129–151.

Hong, S. Y., Noh, Y., and Dudhia, J. (2006). A new vertical diffusion package with an explicit treatment of entrainment processes. *Mon. Weather Rev.* 134, 2318–2341. doi:10.1175/MWR3199.1

Hu, Q., Zhao, Y., Huang, A. N., Ma, P., and Ming, J. (2021). Moisture transport and sources of the extreme precipitation over northern and southern Xinjiang in the summer half-year during 1979–2018. *Front. Earth Sci.* 9, 770877. doi:10.3389/feart.2021.770877

Hu, Z., Li, Q., Chen, X., Teng, Z., Chen, C., Yin, G., et al. (2016). Climate changes in temperature and precipitation extremes in an alpine grassland of central Asia. *Theor. Appl. Climatol.* 126, 519–531. doi:10.1007/s00704-015-1568-x

Hu, Z., Zhang, C., Hu, Q., and Tian, H. (2014). Temperature changes in central Asia from 1979 to 2011 based on multiple datasets. *J. Clim.* 27, 1143–1167. doi:10.1175/JCLI-D-13-00064.1

Hu, Z., Zhou, Q., Chen, X., Qian, C., Wang, S., and Li, J. (2017). Variations and changes of annual precipitation in central Asia over the last century. *Int. J. Climatol.* 37, 157–170. doi:10.1002/joc.4988

Huang, A., Zhou, Y., Zhang, Y., Huang, D., Zhao, Y., and Wu, H. (2014). Changes of the annual precipitation over central Asia in the twenty-first century projected by multimodels of CMIP5. *J. Clim.* 27, 6627–6646. doi:10.1175/JCLI-D-14-00070.1

Huang, W., Feng, S., Chen, J., and Chen, F. (2015). Physical mechanisms of summer precipitation variations in the Tarim Basin in northwestern China. *J. Clim.* 28, 3579–3591. doi:10.1175/JCLI-D-14-00395.1

Iacono, M., Delamere, J. S., Mlawer, E. J., Shephard, M. W., Clough, S. A., and Collins, W. D. (2008). Radiative forcing by long-lived green-house gases: Calculations with the AER radiative transfer models. *J. Geophys. Res.* 113, D13103. doi:10.1029/2008JD009944

IPCC (2021). *Climate change 2021 the physical science basis*. available at: https://www.ipcc.ch/report/ar6/wg1/downloads/report/IPCC_AR6_WGI_Full_Report.pdf.

Janjić, Z. I. (1994). The step-mountain eta coordinate model: Further developments of the convection, viscous sublayer, and turbulence closure schemes. *Mon. Wea. Rev.* 122, 927–945. doi:10.1175/1520-0493(1994)122<0927:TSMECM>2.0

Jiang, J., Zhou, T., Chen, X., and Zhang, L. (2020). Future changes in precipitation over central Asia based on CMIP6 projections. *Environ. Res. Lett.* 15, 054009. doi:10.1088/1748-9326/ab7d03

Jiménez, P. A., Dudhia, J., González-Rouco, J. F., Navarro, J., Montávez, J. P., and García-Bustamante, E. (2012). A revised scheme for the WRF surface layer formulation. *Mon. Weather Rev.* 140, 898–918. doi:10.1175/MWR-D-11-00056.1

Knapp, A. K., Beier, C., Briske, D. D., Classen, A. T., Luo, Y., Reichstein, M., et al. (2008). Consequences of more extreme precipitation regimes for terrestrial ecosystems. *BioScience* 58, 811–821. doi:10.1641/B580908

Leith, C. (1980). Nonlinear normal mode initialization and quasi-geostrophic theory. *J. Atmos. Sci.* 37, 958–968. doi:10.1175/1520-0469(1980)037<0958:NNMIAQ>2.0

Li, Z., Chen, Y., Li, W., Deng, H., and Fang, G. (2015). Potential impacts of climate change on vegetation dynamics in central Asia. *J. Geophys. Res. Atmos.* 120, 12345–12356. doi:10.1002/2015JD023618

Lorenz, E. (1980). Attractor sets and quasi-geostrophic equilibrium. *J. Atmos. Sci.* 37, 1685–1699. doi:10.1175/1520-0469(1980)037<1685

Lorenz, E. (1986). On the existence of a slow manifold. *J. Atmos. Sci.* 43, 1547–1558. doi:10.1175/1520-0469(1986)043<1547

Lynch, P. (1989). Partitioning the wind in a limited domain. *Mon. Wea. Rev.* 117, 1492–1500. doi:10.1175/1520-0493(1989)117<1492

Ma, Q. R., Zhang, J., Ma, Y. J., Game, A. T., Chen, Z. H., Chang, Y., et al. (2021). How do multiscale interactions affect extreme precipitation in eastern central Asia? *J. Clim.* 34, 7475–7491. doi:10.1175/JCLI-D-20-0763.1

Ma, S. P., Cao, J., Zhao, H. J., Zhou, X., and Ran, L. K. (2022). Decomposition of water vapor flux divergence and its application to a blizzard event over Ili Valley in Central Asia during 30 Nov to 1 Dec 2018. *Atmos. Res.* 270, 106079. doi:10.1016/j.atmosres.2022.106079

Maddox, R. A. (1980). An objective technique for separating macroscale and mesoscale features in meteorological data. *Mon. Wea. Rev.* 108, 1108–1121. doi:10.1175/1520-0493(1980)108<1108

Malsy, M., Beek, T. A. D., and Floerke, M. (2015). Evaluation of large-scale precipitation data sets for water resources modelling in Central Asia. *Environ. Earth Sci.* 73, 787–799. doi:10.1007/s12665-014-3107-y

Qin, P. H., Xie, Z. H., Zou, J., Liu, S., and Chen, S. (2021). Future precipitation extremes in China under climate change and their physical quantification based on a regional climate model and CMIP5 model simulations. *Adv. Atmos. Sci.* 38, 460–479. doi:10.1007/s00376-020-0141-4

Renfrew, I. A., Thorpe, A., and Bishop, C. H. (1997). The role of the environmental flow in the development of secondary frontal cyclones. *Q. J. R. Meteorol. Soc.* 123, 1653–1675. doi:10.1002/qj.49712354210

Sangster, W. (1960). A method of representing the horizontal pressure force without reduction of station pressure to sea level. *J. Meteor.* 17, 166–176. doi:10.1175/1520-0469(1960)017<0166:AMORTH>2.0

Seager, R., Naik, N., and Vecchi, G. A. (2010). Thermodynamic and dynamic mechanisms for large-scale changes in the hydrological cycle in response to global warming. *J. Clim.* 23, 4651–4668. doi:10.1175/2010JCLI3655.1

Sun, J. S. (2017). Differences and relationship between flash heavy rain and heavy rainfall (in Chinese). *Torrential Rain Disasters* 36, 498–506. doi:10.3969/j.issn.1004-9045.2017.06.002

Thompson, G., Rasmussen, R. M., and Manning, K. (2004). Explicit forecasts of winter precipitation using an improved bulk microphysics scheme. Part I: Description and sensitivity analysis. *Mon. Wea. Rev.* 132, 519–542. doi:10.1175/15200493(2004)132<0519

Trenberth, K. E., and Guiliemot, C. J. (1995). Evaluation of the global atmospheric moisture budget as seen from analyses. *J. Clim.* 8, 2255–2272. doi:10.1175/1520-0442(1995)008<2255

Ullah, W., Wang, G., Gao, Z., Hagan, D., Bhatti, A., and Zhua, C. (2020). Observed linkage between Tibetan plateau soil moisture and south asian summer precipitation and the possible mechanism. *J. Clim.* 34, 361–377. doi:10.1175/jcli-d-20-0347.1

Ullah, W., Wang, G., Lou, D., Ullah, S., Bhatti, A., Ullah, S., et al. (2021). Large-scale atmospheric circulation patterns associated with extreme monsoon precipitation in Pakistan during 1981-2018. *Atmos. Res.* 232, 105489. doi:10.1016/j.atmosres.2021.105489

Wang, X., and Wang, X. (2021). Spatial distribution and temporal variation characteristics of rainstorm flood disasters with different intensities in southern Xinjiang from 1980 to 2019. *J. Glaciol. Geocryol.* 43, 1818–1828. (in Chinese with English abstract).

Wu, Z. Y., Cao, J., Zhao, W., Ke, Y. H., and Li, X. (2022). An observational analysis of a persistent extreme precipitation event in the post-flood season over a tropical Island in China. *Atmos. (Basel).* 13, 679. doi:10.3390/atmos13050679

Xu, Q. (1992). A geostrophic pseudo-vorticity and geostrophic C-vector forcing-A new look at the Q vector in three dimensions. *J. Atmos. Sci.* 49, 981–990. doi:10.1175/1520-0469(1992)049<0981:APAGCV>2.0.CO;2

Xu, Q., Cao, J., and Gao, S. (2011). Computing streamfunction and velocity potential in a limited domain of arbitrary shape. Part I: Theory and integral formulae. *Adv. Atmos. Sci.* 28, 1433–1444. doi:10.1007/s00376-011-0185-6

Xu, X., Xue, M., Wang, Y., and Huang, H. (2017). Mechanisms of secondary convection within a mei-yu frontal mesoscale convective system in eastern China. *J. Geophys. Res. Atmos.* 122, 47–64. doi:10.1002/2016JD026017

Xue, M., Luo, X., Zhu, K., Sun, Z., and Fei, J. (2018). The controlling role of boundary layer inertial oscillations in Meiyu frontal precipitation and its diurnal cycles over China. *J. Geophys. Res. Atmos.* 123, 5090–5115. doi:10.1029/2018JD028368

Yin, Z. Y., Wang, H., and Liu, X. (2014). A comparative study on precipitation climatology and interannual variability in the lower midlatitude East Asia and central Asia. *J. Clim.* 27, 7830–7848. doi:10.1175/JCLI-D-14-00052.1

Zhang, M., Chen, Y., Shen, Y., and Li, Y. (2017). Changes of precipitation extremes in arid central Asia. *Quat. Int.* 436, 16–27. doi:10.1016/j.quaint.2016.12.024

Zhang, W., Furtado, K., Wu, P., Zhou, T., Chadwick, R., Marzin, C., et al. (2021). Increasing precipitation variability on daily-to-multiyear timescales in a warmer world. *Sci. Adv.* 7, eabf8021. doi:10.1126/sciadv.abf8021

Zhao, Y., and Zhang, H. (2016). Impacts of SST Warming in tropical Indian Ocean on CMIP5 model-projected summer rainfall changes over Central Asia. *Clim. Dyn.* 46, 3223–3238. doi:10.1007/s00382-015-2765-0

Zhou, T. J., and Yu, R. C. (2005). Atmospheric water vapor transport associated with typical anomalous summer rainfall patterns in China. *J. Geophys. Res.* 110, D08104. doi:10.1029/2004JD005413

Zou, H., Wu, S., Yi, X., and Nan, W. (2018). The application of Barnes filter to positioning the center of landed tropical cyclone in numerical models. *Adv. Meteorology* 2018, 1–9. doi:10.1155/2018/1747530

Advantages of publishing in Frontiers

OPEN ACCESS
Articles are free to read for greatest visibility and readership

FAST PUBLICATION
Around 90 days from submission to decision

HIGH QUALITY PEER-REVIEW
Rigorous, collaborative, and constructive peer-review

TRANSPARENT PEER-REVIEW
Editors and reviewers acknowledged by name on published articles

Frontiers
Avenue du Tribunal-Fédéral 34
1005 Lausanne | Switzerland

Visit us: www.frontiersin.org
Contact us: frontiersin.org/about/contact

REPRODUCIBILITY OF RESEARCH
Support open data and methods to enhance research reproducibility

DIGITAL PUBLISHING
Articles designed for optimal readership across devices

FOLLOW US
@frontiersin

IMPACT METRICS
Advanced article metrics track visibility across digital media

EXTENSIVE PROMOTION
Marketing and promotion of impactful research

LOOP RESEARCH NETWORK
Our network increases your article's readership